

# ANNUAL REPORT

2008

and list of publications



Bayerisches Forschungsinstitut  
für Experimentelle Geochemie und Geophysik  
Universität Bayreuth

Bayerisches Geoinstitut  
Universität Bayreuth  
D-95440 Bayreuth  
Germany

Telephone: +49-(0)921-55-3700  
Telefax: +49-(0)921-55-3769  
e-mail: [bayerisches.geoinstitut@uni-bayreuth.de](mailto:bayerisches.geoinstitut@uni-bayreuth.de)  
www: <http://www.bgi.uni-bayreuth.de>

Editorial compilation by: Stefan Keyssner and Petra Buchert  
Section editors: Andreas Audétat, Tiziana Boffa Ballaran, Leonid Dubrovinsky,  
Dan Frost, Florian Heidelbach, Hans Keppler, Falko Langenhorst,  
Catherine McCammon, Nobuyoshi Miyajima, Dave Rubie,  
Henri Samuel, Gerd Steinle-Neumann, Nicolas Walte



**Staff and guests of the Bayerisches Geoinstitut in July 2008:**

**Die Mitarbeiter und Gäste des Bayerischen Geoinstituts im Juli 2008:**

First row, from left (1. Reihe, v. links) Rossana Combes, Valerie Malavergne, Daniela Seifert, Juliane Hopf, Geertje Ganskow, Enikő Bali, Micaela Longo, Polina Gavrilenko, Carmen Capalbo, Nicole Behringer, Vincenzo Stagno

Second row, from left (2. Reihe, v. links) Lydia Kison-Herzing, Nico Walte, Xiang Wu, Tiziana Boffa Ballaran, Sushant Shekhar, Catherine McCammon, Mainak Mookherjee, Petra Buchert, Holger Kriegl, Kyusei Tsuno, Gertrud Gollner

Third row, from left (3. Reihe, v. links) Coralie Weigel, Zhengning Tang, Dave Rubie, Dan Frost, Razvan Caracas, Falko Langenhorst, Davide Novella, David Dolejš, Sven Linhardt, Andreas Audétat, Heinz Fischer, Yuan Li, Elisabeth Herrmann, Federica Schiavi, Stefan Keyssner

Fourth/Fifth row, from left (4./5. Reihe, v. links) Willem van Mierlo, Ulrich Böhm, Robert Minch, Alexander Kurnosov, Konstantin Glazyrin, Kurt Klasinski, Kilian Pollok, Nobuyoshi Miyajima, Florian Heidelberg, Svyatoslav Shcheka, Kazuhiko Otsuka, Diego Bernini, Bernd Hewener, Alexander Konschak, Shantanu Keshav, Detlef Krauß

Last row, from left (Letzte Reihe, v. links) Patrick Cordier, Gudmundur Gudfinnsson, Omar Adjaoud, Wieland Dietrich, Riccardo Pozzobon, Francesco Pandolfo, Hans Keppler, Stefan Übelhack

Absent (Es fehlten) Uwe Dittmann, Leonid Dubrovinsky, Ahmed El Goresy, Alberto Escudero, Olga Narygina, Gerd Ramming, Karen Roscher, Henri Samuel, Hubert Schulze, Gerd Steinle-Neumann, Evgeniya Zarechnaya



## Contents

Foreword/Vorwort .....	9/I
1. Advisory Board and Directorship .....	11
1.1 Advisory Board .....	11
1.2 Leadership .....	11
2. Staff, Funding and Facilities .....	13
2.1 Staff .....	13
2.2 Funding .....	13
2.3 Laboratory and office facilities .....	17
2.4 Experimental and analytical equipment .....	17
3. Forschungsprojekte - Zusammenfassung in deutscher Sprache .....	III
3. Research Projects .....	21
3.1 <i>Earth's Structure and Geodynamics</i> .....	21
a. Core formation in terrestrial planets (H. Samuel and P. Tackley/Zürich) .....	22
b. Heat partitioning in terrestrial planets during core formation (H. Samuel and P. Tackley/Zürich) .....	24
c. The effect of continents as insulating lids on mantle convection dynamics and stirring properties (W. Dietrich/Bayreuth, H. Samuel; W. Zimmermann and F. Busse/Bayreuth) .....	25
d. Optical absorption spectra and radiative thermal conductivity of silicate perovskite to 125 GPa (H. Keppler, L.S. Dubrovinsky, O. Narygina and I.Yu. Kantor) .....	27
e. Low-spin Fe <sup>2+</sup> in silicate perovskite and a possible layer at the base of the lower mantle (C.A. McCammon, L.S. Dubrovinsky, O. Narygina, X. Wu, in collaboration with I. Sergueev and A. Chumakov/Grenoble) .....	29
f. Thermal vs. elastic heterogeneity in high-resolution mantle circulation models (B.S.A. Schuberth and H.-P. Bunge/München; G. Steinle-Neumann) .....	31
3.2 <i>Geochemistry</i> .....	34
a. Estimating the light element content of the Earth's core from models of core formation (D.C. Rubie, D.J. Frost and K. Tsuno, in collaboration with Y. Asahara/Hyogo, U. Mann/Zürich, P. Kegler and A. Holzheid/Kiel, H. Palme/Köln) .....	35
b. Partitioning of oxygen between ferropicriole and liquid Fe-Ni-S alloy at high pressures and temperatures (K. Tsuno, D.J. Frost and D.C. Rubie) .....	36
c. A model to describe the FeO content of the mantle at the core mantle boundary (D.J. Frost and D.C. Rubie, in collaboration with Y. Asahara/Hyogo) .....	38

d.	The oxygen content and temperature at the Fe-FeO eutectic (R. Pozzobon/ Padova and D.J. Frost) .....	40
e.	Carbon solubilities in metal and silicate liquid at high pressure and high temperature (V. Malavergne and R. Combes/Marne La Vallée, in collaboration with D.J. Frost, J.P. Gallien/Saclay and H. Bureau/Paris) .....	41
f.	Ab initio predictions of potassium partitioning between iron and (Mg, Fe)SiO <sub>3</sub> perovskite and post-perovskite (K.K.M. Lee/New Haven, in collaboration with G. Steinle-Neumann, S. Akber-Knutson/San Diego and D. Dolejš/Prague) .....	43
g.	Melting of ferropericlase at lower mantle conditions (J. Pickles, K. Tsuno and D.J. Frost) .....	45
h.	<i>In situ</i> study of iron partitioning between ferropericlase and silicate perovskite at conditions of the Earth's lower mantle (L.S. Dubrovinsky, O. Narygina, X. Wu and G. Aquilanti, in collaboration with S. Pascarelli/Grenoble) .....	47
i.	Oxygen fugacity determined from iron oxidation state of (Mg,Fe)O ferropericlase in lower mantle diamond inclusions (M. Longo and C.A. McCammon, in collaboration with G. Bulanova/Bristol and F. Kaminsky/ Vancouver) .....	48
j.	Carbonatites, kimberlites and diamonds in the Earth's mantle (V. Stagno and D.J. Frost) .....	51
k.	Fe <sup>3+</sup> /Fe <sub>tot</sub> measurements on garnets in equilibrium with carbon/carbonate phases (V. Stagno, C.A. McCammon and D.J. Frost) .....	54
l.	Detailed structure of the carbonated peridotite solidus ledge in the system CaO-MgO-Al <sub>2</sub> O <sub>3</sub> -SiO <sub>2</sub> -CO <sub>2</sub> (S. Ghosh, S. Keshav and G.H. Gudfinnsson) ....	56
m.	Melting phase relations in the system CaO-MgO-Al <sub>2</sub> O <sub>3</sub> -SiO <sub>2</sub> -FeO-Cr <sub>2</sub> O <sub>3</sub> spanning the plagioclase-spinel lherzolite transition at 7 to 10 kbar: Experiments versus thermodynamics (S. Keshav, M. Tirone/Trieste/Miami, G.H. Gudfinnsson and D. Presnall/Richardson) .....	58
n.	Experimental constraints on the storage of phosphorus in the lower mantle (J. Konzett/Innsbruck, in collaboration with D.J. Frost) .....	60
o.	Is molybdenite saturation common in natural rhyolite magmas? (A. Audétat) .....	63
p.	Microstructural controls on pyrrhotite weathering and secondary mineral formation (K. Pollok, D. Harries and F. Langenhorst) .....	65
3.3	<i>Mineralogy, Crystal Chemistry and Phase Transformations</i> .....	67
a.	High-pressure phase transition in SrAl <sub>2</sub> Si <sub>2</sub> O <sub>8</sub> feldspar (T. Boffa Ballaran, F. Pandolfo and F. Nestola/Padova; E. Bruno/Torino and M. Koch-Müller/ Postdam) .....	68
b.	Pressure effect on the crystal structure of tapiolite FeTa <sub>2</sub> O <sub>6</sub> (M. Zema and S.C. Tarantino/Pavia, T. Boffa Ballaran) .....	69

c.	The dehydration reaction gypsum-bassanite-anhydrite at high pressure: A Raman experimental study (P. Comodi and S. Nazzareni/Perugia, A. Kurnosov and L.S. Dubrovinsky) .....	71
d.	Synthesis and single-crystal X-ray diffraction of non-stoichiometric ringwoodite: Evidence of octahedral Si and Al (F. Nestola and R. Pozzobon/Padova, D.J. Frost, T. Boffa Ballaran, R. Spiess/Padova) .....	73
e.	<i>In situ</i> determination of the Fe <sub>3</sub> O <sub>4</sub> – h-Fe <sub>3</sub> O <sub>4</sub> transition at high pressures and temperatures using synchrotron-based XRD measurements (A. Woodland and K. Schollenbruch/Frankfurt/M., in collaboration with D.J. Frost and Y. Wang/Argonne) .....	74
f.	The dilemma of post-spinel structure of MFe <sub>2</sub> O <sub>4</sub> (M=Mg, Co, Zn) ferrite spinels: Mössbauer, Raman and XRD studies (G.Kh. Rozenberg and E. Greenberg/Tel Aviv, in collaboration with A. Kurnosov and L.S. Dubrovinsky) .....	77
g.	Micro-XANES study of the Earth's lower mantle (Mg,Fe)(Si, Al)O <sub>3</sub> perovskite and (Mg,Fe)O ferropericlase (O. Narygina, I.Yu. Kantor, X. Wu and L.S. Dubrovinsky, in collaboration with S. Pascarelli and G. Aquilanti/Grenoble) .....	80
h.	Decomposition of FeTiO <sub>3</sub> perovskite to wüstite and ferropseudobrookite (X. Wu, G. Steinle-Neumann, O. Narygina, I.Yu. Kantor, C.A. McCammon and L.S. Dubrovinsky, in collaboration with V. Prakapenka/Chicago, V. Swamy/Clayton) .....	83
i.	Electronic transition in hexagonal closed packed iron (ε-Fe) at high pressure (K. Glazyrin, O. Narygina, C.A. McCammon, G. Steinle-Neumann and L.S. Dubrovinsky) .....	86
j.	Synthesis of a high density Ni <sub>3</sub> S phase at 20 GPa (D. Charee, in collaboration with Y. Litvin and E. Osadshii/Chernogolovka, O. Narygina, A. Kurnosov and L.S. Dubrovinsky, N.A. Dubrovinskaia/Heidelberg) .....	88
k.	Magnetic structure and electron density of states of Fe <sub>2</sub> SiO <sub>4</sub> fayalite from <i>ab initio</i> computations (Z. Tang and G. Steinle-Neumann) .....	90
l.	High-pressure phase transitions of titanium oxides: Ab initio computations (X. Wu, E. Holbig, G. Steinle-Neumann and L.S. Dubrovinsky) .....	91
m.	Anomalous pressure-evolution of the axial ratio c/a in hcp cobalt: Interplay between structure, magnetism and lattice dynamics (G. Steinle-Neumann, in collaboration with D. Antonangeli, L.R. Benedetti and D.L. Farber/Livermore; A.-L. Auzende and J. Badro/Paris; M. Hanfland and M. Krisch/Grenoble) .....	93
n.	Dense hydrous silicates in the MgFeSiO <sub>4</sub> – H <sub>2</sub> O system up to 25 GPa (G. Ganskow, F. Langenhorst and D.J. Frost) .....	95
o.	TEM examination of sulfide and enstatite dust particles from the Stardust mission (F. Langenhorst; D. Jacob and H. Leroux/Lille; M.E. Zolensky/Houston) .....	96

3.4	<i>Physical Properties of Minerals</i> .....	98
a.	Elasticity of phase-X (M. Mookherjee and G. Steinle-Neumann) .....	98
b.	The dehydrogenation effect on the baric behaviour of amphiboles (C. Capalbo and P. Comodi/Perugia, T. Boffa Ballaran, A. Zanetti/ Pavia, S. Nazzareni/Perugia) .....	101
c.	Compression in He of a perovskite single crystal formed from a basaltic bulk composition (T. Boffa Ballaran and D.J. Frost, R. Pozzobon/Padova) ....	102
d.	Stability of pollucite at high pressure: A potential nuclear waste disposal phase (G.D. Gatta/Milano and T. Boffa Ballaran) .....	103
e.	Comparative TEM study of exsolution in hemo-ilmenite in igneous rock emplaced at 5 kbar and gabbro rapidly uplifted after eclogite-facies metamorphism: Key to contrasting magnetisations (S.A. McEnroe and P. Robinson/Trondheim, N. Miyajima and F. Langenhorst, M.P. Terry/ Rapid City) .....	105
f.	Fe-Ti order transition in quenched synthetic Ilm 60: Magnetic properties and high-resolution TEM imaging (K. Fabian, S.A. McEnroe and P. Robinson/Trondheim, N. Miyajima and T. Boffa Ballaran, B.P. Burton/ Gaithersburg) .....	108
g.	Diffusion of the majorite component in garnet (W. van Mierlo, F. Langenhorst, D.J. Frost and N. Miyajima) .....	112
h.	Cathodoluminescence studies of alluvial diamonds from Archean conglomerates of Eastern Canada (M. Longo and M. Kopylova/Vancouver) .	114
3.5	<i>Fluids and their Interaction with Melts and Minerals</i> .....	117
a.	The solubility of uranium in subduction zone fluids (E. Bali, A. Audétat and H. Keppler) .....	118
b.	The distribution of halogens between fluids and upper mantle minerals (D. Bernini, D. Dolejš and H. Keppler) .....	120
c.	The solubility of noble gases in silicate perovskite (S.S. Shcheka and H. Keppler) .....	121
d.	Water solubility in aluminous diopside (P. Gavrilenko and H. Keppler) .....	123
e.	The influence of microorganisms on biotite dissolution (J. Hopf, F. Langenhorst and K. Pollok, in collaboration with D. Merten and E. Kothe/Jena) .....	124
3.6	<i>Physics and Chemistry of Melts and Magmas</i> .....	125
a.	A general model for CO <sub>2</sub> solubility and speciation in silicate melts (A. Korschak and H. Keppler) .....	125
b.	Interaction of chlorine and carbonate components in jadeitic melts at high pressure (V. Stagno, D. Dolejš and H. Keppler) .....	127
c.	The effect of silica on ferric/ferrous ratio in silicate melts: An experimental investigation (A. Borisov/Moscow, C.A. McCammon) .....	130

d.	Mössbauer spectroscopy at high temperature: A probe for the glass transition of Fe species in silicate glasses (C. Weigel, H. Keppler and C.A. McCammon) .....	131
e.	Liquid-liquid immiscibility between a phosphorous-bearing carbonatite melt and a potassic aluminosiliceous melt coexisting with apatite, K-feldspar and diopside at 2.2 GPa and 1200 °C (T. Guzmics/Budapest; E. Bali and A. Audéat; M. Berkesi and C. Szabó/Budapest) .....	134
f.	Plagioclase growth mechanisms inferred from <i>in situ</i> crystallization experiments performed with the moissanite anvil cell (F. Schiavi, N. Walte and H. Keppler) .....	135
3.7	<i>Rheology</i> .....	139
a.	Comparative viscosity of CaIrO <sub>3</sub> perovskite and post-perovskite (S. Hunt and D. Dobson/ London; N. Walte) .....	140
b.	Deformation microtextures in CaIrO <sub>3</sub> post-perovskite under high stress conditions in a laser-heated DAC (N. Miyajima and F. Heidelbach, in collaboration with K. Niwa, T. Yagi and K. Ohgushi/Tokyo) .....	142
c.	Dislocation microtextures in a Fe,Al-bearing akimotoite (N. Miyajima, J. Pickles, C.A. McCammon and D.J. Frost) .....	144
d.	Texture development in deformed ordered omphacite: A scanning electron microscopy study (D. Novella, N. Walte, F. Langenhorst and F. Heidelbach) .....	146
e.	Pressure-induced slip-system transition in polycrystalline olivine(S. Shekhar, N. Walte, D.J. Frost, F. Heidelbach, F. Langenhorst and D.C. Rubie) .....	148
f.	Pervasive to discrete microstructures in magmatic dense suspensions at HP-HT: Insight from SPO and CPO analysis (D. Picard, L. Arbaret, M. Pichavant and R. Champallier/Orléans; P. Launeau/Nantes and F. Heidelbach) .....	151
3.8	<i>Metamorphism</i> .....	154
a.	Ternary feldspar equilibria and thermodynamic modeling at the granulite-eclogite facies transition (D. Dolejš) .....	154
b.	Microstructural and chemical characteristics of rutile in UHP metamorphic rocks (A. Escudero, N. Miyajima and F. Langenhorst) .....	157
c.	Textural and microstructural analysis of rapidly grown omphacite from eclogite facies pseudotachylytes (K. Pollok, F. Heidelbach and F. Langenhorst, in collaboration with T. John/Oslo) .....	160
d.	Fractional crystallization of olivine melt inclusions in a shock-induced chondritic melt vein (M. Miyahara/Sendai, A. El Goresy; E. Ohtani, S. Ozawa, T. Nagase and M. Nishijima/Sendai) .....	162
e.	Carbon polymorphism in shocked meteorites (T. Ferroir/Lyon, L.S. Dubrovinsky, A. El Goresy, A. Simionovici/Grenoble, T. Nakamura/Fukuoka and P. Gillet/Lyon) .....	165

f.	Transmission electron microscopic study of experimentally shocked dolomite (R. Skála/Prague, N. Miyajima, F. Langenhorst and F. Hörz/Houston) .....	169
3.9	<i>Materials Science</i> .....	171
a.	Synthesis of a high-pressure orthorhombic boron phase (E.Yu. Zarechnaya, L.S. Dubrovinsky, N. Miyajima, A. El Goresy, in collaboration with N.A. Dubrovinskaia/Heidelberg; Y. Filinchuk, D. Chernyshov and V. Dmitriev/Grenoble) .....	172
b.	<i>Ab initio</i> study of the orthorhombic HPHT boron (E.Yu. Zarechnaya, L.S. Dubrovinsky, in collaboration with A. Mikhailushkin, S.I. Simak and I. Abrikosov/Linköping; N.A. Dubrovinskaia/Heidelberg) .....	174
c.	An insight into what superconducts in polycrystalline boron-doped diamonds based on microstructural investigations (N.A. Dubrovinskaia/Heidelberg, R. Wirth/Potsdam, J. Wosnitza and T. Papageorgiou/Dresden, H.F. Braun/Bayreuth, N. Miyajima and L.S. Dubrovinsky) .....	176
d.	A study on the HPHT synthesis of a c-BC <sub>2</sub> N superhard material (W.R. Matizamhuka and I. Sigalas/Johannesburg, L.S. Dubrovinsky, N.A. Dubrovinskaia/Heidelberg, N. Miyajima and O. Narygina, in collaboration with R. Riedel/Darmstadt and G. Mera/Grenoble) .....	178
e.	Diamond anvil cell syntheses and compressibility studies of the spinel-structured gallium oxonitride (C. Zvoriste/Darmstadt, I. Kinski/Dresden, S. Hering/München, H. Huppertz/Innsbruck, R. Riedel/Darmstadt, L.S. Dubrovinsky) .....	180
f.	High pressure hot pressing as a method for obtaining nanostructured Si <sub>3</sub> N <sub>4</sub> containing materials (I. Zalite/Riga, D.J. Frost, N. Zilinska/Riga) .....	181
g.	High pressure and temperature synthesis of metal nitrides (A.J. McGaff and G. Serghiou/Edinburgh, in collaboration with D.J. Frost) .....	182
h.	Structural stability of the $\sigma$ phase FeCr under pressures up to 77 GPa (V.F. Degtyareva/Chernogolovka, L.S. Dubrovinsky, A. Kurnosov and I.Yu. Kantor; V. Prakapenka/Chicago) .....	184
i.	First-principles phase diagram calculations for the HfC-TiC, ZrC-TiC and HfC-ZrC solid solutions (O. Adjaoud and G. Steinle-Neumann, in collaboration with B.P. Burton/ Gaithersburg and A. van de Walle/Pasadena) .....	186
j.	Pressure-induced modifications of crystal and magnetic structure of La <sub>0.33</sub> Ca <sub>0.67</sub> MnO <sub>3</sub> (D.P. Kozlenko/Dubna, L.S. Dubrovinsky, B.N. Savenko/Dubna and V.I. Voronin/Ekaterinburg) .....	187
k.	Raman spectroscopic study of PbCO <sub>3</sub> at high pressure and temperature (R. Minch/Kiel, L.S. Dubrovinsky and A. Kurnosov) .....	189
l.	High-pressure effect on the formation of layered lithium cobaltates with Li occupying the Co-site (R. Stoyanova, E. Shinova and M. Yoncheva/Sofia; C.A. McCammon and T. Boffa Ballaran) .....	190

m.	Elastic behaviour of lithium fluoride under high pressure (A. Kantor, L.S. Dubrovinsky, in collaboration with I.Yu. Kantor, V. Prakapenka, S. Sinogeikin/Chicago) .....	191
n.	High-pressure crystallization of semi-crystalline polypropylene (S. Mazzullo and A. Fait/Ferrara, T. Boffa Ballaran, C.A. McCammon) .....	192
o.	Catalytic oxidative dehydrogenation of ethylbenzene on nanocrystalline iron oxides and carbon nanotubes (K. Pollok, in collaboration with B. Nigrovski, P. Scholz, M. Müller and B. Ondruschka/Jena) .....	194
3.10	<i>Methodological Developments</i> .....	197
a.	Portable laser heating system for diamond anvil cells (L.S. Dubrovinsky, K. Glazyrin, O. Narygina and C.A. McCammon; N.A. Dubrovinskaia/Heidelberg and J. Bock/Gaggenau) .....	197
b.	Universal diamond anvil cell for combined optical and X-ray studies (I.Yu. Kantor, in collaboration with V. Prakapenka and P. Dera/Chicago; L.S. Dubrovinsky) .....	200
c.	A method to synthesize large fluid inclusions in quartz at controlled times and under unfavorable growth conditions (Y. Li and A. Audétat) .....	201
d.	STREAMV: A fast, robust and modular numerical code for modeling various 2D geodynamic scenarios (H. Samuel) .....	203
4.	International Graduate School "Structure, Reactivity and Properties of Oxide Materials" .....	207
5.	Publications, Conference Presentations, Seminars .....	211
5.1	Publications (published); Refereed international journals .....	211
a)	Refereed international journals .....	211
b)	Popular scientific magazines .....	217
5.2	Publications (submitted, in press) .....	218
5.3	Presentations at scientific institutions and at congresses .....	222
5.4	Lectures and seminars at Bayerisches Geoinstitut .....	236
5.5	Conference organization .....	239
6.	Visiting scientists .....	241
6.1	Visiting scientists funded by the Bayerisches Geoinstitut .....	241
6.2	Visiting scientists supported by other externally funded BGI projects .....	243
6.3	Visitors (externally funded) .....	247
7.	Additional scientific activities .....	251
7.1	Ph.D. theses .....	251
7.2	Honours and awards .....	251
7.3	Editorship of scientific journals .....	251
7.4	Membership of scientific advisory bodies .....	252

8. Scientific and Technical Personnel .....	255
Index .....	258

## Foreword

The Bayerisches Geoinstitut has now existed for more than twenty years and, consequently, a generation change in the three professorships of the institute is currently taking place. The professorship formerly occupied by Fritz Seifert has been refilled recently by Falko Langenhorst of the University of Jena. As was the case with his predecessor, Falko Langenhorst is a recipient of the Gottfried Wilhelm Leibniz-Prize of the German Research Foundation, which is the highest scientific award in Germany. It was possible to attract Falko Langenhorst back to Bayreuth due to the generous offers of the University and the Research Ministry. His return to Bayreuth assures continuity in the area of experimental geosciences and also an expansion in the field of planetology.

The current generation change is also associated with a steady increase in the number of personnel and a strong increase in the level of outside research funding which reached almost two million Euros in 2008. A particularly notable achievement in 2008 was the success of Dan Frost with a research proposal for an “Advanced Investigator Grant” of the European Research Council. This ERC programme serves exclusively to support outstanding scientists and Dan Frost’s proposal was one of eight successful proposals from Germany in all disciplines. The research funds will be used over the coming five years to study the elastic properties of mantle minerals under simultaneous high pressures and temperatures.

The infrastructure of the institute has been improved in 2008 through the installation of a new Raman spectroscopy system that is combined with an ultra-violet laser. The installation of a new multianvil press with six independent anvils has been initiated and delivery is expected in the summer of 2009. This press will be used to perform deformation experiments under very high pressures and will also be used to increase the pressure range covered by the existing multianvil presses.

Among the scientific results that are described in this annual report, a study of the optical properties of silicate perovskite up to a pressure of more than a megabar is perhaps worth highlighting. In the past it was always assumed that iron-bearing minerals are opaque at high pressure, which would mean that heat transport in the Earth’s lower mantle could not occur by radiation. Experiments at the Geoinstitut have now shown that both silicate perovskite and ferropericlase, the two main constituents of the lower mantle, remain transparent up to at least a megabar. This means that in the region of the core-mantle boundary, radiative heat transport must be high so that the overall transport of heat is significantly greater than previously believed. This could influence mantle convection and, for example, stabilize so-called “superplumes”. The results of this study were published in *Science* in December 2008. A further interesting result is that noble gases, such as argon, dissolve readily in silicate perovskite at high pressure. Thus a long-standing problem concerning the whereabouts of a hidden noble-gas reservoir may be solved, with noble gases being stored in the lower mantle.

As in previous years, and also on behalf of my colleagues, I would like to thank the *Free State of Bavaria* as represented by the *Bayerisches Staatsministerium für Wissenschaft, Forschung und Kunst* as well as the *Kommission für Geowissenschaftliche Hochdruckforschung* of the *Bavarian Academy of Sciences* for their continuing support and strong commitment to the Bayerisches Geoinstitut. The *President of Bayreuth University*, Prof. Dr. Dr. h. c. Helmut Ruppert always had an open ear for the needs of our institute. We also gratefully acknowledge generous support from external funding agencies, in particular the *Alexander von Humboldt Foundation*, the *European Union*, and the *German Science Foundation*, which have also contributed greatly to the development and success of the Institute.

Bayreuth, March 2008

Hans Keppler

## Vorwort

Das Bayerische Geoinstitut existiert nun seit über zwanzig Jahren und dementsprechend findet gegenwärtig ein Generationswechsel bei den drei Lehrstühlen des Instituts statt. Für den vakanten Lehrstuhl von Fritz Seifert konnte Falko Langenhorst von der Universität Jena gewonnen werden. Wie sein Vorgänger ist Falko Langenhorst Träger des Gottfried Wilhelm Leibniz-Preises der Deutschen Forschungsgemeinschaft, der höchsten wissenschaftlichen Auszeichnung in Deutschland. Herr Langenhorst konnte durch ein äußerst großzügiges Angebot der Universität und des Forschungsministeriums wieder nach Bayreuth zurück berufen werden. Die Berufung von Falko Langenhorst sichert einerseits die wissenschaftliche Kontinuität im Bereich der experimentellen Geowissenschaften, sie erweitert gleichzeitig aber auch die Aktivitäten des Instituts in Richtung auf planetologische Fragestellungen.

Der derzeitige Generationswechsel am Institut äußert sich auch in einer stetigen Zunahme des Personals und einem steilen Anstieg der Drittmiteinnahmen auf nahezu zwei Millionen Euro in diesem Jahr. Ein besonders erfreuliches Ereignis in 2008 war der Erfolg von Dan Frost mit seinem Antrag auf ein "Advanced Investigator Grant" im European Research Council. Dieses Programm des ERC dient ausschließlich zur Unterstützung herausragender Wissenschaftler und Dan Frost war einer von nur acht erfolgreichen Antragsstellern aus ganz Deutschland und in allen Fachgebieten. Die Mittel sollen in den nächsten fünf Jahren verwendet werden, um die elastischen Eigenschaften von Mantel-Mineralen unter hohen Drücken und gleichzeitig hohen Temperaturen zu bestimmen.

Zur Verbesserung der apparativen Infrastruktur am Institut diente die Beschaffung eines neuen Raman-Systems mit Ultraviolett-Lasern. Die Beschaffung einer neuen Multi-Anvil-Pressen mit sechs unabhängigen Stempeln wurde eingeleitet und die Installation dieser Presse wird für Sommer 2009 erwartet. Die Presse soll für Deformationsexperimente bei sehr hohen Drücken eingesetzt werden und außerdem den für Multi-Anvil-Pressen zugänglichen Druckbereich erweitern.

Unter den wissenschaftlichen Resultaten, die in diesem Jahresbericht beschrieben sind, ist vielleicht eine Studie über das optische Verhalten von Silikat-Perowskit bei über einem Megabar besonders hervorzuheben. Bisher war immer angenommen worden, dass Eisenhaltige Minerale bei hohem Druck optisch opak sind, so dass im tiefen Erdmantel keinerlei Wärmeübertragung durch Strahlung möglich ist. Untersuchungen am Geoinstitut zeigten jedoch, dass sowohl Silikat-Perowskit als auch Ferroperiklas, die beiden Hauptbestandteile des unteren Erdmantels, bis in den Megabar-Bereich hinein optisch transparent bleiben. Dies bedeutet, dass nahe der Kern-Mantel-Grenze wahrscheinlich ein erheblicher Teil der Wärme durch Strahlung übertragen wird und dass der Wärmefluss vom Kern in den Mantel wesentlich höher ist als bisher angenommen. Dies kann grundsätzliche Auswirkungen auf die Konvektion im Erdmantel haben und beispielsweise sogenannte „Super-Plumes“ stabilisieren. Die Ergebnisse dieser Studie wurden im Dezember 2008 in *Science* veröffentlicht. Eine

weitere interessante Entdeckung ist, dass Edelgase wie Argon sich in Silikat-Perowskit bei hohem Druck offenbar sehr gut lösen. Damit wurde möglicherweise das seit langem gesuchte verborgene Reservoir von Edelgasen tief im Erdinnern gefunden.

Wie in den vorangegangenen Jahren möchte ich auch im Namen meiner Kollegen dem *Freistaat Bayern*, vertreten durch das *Bayerische Staatsministerium für Wissenschaft, Forschung und Kunst*, als auch der *Kommission für Geowissenschaftliche Hochdruckforschung* der *Bayerischen Akademie der Wissenschaften* danken für ihre fortwährende Unterstützung und ihre enge Verbundenheit mit dem Bayerischen Geoinstitut. Der *Präsident der Universität Bayreuth*, Prof. Dr. Dr. h. c. Helmut Ruppert, hatte immer ein offenes Ohr für die Wünsche des Instituts. Wir sind auch sehr dankbar für die großzügige Förderung durch externe Geldgeber, insbesondere durch die *Alexander von Humboldt-Stiftung*, die *Europäische Union* und die *Deutsche Forschungsgemeinschaft*, die ebenfalls wesentlich zur Entwicklung und zum Erfolg des Bayerischen Geoinstituts beigetragen haben.

Bayreuth, im März 2009

Hans Keppler

## 1. Advisory Board and Directorship

### 1.1 Advisory Board

The *Kommission für Geowissenschaftliche Hochdruckforschung der Bayerischen Akademie der Wissenschaften* advises on the organisation and scientific activities of the institute. Members of this board are:

Prof. Dr. G. BREY	Institut für Geowissenschaften der Johann Wolfgang Goethe-Universität, Frankfurt am Main
Prof. Dr. U. CHRISTENSEN	Max-Planck-Institut für Sonnensystemforschung, Katlenburg-Lindau
Prof. Dr. R. KNIEP	Institut für Chemische Physik fester Stoffe der Max-Planck-Gesellschaft, Dresden
Prof. Dr. H. PALME	Institut für Mineralogie und Geochemie der Universität zu Köln
Prof. Dr. R. RUMMEL	Institut für Astronomische und Physikalische Geodäsie der TU München
Prof. Dr.-Ing. G. SACHS (Chairman)	Lehrstuhl für Flugmechanik und Flugregelung der TU München
Prof. Dr. E. SALJE, FRS, FRSA	Department of Earth Sciences, University of Cambridge
Prof. Dr. H. SOFFEL	Emeritus, Institut für Allgemeine und Angewandte Geophysik der Universität München

The Advisory Board held meetings in Bayreuth (11.04.2008) and in Munich (28.11.2008).

### 1.2 Leadership

Prof. Dr. Hans KEPPLER (Director)  
Prof. Dr. David C. RUBIE  
Prof. Dr. Falko LANGENHORST



## 2. Staff, Funding and Facilities

### 2.1 Staff

At the end of 2008 the following staff positions existed in the Institute:

- Scientific staff \*: **13**
- Technical staff: **14**
- Administrative staff: **2**
- Administrative officer: **1**

\* Including a tenure-track junior professorship in geodynamic modeling initially funded by *Stifterverband für die Deutsche Wissenschaft* for 6 years, started in 2007.

During 2008, 24 scientific (178 months) positions were funded by grants raised externally by staff members of the institute. In addition 9 long-term scientific positions (79 months) were funded by the resources of the BGI Visiting Scientists' Programme (see Sect. 8) which also supported short-term visits for discussing future projects or presenting research results (see Sect. 6). Positions for 5 Ph.D. students and 1 co-ordinator were funded under the BGI International Graduate School under the Elitenetzwerk Bayern "Structure, Reactivity and Properties of Oxide Materials" (see Sect. 4). 3 scientists (19 months) were supported by personal grants (stipends).

### 2.2 Funding

In 2008, the following financial resources were available from the Free State of Bavaria:

- Visiting Scientists' Programme: 325.000 €
- Consumables: 329.000 €
- Investment Funding: 418.000 €

The total amount of national/international external funding ("*Drittmittel*") used for ongoing research projects in 2008 was 1.948.000 € (Positions: 999.000 €; equipment, consumables and travel grants: 949.000 €).

	positions	equipment, consum- ables, travel grants	total
• ENB	281.000 €	65.000 €	346.000 €
• AvH	44.000 €	15.000 €	59.000 €
• DFG	282.000 €	627.000 € <sup>*)</sup>	909.000 €
• EU	320.000 €	186.000 €	506.000 €
• BMBF	14.000 €	3.000 €	17.000 €
• Stifterverband	44.000 €	41.000 €	85.000 €
• Others	14.000 €	12.000 €	<u>26.000 €</u>
			<b>1.948.000 €</b>

(ENB = Int. Graduate School „Oxides“ in the Elite Network of Bavaria; AvH = Alexander von Humboldt Foundation; DFG = German Science Foundation; EU = European Union; BMBF = Federal Ministry of Education and Research; Stifterverband = Stifterverband für die Deutsche Wissenschaft)

<sup>\*)</sup> includes Federal contribution to investment funding (§51B GG)

In the following list only the BGI part of the funding is listed in cases where joint projects involved other research institutions. Principal investigators and duration of the grants are listed in brackets. Total project funding refers to the funding over the entire duration of this project.

<b>Funding institution</b>	<b>Project, Funding</b>	<b>Total Project Funding</b>
BMBF	03G0718A (K. Pollok – 10/08 - 9/11) Nachwuchsgruppe MIMOS Positions: 3 x TV-L 13/2, each 36 months 241.086 € student assistant, (19,75h/month), 48 months 7.894 € Consumables and travel funding: 57.550 € (in 2008: 26.651 €) Total: 306.530 €	306.530 €
DFG	Au 314/1-1 (A. Audétat – 9.08 - 8.10) "Fractionation of sulfur, copper and gold in two-phase fluids" Positions: BAT IIa/2, 24 months 58.800 € Consumables and travel funding: 21.000 €	79.800 €
DFG	BU 2010/3-1 and STE 1105/5-1 (H.-P. Bunge (University of Munich), G. Steinle-Neumann – 02.08 - 01.09) "Geodynamic models with thermodynamically self-consistent mineral physics" Positions: BAT IIa/2, 12 months (Munich) 29.400 € Consumables and travel funding: (Munich) 4.000 € Consumables and travel funding: (BGI) 1.500 €	34.900 €
DFG	Du 393/4-1 (L. Dubrovinsky – 1.08 - 12.08) European Mineral Sciences Initiative (EuroMinSci) "Mineralogy and chemistry of Earth's core", Positions: BAT IIa or E13, 12 month 58.800 € Consumables and travel funding: 12.750 €	71.550 €
DFG	Du 393/6-1 (L.S. Dubrovinsky, H.F. Braun – 9.08 - 8.09) "Synthesis and <i>in situ</i> characterization of boron-doped superhard nanodiamond materials" Positions: BAT IIa/2 or E 13/2, 12 months 29.400 € Consumables and travel funding: 3.600 €	33.000 €
DFG	Fr 1555/4-1 (D.J. Frost – 7.08 - 6.09) "Systematics of the post-spinel transition in Fe-bearing compositions" Consumables and travel funding:	1.815 €
DFG	INST 91/198-1 (H. Keppler) Co-financing of an ultraviolet Raman spectrometer 50 % of 424.474 €	212.237 €

DFG	INST 91/204-1 (H. Keppler) Co-financing of a multianvil press with 6 independent anvils 50 % of 830.918 €	415.459 €
DFG	Ke 501/5-3 (H. Keppler – 1.07 - 12.09) "Übergangsmetallionen und Wasser im Erdmantel" Positions: BAT IIa or E 13, 36 months 176.400 € Consumables and travel funding: 25.200 € Overhead 10.480 €	212.080 €
DFG	Ke 1351/1-1 (H. Keppler – 3.07 - 10.09) ESF-Verbundprojekt "Hydrogen in Minerals" Positions: BAT IIa/2 or E 13/2, 36 months 88.200 € Consumables and travel funding: 15.000 € Overhead 6.800 €	110.000 €
DFG	La 830/9-1 (F. Langenhorst, D.J. Frost, D.C. Rubie – 2.08 - 4.09) "Stability and structures of hydrous minerals in the transition zone of the Martian mantle" Positions: BAT IIa/2, 9 months 22.050 € Consumables and travel funding: 19.150 € Equipment: 50.000 €	91.200 €
DFG	La 830/10-1 (F. Langenhorst, D.J. Frost, D.C. Rubie – 2.08 - 4.09) "Oxygen solubility in Fe-Ni-S alloy at high pressure and implications for the formation and compositions of planetary cores" Positions: student assistant 4.300 € Consumables and travel funding: 8.450 €	12.750 €
DFG	La 830/12-1 (F. Langenhorst, A. Deutsch – 2.08 - 12.08) "Mineralogical and geochemical studies of impact melt products from the Chesapeake Bay impact structure" Positions: BAT IIa/2, 2 months 4.900 € Consumables and travel funding: 8.100 €	13.000 €
DFG	La 830/13-1 (F. Langenhorst, A. Woodland, D.J. Frost – 2.08 - 12.08) "Systematics of the post-spinel transition in Fe-bearing compositions" Positions: BAT IIa/2, 10 months 24.500 € Consumables and travel funding: 6.350 €	30.850 €
DFG	La 830/14-1 (F. Langenhorst – 2.08 - 8.14) Gottfried Wilhelm Leibniz-Preis 2007	2.489.000 €
DFG	La 830/15-3 (F. Langenhorst, A. Deutsch – 2.08 - 1.09) "Mineralogical and geochemical studies of impact melt products from the Chesapeake Bay and the Lake Bosumtwi impact structures (ICDP)" Consumables and travel funding: 10.800 €	10.800 €

DFG	Mc 3/16-1 (C.A. McCammon, L.S. Dubrovinsky – 10.06 - 9.09) "High-pressure high-temperature <sup>57</sup> Fe Mössbauer spectroscopy in laser-heated diamond anvil cells: Applications for the mineralogy of Earth's lower mantle and core" Positions: student assistant (80 h/month), 36 months 22.570 € Consumables and travel funding: 45.800 €	68.370 €
ESF	European Science Foundation Grant for organizing workshop on "Multiscale approach to alloys: advances and challenges" (L.S. Dubrovinsky)	16.200 €
ESF	European Science Foundation Psi-k Grant for organizing "International Alloy Conference" (L.S. Dubrovinsky)	9.500 €
EU	Marie Curie Research Training Network "Crust to core: the fate of subducted material" (2.07 - 1.11) G. Steinle-Neumann (coordinator), G. Fiquet (Paris, France), F. Langenhorst (Bayreuth, Germany), A.I. Beccero (Sevilla, Spain), S. Buiter (Trondheim, Norway), O. Cadek (Prague, Czech Republic), D. Dobson (London, UK), D. Andrault (Clermont-Ferrand, France), P. Jochym (Krakow, Poland), S. Poli (Milan, Italy) and M.W. Schmidt (Zurich, Switzerland) Total funding: 3,3 Mio € BGI funding:	740.000 €
EU	"Research Infrastructures – Transnational Access" Programme (D.C. Rubie – 1.05 - 12.08)	960.000 €
EU	Marie Curie Host Fellowships for Early Stage Research Training "Atomic to Global" (C.A. McCammon – 01.06 - 12.09) Positions, consumables, equipment, travel:	677.952 €
Stifterverband	Stifterverband für die Deutsche Wissenschaft Junior-Professur Geodynamische Modellierung Positions: W1, 72 months 245.200 € Consumables and travel funding: 120.000 €	365.200 €
Industry	Unrestricted Industrial grants (L.S. Dubrovinsky)	70.000 €
Industry	Collaboration with Fa. Anzaplan (F. Heidelbach)	750 €

### *2.3 Laboratory and office facilities*

The institute occupies an area of

ca. 1200 m<sup>2</sup> laboratory space

ca. 480 m<sup>2</sup> infrastructural areas (machine shops, computer facilities, seminar room, library)

ca. 460 m<sup>2</sup> office space

in a building which was completed in 1994.

### *2.4 Experimental and analytical equipment*

The following major equipment is available at Bayerisches Geoinstitut:

#### I. High-pressure apparatus

5000 tonne multianvil press (25 GPa, 3000 K)

1200 tonne multianvil press (25 GPa, 3000 K)

1000 tonne multianvil press (25 GPa, 3000 K)

500 tonne multianvil press (20 GPa, 3000 K)

500 tonne press with a deformation DIA apparatus

4 piston-cylinder presses (4 GPa, 2100 K)

Cold-seal vessels (700 MPa, 1100 K, H<sub>2</sub>O), TZM vessels (300 MPa, 1400 K, gas), rapid-quench device

Internally-heated autoclave (1 GPa, 1600 K)

High-pressure gas loading apparatus for DAC

#### II. Structural and chemical analysis

2 X-ray powder diffractometers

1 X-ray powder diffractometer with furnace and cryostat

Single-crystal X-ray cameras

2 automated single-crystal X-ray diffractometers

High-brilliance X-ray system

1 Mössbauer spectrometer (1.5 - 1300 K)

3 Mössbauer microspectrometers

2 FTIR spectrometers with IR microscope

FEG transmission electron microscope, 200 kV analytical, with EDS and PEELS

FEG scanning electron microscope with BSE detector, EDS, EBSD and CL

3 Micro-Raman spectrometers with ultraviolet and visible lasers

JEOL JXA-8200 electron microprobe; fully-automated with 14 crystals, 5 spectrometer configuration, EDX, capability for light elements

Cameca SX-50 electron microprobe

193 nm Excimer Laser-Ablation ICP-MS

ICP-AES sequential spectrometer  
Water content determination by Karl-Fischer titration  
GC/MS-MS for organic analyses

### III. *In situ* determination of properties

Diamond anvil cells for powder and single crystal X-ray diffraction, Mössbauer, IR, Raman, optical spectroscopy and electrical resistivity measurements up to at least 100 GPa

Facility for *in situ* hydrothermal studies in DAC

Externally heated DACs for *in situ* studies at pressures to 100 GPa and 1200 K

1-atm furnaces to 1950 K, gas mixing to 1600 K, zirconia  $fO_2$  probes

1-atm high-temperature creep apparatus

Gigahertz ultrasonic interferometer with interface to resistance-heated diamond-anvil cells

Heating stage for fluid inclusion studies

Impedance/gain-phase analyser for electrical conductivity studies

Apparatus for *in situ* measurements of thermal diffusivity at high P and T

Laser-heating facility for DAC

### IV. Computational facilities

19 node linux cluster (2x2.4 GHz Xeon, 1 Gb memory), Gb ethernet

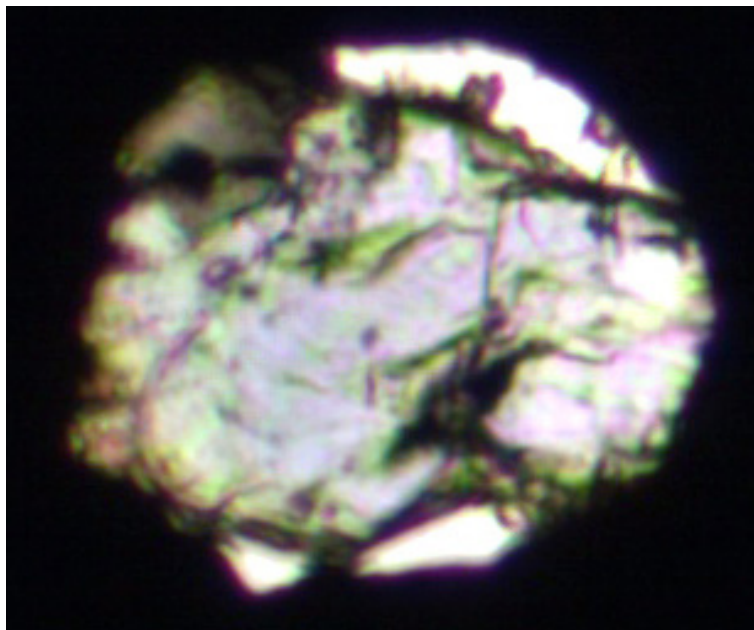
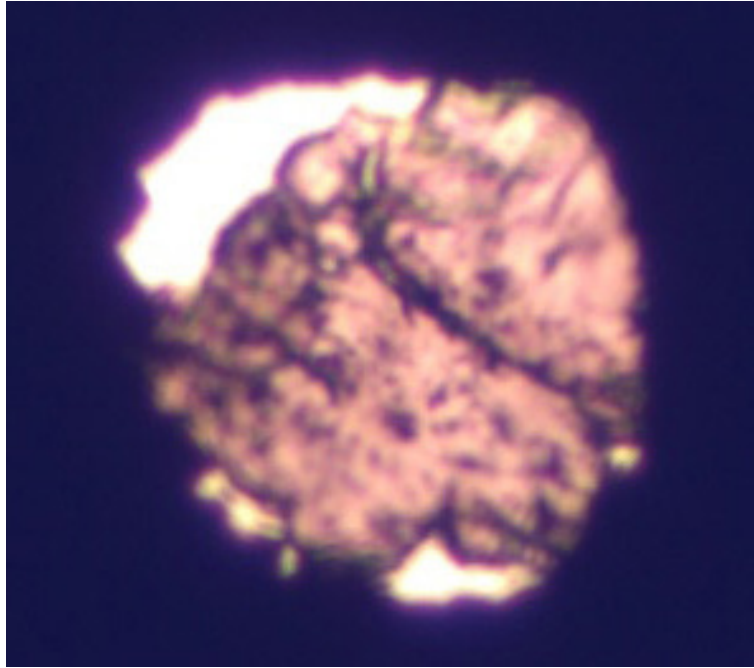
16 node linux cluster (2x3.6 GHz Xeon em64t, 4 Gb memory), Gb ethernet

7 node linux cluster (2x3.0 GHz Xeon Woodcrest Dual Core, 8 Gb memory), InfiniBand

8 node linux cluster (16x2.83 GHz Xeon 5440 Quad Core, 64 Gb memory), InfiniBand

RAID System (6 + 7 Tb storage)

The Geoinstitut is provided with well equipped machine shops, an electronic workshop and sample preparation laboratories. It has also access to the university computer centre.



Silicate perovskite at 125 GPa (top) and ferropericlase at 84 GPa (bottom) in a diamond anvil cell. Width approximately 100  $\mu\text{m}$ . The photographs show that the two main constituents of the lower mantle remain optically transparent even at pressures close to the core mantle boundary. From *Science* 322: 1529 (2008)

Silikat-Perowskit bei 125 GPa (oben) und Ferroperiklas bei 84 GPa (unten) in einer Diamantstempelzelle. Bildbreite etwa 100  $\mu\text{m}$ . Die Photographien zeigen, dass die beiden Hauptbestandteile des unteren Mantels auch bei Drücken nahe der Kern-Mantel-Grenze optisch transparent bleiben. Aus *Science* 322: 1529 (2008)



### 3. Forschungsprojekte

Es wird an dieser Stelle nur über die wichtigsten, derzeit laufenden Projekte berichtet. Informationen über abgeschlossene Teilprojekte sind in den Abschnitten 5.1 und 5.2 in Form von Literaturzitationen angegeben. Die Beiträge des Kapitels 3 sollen nicht zitiert werden.

#### *3.1 Aufbau der Erde und Geodynamik*

Unsere Kenntnisse über die Struktur des tiefen Erdinneren beruhen weitgehend auf Beobachtungen direkt an oder nahe der Erdoberfläche. Der beschränkte Zugang zum Erdinneren führt zu kontroversen Interpretationen hinsichtlich der Temperatur, Zusammensetzung und Mantelströmung, da diese Eigenschaften miteinander gekoppelt sind. Dies erfordert die Kombination von Daten aus der Geochemie und Geophysik mit Labor- und Computeruntersuchungen aus den Bereichen der Mineralogie und Geodynamik. Die Beiträge in diesem Kapitel verfolgen diese Vorgehensweise und untersuchen Prozesse in verschiedenen Tiefen des Erdinneren, zu unterschiedlichen Zeitabschnitten der Erdgeschichte sowie für andere Planeten.

Obwohl die früheste Phase in der Entwicklung der inneren Planeten auf der geologischen Zeitskala einen kurzen Abschnitt darstellt, ist dieser von großer Bedeutung, da er die Anfangsbedingungen der planetaren Entwicklung bestimmt. Die frühe Phase ist charakterisiert durch die Akkretion von Planetesimalen, großvolumiges Aufschmelzen der Planeten und schnelle Durchmischung und Abkühlung durch heftige Konvektion. Diese Vorgänge finden auf einer großen Zeit- und Raumskala statt, so dass die direkte dynamische Simulation der Prozesse nicht möglich ist. Skalierungsgesetze bieten jedoch eine gute Alternative, um die thermische und chemische Entwicklung von Planeten zu modellieren. Die ersten beiden Beiträge dieses Kapitels leiten solche analytischen Skalierungsgesetze her und befassen sich mit der Verteilung von chemischen Elementen und Wärme in Folge der Kernbildung.

Geochemische Messungen an Basalten des mittelozeanischen Rückens und der ozeanischen Inseln zeigen einen deutlichen Unterschied, was oft als Resultat chemischer Heterogenität im Erdmantel interpretiert wird. Da geochemische Daten zeitlich gemittelte Informationen enthalten, erfordert ihre Interpretation die Einarbeitung von geodynamischen Prozessen. Konvektion im Erdmantel kann über geologische Zeitskalen zur Homogenisierung des Mantels führen; aber auch kontinentale Platten an der Oberfläche können die Durchmischung beeinflussen. Der dritte Beitrag dieses Kapitels untersucht die Auswirkungen von ortsfesten isolierenden Platten auf die Durchmischung des Erdmantels.

Die thermische Leitfähigkeit von Mineralen im tiefen Erdmantel hat direkten Einfluss auf den Wärmetransport im Erdmantel und damit auf sein Temperaturprofil und die thermische Entwicklung der Erde. Im vierten Beitrag werden neue Messungen vorgestellt, die zeigen, dass Wärmetransport durch Strahlung im tiefen Erdinneren nicht, wie bisher angenommen, in

thermischen Modellierungen des Erdmantels vernachlässigt werden kann. In diesem Beitrag wird die thermische Leitfähigkeit von Al-haltigen Silikatperowskit bestimmt, der wichtigsten Mineralphase im tiefen Erdmantel.

Der tiefste Erdmantel ist nach wie vor eine rätselhafte Zone, die durch auffällige seismische Eigenschaften wie Anisotropie oder Regionen mit besonders niedriger Geschwindigkeit charakterisiert ist. Um diese seismischen Beobachtungen zu interpretieren, benötigt man Kenntnisse über Phasengleichgewichte und physikalische Eigenschaften wie Dichte und elastische Parameter von Mantelmineralen. Aufgrund des hohen Drucks und der hohen Temperatur im tiefen Erdmantel sind solche Informationen im Labor schwer zugänglich, so dass unsere Kenntnisse über Phasendiagramme und Eigenschaften beschränkt sind. Der fünfte Beitrag zeigt, welchen Effekt die Spin-Paarung in  $\text{Fe}^{2+}$  auf die physikalische Eigenschaften von  $(\text{Mg,Fe})\text{SiO}_3$ -Perowskit hat.

Der letzte Beitrag des Kapitels konzentriert sich auf die Interpretation von gut dokumentierten seismischen Beobachtungen im tiefen Erdmantel: seismische Anomalien mit niedrigen Geschwindigkeiten unter dem Pazifik und Afrika und die Zunahme der Amplitude von seismischen Anomalien mit der Tiefe. Um gekoppelte Effekte von Temperatur, Zusammensetzung und Dynamik in der Inversion zu vermeiden, wird hierbei die elastische Struktur aus einer geodynamischen Konvektionsrechnung mit einheitlicher Zusammensetzung und einem mineralogischen Modell (Phasengleichgewicht und elastische Eigenschaften) berechnet.

### *3.2 Geochemie*

Der Erdkern ist für direkte Untersuchungen unzugänglich. Seine chemische Zusammensetzung und die Bedingungen, unter welchen sich der Kern vom silikatischen Erdmantel getrennt hat, lassen sich jedoch abschätzen. Dazu untersucht man experimentell die relative Verarmung des Erdmantels an siderophilen (= Eisen-liebenden) Elementen und bestimmt deren Verteilungskoeffizienten zwischen Metallschmelzen und Silikaten unter hohen Drücken und Temperaturen. Daraus lässt sich ein Modell zur Entstehung der Erde entwickeln, das sowohl mit den bisher bekannten Daten zur chemischen Zusammensetzung des Erdmantels übereinstimmt, als auch mit neuesten physikalischen Modellen zur Akkretion der Erde. Die bei hohem Druck gemessenen Element-Verteilungskoeffizienten sind teilweise mit großen Unsicherheiten behaftet, die durch die notwendige Extrapolation auf weitaus höhere Druck- und Temperaturbedingungen an der Kern/Mantel-Grenze noch vergrößert werden. Die Erfassung thermodynamischer Eigenschaften, wie z. B. des partiellen Molvolumens, kann die Qualität der Extrapolation deutlich steigern.

Die höchstwahrscheinlich zweithäufigste Mineralphase im unteren Mantel ist  $(\text{Mg,Fe})\text{O}$  Ferroperiklas. Die Zusammensetzung und das Verhalten von Ferroperiklas werden in verschiedenen Projekten untersucht. Schwerpunkte liegen auf dem Schmelzverhalten von Ferroperiklas und der Verteilung von Fe und Mg zwischen dieser Phase und Silikat-Perowskit, einem Thema, das in den letzten Jahren kontrovers diskutiert wurde. Aktuelle

Studien im Geoinstitut kommen bei Anwendung einer neuen Analysetechnik zu dem Schluss, dass Ferropiklas mit zunehmender Tiefe im Erdmantel einen höheren Eisenanteil aufweist. Das  $\text{Fe}^{3+}/\text{Fe}^{2+}$ -Verhältnis in natürlichen Ferropiklas-Einschlüssen in Diamanten erweist sich als recht variabel, was auf unterschiedliche Redoxbedingungen bei ihrer Bildung hinweist.

Der Verteilung und Speziation von Kohlenstoff im Erdmantel widmen sich weitere Projekte. Experimentell werden die Redox-Bedingungen untersucht, unter denen Graphit oder Diamant in aufsteigendem Mantelmaterial zu Carbonat-Schmelzen oxidiert wird. Dieser Prozess steht möglicherweise am Anfang einer partiellen Schmelzbildung in relativ geringen Tiefen unterhalb mittelozeanischer Rücken. Weiterhin werden die Bedingungen erforscht, unter denen carbonatische Schmelzen unter Abgabe von  $\text{CO}_2$  zersetzt werden. Dieser Prozess spielt in Fragen der Mantel-Metasomose und des Ursprungs karbonatischer Schmelzen an der Erdoberfläche eine wichtige Rolle.

Untersuchungen zur Speziation von Phosphor im Erdmantel ergeben, dass in der Übergangszone zwischen oberem und unterem Erdmantel Granat der Hauptträger von Phosphor zu sein scheint, während aufgrund der niedrigen Phosphor-Löslichkeit in gängigen Mineralphasen des unteren Erdmantels das  $\text{Ca}_3(\text{PO}_4)_2$ -Mineral Tuit stabil ist.

Zwei weitere Projekte befassen sich mit erzbildenden Sulfid-Mineralen. Die Erkenntnis, dass zahlreiche rhyolitische Magmen an Molybdänit ( $\text{MoS}_2$ ) gesättigt waren, hat wichtige Konsequenzen für das Verhalten von Molybdän während der magmatischen Fraktionierung und der Bildung von Molybdän-Lagerstätten. Der Molybdän-Gehalt  $\text{MoS}_2$ -gesättigter Schmelzen kann prinzipiell auch dazu genutzt werden, Informationen über deren Bildungsbedingungen (z. B.  $f\text{O}_2$ ,  $f\text{S}_2$ ) zu gewinnen. Ein weiterer Beitrag beschäftigt sich mit Oxidationsprozessen, welche zur Verwitterung von Sulfid-Mineralen führen. Es wird gezeigt, dass die Redoxreaktionen von der Mikrostruktur und den Sekundärphasen im Nanometermaßstab beeinflusst werden.

### *3.3 Mineralogie, Kristallchemie und Phasenumwandlungen*

Die Funktionsweise des Erdinneren zu verstehen, ist das Hauptziel der Forschungsarbeiten am Bayerischen Geoinstitut. Die Untersuchung der Kristallchemie, Kompressibilität und Phasenumwandlungen von Mineralen hinsichtlich ihrer Phasenübergänge bei hohen Drücken und Temperaturen ist dabei eine wesentliche Informationsquelle zur Erreichung dieses Ziels. Die Mehrzahl der Beiträge in diesem Kapitel sind deshalb Hochdruck-/Hochtemperatur-Forschungsarbeiten an verschiedenen Mineralen des Erdinneren, die mit einer Reihe von unterschiedlichen experimentellen Techniken durchgeführt wurden. Die Reihenfolge der Beiträge orientiert sich am inneren Aufbau unseres Planeten, von der Erdkruste zum Erdkern.

Röntgenbeugung an Einkristallen bei hohem Druck dient der Abschätzung des Hochdruck-Verhaltens von  $\text{SrAl}_2\text{Si}_2\text{O}_8$ -Feldspat (isotyp mit Anorthit) und von  $\text{FeTa}_2\text{O}_6$ -Tapiolit mit einer

Tri-Rutil-Struktur. Die Dehydration von Gips und seine Phasenumwandlungen nach Bassanit und Anhydrit als Funktion von Druck und Temperatur werden mit Hilfe der Raman-Spektroskopie bei hohem Druck unter Verwendung einer extern beheizten Diamantstempelzelle untersucht. Um den Effekt einer Aluminium-Substitution auf die Stöchiometrie von Ringwoodit zu erfassen, werden Methoden der Einkristall-Strukturverfeinerung eingesetzt. Der druck- und temperaturabhängige Phasenübergang von Spinell nach Post-Spinell wird dagegen am Beispiel von Magnetit und einer Serie verwandter Ferrit-Spinelle ( $M^{2+}Fe_2O_4$ ) mit Röntgenbeugung, Raman- und Mössbauerspektroskopie erkundet.  $MgSiO_3$ -Perowskit stellt wegen seiner weiten Verbreitung im unteren Erdmantel wohl eines der am intensivsten untersuchten Hochdruckminerale dar. Besonders die Eisen-Substitution in  $MgSiO_3$ -Perowskit steht aufgrund des beobachteten Elektronenspin-Übergangs bei hohem Druck erneut im Mittelpunkt des Forschungsinteresses.

In diesem Kapitel wird auch ein neuer Forschungsansatz beschrieben, bei dem Fe K-Kanten-Röntgenabsorptionsspektroskopie (XANES) in einer Diamantstempelzelle an Silikat-Perowskit betrieben wurde. Dadurch können die elektronische und lokale Struktur von Eisen sowohl in Al-freiem und Al-haltigem  $MgSiO_3$ -Perowskit als auch in Ferroperiklas enger eingegrenzt werden.

Experimente unter den extremen Druck- und Temperaturbedingungen der Kern/Mantel-Grenze stellen eine große Herausforderung dar; die systematische Untersuchung möglicher Phasenübergänge der Post-Perowskit-Struktur des  $CaIrO_3$ -Typs ist daher nicht unkompliziert. Alternativ wird Röntgenbeugung und Mössbauer-Spektroskopie auf  $FeTiO_3$ -Perowskit als ein mögliches Analogon für  $MgSiO_3$ -Perowskit angewendet, um mögliche Post-Perowskit-Übergänge unter Hochdruckbedingungen zu erforschen. Die Mössbauer-Spektroskopie wird auch genutzt, um elektronische Übergänge in hexagonal dichtest gepacktem Eisen und in einer Eisen-Nickellegierung bei hohen Drücken zu untersuchen. Die Entdeckung einer bei hohem Druck stabilen  $Ni_3S$ -Phase mit gleicher Struktur wie  $Fe_3S$  lässt die Existenz einer gewissen Bandbreite von  $(Fe,Ni)_3S$ -Mischkristallen in dem druck- und temperaturbezogenen Stabilitätsfeld der Endglieder  $Fe_3S$  und  $Ni_3S$  vermuten.

Drei weitere Untersuchungen basieren rein auf theoretischen Berechnungen. Diese Untersuchungen haben den Vorteil, dass sich Fragestellungen klären lassen, die experimentell nicht oder nur mit äußerst aufwendigen Methoden beantwortet werden können. So wurde die Dichtefunktionaltheorie angewandt, um die stabile magnetische Struktur von Fayalit sowohl bei Umgebungsdruck als auch unter hohen Drücken zu ergründen und auch verschiedene Hochdruckphasen unterschiedlicher Zusammensetzung im Ti-O-System zu erforschen. Eine kombinierte experimentelle und computergestützte Untersuchung zielt darauf, das anomale elastische Verhalten von Co im Druckbereich zwischen 60 und 80 GPa aufzuklären.

Zwei abschließende Projekte, eines mit Bezug auf die Phasenstabilität eisenreicher, dichter, wasserhaltiger Silikate, das andere zur Untersuchung von Staubpartikeln aus einer Weltraummission zu einem kurz-periodischen Kometen, machen deutlich, wie die Mineralogie dazu

beiträgt, auch das Verhalten anderer Planeten als der Erde, wie dem Merkur oder dem Mars, besser zu verstehen. Materie von Kometen dient dazu, Prozesse in der Frühphase unseres Sonnensystems besser zu verstehen.

### *3.4 Physikalische Eigenschaften von Mineralen*

Zahlreiche Prozesse, die tief in der Erde ablaufen, haben einen Einfluss auf Phänomene, die an der Erdoberfläche zu beobachten sind, wie zum Beispiel Vulkanausbrüche und Erdbeben. Da der größte Teil des Erdinneren für direkte Untersuchungen nicht zugänglich ist, besteht eine erfolgreiche Strategie zur Erforschung des Erdinneren darin, an der Erdoberfläche gewonnene geophysikalische Daten (Seismik, elektromagnetische Feldmessungen) mit Erkenntnissen zu vergleichen, die im Laborexperiment an relevanten Mineralen unter geeigneten Druck- und Temperaturbedingungen erzielt wurden. Dieser Ansatz lässt nicht nur Rückschlüsse auf statische Eigenschaften, wie chemische Zusammensetzung, Mineralogie und Temperaturverteilung im Erdinneren zu, sondern es lassen sich auch Erkenntnisse über die Natur dynamischer erdinnerer Prozesse gewinnen. Die experimentelle Bestimmung physikalischer Eigenschaften von Mineralen im Labor bleibt weiterhin ein zentrales Forschungsziel des Bayerischen Geoinstituts, wie sich in den Beiträgen dieses Jahresberichts widerspiegelt.

Eine bedeutende, immer noch ungeklärte Frage ist das Vorkommen und der Anteil von Wasser im Erdinneren. Durch die Bestimmung von Zustandsgleichungen wird versucht, den Einfluss von Wasser auf elastische Eigenschaften von Mineralen sowie den Prozess der Wasserfreisetzung zu quantifizieren. Ein weiterer Beitrag befasst sich mit elastischen Eigenschaften in tieferen Erdregionen, wo deutliche chemische Gradienten (zum Beispiel  $\text{Fe}^{3+}$ - und Al-Konzentration) zwischen subduzierten Krustenplatten und umgebendem Erdmantel die seismischen Wellengeschwindigkeiten beeinflussen können. Messungen von Zustandsgleichungen stellen ein wichtiges Werkzeug für die Bestimmung von Phasenstabilitäten bei hohen Drücken dar, die zum Beispiel bei der Entsorgung nuklearer Abfälle von entscheidender Bedeutung sind. Das spannende Konzept eines lamellaren Magnetismus wird angeführt, um die extrem hohe magnetische Remanenz in Krustengesteinen zu begründen. Modernste bildgebende Verfahren liefern im atomaren Maßstab einerseits Einblicke in Entmischungsprozesse, die für die Entstehung derartiger Gesteine verantwortlich sind, andererseits mögliche Hinweise darauf, wie sich die Gesteinseigenschaften im Labor für industrielle Anwendungen reproduzieren lassen. Zahlreichen gesteinsbildenden Vorgängen liegt Diffusion als ein weiterer dynamischer Prozess zugrunde. Da es bisher an ausreichenden Daten aus Hochdruck- und Hochtemperatur-Experimenten mangelt, sind Diffusionsvorgänge nur sehr ungenau erfasst. Hier werden Messungen vorgestellt, die sich mit der Lösung von Pyroxen in Granat befassen, ein Vorgang, der sowohl in der Erdkruste als auch im Erdmantel relevant ist. In einem weiteren Projekt werden Kathodenlumineszenz-Messungen an alluvialen Diamanten durchgeführt, um die ursprünglichen Bildungsbedingungen dieser untersuchten Diamanten zu bestimmen.

### *3.5 Fluide und ihre Wechselwirkung mit Schmelzen und Mineralen*

In Subduktionszonen wird Material von der Erdoberfläche wieder in den Mantel zurückgeführt. Die Transportprozesse in Subduktionszonen kontrollieren daher weitgehend die chemische Evolution der Erde in den letzten Milliarden Jahren der Erdgeschichte. Hierzu gehören Schwankungen im Volumen der Ozeane ebenso wie Variationen in der Salinität des Meerwassers. Darüber hinaus sind Subduktionszonen wichtige Quellen von Magmen. Diese Magmen zeigen oft ein charakteristisches Anreicherungsmuster von Spurenelementen, welches verursacht wird durch Prozesse, die tief im Mantel ablaufen. Insbesondere die starke Anreicherung bestimmter inkompatibler Spurenelemente in Laven von Inselbögen beruht wahrscheinlich auf dem bevorzugten Transport dieser Elemente durch Fluide aus der subduzierten Platte heraus in die Zone der Schmelzbildung im Mantelkeil. Eine interessante Beobachtung ist hier, dass Uran und Thorium, die sich normalerweise bei der Schmelzbildung sehr ähnlich verhalten, bei diesem Prozess voneinander entkoppelt werden können. Neue Experimente in diesem Kapitel zeigen, dass die Löslichkeit von Uran in wässrigen Lösungen unter hohem Druck sehr stark mit der Sauerstoffugazität und der Chlor-Konzentration im Fluid ansteigt. Ursache hierfür ist vermutlich die Bildung von Chlor-Komplexen mit sechswertigem Uran. Dieses Verhalten ist für Thorium nicht zu erwarten und das Verhältnis von Uran zu Thorium in kalk-alkalischen Magmen ist daher wahrscheinlich ein Indikator für den Redoxzustand und die Salinität von Fluiden in Subduktionszonen.

Der Halogengehalt von Fluiden in Subduktionszonen kann den Transport bestimmter Spurenelemente durch Komplexbildung beeinflussen. Das Verhalten der Halogene bei der Subduktion ozeanischer Kruste ist darüber hinaus wahrscheinlich ein wesentlicher Faktor, der die Entwicklung der Zusammensetzung des Meerwassers kontrolliert. Die Verteilung von Chlor und Fluor zwischen wässrigen Fluiden und den wichtigsten Mineralen des oberen Erdmantels wurde daher experimentell untersucht. Diese Experimente zeigen, dass Chlor in den Mineralen des oberen Mantels sehr inkompatibel ist. Dies bedeutet, dass das meiste Chlor während der Subduktion durch wässrige Fluide in die Zone der Schmelzbildung hinein transportiert und damit zum größten Teil an die Erdoberfläche zurückgeführt wird.

Der Erdmantel ist ein wichtiges Reservoir für flüchtige Elemente, die man auch in der Atmosphäre findet. Seit langem wurde vermutet, dass ein erheblicher Teil des Gesamtbudgets der Edelgase auf der Erde sich in einem verborgenen Reservoir irgendwo im tiefen Mantel befindet. In einer grundlegenden Studie in diesem Jahresbericht wurde entdeckt, dass Argon in Magnesium-Silikat-Perowskit, dem Hauptbestandteil des unteren Mantels, in erheblichem Maße löslich ist. Der Einbau von Argon in den Perowskit hängt vermutlich mit Sauerstoff-Leerstellen zusammen. Die beobachteten Löslichkeiten sind im Bereich von mehreren Hundert ppm oder darüber, nicht weit entfernt von den Löslichkeiten in depolymerisierten Silikatschmelzen unter vergleichbaren Bedingungen. Dies bedeutet, dass ein erheblicher Teil des Argons möglicherweise während der gesamten Erdgeschichte im tiefen Erdmantel zurückgehalten wurde.

Aluminiumhaltiger Pyroxen ist der Hauptspeicher von Wasser im oberen Mantel. Der scharfe Abfall der Wasserlöslichkeit in Orthopyroxen mit der Tiefe verursacht zusammen mit der steigenden Wasserlöslichkeit in Olivin ein Minimum der Wasserlöslichkeit in der Asthenosphäre. Dieses Minimum der Wasserlöslichkeit in Mineralen führt wahrscheinlich zur Bildung von partieller Schmelze. Da natürliche Klinopyroxene aus Mantel-Xenolithen manchmal sogar mehr Wasser enthalten als Orthopyroxene, wäre es wichtig zu wissen, ob die Wasserlöslichkeit in Klinopyroxenen in einer ähnlichen Weise von Druck und Temperatur abhängt wie für Orthopyroxen. Neue Daten in diesem Jahresbericht zeigen, dass dies tatsächlich der Fall ist. Die Wasserlöslichkeit in Klinopyroxenen nimmt mit der Temperatur stark ab, ähnlich wie für Orthopyroxene. Diese Messungen bestätigen Modelle, die die Asthenosphäre in Verbindung bringen mit einem Minimum der Wasserlöslichkeit in Mantelmineralen in dieser Tiefe.

In den vergangenen Jahren wurde mehr und mehr erkannt, dass viele geologische Prozesse an der Erdoberfläche unter der Mitwirkung von Mikroorganismen ablaufen. Hierzu gehören auch viele Prozesse, die man früher für rein anorganisch gehalten hat. In einem Beitrag in diesem Jahresbericht wurde daher der Einfluss von Mikroorganismen auf die Verwitterung von Biotit untersucht. In Gegenwart von Mikroorganismen wird insbesondere der Ionenaustausch zwischen Kalium und Ammonium in der Zwischenschicht des Biotits verstärkt. Solche Ionenaustauschprozesse sind wichtig, da sie die biologische Verfügbarkeit von Nährstoffen im Boden verbessern.

### *3.6 Physik und Chemie von Schmelzen und Magmen*

Die Aufschmelzung von Gesteinen im Erdinneren und die Verlagerung der daraus resultierenden Magmen stellen den Hauptmechanismus dar, durch den die Erde im Verlauf ihrer 4,5 Milliarden Jahre alten Geschichte differenziert wurde. Material aus dem Erdinneren wird zum Beispiel durch vulkanische Aktivitäten nicht nur an die Erdoberfläche befördert, sondern auch als vulkanische Gase in die Atmosphäre abgegeben. Bildung und Transport von Magmen sind Prozesse, die für die Entwicklung unseres Planeten eine entscheidende Rolle gespielt haben. Die physikalischen und chemischen Eigenschaften der Magmen bestimmen letztlich den Ablauf der Differenzierungsprozesse. Zu den wichtigsten physikalischen Merkmalen zählen rheologische Eigenschaften wie die Viskosität, die Geschwindigkeit und Ausmaß der Magmenmigration steuert. Von den chemischen Merkmalen sind insbesondere die Löslichkeiten volatiler Komponenten in Silikatschmelzen von Bedeutung, da diese z. B. bestimmen, ob der Vulkanismus explosiven Charakter hat und wie die Atmosphäre durch die vulkanischen Eruptionen verändert wird.

Die hier vorgestellten Projekte befassen sich überwiegend mit chemischen Eigenschaften von Magmen. Die Löslichkeit und Speziation von Kohlendioxid in Silikatschmelzen sind wesentliche Parameter für die Freisetzung von CO<sub>2</sub> bei Vulkanausbrüchen, was sich erheblich auf Treibhauseffekt und Klimawechsel auswirkt. Untersuchungen zur Löslichkeit von Chlor

in Silikatschmelzen haben dagegen lagerstättenkundliche Bedeutung, da Chlor eine wichtige Komponente in erzbildenden Fluiden darstellt.

Neben Druck und Temperatur stellt die Sauerstoff fugazität eine bedeutende Variable für Schmelzvorgänge und die sich anschließende Kristallisation von Magmen dar. Die herkömmliche Methode zur Abschätzung der Sauerstoff fugazität beruht auf dem Verhältnis von dreiwertigem zu zweiwertigem Eisen. Neuere Untersuchungen des Geoinstituts zeigen, dass die Beziehung zwischen Sauerstoff fugazität und  $\text{Fe}^{3+}/\text{Fe}^{2+}$ -Verhältnis sich komplexer darstellt als bisher angenommen. Es besteht eine nicht-lineare Abhängigkeit vom  $\text{SiO}_2$ -Gehalt der Schmelze, deren Ursache noch nicht geklärt ist.

Bei vulkanischen Aktivitäten mit explosivem Charakter haben die visko-elastischen Eigenschaften eines Magmas großen Einfluss auf die Deformation und Fragmentierung des Auswurfmaterials. Ein weiteres Projekt setzt die Mössbauer-Spektroskopie ein, um das Relaxationsverhalten sowohl von dreiwertigem als auch zweiwertigem Eisen in Silikatgläsern bei hohen Temperaturen zu studieren. Weitere Forschungsarbeiten befassen sich mit der Entmischung karbonatischer und silikatischer Schmelzen – eine Eigenschaft, die wahrscheinlich für den Ursprung von Karbonatit-Magmen eine große Bedeutung hat – sowie mit detaillierten Untersuchungen von Kristallisationsvorgängen in einer Basaltschmelze bei hohem Druck. Ein hier angewandter neuer Ansatz wird bei Überlegungen zur Kristallisationsgeschichte und Wachstumsgeschwindigkeit von Kristallen, die sich auf Texturen natürlicher Gesteine stützen, sehr hilfreich sein.

### 3.7 Rheologie

Das plastische Deformationsverhalten von Gesteinen wird durch sogenannte Fließgesetze beschrieben, die die angewandte Spannung mit der resultierenden Verformungsrate in Beziehung setzen. Fließgesetze werden aus Deformationsversuchen abgeleitet, bei denen Gesteinsproben unter kontrollierten Bedingungen deviatorischen Spannungen ausgesetzt und die Verformungsraten gemessen werden. Die Anzahl der externen (z. B. Druck, Temperatur, Fugazitäten von Wasser und Sauerstoff) und internen (z. B. Phasengehalt, Mikrostruktur und Textur) Faktoren, die einen Einfluss auf die Gesteinsrheologie haben, ist jedoch relativ groß und gut kontrollierte Deformationsexperimente bei Drücken und Temperaturen des Erdinneren stellen nach wie vor eine große technische Herausforderung dar. Technologische Entwicklungen wie die D-DIA-Vielstempelpresse und die Verwendung von Analogmaterialien (z. B.  $\text{CaIrO}_3$  als Analog for  $\text{MgSiO}_3$ ) können Erkenntnisse über das rheologische Verhalten im tiefen Erdinneren ermöglichen. Eine wichtige Konsequenz großer Verformungsbeträge in Gesteinen ist die Ausbildung charakteristischer Gefüge und physikalischer Anisotropien (z. B. seismische Wellengeschwindigkeiten oder elektrische Leitfähigkeit), die wiederum *in situ* mit geophysikalischen Methoden gemessen werden können.

Das Profil der mechanischen Festigkeit mit zunehmender Tiefe in der Erde ist von großer Bedeutung für das Verständnis und die geodynamische Modellierung der Konvektionsströme im Erdmantel. Von besonderem Interesse sind dabei die Phasenübergänge wie z. B. der Übergang Perowskit–Post-Perowskit oberhalb der Kern-Mantelgrenze, die häufig mit einem scharfen Festigkeitskontrast und veränderter Rheologie einhergehen. Vorläufige Resultate aus Analogexperimenten deuten darauf hin, dass Post-Perowskit deutlich weicher ist als Perowskit, so dass oberhalb der Kern-Mantel-Grenze Verformungsraten bei gleicher Spannung deutlich erhöht wären. Die Wahrscheinlichkeit, dass Mineralphasen seismologisch messbare Anisotropien erzeugen, hängt zum einen ab von ihrer Einkristallanisotropie und zum anderen von ihrer Fähigkeit, sich durch Kriechen von Versetzungen zu deformieren. Letzteres hat eine kristallographische Vorzugsorientierung zur Folge. Detaillierte Untersuchungen mithilfe der Transmissionselektronenmikroskopie zeigen, dass dies sowohl für Post-Perowskit als auch für Akimotoit, der in tief subduzierter ozeanischer Kruste auftritt, der Fall ist, wodurch beide Minerale möglicherweise als Ursache für seismische Anisotropien im tiefen Erdmantel in Frage kommen.

Im oberen Erdmantel werden die Festigkeiten von subduzierten ozeanischen Platten (z. B. Eklogit) und ‚normalem‘ Mantelgestein (Peridotit) durch die Rheologie ihrer Hauptbestandteile Omphazit beziehungsweise Olivin bestimmt. Ein ungelöstes Problem stellt die Frage dar, inwieweit der Phasenübergang von  $C2/c$  (HT) zu  $> P2/n$  (LT)-Symmetrie beim Omphazit die Deformationsmechanismen und die resultierenden Gefüge beeinflusst. Erste experimentelle Resultate zeigen, dass die Gefüge der Niedrigtemperaturphase denen der Hochtemperaturphase ähneln. Die Aktivierung von intrakristallinen Deformationsmechanismen und eine damit verbundene erhöhte Duktilität stellt sich erst bei Zugabe von Wasser in Deformationsversuchen der Niedrigtemperaturphase des Omphazits ein. Deformationsversuche in polykristallinem Olivin bei stark unterschiedlichen Umschließungsdrücken zeigen, dass diese einen Übergang in den aktivierten Gleitsystemen hervorrufen, der zu einem Wechsel in der kristallographischen Vorzugsorientierung und damit der physikalischen Anisotropie mit ansteigender Tiefe führt.

Das rheologische Verhalten von Schmelzen ist wichtig für das Verständnis sowohl intrusiver als auch extrusiver (vulkanischer) magmatischer Prozesse. Einen entscheidenden Faktor stellt dabei der Anteil der festen Kristalle innerhalb des Magmas und ihre Einregelung während des Fließvorgangs dar, da er den Übergang von makroskopisch flüssigem zu festem mechanischen Verhalten kontrolliert. Torsionsversuche mit Kristall-Schmelze-Gemischen zeigen, dass der kritische Anteil von Kristallen für den Übergang zwischen 50 und 60 % liegt, und der Übergang selbst durch einen Wechsel von übergreifenden zu lokalisierten Deformationsstrukturen gekennzeichnet ist.

### *3.8 Metamorphose*

Geologische Prozesse setzen Gesteinseinheiten sich ändernden Temperatur- und Druckbedingungen aus. In den betroffenen Gesteinen und ihren Mineralen wird dabei ein

Prozess der Festkörperumwandlung bewirkt, die Metamorphose. Untersuchungen des metamorphen Mineralbestandes eines Gesteins ermöglichen häufig Rückschlüsse auf seine Druck- und Temperaturgeschichte, wodurch Informationen über nicht direkt zugängliche geologische Prozesse gewonnen werden können. Der Schlüssel zu quantitativen Daten sind Geothermometer und Barometer, Minerale und Mineralvergesellschaftungen, deren chemische Zusammensetzung einen Datenpunkt auf dem Druck-Temperatur-Pfad des Gesteins definiert. Eines der robustesten Geothermometer ist die Analyse von miteinander verwachsenen Orthoklas- und Plagioklaskristallen, die durch Entmischung eines primären Hochtemperatur-Feldspates entstanden sind. Eine kombinierte experimentelle und numerische Studie liefert eine verbesserte Kalibrierung dieses wichtigen Thermometers. Ein weiteres System für die Thermobarometrie ist die Stabilität und der Spurenelement-Einbau unterschiedlicher TiO<sub>2</sub>-Modifikationen. Eine Untersuchung von Rutil-Einschlüssen in Granat aus dem Erzgebirge wird präsentiert, welche ein besseres Verständnis dieses Systems ermöglicht.

Erdbeben bewirken durch Reibungshitze entlang von Verwerfungen häufig die lokale Bildung von Schmelzen, welche als glasreiche Pseudotachylite auskristallisieren. Die kristallisierenden Minerale reflektieren die metamorphe Fazies und die P-T-Bedingungen des Umgebungsgesteins. Im dritten Beitrag wird ein detaillierter Blick auf Omphazite geworfen, die in einem eklogitfaziellen Pseudotachylit entstanden sind. Überraschenderweise wurden Versetzungsmikrostrukturen gefunden, die normalerweise nur mit langfristiger Deformation assoziiert werden. Falls die vorhandene Spannung bei der Omphazit-Kristallisation ausreicht, um diese Mikrostrukturen zu erzeugen, müssten möglicherweise frühere TEM-Untersuchungen von Omphaziten überdacht werden.

Die folgenden Beiträge beschäftigen sich mit intensivem kurzfristigen Aufheizen und Kompaktieren von Gesteinen als Resultat einer Impaktmetamorphose. Eine detaillierte Abfolge fraktionierter Kristallisation von Wadsleyit und Ringwoodit aus einer Impakt-Schmelzader eines Chondriten wird präsentiert. Zusätzlich zu diesen Hochdruckphasen werden in einigen Fällen auch bisher unbekannt Mineralphasen in geschockten Meteoriten gefunden. Hier wird eine neue ultraharte Kohlenstoffmodifikation beschrieben, die möglicherweise materialwissenschaftliche Anwendungen finden könnte. Die Freisetzung von Treibhausgasen aus Karbonatgesteinen ist ein möglicher Beitrag zu Klimaveränderungen nach großen Meteoriteneinschlägen. Im letzten Beitrag wurde ein natürlicher Dolomit experimentell geschockt, um einen Einschlag zu simulieren. Der Dolomit erwies sich als überraschend stabil, so dass unter den experimentellen Bedingungen kein CO<sub>2</sub> freigesetzt wurde.

### *3.9 Materialwissenschaften*

In der Mineralphysik und experimentellen Geochemie werden ähnliche methodische Ansätze verfolgt wie in Teilbereichen der Materialwissenschaften. Die experimentellen Geowissenschaften haben beträchtliche Fortschritte bei der Entwicklung von Hochdruck- und

Hochtemperatur-Apparaturen erzielt, mit denen Volumen, Struktur, elektronische, magnetische und andere physikalische Eigenschaften von Festkörpern gezielt eingestellt werden können. Als Folge dieser Entwicklung sind auch neue materialwissenschaftliche Hochdruck-Forschungszentren in Frankreich, England, Japan und den USA entstanden, während sich die geowissenschaftlich orientierten Hochdruck-Arbeitsgruppen zunehmend mit Themen der Materialwissenschaften, Festkörperphysik und -chemie beschäftigen. Obwohl das Bayerische Geoinstitut kein eigenständiges materialwissenschaftliches Forschungsprogramm besitzt, haben Kooperationen mit Industriepartnern und die Einbindung in internationale und nationale Forschungsprojekte in diesem Jahr zu einer Reihe von Beiträgen auf dem Gebiet der Materialphysik und -chemie geführt. Die materialwissenschaftlichen Projekte reichen von superharten, halb- und supraleitenden Phasen bis hin zu Materialien mit speziellen elektronischen und mechanischen Eigenschaften. Ein Teil dieser Projekte wird im Folgenden kurz erläutert.

Beispiele für potentielle superharte, halb- und supraleitende Materialien sind Bor-haltige Verbindungen. Reines Bor ist eines der vielfältigsten Elemente. Dutzende von Kristallstrukturen wurden für Bor vorgeschlagen, zumeist stellte sich aber später heraus, dass die kristallinen Phasen verunreinigt waren und z. B. Boride darstellten. Eine kombinierte experimentelle und theoretische Studie behandelt die Synthese und Charakterisierung von neuen orthorhombischen Hochdruckphasen des Bors. Diese Phasen bleiben nach Druckentlastung metastabil erhalten und stellen vielversprechende Materialien dar, die sowohl hohe Härte als auch Halbleitereigenschaften aufweisen können.

Die Entdeckung von supraleitenden Bor-dotierten Diamanten war Auslöser für verstärkte Hochdruckstudien an diesem Material, die zum einen die möglichen Anwendungen und zum anderen die Ursache für die Supraleitung ergründen wollten. Die Supraleitung wurde zunächst auf die Dotierung des Diamants mit Bor zurückgeführt, jedoch zeigten detaillierte mikrostrukturelle Untersuchungen, dass die Proben sehr komplex zusammengesetzt sind und wahrscheinlich amorphe Bor-haltige Filme auf Korngrenzen die Supraleitung verursachen.

Obwohl Diamant derzeit als das härteste bekannte Material gilt, wird kontinuierlich versucht, Materialien mit vergleichbarer Härte und höherer thermischer Stabilität zu synthetisieren. Ein solches Material könnte kubisches diamant-strukturiertes  $\text{BC}_2\text{N}$  sein, das in der 5000 Tonnen Presse am BGI hergestellt wird. Eine aktuell wichtige Aufgabe in diesem Projekt ist die Optimierung der Synthesebedingungen wie Beschaffenheit des Ausgangsmaterials, Druck, Temperatur und Heizdauer.

Die Verbesserung optoelektronischer, thermischer und mechanischer Eigenschaften ist das Ziel aktueller Hochdruckstudien an Nitriden und Oxinitriden. Die Optimierung der Synthesebedingungen und die Untersuchung der physikalischen Eigenschaften von spinell-strukturiertem Galliumoxinitrid, neue Methoden zur Sinterung von  $\text{Si}_3\text{N}_4$ -Nanopulvern und die Synthese von einzigartigen Fe-Mg-N-Verbindungen in der Multianvil-Apparatur sind aktuelle Ansätze zur Entwicklung von neuen Verbindungen auf Nitrid-Basis mit möglichen materialwissenschaftlichen Anwendungen.

Eine Aufgabe von genereller technologischer Bedeutung für eine Vielzahl von elektronischen Geräten ist die Entwicklung von elektrischen Speichermaterialien. Lithium-Kobaltate werden als vielversprechende Materialien zur effektiven und preisgünstigen Speicherung von elektrischer Energie in Ionen-Akkus angesehen. Die Kapazität der Batterien hängt direkt von den elektrischen und elektronischen Eigenschaften des Materials und damit auch von deren Kristallstruktur ab. Hochdrucksynthesen erlauben es, neue Kristallstrukturen von Kobaltaten mit nützlichen elektronischen Eigenschaften herzustellen.

Eine wichtige Herausforderung von Hochdruckstudien ist die Kalibrierung des Drucks oberhalb von 10 GPa. Viele Unsicherheiten und Diskrepanzen sind auf fehlende primäre Druckindikatoren zurückzuführen. Lithiumfluorid bietet eine Reihe von Vorteilen für den Einsatz als interner Druckstandard in Diamantstempelzellen-Experimenten. Erste kombinierte Röntgenbeugungsexperimente und Brillouin-Spektroskopie dienen der Erfassung der elastischen Eigenschaften von LiF unter hohem Druck. Die Ergebnisse zeigen, dass dieses Material sogar für die Druckkalibrierung bis in den Mbar-Bereich geeignet ist.

Organische Verbindungen zählen zu den wichtigsten Funktionsstoffen in den Materialwissenschaften, ihre Eigenschaften und ihr Verhalten unter hohem Druck und hoher Temperatur werden aber erst seit kurzem in Experimenten untersucht. Studien zur Kristallisation von Polypropylen belegen erstmals den großen Effekt von selbst geringem Druck und geringer Temperatur (wenige kbar und 250 °C) auf die Eigenschaften von weichen organischen Materialien.

### *3.10 Methodische Entwicklungen*

Die Entwicklung neuartiger experimenteller und analytischer Methoden ist ein wichtiger Zweig der modernen Geowissenschaften. Derartige Entwicklungen sind mit einem relativ großen Zeit- und Kostenaufwand verbunden. Dieser hohe Aufwand ist aber unumgänglich, wenn man fundamentale neue Erkenntnisse in der Wissenschaft erreichen will. In diesem Jahr lagen die Schwerpunkte der methodischen Entwicklungen in der Diamantstempel-Technik, der Synthese von Flüssigkeitseinschlüssen und der numerischen Modellierung.

Ein neues, tragbares Lasersystem zur Beheizung von Diamantstempelzellen ermöglicht den einfachen Transfer dieser Versuchsanordnung zu externen Forschungseinrichtungen. Dies erweist sich als besonders praktisch für *in situ*-Untersuchungen mit Synchrotron-Strahlen, da in entsprechenden Einrichtungen weltweit nur wenige Hochdruck-Messplätze mit (stationären) Laser-Heizsystemen ausgestattet sind. Ein weiterer wesentlicher Fortschritt liegt in der Entwicklung einer neuen Diamantstempelzelle mit Widerstandsheizung mit einem beidseitigen vollständigen 90°-Öffnungswinkel, wodurch die Probenuntersuchung simultan sowohl mit Methoden der optischen Spektroskopie als auch mit Röntgenstreuung durchgeführt werden kann.

Auch auf dem Gebiet der Fluid-Geochemie wurde eine neue Methode entwickelt. Mit ihr lassen sich relativ große Flüssigkeitseinschlüsse unter Bedingungen herstellen, unter denen normalerweise nur kleine Einschlüsse zu erwarten wären. Ein weiterer Vorteil der neuen Methode liegt darin, dass die Fluide gezielt erst nach Erreichen der Gleichgewichtsbedingungen eingefangen werden können.

Ferner wird ein neuer numerischer Code präsentiert, mit dem sich komplexe geodynamische Prozesse zweidimensional mit relativ geringem Rechenaufwand modellieren lassen, so dass die Berechnungen auf gängigen PC's durchgeführt werden können.



### 3.1 Earth's Structure and Geodynamics

Most of our knowledge of the deep structure of the Earth comes from observations collected at the surface or within only the few first kilometers of depth. This uneven data coverage often leads to controversial interpretations of the observations in terms of temperature, composition and flow, due to the possible trade offs between these characteristics. Overcoming this major difficulty requires exploiting the complementarities between the various types of geochemical and geophysical observations, together with geodynamic and mineral physics constraints. The contributions to this chapter follow this approach by focusing on different regions and time windows of the Earth and other terrestrial planets.

The earliest stage of terrestrial planet evolution is a relatively short time window on geological time scales but an essential one as it sets up the initial condition from which planets have evolved until present. These early stages are characterized by the occurrence of many processes acting on various time and length scales such as planetesimal accretion, large scale melting and vigorous convection. This prohibits a direct and simultaneous modeling of all these processes – a good alternative, however, is to perform modeling based on scaling laws. The first two contributions in this chapter focus on these aspects by deriving simple analytical expressions that can be used to investigate chemical equilibration and heat partitioning during core formation by negative diapirism.

Geochemical data show a clear dichotomy between Mid Ocean Ridges and Ocean Island Basalts compositions, often interpreted as the result of mantle heterogeneity. Due to its time-integrated nature, the interpretation of geochemical data needs to be done in the light of geodynamic considerations. Convective motions can potentially homogenize mantle heterogeneities over geological times, but the presence of continental plates at the surface may alter the mixing behaviour. The third contribution to this chapter considers this aspect by investigating the effect of stagnant insulating plates on mixing in the Earth's mantle.

Thermal conductivity of lower mantle phases have a direct primary influence on convective dynamics and hence the thermal state and evolution of the mantle. Recent measurements at BGI have shown that contrary to what was previously thought, radiative heat transport is not negligible in the lower mantle. The fourth contribution to this chapter focuses on determining experimentally the radiative thermal conductivity of Al-bearing silicate perovskite, the main mineral phase in the lower mantle.

The Earth's lowermost mantle remains an enigmatic region characterized by various distinct seismological signatures such as anisotropy and ultra low velocity zones. The knowledge of phase diagrams and physical properties such as density and elastic coefficients is required to interpret these seismic observations. However, this remains particularly challenging in the lowermost mantle, due to the lack of information on mineral properties and phase stability at such high pressures and temperatures. The fifth contribution aims at filling this gap by investigating experimentally the effect of  $\text{Fe}^{2+}$  spin pairing at Earth's lowermost mantle pressure and temperature on the phase diagram of  $(\text{Mg,Fe})\text{SiO}_3$ .

The last contribution focuses on the interpretation of well documented seismological observations of the lowermost mantle: the presence of broad slow velocity anomalies below the Pacific and under Africa as well as the depth increase of the root mean square amplitudes of seismic velocity anomalies. To minimize tradeoffs and couplings between temperature, composition, and flow, the authors use a forward approach combining both geodynamic modeling of an isochemical convective mantle in a spherical shell, and mineral physics considerations.

**a. Core formation in terrestrial planets (H. Samuel and P. Tackley/Zürich)**

Various types of observations have confirmed the presence of metallic cores in several terrestrial planets.  $Hf/W$  chronometry suggests that core formation is a relatively fast process, which may have been completed within less than 100 Myrs for planets such as the Earth or Mars. In addition, the overabundance of siderophile elements in the Earth's mantle suggests that metal silicate equilibration occurred during core formation processes.

We investigate dynamically the timing and metal-silicate equilibration processes during core formation by negative diapirism. We model numerically the sinking of iron-rich diapirs through a viscous silicate mantle in axisymmetric geometry. Shear heating as well as several viscous rheologies are considered and we carried out a parameter study where we vary quantities such as the Rayleigh number, the dissipation number and  $R_d$ , the radius of the iron diapir.

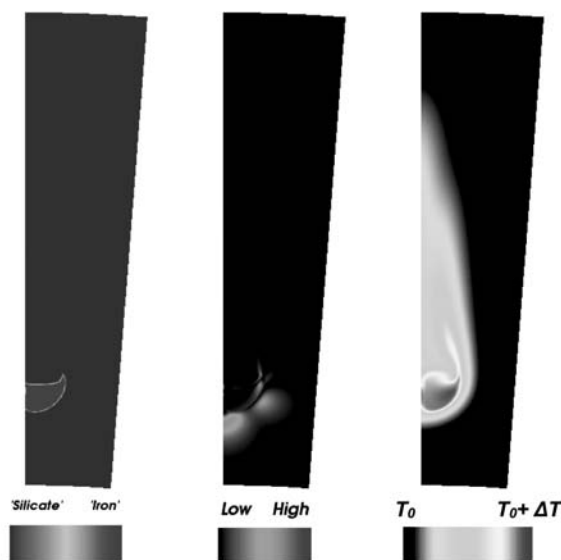


Fig. 3.1-1: Numerical modeling of a metal diapir sinking through a solid or molten silicate mantle. Left: compositional field. Middle: viscous dissipation. Right: dimensionless temperature. As the diapir sinks down its potential energy is converted into thermal energy via viscous heating. Temperature therefore increases at the interface where viscous dissipation is higher, possibly leading to local melting of the silicate.

As the diapir sinks, temperature at the interface between the iron diapir and the surrounding silicate increases due to the conversion of potential energy into thermal energy via viscous heating (Fig. 3.1-1). This significant temperature increase is likely to favor metal-silicate equilibration if the temperatures are high enough to melt the silicates in contact with the metal diapir.

We developed a simplified semi-analytical model that reproduces well the thermal evolution in our numerical experiments, for which only the energy equation has to be solved numerically:

$$\frac{DT}{Dt} = \frac{1}{Pe_T} \nabla^2 T + \Pi_v \Phi_v,$$

where  $t$ ,  $T$  and  $\Phi_v$  are dimensionless time, temperature and dissipation function, respectively. In the above equation the diapir Péclet Number  $Pe_T = V_s R_d$  and the efficiency of viscous heating  $\Pi_v = V_s R_d \eta_0 / (\rho_0 \kappa_T)$  are the only two governing dimensionless parameters, with  $V_s$ ,  $\eta_0$ ,  $\rho_0$ ,  $\kappa_T$  being the diapir sinking velocity, the silicate viscosity, density and thermal diffusivity, respectively. The equation above yields a simple criterion for the generation of a silicate melt layer surrounding the sinking metal diapir:  $Pe_T \Pi_v \sim 10$ .

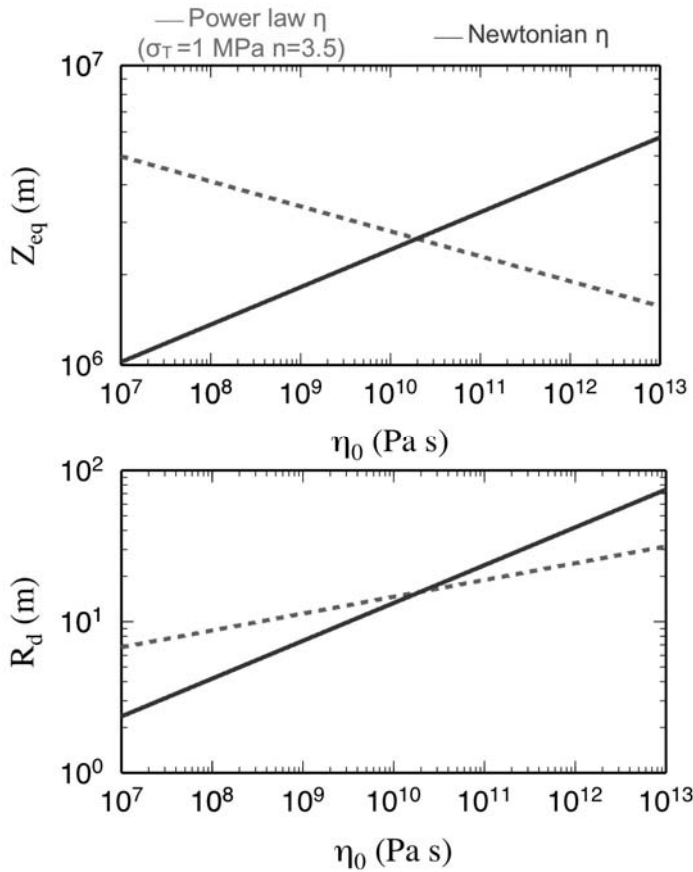


Fig. 3.1-2: Conditions for metal-silicate equilibration during the sinking of the iron diapir for a plausible range of partially molten silicate mantle viscosities. Both Newtonian (solid lines) and power law rheologies (dashed lines) are considered. Top: Radius of the diapir that satisfies the equilibration constraint. Bottom: equilibration distance for a single diapir. We considered three criteria for chemical equilibration between the metal diapir and the surrounding silicates: (1) Chemical equilibration of Ni between the iron diapir and the surrounding silicates up to 99 %. (2) Equilibration time less than 100 Ma, the timescale of core formation as suggested by HF/W chronometry. (3) Equilibration distance  $z_{eq}$  less than a few thousand kilometers for a planet such as the Earth.

Using this criterion we show (Fig. 3.1-2) that metal diapirs of a radius  $\sim 1$ -100 m, sinking through a partially molten silicate mantle can chemically equilibrate within the timescales suggested by geochemical constraints. Therefore, contrary to what was previously assumed, negative diapirism can contribute significantly to metal-silicate equilibration processes during core formation.

**b. Heat partitioning in terrestrial planets during core formation (H. Samuel and P. Tackley/ Zürich)**

Core formation is the first major differentiation event that determines the initial conditions from which terrestrial planets have evolved until present. This separation of metal and silicates in terrestrial planets is likely to generate substantial amounts of heat by conversion of potential energy into thermal energy via viscous heating (see also contribution 3.1.a): the gravitational heat released for an Earth or a Mars-like planet represents a temperature increase of few hundreds to few thousands Kelvin. While estimating the total amount of gravitational heating in a planet is relatively straightforward, determining its partitioning between the silicate and metallic part is not a trivial task.

We therefore derived a simple semi-analytical “sphere-shell” model that considers the heat exchange between the diapir and the surrounding silicate as well as the heat produced by viscous dissipation. This model results in a very simple analytical expression for the mean temperature of a sinking iron diapir  $T_d$  (initially equal to  $T_d^0$ ) as a function of time  $t$ :

$$\bar{T}_d = \Pi_v^* + (\bar{T}_d^0 - \Pi_v^*) \exp\left(-\frac{1}{Pe_T^*} t\right),$$

where  $Pe_T^*$  and  $\Pi_v^*$  have similar meaning as in contribution 3.1.a. As illustrated in Fig. 3.1-3, this simple model is in very good agreement with numerical experiments and has the great advantage of being much simpler to use than solving the differential equation.

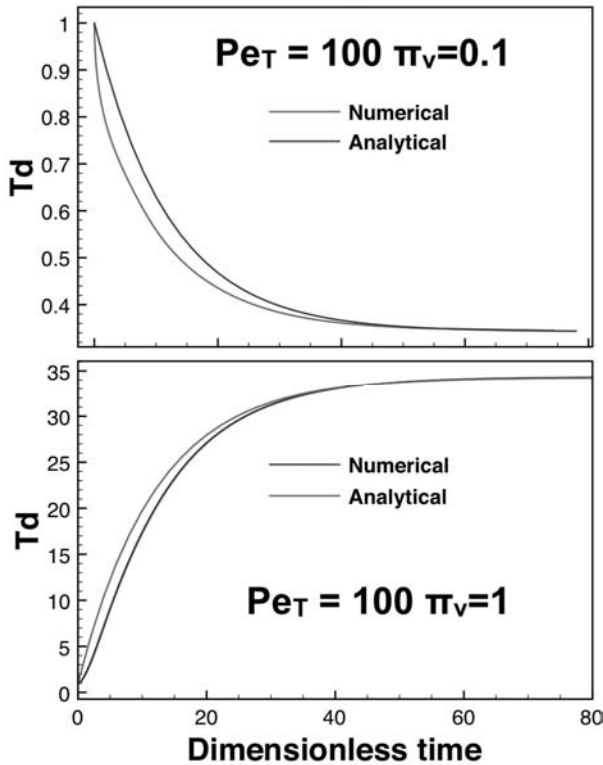


Fig. 3.1-3: Time evolution of the mean temperature of a sinking iron diapir  $T_d$  calculated by solving numerically the differential equation of contribution 3.1.a or using the analytic expression derived here. The good agreement demonstrates the ability of the “sphere-shell” model to capture the essential physics.

These scaling laws are then used to determine the heat distribution within terrestrial planets during their growth and early differentiation (Fig. 3.1-4). Importantly, we show that (i) heat partitioning during core formation is very sensitive to the size distribution of the planetesimals during accretion (ii) simple parameterizations that usually considered in accretion models for heat partitioning (*e.g.*, thermal equilibrium) are unrealistic.

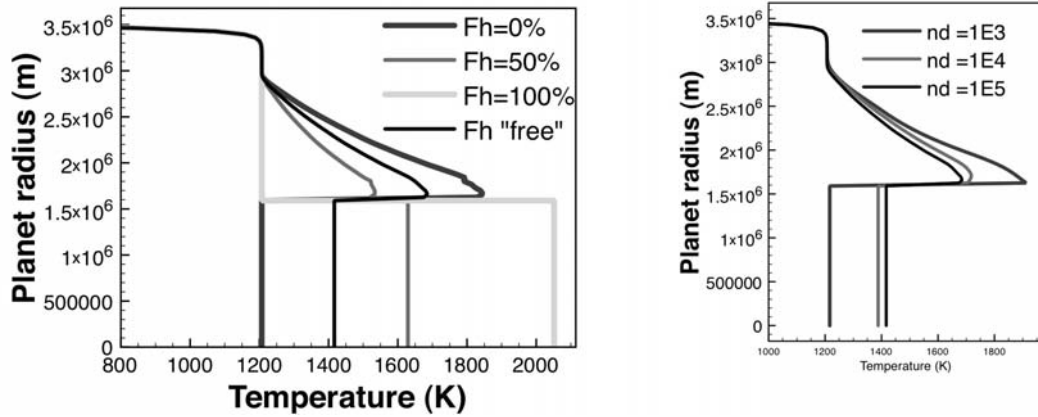


Fig. 3.1-4: Early heat distribution in a Mars-like planet after core formation via negative diapirism. We assume that initially  $n_d$  diapirs are randomly located near the surface and are sinking towards the center of the planet. The gravitational heat partitioning is either arbitrary fixed or determined using the analytical expression (curve labeled as “free”). Left: temperature distribution after core formation. Right: Same as the left figure except that only the analytical expression is used and the total number of diapir  $n_d$  is varied.

**c.** *The effect of continents as insulating lids on mantle convection dynamics and stirring properties (W. Dietrich/Bayreuth, H. Samuel; W. Zimmermann and F. Busse/Bayreuth)*

Active plate tectonics is a unique feature that distinguishes The Earth’s mantle from other terrestrial bodies. Although significant progress have been made in the past years, the dynamics of convective motions in the presence of continental and/or oceanic plates remains a poorly understood phenomenon. Oceanic plates are recycled into the mantle and are characterized by a relatively strong heat flux, while continents are more insulating, lighter, and unsubsductable.

The dichotomy between continents and oceans is likely to have a first order influence on mantle motions, thus on the efficiency of convective stirring over billions of years. Understanding these processes is essential to interpret surface geophysical and geochemical data on Earth, such as the observed isotopic heterogeneities in basalts.

We study the influence of insulating lids (*i.e.*, continents) on the dynamics of the convective system. In particular, we quantify the convective stirring efficiency as a function of Rayleigh number,  $Ra$ , and the size of the insulating lid,  $c$ . We model numerically convection at infinite Prandtl number in a 2D isoviscous, incompressible fluid on a rectangular grid.

Differences between oceanic and continental plates are accounted for by imposing heterogeneous surface boundary conditions: Oceanic plates are described by Dirichlet boundary conditions ( $T=0$ ) while the insulating character of the continents is modeled by imposing zero flux Neumann boundary conditions ( $\partial T/\partial z=0$ ). We use passively advected tracers to quantify the stirring efficiency with various diagnostics such as mixing time, Lyapunov exponents distribution (Figs. 3.1-5 and 3.1-6).

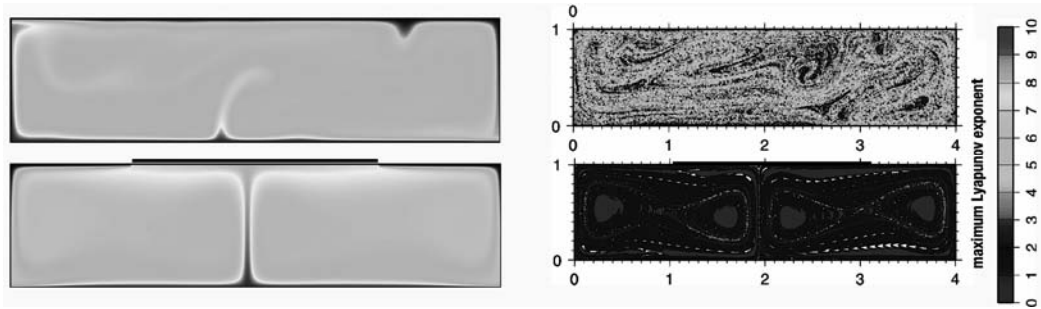


Fig 3.1-5: Temperature field (left) and Lyapunov exponent (right) for two cases without continent (top) and with a fixed insulating continent (bottom) for  $Ra=10^6$ . The presence of continents stabilizes the flow by favoring the presence of convective cells where stirring is less efficient.

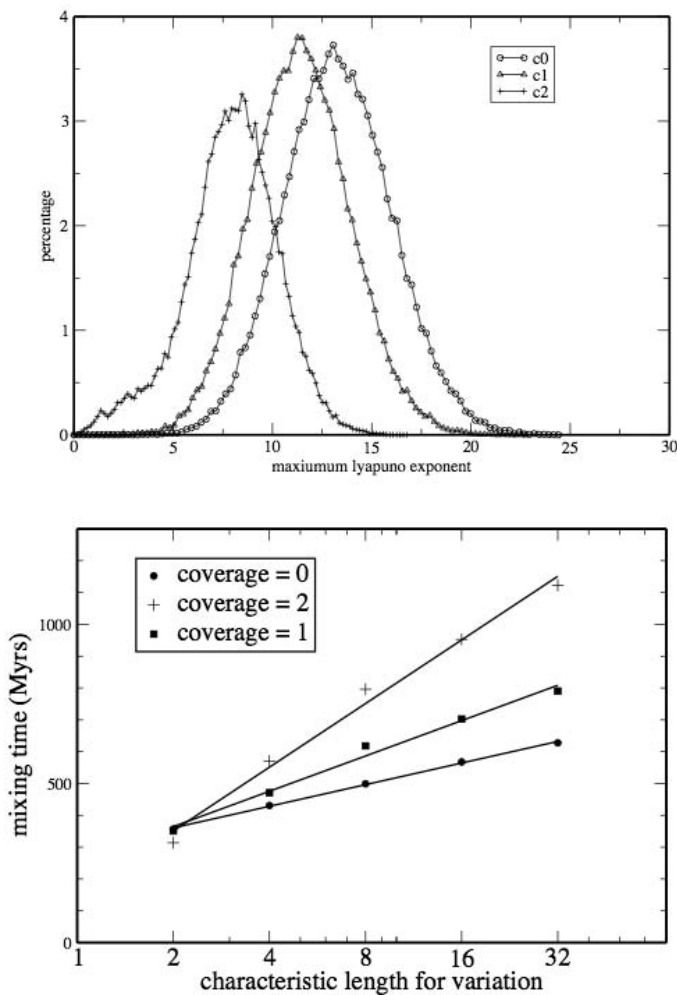


Fig 3.1-6: Top: Lyapunov exponent distribution calculated for  $Ra=10^7$  and three different continental coverage  $c$ . As  $c$  increases, the Lyapunov exponent distributions shift towards lower values, which is synonymous of much lower convective stirring efficiency. Bottom: mixing times as a function of wavelength heterogeneity for  $Ra=10^7$  and three continental coverage.

Our first results clearly demonstrate that the presence of continents strongly affects the mixing efficiency by stabilizing convection cells where the flow is dominated by rotation. As a consequence, mixing via stretching and folding becomes less efficient (Figs. 3.1-5 and 3.1-6). We calculate the mixing times as a function of the continental coverage and the wavelength of the heterogeneity considered (Fig. 3.1-6). This ongoing study will further be extended to more realistic cases in which continents directly act on the flow field as rigid fixed and/or mobile lids, using the *STREAMV* code described in contribution 3.10 d. Additional statistical tools (*e.g.*, tracer age distribution and time evolution of flow parameters) will also be considered.

**d. Optical absorption spectra and radiative thermal conductivity of silicate perovskite to 125 GPa (H. Keppeler, L.S. Dubrovinsky, O. Narygina and I.Yu. Kantor)**

While pressure is very well known in Earth's interior as a function of depth, there is a considerable uncertainty in the temperature profile. This is because seismic wave velocities only indirectly depend on temperature and therefore our main source of information on the properties of Earth's interior cannot be used to reconstruct temperature profiles. Available estimates of the temperature distribution are model dependent and one of the key parameters entering these models is thermal conductivity.

At the temperatures in excess of 3000 K prevailing in the deep part of the lower mantle, one may presume that radiation dominates heat transport, because thermal emission increases with the fourth power of temperature. However, radiative thermal conductivity has usually been neglected in models of heat transfer in the mantle, because mantle minerals were believed to become opaque at high pressure (see p. 19). Recent studies at the Geoinstitut, however, have shown that ferropericlase and ringwoodite of realistic bulk iron content and iron oxidation state remain rather transparent even at deep lower mantle pressures. Therefore, we studied the optical absorption spectrum of an Al-bearing silicate perovskite, the main constituent of Earth's lower mantle, to 125 GPa. The experiments were carried out in a diamond cell with diamonds selected for high optical transparency using neon as pressure medium. Optical and near infrared spectra were measured using a Bruker IFS 125 HR Fourier-transform spectrometer together with an all-reflecting microscope.

The Al content of these perovskite samples is quite important, because the absorption spectra of these aluminous samples (Fig. 3.1-7) are quite different from those of Al-free samples. This is because Al stabilizes  $\text{Fe}^{3+}$  at the expense of  $\text{Fe}^{2+}$  in the perovskite structure and it also changes the distribution of  $\text{Fe}^{3+}$  over the crystallographic sites. Such aluminous samples therefore have to be studied for obtaining realistic estimates of radiative conductivity in the lower mantle.

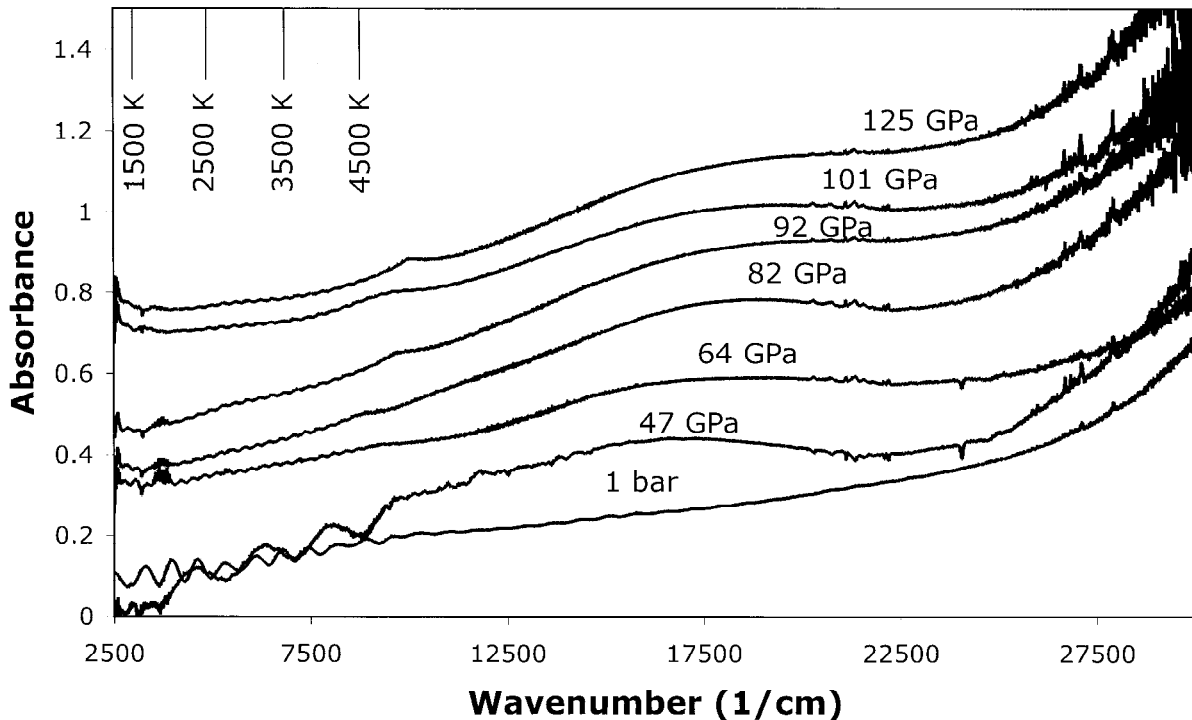


Fig. 3.1-7: Near infrared and optical absorption spectra of silicate perovskite to 125 GPa. The 1 bar spectrum is shown as measured, the other spectra are offset vertically for clarity. Sample thickness is 30  $\mu\text{m}$ . The position of the maxima of thermal blackbody radiation at different temperatures is also shown for reference.

Figure 3.1-7 shows that changes in the absorption spectrum of aluminous perovskite with pressure are relatively subtle and the sample remains quite transparent up to pressures close to the core mantle boundary. The main feature seen in the spectra is a broad band due to  $\text{Fe}^{2+}$ - $\text{Fe}^{3+}$  intervalence charge transfer, while the crystal field bands of  $\text{Fe}^{2+}$  are invisible. The intervalence charge transfer band intensifies between 1 bar and 47 GPa, but its intensity remains essentially unchanged with further increasing pressure. There is no clear evidence for spin-pairing obvious from the spectra.

From the data in Fig. 3.1-7 one can estimate the radiative contribution to thermal conductivity in the deep lower mantle. The values obtained approach  $10 \text{ W m}^{-1}\text{K}^{-1}$  for temperatures around 4000 K at the core mantle boundary. This implies that heat transfer in the lowermost mantle may be dominated by radiation. Since radiative thermal conductivity intrinsically increases with temperature, this effect may stabilize large “superplumes” and it may therefore control the effect of mantle convection in Earth’s interior. However, the increase of radiative conductivity with temperature predicted from our measurements is weaker than the  $T^3$  dependence expected from theory. This is because with increasing temperature, the maximum of blackbody emission moves to higher frequencies, where the sample absorbs more strongly.

**e. Low-spin  $Fe^{2+}$  in silicate perovskite and a possible layer at the base of the lower mantle** (C.A. McCammon, L.S. Dubrovinsky, O. Narygina, X. Wu, in collaboration with I. Sergueev and A. Chumakov/Grenoble)

The base of the lower mantle shows many anomalous properties, a number of which have been explained by the transition of  $(Mg,Fe)(Si,Al)O_3$  perovskite to a post-perovskite structure (*e.g.*, velocity discontinuities, S-wave anisotropy, and possibly the anticorrelation between S-wave and bulk-sound velocities). Other properties, however, remain unexplained (*e.g.*, large P-wave velocity discontinuities, the sharpness of the D'' discontinuity in some regions, high electrical conductivity and the nature of ultralow velocity layers). One possibility that has been considered to account for these observations is lateral variations in chemistry at the base of the lower mantle. However there is another mechanism that can change physical and chemical properties of minerals, namely spin-pairing transitions of iron. Such transitions were predicted to occur within the Earth's interior nearly 50 years ago, but only in the past few years has direct experimental evidence for such transitions at lower mantle conditions been reported. For  $(Mg,Fe)O$ , literature reports of both experimental and computational data confirm a high-spin to low-spin transition of  $Fe^{2+}$  that is expected to occur in the middle part of the lower mantle. For  $(Mg,Fe)(Si,Al)O_3$  perovskite, recent experimental results show a high-spin to intermediate-spin transition of  $Fe^{2+}$  that is expected to occur at the top of the lower mantle, with  $Fe^{2+}$  remaining in the intermediate-spin state throughout the bulk of the lower mantle (BGI Annual Report 2007). Literature data also show that  $Fe^{2+}$  in  $(Mg,Fe)(Si,Al)O_3$  post-perovskite is in the intermediate-spin state. While these results would appear to suggest no further spin transitions within the lower mantle, it is important to note that the P,T region relevant to the base of the lower mantle has not yet been explored with methods that can detect spin transitions. To address this question, we conducted a combined nuclear forward scattering (NFS) and X-ray diffraction experiment on  $(Mg,Fe)SiO_3$  perovskite at the European Synchrotron Radiation Facility (ESRF) combined with conventional Mössbauer measurements at Bayerisches Geoinstitut.

We compressed  $Mg_{0.82}Fe_{0.18}SiO_3$  in a diamond anvil cell (DAC) and transformed it to the perovskite structure using laser heating. We collected room temperature NFS data at pressures from 120 to 170 GPa, with laser heating in between compression steps to reduce deviatoric stress. In all spectra we observed the predominance of intermediate-spin  $Fe^{2+}$ , recognised by its extremely high quadrupole splitting (Fig. 3.1-8). X-ray diffraction data taken of the sample at the same pressures indicated a well crystallised perovskite structure in all cases, even though the sample was laser heated within the post-perovskite stability field, consistent with previous reports of sluggish transformation kinetics. We then heated the sample using a miniature external heater mounted on the DAC, and collected NFS data with increasing temperature. Results clearly showed a transition to low-spin  $Fe^{2+}$ , where the fraction of low-spin  $Fe^{2+}$  increased relative to intermediate-spin  $Fe^{2+}$  with increasing temperature, reaching essentially 100 % low-spin  $Fe^{2+}$  near 1000 K (Fig. 3.1-8). We confirmed the low-spin state using conventional Mössbauer spectroscopy recorded on the same sample in the DAC after returning from ESRF.

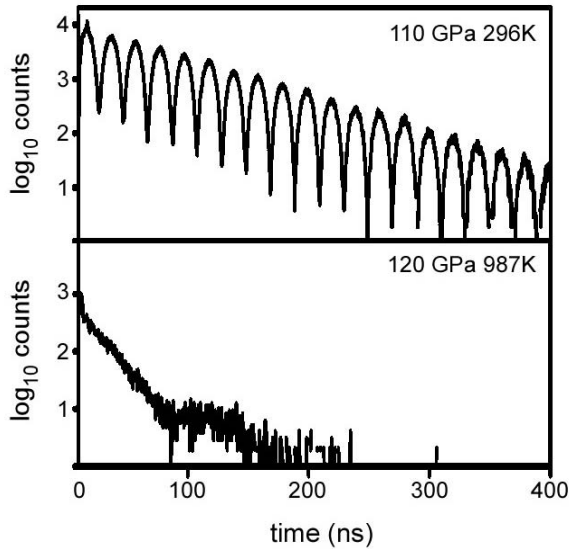


Fig. 3.1-8: Comparison of nuclear forward scattering data of (Mg,Fe)SiO<sub>3</sub> perovskite containing predominantly intermediate-spin Fe<sup>2+</sup> (top) (high quadrupole splitting = high quantum beat frequency) with predominantly low-spin Fe<sup>2+</sup> (bottom) (low quadrupole splitting = low quantum beat frequency). We observed that the proportion of low-spin Fe<sup>2+</sup> increased relative to intermediate-spin Fe<sup>2+</sup> abundance with increasing temperature.

The intermediate-spin to low-spin transition of Fe<sup>2+</sup> in silicate perovskite likely involves an increase in density, and would thus compete thermodynamically and kinetically with the structure transition to the post-perovskite phase. The perovskite structure could therefore be stabilised to higher pressures within the low-spin stability region (Fig. 3.1-9), which could produce a layer at the base of the lower mantle containing low-spin Fe<sup>2+</sup>. Lateral temperature variations within D'' could change the spin-state population, which would influence physical and chemical properties more profoundly than previously estimated. Also, calculations of heat flow based on a double crossing of the pv-ppv phase boundary would be affected by the spin transition, since the perovskite phase adjacent to the core would contain low-spin Fe<sup>2+</sup>.

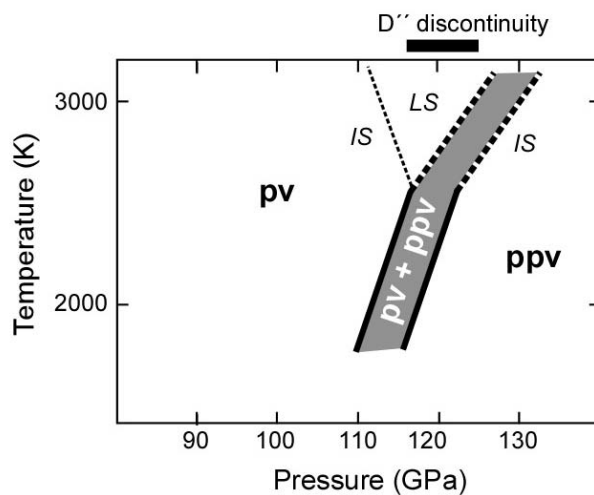


Fig. 3.1-9: Proposed phase diagram of (Mg,Fe)(Si,Al)O<sub>3</sub>. The perovskite (pv) to post-perovskite (ppv) phase boundary for pyrolite (solid bold lines) [Ohta *et al.*, 2008, Earth Planet. Sci. Lett. 267: 107-117] may be deflected to higher pressures (dashed bold lines) due to an intermediate-spin (IS) to low-spin (LS) transition in the perovskite phase which stabilises the structure to higher pressures, leading to a layer of low-spin Fe<sup>2+</sup> silicate perovskite in the deep mantle.

**f.** *Thermal vs. elastic heterogeneity in high-resolution mantle circulation models (B.S.A. Schubert and H.-P. Bunge/München; G. Steinle-Neumann)*

Seismic tomography has revealed two robust features of lower mantle heterogeneity: One is a long wavelength fast seismic velocity anomaly in the circum-Pacific and regions under Asia, reflecting past subduction. Less certain is the origin of another feature consisting of two pronounced low seismic velocity anomalies located beneath the Pacific and under Africa. Hot buoyant mantle from a strong thermal boundary layer at the core-mantle boundary (CMB) would provide a straightforward explanation for these anomalies. However, several studies argue that these regions are characterized by a different bulk composition from the surrounding mantle. These observations have prompted geodynamicists to investigate the behaviour of mantle flow with compositional variations. However, relating temperature and compositional anomalies from mantle convection to seismic wave velocities depends on material properties of mantle minerals, and trade-offs between thermal and chemical effects have limited the identification of the cause of heterogeneity. Here we test in a forward modeling approach under what conditions geodynamic simulations for isochemical mantle composition (pyrolite) can result in elastic heterogeneity compatible with seismic observations. For the conversion of temperatures into elastic parameters we use a thermodynamic model of mantle mineralogy in the CFMAS system (CaO-FeO-MgO-Al<sub>2</sub>O<sub>3</sub>-SiO<sub>2</sub>), including information on the shear modulus.

We compute global mantle flow with the parallel finite element code TERRA, solving the momentum and energy balance at infinite Prandtl number (no inertial forces) in a spherical shell. The horizontal resolution is 30 km at the surface, and decreases to half that value at the CMB, while a uniform radial grid spacing of 25 km is applied. This fine grid allows us to explore large-scale mantle flow at earth-like convective vigor: we are able to resolve a characteristic thermal boundary layer thickness on the order of 100 km, comparable to that of oceanic lithosphere. We apply a an internal heating rate of  $6.0 \times 10^{-12} \text{ W kg}^{-1}$  throughout this study, roughly the chondritic value; thermal boundary conditions are constant temperature at the surface (300 K) and the CMB. The latter is chosen such as to produce models with weak or strong core heat flux. Here we focus on results that arise from two different models with core heat flux of 1.5 (M1) and 12 TW (M2), respectively (roughly 5 % and 35 % of the surface heat flow). Our radial viscosity profiles account for the lithosphere, the upper and the lower mantle, separated at 100 km and 660 km depth. At the surface, velocities are specified according to a plate motion history model. Finally, the temperature fields from the mantle circulation models are post-processed and mapped to seismic velocities using the thermodynamic model of mantle mineralogy. In this simple approach, phase transitions of upper mantle minerals are therefore incorporated in our elastic models, even though their dynamic effects on the flow are not included in the calculations.

The earth-like convective vigor produces a narrow, upper thermal boundary layer with a thickness of about 100 km, and correspondingly thin and elongated downwellings in regions

of plate convergence. A remarkable feature is the spontaneous emergence of the asthenosphere as a region of relatively uniform temperature with strongly reduced thermal heterogeneity (Fig. 3.1-10). This agrees well with petrological studies, which infer only minor melting temperature variations beneath the global mid-ocean ridge system.

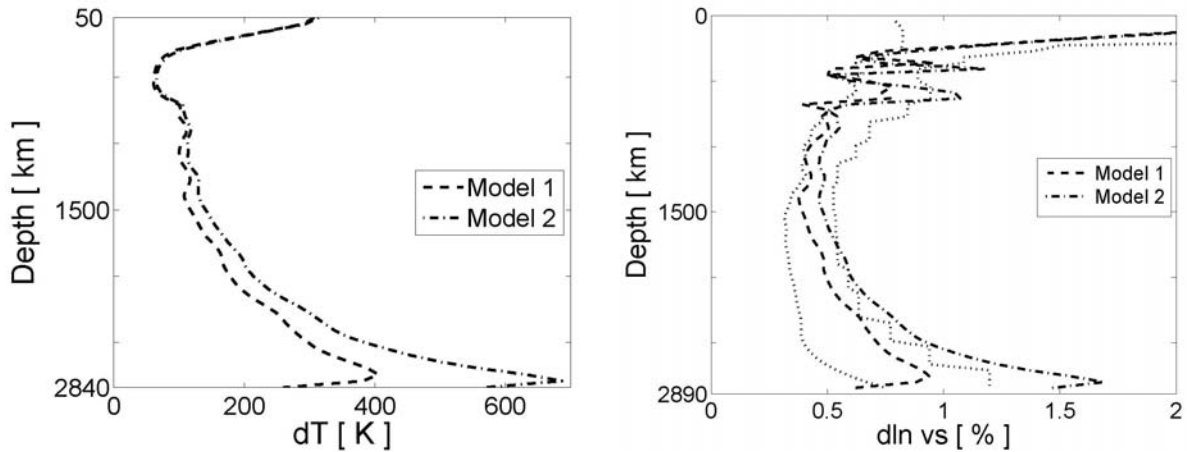


Fig. 3.1-10: Lateral variations (root-mean-square amplitudes) in temperature for the geodynamic models with low and high bottom heating (left) and corresponding variations in the shear wave velocities (right). For comparison with seismic tomography an envelope from seismic observations (dotted lines) is included.

In one-dimensional profiles relative variations in S-wave velocity (Fig. 3.1-10) mimic the shape of temperature variations, except for the transition zone, where changes in the transition depth of mineral phases cause large lateral variations in  $v_s$ . Variations in  $v_s$  occur at all length scales in the upper mantle, but only at long wavelengths in the uppermost lower mantle. This could be interpreted as a change in convection style. However temperature variations do not support this notion, as in the uppermost lower mantle fluctuations occur over a wider spectral range than in the upper mantle.

The most pronounced differences between M1 and M2 occur for hot anomalies, *i.e.*, plumes rising from the thermal boundary layer above the CMB. Model M1 with a low core heat flux and a correspondingly weak lower thermal boundary layer is characterized by low amplitude positive temperature variations with magnitudes less than 500 K. In contrast for M2 we see large positive values in the lower mantle and a strong decrease of plume excess temperatures as the material rises adiabatically in the otherwise subadiabatic mantle. In these models, hot anomalies are reduced from around 1000-1500 K at the CMB to 200-300 K in the upper mantle.

One robust property inferred from tomography is an increase in the root-mean-square (RMS) amplitude of seismic heterogeneity below 2000 km depth (Fig. 3.1-10), often taken as an indication for deep mantle chemical heterogeneity. In Fig. 3.1-10 we plot the envelope of

RMS profiles of four tomographic S-wave models, all of which show a gradual increase from a minimum in the mid-mantle to values of around 1 % close to the CMB. The geodynamic computed RMS profiles of  $v_S$  lie within these bounds for M1, and M2 gives larger values in the lowermost mantle. At the transition zone discontinuities, the RMS amplitudes of both models show strong variations and large values as noted before. Lower values and less variation in the tomographic models may be related to vertical smearing of heterogeneity from the transition zone into the uppermost lower mantle, where the geodynamic models show values at the lower bound.

### 3.2 Geochemistry

From knowledge of the depletions of siderophile (iron loving) elements in the Earth's mantle and measurements of the partition coefficients of these elements at high pressures and temperatures, an assessment can be made of the composition of the Earth's metallic core and the conditions under which it separated from the silicate mantle. The opening 6 studies in this section detail experiments and models designed to fulfil this aim with the first study proposing a model for the formation of the Earth that fits the available mantle chemical constraints and follows a scenario consistent with recent physical models for Earth's accretion. Uncertainties in element partitioning measurements at high pressures can be very large and extrapolation of the results to conditions of the core mantle boundary compounds these errors. These extrapolations can be made more rigorous, however, using constraints provided from simpler experimental measurements of properties, such as partial molar volumes, that act to control inter-phase partitioning, as reported in the third project in this section.

The next 3 studies examine the composition and behaviour of (Mg,Fe)O or ferropericlase, which is likely to be the second most abundant phase in the lower mantle. While the first of these examines the melting behaviour of ferropericlase the second deals with the partitioning of Fe and Mg between this phase and silicate perovskite, a topic of significant controversy in recent years. This new study, which also utilises a new analysis technique for these measurements, indicates that ferropericlase is likely to become progressively richer in Fe with increasing depth in the Earth's mantle. In the last of these three studies the  $\text{Fe}^{3+}/\text{Fe}^{2+}$  ratios of natural diamond inclusions of ferropericlase are examined. This ratio is found to be quite variable throughout the sample set, indicating significant heterogeneity in the redox state at which diamonds containing ferropericlase form.

The importance of carbon speciation and its behaviour in the Earth are underlined in the three following studies. The first two deal with the experimental determination of the redox conditions at which graphite or diamond in up welling mantle would become oxidised to form carbonate melts. This redox melting process may mark the onset of melting beneath mid ocean ridges but the experiments described in this study seem to indicate that this process may only occur at relatively shallow depths in the mantle. A further study in this carbon subsection deals with the decarbonation of carbonatitic magmas by defining the conditions in the mantle at which carbonate melts breakdown to release  $\text{CO}_2$ . This process may be important for metasomatism and for determining if carbonatite lavas have a primary mantle origin.

Towards the end of this section is a study on the speciation of phosphorous in the mantle. Garnet is found to be a major host for P in Earth's transition zone, however, the low solubility of P in lower mantle minerals forces the  $\text{Ca}_3(\text{PO}_4)_2$  mineral tuite to be the major host of P in the deep mantle.

The final two contributions in this section deal with sulphide ore-forming minerals. The first details the discovery of ubiquitous molybdenum sulphide inclusions in rhyolitic magmas from many localities. The saturation of the magma by  $\text{MoS}_2$  has important implications for the distribution of Mo-ore deposits around rhyolitic intrusions. The solubility of Mo in the melt phase could also be used as a probe to examine the conditions (*e.g.*,  $f\text{O}_2$ ,  $f\text{S}_2$ ) at which Mo-deposits formed, following a somewhat similar methodology to the studies of core formation described at the start of this section. The second of these contributions deals with the oxidation processes that lead to weathering of such sulphide ores and finds that redox reactions are controlled by microstructure and secondary phases at nanometer scale.

**a.** *Estimating the light element content of the Earth's core from models of core formation (D.C. Rubie, D.J. Frost and K. Tsuno, in collaboration with Y. Asahara/Hyogo, U. Mann/Zürich, P. Kegler and A. Holzheid/Kiel, H. Palme/Köln)*

It has been known for about fifty years that the Earth's metallic Fe-Ni core contains approximately 10 wt.% light elements, with possible candidates being S, O, Si, C, N, and H. Knowledge of the light element content is crucial for understanding compositional convection that is considered to play an major role in generating the Earth's magnetic field. Because chemical interaction between the core and mantle has likely been very limited during Earth's history, the light element content is expected to have been established by chemical reactions between liquid metal and liquid silicate during core formation. We estimate the concentrations of oxygen and silicon in the core through a new multi-stage model of core formation that is constrained by the concentrations of both siderophile and lithophile elements in the Earth's mantle (in particular, Fe, Ni, Co, W, Si, V, Nb, Ta and Cr). The Earth accretes through a series of collisions with smaller planetary bodies that had already differentiated. Each impact results in a magma ocean in which the core of the impactor reequilibrates with silicate liquid at pressures that increase during accretion, *e.g.*, from 3 to 90 GPa, before merging with the Earth's proto-core. The bulk compositions of the proto-Earth and impactors are chondritic with oxidation states (*i.e.*, bulk oxygen contents) that can be varied. The compositions of coexisting liquid metal and liquid silicate in the magma ocean are determined by mass balance calculations that are based on experimental determinations of the metal-silicate partitioning of FeO and Si, together with a range of trace elements including Ni, Co, V, Cr, Ta and Nb. The partitioning behaviour of FeO is particularly crucial because it determines the oxygen fugacity for a given bulk composition. Our newly-developed thermodynamic model for FeO partitioning is consistent with experimental data obtained up to > 100 GPa and shows that partitioning has a compositional dependence, particularly at pressures greater than 25 GPa.

Models that reproduce mantle geochemistry best involve heterogeneous accretion in which the oxygen content of the accreting material increases, thus causing oxygen fugacity to increase as the Earth grows. Specifically, the initial 70-80 % of the Earth accretes from highly reduced material (with an oxidation state comparable to that of enstatite chondrites). The FeO

content of the silicate material is initially extremely low but increases during accretion and differentiation as Si dissolves into the proto-core (Fig. 3.2-1). The final 2-3 giant impacts involve the accretion of much more oxidised material in order to achieve the current mantle FeO content of 8 wt.%. In addition, during the final few impacts only a fraction (10-30 %) of the metallic cores of the impactors reequilibrate with the silicate magma ocean at high pressure – which would be the consequence of becoming only partially emulsified in the magma ocean following the impact. Results predict that Si is the dominant light element in the core (8-9 wt.%) and that the oxygen content is very low (< 1 wt.%). Together with ~ 2 wt.% S, these concentrations are sufficient to satisfy recent estimates of the density deficit of the outer core.

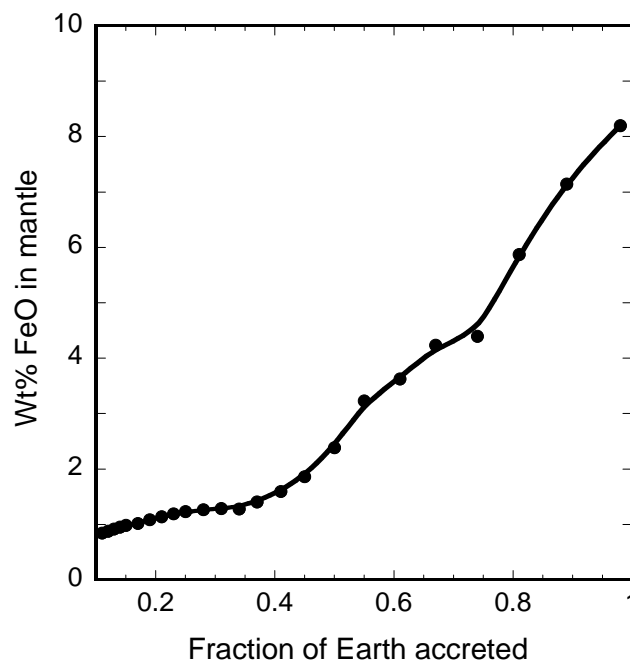


Fig. 3.2-1: Evolution of the FeO content of the mantle during accretion. The initial increase in FeO content is caused by Si dissolving progressively into the core. During accretion of the final 20 % of the Earth, the FeO content increases to its current value of 8 wt.% as a consequence of the final giant impactors being relatively oxidised. Each symbol represents the accretion of a new impactor.

**b. Partitioning of oxygen between ferropericlase and liquid Fe-Ni-S alloy at high pressures and temperatures (K. Tsuno, D.J. Frost and D.C. Rubie)**

The Earth's outer core is composed of liquid Fe-Ni alloy together with approximately 10 wt.% light elements. Oxygen is one of the potential light elements in the core based on the results of previous experimental studies of the partitioning of oxygen between ferropericlase and liquid Fe(-Ni) at high pressures and temperatures (*e.g.*, Tsuno *et al.* 2007, BGI Annual Report, page 34). Sulphur is also a potential light element because it is more depleted in the Earth's mantle than other elements of similar volatility, implying that some amount of sulphur (*e.g.*, ~ 2

wt.%) resides in the core. In this study, we have investigated the partitioning of oxygen between ferropericlase and liquid Fe-Ni-S at high pressures and temperatures in order to clarify the effects of sulphur on the partitioning behaviour.

High-pressure experiments were conducted using a 1000-ton multianvil apparatus at pressures of 15-24.5 GPa and a temperature of 2473 K. Metallic starting compositions were (1) Fe containing 0-20 wt.% S and (2) Fe-10 wt.% Ni containing 0-20 wt.% S, to which 1.5 wt.% O was also added. Both starting compositions were run simultaneously in each experiment in double-chamber polycrystalline MgO capsules which reacted with the liquid metal to form ferropericlase during the experiments. Evaluation of oxygen partitioning is described by

$$K_d = \frac{X_O^{metal} X_{Fe}^{metal}}{X_{FeO}^{ferropericlase}}$$

where  $X_O^{metal}$  and  $X_{Fe}^{metal}$  are the mole fractions of O and Fe in the metal, respectively, and  $X_{FeO}^{ferropericlase}$  is the mole fraction of FeO in ferropericlase.

Figure 3.2-2 shows the  $\ln K_d$  values between ferropericlase and liquid Fe(-Ni)-S as a function of sulphur content. The value of  $K_d$  clearly increases with increasing sulphur content, but the effect of pressure is weak. These results imply that the proportion of oxygen that may have partitioned into Earth's core may be slightly higher than previous estimates that were based on sulphur free experiments.

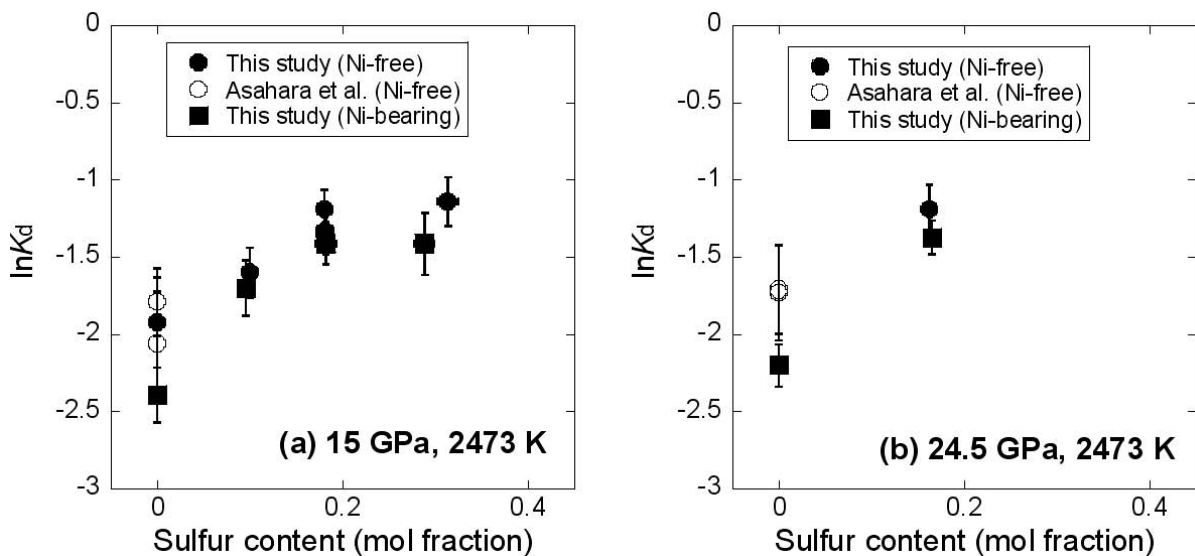


Fig. 3.2-2: The relationship between  $\ln K_d$  and sulphur content of the liquid metal at 2473 K and pressures of (a) 15 GPa and (b) 24.5 GPa. The data from this study are plotted as filled circles (partitioning between ferropericlase and liquid Fe-S) and filled squares (ferropericlase and liquid Fe-Ni-S). Values of  $\ln K_d$  between ferropericlase and pure liquid Fe from our earlier study (Asahara *et al.* EPSL 257, 435, 2007) are also shown as open circles.

c. *A model to describe the FeO content of the mantle at the core mantle boundary (D.J. Frost and D.C. Rubie, in collaboration with Y. Asahara/Hyogo)*

Oxygen is a potential light alloying element in the Earth's outer core. The Fe-FeO system is the simplest through which to understanding and model the oxygen content of liquid Fe metal. In this study experimental results on the oxygen contents of coexisting immiscible metallic and ionic liquids in the Fe-FeO system have been used to extract thermodynamic properties that describe oxygen solubility, and FeO activities in Fe metal as a function of pressure and temperature. These properties have been used to independently calculate oxygen partitioning in the Fe-Mg-O system, whereby reactions between ferropericlase, a proxy for the Earth's silicate mantle, and O-bearing liquid metal can be assessed.

Multianvil experiments on the miscibility gap between liquid metallic Fe and liquid FeO have been performed to pressures of 25 GPa (see annual report 2007). These results show that the miscibility gap closes with both increasing pressure and temperature. By fitting a thermodynamic model to these results the activity composition relations of the FeO component in metallic Fe liquid can be determined as a function of P and T. By equating the chemical potential of FeO in both liquid Fe and ferropericlase, a thermodynamic equation can be written to determine the FeO content of metallic liquid as a function of P,T and the FeO content of ferropericlase. A crucial term in the equations is the difference in the standard state chemical potential for pure FeO in both liquid Fe and ferropericlase. This term can be derived using data on the melting curve of FeO, which has been studied up to 80 GPa.

In Figure 3.2-3a curves calculated for the O  $K_d$  (where  $K_d = X_O^{metal} X_{Fe}^{metal} / X_{FeO}^{Mw}$  and  $X_{FeO}^{mw}$ ,  $X_{Fe}^{met}$  and  $X_O^{met}$  are the mole fractions of FeO in ferropericlase and Fe and O in liquid metal respectively) are calculated using this model and are shown to be in very good agreement with experimental data from the multianvil. In Figure 3.2-3b the model is compared with laser heated diamond anvil cell results with curves calculated for the ferropericlase compositions of the individual experiments. Below 25 GPa the model predicts that  $K_d$  is independent of composition, but above 25 GPa  $K_d$  becomes strongly dependent on the ferropericlase FeO-content. In Figure 3.2-3b , for example, the curve calculated at 3500K for a ferropericlase Fe/(Fe+Mg) ratio of 0.19 flattens out and crosses beneath that calculated for a lower temperature and lower ferropericlase Fe content. This behaviour is mirrored exactly by the experimental data with which the model is in excellent agreement, even though it has been derived completely independently.

In Figure 3.2-4 the model is extrapolated to conditions of the core mantle boundary (136 GPa) in order to calculate the Fe/(Fe+Mg) ratio of ferropericlase as a function of the oxygen content of the core. Estimates for the temperature at the boundary range between 3500-4500 K and if oxygen is the sole cause of the core's density deficit the oxygen content of the core would need to be in the range 6-9 wt.%. The Fe/(Fe+Mg) ratio of ferropericlase in the mantle

in equilibrium with this core O content is 0.02-0.08 over the estimated temperature range, which is far below that expected for the bulk of the mantle. The mantle at the core mantle boundary will consequently become depleted in FeO in order to achieve local equilibrium with the core.

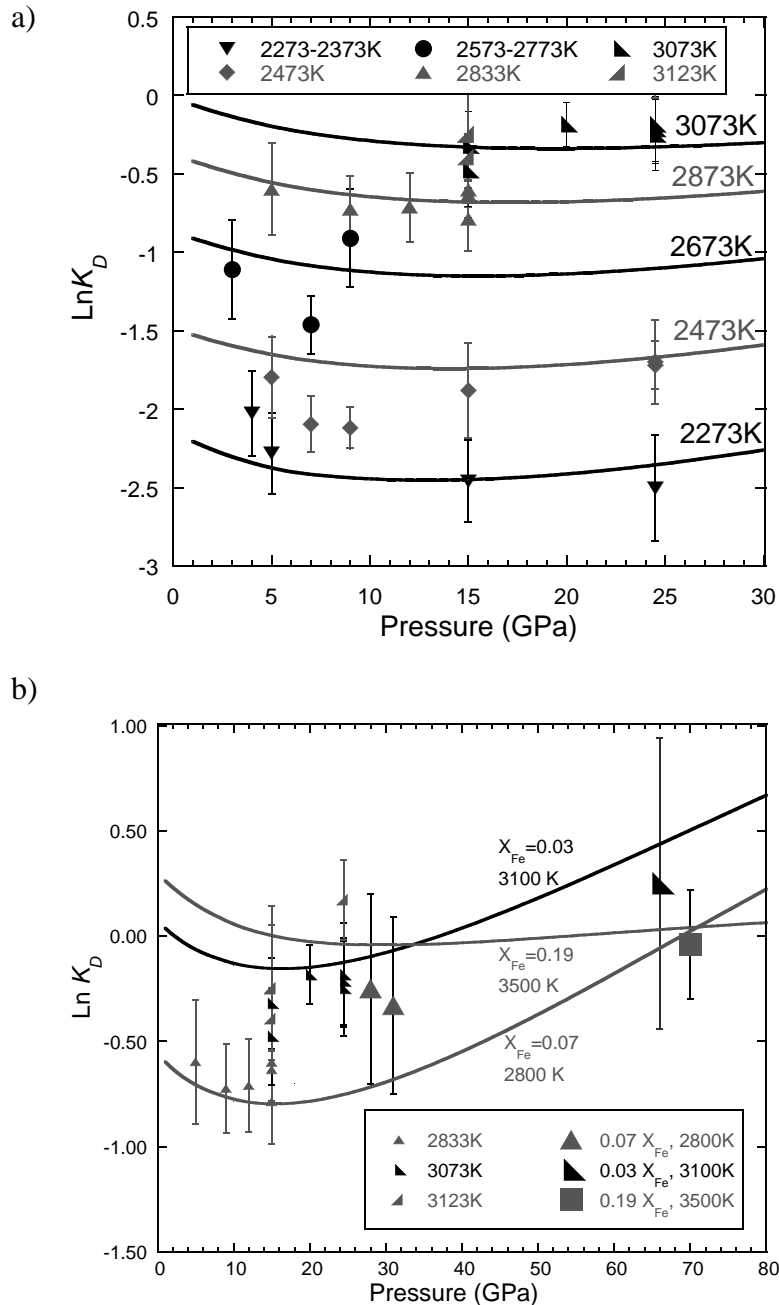


Fig. 3.2-3: Oxygen distribution coefficients calculated with the thermodynamic model described in the text (solid curves) are compared with experimental multianvil data in **a)** and with laser heated diamond anvil cell data in **b)**, where model curves are calculated for the individual experimentally-observed ferropericlaste Fe/(Fe+Mg) ratios. At high pressure the model predicts that  $K_d$  becomes compositionally dependent, in good agreement with the experimental data.

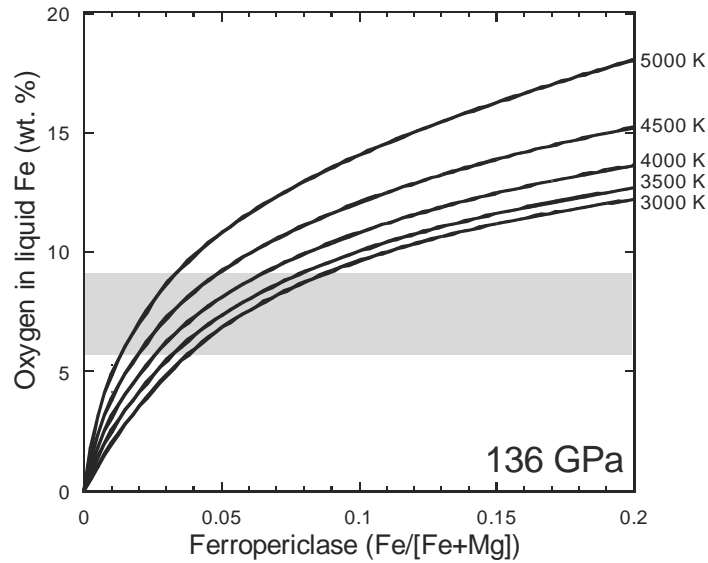


Fig. 3.2-4: The mole fraction of FeO in ferropericlasite at the core mantle boundary as a function of the oxygen content of the liquid outer core. The temperature at the core mantle boundary is likely to be in the range 3500-4500 K. The shaded region indicates the uncertainty in the oxygen content of the core if it is the only light alloying element. A layer of ferropericlasite at the core mantle boundary will become depleted in FeO compared to the bulk of the mantle in order to maintain equilibrium with the core.

**d.** *The oxygen content and temperature at the Fe-FeO eutectic (R. Pozzobon/Padova and D.J. Frost)*

Oxygen is a potential light element in the Earth's outer core. At the ambient pressure eutectic melting point between Fe and FeO solid Fe contains less than 0.01 wt.% O, while liquid Fe contains less than 0.2 wt.%. As a result of the low O concentration the eutectic temperature is only 14 °C lower than the melting temperature of pure Fe at these conditions. In the literature it is reported, however, that at 16 GPa the eutectic liquid contains approximately 3 wt.% O and as a result the eutectic temperature is over 250 °C below the melting temperature of pure Fe. The solubility of O in solid metal even at high pressure is very low, however, which means that if O is in the liquid outer core it can explain why the Earth's solid inner core has a much smaller light element density deficit. In this study we are attempting to examine the melting phase relations in this system as a function of pressure in order to refine a thermodynamic model that can ultimately describe the partitioning of O between the inner and outer core.

Samples of Fe mixed with FeO in varying proportions were placed in double Al<sub>2</sub>O<sub>3</sub> capsules made of two-hole thermocouple ceramic. In each experiment we included a sample of FeO containing 10 or 20 wt.% Fe and a sample of Fe containing either 10 or 20 wt.% FeO. Samples were run in the multianvil apparatus at 7 and 10 GPa and at temperatures between 1700 °C and 1500 °C. In addition experiments on pure Fe metal were performed by placing samples of Fe rod in an MgO capsule that was further encapsulated in molybdenum foil, to

ensure the exclusion of oxygen. After recovering the samples they were polished for analysis with scanning electron microscopy and the electron microprobe.

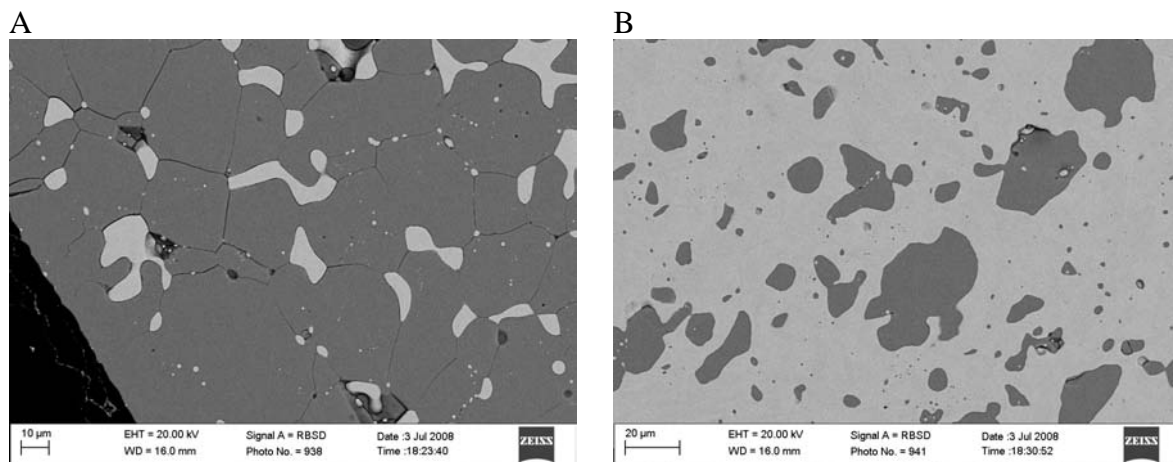


Fig. 3.2-5: Back scattered electron images showing two samples containing different proportions of solid FeO (dark) and liquid Fe from the same experiment performed at 11 GPa and 1500 °C.

Figure 3.2-5 shows a back-scattered electron image of two samples from a pressure of 11 GPa and 1500 °C. One sample contained excess FeO and only 10 wt.% Fe while these proportions are reversed in the other sample. Melting textures within the charges were difficult to interpret in some instances. In Figure 3.2-5A it is quite clear that solid FeO displaying equilibrium triple junctions coexists with lesser amounts of liquid Fe metal that is trapped at grain boundaries. In Figure 3.2-5B, however, solid grains of FeO in the liquid Fe matrix appear rounded and might be interpreted as molten if considered in isolation.

The resulting bracket of the Fe-FeO eutectic melting point at 11 GPa occurs at a nominal thermocouple temperature of 1580 °C. However, we bracketed the melting point of pure Fe at the same pressure at approximately 1700 °C, which is 170 °C below the published melting curve of pure Fe. The cause of this discrepancy is at present unclear; however, this means that the eutectic is actually only ~ 100 °C below the pure Fe melting point at 11 GPa. The smaller depression in the eutectic compared to previous studies is in better agreement with the expectations of simple freezing point depression calculations based on the O content of the liquid.

*e. Carbon solubilities in metal and silicate liquid at high pressure and high temperature (V. Malavergne and R. Combes/Marne La Vallée, in collaboration with D.J. Frost, J.P. Gallien/Saclay and H. Bureau/Paris)*

Metal-silicate segregation took place in many planetary bodies during the early history of the solar system. The Earth's core is likely enriched in light elements but the nature of this light

element is still unknown. The most probable candidates for the Earth are: Si, O, S, H and C but the answer depends on the exact conditions of the core formation process. C is the fourth most abundant element in the solar system. C is also known for its high solubility in Fe-Ni alloys at high pressure (HP) and high temperature (HT). Several HP-HT studies have tried to evaluate the likelihood that C partitioning into the core through studies of its effect on elemental partitioning behaviour, by examining metal-carbonate reactions with Si or S, or through measurements of the solubility of C in metallic alloys. None of these studies, however, have benefited from direct C measurements. Direct analysis with classical techniques (such as electron or ion microprobes) are complicated because of (i) the deposition of C on the sample by the beam, resulting in an artificial increased of its concentration, (ii) lack of reliable and homogeneous C standards. The present study attempts to evaluate the solubility of carbon in metallic and silicate phases at HP-HT employing a less classical technical: the nuclear microprobe of the Laboratoire Pierre Süe, CEA Saclay (France). This microprobe has the major advantages of being independent of the C deposition (because its beam probes deeper into the sample) and the choice of the standards is less critical than with electron or ion probes.

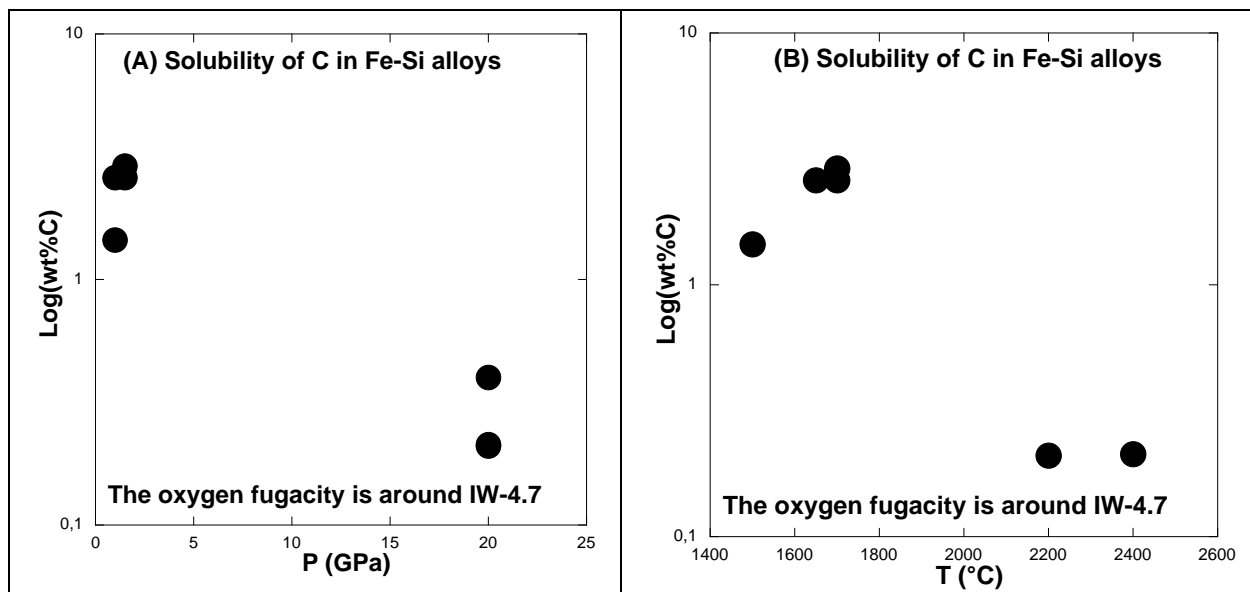


Fig. 3.2-6: C solubility in Fe-Si alloys as a function of pressure (A) and temperature (B).

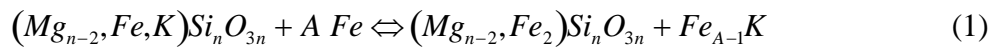
Our preliminary results indicate that C solubility in metallic phases decreases at HP-HT (Fig. 3.2-6). These results suggest that: (i) the solubility of C in Fe-S phases shows no obvious correlation with P, T or  $fO_2$ . Its limit is very low, well below 1 wt.%. (ii) the solubility of C in Fe-Si alloys shows a light correlation with P, T compared to the Fe-S phases. Its limit is high at 1 GPa (between 3 and 1.5 wt.%) and decreases at 20 GPa to around 0.3 wt.% (Fig. 3.2-6). These first results confirm that the association of Si and C as light elements in the Earth's core is more likely than the association of S and C. Recent experiments performed at 5, 10 and 15 GPa, are awaiting analysis.

**f.** *Ab initio predictions of potassium partitioning between iron and (Mg, Fe)SiO<sub>3</sub> perovskite and post-perovskite (K.K.M. Lee/New Haven, in collaboration with G. Steinle-Neumann, S. Akber-Knutson/San Diego and D. Dolejš/Prague)*

The core, although relatively simple in constitution, is a vast inaccessible part of the Earth. Comprising ~ 15 % of the Earth's volume and ~ one-third of its mass, the core is composed of an iron-rich (Fe-) alloy that must contain some light element(s) to account for its density. In addition to various light elements, the core has often been considered to host other geochemically important elements, including noble gases and radiogenic isotopes. Recent research has inferred high solubility of potassium (K) in iron at high pressures and temperatures, allowing for the possibility of a core reservoir of the important radiogenic isotope <sup>40</sup>K. Energy from radioactive decay of <sup>40</sup>K in the core could be important for driving the geodynamo and mantle dynamics. In order to assess the possibility of such a reservoir partitioning of K between the rocky mantle and iron-rich core both during core formation and at current is of great importance to the thermal state and history of Earth's deep interior.

In this study, we test the partitioning of K between the major silicate phase of the Earth's mantle, an Fe-bearing MgSiO<sub>3</sub> perovskite (pv) and its high-pressure polymorph post-perovskite (ppv), and pure iron by means of density-functional theory-based (DFT) computations. We use the generalized gradient approximation (GGA) for exchange and correlation in all of our computations. We use the projector augmented wave method (PAW) as implemented in the Vienna *Ab initio* Simulation Package (VASP). For the iron-bearing silicates, we perform spin-polarized computations.

To determine how potassium partitions between iron and the silicate we compute the Gibbs free energy difference at static conditions (*i.e.*, enthalpy) for the equilibrium reaction,



where n is either 16 or 32 for an 80 or 160-atom silicate supercells, and A is the size of the Fe-K supercell (24, 32, 48 or 96). The distribution coefficient of potassium  $K_D$  between iron and the silicate phase (either pv or ppv) is

$$K_D(pv \text{ or } ppv, Fe) = \exp\left(\frac{-\Delta G}{k_B T}\right) = \frac{(x_{K,pv \text{ or } ppv})(1 - x_{K,Fe})}{(x_{K,Fe})(1 - x_{K,pv \text{ or } ppv})} \quad (2)$$

We find that for all K concentrations and entire pressure range tested, K is energetically favored to remain in the pv or ppv (Mg<sub>n-2</sub>FeK)Si<sub>n</sub>O<sub>3n</sub> rather than enter the Fe supercell (Fig. 3.2-7). Our results imply that very little potassium is partitioned into iron over an iron-bearing MgSiO<sub>3</sub> in either pv or ppv forms, making the core an unlikely potassium reservoir in the Earth's interior.

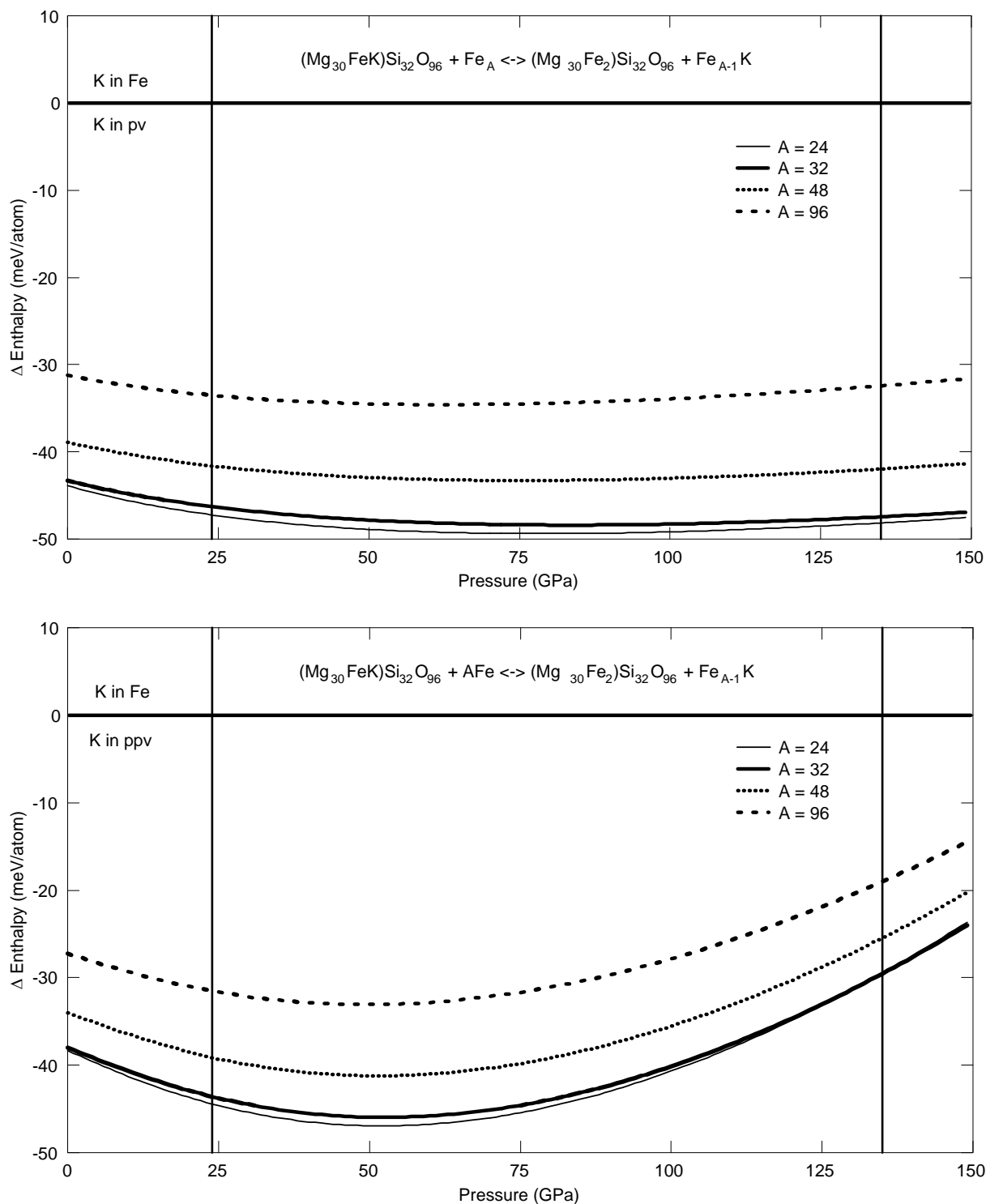


Fig. 3.2-7:  $\Delta H$  per atom versus pressure for the 160-atom reaction:  $(\text{Mg}_{30}\text{FeK})\text{Si}_{32}\text{O}_{96} + \text{AFe} \leftrightarrow (\text{Mg}_{30}\text{Fe}_2)\text{Si}_{32}\text{O}_{96} + \text{Fe}_{A-1}\text{K}$  for perovskite (Top) and post-perovskite (Bottom). Thin solid lines correspond to an iron supercell size  $A = 24$ , thick solid lines ( $A = 32$ ), dotted lines ( $A = 48$ ) and dashed lines ( $A = 96$ ). Negative  $\Delta H$  values correspond to K remaining in the silicate structures, whereas positive values correspond to energetically favorable K in Fe. Two vertical lines correspond to the pressures of the upper-lower mantle ( $\sim 24$  GPa) and core-mantle boundary ( $\sim 136$  GPa).

**g. Melting of ferropericlase at lower mantle conditions (J. Pickles, K. Tsuno and D.J. Frost)**

Ferropericlase is an important mineral phase in the Earth's lower mantle. Studying the melting of ferropericlase is important for two reasons. Firstly, if the two-phase region between FeO-MgO liquid and solid can be studied as a function of composition and temperature over a wide enough compositional range then the results can be extrapolated to determine the melting temperature of pure MgO. Large discrepancies exist between experimental and theoretically determined MgO melting curves at high pressures with differences of over 2000 °C between studies. Secondly the melting of FeO-MgO represents an important chemical join in the study of deep melting phase relations applicable the crystallization of a terrestrial magma ocean. In this study the melting of MgO-FeO has been studied as a function of temperature at 25 GPa. In addition, however starting materials were mixed with Fe metal in order to ensure the ferric Fe content of FeO-rich liquids remained low. This, however, led to the creation of miscible Fe-FeO-MgO liquids, which have interesting chemical properties and some implications for core formation.

Samples of FeO powder, reduced from Fe<sub>2</sub>O<sub>3</sub> in a gas mixing furnace, mixed with either 10, or 50 mol.% Fe were placed inside single crystal MgO capsules. The capsules were placed inside a LaCrO<sub>3</sub> heater in a 10/4 multianvil assembly. Experiments were performed at 25 GPa and temperatures between 2000-3000 K. Recovered samples were polished for analysis with the electron microprobe and scanning electron microscope.

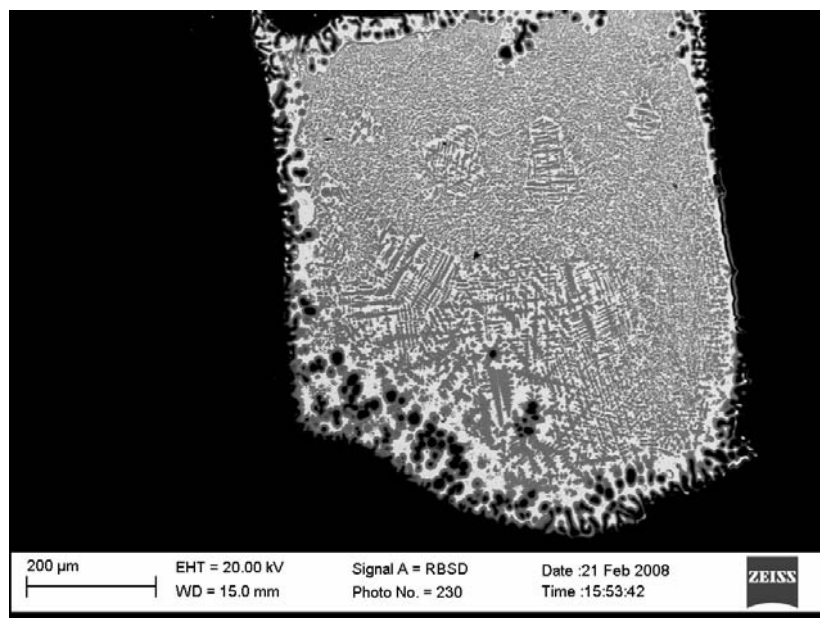


Fig. 3.2-8: Back scattered electron image showing a quenched 1:1 mixture of Fe-FeO liquid inside an MgO capsule (black). The capsule has become an MgO-FeO solid solution at the boundary. Small rounded crystals of MgO-FeO that were likely solid during the experiment can be seen at the boundary of the capsule.

Figure 3.2-8 shows a recovered sample from 2500 K and 25 GPa. The starting material was a 1:1 mixture of FeO and Fe. During the experiment FeO from the liquid sample dissolves into the MgO capsule to create an MgO-FeO solid solution. The liquid crystallizes on quenching but the texture indicates that a single Fe-FeO liquid existed at the conditions of the experiment. This means that the large miscibility gap between ionic FeO liquid and metallic Fe liquid that exists at one bar is completely closed at these conditions and a single miscible liquid exists between Fe metal and FeO. In addition this liquid also contains approximately 0.4 mol.% MgO. The MgO content of the liquid is does not vary as a function of the metallic Fe content of the liquid and increases only very slightly with temperature up to 0.7 mol.% at 2700 K. The coexisting ferropericlase increases in MgO content very strongly with temperature to over 70 mol.% at 2700 K. This results in a very wide compositional two phase region shown in Fig. 3.2-9 which is quite different in shape to that observed by Zhang and Fei [GRL, 35,L13302, 2008] in a similar study performed to 7 GPa. The Fe-Mg exchange coefficient  $(Fe/Mg_{liquid}) / (Fe/Mg_{solid})$ , for example, is greater by one order of magnitude at 25 GPa compared to 7 GPa. This indicates very strong non-ideality in the mixing between MgO and FeO at high pressures that may be related to the metallization of FeO. Further experiments performed at 3000K await analysis, however, the very low liquid MgO contents imply that the melting curve of pure MgO is likely to be at much higher temperature than that reported in laser heated diamond anvil cell experiments.

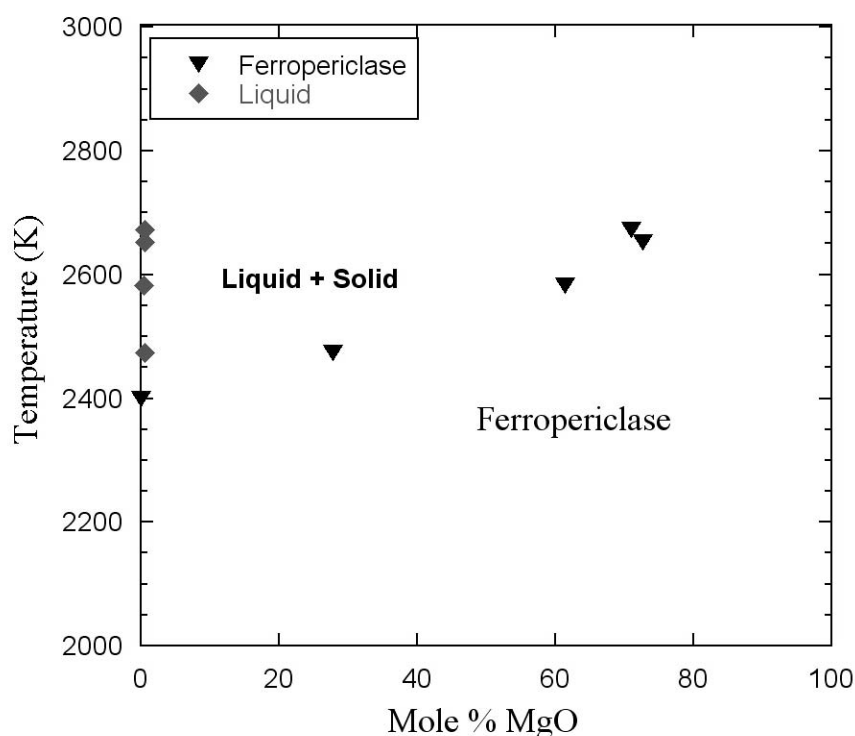


Fig. 3.2-9: Coexisting ferropericlase and liquid compositions at 25 GPa as a function of temperature. While the ferropericlase composition increases strongly in MgO content with temperature the coexisting liquid contains very low levels of MgO. The extremely asymmetric two phase region is quite different from that reported at lower pressure.

**h.** *In situ* study of iron partitioning between ferropericlase and silicate perovskite at conditions of the Earth's lower mantle (L.S. Dubrovinsky, O. Narygina, X. Wu and G. Aquilanti, in collaboration with S. Pascarelli/Grenoble)

One of the major goals in geosciences is the study of the dynamics of the solid Earth and the properties of each of Earth's reservoirs. This requires a detailed knowledge of the properties of the main mineral phases which compose the Earth's mantle, core, subducting slabs and ascending plumes at pressure and temperature conditions that may exceed 150 GPa and 5000 K, respectively. The study of chemical reactions in complex systems approaching natural rocks at conditions prevailing in the Earth's interior is essential to model the mineralogy and the chemistry of our planet. Although diamond anvil cells (DACs) coupled with laser heating techniques allow us to reach such thermodynamic conditions, the experiments at these conditions are usually associated with big challenges. These include: limited sample amount in the DAC (of the order of  $10^{-10}$  g), significant pressure and temperature gradients, and the fact that many phases are not quenchable. Moreover, pressure and temperature gradients give rise to a complex spatial distribution even inside the small volume of the DACs. A probe with a spatial resolution at the micrometer scale, a high chemical sensitivity and allowing *in situ* investigation would fulfill the constraints of such kinds of experiments.

Recently, the energy dispersive XAS beamline, ID24, has been used for  $\mu$ -XAS applications with a spatial resolution at the micrometer scale, resulting in two-dimensional XANES (X-ray absorption near edge structure) maps where each pixel contains full XANES information.  $\mu$ -XAS two-dimensional mapping has previously been used in fluorescence mode to investigate the abundance, redox state and speciation of iron in a natural rock thin sections. The small size and stable spot of  $5 \times 5 \mu\text{m}$  (FWHM) allows to probe small sample regions within the laser spot in DAC to characterize mineralogical transformations in the hottest region as well as along thermal and pressure gradients within the sample volume.

The determination of the (Mg,Fe) partitioning coefficient ( $K_{\text{Fe}}^{\text{Fp/Pv}}$ ) between ferropericlase (Fp) and silicate perovskite (Pv) is crucial to understand the composition and the physics of the lower mantle as well as the interactions between the lower mantle and the liquid core. Until now, the  $K_{\text{Fe}}^{\text{Fp/Pv}}$  values reported using different techniques remain strongly controversial, rendering a major aspect of mantle geochemistry essentially unconstrained. We show how 2D XAS mapping offers an alternative and unique tool to provide information on the partitioning between the Pv and Fp at high P and T.

As starting material, a natural sample of San Carlos olivine with  $(\text{Fe}_{0.12}, \text{Mg}_{0.88})_2\text{SiO}_4$  composition was used. Its chemical and phase homogeneity was confirmed by X-ray powder diffraction and microprobe chemical analyses. A double-sided polished, irregularly shaped sample of  $\sim 10 \mu\text{m}$  of thickness was loaded into a hole drilled into a Re gasket, together with two small (about  $2 \mu\text{m}$  in diameter) rubies. As pressure transmitting medium, Ar loaded under a pressure of 1.4 kbar was used. We employed diamonds of 1.6 mm height featuring culets of  $300 \mu\text{m}$  diameter. The sample in the DAC was compressed to pressures of 27-115 GPa, and three  $15 \times 15 \mu\text{m}^2$  areas of the sample were then double-sided laser heated to temperatures of

1700(50) K, 1950(50) K, and 2300(50) K using a YAG laser. At each pressure 2D  $\mu$ -XANES maps were collected and used for extracting information about the partitioning coefficient  $K_{\text{Fe}}^{\text{Fp/Pv}}$  (Fig. 3.2-10). Our data suggest that  $K_{\text{Fe}}^{\text{Fp/Pv}}$  significantly depends on pressure and temperature.

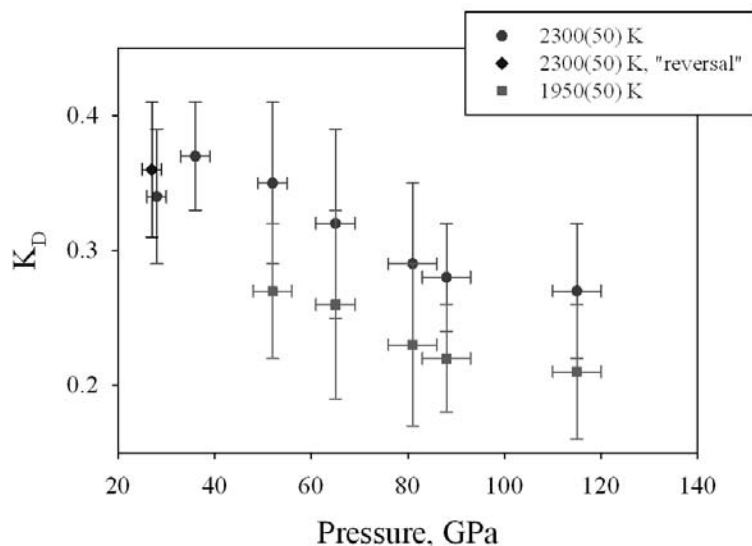


Fig. 3.2-10: Partitioning coefficient of iron ( $K_{\text{Fe}}^{\text{Fp/Pv}}$ ) between ferroperricite (Fp) and silicate perovskite (Pv), as determined by XANES spectroscopy for a natural sample of San Carlos olivine with  $(\text{Fe}_{0.12}, \text{Mg}_{0.88})_2\text{SiO}_4$  starting composition. "Reversal" means that the sample was heated at 81(3) GPa to 2300(50) K, then decompressed to 27(1) GPa and re-heated to 2300(50) K.

**i. Oxygen fugacity determined from iron oxidation state of (Mg,Fe)O ferroperricite in lower mantle diamond inclusions (M. Longo and C.A. McCammon, in collaboration with G. Bulanova/Bristol and F. Kaminsky/Vancouver)**

The most common mineral found in diamonds originating in the lower mantle is (Mg,Fe)O ferroperricite (more than 50 % of occurrences). Since it is well known that the  $\text{Fe}^{3+}$  concentration in (Mg,Fe)O is sensitive to oxygen fugacity, even at high pressure (see earlier BGI Annual Reports), determination of  $\text{Fe}^{3+}/\Sigma\text{Fe}$  in such inclusions provides a direct method for investigating lower mantle redox conditions during diamond formation. The goal of this study is to measure  $\text{Fe}^{3+}$  in (Mg,Fe)O lower mantle diamond inclusions from a wide range of sites worldwide in order to explore the variation of oxygen fugacity with chemical, physical and geographic parameters.

For the first part of the study we investigated four (Mg,Fe)O inclusions from Juina, Brazil and two inclusions from Machado River, Brazil. The composition of the inclusions ranges from  $x_{\text{Fe}} = 0.1$  to 0.3, and they contain varying amounts of Na and Cr. All of the inclusions are less than 50  $\mu\text{m}$  in diameter, which is too small for analysis using Mössbauer spectroscopy, so we used the flank method based on X-ray emission spectra analysis from the electron microprobe to determine  $\text{Fe}^{3+}$ . We updated our previous calibration (see BGI Annual Reports 2006 and 2007) based on synthetic (Mg,Fe)O samples to the following:

$$\text{Fe}^{2+} = 46.238 + 8.161 \cdot \ln(\Sigma\text{Fe}) - 137.01(L\beta/L\alpha) + 85.57(L\beta/L\alpha)^2 \quad R^2=0.9967$$

where  $\Sigma\text{Fe}$  and  $\text{Fe}^{2+}$  are in wt.%. Results for synthetic (Mg,Fe)O samples show good agreement with  $\text{Fe}^{3+}/\Sigma\text{Fe}$  determined by Mössbauer spectroscopy (Fig. 3.2-11).

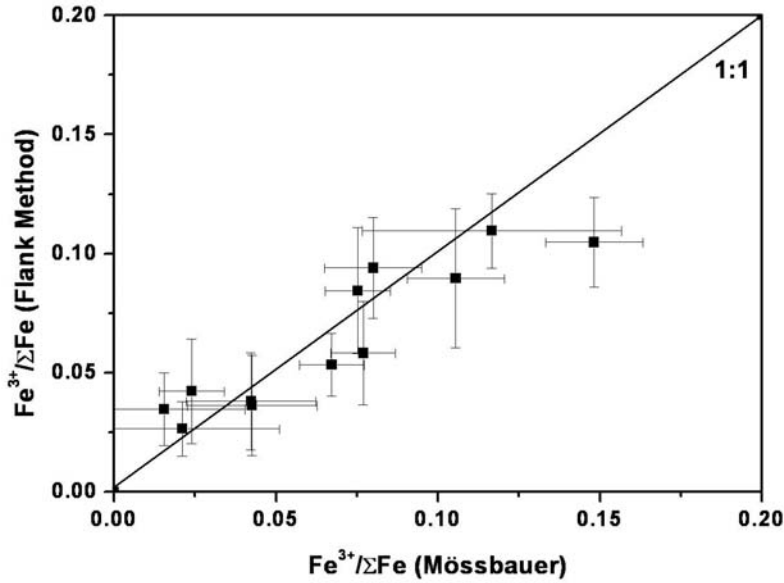


Fig. 3.2-11:  $\text{Fe}^{3+}/\Sigma\text{Fe}$  determined in synthetic (Mg,Fe)O crystals using the flank method according to equation (1) vs.  $\text{Fe}^{3+}/\Sigma\text{Fe}$  determined using Mössbauer spectroscopy.

We first examined the variation of the  $L\beta/L\alpha$  ratio with  $\text{Fe}^{2+}$  for the (Mg,Fe)O inclusions to test for phase homogeneity. Since the flank method shows high sensitivity to the chemical composition, the presence of extra phases affects the  $L\beta/L\alpha$  ratios. Our results for the (Mg,Fe)O inclusions show good agreement with the theoretical trend described by the synthetic samples (Fig. 3.2-12), which confirms high phase homogeneity for most of the samples. Only one of the inclusions plots slightly below the theoretical line, suggesting the presence of additional phase(s), which is most likely due to exsolution of magnesioferrite from (Mg,Fe)O.

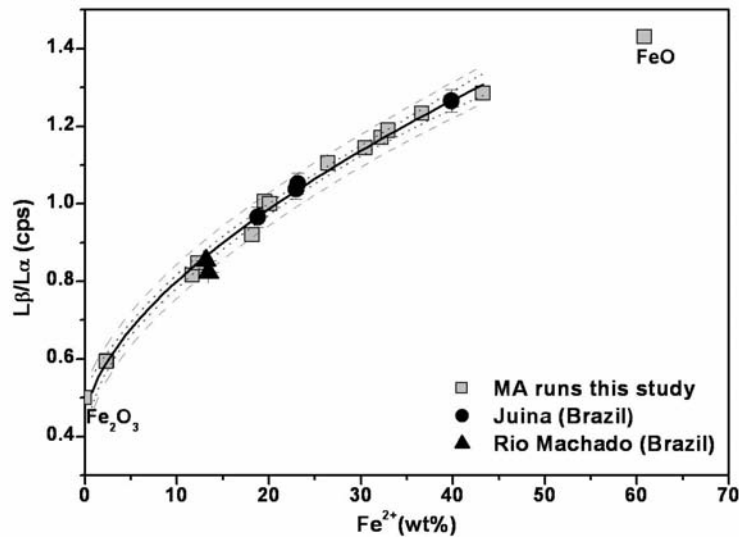


Fig. 3.2-12:  $L\beta/L\alpha$  ratio variation as a function of  $\text{Fe}^{2+}$  (wt.%) for (Mg,Fe)O inclusions from lower mantle diamonds compared to the theoretical trend for synthetic (Mg,Fe)O samples grown in multianvil (MA) experiments.

The deviation of data for (Mg,Fe)O inclusions from the 1:1 trend between monovalent and trivalent cations provides a measure of the number of vacancies required to balance charge in the structure (Fig. 3.2-13a), and the variation of these vacancy concentrations with total iron content provides a measure of oxygen fugacity (Fig. 3.2-13b). Our results show a large range of redox conditions, similar to results for a suite of much larger inclusions that were studied using Mössbauer spectroscopy (BGI Annual Report 2003). To improve the size of the dataset, further work is planned on 12 (Mg,Fe)O diamond inclusions from Australian Jurassic kimberlites.

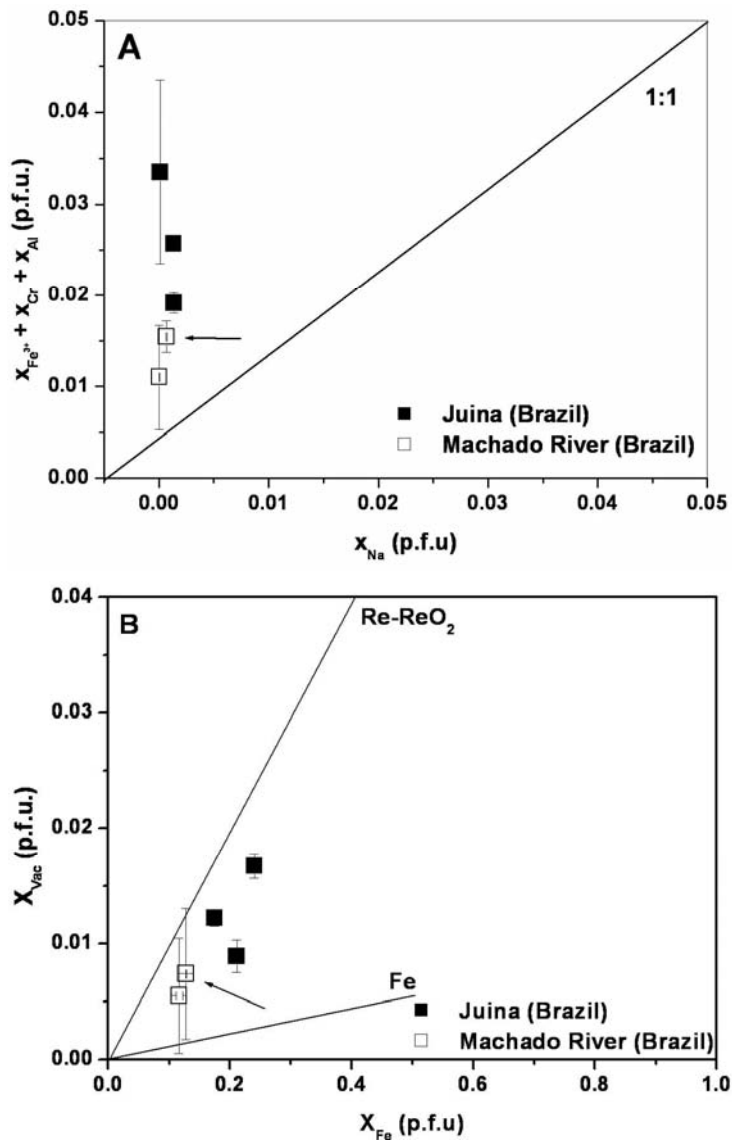
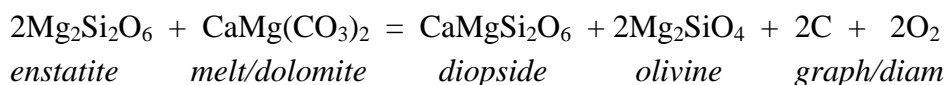


Fig. 3.2-13: a) Trivalent cation abundance versus Na abundance for (Mg,Fe)O inclusions in lower mantle diamonds, expressed in cations per formula unit. The 1:1 line represents stoichiometric charge balance. b) Cation vacancy concentration determined from Fig. 3.2-13a ( $= \frac{1}{2} (x_{Fe^{3+}} + x_{Al} + x_{Cr} - x_{Na})$ ) as a function of total iron content. The solid lines indicate the variations reported in the literature for Fe-(Mg,Fe)O and Re-ReO<sub>2</sub> equilibria. The arrow refers to the (Mg,Fe)O inclusion with possible ferrite exsolution.

**j. Carbonatites, kimberlites and diamonds in the Earth's mantle (V. Stagno and D.J. Frost)**

Carbonatites or carbonate-rich melts are likely to be the first liquids produced during mantle up-welling. There is evidence of deep melting in mid ocean ridges from seismological anomalies located beneath the East Pacific Rise. Although the formation of carbonate-bearing melts, including carbonatites and kimberlites, has been well studied in terms of solidus temperature, composition and volatile content, the role of the oxygen fugacity is generally overlooked. Naturally occurring xenolith assemblages of graphite or diamond in equilibrium with typical mantle assemblages imply seemingly widespread redox conditions in the Earth where carbonates would not be stable.

The aim of this study is to provide knowledge on the stability of carbon/carbonate equilibria with respect to oxygen fugacity up to conditions above the carbonated mantle solidus where the composition of the coexistent melt is also an important factor. Experiments are performed in the Fe-Ca-Mg-Si-C-O system. Mineral starting mixtures of olivine, enstatite, diopside, graphite, MgCO<sub>3</sub> and CaCO<sub>3</sub> were employed to make mixtures of the following equilibria:



where the oxygen fugacity consequently becomes dependent on the purity of the carbonate melt phase above the solidus. The oxygen fugacity imposed by the carbon - carbonate equilibrium was experimentally determined as function of pressure and temperature by using Ir-Fe alloy as a redox sensor based on the equilibrium,



where the Fe alloys with the Ir metal to equilibrate with the oxygen fugacity imposed by the equilibrium between carbonate minerals/melts and graphite/diamond during the experiments. The experiments were carried out in a multianvil apparatus at pressures from 3 to 24 GPa and temperatures from 1200-1550 °C. Textural observations of the run products were performed using a scanning electron microscope. The chemical composition of the melts and mineral phases were obtained using a Jeol JXA-8200 electron microprobe. The ferric iron contents of the iron-bearing solid phases were determined by <sup>57</sup>Mössbauer spectroscopy.

Results show that the measured redox conditions for Ca-free subsolidus assemblages at 3 GPa are in agreement with those determined by Eggler and Baker [High-Pressure Res. Geophys.

237-250, 1982] whereas, in the Ca-bearing system the  $fO_2$  is shifted of about 0.4 log units. However, the onset of melting drives the equilibrium oxygen fugacities down as the carbonate melt becomes silicate-rich with increasing temperature. As shown in Fig. 3.2-14, as the silicate content increases from 2 to 20 wt.% in the melt, the  $fO_2$  drops by approximately 0.8 log units at 3 GPa. With increasing temperature the melt composition shifts from carbonatitic to carbonate-silicate as a function of temperature and the increase of silica content in the melt follows a similar trend as reported in previous studies.

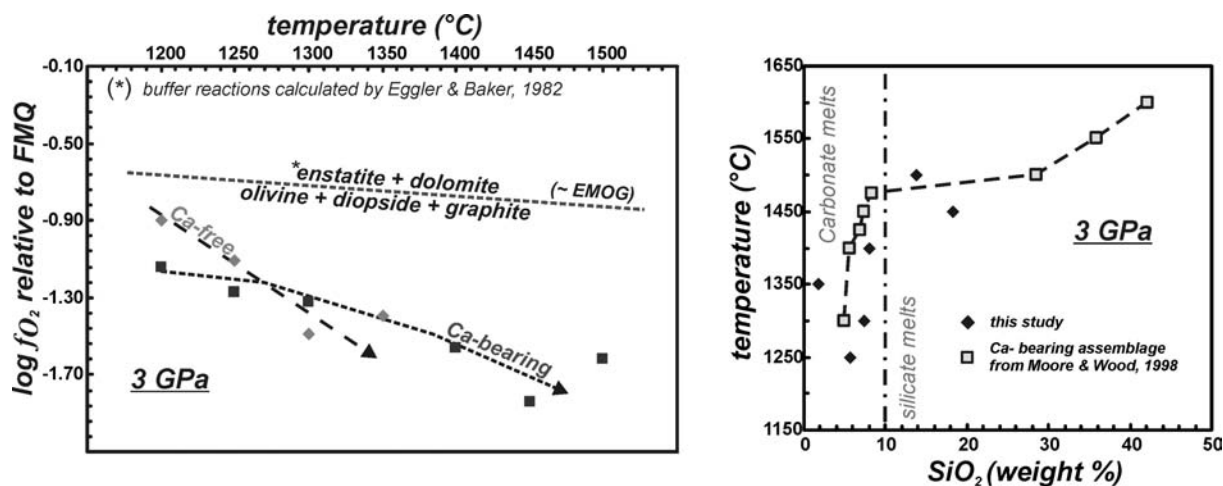


Fig. 3.2-14: (a) the  $fO_2$  of carbonate melt bearing assemblages in Ca-rich and Ca free systems as a function of temperature at 3 GPa.. (b) Melt  $SiO_2$  content increases from 2 wt.% at the solidus to 20 wt.% at 1400 °C. Determinations for the solid buffering assemblages from Egger and Baker [High-Pressure Res. Geophys. 237-250, 1982] are shown for comparison.

shows a negative trend as the temperature increases although, the presence of calcium seems to play an important role in order to stabilize the carbon phase at more oxidized values than the Ca-free harzburgitic assemblage. The melt exhibited a quenched texture and was compositionally inhomogeneous with a typical silica content of kimberlitic products to 20 - 30 wt.% (Fig. 3.2-15b).

The oxygen fugacity imposed by the equilibrium between carbonate minerals, melts and graphite/diamond in Ca-bearing and Ca-free systems has been determined also at 7 and 11 GPa with a synthetic garnet lherzolite and at 16 and 24 GPa into the stability field of wadsleyite and magnesiowüstite. Experimental results are compared to literature data on the  $fO_2$  recorded by garnet-bearing mantle xenoliths in Fig 3.2-16 with the following geological implications: (1) the measured  $fO_2$  values plotted versus depth seem to exclude the occurrence of carbonate-rich melts at depths greater than 100 km as argued in previous studies; (2) carbonate rich magmas of deep origin must originate from relatively oxidised mantle sources; (3) with increasing depth, the stability field of carbonates expands with respect to  $fO_2$ , which may limit diamond formation to regions between 160-700 km.

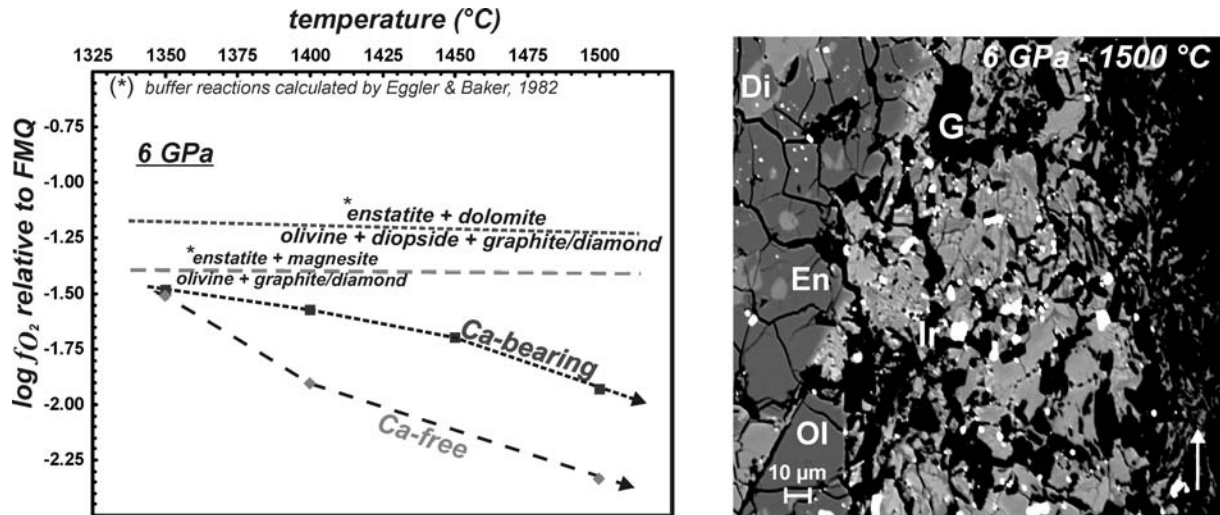


Fig. 3.2-15: (a) Experiments at 6 GPa plotting  $\log fO_2$  vs. T ( $^{\circ}C$ ) for the graphite/carbonate melt equilibrium in the Fe-Ca-Mg-Si-C-O (squares) and Ca-free system (diamonds). (b) Back scattered electron image of recovered enstatite (En), diopside (Di), olivine (Ol), Ir-Fe alloy (Ir), graphite (G) and quenched melt (light grey region) recovered at 6 GPa and 1500  $^{\circ}C$ .

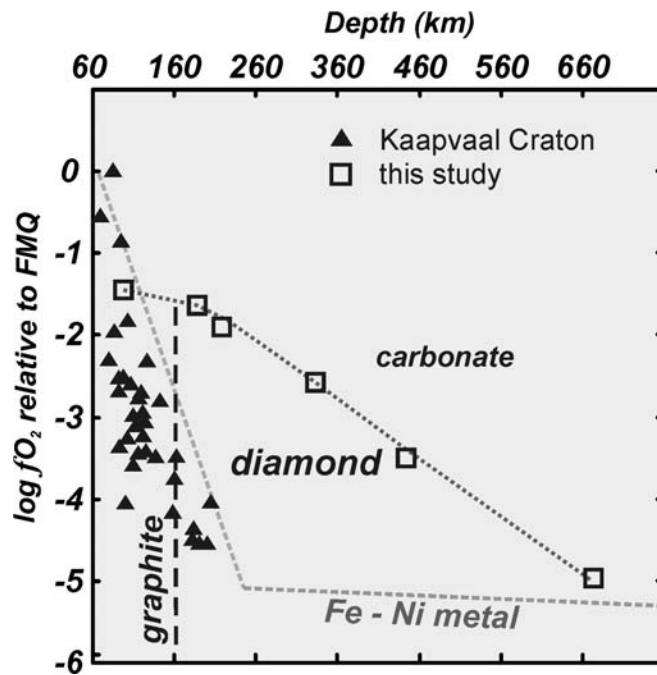


Fig. 3.2-16: The experimentally determined oxygen fugacity of the carbon - carbonate equilibria in a Ca-free system is shown as a function of depth (squares) compared to the  $fO_2$  calculated for garnet peridotite xenoliths from the literature (triangles). The vertical black dashed line indicates the graphite-diamond transition; the dashed grey line shows the predicted average mantle  $fO_2$ ; the dotted black line shows the boundary between the stability fields of carbon minerals and carbonate minerals and melts along an average mantle adiabat.

**k.**  $Fe^{3+}/Fe_{tot}$  measurements on garnets in equilibrium with carbon/carbonate phases (V. Stagno, C.A. McCammon and D.J. Frost)

The oxygen fugacity of the Earth's mantle can be determined by examining ferric and ferrous iron bearing mineral equilibria in mantle xenoliths. At depths below 50 km garnet-bearing assemblages are employed for this purpose through equilibria that consider the garnet end-member skiaigite  $Fe_3Fe_2^{3+}Si_3O_{12}$ , a component in natural garnets which has ferric and ferrous iron in octahedral and dodecahedral coordination respectively. The effect of pressure on the garnet-bearing equilibria should act to drive the oxygen fugacity down with increasing depth in the mantle, even if the bulk ferric Fe content remains constant. In this study, the Fe redox state in garnet was investigated as a function of pressure and temperature by employing a carbonate and graphite/diamond bearing assemblage that fixed the oxygen fugacity at a given set of conditions. The reasons for performing this study are twofold. Firstly, the level of ferric Fe in garnet consistent with the formation of carbonate bearing minerals and melts can be determined; secondly, oxythermobarometers for determining the oxygen fugacity of garnet bearing assemblages can be tested at pressures where they have to date not been calibrated.

The experiments were performed in a multianvil apparatus at pressures from 7 to 16 GPa and temperatures from 1400-1550 °C. Mg, Fe- and Ca, Fe, Mg - bearing garnets were synthesized as glasses at 1600 °C and then reduced in a gas mixing furnace so that no  $Fe^{3+}$  was present. Figure 3.2-17 shows the experimental arrangement with a monomineralic garnet layer sandwiched respectively between Ca- free and Ca- bearing buffering assemblages representative of harzburgitic and lherzolitic compositions mixed with 10 wt.% of carbon. The oxygen fugacity was, therefore, imposed by the mineral starting mixtures of olivine, enstatite, diopside, graphite,  $MgCO_3$  and  $CaCO_3$  (*i.e.*, EMOD and EDDOG buffers). The

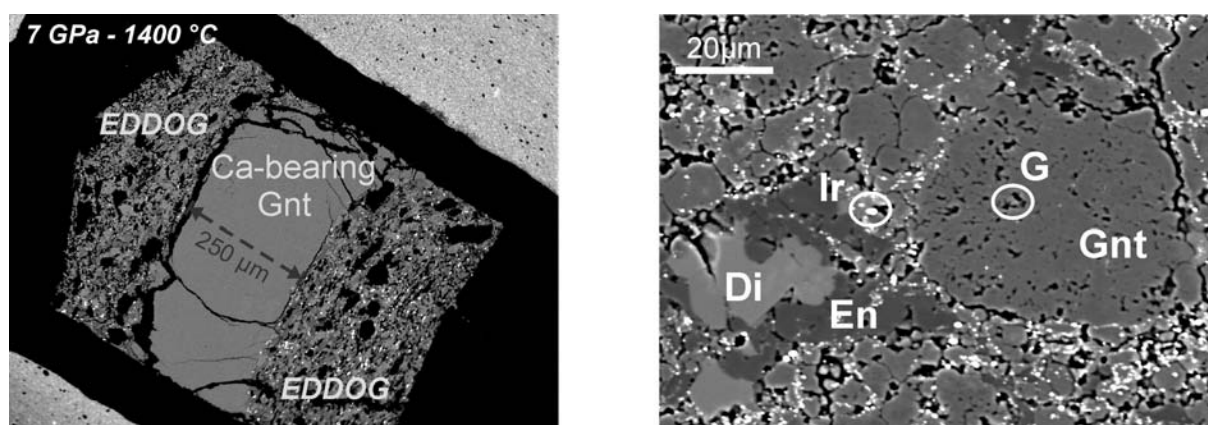


Fig. 3.2-17: Back scattered electron image of a garnet layer sandwiched between a Ca-bearing assemblage containing ortho and clinopyroxene, olivine, dolomite and graphite recovered from 7 GPa and 1400 °C. An enlargement on the right shows the garnet layer contains graphite inclusions as a result of carbonate melt infiltration and reduction. G is graphite, Gnt garnet, Di diopside, En enstatite and Ir iridium.

sample layering was required for Mössbauer measurements. In some experiments layers of olivine were sandwiched between one of the two buffering assemblages in order to that the  $\text{Fe}^{3+}/\sum\text{Fe}$  ratio of wadsleyite buffered by carbon-carbonate equilibria could also be measured. In some experiments 10 wt.% of the buffering assemblage was also added to the monomineralic layer to ensure equilibrium. Metallic iridium was added in small amounts (5 wt.%) as a redox sensor so that the oxygen fugacity could be determined. The chemical compositions of mineral phases was obtained using the electron microprobe. The ferric iron contents of the garnet and wadsleyite layers were determined by  $^{57}\text{Fe}$  Mössbauer spectroscopy at room temperature.

The oxidation of  $\text{Fe}^{2+}$  by the reduction of carbonate can be observed in Fig. 3.2-17 where graphite inclusions developed in the garnet layers. Although, the starting materials for these sandwiched layers were ferric iron free, Mössbauer spectra confirmed the oxidation of iron in these phases as shown in Fig. 3.2-18.

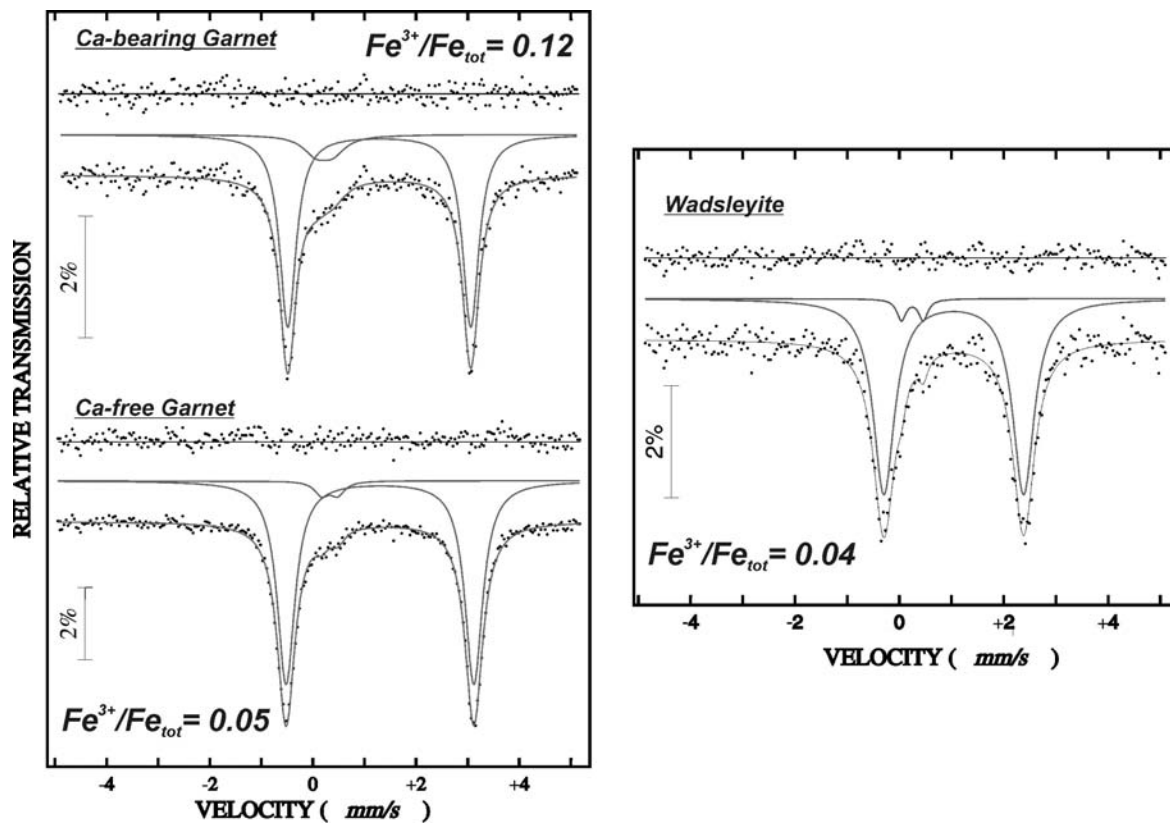


Fig. 3.2-18: Mössbauer spectra at 298 K of Ca-bearing and Mg-rich garnet on the left side after experiments at 7 GPa and 1400 °C. On the right is shown the spectrum of wadsleyite from 16 GPa and 1500 °C.

The nominal composition of the garnets was  $\text{Py}_{85}\text{Alm}_{15}$  and  $\text{Py}_{79}\text{Alm}_{16}\text{Gr}_5$ . After the experiment 1 wt.% of the skiaegite ( $\text{Fe}_3\text{Fe}_2^+\text{Si}_3\text{O}_{12}$ ) component entered Ca-free garnet and about 2 wt.% in the Ca-bearing garnet. The  $\text{Fe}^{3+}/\sum\text{Fe}$  ratio measured for Ca-bearing garnets

in these experiments is similar to values found in natural garnets in mantle xenoliths from South Africa from similar pressures. Experiments at 1500 °C show slightly higher ferric iron contents in garnets whereas, the total amount of iron decreases. Our measurements of  $\text{Fe}^{3+}/\Sigma\text{Fe}$  ratios of garnets in equilibrium with graphite and carbonates are slightly inconsistent with the predictions of oxythermobarometers. The  $\text{Fe}^{3+}/\Sigma\text{Fe}$  ratio in wadsleyite was found to be relatively low (~ 4 %) in equilibrium with diamond/carbonate phases. Previous experiments have reported  $\text{Fe}^{3+}/\Sigma\text{Fe}$  ratios of ~ 2 % in wadsleyite in equilibrium with metallic iron. The relatively low wadsleyite  $\text{Fe}^{3+}/\Sigma\text{Fe}$  ratios imply that high levels of ferric iron may not be necessary for the development of carbonate bearing assemblages in the transition zone.

**1. Detailed structure of the carbonated peridotite solidus ledge in the system  $\text{CaO-MgO-Al}_2\text{O}_3\text{-SiO}_2\text{-CO}_2$  (S. Ghosh, S. Keshav and G.H. Gudfinnsson)**

The so-called ‘carbonate ledge’ is a prominent feature of the solidus topology of carbonated peridotite at pressures of ~ 25-30 kbar is (Fig. 3.2-19). The ledge is caused by the appearance of crystalline carbonate on the high-pressure side of the carbonated peridotite phase diagram, at the expense of  $\text{CO}_2$  vapor that exists on the low-pressure side. Owing to the creation of crystalline carbonate, at the ledge, the solidus temperatures of carbonated peridotite decreases by ~ 200 °C. The ledge was first reported in the system  $\text{CaO-MgO-SiO}_2\text{-CO}_2$  (CMS- $\text{CO}_2$ ) carbonated peridotite, and does not vanish in the slightly more complex system  $\text{CaO-MgO-Al}_2\text{O}_3\text{-SiO}_2\text{-CO}_2$  (CMAS- $\text{CO}_2$ ; Fig. 3.2-18). Clearly, temperatures at which the mantle melts and the melt compositions that result are fundamentally dependent on whether  $\text{CO}_2$  is present either in vapor or crystalline form, and therefore, the importance of  $\text{CO}_2$  in mantle melting processes cannot be overemphasized.

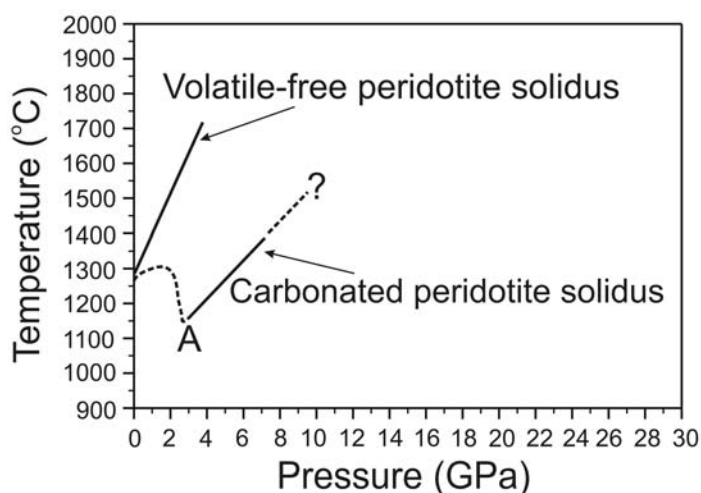


Fig. 3.2-19: Solidus curves for volatile-free ( $\text{CaO-MgO-Al}_2\text{O}_3\text{-SiO}_2$ ; CMAS) and carbonated (CMAS- $\text{CO}_2$ ) peridotite. The dashed curves shows segments of the carbonated peridotite solidus that are not yet experimentally determined. The dashed curve with a negative P-T slope along the carbonated peridotite solidus is the so-called carbonate ledge. Only the solid portion in carbonated peridotite is experimentally known, although not at pressures < 7 GPa.

Owing to the significance of the carbonate ledge, at this point it is rather imperative to evaluate the possible relationship between the carbonate ledge and associated features in slight more detail. The following are to be noted in Fig. 3.2-20: (1) B and C identify the assemblages fo+opx+cpx+spinel+garnet+CO<sub>2</sub>-vapor+melt and fo+opx+cpx+plagioclase+spinel+CO<sub>2</sub>-vapor+melt, respectively; (2) A comprises fo+opx+cpx+garnet+CO<sub>2</sub>-vapor+dolomite+melt; (3) F consists of fo+opx+cpx+garnet+dolomite+magnesite+melt. The region existing between the vertical line (initiating from point E on the dry peridotite solidus curve, down to the carbonated peridotite solidus between points A and F) and the dashed curve is not known at all, and is hence, a geometrical construct; (4) D and E consist of fo+opx+cpx+plagioclase+spinel+melt and fo+opx+cpx+spinel+garnet+melt, respectively.

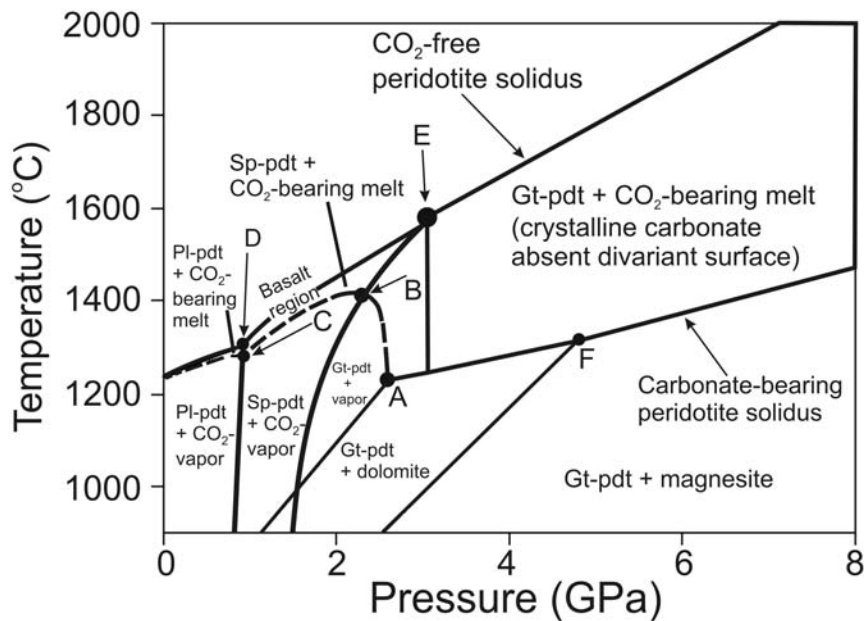


Fig. 3.2-20: Pressure-temperature projection depicting phase relations of carbonated and volatile-free in the systems CMAS and CMAS-CO<sub>2</sub>.

In this work melts in equilibrium with the crystalline assemblage and CO<sub>2</sub>-vapor do not show signs of liquid immiscibility. The solidus of model carbonated peridotite is defined by the following assemblages:

- 2.1 GPa and 1425 °C - forsterite + opx + cpx + spinel + CO<sub>2</sub>-vapor + melt
- 2.3 GPa/1425 °C, 2.4 GPa/1415 °C, 2.6 GPa/1375 °C, 2.7 GPa/1325 °C, and 2.8 GPa/1275 °C - forsterite + opx + cpx + garnet + CO<sub>2</sub>-vapor + melt
- 3.0 GPa and 1225 °C - forsterite + opx + cpx + garnet + CO<sub>2</sub>-vapor + magnesian calcite + melt

Significantly, the melt compositions in equilibrium with all the relevant assemblages over the studied pressure range are carbonatitic, having roughly 42-45 wt.% dissolved CO<sub>2</sub>. The experimentally produced liquids are also highly calcic and in this respect overlap the

compositions of surficially erupted calciocarbonatites. The invariant point located at 3.0 GPa and 1225 °C is at least 0.5-0.6 GPa *higher* than in previous topological constructs, and the knowledge of its precise location cannot be overemphasized. On the basis of melting phase relations determined, the following can be concluded: (a) since two different isobarically invariant assemblages exist at 2.3 and 2.1 GPa, there must exist a lower-pressure invariant point at about 2.2 GPa and 1425 °C. This invariant point consists of forsterite + orthopyroxene + clinopyroxene + spinel + garnet + CO<sub>2</sub>-vapor + melt.; (b) melt compositions must be carbonatitic at this invariant point; (c) since the solidus temperatures (1425 °C) at 2.1 and 2.3 GPa are identical, the carbonate ledge has to begin at 2.3 GPa and 1425 °C and end at 3.0 GPa and 1225 °C. These two points define the upper and lower extremities of the carbonate ledge; (d) the solidus of carbonated peridotite resembles a plateau from 2.3 and down to at least 2.1 GPa; (g) generation of carbonatites in equilibrium with CO<sub>2</sub>-vapor at pressures as low as 2.1 GPa is contrary to all previous reports, where such melts were hypothesized to be generated at pressures much higher than reported here. This experimental observation has tremendous implications for our understanding of carbonatites as primary (straight) mantle melts, the depth at which their geochemical signatures on the surrounding mantle start to become prominent, their possible relation with other magmas generated at these or shallower depths, and the depth-dependent nature of CO<sub>2</sub> solubility in mantle-derived magmas.

**m.** *Melting phase relations in the system CaO-MgO-Al<sub>2</sub>O<sub>3</sub>-SiO<sub>2</sub>-FeO-Cr<sub>2</sub>O<sub>3</sub> spanning the plagioclase-spinel lherzolite transition at 7 to 10 kbar: Experiments versus thermodynamics (S. Keshav, M. Tirone/Trieste/Miami, G.H. Gudfinnsson and D. Presnall/Richardson)*

Voluminous basaltic magmas erupt at mid-ocean ridges (MORB) as a consequence of passive mantle upwelling and melting beneath spreading plates. The major element composition of MORB magmas is generally well-explained by extraction of integrated, small-degree partial melts from polybaric melting zones. Models on the basis of major element systematics of most primitive MORB compositions indicate mantle potential temperatures generally in the range of ~ 1250-1350 °C. On the basis of phase relations for model fertile mantle, MORB melting is generally expected to occur entirely within the stability fields of spinel and plagioclase lherzolite, and a significant role for melting in the region of lowered solidus temperature caused by the plagioclase to spinel transition is implicated. A critical yet unresolved question, however, is how phase transitions within a polybaric melting zone affect melt productivity and thereby, possibly exert control on major and trace element composition of erupted magmas. Currently, the disagreements on these issues are fundamental, with great consequences that extend beyond petrology to global issues of potential temperatures, mantle melting, mantle heterogeneity, and mantle dynamics. Thermodynamics show that melt productivity depends critically on the transition reaction, and melting can in principle increase, decrease, or even stop at a transition. Phase equilibrium work from both systems CaO-MgO-Al<sub>2</sub>O<sub>3</sub>-SiO<sub>2</sub>-Na<sub>2</sub>O (CMASN; Fig. 3.2-21) and CMAS-FeO (CMASF; Fig. 3.2-21) have been used to argue that melt productivity may increase at the plagioclase-spinel (pl-sp) transition because the univariant solidus transition reaction has a positive dT/dP slope in these

systems, moving to higher pressure relative to the CMAS system (Fig. 3.2-21). However, melting models derived on the basis of MELTS and pMELTS show that the solidus has a *negative slope* on the plagioclase-spinel transition (Fig. 3.2-21). If correct, this would cause suppression of melting as the mantle decompresses along a pertinent adiabat. Here it is also perhaps worth emphasizing that the extant data for melting natural lherzolite compositions, or calculated melting using the MELTS algorithm, *are just not refined enough* to make reliable estimations for melting along solidus transitions.

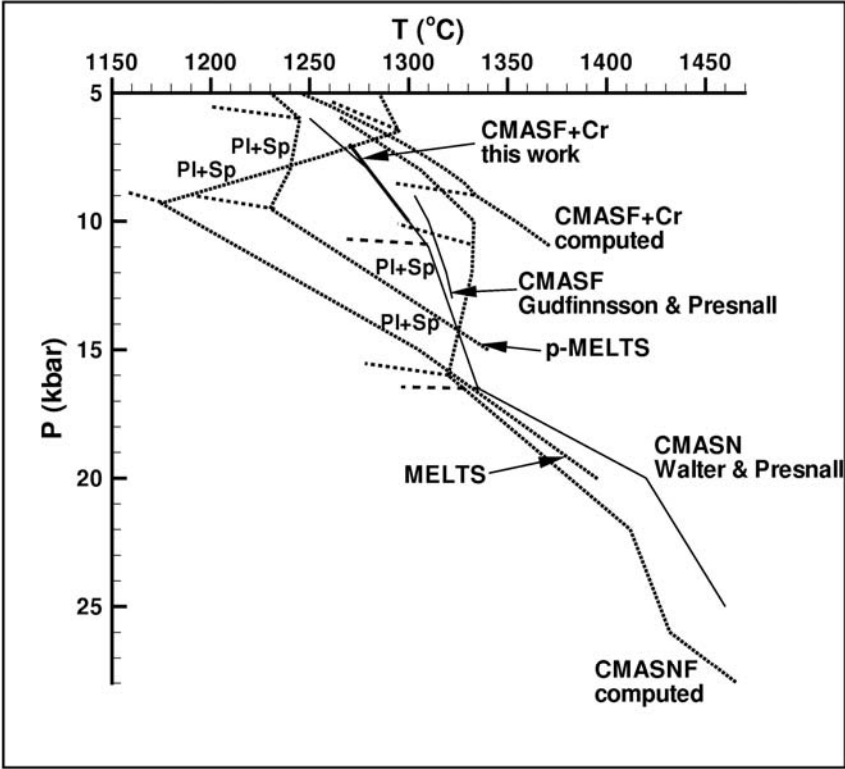


Fig. 3.2-21: A detailed comparison of solidi curves of fertile peridotite determined using experimental and theoretical methods in several systems. The solidus curves calculated using MELTS and pMELTS algorithms are shown as well in this pressure-temperature projection. Using these two algorithms, the plagioclase-spinel transitions at the solidus in *natural* compositions (with Cr) shows a *trench* trajectory, which is further accentuated when using MELTS. Solidus melting phase relations in the system CMAS-Fe-Cr (CMASF+Cr, this work) spanning the plagioclase-spinel lherzolite transition are also shown. Further, calculations performed using revised thermodynamic databases in the systems CMASF+Cr and CMASNF are also shown.

In this work we present melting phase relations in the system CMASFCr at the plagioclase-spinel lherzolite transition from 7 to 10 kbar. Further, using modified approaches to current understanding of mantle melting, we also draw comparisons between experimental data and the results of numerical simulations employing thermodynamics. The significance of Cr to melting phase relations at least in the shallow upper mantle comes from the following: even though Fe is more abundant in natural lherzolite compositions (~ 8 % FeO and ~ 0.5 %

Cr<sub>2</sub>O<sub>3</sub>), addition of Cr (which is highly soluble in Mg-Fe-Al spinels) to the system CMAS has been shown to shift the plagioclase-spinel transition to 1 atm, that has implications for mantle melting at very shallow depths near the ridges and record of melting in the dredged abyssal peridotites. It has also been recently shown that the addition of Cr to CMAS has an unusually large effect on Ca/Al of melt compositions at 1.1 GPa. On the other hand, with the addition of iron (Fe) and sodium (Na) to CMAS, the plagioclase-spinel transition at the solidus is shifted to higher pressures (Fig. 3.2-21). Hence, taken together, Fe and Cr will have predominant control over the melting relations along the transition.

Geometrically, with six phases in the system CMASFCr, melting phase relations at a given P and T are invariant, and the solidus spans a divariant surface in P-T space. In the experiments reported here, at all pressures, the charges contain olivine + opx + cpx + plagioclase + spinel + melt, and completely define the transition from plagioclase to spinel-bearing lherzolite on the solidus. The solidus at 7, 8, 9, and 10 kbar is located at 1270, 1280, 1290, and 1300 C, respectively, and is linear in P-T space (Fig. 3.2-21).

In the system CMASFCr, the experimentally determined plagioclase-spinel lherzolite transition at the solidus moves to lower pressures (Fig. 3.2-21), but this solidus curve overlies that of plagioclase-lherzolite in the system CMASN. Significantly, as compared either with MELTS or pMELTS, the experimentally determined solidus has a *positive* slope in P-T space. Recently developed thermodynamic databases optimized for peridotite melting in the system CMASNF predict a solidus with a slightly negative slope (fairly similar to that observed using pMELTS; Fig. 3.2-21) in the plagioclase-spinel lherzolite stability field. In the system CMASFCr the slope becomes positive, in accordance with the experimental data of this work. In Figure 3.2-21, the computed plagioclase-spinel transition at the solidus in the system CMASFCr is bound at about 8 kbar, extending all the way down to 1 atm. Both the experimental and modeling results suggest that the effect of Cr is to increase the stability of spinel at lower pressure. However, the *computed* solidus curve in CMASF+Cr consistently lies at temperatures higher than those determined experimentally. This difference in the solidus temperatures can partially be ascribed to the approaches employed to address solidus melting relations: in the experiments reported here, as long as all the six relevant phases are present in the charges, the solidus temperatures are independent of the bulk composition; while in computations a fertile peridotite composition, reduction to six-space tends to overestimate the solidus temperatures.

**n.** *Experimental constraints on the storage of phosphorus in the lower mantle (J. Konzett/Innsbruck, in collaboration with D.J. Frost)*

Phosphorus is one of the essential elements for life on Earth. The long term evolution of ecosystems requires a thorough understanding of the global P-cycle which again must be

based on an understanding of the processes by which P is stored and transported in the Earth's interior. Because the initial source of P available to terrestrial ecosystems is through chemical and physical weathering of crustal magmatic and metamorphic rocks, it is important to gain insight into the mechanisms that control the exchange of P between the Earth's crust and mantle and to identify those phases that are capable of storing and transporting P in the upper and lower mantle. Under upper mantle *P-T* conditions apatite is a major host for P, REE, LILE and halogens to a depth of approximately 200 km. At higher depths, apatite breaks down to form the anhydrous Ca-phosphate tuite [ $\gamma$ -Ca<sub>3</sub>(PO<sub>4</sub>)<sub>2</sub>] that continues to act as a major host for P, REE and LILE. No information, however, is available on the P storage capacity of the common lower mantle phases or on the stability of phosphate phases under lower mantle *P-T* conditions. For this reason exploratory experiments have been conducted to study the P-incorporation in lower mantle assemblages for peridotitic and MORB-type bulk compositions.

Experiments were carried out in a 1000 t multianvil press with 10/4 assemblies at 25 GPa and 2000 °C using 1.0 mm outer diameter Re-capsules. Run durations ranged between 1 and 2 hours. Three different starting materials were used: (1) an average MORB doped with 3 % synthetic OH-apatite (run B07-12); (2) a synthetic simplified MORB-equivalent in the system Na<sub>2</sub>O-CaO-MgO-Al<sub>2</sub>O<sub>3</sub>-TiO<sub>2</sub>-SiO<sub>2</sub> doped with 3 % synthetic OH-apatite (run B07-14), and (3) a moderately fertile lherzolite doped with 3 % synthetic  $\beta$ -Ca<sub>3</sub>(PO<sub>4</sub>)<sub>2</sub> (run B08-11). Mineral compositions were analyzed with the electron microprobe using polished sections through the sample capsules. In order to obtain accurate P-analyses at low concentrations, P was analyzed in a separate analytical session using 15 kV acceleration voltage and 150 nA beam current with counting times of 300 sec on the peak and 150 sec on the backgrounds of the P-K<sub>a</sub> X-ray line. Precision and accuracy of the P-analyses were tested using synthetic glass standards doped with P on a concentration level of 100-1000 ppm P<sub>2</sub>O<sub>5</sub>.

Run B07-12 produced an assemblage garnet + Ca-perovskite + stishovite + Ca-Al-phase + metallic iron. The latter phase is present as globules with  $\leq 1$   $\mu$ m diameter and a modal amount of < 1 % and has not been observed in earlier experiments in the *P-T* range 6-15 GPa and 950-1800 °C. A possible explanation for the presence of metallic iron in the MORB bulk is disproportionation of ferrous iron according to  $3 \text{FeO} = \text{Fe} + \text{Fe}_2\text{O}_3$  as suggested in previous studies for the Earth's lower mantle where the presence of Mg-perovskite with high Fe<sup>3+</sup>/Fe<sub>tot</sub> requires the stability of small amounts of metallic Fe under the assumption that the Fe<sup>3+</sup>/Fe<sub>tot</sub> ratios of upper and lower mantle are similar. In case of the MORB bulk composition the only phase capable of acting as a host for Fe<sup>3+</sup> and present in sufficient quantities is majoritic garnet. An analysis of the Fe<sup>3+</sup>/Fe<sub>tot</sub> ratio of this garnet is in progress. In run B07-12 the only phases containing significant P are Na-Ti-rich majoritic garnet with 1.04 $\pm$ 0.24 wt.% P<sub>2</sub>O<sub>5</sub> (n=16) and metallic Fe. The latter could not be analyzed quantitatively due to the small grain size but EDS-spectra showed a strong P-peak indicative of the presence of substantial P. In case of Ca-perovskite, stishovite and the Ca-Al-phase qualitative WDS-scans did not provide any evidence for measurable P.

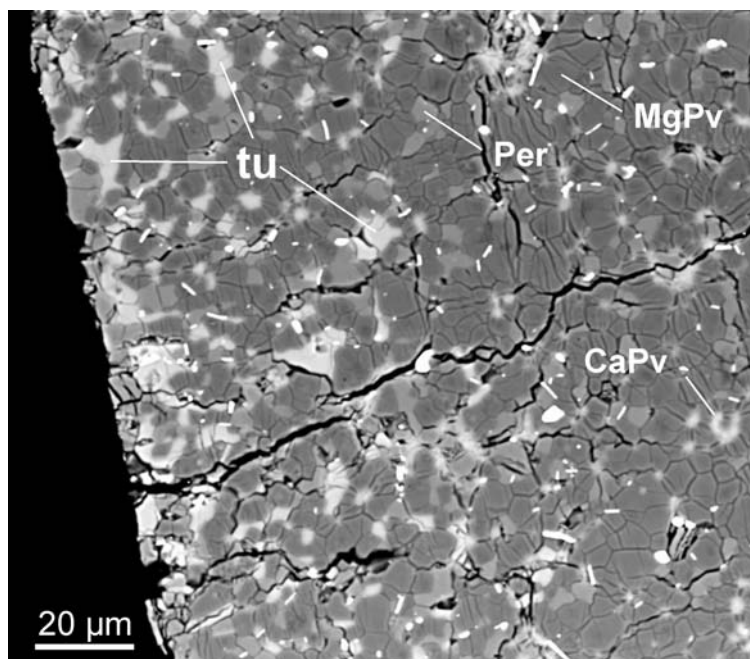


Fig. 3.2-22: BSE-photomicrograph of run B08-11 showing a texturally well equilibrated assemblage of Mg-perovskite (MgPv) + Ca-Perovskite (CaPv) + Fe-periclase (Per) + tuite (tu)

Run B08-11 (Fig. 3.2-22) contains the typical lower mantle assemblage Mg-perovskite + Ca-perovskite + Fe-periclase + traces of melt and a Ca-phosphate. EMPA and Raman analyses showed that the calcium phosphate is tuite [ $\gamma\text{-Ca}_3(\text{PO}_4)_2$ ]. In this bulk composition P is to a first approximation exclusively partitioned between the Ca-phosphate and P-rich melt containing 5.3 wt.%  $\text{P}_2\text{O}_5$ . Neither Mg-perovskite nor Fe-periclase contain measurable P, and Ca-perovskite was too small to be analyzed.

Under subsolidus conditions garnet shows an extreme preference for P at  $P$ - $T$  conditions of the uppermost lower mantle and will be the major P-reservoir. Therefore, no other solid silicate phase is likely to accommodate significant P in the presence of garnet. If garnet is able to accommodate significant  $\text{Fe}^{3+}$ , then disproportionation of  $\text{Fe}^{2+}$  into metallic Fe +  $\text{Fe}^{3+}$  would be a possible mechanism to explain the presence of metallic Fe coexisting with garnet + stishovite + Ca-Al-phase in the MORB bulk at 25 GPa and 2000 °C. If present, metallic Fe will store a significant portion of the bulk P and siderophile trace elements.  $\gamma\text{-Ca}_3(\text{PO}_4)_2$  is stable in a peridotite bulk under  $P$ - $T$  conditions of the uppermost lower mantle. This phase will also be a major reservoir for light rare earth and large ion lithophile elements. Low percentage partial melting of moderately fertile P-enriched peridotitic mantle produces very P-rich melts because P retains its incompatible character to lower mantle  $P$ - $T$  conditions. At 25 GPa and 2000 °C a melt with 5.3 wt.%  $\text{P}_2\text{O}_5$  is saturated in  $\text{Ca}_3(\text{PO}_4)_2$ . By comparison, Na is no longer incompatible at these  $P$ - $T$  conditions because it is strongly partitioned into Fe-periclase.

o. *Is molybdenite saturation common in natural rhyolite magmas? (A. Audétat)*

Molybdenite ( $\text{MoS}_2$ ) is considered an uncommon magmatic phase in terrestrial magmas. So far, the only known occurrence of magmatic molybdenite is in peralkaline rhyolites from Pantelleria, Italy. Small, hexagonal platelets of molybdenite included in quartz phenocrysts have now been found in several rhyolite samples from the western United States. The identity of the molybdenite was confirmed by both Raman spectroscopy and LA-ICP-MS. Based on their isolated occurrence within the quartz host (with no cracks or fluid inclusion trails leading to them) and the fact that some have glassy melt inclusions attached to them, there is no doubt that these molybdenite inclusions represent a magmatic phase (Figs. 3.2-23, 24).

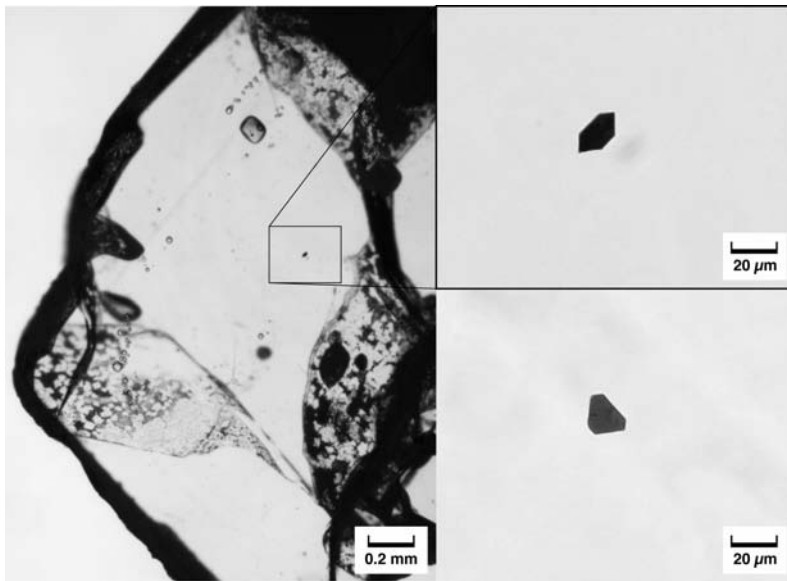


Fig. 3.2-23: Photomicrograph of molybdenite inclusions in quartz phenocrysts from the Pine Grove tuff, Utah (basal layer of air fall unit). Also visible in the picture on the left are arrays of glassy melt inclusions.

	<b>Stronghold</b> (Arizona)	<b>Pine Grove</b> (Utah)	<b>Bandelier Tuff</b> (New Mexico)	<b>Treasure Mt.</b> (Colorado)	<b>Amalia Tuff</b> (New Mexico)	<b>Y-TPI, PCI</b> (unknown)
number of quartz phenocrysts examined	~50	~50	26	~40	~40	~90
number of phenocrysts with molybdenite inclusions	7	12	6	2	7	8
number of coexisting melt inclusions measured	16	16	4	2	3	2
Mo-content of coexisting melt inclusions (ppm)	4-5	2	9-10	1-2	3-4	9-10

Table 3.2-1: Abundance of molybdenite inclusions and Mo content of cogenetic melt inclusions analyzed by LA-ICP-MS

Systematic inspection of quartz phenocrysts in rhyolitic samples from 14 magma systems in the western United States revealed molybdenite inclusions at the following six locations: Stronghold granite, Arizona (rhyolite dike); Pine Grove, Utah (rhyolitic ignimbrite); Bandelier Tuff, New Mexico (rhyolitic ignimbrite); Treasure Mountain Dome, Colorado (high-silica rhyolite / granite porphyry below the roof); Amalia Tuff, New Mexico (main eruption of the Questa Caldera); plus in two rhyolite samples from an unknown locality in North America. LA-ICP-MS analyses of cogenetic melt inclusions indicate Mo-concentrations of 2-10 ppm Mo (Table 3.2-1).

The fact that magmatic molybdenite was observed in six out of fourteen investigated magma systems suggests that molybdenite saturation in rhyolitic magmas may be far more widespread than assumed. Three of the molybdenite-bearing magmas are either directly (Pine Grove) or indirectly (Treasure Mt. dome; Amalia tuff) related to porphyry-Mo mineralization, suggesting a potential link between molybdenum saturation and porphyry-Mo formation.

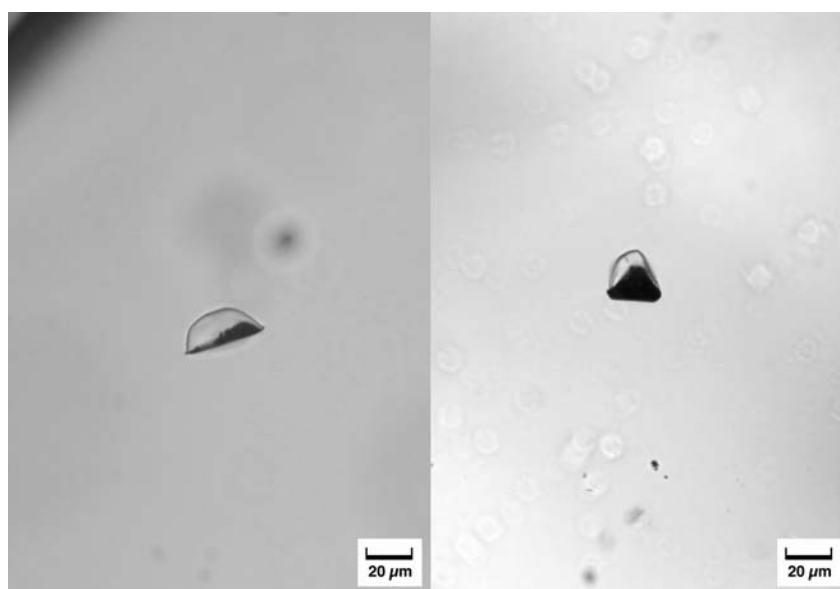


Fig. 3.2-24: Photomicrograph of molybdenite inclusions with attached melt inclusions (quenched to glass) in quartz phenocrysts from the Otowi Member of the Bandelier tuff, New Mexico.

The implications of molybdenite saturation in felsic melts are manifold. Most importantly, the crystallization of a Mo-rich mineral will lead to an efficient buffering of the Mo concentration in the residual melt. The exact saturation value depends on  $fO_2$  and  $fS_2$  (amongst other parameters), which means that it will become possible to constrain either of these values once the influence of all major parameters affecting molybdenite saturation has been quantified. Furthermore, fluids that exsolve from molybdenite saturated magmas are likely to precipitate hydrothermal molybdenite close to their magmatic source, as any decrease in temperature and/or pressure will cause them to get supersaturated. This may explain why the ore shells in porphyry-Mo systems typically are found immediately above the mineralizing intrusions.

**p.** *Microstructural controls on pyrrhotite weathering and secondary mineral formation (K. Pollok, D. Harries and F. Langenhorst)*

The oxidative alteration of sulfidic ores due to natural events and mining activities leads to the production of acid rock drainage (ARD) and acid mine drainage (AMD), respectively. It releases acidity (low pH) as well as high heavy metal and sulphate concentration into the environment and is an environmental problem for the water quality of ground and surface waters worldwide. Pyrrhotite ( $\text{Fe}_{1-x}\text{S}$ , with  $x = 0 - 0.125$ ) is, after pyrite, the second most frequent iron sulphide in nature and is found in a wide range of magmatic and metamorphic rocks as well as in massive sulphide deposits. The oxidation rates of pyrrhotite are on the order of 20 to 100 times higher compared with pyrite.

The incorporation of variable amounts of  $\text{Fe}^{3+}$  results in cation vacancies and thus non-stoichiometry of pyrrhotite. Ordering of these vacancies yields a number of superstructures with various stacking sequences. Therefore, stacking faults and twinning are common in natural samples. In this study the influence of the defect microstructure on the weathering behaviour, the spatial relationship between the primary mineral, and the formation of secondary phases in a natural sample from Dalnegorsk (Russia) are addressed.

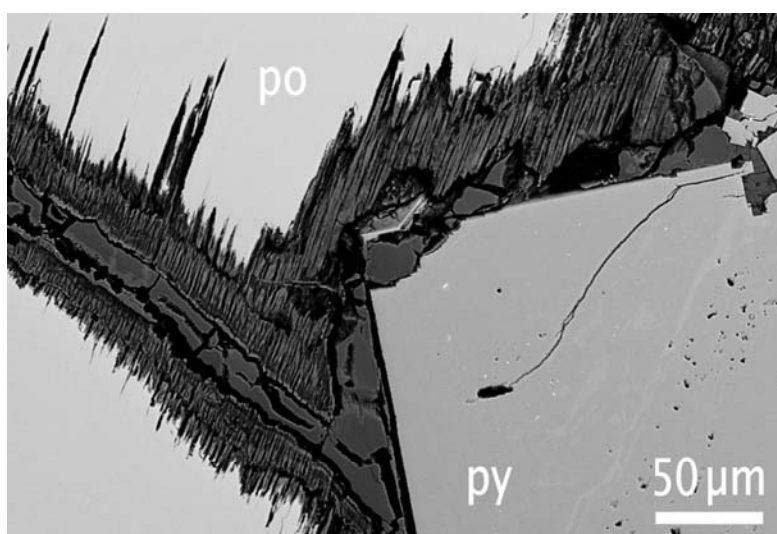


Fig. 3.2-25: Backscattered electron image of partially weathered pyrrhotite (po) and newly grown pyrite (py). 4 iron (hydr)oxides plus elemental sulphur and chalcocite have been identified in the reaction zone by Raman spectroscopy and TEM.

SEM, EDX mapping and Raman spectroscopy reveal the heterogeneity of the alteration veins (Fig. 3.2-25). Goethite and pyrite are formed as (metastable) results of pyrrhotite weathering. However, the high number of transient secondary phases (elemental sulfur [S], chalcocite [ $\text{Cu}_2\text{S}$ ], marcasite [ $\text{FeS}_2$ ], lepidocrocite [ $\gamma\text{-FeOOH}$ ], and hematite [ $\alpha\text{-Fe}_2\text{O}_3$ ]) indicate a complex reaction sequence which involve redox processes and element transport. HRTEM

and selected area diffraction reveal a superstructure consistent with 4C and multiple microtwinning. In addition, a small degree of stacking disorder and a NA superstructure were found. Unexpectedly, nanocrystalline, Si-bearing magnetite with a grain size of 15-30 nm was found to be the first alteration product. The formation of magnetite at the surface of pyrrhotite indicates that the alteration is not primarily driven by the oxidation of Fe. For this sample, partial oxidation of sulphur is inferred by the formation of elemental sulfur. Further reaction steps must involve the oxidation of Fe (from magnetite and/or pyrrhotite) and the subsequent formation of iron (hydr)oxides. This process could be coupled with the reduction of sulphur to form the secondary pyrite.

### 3.3 Mineralogy, Crystal Chemistry and Phase Transformations

Understanding the behaviour of the Earth's interior is a major aim of the ongoing research at the Bayerisches Geoinstitut. The study of the crystal chemistry of minerals, their compressibility and their phase transformations at high pressures and temperatures is an essential tool to reach such a goal. It is, therefore, not surprising that most of the contributions in this section describe high-pressure and high-temperature studies of different minerals performed using a variety of experimental techniques. The order of the contributions follows the sequence of our planet's interior: from crust to core. High-pressure single-crystal diffraction studies constrained the high-pressure behaviour of a  $\text{SrAl}_2\text{Si}_2\text{O}_8$  feldspar (isochemical with anorthite) and of the trirutile-type structure of  $\text{FeTa}_2\text{O}_6$  tapiolite. High-pressure Raman spectroscopy has been used with an externally heated diamond anvil cell to follow the dehydration of gypsum and its phase transformations to bassanite and anhydrite as a function of pressure and temperature. The effect of Al substitution on the stoichiometry of ringwoodite has been addressed by means of single-crystal structural refinements, whereas the spinel to post-spinel phase transformation occurring as a function of pressure and temperature has been investigated for magnetite and for a series of related ferrite spinels,  $\text{M}^{2+}\text{Fe}_2\text{O}_4$  by means of X-ray diffraction, Raman and Mössbauer spectroscopies.  $\text{MgSiO}_3$ -perovskite is one of the high-pressure mineral phases most studied due to its abundance in the Earth's lower mantle. In particular Fe substitution in  $\text{MgSiO}_3$ -perovskite has been the center of a renewed interest due to its spin crossover transition at high pressures. In this section a novel approach has been tested, which makes use of the Fe K-edge absorption (XANES) coupled with the diamond anvil cell, in order to better constrain the electronic and local structure of Fe substituted in an Al-free and in an Al-bearing  $\text{MgSiO}_3$ -perovskite as well as that of ferropericlase. Experimental studies at the extreme pressure and temperature conditions of the core-mantle boundary are very challenging and therefore a systematic study of possible phase transformations of the  $\text{CaIrO}_3$ -type post-perovskite structure is not straightforward. Instead  $\text{FeTiO}_3$ -perovskite has been studied at high pressures and temperatures by means of X-ray diffraction and Mössbauer spectroscopy as a possible analogue of  $\text{MgSiO}_3$ -perovskite to explore the possible high-pressure post-postperovskite transitions. Mössbauer spectroscopy has also been used to investigate the high-pressure electronic transition in hexagonal close packed iron and in an iron-nickel alloy. To conclude this first part of experimental studies a contribution describes the finding of the high-pressure phase  $\text{Ni}_3\text{S}$  isostructural with  $\text{Fe}_3\text{S}$  suggesting the presence of a possible range of  $(\text{Fe,Ni})_3\text{S}$  solid solutions in the pressure-temperature stability region of the  $\text{Fe}_3\text{S}$  and  $\text{Ni}_3\text{S}$  end-members.

After these experimental studies, three contributions present results obtained using theoretical computations which often have the advantage of addressing questions which cannot or can only with extreme difficulty be answered by experimental studies. Density functional theory has been, thus, applied to establish the stable magnetic structure of fayalite both at room and at high pressure, as well as to explore the several high-pressure phases of the different compounds in the Ti-O system. A combined experimental and computational study, in the end, is aimed to elucidate the anomalous elastic behaviour of Co in the pressure range between 60 and 80 GPa.

At last, two studies, one relative to the phase stability of iron-rich dense hydrous silicates and the other characterising dust particles from a return mission to a short-period comet, show how mineralogy can help to understand not only the behaviour of the Earth, but also that of other planets as Mercury or Mars, as well as to constrain the cometary matter in an effort to understand the processes of the early solar system.

**a. High-pressure phase transition in  $\text{SrAl}_2\text{Si}_2\text{O}_8$  feldspar (T. Boffa Ballaran, F. Pandolfo and F. Nestola/Padova; E. Bruno/Torino and M. Koch-Müller/Postdam)**

Feldspars are among the most common minerals in crustal rocks and hence their physical-chemical properties have been widely investigated. The high-pressure behaviour of these minerals, however, appears to be very complex. Recent experiments, for example, have documented elastic softening in albite and have found completely new symmetries and sequences of phase transformations for feldspars with different compositions. Moreover, it has been found that a 4<sup>th</sup> order Birch-Murnaghan Equation of state (BM-EoS) needs to be used to fit the  $P$ - $V$  data of some plagioclase and anorthoclase samples, *i.e.*, the fitting of the second pressure derivative of the bulk modulus is required to correctly describe their high-pressure behaviour.

$\text{SrAl}_2\text{Si}_2\text{O}_8$  feldspar is isochemical with anorthite ( $\text{CaAl}_2\text{Si}_2\text{O}_8$ ), but is monoclinic  $I2/c$  instead of triclinic  $P\bar{1}$  due to the substitution of the larger Sr into the anorthite structure. The anorthite -  $\text{SrAl}_2\text{Si}_2\text{O}_8$  system presents a complex path ways of phase transformation as a function of composition, temperature and pressure. However, whereas the behaviour of this system has been well characterised as a function of composition and temperature; there are still some open questions about its high-pressure behaviour. Anorthite transforms to a  $I\bar{1}$  structure above 2.5 GPa; another phase transformation has been observed by means of Raman spectroscopy above 10 GPa, but the structural details are still undefined.  $\text{Ca}_{0.2}\text{Sr}_{0.8}\text{Al}_2\text{Si}_2\text{O}_8$  feldspar has a  $I\bar{1}$  structure at room pressure and transforms to monoclinic  $I2/c$  above 4 GPa and to monoclinic  $P2_1/c$  above 7 GPa. The behaviour of the  $\text{SrAl}_2\text{Si}_2\text{O}_8$  end-member at high pressure is still not clear. It appears to become triclinic above 3.2 GPa, but the bulk modulus of the monoclinic phase is much larger than any other feldspar structure, suggesting that the data presented in the literature may be affected by some systematic errors. Moreover a recent IR study on a hydrous  $\text{SrAl}_2\text{Si}_2\text{O}_8$  feldspar containing 1100 ppm water suggests the presence of a phase transformation only above 8 GPa.

Two single-crystals of  $\text{SrAl}_2\text{Si}_2\text{O}_8$  feldspar, one anhydrous and one containing about 1100 ppm of structural OH and  $\text{H}_2\text{O}$  have been studied by means of high-pressure single-crystal X-ray diffraction up to 5.1 and 7.9 GPa, respectively. There is no discontinuity in the  $P$ - $V$  data of the anhydrous feldspar up to 5.1 GPa, pressure at which the crystal bridged the diamonds. Above 6.5 GPa the  $I2/c$  hydrous feldspar transforms to a monoclinic structure which has likely the  $P2_1/c$  space group as the phase reported for the analogue  $\text{Ca}_{0.2}\text{Sr}_{0.8}\text{Al}_2\text{Si}_2\text{O}_8$  feldspar.

This phase transformation is first ordered in character with a  $\sim 2\%$  decrease in volume. The monoclinic  $I2/c$   $P$ - $V$  data of the two crystals follow almost the same curve, although the normalised stress  $F_E$  vs the eulerian strain  $f_E$  plot suggests that the anhydrous sample is slightly more compressible than the hydrous feldspar (Fig. 3.3-1). Moreover the curvature of the  $F - f$  plot clearly indicate that these data can be properly described only by using a 4<sup>th</sup> order Birch-Murnaghan equation of state. Further investigations are at the moment undertaken to better constrain the EoS of the two samples and to determine if water has any effect on the transition pressure of  $\text{SrAl}_2\text{Si}_2\text{O}_8$  feldspar.

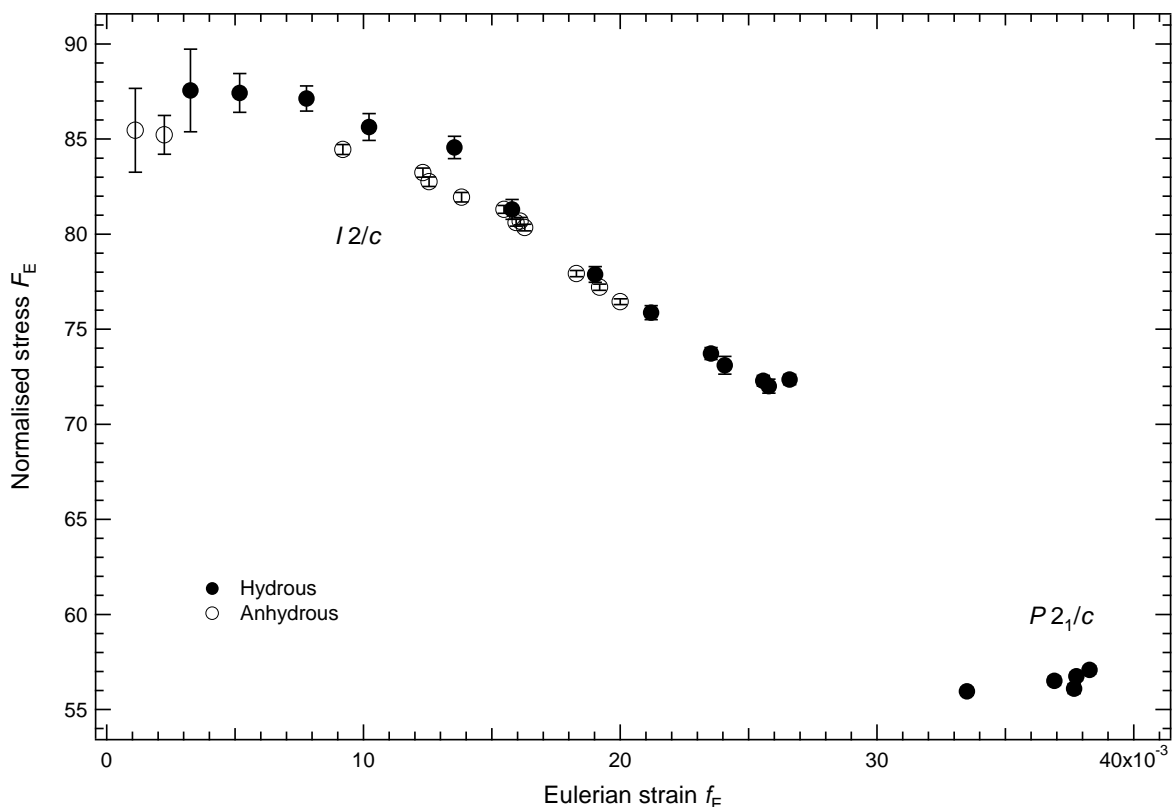


Fig. 3.3-1: Normalised stress (GPa) vs eulerian strain plot for the  $P$ - $V$  data of the two  $\text{SrAl}_2\text{Si}_2\text{O}_8$  feldspar crystals. Note that the  $I2/c$  data do not plot on a straight line indicating that a 4<sup>th</sup> order BM-EoS is necessary to fit them correctly.

**b. Pressure effect on the crystal structure of tapiolite  $\text{FeTa}_2\text{O}_6$  (M. Zema and S.C. Tarantino/Pavia, T. Boffa Ballaran)**

High-pressure behaviour of  $\text{MO}_2$ -type compounds with the rutile-type structure has attracted great interest in geophysics, since rutile-structured  $\text{SiO}_2$  (stishovite) was found. A number of high-pressure XRD studies of rutile, which provides an analogue to the  $\text{SiO}_2$  system, have been performed. At room temperature  $\text{TiO}_2$  is known to transform to its baddeleyite ( $\text{ZrO}_2$ )-type polymorph at 12 GPa and, upon decompression, it transforms at 7 GPa to a phase which is isostructural with orthorhombic  $\alpha$ - $\text{PbO}_2$  structure. This phase is metastable at ambient

pressure and can also be prepared from other  $\text{TiO}_2$  polymorphs, *i.e.*, anatase and brookite. The phase transitions in trirutile  $\text{AB}_2\text{X}_6$  structures are expected to be analogous to the ones observed for the  $\text{AX}_2$  compounds. Galy and Anderson [*J. Solid State Chem.* 3, 525, 1973] proposed simple transformation mechanisms of the  $\text{Li}_2\text{ZrF}_6$  trirutile (s.g.  $P4_2/mnm$ ) structure types at high pressures through cation rearrangements in the anionic array. They suggested also that these materials would be expected to transform at high pressures to the columbite  $\text{FeNb}_2\text{O}_6$  structure that is an ordered analogue of the  $\alpha\text{-PbO}_2$  type (s.g.  $Pbcn$ ).

The mineral ferrotapiolite  $\text{FeTa}_2\text{O}_6$ , occurring primarily as accessory phase in rare-element granitic pegmatites and usually associated with other Nb,Ta-bearing minerals such as columbite-tantalite or wodginite, crystallizes with the trirutile structure in space group  $P4_2/mnm$  (Fig. 3.3-2). The rutile and trirutile structures are related by an isomorphic transformation of index three, hence they have the same symmetry and the relationship between their unit cells is  $a_{\text{trirutile}} = a_{\text{rutile}}$  and  $c_{\text{trirutile}} = 3c_{\text{rutile}}$ . In tapiolite, the tripling of the  $c$  cell parameter is related to long-range ordering of  $\text{Fe}^{2+}$  and  $\text{Ta}^{5+}$  in the two octahedral sites A and B.

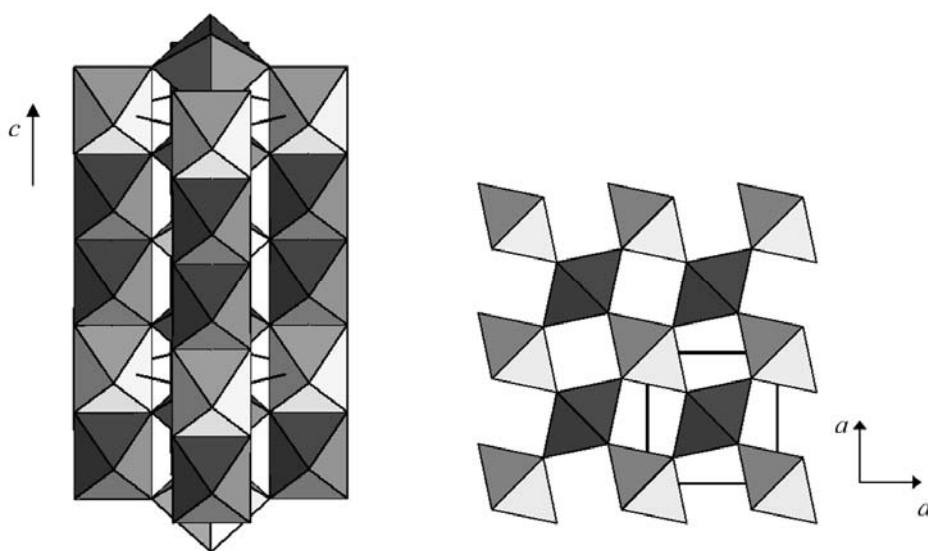


Fig. 3.3-2: The crystal structure of tapiolite

In this study structural investigations at high pressure were carried out using a single-crystal of natural tapiolite ( $110 \times 80 \times 50 \mu\text{m}$ ) from Kimito (Finland). Preliminary high-temperature investigations on the same sample revealed that axial thermal expansion is linear and positive up to  $750^\circ\text{C}$  with a slight anisotropy, the  $c$  dimension showing the largest variations with temperature. Accurate lattice parameters were first measured in air by X-ray diffraction on a Huber four-circle diffractometer (non-monochromatized Mo-K $\alpha$  radiation) operating at 50 kV and 40 mA by using eight-position centring of 18 Bragg reflections. The crystal of tapiolite, already studied in air, was loaded into a BGI-type diamond anvil cell (DAC) together with 2 ruby chips for pressure measurements. Stainless steel T301 foil,  $300 \mu\text{m}$  thick, pre-indented to

a thickness of about 110  $\mu\text{m}$  and with a 250  $\mu\text{m}$  hole obtained by electro-spark erosion, was used as a gasket. A mixture of methanol: ethanol (4:1) was used as hydrostatic pressure-transmitting medium. Accurate lattice parameters were measured at 16 different pressures up to 8.7 GPa following the same procedure as used for the crystal in air. Two measurements were performed upon decompression. The unit-cell parameters show a continuous behaviour with pressure and no evidence for phase transitions was found in the investigated pressure range. The equation of state at room temperature was determined from unit-cell volume ( $P$ - $V$ ) data using the EOSFIT 5.2 program and refining simultaneously the unit-cell volume at room pressure  $V_0$ , the bulk modulus  $K_{T0}$  and the first pressure derivative  $K'$  (third-order Birch-Murnhagan equation of state:  $V_0 = 208.29(3) \text{ \AA}^3$ ,  $K_{T0} = 197(2) \text{ GPa}$ ,  $K' = 2.9(5)$ ). Four complete datasets have also been collected at 0, 3.0, 4.8 and 6.9 GPa using the Oxford Xcalibur four-circle diffractometer equipped with a CCD detector. All diffracted intensities were checked and only reflections whose intensity was not affected by diffraction effects from diamond, Be or ruby chips were kept. Preliminary structure refinements converged to discrepancy factors  $R$  of about 7 %.

*c. The dehydration reaction gypsum-bassanite-anhydrite at high pressure: A Raman experimental study (P. Comodi and S. Nazzareni/Perugia, A. Kurnosov and L.S. Dubrovinsky)*

Sulphates are important minerals in Earth sciences (for example gypsum, together with anhydrite, halite and Ca-Mg carbonates is one of the major minerals forming evaporitic sequences, where it plays an important role in localising deformations) in planetology, given the strong evidence of the presence of gypsum in planetary bodies (for example in Martian soil) as well as in material sciences since sulphates are commonly used in medical and concrete industries. However, although the dehydration of gypsum has been the focus of many high-temperature studies, little is known about its behaviour as a function of pressure and in particular the  $P/T$  gradient of the dehydration is poorly constrained.

In this study, the dehydration sequence on the  $\text{CaSO}_4\text{-H}_2\text{O}$  system was investigated under simultaneously high-pressure and high-temperature conditions by collecting Raman spectra from an external heated diamond anvil cell up to 360  $^\circ\text{C}$  and 3 GPa.

The study revealed that bassanite was formed directly from gypsum at 1.5 GPa at 160  $^\circ\text{C}$  and remained stable up to 210  $^\circ\text{C}$  at about 1 GPa when  $\gamma$ -anhydrite formed. Raman spectra of  $\gamma$ -anhydrite, in the low frequency region between 200 and 1200  $\text{cm}^{-1}$ , were extremely similar to that of bassanite due to the strong similarity of the two structures (Fig. 3.3-3). However, in the high frequency region, from 3200 to 3700  $\text{cm}^{-1}$  (Fig. 3.3-4), the dehydration from gypsum to bassanite to  $\gamma$ -anhydrite was more evident. In fact the two OH stretching modes of gypsum shifted to higher frequency as bassanite formed, due to the hydrogen bond weakness in bassanite with respect to the stronger hydrogen bonds of gypsum. No OH peaks were present in the spectra of  $\gamma$ -anhydrite.

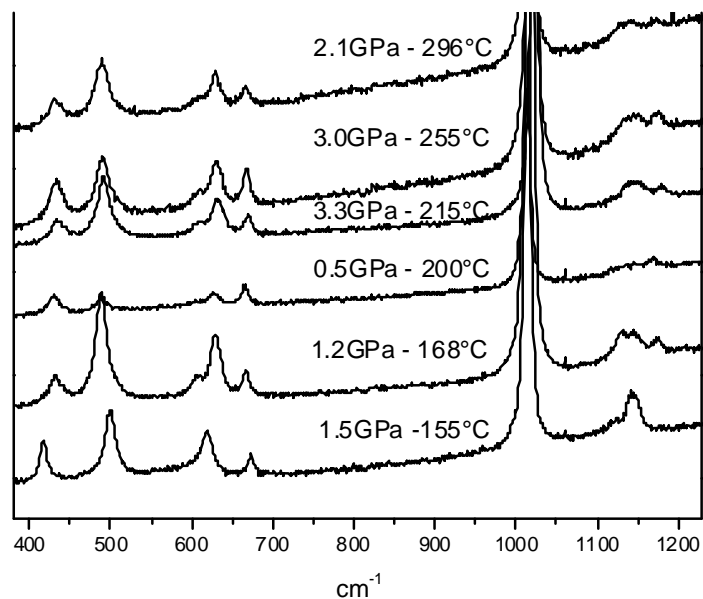


Fig. 3.3-3: Raman spectra of Ca-Sulphates at different P-T conditions

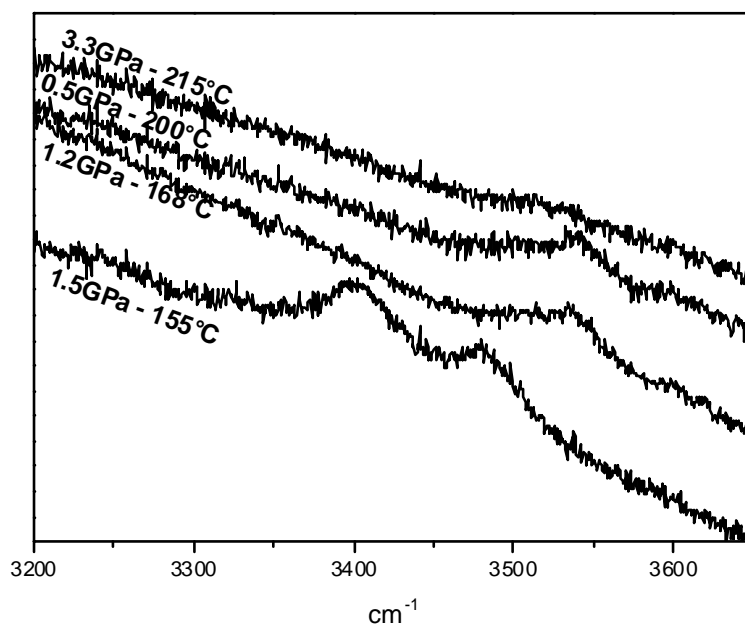


Fig. 3.3-4: Raman spectra of Ca-sulphates in the OH stretching region (3200-3700 cm<sup>-1</sup>) at different P-T conditions

At temperature higher than 360 °C and at 1.5 GPa, the strong change in the Raman spectrum indicated the occurrence of the phase transformation from  $\gamma$ -anhydrite to  $\beta$ -anhydrite. The transformation of  $\beta$ -anhydrite to the monazite-type structure was followed at room condition in decompression from 25 GPa to 0.001 GPa (Fig. 3.3-5). Evidence of the phase transition from the monazite structure to the anhydrite phase was observed at about 2 GPa at room temperature.

These data combined with the HP single-crystal X-ray diffraction data collected at the University of Perugia and with powder X-ray diffraction data collected at APS (GSECARS-BM13, Argonne, Chicago, USA) and at ESRF (ID09 beamline) allow to constrain the stability of the various phases in the CaSO<sub>4</sub>-H<sub>2</sub>O system.

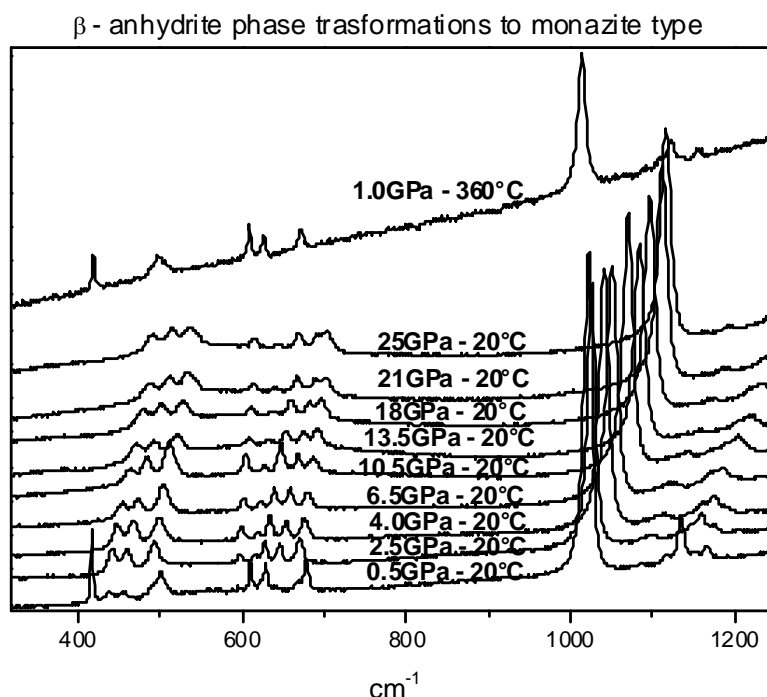


Fig. 3.3-5: Raman spectra of β-anhydrite at 1.0 GPa - 360 °C and from 25 GPa to 0.001 GPa at room temperature. The phase transformation from monazite type to β-anhydrite results evident at about 2 GPa.

**d.** *Synthesis and single-crystal X-ray diffraction of non-stoichiometric ringwoodite: Evidence of octahedral Si and Al (F. Nestola and R. Pozzobon/Padova, D.J. Frost, T. Boffa Ballaran, R. Spiess/Padova)*

It is well known that Mg<sub>2</sub>SiO<sub>4</sub> spinel, *i.e.*, ringwoodite, is the most abundant phase in the lower part of the transition zone and is stable down to 660 km where it decomposes to MgSiO<sub>3</sub> perovskite + periclase (MgO). The crystal-chemistry of ringwoodite has been investigated extensively, in particular with respect to the effect of Fe and/or H<sub>2</sub>O substitution on its structural properties. No data are present in the literature, however, concerning the substitution of Al in ringwoodite, likely because majoritic garnets in the transition zone are probably the major host of Al. However, at equilibrium conditions, some Al will partition into ringwoodite affecting the concentration of either vacancies or other defects such as hydrogen.

In the present study, we have synthesised a ringwoodite sample at 21 GPa and 1850 °C using a mixture of Mg<sub>2</sub>SiO<sub>4</sub> forsterite, Mg(OH)<sub>2</sub> and Al<sub>2</sub>O<sub>3</sub> as starting material. Crystals of a few

hundred micron were selected from the run products and were characterised using an electron microprobe in wavelength dispersive mode and single-crystal X-ray diffraction. The chemical analysis indicates that only a very small amount of Al ( $0.011 \text{ pfu} \pm 3$ ) is substituted into the ringwoodite structure. Moreover there is a slight excess of Si ( $1.040 \text{ pfu} \pm 7$ ) and deficit of Mg ( $1.897 \text{ pfu} \pm 7$ ). The crystals are of very high quality and structural refinements converged to a discrepancy factor of 1.8 %. Octahedral bond distances are consistent with some Si occupying the octahedral site since the M-O bond length is shorter than that of pure  $\text{Mg}_2\text{SiO}_4$  ringwoodite, whereas the tetrahedral bond distance suggests the presence of Al or/and Mg in the tetrahedral site since the T-O bond length is longer than that of pure  $\text{Mg}_2\text{SiO}_4$  ringwoodite. Further analysis are in progress to determine the coordination of Al and Si as well as the vacancy content of this sample and to characterise the high-pressure behaviour of Al-ringwoodite.

**e.** *In situ* determination of the  $\text{Fe}_3\text{O}_4 - h\text{-Fe}_3\text{O}_4$  transition at high pressures and temperatures using synchrotron-based XRD measurements (A. Woodland and K. Schollenbruch/Frankfurt/M., in collaboration with D.J. Frost and Y. Wang/Argonne)

Understanding the properties of chemically simple oxides like  $\text{Fe}_3\text{O}_4$  is fundamental to modelling more complex systems. In addition, the rare occurrence of magnetite as inclusions in diamonds means that this phase has a direct relevance to certain processes in the Earth's mantle, possibly those responsible for diamond formation. Therefore it is essential to determine the thermodynamic behaviour of  $\text{Fe}_3\text{O}_4$  at high pressures and temperatures. Magnetite is known to transform to the orthorhombic  $h\text{-Fe}_3\text{O}_4$  at 21 GPa and room temperature. However, the position of the phase boundary in  $P$ - $T$  space remains only poorly constrained. Recent electrical resistivity experiments performed by us at the BGI suggested that the  $dP/dT$  of the magnetite –  $h\text{-Fe}_3\text{O}_4$  is very shallow, but being an indirect method, the correct interpretation of these results remained open.

The position of this phase transition has been further investigated through the combination of a multianvil press and *in situ* X-ray diffraction measurements performed at the Advanced Photon Source (APS) at Argonne National Laboratory, U.S.A. For the experiments, we used the 10 mm edge length COMPRES-multianvil assembly with a Re furnace and a  $\text{W}_{95}\text{Re}_5\text{-W}_{84}\text{Re}_{26}$  thermocouple. Slits cut in the Re furnace allowed passage of the radiation through the sample to an energy dispersive detector. An advantage of such a setup is that the pressure can be determined *in situ* by measuring the cell parameter of a standard for which the equation of state is well known. Both MgO and Pt were used for this purpose. A 1 mm long cylinder of magnetite was placed directly below the standard material, surrounded by a MgO sleeve. The positioning of the sample or standard relative to the incident radiation was determined using X-ray imaging (Fig. 3.3-6). In measurement mode, the analysed spot was  $\sim 30 \mu\text{m}$  in diameter. *In situ* pressure determination also made it feasible to change pressure while at high temperature, permitting a very different  $P$ - $T$  trajectory during the experiments

than is possible with standard methods. For example, we were able to pressurise and depressurise over a range of  $\sim 5$  GPa while the experiments were held at temperatures between 800 °C and 1400 °C.

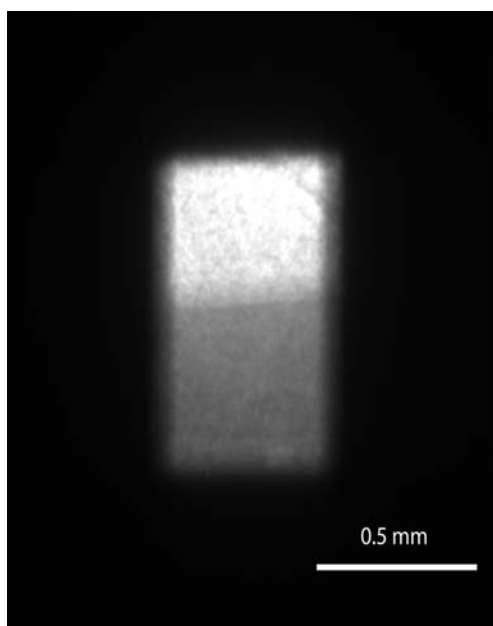


Fig. 3.3-6: X-ray image of the  $\text{Fe}_3\text{O}_4$  sample (grey area) and the pressure standards MgO + Pt (white area).

Up to 9-10 GPa only magnetite peaks were detected in the diffraction patterns, consistent with our observations during the electrical resistivity experiments (see annual report 2007). At  $\sim 10$  GPa peaks related to the  $h\text{-Fe}_3\text{O}_4$  phase began to appear. Rapid changes in peak intensities have been observed and often magnetite peaks re-grew in intensity until further pressure was applied. This behaviour is attributed to pressure buffering during the phase transition, causing a decrease in sample pressure that re-stabilised the lower pressure magnetite (sample pressure was indeed found to decrease slightly, or initially remain constant during further pressurisation). Even at pressures of  $\sim 15$  GPa, a few weak magnetite peaks were still present in the diffraction patterns. Rapidly changing intensities of peaks related to magnetite and  $h\text{-Fe}_3\text{O}_4$  were also observed during depressurisation, at about the same pressure range. This behaviour was observed in several experiments performed at temperatures of 800 °C, 1000 °C, 1300 °C and 1400 °C. These results imply that the magnetite –  $h\text{-Fe}_3\text{O}_4$  phase boundary is practically isobaric and lies around 10 GPa over a range of 600 degrees (Fig. 3.3-7). The electrical resistivity experiments are broadly consistent with such a boundary, considering that those measurements were always made during heating at a more or less constant pressure. In this later case, the phase transition would appear at a given elevated temperature due to the thermally-driven reaction kinetics, even if the pressure was high enough to stabilise the  $h\text{-Fe}_3\text{O}_4$  phase.

Preliminary analysis by SEM indicates some reaction occurred between the MgO and  $\text{Fe}_3\text{O}_4$ , particularly in the experiments performed at high temperatures, producing a (Mg,Fe)O solid solution. However, this observed effect (Fig. 3.3-8) represents the cumulative process during

the entire experiment and is considered to have little or no influence on our pressure determinations. The small diameter of the X-ray beam meant that the standard was measured well away from the interface with the magnetite. In addition, no systematic discrepancies in the pressures calculated from the MgO and Pt cell parameters are apparent. Further analysis of the diffraction patterns containing the  $h$ -Fe<sub>3</sub>O<sub>4</sub> phase are underway and the samples are being investigated by TEM to look for relicts of the high-pressure polymorph.

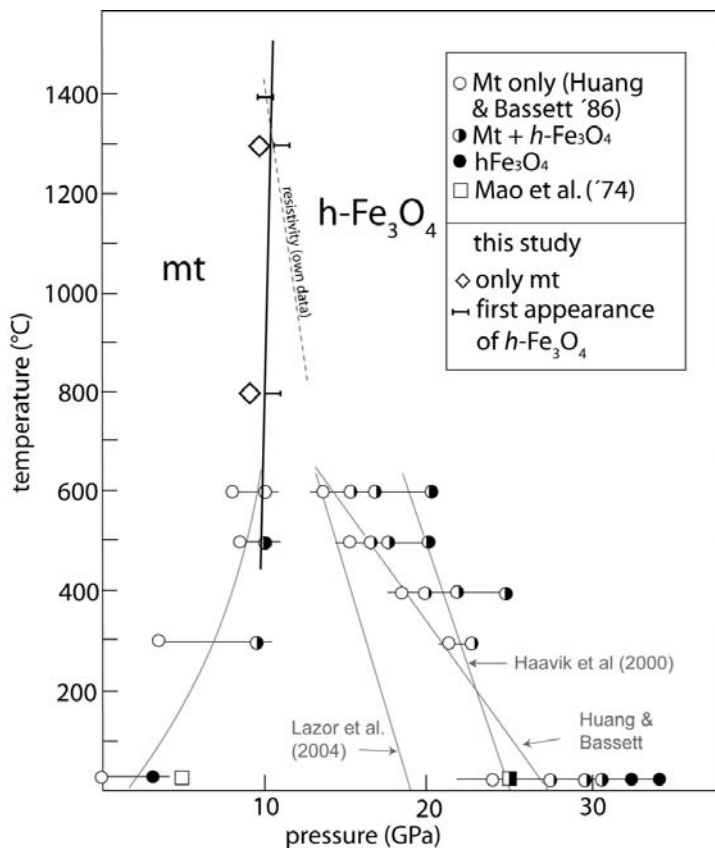


Fig. 3.3-7: Phase boundary (dashed line) is nearly isobaric and might, in contrast to the hitherto published boundaries, even be positive.

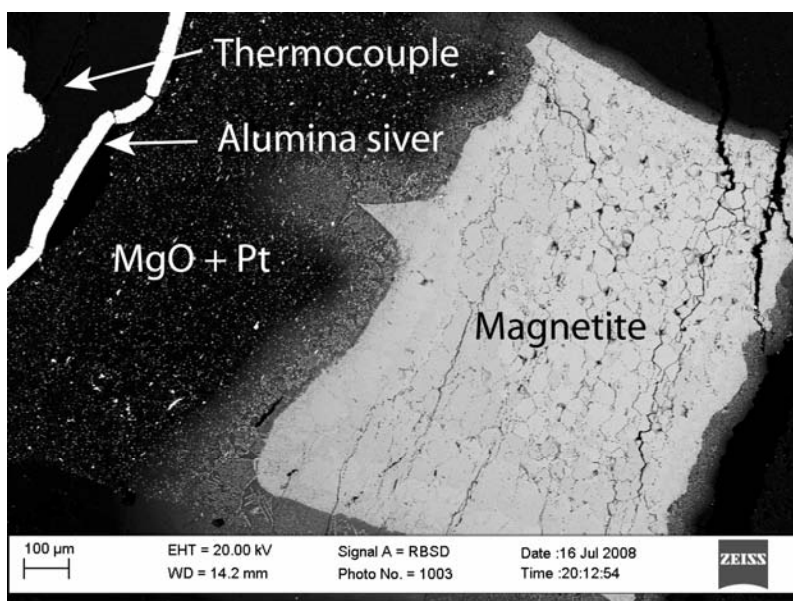


Fig. 3.3-8: SEM picture of a sample after 11 GPa and 1300 °C. On the left side are the two pressure calibrants MgO (dark phase) and Pt (bright spots) covered by an aluminium sliver. On the left rim a part of the thermocouple is visible. In contact to MgO a larger crystal growth in the Fe<sub>3</sub>O<sub>4</sub> can be observed.

**f.** *The dilemma of post-spinel structure of  $M\text{Fe}_2\text{O}_4$  ( $M=\text{Mg}, \text{Co}, \text{Zn}$ ) ferrite spinels: Mössbauer, Raman and XRD studies (G.Kh. Rozenberg and E. Greenberg/Tel Aviv, in collaboration with A. Kurnosov and L.S. Dubrovinsky)*

The spinel structure and its high-pressure (HP) modifications are adopted by many minerals of the upper Earth and play an important role in modeling major mineral phases of Earth's mantle. Therefore the behaviour of spinels under non-ambient conditions is of considerable geophysical importance and has been the subject of several studies, in terms of equilibrium properties and phase transformations.

The present study stems from our recent extensive high-pressure magnetic ( $^{57}\text{Fe}$  Mössbauer Spectroscopy (MS)) studies on magnetite ( $\text{Fe}_3\text{O}_4$ ). These studies up to 100 GPa revealed, in good agreement with recent XRD studies, a pressure-induced first order phase transition in the pressure range 25-35 GPa. However, in the high-pressure phase two  $\text{Fe}^{3+}$  sites with different hyperfine interaction parameters have been observed. These MS results are incompatible with the XRD studies suggesting that the  $h\text{-Fe}_3\text{O}_4$  phase has the  $\text{CaMn}_2\text{O}_4$ - (CML) or  $\text{CaTi}_2\text{O}_4$ -like (CTL) structures, where  $\text{Fe}^{3+}$  ions are in identical crystallographic sites. This discrepancy with the X-ray results initiated the present studies of a series of related normal and inverse ferrite spinels  $M\text{Fe}_2\text{O}_4$  ( $M=\text{Co}, \text{Zn}, \text{Mg}$ ); the main objective being a thorough structural and magnetic study and data analysis to clarify the post-spinel structure of ferrite spinels.

We addressed most of the objectives by conducting high-pressure studies up to 110 GPa with diamond anvil cells and employing X-ray diffraction using the rotating anode X-ray system at Bayerisches Geoinstitut and synchrotron radiation facilities as a means of probing phase transitions and performing precise structural studies at pressures above 30 GPa, beyond the spinel phase. Up to 55 GPa the pressure evolution of the vibrational properties of  $M\text{Fe}_2\text{O}_4$  ( $M=\text{Co}, \text{Zn}, \text{Mg}$ ) ferrite spinels also have been studied by means of Raman spectroscopy to identify possible subtle structural modifications. The obtained XRD and Raman spectroscopy data have been analysed taking into account the detailed results of  $^{57}\text{Fe}$  Mössbauer spectroscopy.

MS studies up to 110 GPa revealed for all materials a pressure-induced first order phase transition in the pressure range 25-40 GPa shown by the dramatic changes of the hyperfine interaction parameters. Similar to magnetite, in the HP phase of  $M\text{Fe}_2\text{O}_4$  ferrites two  $\text{Fe}^{3+}$  sites characterized by different quadrupole splitting (QS) and isomer shift (IS) values have been observed. A strong magnetic relaxation effect has been observed around the magnetic ordering temperature which decreases at elevated pressures, implying a ferromagnetic coupling in the HP phase. Up to the highest pressure measured, the ferric ions remain in the high-spin state as shown by the magnetic ordering taking place at low temperature. These HP phases are not quenchable.

Raman studies revealed a significant pressure evolution of the Raman spectra (Fig. 3.3-9). The modes shift towards higher energy and broaden with increasing pressure. In the pressure range between 25 and 40 GPa a significant change of the Raman spectra has been observed for all studied ferrite spinels. These observations are in good agreement with the XRD studies which revealed structural phase transitions in almost the same pressure ranges.

XRD studies show structural phase transitions to post-spinel HP structures at 25-40 GPa range. These HP phases are not quenchable. Based on MS studies the post-spinel phases of  $M\text{Fe}_2\text{O}_4$  ferrite spinels cannot be the  $\text{CaMn}_2\text{O}_4$  ( $Pbcm$ ) or  $\text{CaTi}_2\text{O}_4$  ( $Bbmm$ )-type structures. The only possible structure from an earlier proposed model characterized by two different  $\text{Fe}^{3+}$  sites is the  $\text{CaFe}_2\text{O}_4$ -(CFL) ( $Pnma$ )-type structure. A fit of the powder diffraction data using this structural model gives rather good results in the case of LeBail F(calc) Weighted (Model biased) refinement (Fig. 3.3-10) but poor results in the case of full-profile Rietveld refinement. Further careful experimental XRD studies, using He or Ne pressure medium, and thorough structural analysis are necessary to resolve the dilemma of the post-spinel structure of ferrite spinels.

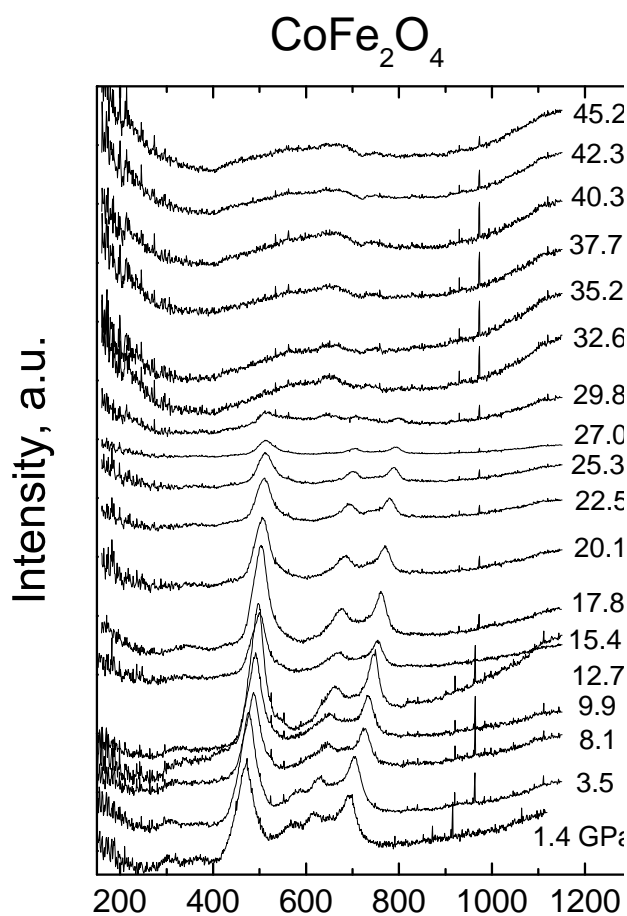


Fig. 3.3-9: Raman spectra of  $\text{CoFe}_2\text{O}_4$  recorded under compression.

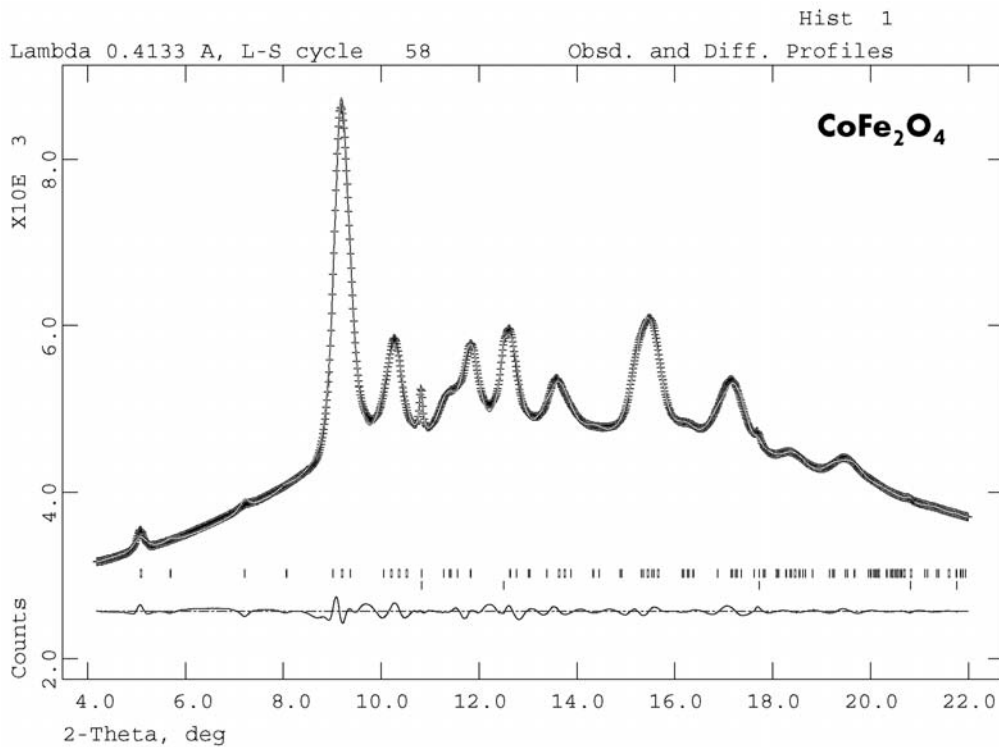
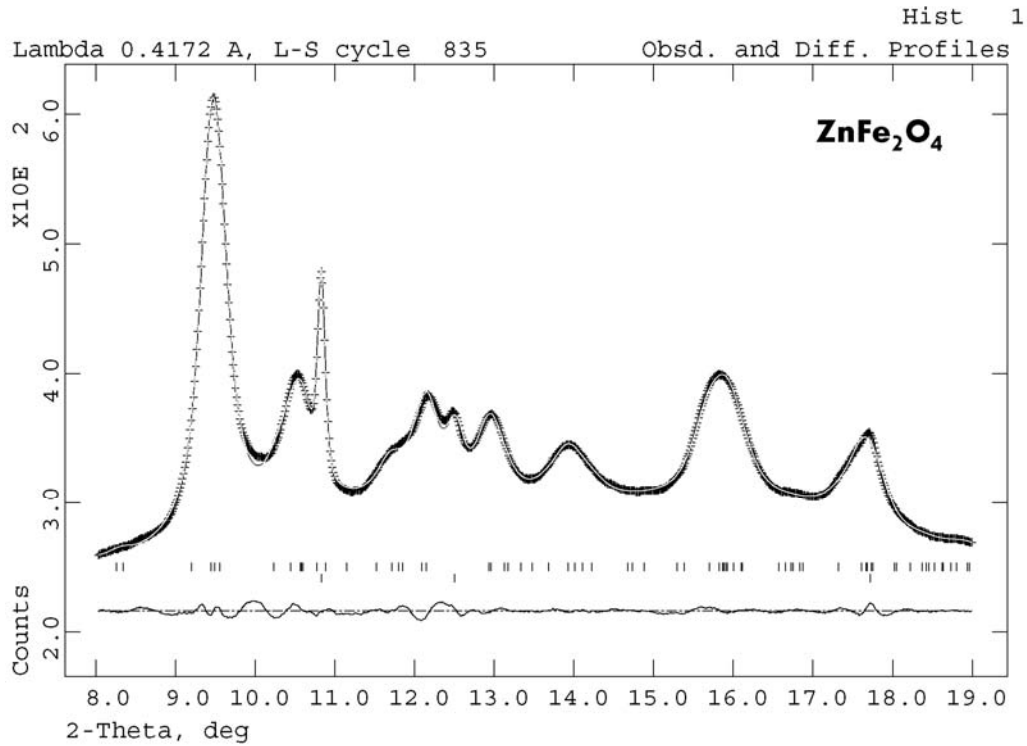


Fig. 3.3-10: Typical examples of analysed integrated patterns of spectra collected for  $ZnFe_2O_4$  (HP – upper ticks, Au – lower ticks), and  $CoFe_2O_4$  (HP – upper ticks, Pt – lower ticks) at 30.5 and 52.5 GPa respectively assuming  $CaFe_2O_4$ - model for HP ( $Pnma$ ). The GSAS program package was used for LeBail F(calc) Weighted (Model biased) refinement.

**g.** *Micro-XANES study of the Earth's lower mantle (Mg,Fe)(Si, Al)O<sub>3</sub> perovskite and (Mg,Fe)O ferropericlyase (O. Narygina, I.Yu. Kantor, X. Wu and L.S. Dubrovinsky, in collaboration with S. Pascarelli and G. Aquilanti/Grenoble)*

The Earth's lower mantle is believed to be composed predominantly by (Fe,Mg)(Si,Al)O<sub>3</sub> perovskite with a smaller amount of (Mg,Fe)O ferropericlyase and CaSiO<sub>3</sub> perovskite. It is also known that under high pressure the iron present in these phases undergoes a spin crossover transition which might influence the physical properties of these materials such as elasticity, electrical and thermal conductivity, element partitioning between phases, etc.

It is well established that Fe<sup>2+</sup> in (Mg,Fe)O ferropericlyase undergoes gradual high spin -low spin crossover at pressures above 40 GPa depending on composition. However the spin state of iron in (Mg,Fe)(Si,Al)O<sub>3</sub> perovskite under pressure is still controversial. According to K<sub>β</sub> X-ray emission spectroscopy, iron in silicate perovskite undergoes a crossover from the high spin (HS) to an intermediate spin state at 70 GPa with a following transition to the low spin state (LS) at 120 GPa. Published synchrotron Mössbauer spectroscopy (SMS) data suggest a HS-LS crossover at 70 GPa in Fe<sup>3+</sup>; whereas Fe<sup>2+</sup> remains in the HS state throughout the studied pressure interval. It is obvious that XES and Mössbauer spectroscopy techniques alone cannot provide a conclusive answer on the iron spin state in silicate perovskite under pressure.

X-ray Absorption Near Edge structure (XANES) is one of the most precise experimental techniques for following the electronic and local structure around Fe along with Electron Energy Loss Spectroscopy (EELS), and conventional and synchrotron Mössbauer spectroscopies (nuclear forward scattering: NFS). Taking advantage of the 3<sup>rd</sup> generation synchrotron sources, XANES can be relatively easily combined with the diamond anvil cell (DAC) technique for *in situ* measurements at high pressure and temperature conditions. The aim of this study was therefore to perform for the first time a systematic Fe K-edge XANES study of (Mg,Fe)SiO<sub>3</sub>, (Mg,Fe)(Si,Al)O<sub>3</sub> perovskites and (Mg,Fe)O ferropericlyase under pressure in order to test the strengths and limitations of this technique in complementing the information on the electronic state of iron in these compounds, and to define the abilities of the method to investigate spin transitions, particularly in Fe-bearing silicate perovskites.

*In situ* high-pressure micro-XANES measurements of Mg<sub>0.88</sub>Fe<sub>0.12</sub>SiO<sub>3</sub>, Mg<sub>0.86</sub>Fe<sub>0.14</sub>Si<sub>0.98</sub>Al<sub>0.02</sub>O<sub>3</sub> perovskite and Mg<sub>0.8</sub>Fe<sub>0.2</sub>O ferropericlyase samples were performed at the European Synchrotron Radiation Facility at the energy dispersive XAS beamline ID24, using diamond anvil cells with 300 μm culet size diamonds.

Measured Fe K-edges of ferropericlyase are presented as a function of pressure in Fig. 3.3-11a. With compression there is a gradual shift of the absorption edge position towards higher energies, however, some other changes also can be observed: (i) with increasing pressure the small peak at 7135 eV (feature B) gradually shifts to higher energies and finally “disappears”

converging with the peak at 7142 eV (feature C) at about 78GPa; (ii) the ratio between amplitudes of the peaks at 7130 eV (feature A) and 7170 eV (feature D) change significantly between 45 and 80 GPa (Fig. 3.3-11b). This change in absorption ratio is in agreement with previous results, obtained by XES and Mössbauer spectroscopy, that suggest a gradual HS-LS crossover in  $\text{Mg}_{0.80}\text{Fe}_{0.20}\text{O}$  starting at about 45-50 GPa.

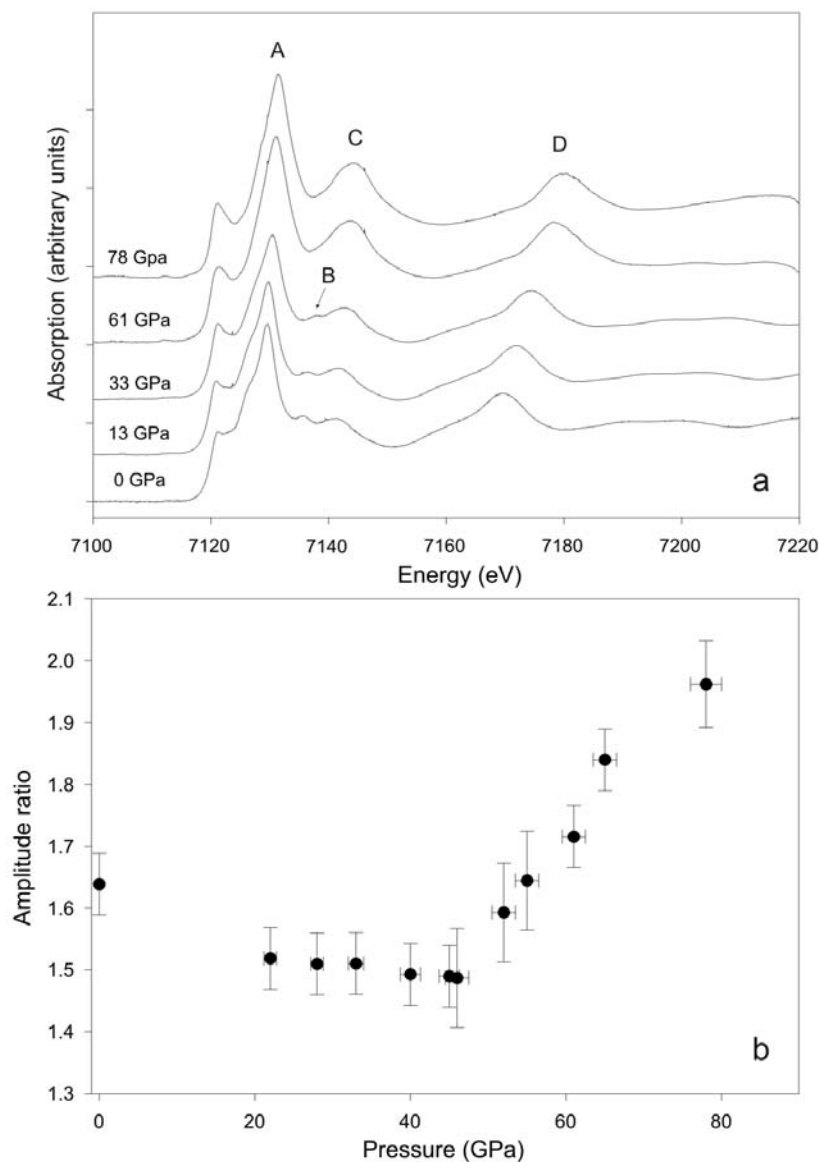


Fig. 3.3-11: (a) Pressure evolution of the  $(\text{Mg}_{0.8}\text{Fe}_{0.2})\text{O}$  XANES spectra taken at room temperature; and (b) the amplitude ratio between peaks at 7130 eV and 7170 eV of  $(\text{Mg,Fe})\text{O}$  XANES spectra as a function of pressure.

XANES spectra of both Al-free and Al-bearing perovskites (Fig. 3.3-12a,b) also show some changes at pressures between 30 and 80 GPa: (i) in the low energy region a small shoulder on the first broad peak appears with increasing pressure (feature A); (ii) in the high-energy region, the two peaks that are resolved at low pressures converge and eventually form one broad peak at 80 GPa (feature B); (iii) the amplitude ratio between two main peaks of the XANES spectra (at 7130 eV and 7170 eV) for both Al-free and Al-bearing silicate

perovskites decreases up to about 35 GPa and then remains constant (within the uncertainties) up to the highest reached pressure at 85GPa (Fig. 3.3-12c). This pressure interval corresponds to the gradual high spin-intermediate spin crossover in Fe-bearing silicate perovskite, that we recently detected by Mössbauer spectroscopy.

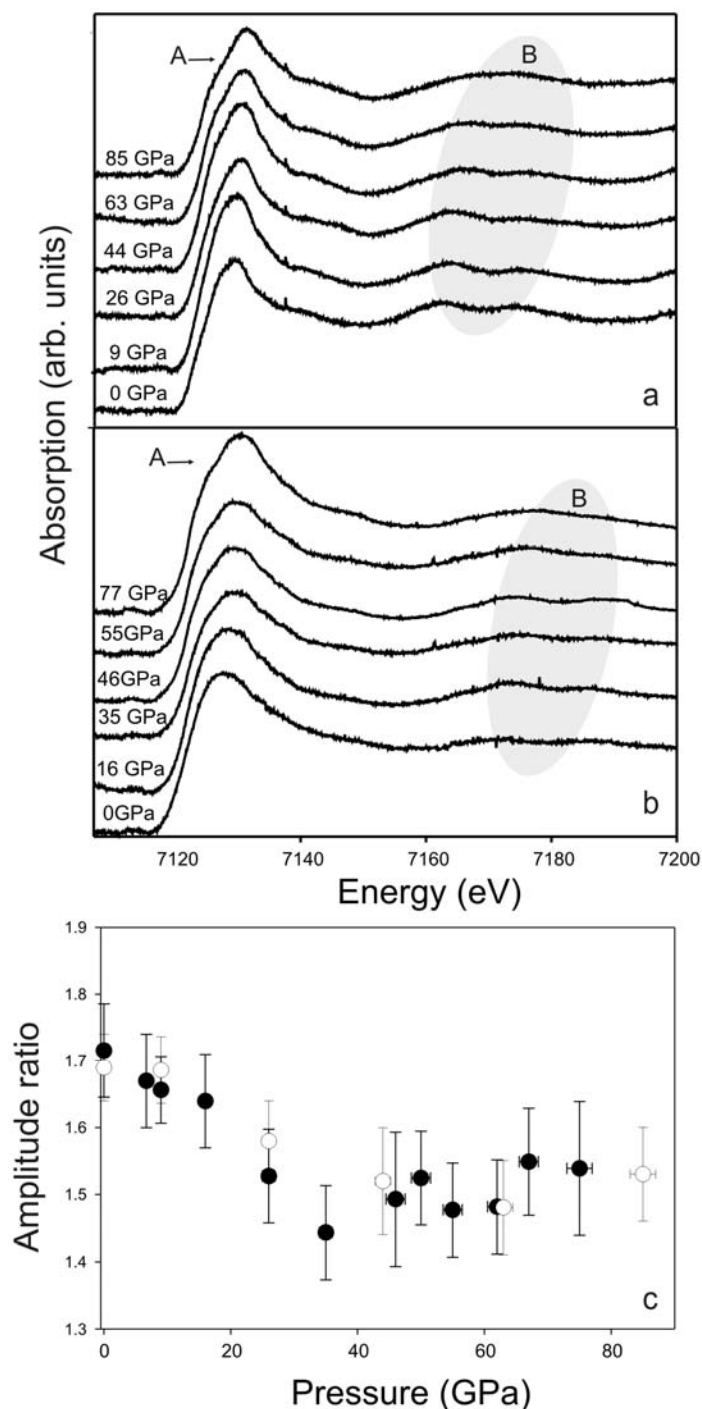


Fig. 3.3-12: Pressure evolution of the XANES spectra of (a) (Mg,Fe)SiO<sub>3</sub> and (b) (Mg,Fe)(Si,Al)O<sub>3</sub> perovskites. (c) The amplitude ratio between peaks at 7130 eV and 7170 eV of XANES spectra as a function of pressure for both Al-free (open circles) and Al-bearing (filled circles) silicate perovskites.

The effect of the iron spin state transition on the amplitude ratios between main XANES peaks is weaker in perovskite with respect to ferropericlyase. This could be related to the type of the transition. It is known that HS-LS crossover in (Mg,Fe)O is accompanied by a change in compressibility suggesting major changes in the local environment of iron with consequent visible changes in the XANES absorption features. In the other end, the crossover from HS to intermediate spin state in perovskite may not induce a significant change in the local environment of Fe as suggested by the weaker effect on the Fe K-edge.

To summarize, we performed for the first time a systematic Fe K-edge XANES study of (Mg,Fe)O ferropericlyase, (Mg,Fe)SiO<sub>3</sub> and (Mg,Fe)(Si,Al)O<sub>3</sub> perovskites at pressures up to 80 GPa. We conclude that the sensitivity of Fe K-edge XANES absorption to the changes in the spin state of iron depends on the type of transition. If the modification of the iron spin state is significant then the transition has a great effect on the absorption features, as we observed for (Mg,Fe)O ferropericlyase. In the case of (Mg,Fe)(Si,Al)O<sub>3</sub> perovskite the effect of the spin crossover on the absorption properties is weaker but can still be detected.

**h.** *Decomposition of FeTiO<sub>3</sub> perovskite to wüstite and ferropseudobrookite (X. Wu, G. Steinle-Neumann, O. Narygina, I.Yu. Kantor, C.A. McCammon and L.S. Dubrovinsky, in collaboration with V. Prakapenka/Chicago, V. Swamy/Clayton)*

(Mg,Fe)(Si,Al)O<sub>3</sub> silicate perovskite (pv) is believed to be the most abundant mineral of the Earth's lower mantle. At pressures > 120 GPa, it transforms into the CaIrO<sub>3</sub>-type post-perovskite (ppv) phase. Quite naturally, the high-pressure transitions of ppv have attracted the attention of numerous researchers. ppv-NaMgF<sub>3</sub> transforms to a phase with the *Pnmm* space group and becomes amorphous at lower pressures. First-principles computations indicated that ppv-NaMgF<sub>3</sub> transforms to a metastable phase *Pnma* at 43 GPa and then to another metastable *P6<sub>3</sub>/mmc* structure at 223 GPa. Recently, ppv-Al<sub>2</sub>O<sub>3</sub> has been predicted to transform to the U<sub>2</sub>S<sub>3</sub>-type (*Pnma*) phase at 370 GPa. Generally, ABX<sub>3</sub>-type perovskites are thought to dissociate into AX (CsCl-type) and BX<sub>2</sub> (cotunnite-type) at high temperature and high pressure. Similar to MgSiO<sub>3</sub>, FeTiO<sub>3</sub> crystallizes in an orthorhombic perovskite structure at pressures higher than 20 GPa. A recovery shock wave experiment indicates that FeTiO<sub>3</sub> separates into a mixture of FeO and TiO<sub>2</sub> at pressure above 65 GPa, and theoretical calculations have predicted a ppv phase of FeTiO<sub>3</sub> before the dissociation. Therefore, FeTiO<sub>3</sub> is a suitable analogue for MgSiO<sub>3</sub> perovskite to explore the high-pressure post-ppv phase transitions at relatively low pressures.

Here we present results of a study of FeTiO<sub>3</sub> at high temperatures and high pressures by *in situ* X-ray diffraction and <sup>57</sup>Fe Mössbauer spectroscopy using diamond anvil cell technique. Compared with the diffraction pattern obtained at 48 GPa (Fig. 3.3-13a), the intensities of the main peaks at 53 GPa around d-values of 2.5 Å (Fig. 3.3-13b) changed and some new peaks appeared, indicating the occurrence of a phase transformation. The sample was subsequently

heated to 2000 ( $\pm 200$ ) K. At high temperatures, we observed *in situ* a completely new XRD pattern (Fig. 3.3-13c); most diffraction peaks were preserved after quenching to room temperature, while two peaks are split (indicated by asterisks in Figs. 3.3-13c and 3.3-13d). These diffraction peaks can not be assigned to pv, ppv, or a mixture of known FeO and TiO<sub>2</sub> phases. By following the behaviour of these peaks on decompression, we were able to divide all reflections into three groups: one belonging to the pressure-transmitting medium (NaCl, labeled N); a second attributed to wüstite (W); and a third group of reflections that broaden upon decompression and disappear below 9 GPa. We assign these latter peaks to a new high-pressure form of FeTi<sub>2</sub>O<sub>5</sub> ferropseudobrookite (C2/c, Z=4), which is confirmed in the pure FeTi<sub>2</sub>O<sub>5</sub> experiments (Figs. 3-3.13f and 3-3.13g).

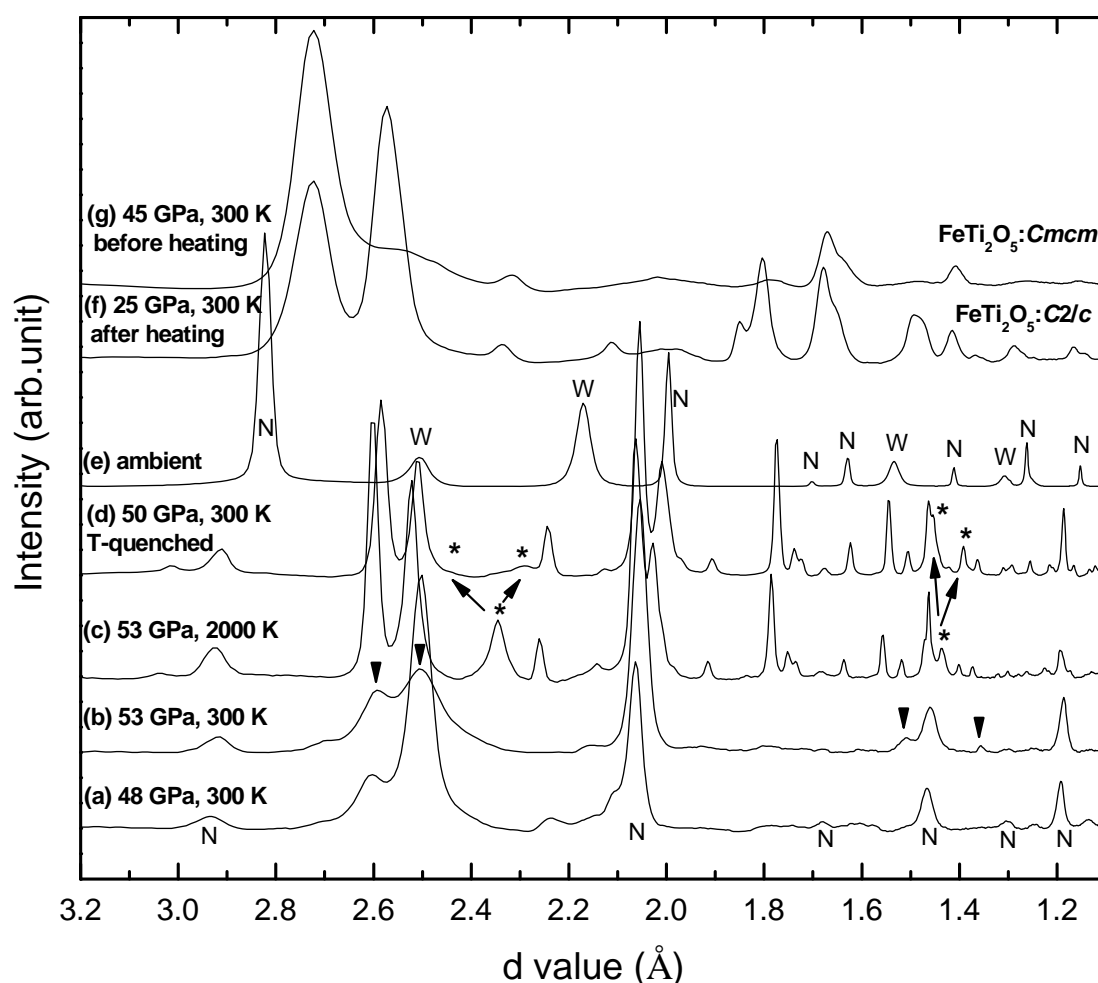


Fig. 3.3-13: Background subtracted XRD patterns of FeTiO<sub>3</sub> (a-e) and FeTi<sub>2</sub>O<sub>5</sub> (f-g). Peak labels: N - NaCl and W - wüstite.

At 45 GPa and room temperature, the Mössbauer spectrum of <sup>57</sup>FeTiO<sub>3</sub> shows a simple doublet due to the Fe<sup>2+</sup> component (Fig. 3.3-14a). On increasing pressure to 50 GPa, the spectrum changes (Fig. 3.3-14b) suggesting a phase transformation, consistent with the above XRD results. The sample was heated to ~ 2000 K at 50 GPa and subsequently quenched to

room temperature. According to the XRD results, the corresponding spectrum should be made of ferropseudobrookite and wüstite (Fig. 3.3-14c). However, the magnetic ordering of wüstite reported in previous work was not observed in the present experiments. Mössbauer spectra of the products of  $\text{FeTiO}_3$  dissociation were fitted (Figs. 3.3-14c and 3.3-14d). An additional  $\text{Fe}^{3+}$  component appeared in Fig. 3.3-14c and disappeared in Fig. 3.3-14d, which implies that charge transfer occurred in the products of  $\text{FeTiO}_3$  dissociation on decompression. According to the Fe component ratio of  $\Sigma$ ferropseudobrookite/ $\Sigma$ wüstite,  $\text{Fe}^{3+}$  is believed to be associated with ferropseudobrookite composition. Hyperfine parameters (isomer shift  $\delta$  and quadrupole splitting  $\Delta E_Q$ ) of  $\text{Fe}^{2+}$  components in the high-pressure ferropseudobrookite and amorphous ferropseudobrookite phase resulting from the  $\text{FeTiO}_3$  dissociation are consistent with those of pure  $\text{FeTi}_2\text{O}_5$ .

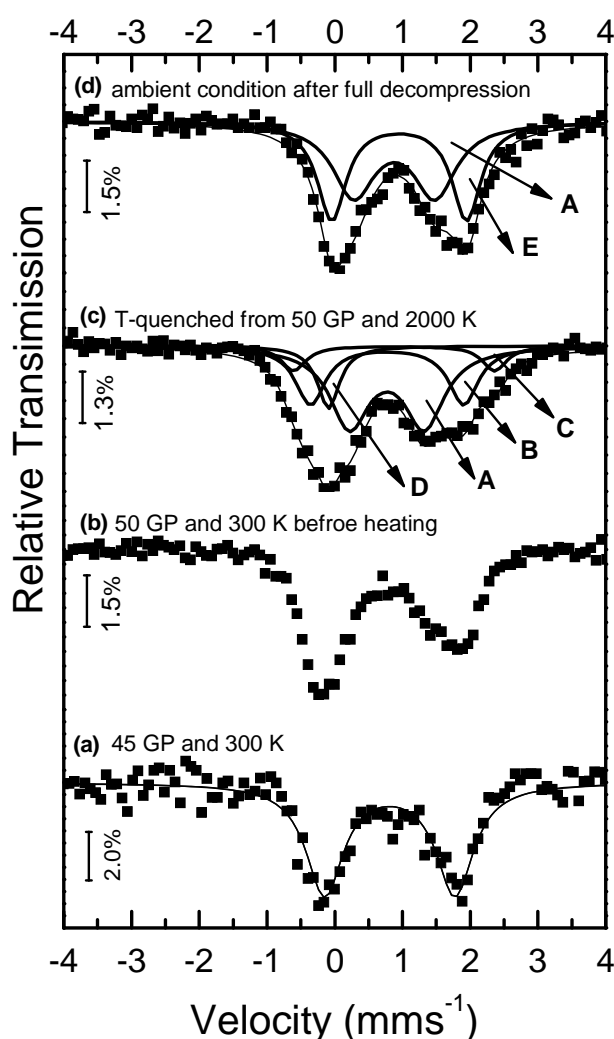


Fig. 3.3-14:  $^{57}\text{Fe}$  Mössbauer spectra at (a) 45 GPa and 300 K, (b) 50 GPa and 300 K before laser heating, (c) 43 GPa and 300 K from sample quenched from 50 GPa and  $\sim 2000$  K, and (d) ambient conditions after full decompression. A, B, C, D, and E denote different iron components. A is attributed to wüstite, B is attributed to the 4d iron site of ferropseudobrookite, and C belongs to the 8f iron site of ferropseudobrookite. There is a  $\text{Fe}^{3+}$  component “D”, while E is attributed to the amorphous ferropseudobrookite.

**i. Electronic transition in hexagonal closed packed iron ( $\epsilon$ -Fe) at high pressure (K. Glazyrin, O. Narygina, C.A. McCammon, G. Steinle-Neumann and L.S. Dubrovinsky)**

Iron is the most abundant transition element on our planet. Iron-nickel alloy with 5 to 15 % Ni is believed to be the major component of the Earth's core. For correct interpretation of seismic data or core dynamics modeling it is crucial to have a complete picture of different iron or iron nickel alloys properties.

The pressure-temperature ( $P$ - $T$ ) phase diagram of iron below 100 GPa is well established. There are only four stable phases:  $\alpha$ - and  $\delta$ -Fe (body centered cubic, *bcc*),  $\gamma$ -Fe (face centered cubic, *fcc*) and  $\epsilon$ -Fe (hexagonal closed packed, *hcp*). The  $\gamma$ -Fe is a high-temperature phase, and the  $\epsilon$ -Fe phase is observed only above  $\sim 12$  GPa and cannot be quenched. The  $\alpha$ -Fe phase is ferromagnetic at ambient conditions, and it undergoes a phase transition to the *hcp* Fe phase which was believed to be nonmagnetic. However, recent theoretical works suggest that an antiferromagnetic state (afm-II or afm-III) is more likely than a nonmagnetic state. Although these antiferromagnetic phases cannot be resolved in Mössbauer experiments, the calculated equations of state (EOS) for these phases show a better agreement with experimental data.

The phase diagram of iron-nickel alloys with low Ni content ( $< 25$  at.%) is similar to pure iron. As a result of compression, the  $\alpha$ -phase (*bcc*) of  $\text{Fe}_{1-x}\text{Ni}_x$  transforms directly to the  $\epsilon$ -phase (*hcp*). According to theoretical calculations the *hcp* phase is described best by the same afm-II magnetic model. Although nickel atoms should enhance magnetic moments on neighboring iron atoms, there are no evidences that  $\epsilon\text{-Fe}_{1-x}\text{Ni}_x$  ( $x < 0.25$ ) is static antiferromagnetic down to 11 K at 21 GPa.

Theoretical studies predict a magnetic transition of the afm-II antiferromagnetic phase to a paramagnetic phase at pressures of about 50-60 GPa. Sound velocities obtained in nuclear resonance inelastic X-ray scattering (NRIXS) measurements and impulsive stimulated light scattering (ISLS) measurements for pure  $\epsilon$ -Fe and for  $\epsilon\text{-Fe}_{0.92}\text{Ni}_{0.08}$  and  $\epsilon\text{-Fe}_{0.9}\text{Ni}_{0.1}$  show changes in slope of the mean sound velocity at pressures of about 40-50.

Previous X-ray diffraction studies at high pressures did not reveal any structural changes with compression at ambient temperature of *hcp* phase in iron and iron-nickel alloy. Without any evidences of a transition, softening of mean sound velocities  $v_m$  could be associated with changes in electronic/magnetic state of *hcp*-phase of Fe or Fe-Ni alloy. In order to test this hypothesis we conducted a Mössbauer spectroscopic study of pure Fe and of a  $\text{Fe}_{0.9}\text{Ni}_{0.1}$  alloy at pressures up to 60 GPa in diamond anvil cells (DAC) loaded with He as pressure transmitting medium. The diamonds culet sizes and holes diameters of the Re gaskets were 250  $\mu\text{m}$  and 120  $\mu\text{m}$  respectively.

For the preparation of the iron sample we used enriched  $^{57}\text{Fe}$  of 99.99 % purity. The  $\text{Fe}_{90}\text{Ni}_{10}$  sample was prepared by mixing appropriate amounts of  $^{57}\text{Fe}$  enriched iron and nickel powder

of 99.999 % purity. The mixture was compressed to 2 GPa in a piston-cylinder apparatus, heated above the melting point and subsequently quenched.  $^{57}\text{Fe}$  Mössbauer spectra (MS) were recorded at room temperature in transmission mode on a constant acceleration Mössbauer spectrometer using a nominal 370 MBq  $^{57}\text{Co}$  high specific activity source in a 12  $\mu\text{m}$  Rh matrix (point source). The velocity scale was calibrated relative to 25  $\mu\text{m}$   $\alpha$ -Fe foil. Mössbauer spectra were fitted to Lorentzian lineshapes using the commercially available fitting program NORMOS. Collection time for each spectrum varied from 24 to 48 h.

At pressures of 10-13 GPa, in good agreement with the data reported in the literature, the *bcc*  $\alpha$ -phase transforms to  $\epsilon$ -phase, which is associated with the absence of ferromagnetic order and with a lower value of Mossbauer central shift (Fig. 3.3-15, Fig. 3.3-16). The central shift of  $\epsilon$ -phase in pure Fe and  $\text{Fe}_{0.9}\text{Ni}_{0.1}$  gradually decreases with increasing pressure up to 40-45 GPa. At these pressures we observe an abruptly increase of the central shift by  $\sim 0.05$  mm/s in pure iron and  $\sim 0.15$  mm/s in the iron-nickel alloy (Fig. 3.3-15, Fig. 3.3-16). A further compression to 60 GPa shows again a continuous decrease of the central shift. The changes are reversible on decompression and were observed in several independent DACs loadings.

We have tested the hypothesis that the anomalous IS behaviour is caused by a transition from *afmII* to a non-magnetic phase by *ab initio* computations. While there is a slightly higher electron density at the nucleus (from the s electrons) for the *afmII* phase than the nm phase, the predicted difference is too small to be detectable in Mössbauer experiments. Additional computations will address changes in the electronic structure of iron and the FeNi alloy

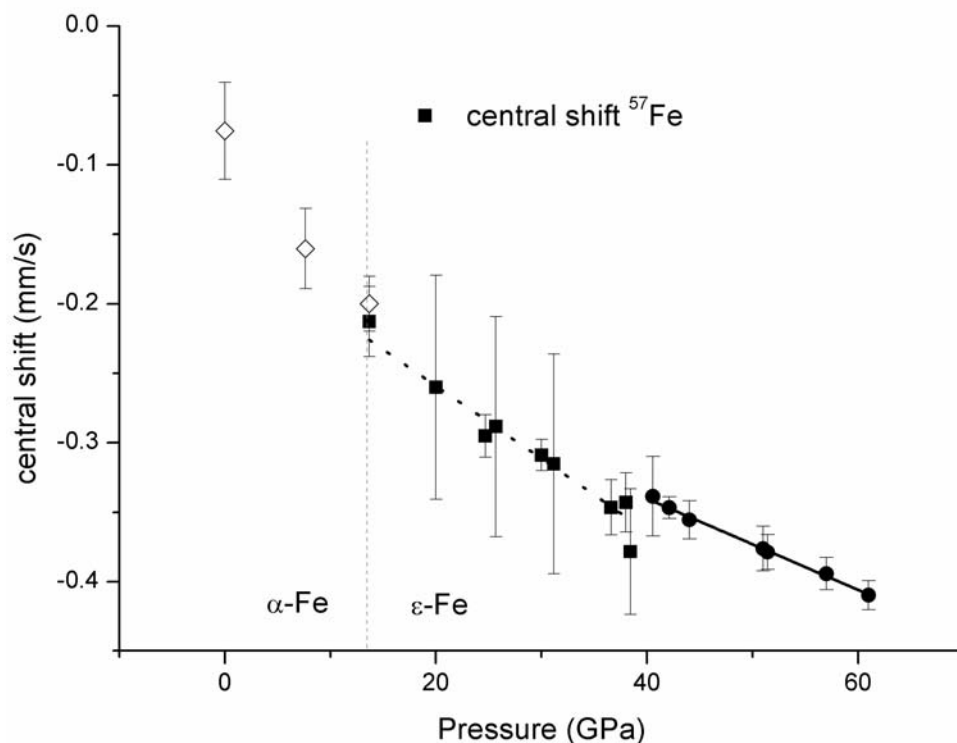


Fig. 3.3-15: The Mössbauer central shift pressure dependence for pure iron.

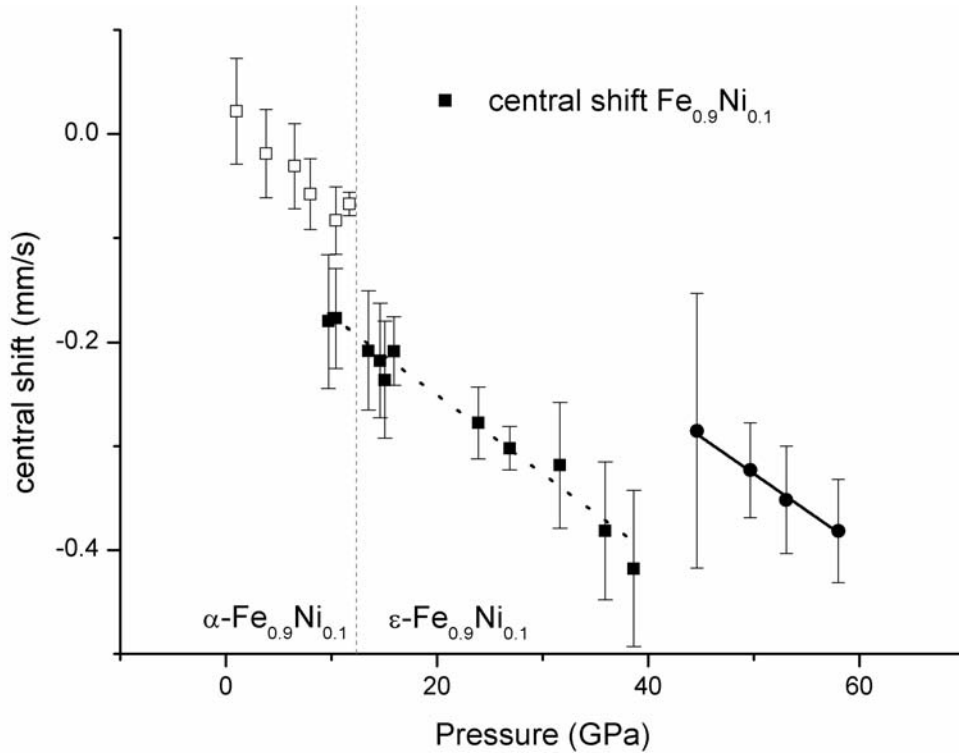


Fig. 3.3-16: The Mössbauer central shift pressure dependence for Fe<sub>0.9</sub>Ni<sub>0.1</sub>.

**j.** *Synthesis of a high density Ni<sub>3</sub>S phase at 20 GPa (D. Charee, in collaboration with Y. Litvin and E. Osadshii/Chernogolovka, O. Narygina, A. Kurnosov and L.S. Dubrovinsky, N.A. Dubrovinskaia/Heidelberg)*

It is generally accepted that the Earth's core is mainly composed of iron-nickel alloy with a certain minor amount of light element(s). H, C, O, Si and S are considered to be the most plausible candidates for the light component in the core. According to geochemical estimations the amount of sulphur in the Earth's core may be as high as 1.8 - 4.1 wt.%, which implies that iron and nickel sulphides may play an important role in determining certain properties of the core. While there are several experimental studies on phase relations in the Fe-S system, the Ni-S system is still poorly investigated.

We performed a series of high-pressure/high-temperature experiments in order to study phase relations in the Ni-S system within the compositional range from pure Ni to Ni<sub>3</sub>S<sub>2</sub>, and to synthesize the high-pressure phase Ni<sub>3</sub>S, which is not stable at ambient pressure. Homogeneous mixtures of metallic Ni and Ni<sub>3</sub>S<sub>2</sub> with appropriate compositions, including the Ni<sub>3</sub>S stoichiometry, were used as starting materials for large-volume multianvil press experiments at pressures up to 20(1) GPa at 800(20) °C. Quenched samples were analyzed by microprobe and X-ray diffraction techniques.

We observed the formation of the new Ni<sub>3</sub>S sulphide phase at 20 GPa (the corresponding XRD pattern is presented in Fig. 3.3-17). This phase has a body-centered lattice with

tetragonal symmetry and belongs to the  $I\bar{4}$  space group, the same as  $\text{Fe}_3\text{S}$ . The lattice parameters of the obtained  $\text{Ni}_3\text{S}$  phase are  $a=8.831(5)$  Å, and  $c = 4.455(3)$  Å. Atom coordinates and occupancies are presented in Table 3.3-1.

Atom	Wyck	Occ.	x	y	Z
Ni1	8g	0.851	0.0807	0.1091	0.2765
Ni2	8g	1.0	0.1288	0.4792	0.0209
Ni3	8g	0.846	0.3347	0.2764	0.2625
S	8g	1.0	0.3036	0.0469	0.0081

Table 3.3-1: Atom coordinates and substitution parameters (in  $E^2$ ) for the  $\text{Ni}_3\text{S}$  phase.

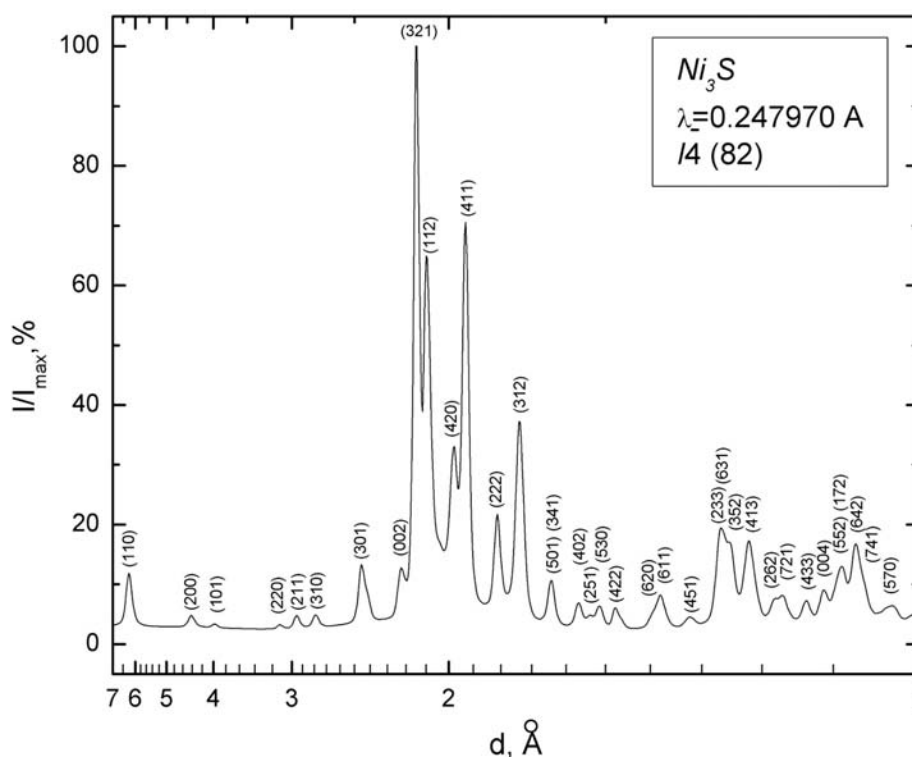


Fig. 3.3-17: X-ray diffraction pattern of the high-pressure phase of  $\text{Ni}_3\text{S}$  synthesized at 20 GPa and 800 °C.

In summary we synthesized a new high-pressure  $\text{Ni}_3\text{S}$  phase which crystallized in the  $\text{Fe}_3\text{P}$  – type structure. The phase is stable at pressures above 9-10 GPa. Structural identity of the  $\text{Fe}_3\text{S}$  and  $\text{Ni}_3\text{S}$  high-pressure phases and the fact that iron and nickel have similar chemical properties suggests the existence of a range of solid  $(\text{Fe,Ni})_3\text{S}$  solutions in the pressure-temperature stability region of the end-members ( $\text{Fe}_3\text{S}$  and  $\text{Ni}_3\text{S}$ ).

**k.** *Magnetic structure and electron density of states of Fe<sub>2</sub>SiO<sub>4</sub> fayalite from ab initio computations (Z. Tang and G. Steinle-Neumann)*

The incorporation of Fe into the olivine structure can considerably change its physical properties: for example variations in Fe content will affect the phase transitions occurring as a function of pressure as well as their sharpness. In order to fully understand the variation of properties in the (Mg,Fe)<sub>2</sub>SiO<sub>4</sub> olivine solid solution a good characterisation of the end-members is of critical importance. While forsterite has been studied extensively at high pressure in both experiments and computations, information on Fe<sub>2</sub>SiO<sub>4</sub> fayalite is limited. This is true in particular for the magnetic structure of Fe<sub>2</sub>SiO<sub>4</sub>, even at ambient pressure. At cryogenic temperature below ~ 65 K, Fe<sub>2</sub>SiO<sub>4</sub> is reported to show non-collinear anti-ferromagnetic (afm) order. The olivine structure has two distinct Mg/Fe (M1 and M2) sites that connect the isolated SiO<sub>4</sub> tetrahedra. While experiments show that the Fe atoms order anti-ferromagnetically on the Fe-M2 sublattice, on the M1-sublattice the magnetic moments are canted from collinear afm alignment. The coupling between these two sublattices can not be resolved experimentally and an ambiguity exists (afmI vs. afmII). Density functional theory (DFT) based computations on the collinear approximation to the afm structure were able to establish which of the magnetic structures is energetically favored at ambient pressure (afmI).

Here we explore the stability of the afmI configuration under pressure relative to afmII and ferromagnetic alignment by means of DFT-based computations, implemented in the projector-augmented-wave (PAW) method in the VASP software package, using both the generalized gradient approximation to the exchange and correlation potential as well as the LDA+U method which corrects for self-interaction of the localized electrons for Fe. We find that over the whole compression range considered ( $0.7 < V/V_0 < 1.1$ ) the afmI structure remains energetically favored. The magnetic moments in the afmI structure decrease only slightly over the compression range considered due to delocalization effects (Fig. 3.3-18). However, under

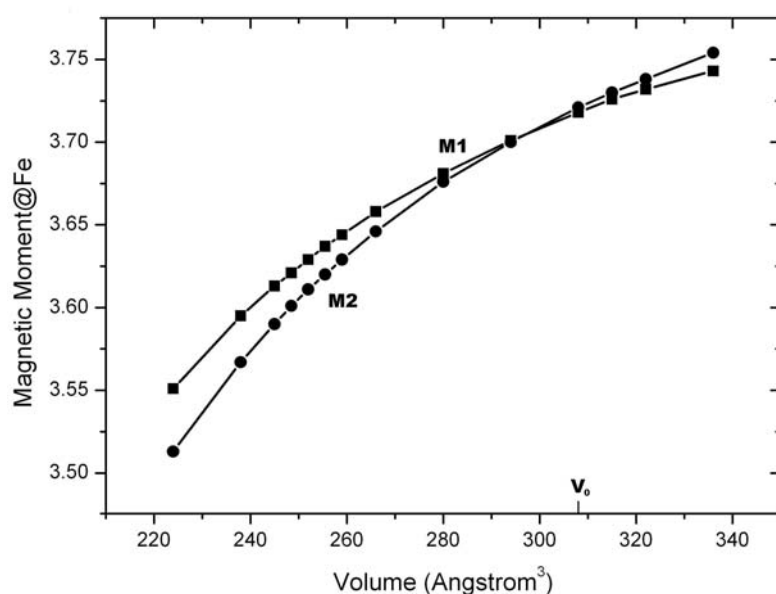


Fig. 3.3-18: Magnetic moments of collinear afmI fayalite as a function of volume from LDA+U computations. Filled circles show the magnetic moment for the M2 site, filled squares the moments for the M1 site.

compression the moment on the M1 site is larger than that on the M2 site, opposite to the situation at ambient pressure.

**1. High-pressure phase transitions of titanium oxides: Ab initio computations (X. Wu, E. Holbig, G. Steinle-Neumann and L.S. Dubrovinsky)**

Due to the various valence states of Ti many different mineral phases exist in the Ti-O system, including TiO, Ti<sub>2</sub>O<sub>3</sub>, Ti<sub>3</sub>O<sub>5</sub>, Ti<sub>4</sub>O<sub>7</sub>, Ti<sub>5</sub>O<sub>9</sub>, and TiO<sub>2</sub>. Diverse physical and chemical properties of these compounds are of considerable interest in material sciences. High-pressure behaviour of titanium oxides has also attracted interest in Geosciences because they are regarded as analogues for the components of the Earth's mantle; for example, the high-pressure structural stability of TiO<sub>2</sub> is similar to that of SiO<sub>2</sub> at high pressure. Ti<sub>3</sub>O<sub>5</sub> (TiTi<sub>2</sub>O<sub>5</sub>) provides a basis for discussing many AB<sub>2</sub>O<sub>5</sub> compounds, removing complications of cation ordering/disordering, especially in theoretical simulations. Ti<sub>2</sub>O<sub>3</sub> is another suitable composition to explore phase relations in A<sub>2</sub>O<sub>3</sub> compounds, such as the Rh<sub>2</sub>O<sub>3</sub>II, perovskite, post-perovskite, U<sub>2</sub>S<sub>3</sub> and  $\alpha$ -Gd<sub>2</sub>S<sub>3</sub> structures as well as its decomposition in constituting oxides (*i.e.*, TiO+Ti<sub>3</sub>O<sub>5</sub> or TiO+TiO<sub>2</sub>), possibility explored also for Al<sub>2</sub>O<sub>3</sub>, Fe<sub>2</sub>O<sub>3</sub> and also MgSiO<sub>3</sub>.

The calculations performed here are based on the density functional theory (DFT) with the generalized gradient approximation (GGA), as implemented in the VASP and WIEN2K software packages. For TiO, a phase transition occurs at 70 GPa from the B1 to the B2 phase. The perfectly ordered TiO is proposed with a lattice constant of 4.2912 Å, bigger than that of vacancy-containing TiO. For rutile TiO<sub>2</sub> (*P4<sub>2</sub>/mnm*, Z=2), four experimentally observed high-pressure polymorphs are considered: TiO<sub>2</sub>II (*Pbcn*, Z=4), MI (*P2<sub>1</sub>/c*, Z=4), OI (*Pbca*, Z=8) and OII (*Pnma*, Z=4). In our computations rutile transforms to MI at 6 GPa, then to OI at 27 GPa, finally to OII at 40 GPa (Fig. 3.3-19), which is consistent with the experimental results at 12 GP, 30 GPa, and 48 GPa. Here we found that the TiO<sub>2</sub>II has a lower energy than that of the rutile at lower pressure, which can explain the reason of the TiO<sub>2</sub>II absence on compression and its occurrence on decompression. For Ti<sub>3</sub>O<sub>5</sub>, the high-pressure phase (*C2/c*, Z=4) observed for FeTi<sub>2</sub>O<sub>5</sub> is confirmed to be a stable phase at high pressure. For Ti<sub>2</sub>O<sub>3</sub>, the sequence of phase transitions is from corundum to U<sub>2</sub>S<sub>3</sub> (*Pnma*, Z=4) at 2.5 GPa, then to TiO (B2) + TiO<sub>2</sub> (cotunnite) at 154 GPa (Fig. 3.3-20). In our computations Ti<sub>2</sub>O<sub>3</sub> does not adopt the Rh<sub>2</sub>O<sub>3</sub>II, perovskite, post-perovskite, or  $\alpha$ -Gd<sub>2</sub>S<sub>3</sub> structures, unlike many other sesquioxides. The U<sub>2</sub>S<sub>3</sub> phase with sevenfold and eightfold coordinated cations is proposed to be a potential post-ppv phase for Al<sub>2</sub>O<sub>3</sub> at pressures above 370 GPa, which means it is very hard to verify the prediction with the present experimental technologies. The very low transition pressure to the U<sub>2</sub>S<sub>3</sub> phase makes of Ti<sub>2</sub>O<sub>3</sub> a suitable analogue to explore the properties of this possible post-ppv structure.

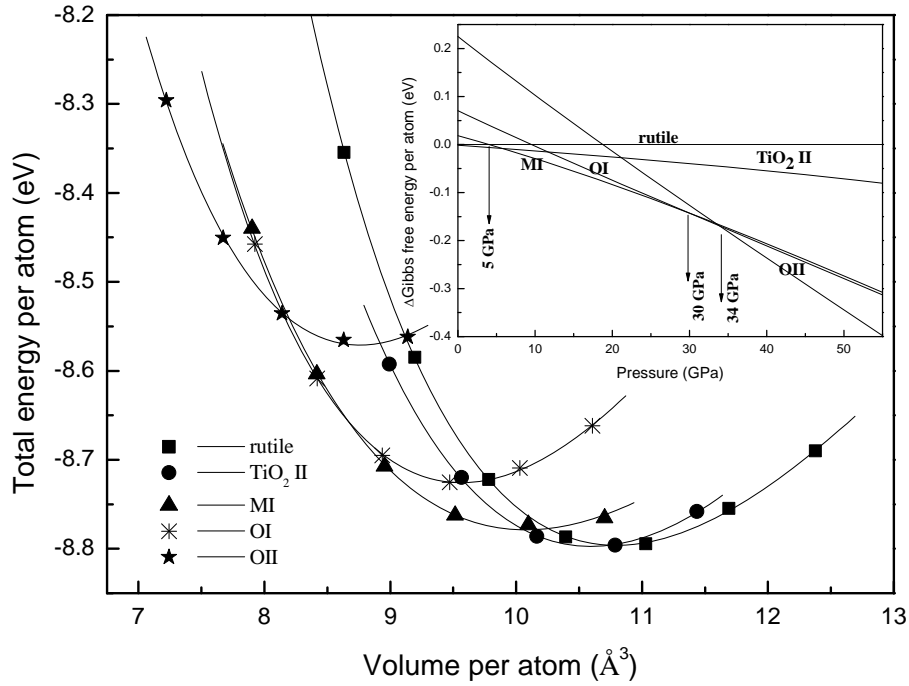


Fig. 3.3-19: Calculation of the total energy vs. volume for  $\text{TiO}_2$  with the rutile,  $\text{TiO}_2$  II, MI, OI and OII phases. Inset: calculated different Gibbs free energy vs. pressure for all phases. The corresponding phase-transition pressures are marked.

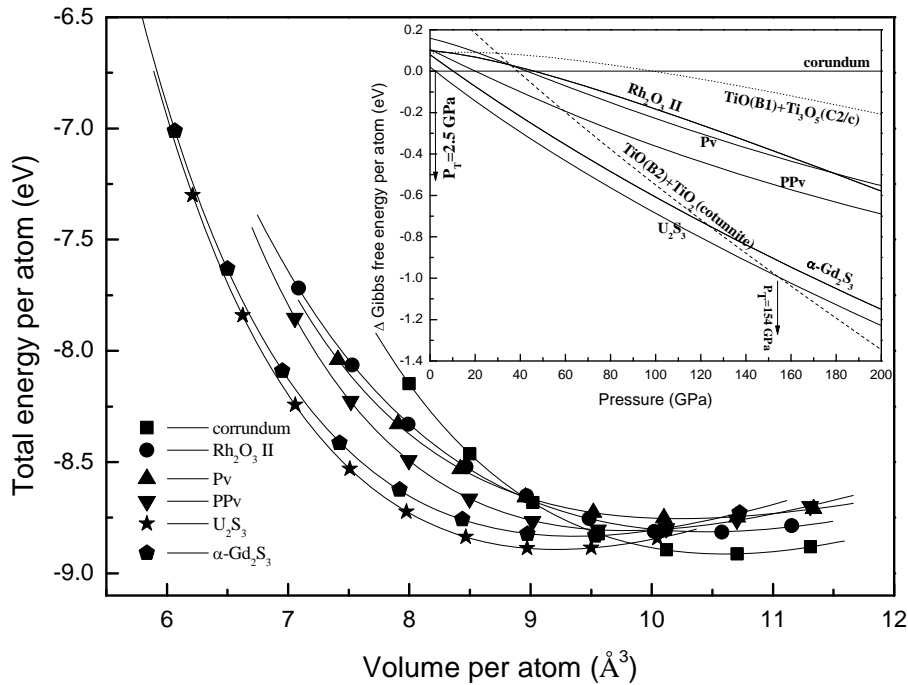


Fig. 3.3-20: Calculation of the total energy vs. volume for  $\text{Ti}_2\text{O}_3$  with the corundum,  $\text{Rh}_2\text{O}_3$  II, pv, ppv,  $\alpha\text{-Gd}_2\text{S}_3$ , and  $\text{U}_2\text{S}_3$  phases, and the possible dissociation assemblages. Inset: calculated different Gibbs free energy vs. pressure for all phases. The corresponding phase-transition pressures are marked.

**m.** *Anomalous pressure-evolution of the axial ratio  $c/a$  in hcp cobalt: Interplay between structure, magnetism and lattice dynamics (G. Steinle-Neumann, in collaboration with D. Antonangeli, L.R. Benedetti and D.L. Farber/Livermore; A.-L. Auzende and J. Badro/Paris; M. Hanfland and M. Krisch/Grenoble)*

The structure and elastic properties of 3d transition metals strongly depend on the d-electron occupancy and their magnetic state. At ambient conditions, progressive filling of the 3d bands drives the stable elemental phase from bcc (iron), to hcp (cobalt), and finally fcc (nickel). Increasing pressure also stabilizes the hcp and then the fcc structure over the bcc structure. In both cases, suppression of the magnetic moment is considered the driving parameter. Indeed, compression leads to a broadening of the electronic bands and hence to a reduction of the density of states at the Fermi level, eventually driving the system to a non-magnetic state. Among all the elements or ordered compounds, cobalt exhibits a non-zero magnetic moment over the largest  $P$ - $T$  domain. Under compression the hcp phase is stable up to 100 GPa, where it transforms martensitically to an fcc phase. Well below the high-pressure hcp-fcc transition, the elastic and vibrational properties of cobalt display anomalous behaviour: the aggregate sound velocities show a departure from the linear evolution with density. Similarly, a decrease in the E2g mode Grüneisen parameter is observed in the 70-80 GPa range. While it is clear that there are strong elastic anomalies in this pressure range, quite surprisingly, there has been no indication of any structural discontinuity.

In a combined experimental and computational study we explored the structure of Co over this pressure range in more detail to elucidate this anomalous behaviour. In high resolution angle-dispersive X-ray diffraction measurements we observe a markedly different behaviour in the  $c/a$  axial ratio from that of previous experimental work and *ab initio* calculations. Our data display a monotonic decrease in the axial ratio with a minimum near 70-75 GPa. Above this pressure,  $c/a$  has positive pressure dependence (Fig. 3.3-21). The inversion in the pressure evolution of the axial ratio takes place in the same pressure interval where the anomalies in the elastic and vibrational properties have been observed. To shed light on the origin of the axial ratio anomaly and on the potential link with the elastic and vibrational properties, we performed full-potential linearized augmented plane-wave calculations, implemented in the Wien2k code, using the generalized gradient approximation to the exchange-correlation potential. We carried out computations for volumes corresponding to pressure of 0-140 GPa with a dense pressure sampling. Total energies were evaluated for  $c/a$  ratios between 1.55 and 1.69, in steps of 0.01. The equilibrium  $c/a$  was obtained from fitting a quadratic polynomial to the E- $c/a$  curve at constant volume. The computed equilibrium values for the axial ratio are reported in the inset of Fig. 3.3-21. In spite of a slight offset in the absolute values at low compression, the spin-polarized calculations compare favorably with the measurements. Most importantly, the  $c/a$  ratio of ferromagnetic hcp cobalt decreases with pressure to 75 GPa and then increases, progressively approaching the values computed for the non-magnetic phase, which, conversely, monotonically increases over the entire pressure range. A comparison with

the pressure evolution of the magnetic moment (inset Fig. 3.3-21) provides the most direct explanation for the observed behaviour: compression induces a slow reduction of the magnetic moment up to 70-80 GPa, above which the magnetism is rapidly lost and the axial ratio  $c/a$  of ferromagnetic cobalt changes its pressure derivative, coming up to match the  $c/a$  values of non-magnetic cobalt. This scenario is also supported by the linear decrease of the magnetization energy with compression, which reaches zero near 130 GPa. This magneto-elastic coupling likely also drives a softening of the elastic moduli and provides an explanation for the deviation from linear density dependence seen in the aggregate sound velocities.

While the proposed model is consistent with previous experimental and computational work, recent X-ray magnetic circular dichroism measurements report a rapid and uniform decrease of the magnetic dichroism with compression, suggesting a constant decline in magnetic moment over the entire hcp phase stability range. These results differ from the predictions of density functional theory and measurements of the pressure dependence of the Curie temperature. Resolving these issues will critically hinge on future confirmation of the X-ray magnetic circular dichroism measurements.

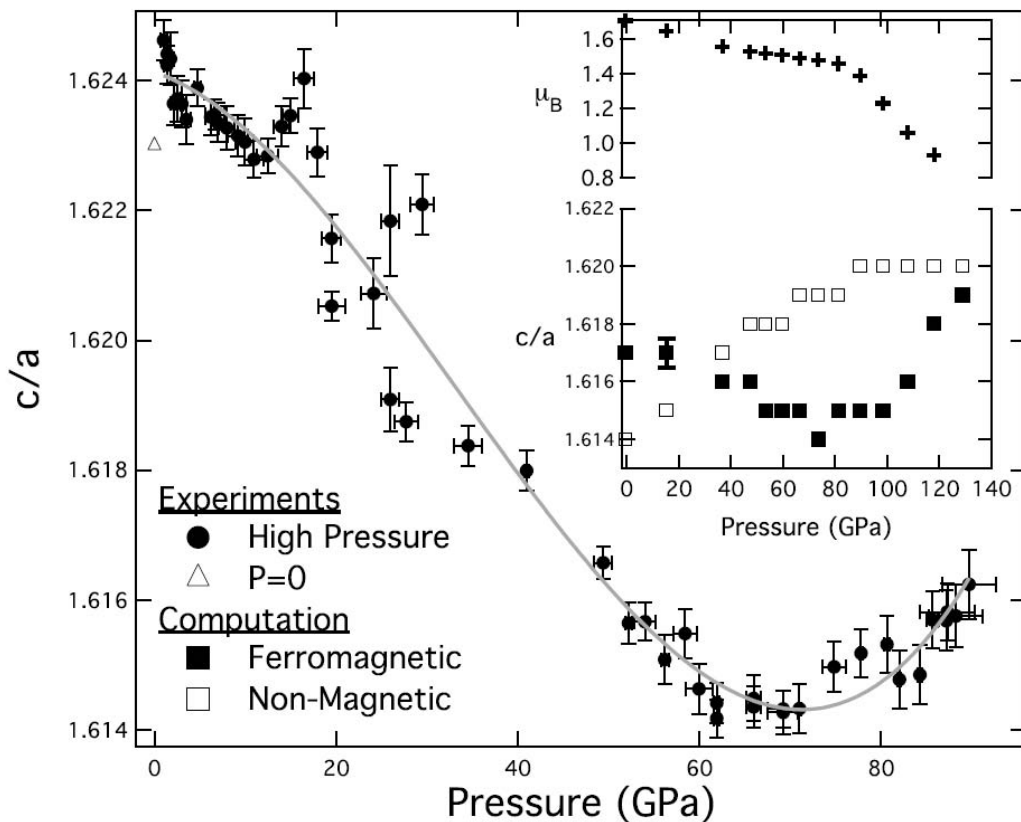


Fig. 3.3-21: Pressure evolution of the  $c/a$  axial ratio. The solid curve is a polynomial fit to the experimental data. Inset: theoretically predicted pressure evolution of the magnetic moment and computed values of  $c/a$  for magnetic (filled symbols) and non-magnetic (open symbols) hcp Co.

**n. Dense hydrous silicates in the  $MgFeSiO_4 - H_2O$  system up to 25 GPa (G. Ganskow, F. Langenhorst and D.J. Frost)**

A number of high-pressure studies have clarified the stability of dense hydrous magnesium silicates (DHMS) in magnesium-rich peridotite systems relevant for the Earth's interior. These studies reveal that DHMS may be stable at the low temperatures representative of subduction conditions; they are certainly not stable along the normal mantle geotherm. On the contrary, the stability of dense hydrous silicates in iron-rich silicate systems is much less explored. Such data is however essential to assess the water budgets and storage capacities of more iron-rich planetary mantles such as those of Mercury and Mars. To determine the possible iron-rich high-pressure phase assemblages under water-saturated conditions, we have carried out systematic high-pressure experiments on a  $MgFeSiO_4 - H_2O$  starting composition.

As starting material we used a powder made of brucite, fayalite, and quartz mixed in the following proportions:  $2 Mg(OH)_2 + Fe_2SiO_4 + SiO_2$  (nominally  $Fe_{50}$  composition). Multianvil experiments were carried out at pressures between 6 and 25 GPa and at temperatures between 500 °C and 1500 °C. Subsequently, recovered samples were examined by electron microprobe, transmission electron microscopy, X-ray diffraction, Raman and FTIR spectroscopies.

Dense hydrous silicates (phases A, D, and superhydrous B) are dominant phases at low temperatures; they can accommodate low yet variable amounts of iron and occur in distinct phase assemblages. Phase A accommodates 15 mol.% iron and is stable at temperatures and pressures up to 800 °C and 15 GPa, pressure at which it coexists with ringwoodite. Phase D occurs first at 18 GPa and 750 °C, forming an assemblage with ringwoodite and brucite; and it is stable up to 23 GPa and 1300 °C. At pressures of ~ 20 - 23 GPa, phase D (Fig. 3.3-22) occurs in phase assemblages with superhydrous B and magnesiowüstite (1150-950 °C) as well as with ringwoodite and magnesiowüstite (1300-1150 °C). In all these experiments, phase D retains a composition with 5 mol.% iron, whereas superhydrous B contains about 10 mol.% Fe. Beyond the stability limits of the dense hydrous silicates, ringwoodite is the dominant phase either as single phase (15 GPa, 950-1150 °C) or in assemblages with stishovite and magnesiowüstite (18-23 GPa, 1150-1500 °C).

These results show that the dense hydrous silicates are also stable in the  $MgFeSiO_4 - H_2O$  system with a maximum uptake of 15 mol.% iron. Moreover, the incorporation of iron in the dense hydrous silicates affects strongly their stabilities. Whereas phase D is stable at 18 GPa up to 1100 °C in the  $MgSiO_4 - H_2O$  system, it is only stable up to 800 °C at the same pressure in the  $MgFeSiO_4 - H_2O$  system. An enormous difference has been also found for the decomposition of superhydrous B. The addition of iron seems to lower the decomposition boundary of superhydrous B by about 7 GPa. Since the stability of phase D is limited to 1300 °C at 20 GPa in an iron-rich composition, the dense hydrous silicates are not stable along the currently assumed thermal gradient of Mars. This implies that the water storage capacity in an

iron-rich mantle is mainly determined by the water solubility in nominally anhydrous phases (olivine, wadsleyite, and ringwoodite).

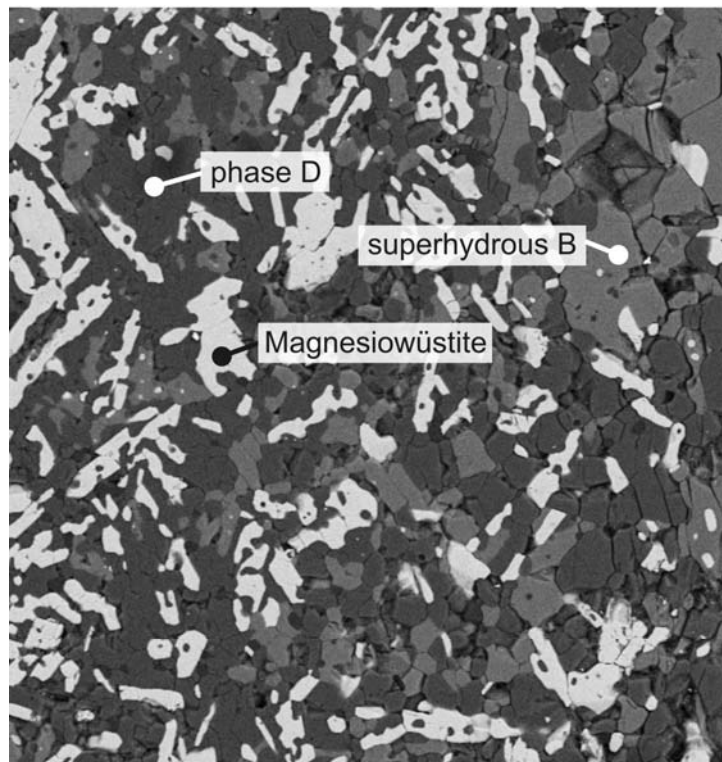


Fig. 3.3-22: SEM image of the sample GG2737, indicating a phase assemblage of magnesiowüstite, phase D and superhydrous B.

o. *TEM examination of sulfide and enstatite dust particles from the Stardust mission (F. Langenhorst; D. Jacob and H. Leroux/Lille; M.E. Zolensky/Houston)*

NASA's Stardust mission is a sample return mission to a known short-period comet (81P/Wild2); it aims at revealing the origin of cometary matter and at understanding the processes in the early solar system. In 2004, the Stardust spacecraft collected cometary dust particles during a flyby operation through the tail of the comet. The dust particles were captured in an aerogel collector at a relative velocity of 6.1 km/s. During the capture process particles deeply penetrated into the aerogel collector and were scattered along up to millimeters long tracks. Samples were returned to Earth in 2006 and are since then under study by an international consortium of scientists. In this context we have characterized dust particles from tracks 32, 35, and 41 of the collector, using transmission electron microscopy.

Dust particles recovered from tracks measure no more than several microns in diameter. Among the unexpected finds is the ubiquitous presence of monosulfides, which were not predicted by other comet missions such as Deep Impact. Monosulfides are particularly

abundant in tracks 35 and 41 but most of them were apparently melted during the capture process due to the high post-shock temperatures. The monosulfides occur as droplets forming a foamy mantle around a core of metallic FeNi. This structure was probably established during the capture process. Besides this, the tracks 35 and 41 do also contain two sulfide grains, which were obviously not melted during capture. Electron diffraction reveals that these grains are stoichiometric troilite.

Two dust particles were provided from track 32. These particles represent terminal grains, which penetrated deepest into the aerogel collector and underwent only little thermal overprint during capture. Both grains are orthoenstatite with  $\text{En}_{85}\text{Fs}_{13}\text{Wo}_2$  and  $\text{En}_{89}\text{Fs}_8\text{Wo}_3$  compositions; other detectable elements are Cr and Mn. The grains contain pervasive clinoenstatite lamellae parallel to the (100) plane of orthoenstatite (Fig. 3.3-23) and few dislocations in glide configuration.

The occurrence of enstatite and sulfide grains substantiate the conclusion that the Wild 2 dust particles are mostly not of presolar origin yet they must have formed in the inner part of the solar nebula. Subsequently particles were transported outward into the Kuiper belt to be finally accreted into comets. The find of stoichiometric troilite is consistent with a condensation from the solar nebula at low C/O ratios  $< 1$ . The formation of clinoenstatite lamellae in orthoenstatite can be explained by shock metamorphism, which has either occurred during capture or by a hypervelocity impact in the early solar system.

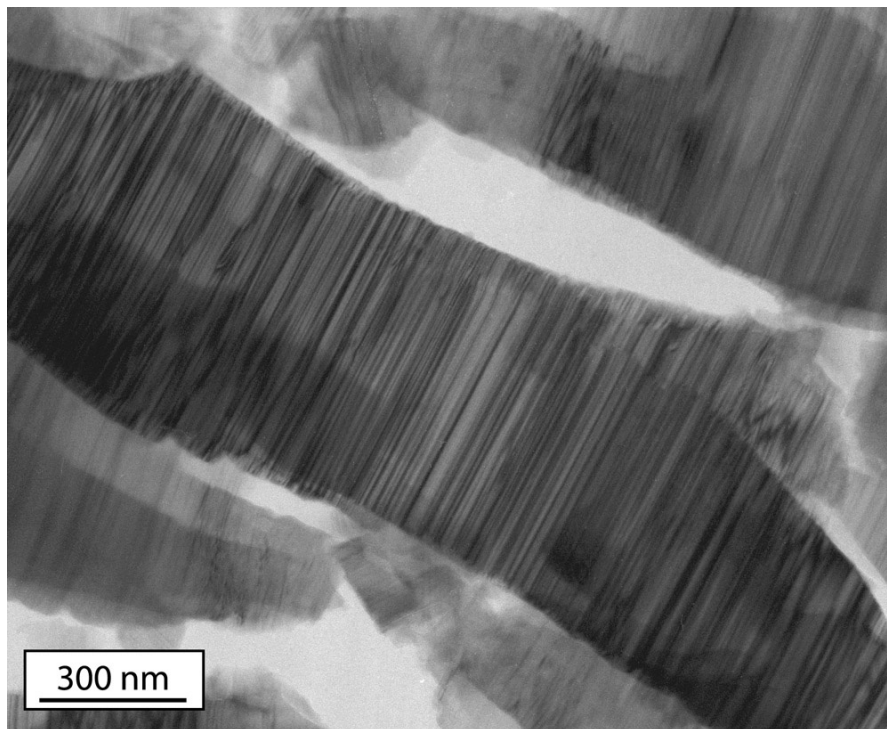


Fig. 3.3-23: Bright-field TEM image of a terminal grain from track 32. The orthoenstatite contains abundant clinoenstatite lamellae parallel to (100).

### 3.4 Physical Properties of Minerals

The bulk of the Earth's interior is not directly accessible, yet processes occurring deep within the Earth drive many of the events observed at its surface, such as volcanic eruptions and earthquakes. One successful strategy for probing the Earth's interior has been the comparison of geophysical measurements made at the surface, such as from seismology and electromagnetism, with studies of the relevant minerals at the appropriate  $P, T$  conditions in the laboratory. This approach has yielded not only static properties of the Earth's interior such as chemistry, mineralogy and temperature, but also has helped to reveal the nature of dynamic processes. Measurement of the physical properties of minerals in the laboratory continues to be a focal point of research at Bayerisches Geoinstitut, as reflected in the contributions to this year's report. The abundance of water within the Earth's interior remains an open yet important question, which is addressed by equation of state measurements to quantify the effect of water on elastic properties and the dehydrogenation process. Another contribution addresses elastic properties in deeper regions, where contrasting chemistry (*e.g.*,  $\text{Fe}^{3+}$  and Al concentration) between subducting slabs and the surrounding mantle may influence seismic velocities. Equation-of-state measurements are also important for determining the high-pressure stability of phases, which can be critical for applications such as nuclear waste disposal. The intriguing concept of lamellar magnetism has been proposed to account for extremely high magnetic remanence in crustal rocks, and state-of-the-art imaging at the atomic scale provides insight into the exsolution processes that created such rocks, as well as potential clues to reproducing their properties in the laboratory for industrial applications. The dynamic process of diffusion underlies many of the rock-forming events within the Earth, but is poorly constrained due to the lack of experimental data at high pressures and temperatures. Measurements involving the solution of pyroxene in garnet are reported, which is relevant for both crustal and mantle reactions. The final contribution seeks to apply cathodoluminescence measurements of alluvial diamonds as a tool to determine the conditions under which the diamonds originally formed.

#### **a.** *Elasticity of phase-X (M. Mookherjee and G. Steinle-Neuman)*

Potassium is an important element in the Earth. In the form of  $^{40}\text{K}$ , it contributes significantly to Earth's heat budget. The estimated  $\text{K}_2\text{O}$  content of a pyrolite mantle varies between 0.03 wt.% to 0.15 wt.%. As peridotite melts to generate basalt, potassium being a large ion lithophile element (LILE), readily fractionates to basalt. The  $\text{K}_2\text{O}$  content of various basalt that constitutes oceanic crust varies from 0.3-4.1 % (sub alkaline basaltic rocks) and 1.2-5.1 % (alkali olivine basalts). In the basaltic rocks, potassium is primarily hosted by amphibole. In the continental crust, potassium occurs in common crustal minerals such as feldspar, micas and amphiboles. As plates subduct, they transport oceanic crust (basalt) and overlying sediments into the mantle, both containing potassium in varying amounts. Most potassium bearing phases are also hydrous (micas and amphibole) and they have limited pressure and temperature stability. Most of them dehydrate with increasing pressure and temperature, releasing fluid and potassium along with other LIL elements that are transported in to arc

volcanoes. A systematic increase in the  $K_2O$  content of volcanic arc magmas is commonly observed with depth of subduction zones below arc volcanoes. It has been suggested that subducting slabs release potassium when amphibole breaks down at around 2.5 GPa. Later, it was demonstrated that phengite mica is a plausible host for K at least to a depth of 300 km (9.5-10 GPa, 750-1050 °C) where it breaks down and releases fluids and potassium. More recently, experimental studies have shown that with certain bulk composition K-rich amphibole can form which is stable to greater pressures and temperatures and finally transforms to phase-X.

Phase-X has a wide compositional range with a general formula  $A_2B_2Si_2O_7$  (Fig. 3.4-1), with potassium (K), sodium (Na) and hydrogen (H) occupying the A site and magnesium (Mg), aluminium (Al) and calcium (Ca) occupying the B site. Phase-X is stable under upper mantle and transition zone conditions (10-23 GPa, 800-1800 °C) and is likely to store both potassium and water under typical mantle geotherm.

In the present study we explore high-pressure behaviour of anhydrous potassium and sodium phase-X by means of density functional based computations, focusing on the role of chemistry on physical properties.

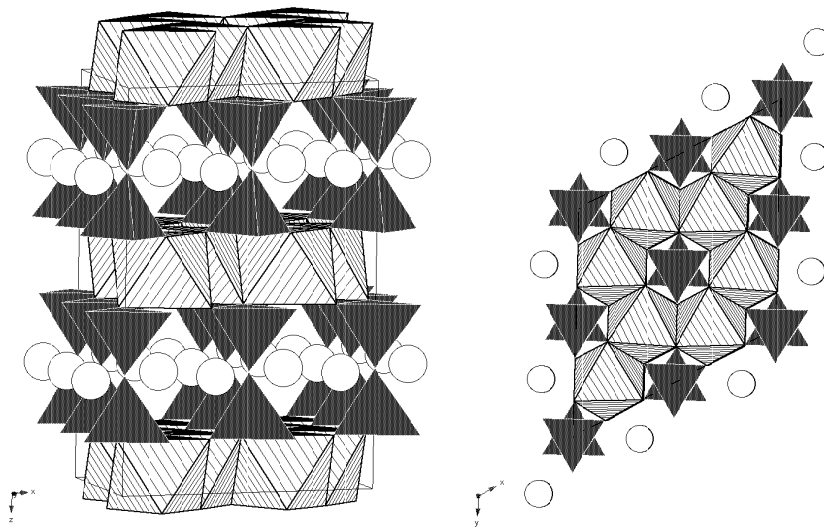


Fig.: 3.4-1: **left:** Three dimensional view of phase-X structure. Di-octahedral layer of  $MgO_6$  octahedra (white striped polyhedra) are linked by  $Si_2O_7$  di-silicate groups (dark polyhedra). The K atoms (white circles) occupy a cavity connected by channels along [100], [110], and [010]; **right:** down [001] direction, showing hexagonal outline of the unit cell,  $MgO_6$  octahedra in dioctahedral pattern and interlinked by di-silicate groups.

All computations are performed in a 104 atom cell consisting of a  $2 \times 2 \times 1$  super cell based on a 26 atom primitive unit cell. We use an energy cutoff  $E_{cut} = 400$  eV, and reciprocal space sampling is restricted to the  $\Gamma$ -point. We used plane-wave pseudopotential method, as implemented in the VASP software.

We find that the pressure-volume results for anhydrous phase-X are well represented by a third order Birch-Murnaghan formulation, with  $K_0 = 132$  GPa,  $K'_0 = 4.4$  and  $V_0 = 284.6 \text{ \AA}^3$  for the potassium (K) end member and  $K_0 = 128$  GPa,  $K'_0 = 4.0$  and  $V_0 = 265.9 \text{ \AA}^3$  for the sodium (Na) end member. The full elastic constant tensor reveals significantly larger stiffness along the [001] direction than in the [100] plane (Fig. 3.4-2). We attribute such stiffness to the  $180^\circ$  angle of Si-O-Si units and their orientation parallel to the [001] direction.

The effect of chemistry (substitution of potassium with sodium) on shear elastic constant is very similar to that of Fe or hydrogen on mantle minerals, where a major change is observed in the shear modulus. Assuming ideal behaviour between Na and K end member phase-X the shear modulus might vary as a function of sodium content as  $G = [84 - 0.14 \times Na(\text{wt}\%)]$  GPa. We anticipate hydration of phase-X will affect mostly the shear modulus and might lead to a further reduction in shear wave velocity.

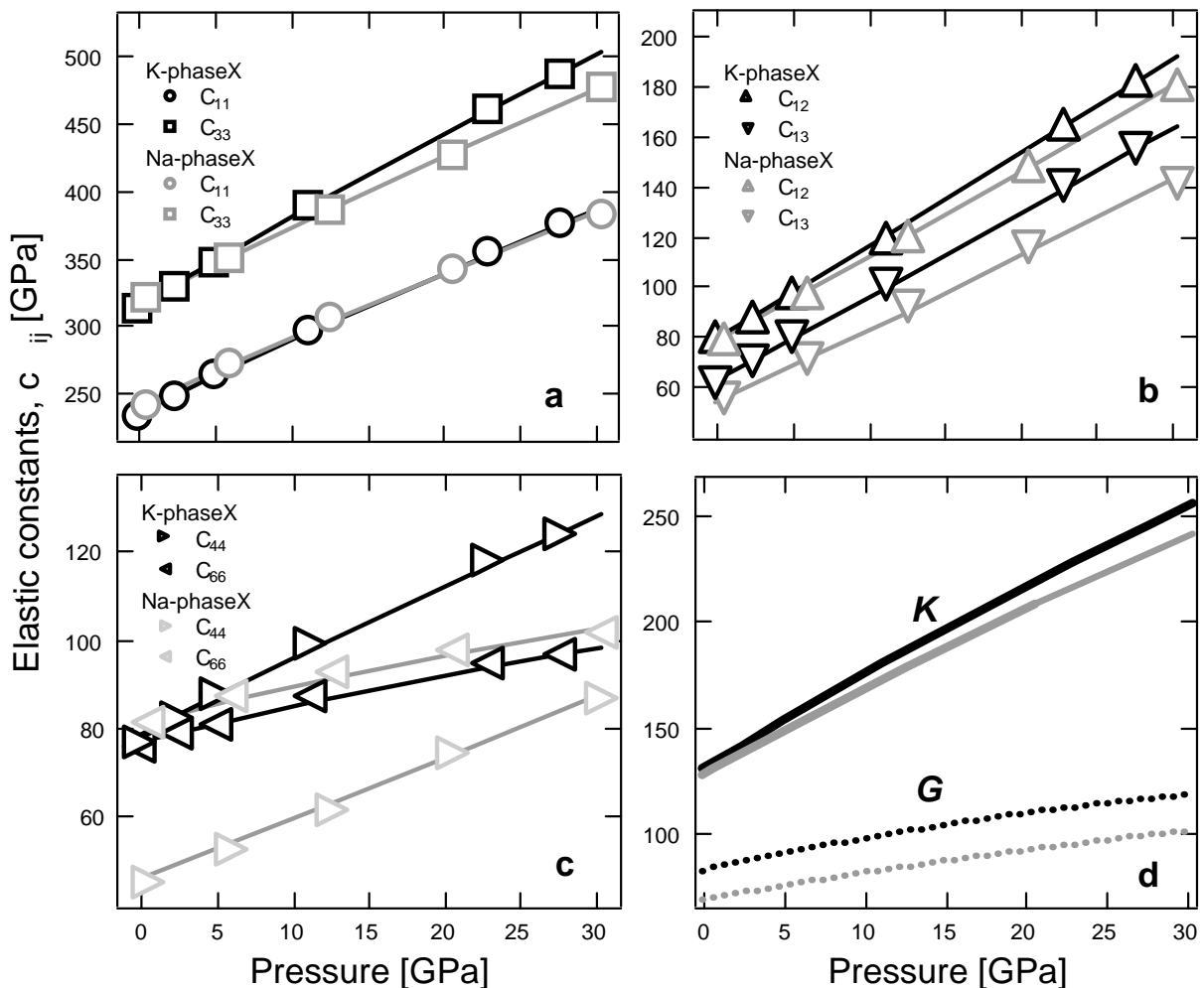


Fig. 3.4-2: Calculated elastic constants: (a) longitudinal elastic constants and; (b) off-diagonal elastic constants; (c) shear elastic constants and (d) Bulk (K) and shear (G) moduli for K (black) and Na phase-X (gray). Lines are finite strain fits to the elastic constants.

**b. The dehydrogenation effect on the baric behaviour of amphiboles (C. Capalbo and P. Comodi/Perugia, T. Boffa Ballaran, A. Zanetti/Pavia, S. Nazzareni/Perugia)**

Amphiboles represent one of the most important hydrous phases in the upper mantle. Mantle amphiboles are often H-deficient, described as oxo-amphiboles which have commonly the compositions of titanian pargasite and kaersutite. It has recently been shown that (i) the degree of oxo-component correlates inversely with the H<sub>2</sub>O concentration in coexisting melts and (ii) the oxo-component is locally balanced by Ti at the M1 site or by the presence of Fe<sup>3+</sup>. It has also been found that the oxo-component increases the thermal stability of amphibole, although its effect on the pressure behaviour is still not well constrained. To better understand the effect of dehydrogenation on the compressibility of amphibole, two natural samples (FR11 and FR12) from alkaline basalts with similar cation compositions but different OH contents were studied by single-crystal X-ray diffraction using a diamond anvil cell. The oxo-component in FR11 is balanced by a substitution mechanism involving both Ti and Fe<sup>3+</sup>, whereas the electrostatic balance of the larger OH-deficiency in FR12 is essentially achieved through the Fe<sup>2+</sup> + OH<sup>-</sup> = Fe<sup>3+</sup> + O<sup>2-</sup> + 1/2 H<sub>2</sub> reaction.

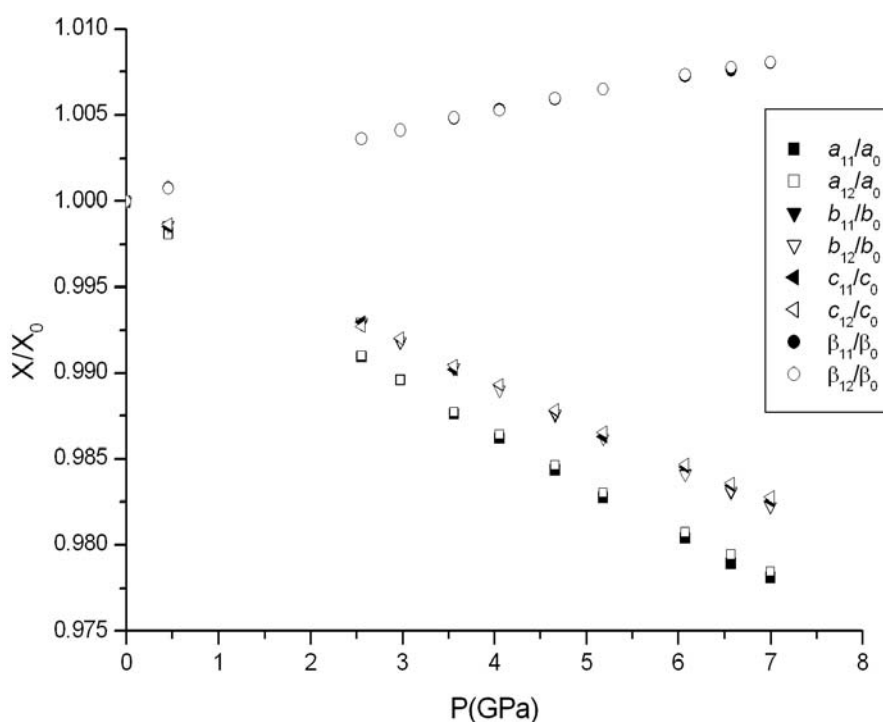


Fig. 3.4-3: Evolution of lattice parameters with pressure normalised to values at room conditions. Solid symbols refer to the FR11 sample, while open symbols refer to the FR12 sample.

Two crystals, one for each sample, were loaded together into a diamond anvil cell with a ruby chip as internal pressure calibrant and a 4:1 methanol:ethanol mixture as pressure transmitting medium. Unit-cell parameters were collected up to 7 GPa. A third-order Birch-Murnaghan

equation of state (EoS) was used to fit the  $P$ - $V$  data of the two amphibole crystals and the following EoS parameters were obtained:  $V_0 = 905.69(10) \text{ \AA}^3$ ;  $K_0 = 94(1) \text{ GPa}$ ,  $K' = 5.9(5)$  for sample FR11 and  $V_0 = 903.62(6) \text{ \AA}^3$ ,  $K_0 = 93.7(8) \text{ GPa}$ , and  $K' = 6.4(4)$  for sample FR12. There is no significant difference in compressibility between the two samples. These bulk moduli values are slightly smaller than the value reported in the literature for a natural pargasite with OH = 2 atoms per formula unit, suggesting that oxo-amphiboles are slightly more compressible than completely hydrated amphiboles. Also a small difference in compressibility of the  $a$  axis (Fig. 3.4-3) between sample FR11 and FR12 was observed, indicating that this direction may be the most sensitive to the  $\text{Fe}^{2+} + \text{OH}^- = \text{Fe}^{3+} + \text{O}^{2-} + \frac{1}{2} \text{H}_2$  substitution. Refinements of high-pressure single-crystal X-ray diffraction data are in progress to study in detail the structural evolution of these two samples and clarify the compressibility mechanism which gives rise to the difference in the compressibility of the  $a$  axis.

*c. Compression in He of a perovskite single crystal formed from a basaltic bulk composition (T. Boffa Ballaran and D.J. Frost, R. Pozzobon/Padova)*

Throughout the bulk of the Earth's lower mantle,  $\text{MgSiO}_3$  perovskite is expected to contain significant proportions of both Al and Fe, with Fe potentially in both 2+ and 3+ oxidation states. Silicate perovskite formed in subduction zones from oceanic crust, however, will be far more enriched in Fe and Al. If the substitution of the trivalent cations Al and  $\text{Fe}^{3+}$  influences the elastic properties of silicate perovskite, strong differences in sound velocities might be expected between regions of remnant-subducted crust and the ambient lower mantle.

Recently we studied the single-crystal properties of  $\text{MgSiO}_3$  perovskite containing up to 0.36 atoms per formula unit of Al and  $\text{Fe}^{3+}$  (see BGI Annual Report 2007). The recovered large single crystals of perovskite could be well characterised in terms of both bulk composition and in particular  $\text{Fe}^{3+}/\text{Fe}_{\text{tot}}$  ratio. Compressibility studies on these samples demonstrated that below 10 GPa perovskite exhibits a modest increase in compressibility with increasing Fe and Al incorporation compared to the  $\text{MgSiO}_3$  perovskite end-member. These studies also indicated that there is an increase in  $K'$ , the pressure derivative of the bulk modulus, with increasing Fe/Al content, which will result in Fe-Al-bearing perovskites becoming less compressible than  $\text{MgSiO}_3$  perovskite at pressures > 10 GPa. By extrapolating these results, a pronounced effect of composition on elasticity and density is predicted throughout the lower mantle. With the current  $P$ - $V$  data sets, however, which are limited to pressures < 9 GPa, we cannot exclude the possibility that an even higher order equation of state may be required to correctly reproduce perovskite elasticity at lower mantle conditions. We have therefore undertaken a compression study of a perovskite sample containing 0.68 trivalent cations per formula unit using a diamond anvil cell loaded with He as a pressure transmitting medium in order to extend the pressure range of hydrostatic measurement above the 10 GPa limit where a methanol:ethanol mixture is no longer hydrostatic.

We synthesised large single-crystals of Fe-Al-perovskite from a MORB tholeiitic bulk composition at 25 GPa and 1800 °C. The compressibility of a single crystal from this sample

was studied at ambient temperature by means of X-ray diffraction using ethanol:methanol as a pressure transmitting medium, and then the same crystal was loaded into a diamond anvil cell with He as a pressure transmitting medium. The data collected so far are in excellent agreement with the  $P$ - $V$  data set collected with methanol:ethanol (Fig. 3.4-4). Fitting both sets of data together with a third-order Birch-Murnaghan equation of state results in a decrease in bulk modulus but a significant increase of  $K'$  with respect to pure  $\text{MgSiO}_3$  and peridotitic perovskite. The change in compressibility is mainly due to softening of the  $c$  axis.

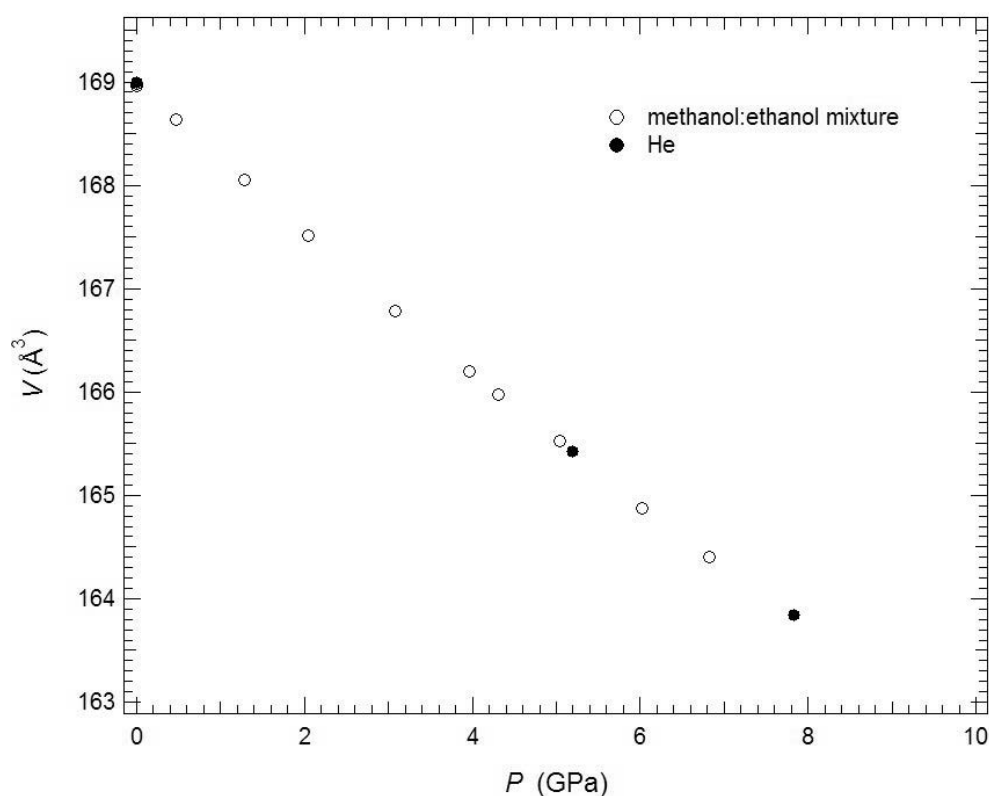


Fig. 3.4-4: Variation of the unit-cell volume of Fe-Al-perovskite with increasing pressure.

**d. Stability of pollucite at high pressure: A potential nuclear waste disposal phase (G.D. Gatta/Milano and T. Boffa Ballaran)**

Pollucite  $[\text{Cs}_x\text{Na}_y\text{Al}_{x+y}\text{Si}_{48-x-y}\text{O}_{96}\cdot(16-x)\text{H}_2\text{O}]$ , in which  $2y \geq 16-x \geq y$  is one of the natural Cs-bearing minerals, with an amount of  $\text{Cs}_2\text{O}$  of about 36 wt.%. Pollucite is an open-framework silicate (defined as feldspathoids or zeolites in the literature) and its crystal structure is built on the combination of two secondary building units (SBU): 4 and 6 SBU (4 and 6-membered ring of tetrahedra) (Fig. 3.4-5). The framework topology (ANA-analcime framework type) shows the maximum symmetry ( $Ia-3d$ ). At room conditions the general symmetry of pollucite is cubic  $Ia-3d$  with  $a \sim 13.68 \text{ \AA}$  and a statistical Si/Al-distribution in the tetrahedral framework, with Cs, Na and  $\text{H}_2\text{O}$  as extra-framework constituents. The water molecules occupy the voids that are not occupied by the caesium atoms (*i.e.*, Cs and  $\text{H}_2\text{O}$  share the same extra-framework

site). The topological configuration of the Cs-polyhedron (and its bonding environment), the small dimension of the sub-nanopores and the high flexibility of the ANA framework type implies a better thermal and elastic stability of pollucite than those of other synthetic microporous and mesoporous Cs-aluminosilicates. In addition, pollucite should retain Cs better when immersed in a fluid phase compared to several other Cs-bearing zeolites. In this light, pollucite can be considered as a functional material potentially usable for fixation and deposition of radioactive isotopes of Cs and can also be considered as a potential solid host for a  $^{137}\text{Cs}$   $\gamma$ -radiation source to be used in sterilisation applications. For these reasons, several studies have been devoted to the thermal stability of this open-framework material, but little is known about its high-pressure behaviour.

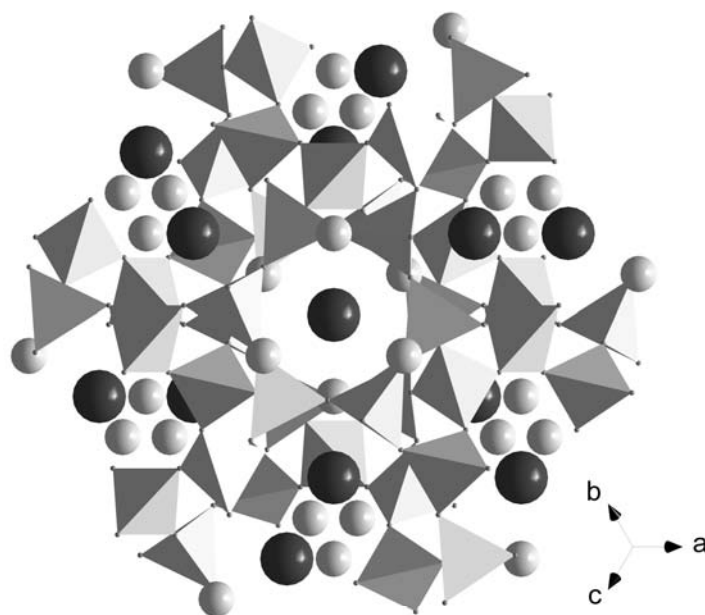


Fig. 3.4-5: The crystal structure of pollucite viewed down [111]. The large black spheres represent the Cs/H<sub>2</sub>O sites, whereas the small light grey spheres indicate the Na sites.

We investigated a crystal of natural pollucite up to about 9 GPa by means of *in situ* high-pressure single-crystal X-ray diffraction using a diamond anvil cell. A preliminary structural refinement at room conditions was performed, yielding 66 % (Cs) + 34 % (H<sub>2</sub>O) at the mixed Cs/H<sub>2</sub>O-site. A phase-transition was observed at  $P=0.66\pm 0.12$  GPa from cubic to triclinic symmetry (Fig. 3.4-6). The transition pressure was bracketed by several measurements in compression and decompression, and the phase transition was found to be completely reversible without any appreciable hysteresis. No further phase transition was observed up to at least 9 GPa. Any pressure-induced structural effects up to 9 GPa were found to be completely reversible. Fitting the pressure-volume data of the cubic polymorph with a second-order Birch-Murnaghan equation of state (BM-EoS), we obtained:  $V_0=2558.3 \text{ \AA}^3$  (fixed),  $K=41(2)$  GPa and  $K'=4$  (fixed). For the triclinic polymorph, a third-order BM-EoS-fit gave:

$V_0=2577(4) \text{ \AA}^3$ ,  $K=25(1) \text{ GPa}$  and  $K'=6.5(4)$ . Axial bulk moduli of the high-pressure triclinic polymorph and their pressure derivatives calculated with a linearised third-order BM-EoS were:  $K(a)=25(2) \text{ GPa}$  and  $K'(a)=6.8(6)$ ,  $K(b)=23(1) \text{ GPa}$  and  $K'(b)=7.7(7)$ ,  $K(c)=25(1) \text{ GPa}$  and  $K'(c)=6.9(4)$ . The elastic behaviour of the high-pressure polymorph appears to be isotropic. As already observed for the isotypic analcime, the relevant structural variations in response to the cubic-to-triclinic phase transition in pollucite are expected to be due to tetrahedral tilting.

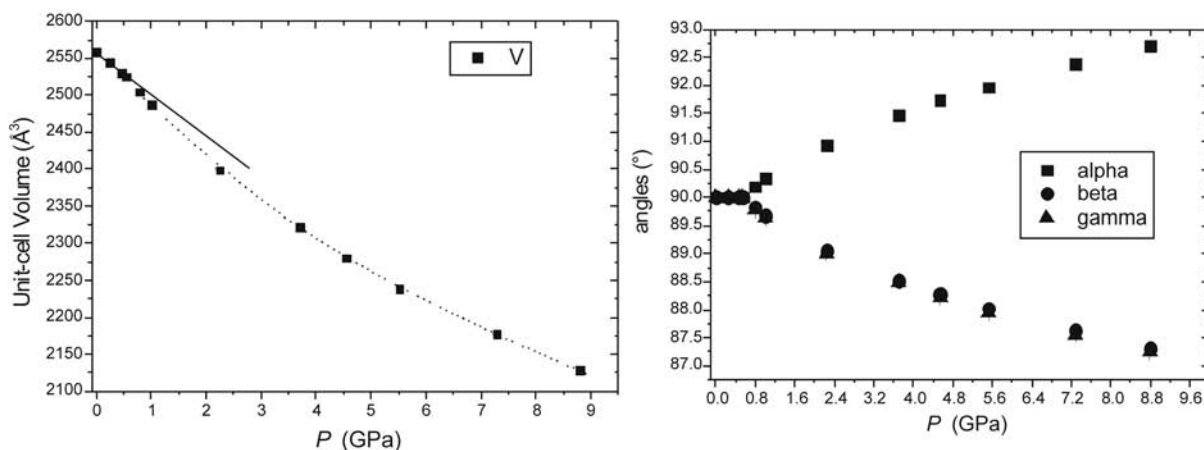


Fig. 3.4-6: Evolution of the unit-cell volume (top) and unit-cell angles (bottom) of pollucite with pressure. The solid line in the upper figure represents the second-order BM-EoS for the low- $P$  cubic polymorph, whereas the dotted line represents the third-order BM-EoS fit for the high- $P$  triclinic polymorph.

**e. Comparative TEM study of exsolution in hemo-ilmenite in igneous rock emplaced at 5 kbar and gabbro rapidly uplifted after eclogite-facies metamorphism: Key to contrasting magnetisations (S.A. McEnroe and P. Robinson/Trondheim, N. Miyajima and F. Langenhorst, M.P. Terry/Rapid City)**

Extensive studies of hemo-ilmenite- and ilmeno-hematite-bearing igneous and metamorphic rocks from South Norway, from the granulite region of southwest Sweden, and from the Grenville Province of Canada and adjacent USA, have shown that the magnetisation is closely tied to the abundance of fine exsolution lamellae, either of ilmenite in a hematite host or of hematite in an ilmenite host. The abundance of lamellar phase interfaces produces a strong magnetism parallel to the interfaces and to the sublattice magnetisations of the adjacent hematite, called 'lamellar magnetism'. The abundance of fine exsolution appears to be related to a long cooling history in which the main magnetisation is a chemical remanence formed at the time of fine exsolution in the phase field CAF hematite +  $R3$  ilmenite, at a temperature below the eutectoid point of the phase diagram at about 520 °C. Chemically and mineralogically similar rocks in the eclogite facies of the Western Gneiss Region, Norway

contain much weaker and less stable remanent magnetizations. Our recent objective is to determine why the magnetic intensity and behaviour is different in eclogite-facies rocks.

Sample 642, selected for initial investigation, is typical of a Proterozoic (~1450-1250 Ma) mafic igneous rock containing hemo-ilmenite which has undergone exsolution after having been treated to about 800 °C and pressure at least 20 kbar during Scandian (415-400 Ma) eclogite-facies metamorphism, and then uplifted rapidly about 395 Ma and cooled. The exsolution occurred at the end of the metamorphism because such exsolution occurs in mylonitic corona gabbro, where intense shearing followed by static growth of garnet came before the oxide exsolution. Because the overall character of these hemo-ilmenites is similar to those found in Rogaland (5 kbar conditions), we think the magnetic difference may lie in different exsolution microstructures related to a different *P-T* history. These are being investigated using TEM, already used in several earlier studies.

Sample 642 can be compared with two other samples studied in detail earlier. Sample AL36b from the Lac Tio hemo-ilmenite deposit, Allard Lake, Quebec, is notable for its high hematite component (bulk composition Ilm 72.5). This led to exsolution at high temperature and the development of coarse hematite exsolution lamellae up to 40 µm thick. The intensity and stability of lamellar magnetism is enhanced when a higher proportion of the exsolution lamellae are ilmenite in a hematite host, in this case early thick hematite exsolution lamellae. Sample 004-3 from the Frøytlog hemo-ilmenite deposit, Rogaland, Norway has a bulk composition Ilm 84, which led to exsolution at lower temperature with initial lamellae only up to ~3.6 µm thick (Fig. 3.4-7a). Sample 642 (Fig. 3.4-7b) has a similar bulk composition, Ilm 83, with thinner and straighter initial lamellae at ~1.8 µm.

Electron microprobe (EMP) and TEM analyses of 004-3 and EMP analyses of 642 were performed. The maximum EMP ilmenite composition is Ilm 94 and 95, respectively, and the minimum obtained in areas of coarsest hematite is Ilm 23 in both. The MgTiO<sub>3</sub> component of ilmenite, which may affect exsolution temperatures, is ~ 20 % in 004-3, but only ~ 4.5 % in 642 (~ 14 % in AL36b). TEM analyses for 004-3 suggest host compositions between fine lamellae of Ilm 98 and Ilm 13-15. TEM analyses have yet to be performed for 642.

The very finest exsolution lamellae, particularly of ilmenite in a hematite host, may provide the most abundant and strongest lamellar magnetism, because fine lamellae provide the largest surface area of phase interfaces that are the host for uncompensated magnetic spins. A moderately high resolution TEM image of 004-3 (Fig. 3.4-8a) shows lamellae clearly defined (see inset) at 3.6 nm, but with clouding suggesting exsolution at a finer scale probably down to unit-cell scale. TEM images of 642 (Fig. 3.4-8b) show similar patterns of exsolution in the ilmenite host, with precipitate-free zones adjacent to coarse hematite lamellae, but more precise characterisation of the sizes and distributions of the finest ilmenite within the coarse hematite awaits the acquisition of new higher-resolution images. These may answer our questions concerning the different magnetic properties.

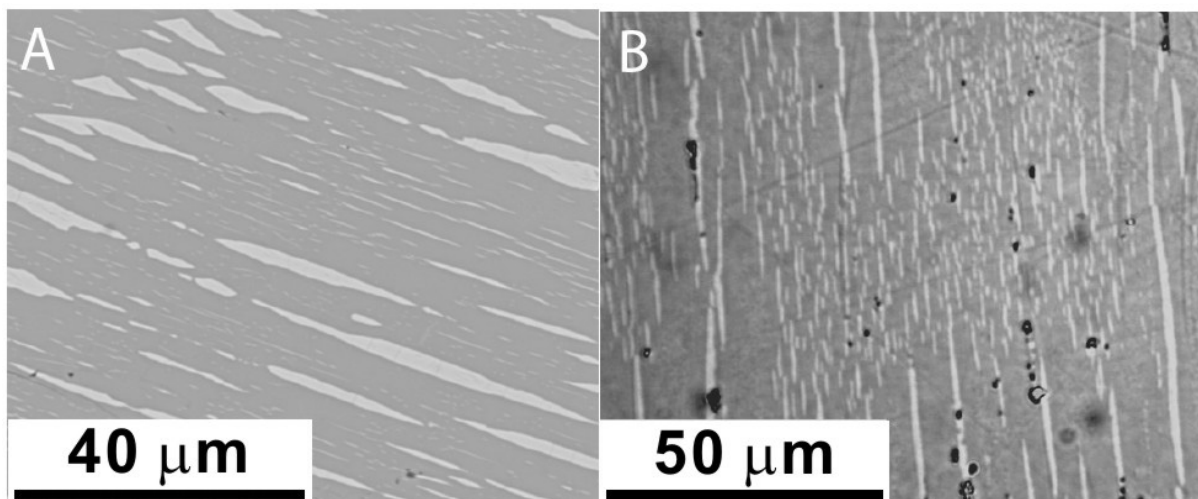


Fig. 3.4-7: Low-resolution images of ilmenite (dark) with multiple generations of hematite exsolution lamellae (white). **A**: SEM electron backscatter image from Froytløgg massive ore deposit, sample 004-3, south Rogaland, Norway. Large lamellae are  $\sim 3.5$   $\mu\text{m}$  thick. **B**: Reflected-light micrograph of hemo-ilmenite from Lauvsundholmen Gabbro, Lepsøy, Western Gneiss Region, sample 642. Thickest lamellae are  $\sim 1.8$   $\mu\text{m}$  thick. Lamellae are more parallel-sided, less curved than in (A).

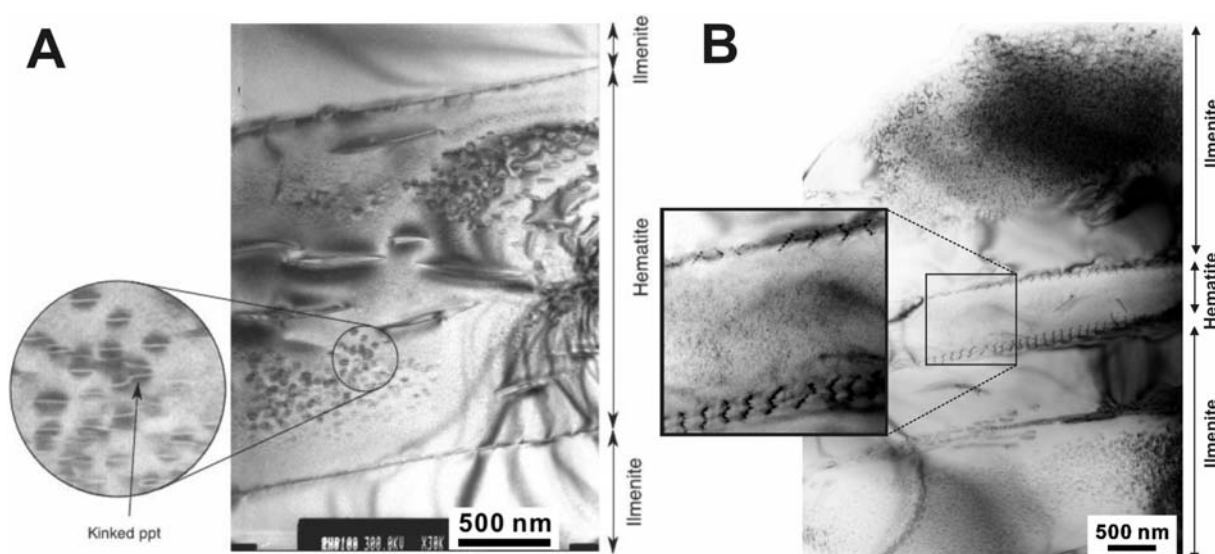


Fig. 3.4-8: Bright-field TEM images of large hematite lamellae in ilmenite with different sizes of enclosed ilmenite lamellae from **A**: sample 004-3 and **B**: sample 642. Inset in (A) shows details of intermediate-sized ilmenite lamellae that are about 3.8 nm ( $\sim 3$  unit cells) thick, with coherent strain shadows. The main image shows areas with even finer lamellae. In (B) bordering the coarse hematite are apparently lamellar-free zones, then rare rhomb-shaped hematite patches and even finer hematite lamellae. The inset shows the abundance of very fine ilmenite lamellae enclosed in the coarse hematite, but their sizes and surrounding host compositions, which may be a key to magnetic properties, have not yet been studied at high resolution.

**f. Fe-Ti order transition in quenched synthetic Ilm 60: Magnetic properties and high-resolution TEM imaging (K. Fabian, S.A. McEnroe and P. Robinson/Trondheim, N. Miyajima and T. Boffa Ballaran, B.P. Burton/Gaithersburg)**

Our long-term research target has been to understand the magnetic properties of the hematite-ilmenite ( $\text{Fe}_2\text{O}_3\text{-FeTiO}_3$ ) solid solution series, and, most recently, low-temperature properties in the composition range  $X_{\text{FeTiO}_3} = 0.6\text{-}1.0$  between 0 and 500 K as an adjunct to understanding the magnetism of the Earth's crust. Most of these samples were annealed below the Fe-Ti ordering transition, hence those with  $X_{\text{FeTiO}_3} < 0.87$  produce the properties of a ferrimagnet from adjacent-layer magnetic interactions at moderately low temperature. Those with  $X_{\text{FeTiO}_3} < 0.98$  produce additional properties below 57 K, thought to be associated with spin glass from double-layer magnetic interactions in ilmenite-rich regions. The ferri-ilmenite sample studied here was unusual in that it had been annealed at 1055 °C, above the order-disorder transition, before quench.

The first indication of unusual properties came from low-temperature hysteresis loops on small samples (Fig. 3.4-9) showing a strong magnetic exchange bias demonstrated by highly asymmetric hysteresis. In this case a very strong field of 5 T was applied at 300 K. The sample was then cooled in this field to 5 K before performing the hysteresis measurement. The observed loop shift is due to magnetic exchange bias, a property that requires strong magnetic coupling across an interface between two magnetic phases with different properties, so the experiment demonstrated that the sample is a mixture of at least two closely intergrown phases. Our interest in exchange bias in the hematite-ilmenite solid solution developed from the previous observation of giant exchange bias in a lamellar hematite-ilmenite intergrowth.

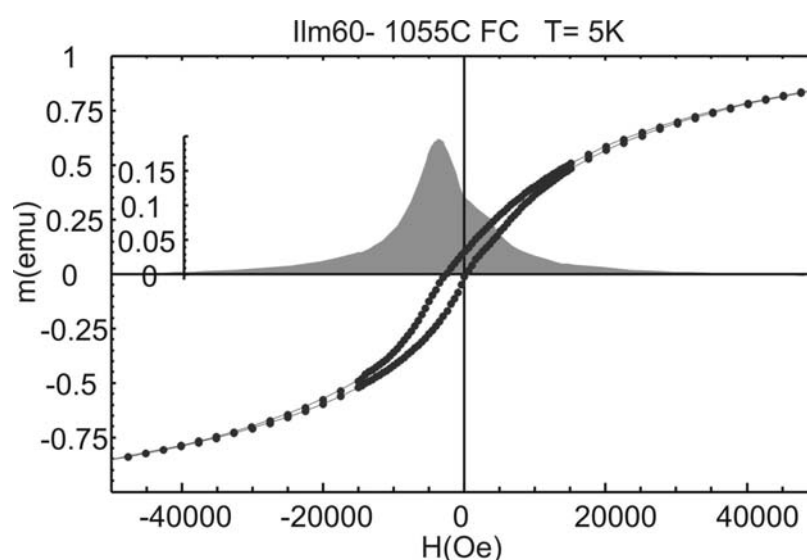


Fig. 3.4-9: Low-temperature magnetic hysteresis loop measured at 5 K after cooling in a 5 T field. The loop is noticeably shifted, indicating exchange bias due to magnetic exchange coupling across nanoscale interfaces. The average shift of irreversible magnetisations is more than 2000 Oe (corresponding to 200 mT).

A second hysteresis experiment was performed on the material at room temperature. The peculiar hysteresis loop (Fig. 3.4-10) also showed the presence of two phases, one with high coercivity and low magnetisation, and a second with high magnetisation and lower coercivity. By comparing the saturation magnetization  $M_s$  of the two-phase sample ( $2.57 \text{ Am}^2/\text{kg}$ ) with the  $M_s$  ( $25.1 \text{ Am}^2/\text{kg}$ ) of a completely ordered phase of composition  $X_{\text{FeTiO}_3}=0.6$ , it was possible to infer that an ordered phase contributes about 10 % of the magnetisation to the two-phase sample. However, this experiment is less definitive for two intergrown phases than the low-temperature experiment, because the two parts of the loop could come from separate grains within the sample. The two sets of experiments together, strongly indicated the need for detailed investigations by TEM.

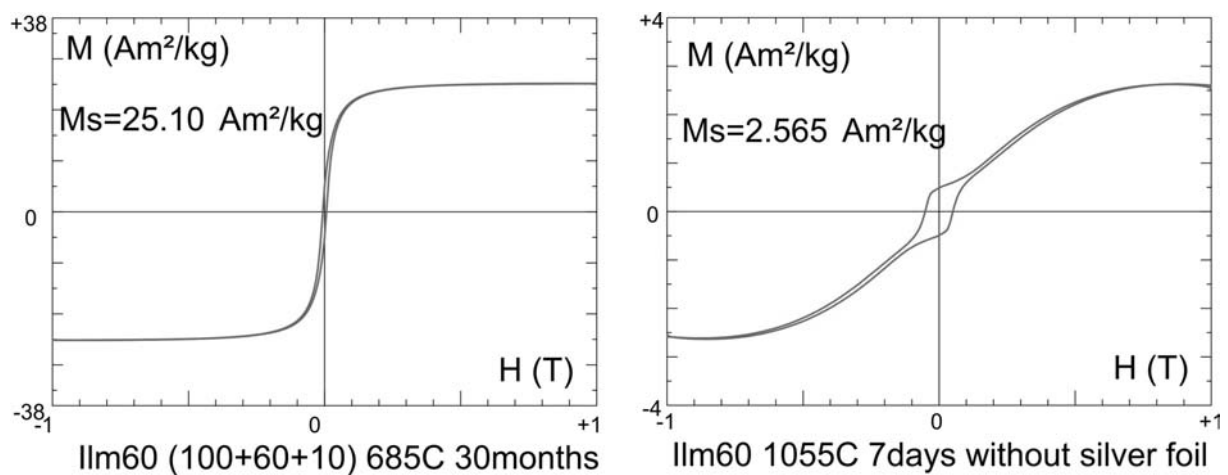


Fig. 3.4-10: Room-temperature hysteresis loops of a completely ordered Ilm60 sample (left) and the sample investigated here (right) show significant differences. Saturation magnetisation  $M_s$  of the right sample is only  $\sim 10\%$  of the ordered  $M_s$  value, but coercivity  $H_c$  is much higher in the partly disordered sample. Also hysteresis shape indicates the presence of two phases with markedly different coercivity.

The first TEM observations showed a homogenous phase with no indication of exsolution or any foreign material. Strong (006) reflections in electron diffraction suggested the presence of a predominant disordered phase consistent with the annealing temperature of the sample. However there are also weak (003) reflections, only possible for the Fe-Ti ordered phase. When a dark field image is taken through the (003) diffraction spot (Fig. 3.4-11), the sample shows predominantly dark regions reflecting disorder, with small illuminated regions where an Fe-Ti ordered phase runs completely through the sample thickness. The image is of a crushed grain where the thinnest edge is to the left, but the centre is also thin, probably as a result of conchoidal fracture during grain preparation. The largest “see through” ordered regions are about 8 nm thick (five to six 6-layer unit cells of Ilm 60), and they are also clearly elongated parallel to the (0001) basal plane. This latter feature, also reported in electron micrographs from the Mt. Pinatubo ash, can be explained easily, because there is little to no

change in the  $a$  lattice parameter during the phase transition, whereas  $c$  expands, inhibiting growth of the ordered phase in that direction. This effect can also be seen in very close examination of the (006) electron diffraction spots, which show a smaller  $2\theta$  angle (hence larger  $c$  lattice parameter) for the minority ordered phase, compared to the disordered phase.

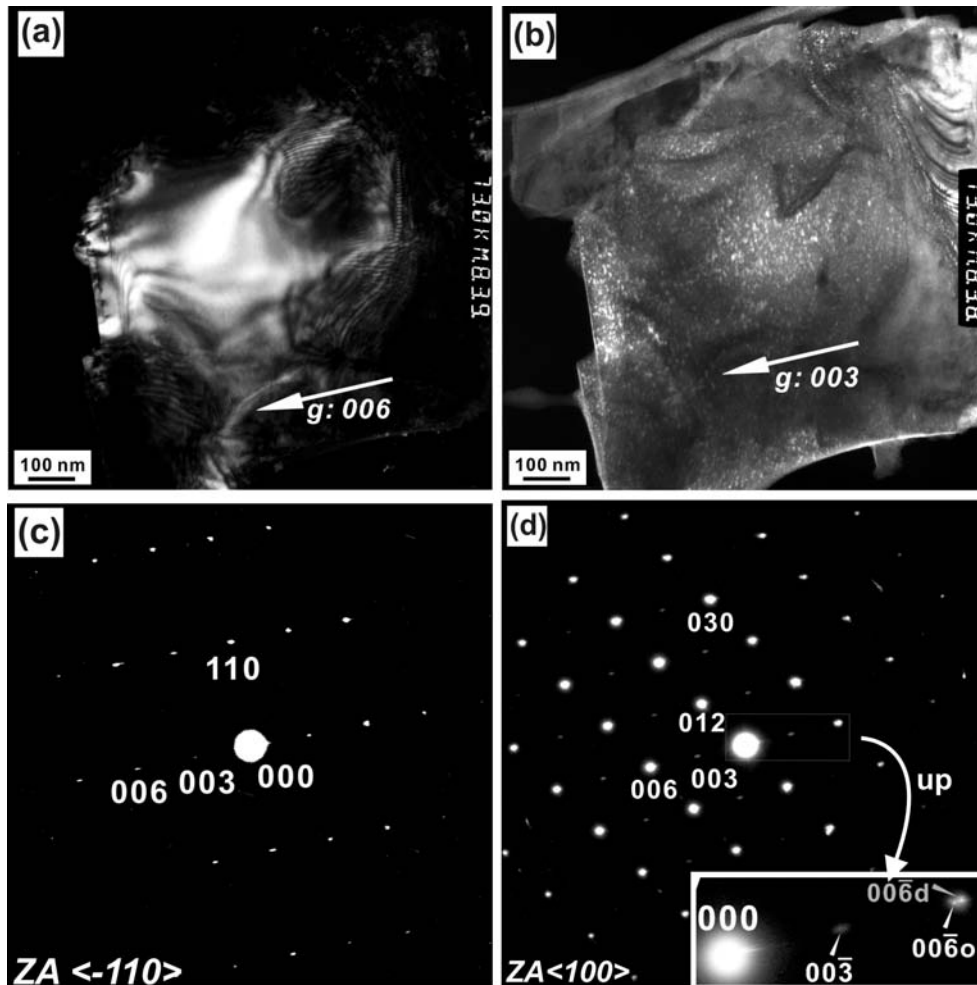


Fig. 3.4-11: Dark field TEM images of Ilm60 (1055 °C) with the hematite-like disordered reflection (a)  $g = 006$  and the ilmenite-like ordered reflection (b)  $g = 003$ . Selected area electron diffraction patterns are shown in (c) the  $\langle -110 \rangle$  zone axis and (d) the  $\langle 100 \rangle$  zone axis. Image (a) taken through 006, shows no remarkable contrasts in illumination, but in (b) taken through 003 only the ordered regions are illuminated, representing a minority of the sample.

When Fe-Ti ordering occurs during cooling in a rhombohedral Fe-Ti oxide, the initial placement of alternate Ti layers occurs at random through the structure. Ordered domains with opposed placement but identical structure grow outward until they impinge on each other, producing narrow regions where the phases are chemically out-of-phase, described as anti-phase domains or twins. Such boundaries are energetically unfavourable and tend toward elimination with progressive cooling. Detailed cooling experiments by another research group

on similar compositions using TEM imaging of the (003) reflection showed that a high density of such boundaries (shown by thin dark regions of disorder) is only preserved with annealing times well less than one hour below the ordering transition. It seems likely, then, that the partial ordering in our sample occurred entirely during the quench.

In order to gain a fuller understanding of the ordering relationships, high-resolution imaging, not available in earlier oxide studies, was used (Fig. 3.4-12). Here the resolution is so high that individual alternating Fe-rich and Ti-rich layers can be seen as alternating light and dark stripes parallel to the basal plane. The alternating light and dark stripes (three of each per unit cell thickness) are indeed what cause the (003) reflections in the electron diffraction images. What is so remarkable about this image is that the light layers at the extreme left and right of the image are lined up with each other, but in the middle of the image dark layers are lined up with light layers to either side (white lines are added to guide the eye). Thus, the region in the centre is an antiphase domain separated from the surroundings by two antiphase domain boundaries. Here it is not completely clear whether there is or is not a finite region of disordered structure along the boundary (perhaps up to 2-3 nm thick), or whether the two ordered phases are in direct contact.

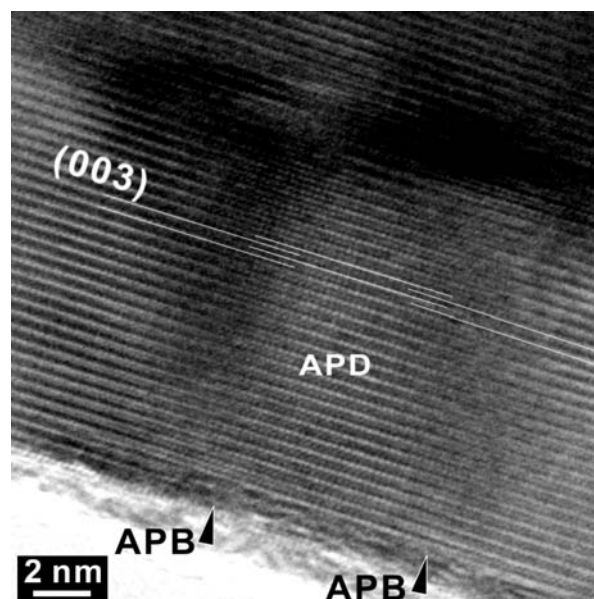


Fig. 3.4-12: HRTEM image showing an antiphase domain (APD) within the ordered phase and the corresponding antiphase boundaries (APBs) in Ilm60 (1055 °C).

Our sample bears considerable resemblance to the famous quenched ferri-ilmenite samples from the Huruna dacite in Japan and the Pinatubo ash from the Philippines. Such samples played a vexing role in the history of geomagnetism, because they definitely did acquire a magnetisation reversed from the present field magnetisation. Early on it was proposed that all magnetically reversed lavas and sediments acquired these properties through self-reversal, and that the Earth field itself does not reverse. Only a few years later it was proved that such

compositions are unusual, and that lavas and sediments of normal composition do contain a robust record of earth-field reversals. The geographic record of such reversals, indelibly preserved in the remanent magnetism of sea-floor basalts, provided the decisive key to our present ruling paradigm of global sea floor spreading and plate tectonics.

Most, but not all, models for the self-reversal process call upon two coexisting phases, a disordered hematite-like phase with high coercivity, low magnetisation, and higher Néel temperature, and an ordered lower coercivity, ferrimagnetic phase, with a lower Néel temperature. A key part of several self-reversal models is that during ordering, the residual disordered hematite-like phase acquires a higher Fe content, hence a higher Néel temperature, whereas the ordered ferrimagnetic phase acquires a lower Fe content, hence a lower Néel temperature. This question of whether there is or is not composition change along the Fe-Ti ordering boundary also appears in alternate versions of the phase diagram. It must also be remembered that when alternate ordered antiphase domains pass through their magnetic ordering temperature ( $\approx 150$  °C), the alternate Fe-rich layers may acquire the same direction of ferrimagnetism, but if so, one will be magnetically out-of-phase, both with the other ordered phase or with any adjacent disordered phase.

In our sample there is no doubt that the ordered phase has a larger  $c$  dimension than the disordered phase, but this difference would still show, whether due only to the ordering or to a Ti difference. Theoretical considerations suggest that an ordered phase of a given composition would have a higher Néel temperature than a disordered phase. This implies that we may solve the problem, for our sample at least, by detailed hysteresis loops in the range 450-400 K (175-125 °C), where we may learn whether the high-coercivity or low-coercivity phase has the higher Néel temperature. The question of Fe enrichment at a very fine scale may also possibly be resolved by high-resolution TEM EDS or EELS analyses. The origin of the low-temperature magnetic exchange bias, revealed in the earliest experiments, also requires resolution with additional closely controlled experiments to reveal the exact temperature of onset. In summary, what might have been a single solid-solution phase has proved to be a complex two-phase intergrowth likely related to an ordering transition, with implications concerning possible composition changes, the self-reversal mechanism, and low-temperature exchange bias possibly involving spin-glass behaviour.

**g.** *Diffusion of the majorite component in garnet (W. van Mierlo, F. Langenhorst, D.J. Frost and N. Miyajima)*

Garnets obtained from UHP metamorphic provinces such as the Western Gneiss Region in Norway or Dabie Sulu in China show exsolution needles or lamellae of pyroxene. These textures are usually interpreted as indications for (ortho)pyroxene solubility in garnet at UHP conditions, which has been confirmed experimentally. Also, experiments in the (C)MAS system have shown that at transition zone conditions there is an extensive solubility of

pyroxene in garnet, and above ~ 16.5 GPa a complete miscibility between majorite, the high-pressure polymorph of enstatite, and pyrope, resulting in only two major phases present in the transition zone: wadsleyite/ringwoodite (~ 55 vol.%) and (majoritic) garnet (~ 40-45 %). For subducted oceanic crust the garnet fraction might be as high as 90 % in the transition zone. Since majoritic garnet is thus a major constituent of the transition zone it is essential to understand its transport properties. Therefore an experimental high-pressure study has been performed on the diffusivity of the majorite component in garnet, as this will make it possible to better assess the rates of pyroxene dissolution in garnet. This will also improve our understanding of the timescales of UHP metamorphic events.

Two types of experiments were performed, namely diffusion experiments and equilibration experiments. The latter were performed to determine the equilibrium composition of garnet at the pressure and temperature conditions corresponding to the diffusion experiments, and thus were performed at the same *P-T* conditions. Both types of experiments were performed using the multianvil apparatus at BGI. For the equilibration experiments mixtures of pyrope, enstatite and diopside glass powders, which were molten and fused from CaO, MgO, SiO<sub>2</sub>, and Al<sub>2</sub>O<sub>3</sub> powders and subsequently ground to a fine powder, were put in a capsule and pressurised to 10, 15 and 16 GPa at 1600 °C. The capsules were made of 4- (4 GPa) or 6- (10 GPa) bore alumina thermocouple tubes with a rhenium or molybdenum foil mantle, making it possible to do 4 or 6 “experiments” at the same time.

The results, which are displayed in Fig. 3.4-13, show an increase in majorite component from 15 % at 10 GPa to 45 % at 16 GPa. Diopside-pyrope mixtures at 10 and 15 GPa give the following equilibrium compositions:

Ca<sub>0.70</sub>Mg<sub>2.37</sub>Al<sub>1.75</sub>Si<sub>3.14</sub>O<sub>12</sub> garnet - Ca<sub>1.65</sub>Mg<sub>2.09</sub>Al<sub>0.19</sub>Si<sub>3.99</sub>O<sub>12</sub> diopside (at 10 GPa) and  
 Ca<sub>0.63</sub>Mg<sub>2.60</sub>Al<sub>1.48</sub>Si<sub>3.27</sub>O<sub>12</sub> garnet - Ca<sub>1.88</sub>Mg<sub>1.93</sub>Al<sub>0.24</sub>Si<sub>3.91</sub>O<sub>12</sub> diopside (at 15 GPa).

Starting compositions were the same and thus the dissolution of clinopyroxene into garnet can be almost purely described by the dissolution of the enstatite end-member in clinopyroxene into garnet, reflecting that the large Ca<sup>2+</sup> cation cannot be accommodated in the octahedral site of garnet.

Diffusion experiments were conducted at 10 GPa and both 1400 °C and 1600 °C with pyrope-enstatite diffusion couples. Enstatite and pyrope were synthesised from glasses in a piston-cylinder (enstatite) or multi-avil apparatus (pyrope), cut into ~ 500 µm thick disks, polished and put together in a platinum capsule. At 1400 °C no discernible diffusion profiles could be observed using either the electron microprobe or the TEM. Since the beam size used in the TEM was ~ 200 nm, this means that at these conditions the diffusion coefficient for silicon in pyrope should be at most ~ 10<sup>-15</sup> cm<sup>2</sup>s<sup>-1</sup>, which indicates that diffusion of silicon in garnet is at least one to two orders of magnitude slower than the diffusion of magnesium. At 1600 °C diffusion profiles could be observed, but only under the TEM. However, an accurate diffusion

coefficient could not be calculated since the diffusion profiles were larger than the size of the pyrope grains ( $\sim 3 \mu\text{m}$ ) and the analysed grain was almost been fully equilibrated during the run. To overcome the above mentioned problems with small grain sizes of the synthesised pyrope, new experiments will be conducted using natural Dora Maira pyrope and a more coarse-grained synthetic pyrope.

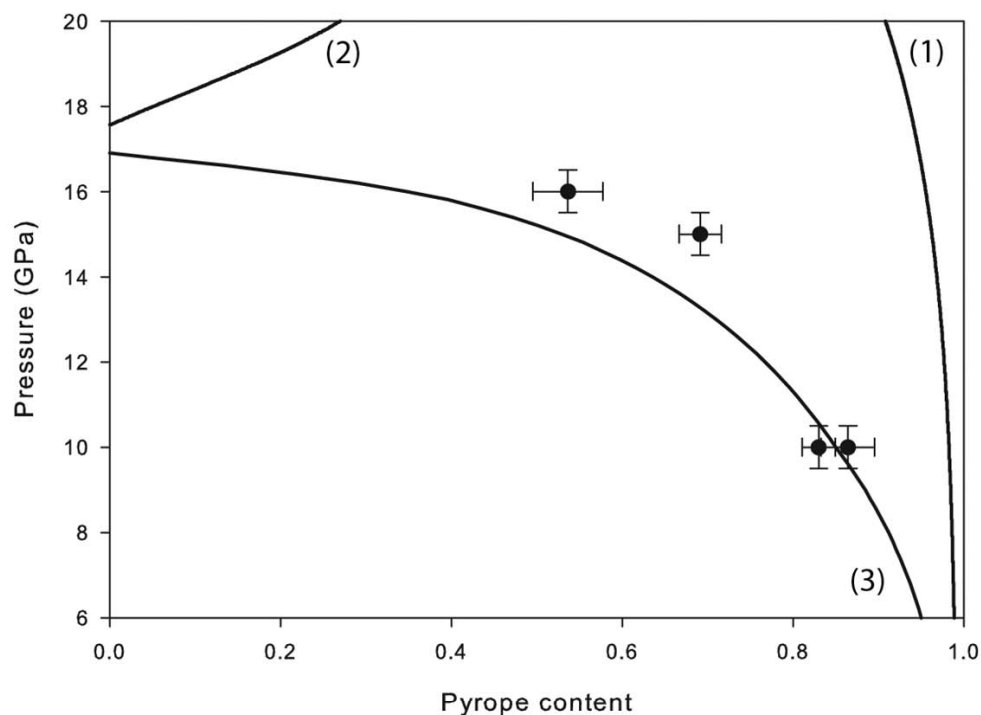


Fig. 3.4-13: Garnet composition in equilibrium with (1) corundum, (2) akimotoite and (3) (clino-)enstatite in the MAS system as function of pressure for a given temperature of 1600 °C. Solid lines are equilibrium compositions calculated from literature thermodynamic data, while dots represent results from this study.

#### **h.** Cathodoluminescence studies of alluvial diamonds from Archean conglomerates of Eastern Canada (M. Longo and M. Kopylova/Vancouver)

Diamonds form at a minimum depth of 150 km in the Earth's interior and are brought to the surface via kimberlitic eruptions; hence diamonds normally occur in volcanic rocks that originated below the Earth's crust. However subsequent erosion can re-deposit diamonds in alluvial or marine beach sands and gravels that are later lithified into sedimentary rocks and thereby obscure their origin. In order to investigate potential methods for extraction of the conditions under which alluvial diamonds originally formed, we undertook a cathodoluminescence (CL) study of diamonds recovered from sedimentary conglomerates of the Superior craton (Eastern Canada) dated at 2.7 Ga. The CL colour in diamonds is related to the degree of nitrogen aggregation, which can be used as a tool for determining the conditions under which the diamonds originally formed.

We selected 40 macro diamonds (< 500  $\mu\text{m}$ ) from a total of 1234 stones (both macro and micro diamonds) for CL studies. The diamonds studied so far show variable crystal morphology. Crystal habits are octahedral (Fig. 3.4-14), single or aggregates, macle (octahedral twins) and cubic. In the conglomerates examined, macro diamonds (size > 500  $\mu\text{m}$ ) are less abundant than micro diamonds, dividing the population clearly into two distinct groups. In macro diamonds the most common CL colour observed is green, followed by yellow, orange and pink. In contrast, micro diamonds tend to be mostly yellow, orange or red, but are rarely green. These CL colours are very similar to those observed in diamonds recovered from Archean calc-alkaline lamprophyres in the same area, and very different from colours that diamonds would normally exhibit.

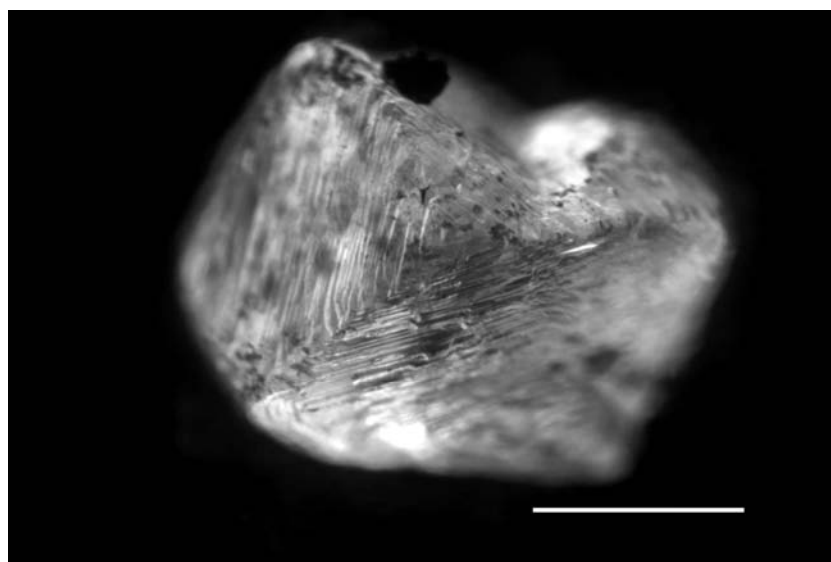


Fig. 3.4-14: Optical CL photograph selected from one of the 40 macro diamonds studied. The scale bar corresponds to 500  $\mu\text{m}$ . Trigonal etch pits (surface features) are recognisable on the surface of the diamond.

The macro diamonds studied mostly show a maximum peak at 520 nm, in the green region. The second group of CL spectra (micro diamonds) show two maximum peaks at about 576 and 600 nm, in the yellow (560-690 nm) and orange region (590-630 nm), respectively. None of the diamonds show a maximum peak at 420 nm, in the blue region, in contrast to the majority of diamonds worldwide. This band is related to the presence of N impurities in so-called A centers (nitrogen aggregated in pairs). Most interestingly, alluvial diamonds with polycrystalline morphology show distinct and peculiar spectra for different intergrown crystals in the same sample (Fig. 3.4-15), not observed in any other diamond. Further work will involve photoluminescence studies at low temperature on some of the samples presenting complex spectra, which will allow a better resolution of each peak contributing to the overall spectrum and will assist in the interpretation of correlations between the CL emission peaks

and the diamond formation processes. Nitrogen contents and aggregation state will be subsequently be determined by Fourier transform infrared measurements in order to classify the diamonds.

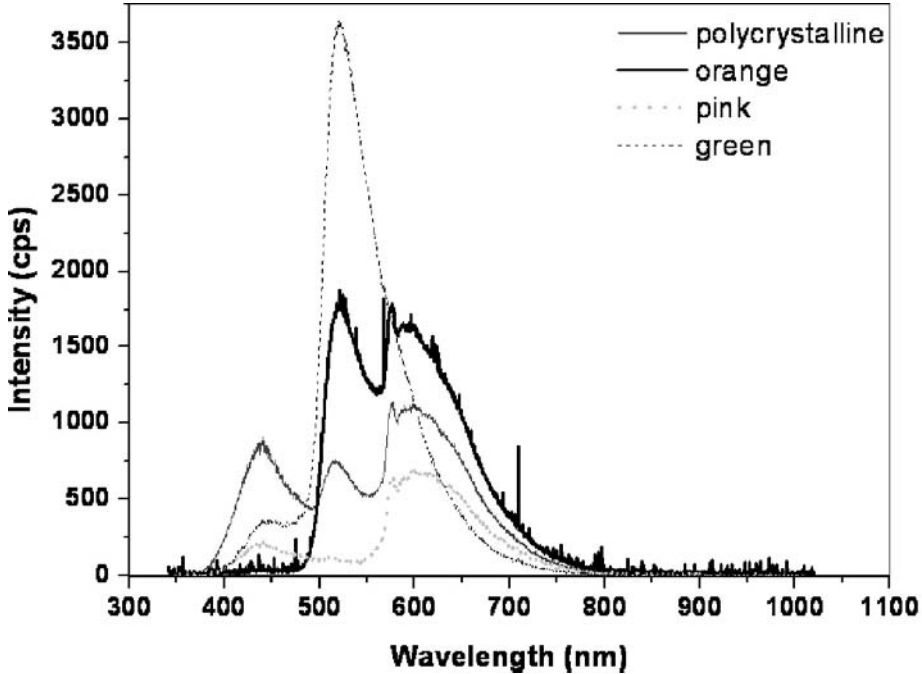


Fig. 3.4-15: Comparison of CL emittance intensities (counts per seconds) of polycrystalline alluvial diamond with spectra from diamonds that show either orange, pink or green CL colours.

### 3.5 Fluids and their Interaction with Melts and Minerals

In subduction zones, material from the Earth's surface is recycled back into the mantle. The element fluxes at subduction zones therefore largely determine the chemical evolution of the Earth during the last billions of years of geologic history. Variations in the volume of water on Earth's surface as well as variations in the salinity of the oceans are linked to these processes. Moreover, subduction zones are one of the main sites of magma generation in the present day Earth. These magmas often have characteristic trace element signatures that may be linked to processes occurring deep in the mantle. In particular, the strong enrichment of some incompatible trace elements in arc lavas has been attributed to the preferential transport of these elements in fluids release from the subducted slab to the zone of melting in the mantle wedge. One interesting observation here is that two trace elements, uranium and thorium, that should normally behave in a similar way during melting, are sometimes strongly decoupled. This problem is addressed in the first contribution in this chapter, which shows that the solubility of uranium in high-pressure aqueous fluids strongly increases with oxidation state and chlorine concentration in the fluid, probably due to the formation of chloro-complexes of hexavalent uranium. This is not expected to happen with thorium and therefore the ratio of uranium and thorium in arc lavas may actually reflect the oxidation state and salinity of subduction zone fluids.

Halogens in subduction zone fluids may influence the transport of some trace elements by the formation of halogen complexes. At the same time, the behaviour of halogens in subduction zones is interesting in its own right, because the recycling of halogens into the mantle is one of the key factors determining the evolution of ocean chemistry. In another study in this chapter, the distribution of halogens between aqueous fluids and major mantle minerals was studied. These experiments show that chlorine is highly incompatible in upper mantle minerals, implying that most of the chlorine entering subduction zones will be sequestered by aqueous fluids that ultimately end up in arc magmas, implying a recycling back to the surface of most of the chlorine entering a subduction zone.

The mantle is a major host of volatile elements. For noble gases, it was suspected for a long time that a considerable part of the bulk noble gas budget of the Earth must still be hidden somewhere in the deeper mantle. In a pioneering study in this report, significant argon solubility was discovered in magnesium silicate perovskite, the main constituent of the lower mantle. The dissolution of argon in perovskite is probably related to oxygen vacancies. Observed solubilities are in the range of several hundred ppm or higher, not very far away from the solubilities expected in depolymerized silicate melts under high pressure. This implies that most argon may well have been retained deep in Earth's mantle for all of Earth's history.

Aluminous pyroxenes have been recognized as the most important host of water in the upper mantle. The sharp decrease in water solubility in orthopyroxene with depth, together with the

simultaneous increase of water solubility in olivine probably causes a minimum of water solubility in the asthenosphere. This may cause the generation of a small degree of partial melting in the asthenosphere. Since natural clinopyroxenes from mantle xenoliths sometimes contain even more water than orthopyroxene, it is important to check if the water solubility in clinopyroxenes shows a similar dependence on pressure and temperature as observed for orthopyroxene. New data in this annual report show that indeed water solubility in clinopyroxenes sharply drops with temperature, as observed for orthopyroxenes and consistent with recent models on the origin of the asthenosphere.

In recent years, it has been more and more recognized that many processes occurring at the surface of the Earth involve microorganisms, even processes that were previously believed to be completely inorganic in nature. In the last contribution to this chapter, experiments show that microorganisms affect the weathering of biotite, in particular by enhancing ion exchange between potassium and ammonium in the interlayer of biotite. Such exchange processes are important for improving the bioavailability of elements in soils.

**a. The solubility of uranium in subduction zone fluids (E. Bali, A. Audétat and H. Keppler)**

Volcanic arc lavas show characteristic signatures in incompatible elements that may be related to the composition of the subducted material and to processes during partial melting. Interestingly, the enrichment of Th and U is decoupled in most cases, which cannot be explained by mineral-melt equilibria during partial melting. This difference may be due to the fact that unlike thorium, uranium can be oxidized from the  $U^{4+}$  to the  $U^{6+}$  oxidation state and compounds of  $U^{6+}$  may be highly soluble in aqueous fluids, particularly in the presence of complexing agents such as chloride. However, at present no experimental data exist for subduction zone pressures and temperatures to test this hypothesis.

To clarify which factors control U-solubility in aqueous fluids in subduction zone environments we carried out a series of experiments in which  $UO_2$ -solubility was measured as a function of P, T, oxidation state and fluid salinity. We used the Re- $ReO_2$  and iron-wustite oxygen fugacity buffers to maintain oxidizing and reducing conditions, respectively. Fluid salinity varied between 0.3 and 41.7 wt.% NaCl. We trapped the fluid as synthetic fluid inclusions in quartz (Fig. 3.5-1). In order to produce these inclusions, a quartz single crystal and one or two single crystals of natural  $UO_2$  were loaded into Pt/Rh capsules with aqueous solution. During a one-day experiment, large (up to 200  $\mu m$ ), negative crystal shaped, primary inclusions (Fig. 3.5-1) formed in the overgrowing quartz. Fluid inclusions were analyzed by laser ablation ICPMS.

The results show that U-solubility increases with pressure (Fig. 3.5-2a). At oxidizing conditions, U-solubility increases an order of magnitude between 7.5 and 27.5 kbars (from ~ 80 to ~ 900 ppm in the presence of an aqueous solution with 13.7 wt.% dissolved NaCl). This means that available low-pressure data cannot be directly applied to mantle conditions.

At oxidizing conditions, the solubility of U is much higher than at reducing conditions for all investigated fluid salinities (Fig. 3.5-2b). In fact, U concentrations in all fluid inclusions synthesized at the iron-wustite buffer were below the detection limit of 2-30 ppm. Furthermore, at oxidizing conditions the U-solubility increases dramatically with increasing fluid-salinity (from ~ 20 ppm to ~ 900 ppm U when the NaCl content of the fluid increases from 0.3 to 13.7 wt.%) (Fig. 3.5-2b).

Our results suggest that oxidized, saline aqueous fluids in subduction zone settings can dissolve large amounts of uranium and thus possess the potential to enrich U over Th as observed in many subduction zone magmas. The U/Th ratio may therefore be an indicator of the oxidation state and the salinity of subduction zone.

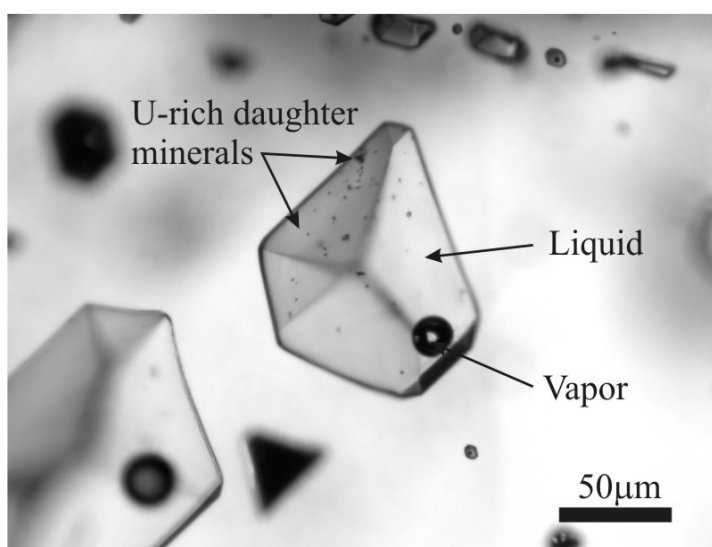


Fig. 3.5-1: Negative crystal shaped synthetic fluid inclusions in quartz, trapped at 15 kbar and 800 °C. The inclusions contain a liquid phase, a vapor bubble and tiny uranium-rich daughter crystals precipitated during cooling

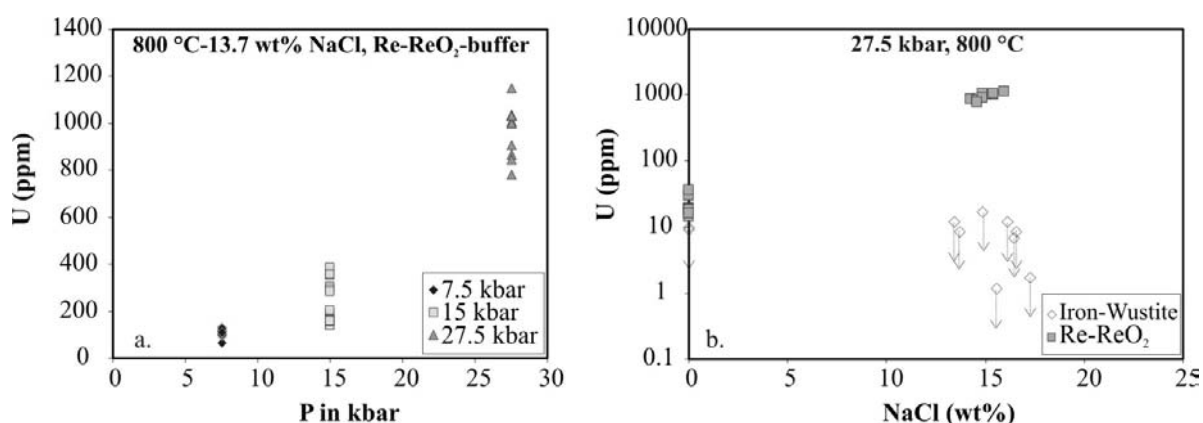


Fig. 3.5-2: UO<sub>2</sub> solubility in aqueous fluids at high pressure and temperature. a: Pressure dependence of UO<sub>2</sub>-solubility in a fluid containing 13.7 wt.% NaCl at oxidizing conditions (buffered by Re-ReO<sub>2</sub>). b: Dependence on oxygen fugacity and fluid salinity at 27.5 kbar and 800 °C. U-solubilities at the iron-wustite buffer are maxima defined by detection limits.

**b. The distribution of halogens between fluids and upper mantle minerals (D. Bernini, D. Dolejš and H. Keppler)**

The behaviour of halogens in subduction zones controls the exchange of chlorine and fluorine between the Earth's mantle and the oceans. In addition, the distribution of halogens between aqueous fluids and mantle minerals will have a strong effect on the ability of these fluids to transport trace elements, because there is increasing evidence for complexing of some trace elements by chlorine in the fluid. Halogens are incorporated in subducting hydrous silicates, oceanic evaporites and pore water. However, forearc fluids and arc magmas typically show a decoupling and a wide scatter of fluorine and chlorine concentrations, respectively. In addition, halogens are frequently more enriched in undegassed volcanics than other fluid-mobile lithophile cations. Until now, there are no experimental data on the behaviour of halogens in subduction zones and their fate during dehydration metamorphic reactions and fluid migration across the slab-mantle interface are not known.

In this study we investigate the incorporation of chlorine and fluorine in forsterite, enstatite and pyrope under upper-mantle conditions. Experiments were performed with oxide-hydroxide mixtures, synthetic glasses (with seeds of natural minerals), and chlorides, fluorides, and halogen-bearing aqueous fluids as halogen sources. Runs were carried out in a piston cylinder apparatus at 800-1400 °C and 1.5-3.0 GPa, and major-element and halogen concentrations were determined by electron microprobe (Fig. 3.5-3).

Some experiments were performed with synthetic glass (30.0 wt.% MgO, 25.3 wt.% Al<sub>2</sub>O<sub>3</sub> and 44.7 wt.% SiO<sub>2</sub>) buffered with NaCl or KCl at 1400 °C and 3 GPa. They yielded a three-phase assemblage of forsterite, enstatite and pyrope. Chlorine concentrations in all silicate phases are lower than 400 ppm 60-140 ppm Cl in forsterite, 40-360 ppm in enstatite and 70-100 ppm Cl in pyrope. The elevated chlorine concentrations in enstatite are related to a minor substitution of a jadeitic component, which appears to enhance the solubility of halogens.

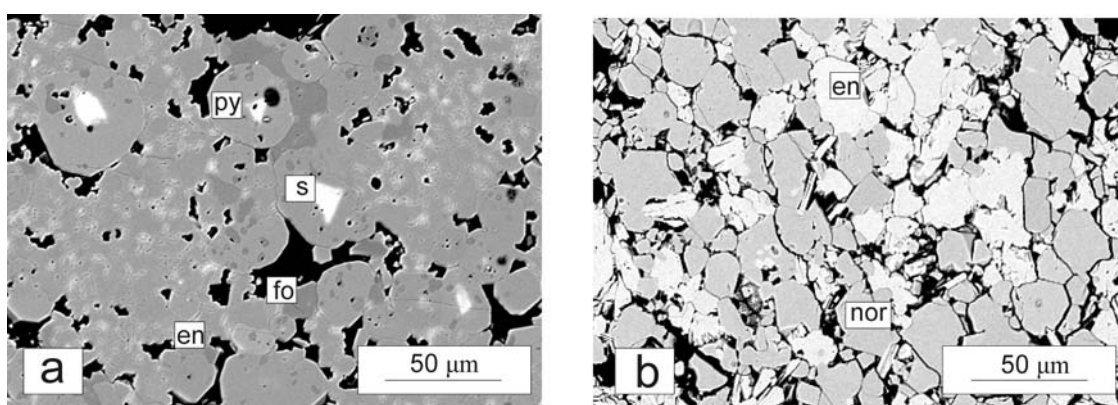


Fig. 3.5-3: Photomicrographs in backscattered electron mode of experimental run products: (a) forsterite (fo), enstatite (en) and pyrope (py) formed at 1400 °C and 3 GPa with NaCl buffer, pyrope seeds (s) were used; and (b) enstatite (en) with fluoronorbergite (nor) produced in the presence of a fluorine-bearing aqueous fluid at 1100 °C and 3 GPa.

Runs in the system MgO-SiO<sub>2</sub>-H<sub>2</sub>O-MgCl<sub>2</sub> at 1100 °C and 3 GPa produced a four-phase assemblage of forsterite, enstatite, Cl-bearing hydrous silicate melt and aqueous fluid (brine). Chlorine partitions preferentially into hydrous silicate melt over solid phases. Individual chlorine concentrations were: 31 ppm Cl in forsterite, 24 ppm Cl in enstatite, 0.46 wt.% Cl in the melt and 16.3 wt.% Cl in the brine (estimated by mass balance). Chlorine partition coefficients between brine, minerals and melt are  $D^{fl/fo} \sim 5 \cdot 10^3$ ,  $D^{fl/en} \sim 7 \cdot 10^3$  and  $D^{fl/melt} = 36$ . Additional experiments in the system MgO-Al<sub>2</sub>O<sub>3</sub>-SiO<sub>2</sub>-H<sub>2</sub>O-MgCl<sub>2</sub> at 1100 °C and 3 GPa addressed the incorporation of chlorine into pyrope. These experiments yielded 15 ppm Cl in pyrope, 0.55-0.74 wt.% Cl in the melt and 46.3 wt.% Cl in the aqueous fluid. The calculated chlorine partition coefficients are  $D^{fl/py} \sim 3 \cdot 10^4$  and  $D^{fl/melt} = 63$ .

Several experiments in the system CaO-MgO-Al<sub>2</sub>O<sub>3</sub>-SiO<sub>2</sub>-H<sub>2</sub>O-MgCl<sub>2</sub>/MgF<sub>2</sub> at 1100 °C and 3.0 GPa intersected the stability fields of hydrous phases, which contain appreciable amounts of halogens. In chlorine-bearing compositions, pyrope coexists with chlorobrucite (1.00 wt.% Cl) whereas in fluorine-bearing runs, calcian pyrope is stable with fluorobrucite (0.86 wt.% F) and aluminous enstatite occurs together with fluoronorbergite, Mg<sub>3</sub>SiO<sub>4</sub>(F,OH)<sub>2</sub> with 11.3 wt.% F and fluorochondrodite, Mg<sub>5</sub>Si<sub>2</sub>O<sub>8</sub>(F,OH)<sub>2</sub> with 6.5 wt.% F.

Our preliminary experimental results demonstrate that (1) solubility of chlorine in forsterite, enstatite and pyrope at 1100-1400 °C and 1.5-3.0 GPa is low and it ranges from 60 to 400 ppm; (2) partition coefficients for chlorine between aqueous fluid (brine) and silicate minerals are high,  $5 \cdot 10^3$  to  $3 \cdot 10^4$ , and those between hydrous melt and minerals range from  $1.4 \cdot 10^2$  to  $4.8 \cdot 10^2$ . Therefore, both the aqueous fluids and silicate melts efficiently sequester chlorine from anhydrous silicate minerals; (3) halogens promote the stability of hydroxyphases, *e.g.*, Mg(OH,Cl,F)<sub>2</sub>, Mg<sub>3</sub>SiO<sub>4</sub>(F,OH)<sub>2</sub> and Mg<sub>5</sub>Si<sub>2</sub>O<sub>8</sub>(F,OH)<sub>2</sub>, which can act as storage or transport agents for halogens in the subducting slab.

### *c. The solubility of noble gases in silicate perovskite (S.S. Shcheka and H. Keppler)*

Noble gases are traditionally believed to be highly incompatible during partial melting. Accordingly, high contents of primary noble gases are considered to be diagnostic for primitive reservoirs in the mantle. There are various lines of evidence that suggest the occurrence of a hidden primitive noble gas reservoirs deep in the mantle. In particular, the relative abundance of Xe among the noble gases the Earth's atmosphere is significantly lower than expected from the noble gas pattern of the other planetary bodies, the sun or meteorites. Moreover, the amount of <sup>40</sup>Ar found in Earth's atmosphere and near-surface reservoirs is less than half of the <sup>40</sup>Ar expected to be produced by radioactive decay of <sup>40</sup>K over Earth's history.

Al-bearing MgSiO<sub>3</sub> perovskite could potentially be an appropriate candidate to store noble gases. Most of the aluminium (4-5 mol.% of Al<sub>2</sub>O<sub>3</sub>) in the lower mantle is believed to be incorporated in silicate perovskite by two major substitution mechanisms: (a) a Tschermak-like substitution, where 2 Al<sup>3+</sup> substitute for Mg<sup>2+</sup> + Si<sup>4+</sup>; and (b) an O-vacancies substitution where the substitution of Al<sup>3+</sup> for Si<sup>4+</sup> is charge compensated by oxygen vacancies. The latter

mechanism is well established for ceramic perovskites. In silicate perovskite, oxygen vacancy mechanism is favored by excess of MgO, which should create some oxygen vacancies in the perovskite of Earth's lower mantle. Several studies of the equation-of-state of such "non-stoichiometric" Al-bearing perovskites produced contradictory results. For instance, the bulk modulus of perovskite, synthesized in multianvil presses decreases with Al, whereas the opposite behaviour was observed for perovskite synthesized in the diamond anvil cell (DAC) with Ar as pressure medium. If argon were soluble in perovskite, this discrepancy may be due to the effect of argon on the equation of state. A significant noble gas solubility in perovskite could also provide a major reservoir of noble gases in Earth's deep interior.

To measure the solubility of Xe and Ar in silicate perovskite, starting glasses of compositions corresponding to perovskite with 0, 1, 3 and 5 mol.% Al saturated with Ar and Xe were first synthesized in a piston-cylinder apparatus at 10 kbar and 1800 °C. Perovskite growth experiments were carried out using the 1000t and 1200t multianvil presses ( $P = \sim 25$  GPa;  $T = 1600$ -1800 °C). Ar contents in the starting glasses were in the range of 250-400 wt. ppm. Electron microprobe analyses of recovered perovskites show that most of the Ar loaded into the capsule is incorporated in perovskite. Sometimes, the formation of submicroscopic bubbles was observed during electron microprobe analyses of perovskite crystals (Fig. 3.5-4a), indicating argon release under the electron beam. The maximum solubility of Ar in perovskite is probably higher than 200-400 wt. ppm, because no unambiguous evidence for saturation with Ar was found and the observed concentrations simply reflect the argon concentrations in the starting material. In majorite, on the other hand, argon contents measured by electron microprobe are below detection limit and the samples contain numerous bubbles, which appear to be primary, reflecting argon saturation during the experiment (Fig. 3.5-4b). Our results imply that silicate perovskite could easily store all of the argon produced by decay of  $^{40}\text{K}$  in Earth's interior. Moreover, the inferred solubilities are comparable to argon solubilities in depolymerized silicate melts at high pressure, implying that melt extraction would not necessarily strongly deplete the lower mantle of noble gases.

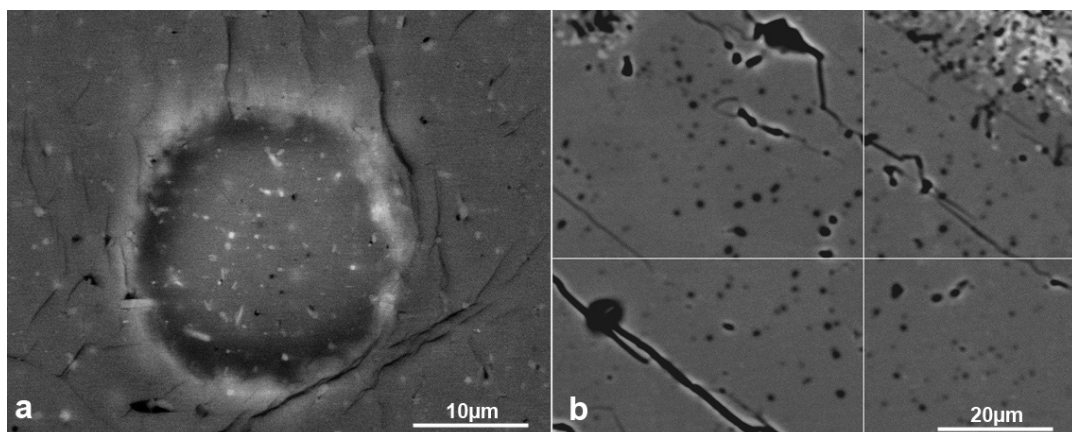


Fig. 3.5-4: BSE images of  $\text{MgSiO}_3$ -perovskite (a) and majoritic garnet (b), grown in the presence of Ar. The bubbles in the perovskite only formed during microprobe analysis and indicate argon release from the sample under the electron beam, while the bubbles in the garnet appear to be primary features.

**d. Water solubility in aluminous diopside (P. Gavrilenko and H. Keppler)**

Among the nominally anhydrous minerals of the upper mantle, clinopyroxenes usually have the highest water contents in mantle xenoliths. Previous studies have shown that the dissolution of water in pyroxenes is primarily coupled to aluminium. In aluminous orthopyroxenes, water solubility is known to strongly decrease with pressure and temperature. Together with the opposite effect observed for olivine, this causes a minimum of water solubility in the bulk mantle at a certain depth, which may be responsible for the formation of partial melts in the asthenosphere. However, so far it was not known whether water solubility in aluminous clinopyroxenes shows a similar dependence on pressure and temperature as observed for orthopyroxenes. Although the modal abundance of clinopyroxene is small, its high water contents could make a significant contribution to the bulk water content in the mantle. Therefore, the temperature dependence of water solubility in aluminous clinopyroxene was systematically studied.

Clinopyroxenes along the join diopside  $\text{CaMgSi}_2\text{O}_6$  - Ca Tschermak component  $\text{CaAlAlSiO}_6$  were synthesized from oxide mixtures under water-saturated conditions in piston cylinder experiments. Water contents were determined from polarized infrared spectra obtained on oriented single crystals. The results (Fig. 3.5-5) show that – as with orthopyroxenes – water solubility strongly decreases with temperature. Together with existing data for olivine and orthopyroxene, these data are in agreement with models that link the Earth’s asthenosphere to a zone with a minimum in water solubility in Earth’s mantle.

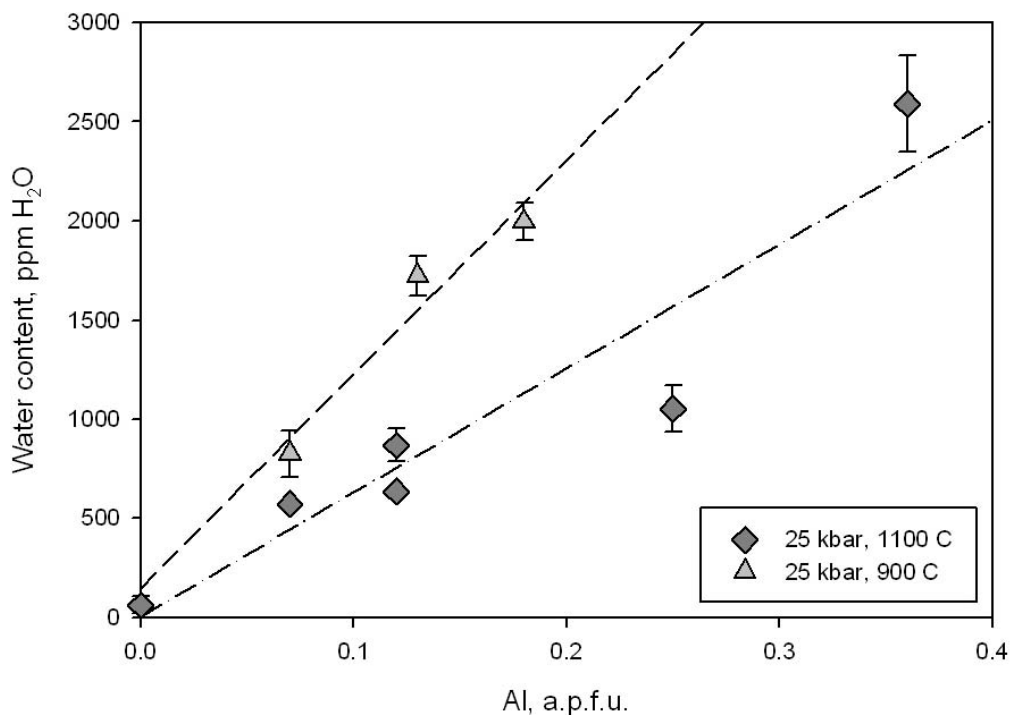


Fig. 3.5-5: Temperature dependence of water solubility in aluminous diopside.

e. *The influence of microorganisms on biotite dissolution (J. Hopf, F. Langenhorst and K. Pollok, in collaboration with D. Merten and E. Kothe/Jena)*

The biogeochemical alteration of biotite plays an important role for the bioavailability of inorganic nutrients like K, Mg, and Fe during soil formation and for redox and pH conditions affecting groundwater chemistry. In this context, microorganisms can influence the mechanism and rate of mineral dissolution in a number of ways, *e.g.*, as a result of the microbial metabolism (energy generation), by the production of organic and inorganic acids, and by the absorption or complexation of desired nutrients.

We evaluated the rates and mechanisms of elemental release during the interaction of four environmentally important species (*Bacillus subtilis*, *Shewanella putrefaciens*, *Streptomyces acidiscabies*, and *Schizophyllum commune*) with biotite using batch reactor dissolution experiments. Biotite powder, fresh bacteria, and growth medium were incubated at 28 °C and at slightly alkaline pH conditions (~ pH 9.5) for 35 days. One experiment without microbes served as a reference. The composition of the growth medium was free of major cations available from biotite in order to provide evidence of microbial influence on the dissolution process. Aliquots of solution were removed at 7 days intervals to measure the release of major and minor elements (Al, Fe, K, Mg, Mn, Si and Ti) by ICP-OES. Concentrations of Mg, Si and K increased linearly after 14 days of incubation indicating a predominantly surface-controlled process. All experiments showed that biotite dissolves incongruently with a preferential release of K (interlayer cation) followed by Mg (octahedral site) and subsequently Si (tetrahedral site). Especially the release of K and Mg was significantly enhanced by microorganisms and *Bacillus subtilis* was found to be most efficient.

Structural and chemical changes in biotite after 35 days were analyzed by a directly evolved gas analysis system (DEGAS) and transmission electron microscopy (TEM) coupled with electron energy loss spectroscopy (EELS) and energy-dispersive X-ray (EDX) analysis. TEM images of the bacteria-treated biotite flakes displayed frayed rims and etch-pits-like structures whereas the starting and control biotite was unaltered. Compositionally, the biotite evolves to a chlorite stoichiometry with a constant Al:Si ratio. Valence states of iron, manganese, and titanium in biotite determined by EELS demonstrated that the microorganisms have apparently no influence on the valence states of these transition metals. Degassing analyses reveal that microorganisms facilitate the exchange of  $\text{H}_3\text{O}^+$  and  $\text{NH}_4^+$  for K in the biotite interlayer in experiments with *Shewanella putrefaciens* and *Bacillus subtilis*. These results substantiate the considerable influence of microorganisms on the dissolution and ion exchange processes of biotite.

### 3.6 Physics and Chemistry of Melts and Magmas

Melting of rocks in the Earth's interior and the migration of the resulting partially-molten rock (magma) is the main mechanism by which the Earth has differentiated during its 4.5 billion year history. Through volcanism, for example, material is extracted from the Earth's interior and is delivered not only onto the surface but also into the atmosphere in the form of volcanic gases. The formation and movement of magma are processes that are critical to the evolution of the planet. How processes of differentiation operate in detail depends on the physical and chemical properties of magmas. Important physical properties include rheological properties, such as viscosity, which control rates of melt migration. A wide range of chemical properties are important, especially the solubilities of volatile species in silicate liquids because these determine, for example, whether volcanism is explosive and how the atmosphere is modified during volcanic eruptions.

The contributions presented here deal especially with chemical properties. The solubility and speciation of carbon dioxide in silicate melts, for example, is a topic that is closely related to the delivery of CO<sub>2</sub> into the atmosphere during volcanic eruptions, which has major implications for the greenhouse effect and climate change. The second contribution is concerned with the solubility of chlorine in silicate melts and how this changes with melt composition: this theme is directly related to ore formation because chlorine is an important component in ore-forming fluids.

In addition to pressure and temperature, oxygen fugacity is an important variable during melting and the subsequent crystallization of magmas. Traditionally, oxygen fugacity is estimated based on the ratio of ferric to ferrous iron. In the third contribution of this section, it is shown that the relationship between oxygen fugacity and the Fe<sup>3+</sup>/Fe<sup>2+</sup> ratio is more complex than previously believed and shows a non-linear dependence on the SiO<sub>2</sub> content of the melt. The cause of this dependence is not yet understood.

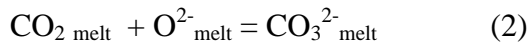
During explosive volcanism, the viscoelastic properties of magma are important for controlling how deformation and fragmentation occur. In the fourth contribution of this section, Mössbauer spectroscopy is used to study the relaxation behaviour of both ferrous and ferric iron in silicate glasses at high temperature. The final contributions are concerned with (i) liquid immiscibility between carbonatite and silicate melts – a property that is likely to be of major importance for the origin of carbonatite magmas, and (ii) a detailed *in situ* study of the crystallization of a basaltic melt at high pressure. In this latter study, the novel approach used will be of great benefit for making deductions about crystallisation history and crystal growth rates based on studies of the textures of natural rocks.

**a.** *A general model for CO<sub>2</sub> solubility and speciation in silicate melts (A. Korschak and H. Keppler)*

Unlike water, the solubility of carbon dioxide in silicate melts depends strongly on the melt composition, in addition to pressure and temperature. This partially reflects the fact that CO<sub>2</sub>

speciation in silicate melts is a strong function of composition, with molecular CO<sub>2</sub> dominating in polymerized, siliceous melts, while carbonate is believed to dominate in basic melts. The equilibria between these two species, however, are poorly known. Therefore, no general thermodynamic model for CO<sub>2</sub> speciation and solubility exists for silicate melt, despite the importance of CO<sub>2</sub> in the generation of basaltic melts in the mantle and its effect on the style of volcanic eruptions.

CO<sub>2</sub> solubility and speciation in silicate melts can be described by two equilibria:



In the last years, we have been able to measure the equilibrium between molecular CO<sub>2</sub> and carbonate in silicate melts of variable composition by *in situ* FTIR spectroscopy. The enthalpies of reaction (2) were found to systematically increase with NBO/T. Using these results and published data on CO<sub>2</sub> solubility over a wide range of pressures, temperatures and bulk compositions, we were able to derive a general model of CO<sub>2</sub> solubility and speciation in silicate melts. We parameterized the equilibrium constants of reactions (1) and (2) in the form

$$\ln K_1 = a_1/T + b_1$$

$$\ln K_2 = a_2/T + b_2$$

where  $a_1$ ,  $a_2$ ,  $b_1$ , and  $b_2$  are linear functions of NBO/T, the number of non-bridging oxygen atoms per silicate tetrahedron in the melt. With this model, we can correctly predict CO<sub>2</sub> solubility over a wide range of melt compositions, pressure and temperature. Figure 3.6-1 shows one example for a pressure of 15 kbar.

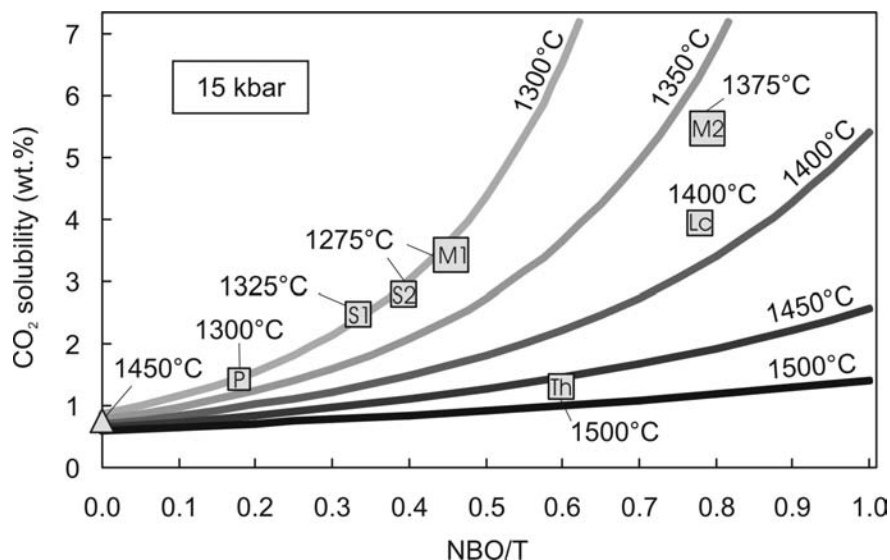


Fig. 3.6-1: Calculated and measured CO<sub>2</sub> solubilities at 15 kbar in a variety of silicate melt compositions, as represented by the NBO/T parameter. Solubility data are from the literature.

Our model also predicts that at temperatures of 1400 °C or more, most of the CO<sub>2</sub> is dissolved in molecular form even in basalts. This is in agreement with measurements of diffusion coefficients, which only weakly depend on bulk composition at these temperatures. However, close to the solidus, speciation is predicted to depend much more strongly on composition, which should lead to a pronounced compositional dependence of diffusion coefficients.

**b. Interaction of chlorine and carbonate components in jadeitic melts at high pressure (V. Stagno, D. Dolejš and H. Keppler)**

Chlorine is one of the most important volatile constituents in natural magmas and associated ore-forming fluids. It also exerts fundamental control on trace element partitioning in volatile-rich magmatic systems. In contrast to the system H<sub>2</sub>O-NaCl, interactions between chlorine and other volatiles, *e.g.*, CO<sub>2</sub>, in silicate melts are virtually unknown. Observations on melt inclusions from natural arc and back-arc magmas suggest that chlorine and carbon dioxide may be present in high and comparable amounts (up to 0.2 wt.% each) and these systems may provide insights into distinct solubility behaviours owing to the distinct and multiple speciation mechanisms of carbon in silicate melts.

In order to eliminate additional effects arising from element partitioning between silicate melt and aqueous fluid we have focused on a compositionally simple and anhydrous model system. We investigated chlorine solubility in CO<sub>2</sub>-free and CO<sub>2</sub>-saturated jadeitic melt from 5 to 30 kbar at a temperature of 1400 °C. The solubility and speciation of dissolved carbonate species were measured using Fourier transform infrared spectroscopy.

The starting composition was a synthetic oxide-carbonate mixture of jadeitic composition (NaAlSi<sub>2</sub>O<sub>6</sub>). For CO<sub>2</sub>-free experiments, the starting mixture was slowly decarbonated and repeatedly melted to provide glass whereas for CO<sub>2</sub>-bearing experiments, a portion of the raw carbonate-bearing mixture was used together with the glass. All starting materials were doped with 5 wt.% of pure NaCl as a chlorine source. Experiments were carried out in an end-loaded piston cylinder apparatus at 1400 °C and 5 to 30 kbar. At run conditions, jadeitic melt is saturated with molten NaCl and a CO<sub>2</sub> fluid. Chlorine solubility was measured by electron microprobe whereas the solubility and speciation of CO<sub>2</sub> was determined by Fourier transform infrared (FTIR) spectroscopy. Infrared spectra were collected at room temperature on doubly-polished glass plates using a microscope attachment to the FTIR spectrometer operating between 1000 and 5000 cm<sup>-1</sup>. The density of the glasses was estimated on a chlorine and water-free basis by using partial molar volumes of oxide components. FTIR spectra revealed that only a negligible amount of CO<sub>2</sub> was reduced to CO during experiments (Fig. 3.6-2).

Chlorine solubility in CO<sub>2</sub>-free jadeitic melts at 1400 °C ranges between 0.61 wt.% Cl at 1 atm and 2.26 wt.% Cl at 30 kbar (Fig. 3.6-3). The increase in chlorine solubility with pressure

is nearly linear, about 0.055 wt.% Cl/kbar. This behaviour is in excellent agreement with our previous experimental results on several other melt compositions in the system  $\text{Na}_2\text{O}-\text{Al}_2\text{O}_3-\text{SiO}_2$ , which yielded 0.044-0.062 wt.% Cl/kbar. This pressure dependence suggests that chloride dissolution into silicate melts is associated with a negative volume change, that is, local contraction of the tetrahedral silicate melt structure.

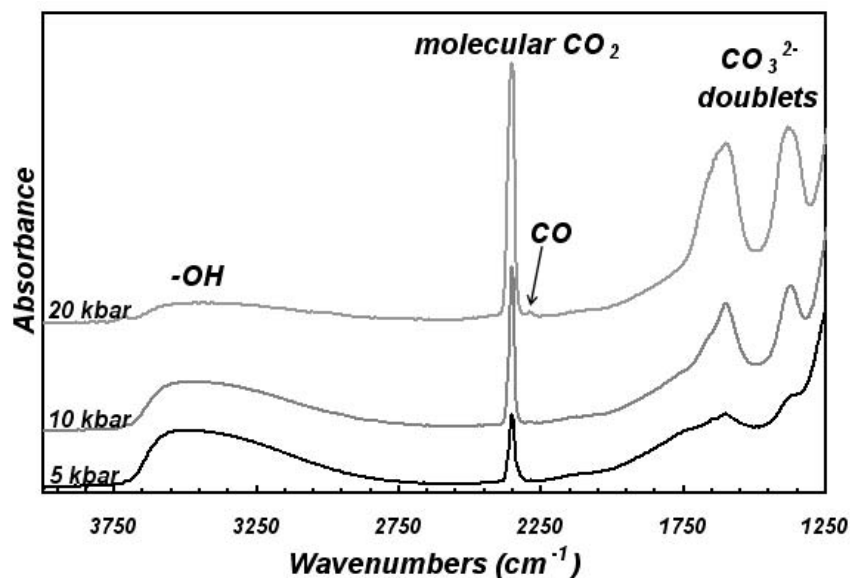


Fig. 3.6-2: FTIR spectra of  $\text{CO}_2$ -bearing jadeitic glasses produced at  $1400\text{ }^\circ\text{C}$  and 5, 10 and 20 kbar, respectively, illustrating relative abundances of molecular CO, molecular  $\text{CO}_2$  and carbonate  $\text{CO}_3^{2-}$  species.

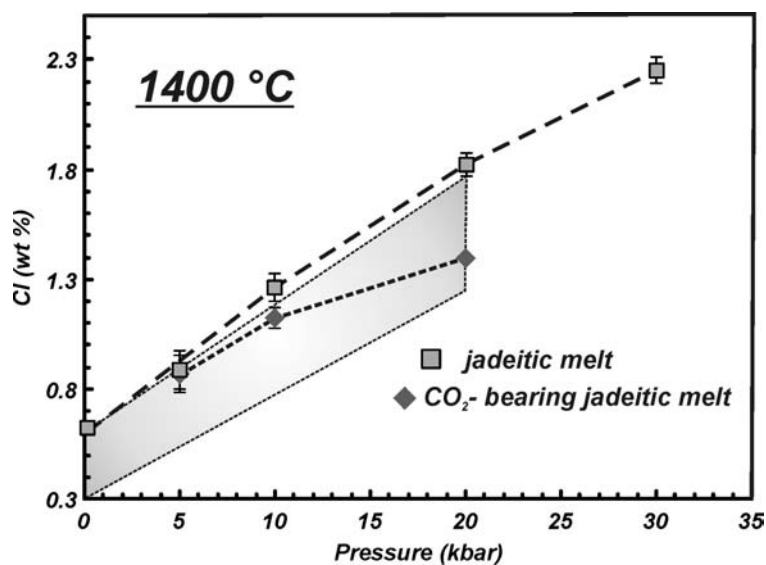


Fig. 3.6-3: Chlorine solubility in  $\text{CO}_2$ -free and -bearing jadeitic melts at  $1400\text{ }^\circ\text{C}$ . The shaded area shows the Cl solubility trends of aluminosilicate melts previously investigated.

In CO<sub>2</sub>-saturated jadeitic melts the chlorine solubility is lower than under CO<sub>2</sub>-free conditions and this difference becomes more prominent at higher pressure (Fig. 3.6-3). At 20 kbar, the chlorine solubility is 1.39 wt.% Cl, which is 76 % of the chlorine budget in a CO<sub>2</sub>-free system. The average increase in chlorine solubility in CO<sub>2</sub>-saturated melts is 0.028 wt.% Cl/kbar and is therefore also relatively low.

The total CO<sub>2</sub> solubility in chloride-saturated jadeitic melts at 1400 °C increases from 0.37 wt.% CO<sub>2</sub> at 5 kbar to 1.56 wt.% CO<sub>2</sub> at 20 kbar and this is in a good agreement with previous experimental results in CO<sub>2</sub>-free melts. Our observations imply that chlorine exerts no effect on CO<sub>2</sub> solubility in jadeitic melts. The ratio of molecular and total CO<sub>2</sub> in quenched glasses varies between 0.23 and 0.28, and it is nearly independent of pressure. These values are slightly lower than results of Brooker *et al.*, (1999, *Geochim. Cosmochim. Acta* 63, 3549-3565) owing to a weak positive temperature dependence (Fig. 3.6-4).

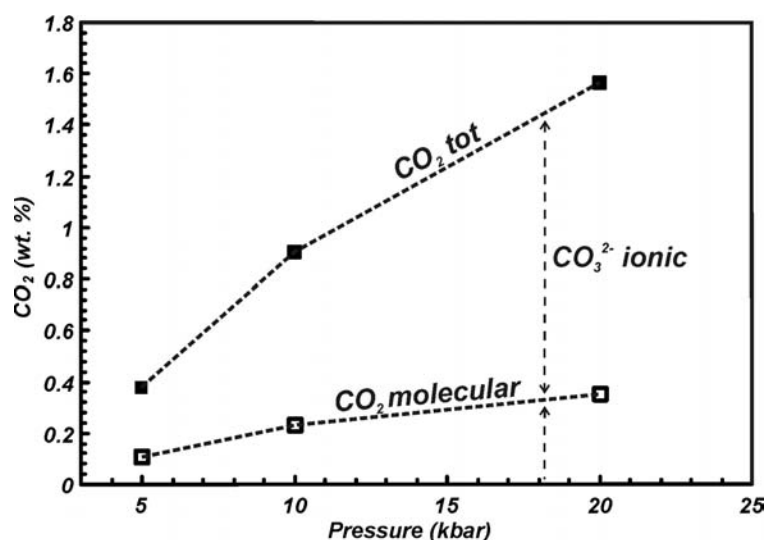


Fig. 3.6-4: CO<sub>2</sub> solubility and speciation in NaCl-saturated jadeitic melts at 1400 °C.

In summary, the presence of CO<sub>2</sub> in jadeitic melts causes a decrease in the chlorine solubility but, interestingly, the opposite effect has not been observed. The magnitude of decrease in chlorine concentration is, however, comparable to the equimolar amount of molecular CO<sub>2</sub> dissolved in the melt. Our previous study has demonstrated that chlorine dissolves in the melt in the form of associated alkali chloride species without any energetic (enthalpic) interaction with the melt structure. We propose that a decrease in chlorine solubility in favour of molecular CO<sub>2</sub> is a result of competition for sites or free volume in the silicate melt structure.

Our experimental results imply that dissolved CO<sub>2</sub> and Cl in natural magmas may cause saturation with multiple volatile phases, *e.g.*, CO<sub>2</sub>-rich fluid and NaCl-rich hydrosaline liquid. The Cl/CO<sub>2</sub> ratio in the melt at simultaneous halide-fluid saturation changes between 1.0 at 20

kbar and 2.4 at 5 kbar (Fig. 3.6-5). Lowering by CO<sub>2</sub> of the chlorine solubility in silicate melts suggests that carbon dioxide promotes early halide saturation in natural magmas.

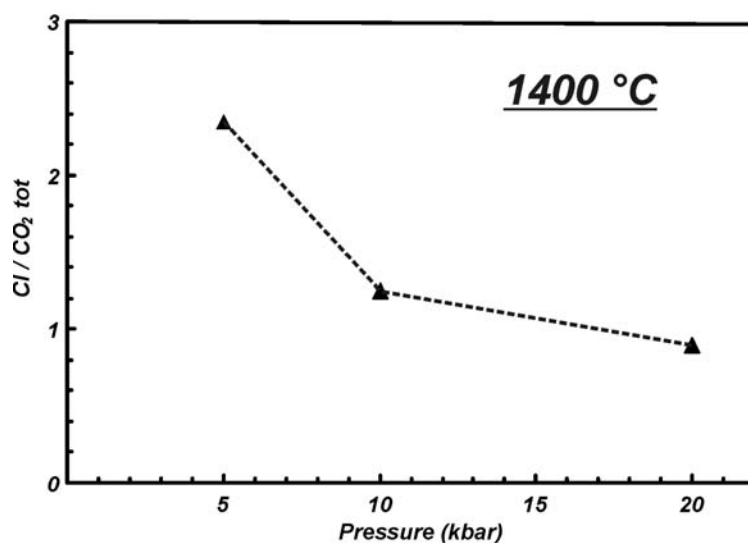


Fig. 3.6-5: Variation of Cl/CO<sub>2</sub> ratio in jadeitic melts at 1400 °C and simultaneous fluid-halide saturation as a function of pressure.

**c. The effect of silica on ferric/ferrous ratio in silicate melts: An experimental investigation (A. Borisov/Moscow, C.A. McCammon)**

The ferric/ferrous ratio is an important parameter of natural silicate melts which not only controls magnetite and spinel crystallization and physical properties of silicate melts, but also is widely used for estimating the redox conditions of magmas. Many different empirical equations have been suggested, but most of them assume a linear dependence of log (Fe<sup>3+</sup>/Fe<sup>2+</sup>) on the mole fractions of the main components of the silicate melts. To investigate this assumption, we studied the Fe<sup>3+</sup>/Fe<sup>2+</sup> ratio in Fe-doped Di-An eutectic compositions modified with different amounts of silica. Experiments were performed with a loop technique in air over a temperature range from 1400 to 1570 °C. <sup>57</sup>Fe Mössbauer spectroscopy was used to analyze the ferric/ferrous ratios in quenched glasses. A three-distribution fitting model was applied to the spectra, with one Fe<sup>2+</sup> and one Fe<sup>3+</sup> paramagnetic distribution, and one Fe<sup>3+</sup> magnetic distribution.

We observed a marked effect of silica on the ferric/ferrous ratio for all experimental compositions, which follows the solubility trend of iron in the melt as shown in previous experiments (Fig. 3.6-6). At fixed T-fO<sub>2</sub> conditions, a minimum in the ferric/ferrous ratio in our melts extends from 56 to 63 wt.% SiO<sub>2</sub>; more basic and more silicic melts show significantly higher ferric/ferrous ratios. For this reason calibrations of Fe<sup>3+</sup>/Fe<sup>2+</sup> versus oxygen fugacity made with a dataset based on basaltic compositions may not be valid for relatively silicic liquids.

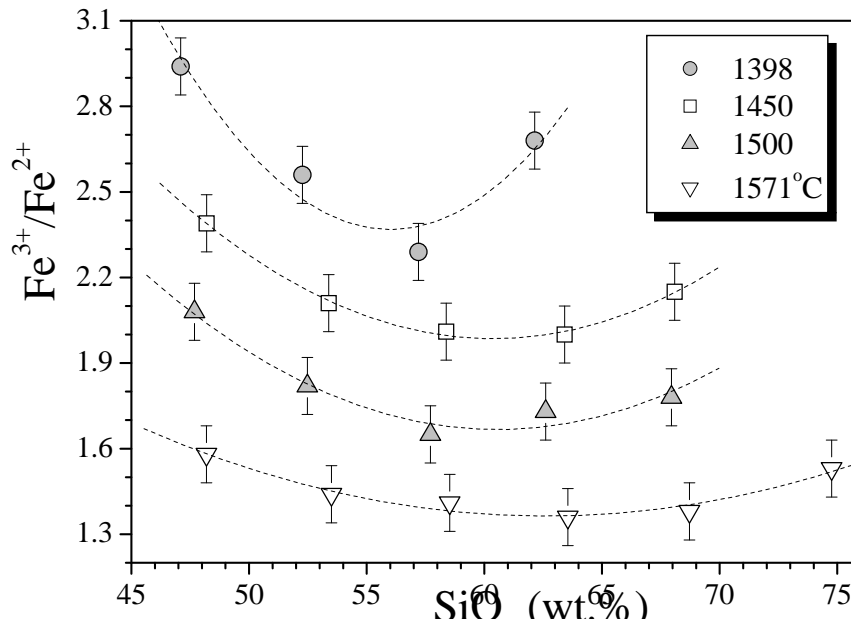


Fig. 3.6-6: Effects of silica on the ferric/ferrous ratio in silicate melts of  $x\text{DiAn}_{\text{eu}} \cdot 5\text{FeO} \cdot (95-x)\text{SiO}_2$  (wt.) composition.

**d. Mössbauer spectroscopy at high temperature: A probe for the glass transition of Fe species in silicate glasses (C. Weigel, H. Keppler and C.A. McCammon)**

Silicate melts exhibit viscoelastic properties, which means that their structures require some time to reach an equilibrium state after a perturbation. This property is a function of the relaxation time, controls the rheology of natural silicate melts, and is ultimately related to the dynamics of the melt structure. Experimentally, the most straightforward way to investigate structural relaxation is to carry out viscosity measurements. Measurements of  $^{29}\text{Si}$  NMR spectra at high temperature provide a direct insight into the relaxation time of Si-O bonds and this relaxation time can sometimes be related to measured viscosities. In a silicate melt of complex composition, however, viscous flow does not only involve rearrangement of the Si-O bonds, but also of other structural units. A deeper understanding of the dynamics of silicate melts therefore requires experiments that shed light on the relaxation timescales around various cations in the silicate glass and melt.

The Mössbauer effect arises from the recoilless absorption and emission of  $\gamma$ -rays by specific nuclei. It is generally used to study the local environment of iron in rock-forming minerals and glasses. Indeed, the intensity of Mössbauer spectra depends on the efficiency of recoilless absorption and is proportional to the recoilless fraction. The recoilless fraction in a solid decreases with temperature up to the melting point, where the Mössbauer effect is not observed anymore. But according to the characteristic time scale of a Mössbauer transition of  $\sim 10^{-8}$  s, it should be possible to record the spectra of  $\text{Fe}^{2+}$  and  $\text{Fe}^{3+}$  in a viscoelastic liquid: in

such a liquid, the relaxation time may be larger than  $10^{-8}$  s which would result in a significant recoilless fraction.

The spectra of Fe-doped albite glass (composition  $\text{NaAlFe}_{0.04}\text{Si}_3\text{O}_8$ , with Fe enriched at 90 % in the isotope  $^{57}\text{Fe}$ ) have been recorded in an argon atmosphere from room temperature to 900 °C at 100 °C intervals, using a cylindrical furnace specially designed for the Mössbauer spectrometer. The spectra have been fitted using the Extended Voigt Based Fitting method (Fig. 3.6-7) to determine the hyperfine parameters for each Fe site and the relative abundance of these sites (Fig. 3.6-8). This fitting method assumes that the hyperfine parameters are distributed according to a two-dimensional Gaussian distribution. The method is particularly adapted to disordered materials such as glasses or viscous liquids. Three components were used to fit the spectra, two for paramagnetic  $\text{Fe}^{2+}$  and  $\text{Fe}^{3+}$  sites and one for magnetic  $\text{Fe}^{3+}$ . The fits obtained for four temperatures are shown in Fig. 3.6-7. The hyperfine parameters have been fixed to their room temperature values for  $\text{Fe}^{2+}$  and for magnetic  $\text{Fe}^{3+}$ . Only the center shift (CS) and the quadrupole splitting (QS) of paramagnetic  $\text{Fe}^{3+}$  were allowed to vary as well as the areas of each sub-spectra. The evolution of the abundance of each Fe site and of the CS and QS for paramagnetic  $\text{Fe}^{3+}$  as a function of temperature is represented in Fig. 3.6-8.

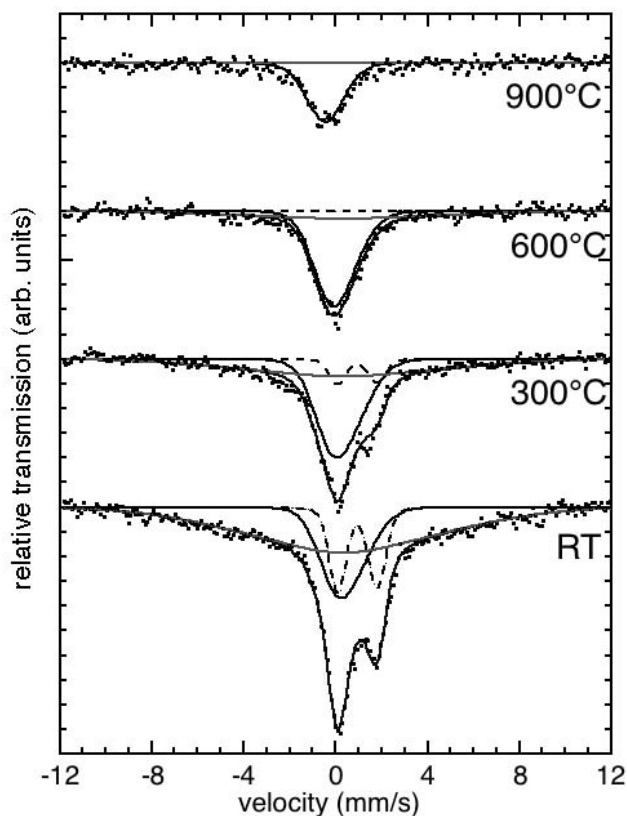


Fig. 3.6-7: Extended Voigt Based Fitting of Mössbauer spectra of Fe-doped albite glass at different temperatures. The dots represent the experimental points, which are plotted together with the total fit, and the three components are also represented: paramagnetic  $\text{Fe}^{3+}$  site (black solid line), paramagnetic  $\text{Fe}^{2+}$  (dashed black line) and the magnetic  $\text{Fe}^{3+}$  site (grey solid line).

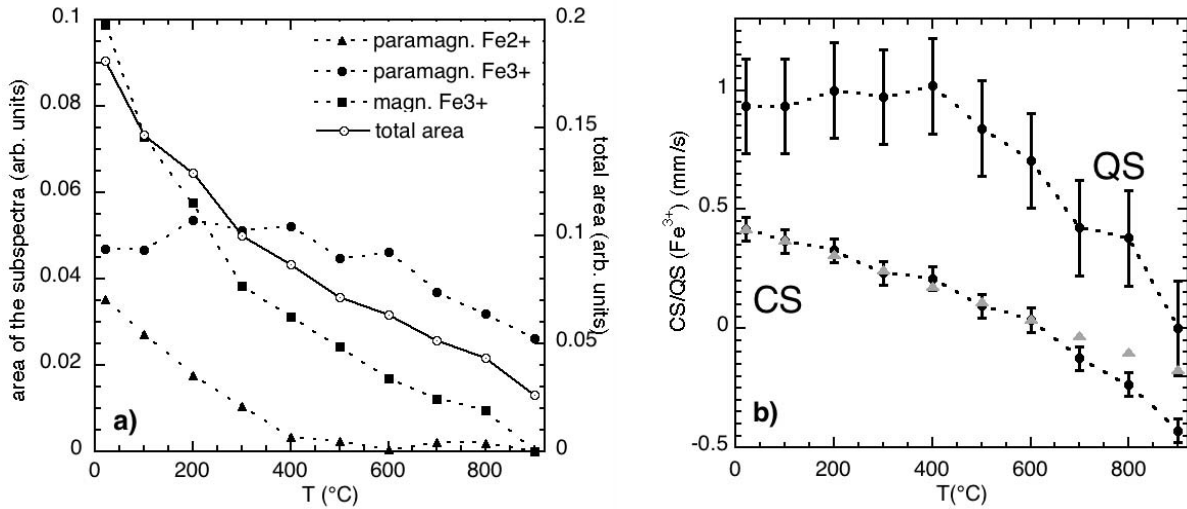


Fig. 3.6-8 : a) Areas of the sub-spectra of each of the three Fe sites, and total spectral area as a function of temperature. b) Center shift (CS) and quadrupole splitting (QS) for the paramagnetic  $\text{Fe}^{3+}$  site as a function of temperature. The experimental points are represented with error bars, and the grey triangles represent a fit to the Debye model up to 600 °C.

The total area of the Mössbauer spectra decreases as temperature increases, which reflects the general decrease of the recoil-free fraction for Fe species. The contribution of the paramagnetic  $\text{Fe}^{2+}$  site decreases as the temperature increases up to  $\sim 400$  °C, where this contribution disappears while paramagnetic  $\text{Fe}^{3+}$  is still intense. The spectrum of the recovered sample is indistinguishable from the original spectrum at room temperature. This behaviour rules out the oxidation of the sample, which could explain the disappearance of the  $\text{Fe}^{2+}$  contribution. Therefore, the  $\text{Fe}^{2+}$  signal probably disappears because the relaxation time around the  $\text{Fe}^{2+}$  ion becomes comparable to the time scale of the Mössbauer experiment of  $10^{-8}$  sec. This may be interpreted as a glass transition of  $\text{Fe}^{2+}$ . Such a phenomenon is not observed for  $\text{Fe}^{3+}$ , which can be detected in the spectrum from room temperature to 900 °C. This can be explained by the different structural behaviour of the two cations,  $\text{Fe}^{3+}$  acting as a network former and  $\text{Fe}^{2+}$  acting as a network modifier, the former one being more tightly bound to the network.

The decrease of the intensity of the magnetic  $\text{Fe}^{3+}$  contribution as  $T$  increases is attributed to the decrease of the relaxation times at high temperature. In paramagnetic  $\text{Fe}^{3+}$ -bearing materials, spin-spin interactions usually dominate, which means that the relaxation times can be slowed down when exchange coupling becomes negligible. This is the case for dilute systems in which the  $\text{Fe}^{3+}$  atoms are too far away from each other to interact appreciably. In this case, the spin-spin relaxation mechanism is slowed down, which can lengthen the atomic relaxation time up to the point where an essentially static magnetic field is experienced by the nucleus, hence giving rise to hyperfine magnetic splitting even though the bulk material is paramagnetic. This is what is observed at room temperature. But as the temperature increases,

thermal movement overcomes the spin-spin interaction, which leads to a time-averaged magnetic field equal to zero and the hyperfine magnetic splitting is not observed anymore, which causes the decrease of the area of the magnetic Fe<sup>3+</sup> component.

The center shift of paramagnetic Fe<sup>3+</sup> decreases as temperature increases. This can be explained by the variation of the second-order Doppler shift (SOD) as a function of temperature. The Center Shift (CS) measured in Mössbauer spectroscopy consists of the intrinsic isomer shift ( $\delta_I$ , related to the s-electron density at the nucleus) and the second order Doppler shift (related to the mean-square velocity of the nucleus). The temperature dependence of the intrinsic isomer shift is generally very small, so the temperature dependence of the center shift can be primarily described by the evolution of the SOD, which can be expressed using the Debye model for the lattice vibrations:

$$CS(T) = \delta_I - \frac{9}{2} \frac{k_B T}{mc} \left( \frac{T}{\theta_M} \right)^3 \int_0^{\theta_M/T} \frac{x^3 dx}{e^x - 1} \quad (1)$$

where  $k_B$  is the Boltzmann constant, T is the temperature in Kelvin, c is the velocity of light, m is the mass of the absorber nucleus and  $\theta_M$  is the characteristic Mössbauer temperature. The experimental data were fitted to equation (1) up to 600 °C using a series approximation to the Debye integral; the best-fit parameters are  $\delta_I = 0.49$  mm/s and  $\theta_M = 786$ K. It was not possible to fit the data over the whole temperature range. This is probably because the Debye Model is valid only at low temperatures, which explains why we cannot fit the data above 600 °C. It also shows that there is no major structural modification of Fe<sup>3+</sup> below 600 °C.

The quadrupole splitting of paramagnetic Fe<sup>3+</sup> is stable up to 400 °C and then decreases. The quadrupole splitting is often considered as a measure of site distortion. The Fe<sup>3+</sup> sites would then remain unchanged up to 400 °C; above this temperature the thermal movement would release the constraints on the distorted sites leading to more regular sites, which can explain the decrease of QS.

This work shows that it is possible to measure the Mössbauer spectra of glasses at high temperature, and highlights the different relaxation timescales of Fe<sup>2+</sup> and Fe<sup>3+</sup> in the glass investigated. Further work will be extended to higher temperature to observe the glass transition for Fe<sup>3+</sup>. Optical absorption spectroscopy at high temperature is planned on the same sample to demonstrate that Fe<sup>2+</sup> is not oxidized during the experiment.

*e. Liquid-liquid immiscibility between a phosphorous-bearing carbonatite melt and a potassic aluminosiliceous melt coexisting with apatite, K-feldspar and diopside at 2.2 GPa and 1200 °C (T. Guzmics/Budapest; E. Bali and A. Audétat; M. Berkesi and C. Szabó/Budapest)*

Based on previous research on natural carbonatite melt inclusions, found in clinopyroxene-apatite-K-feldspar-phlogopite mantle xenoliths, the aim of our study was to demonstrate that

apatite and K-feldspar can be in equilibrium with two immiscible melts, namely carbonatite melt and alkali aluminosiliceous melt, at mantle pressures and at CO<sub>2</sub> saturation. We performed piston-cylinder experiments on the system apatite–K-feldspar–calcite–magnesite at 2.2 GPa and 1200 °C, with 18 hours duration time. Focusing on healed cracks within K-feldspar crystals after quenching (Fig. 3.6-9), it is observed that newly formed K-feldspar, apatite and clinopyroxene exist together with three liquids: a phosphorous-bearing carbonatite melt, a potassic aluminosilicate melt and a CO<sub>2</sub>-rich fluid. Although textural equilibrium was not attained (Fig. 3.6-9), the co-existence of the newly formed phases suggest that K-feldspar and apatite can crystallize from coexisting carbonatite and aluminosilicate melts (CO<sub>2</sub> saturated) in a metasomatized (clinopyroxenite) mantle. Our experimental results are in good accordance with natural observations on apatite- and K-feldspar-hosted melt inclusions showing that there was a liquid immiscibility between a carbonate-bearing potassic aluminosilicate melt and a phosphorous-bearing carbonatite melt. Both experimental and natural studies support the idea that immiscible carbonatite and aluminosilicate melts play an important role in mantle metasomatism that is associated with crystallization of unique phases such as apatite and K-feldspar.

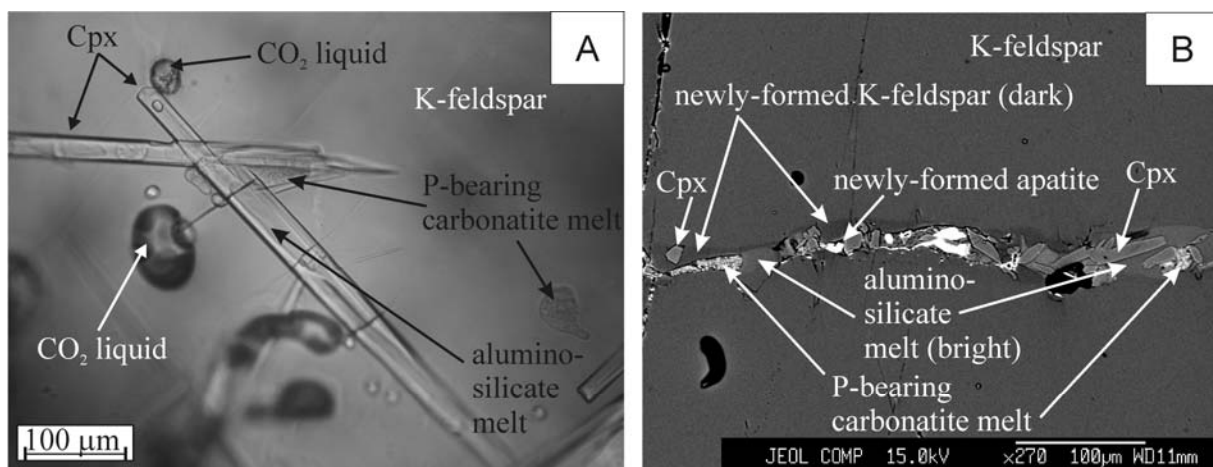


Fig. 3.6-9: Photomicrograph (A), taken in non-polarized light, and BSE image (B) of K-feldspar-hosted melt-, fluid- and solid inclusions trapped along cracks in K-feldspar at 2.2 GPa and 1200 °C. Cpx – clinopyroxene.

**f. Plagioclase growth mechanisms inferred from *in situ* crystallization experiments performed with the moissanite anvil cell (F. Schiavi, N. Walte and H. Keppler)**

The development of crystalline textures in igneous rocks depends on numerous factors among which the kinetics of nucleation and crystal growth play a central role. Thus, igneous textures yield important information on mechanisms, timescales and rates of rock solidification, whenever their investigation is possible and their interpretation correct. However, early stages of crystallization, as well as the evolution of igneous textures with complex histories such as

cycles of cooling and heating, are usually difficult to infer, since early stages of solidification are rarely preserved in natural rock samples.

In the following we focus on the crystal growth kinetics during the crystallization of a basaltic-andesitic supercooled liquid at constant temperature (900 °C) and pressure (1 bar), as observed in a moissanite anvil cell. Plagioclase was the only crystallizing phase over the whole duration of the experiment. The texture development from crystal nucleation to almost complete crystallization was examined. With increasing crystallinity, a framework of clustered and individual crystals developed to a packed clustered-chain distribution. A detailed quantitative analysis was performed on digital images, recorded during the experiment, of three representative stages characterized by distinct plagioclase modal fractions (0.06, 0.24 and 0.38 for steps 1, 2 and 3, respectively). 2D measurements of crystal length and width were used to convert 2D data to 3D crystal size distributions (CSDs, Fig. 3.6-10). Moreover, the actual estimates of crystal growth rate were precisely determined on selected grains by measuring variations of crystal lengths during known time intervals.

In the recovered CSDs, log population densities are approximately linear functions of the crystal size over a large size range, but they decrease for the lowest size interval. In addition, with progressive crystallization the curves rotate to produce a fan-like shaped distribution. These features resemble those seen in the CSD evolution of natural rock samples and can be explained by processes that are able to raise the number of large grains at the expenses of small ones. A careful visual inspection of the textural development helped us in identifying one such process, by allowing, for the first time, the *in situ* observation of crystal coalescence (Fig. 3.6-11). Additionally, the increase of crystallinity would reasonably favor a decrease of the nucleation rate (probably after step 2). Crystal coalescence caused strong increases in growth rates of individual crystals up to about one order of magnitude if compared to typical rates of free growing crystals ( $\sim 1.9 \times 10^{-5}$  mm/s vs.  $2.3\text{-}4.8 \times 10^{-6}$  mm/s), as shown in Fig. 3.6-12 (intervals C vs. intervals A). On the contrary, significant reduction of growth rate (down to  $\sim 8 \times 10^{-7}$  mm/s) occurred as a result of crystal impingement, which became important for plagioclase modal fractions higher than 0.3-0.4. In the performed experiment, all crystals experienced impingement, but at different times (see for comparison Crystals 1, 2 and 3 of Fig. 3.6-12). Noteworthy, although each crystal followed its own growth path, average growth rates calculated for single grains during the examined growth interval (crystallinity ranging between  $\sim 6$  and 70 %), showed very little variation ( $2.9 \times 10^{-6} \pm 8 \times 10^{-7}$  mm/s). This observation is in agreement with the nearly linear correlation between time and mean crystal lengths measured on the whole crystal set at Steps 1, 2 and 3. Thus, our results suggest, on the one hand, that the linear relationship between mean crystal size and time observed in natural samples results from the combination of different growth histories for individual grains. On the other hand, they indicate that the overall decrease of growth rate expected for diffusion-controlled growth, as the result of impingement and consequent depletion of diffusion halos, is negligible over the analyzed range of crystallinity.

This work highlights the importance of combining information obtained by continuous and direct observation of crystallizing samples with data provided from the subsequent

quantification of recovered textures for a correct interpretation of crystal growth mechanisms. By this method, variations in bulk textural parameters can be compared and better explained by examinations at the single crystal scale. This study confirms the importance of grain coalescence as a coarsening mechanism in natural basaltic melts and shows the effects that it can exert on the shape of crystal size distribution patterns. Despite some uncertainties that still remain about the processes operating during solidification, the plagioclase crystal mush produced experimentally will help to clarify crystal growth kinetics operating in batch systems during *in situ* crystallization at magma chamber margins. In particular, this type of research can help understand the early stages of texture evolution of crystallizing magmas that are rarely preserved in natural rocks.

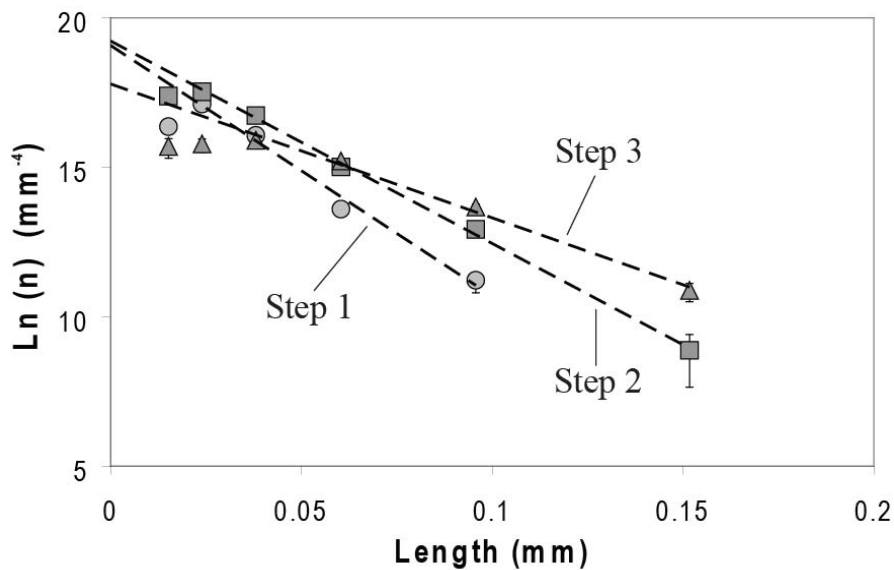


Fig. 3.6-10: Crystal size distributions for three steps of textural evolution. The steps 2 and 3 occurred 15 and 40 minutes, respectively, after the step 1.

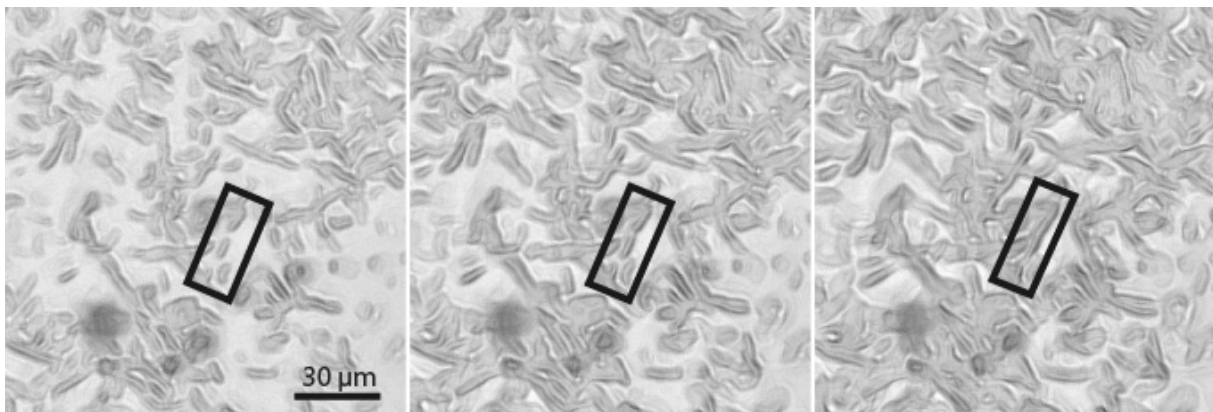


Fig. 3.6-11: Time-lapse pictures of three stages of textural evolution showing coarsening and subsequent coalescence of three neighboring plagioclase crystals of comparable size, oriented in the same direction, which merge together to form one single grain.

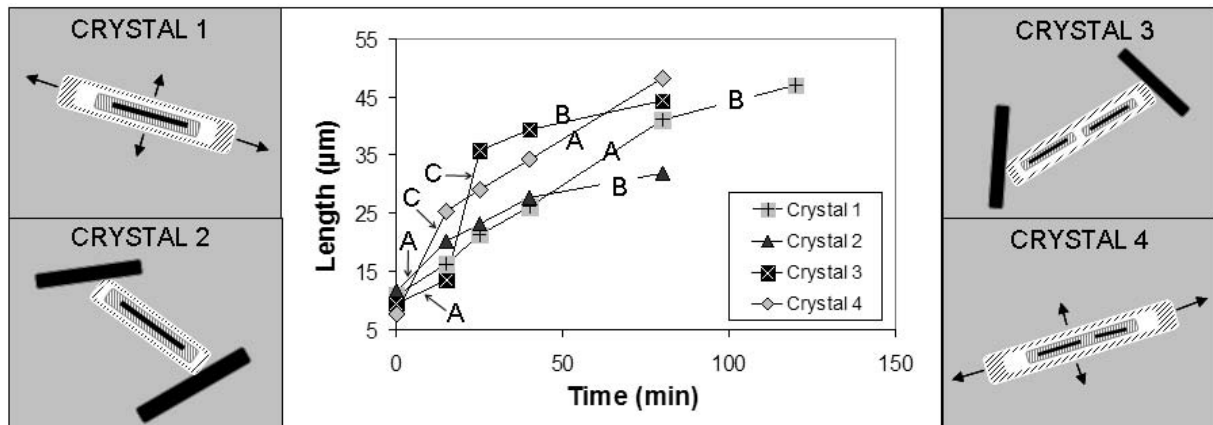


Fig. 3.6-12: The central diagram shows the temporal variations of lengths measured on four representative plagioclase crystals. The starting point at time zero corresponds to the Step 1 in Fig. 3.6-10. The linear intervals characterized by different slopes and indicated by the letters A, B and C are related to free growth, impingement and crystal coalescence, respectively. The sketches are schematic representations of the four growing crystals. The growth history of each crystal is traced in four steps (at 0, 15, 40 and 80 minutes). Black crystals represent neighboring crystals that caused impingement.

### 3.7 Rheology

The plastic deformation behaviour of rocks is described by flow laws, which relate the applied stresses to the equilibrium strain rate. The flow laws are derived from deformation experiments where materials are subjected to deviatoric stresses under controlled conditions. The number of external (*e.g.*, pressure, temperature, oxygen and water fugacity) and internal (*e.g.*, phase content, microstructure, texture) parameters influencing the deformation behaviour of a rock is however rather large and controlled deformation experiments at pressures and temperatures pertaining to the Earth's interior remain challenging. Technological developments such as the D-Dia multianvil apparatus and the use of low pressure analogue materials, *e.g.*,  $\text{CaIrO}_3$  as analogue for  $\text{MgSiO}_3$  perovskite/post-perovskite, give nevertheless insights into the rheological behaviour of the Earth's deep interior. An important consequence of large strains in rocks is the development of characteristic deformation microstructures and physical anisotropies which can be detected indirectly in the deep Earth by geophysical methods such as seismological or geoelectrical measurements.

The profile of mechanical strength vs. depth inside the Earth is extremely important for the understanding and geodynamic modelling of convective flow patterns in the Earth's mantle. Of special interest are phase transitions such as the perovskite – post-perovskite transition above the core mantle boundary and their associated change in strength as well as deformation mechanism. Preliminary results from analogue experiments indicate that post-perovskite may be somewhat weaker than perovskite indicating that deformation will be enhanced near the CMB. The ability of mineral phases to produce seismologically detectable anisotropies depends on their single crystal anisotropy and on their ability to deform in dislocation creep, which produces a crystallographic preferred orientation. Detailed transmission electron microscopy studies have shown that this is the case for post-perovskite as well as akimotoite, which likely occurs in larger proportions in deeply subducted slabs, making both of them candidates for producing seismic anisotropies in the deep mantle.

In the upper mantle the strengths of subducting slabs (*e.g.*, eclogite) and average mantle material (*e.g.*, peridotite) are largely determined by their main constituents, that is omphacite and olivine, respectively. A long-standing debate concerns the question if the  $C2/c$  (HT)  $\rightarrow$   $P2/n$  (LT) phase transition influences the deformation mechanisms of omphacite and how this may affect the resulting textures. First results indicate that textures in omphacite deformed in the  $P2/n$  are similar to the high temperature ( $C2/c$ ) fabrics known from literature. However, deformation experiments with added water show an enhanced ductility and activation of intracrystalline deformation mechanisms in omphacite. Deformation studies of olivine indicate that there is a pressure dependence of the active intracrystalline slip systems yielding a change in crystallographic preferred orientation and seismic anisotropy with increasing depth.

The rheological behaviour of melts is important for the understanding of intrusive as well as extrusive (volcanic) magmatic processes. A crucial factor is the percentage of solid crystals in the magma and their alignment during flow which governs the transition from liquid to solid

behaviour. Torsion experiments with melt-crystal mixtures show that the critical amount of crystals lies between 50 and 60 % and that the transition is characterized by a change from pervasive to discrete deformation structures.

**a. Comparative viscosity of  $\text{CaIrO}_3$  perovskite and post-perovskite (S. Hunt and D. Dobson/ London; N. Walte)**

The transition from the Earth's lower mantle into the 200-300 km thick D'' layer near the core-mantle boundary is now widely thought to coincide with the phase transition from  $(\text{Mg,Fe})\text{SiO}_3$  perovskite (pv) to post-perovskite (ppv). Deformation studies with diamond anvil cell experiments and using ppv analogue materials such as  $\text{CaIrO}_3$  suggest that part of the anomalous seismic anisotropy of the D'' layer can be explained by a lattice preferred orientation in the post-perovskite phase. However, even though the possible formation of a lattice preferred orientation indicates dislocation creep as the dominant deformation mechanism of ppv under D'' conditions, the rheology of ppv and its relative viscosity versus perovskite are largely unknown. The extremely high pressures necessary to form ppv preclude direct studies of rheology on  $\text{MgSiO}_3$  ppv; even the rheology of  $\text{MgSiO}_3$  pv has not yet been determined. Geodynamic simulations indicate that ppv could be up to three orders of magnitude less viscous than pv. Such a high viscosity contrast could cause a decoupling of the D'' layer from the lower mantle, which would mean that D'' could act as a geochemically distinct reservoir in the deep Earth. For this study we have investigated the relative rheology contrast of  $\text{CaIrO}_3$  pv and ppv versus MgO.  $\text{CaIrO}_3$  is an isostructural analogue for  $\text{MgSiO}_3$ , forming both a pv and a ppv structure. Assuming that a viscosity contrast between pv and ppv in the Earth is mainly controlled by the different crystal structures of both phases, we suggest that the determination of the viscosity contrast between  $\text{CaIrO}_3$  pv and ppv is a valid approach to understand viscosity in the deep Earth. We performed deformation experiments with  $\text{CaIrO}_3$  pv and ppv versus MgO to determine the relative viscosity contrast between these phases.

The experiments were performed with the deformation-DIA in axial compression. Each assembly contained two Pt capsules of initially identical length filled with MgO and  $\text{CaIrO}_3$  powder (Fig. 3.7-1). Since the flow strength of crystalline material depends more on temperature than on pressure, the pressure was varied between 1 and 3 GPa at a constant temperature of ca. 1420 °C to deform in the pv and ppv field, respectively. The strain rates were held constant in both experiments at ca.  $9 \times 10^{-5} \text{ s}^{-1}$  to ensure comparability between pv and ppv experiments.

After deformation the assemblies were cut with a diamond wire saw and polished. The samples indicate a clear competence contrast between pv, ppv, and MgO (Fig. 3.7-1). The first experiment in the pv stability field shows that pv has a higher competence than MgO, since the MgO capsule is more deformed than the  $\text{CaIrO}_3$  pv capsule. The opposite result can be observed in the ppv experiment. Here, the  $\text{CaIrO}_3$  ppv is more deformed than the MgO

capsule. Hence, under our experimental conditions  $pv > MgO > ppv$  (> denotes more viscous), hence, ppv is weaker than pv by ca. 4 times.

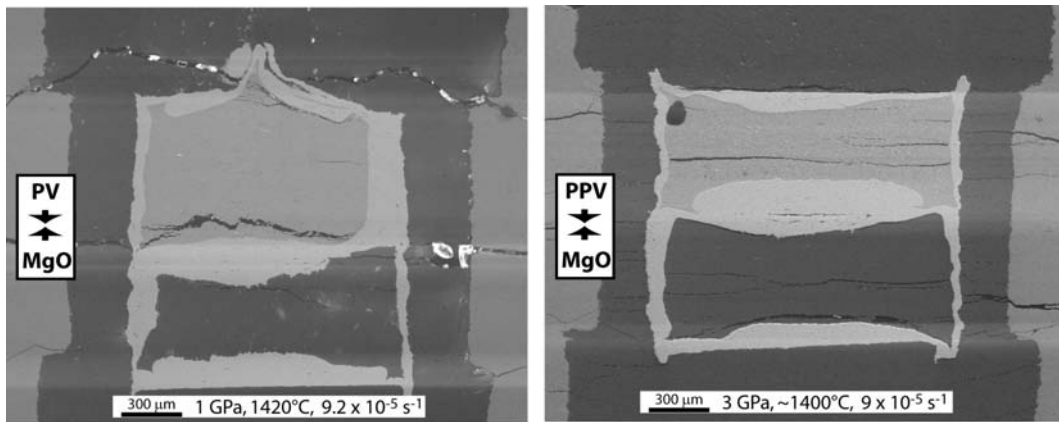


Fig. 3.7-1: Secondary electron image of  $CaIrO_3$  perovskite-MgO (left) and post-perovskite-MgO deformation (right). Capsules in both experiments were identical in length before deformation. The experiments show that  $CaIrO_3$  pv is more viscous and ppv is less viscous than MgO under experimental conditions.

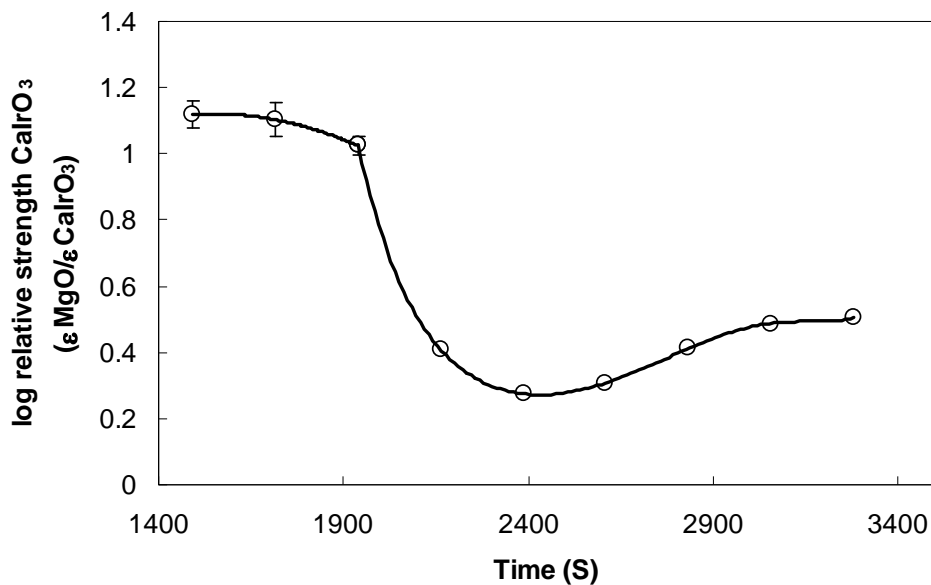


Fig. 3.7-2: Relative strength of  $CaIrO_3$  during the transformation from perovskite to post-perovskite determined by X-radiography during a deformation experiment at 4 GPa and 1400 C. The sample is entirely perovskite at 1500 s and has completely transformed by 3200 s. There is an initial weakening by almost 1 order of magnitude but the post-perovskite recovers by a factor of two by the end of the experiment.

Further experiments were performed at beamline X17B2 of the NSLS, in which  $CaIrO_3$  samples were deformed during the transformation from pv to ppv with continuous radiographic monitoring. Figure 3.7-2 shows the relative strength of  $CaIrO_3$  to MgO during

the transformation at constant temperature and pressure. Perovskite is stronger than ppv by a factor of  $\sim 5$ , similar to the quenching experiments. Furthermore, there is a factor of 2 extra weakening during the transformation.

If our results can be scaled to  $\text{MgSiO}_3$  under lower mantle conditions and strain rates, we can conclude that ppv is softer than pv, as was predicted based on geodynamic modeling, but by less than an order of magnitude. A weakening of 5-times is, however, sufficient to change D'' dynamics, resulting in laminar convection within the field of ppv stability and increasing the complexity of seismic anisotropy observed from D''.

**b. Deformation microtextures in  $\text{CaIrO}_3$  post-perovskite under high stress conditions in a laser-heated DAC (N. Miyajima and F. Heidelbach, in collaboration with K. Niwa, T. Yagi and K. Ohgushi/Tokyo)**

The structure and behaviour of  $\text{CaIrO}_3$  under high pressure and high temperature are of interest in high-pressure mineral physics, because  $\text{MgSiO}_3$  perovskite transforms into a denser polymorph at 130 GPa and 2000 K which has the same structure as  $\text{CaIrO}_3$  at ambient conditions. This post-perovskite phase (ppv) has a layered structure and displays a strong elastic anisotropy. Knowledge of the plastic properties of the  $\text{CaIrO}_3$  phase would help to constrain that of the  $\text{MgSiO}_3$  post-perovskite phase, especially in relation to the polarized seismic anisotropy (*e.g.*,  $V_{\text{SH}} > V_{\text{SV}}$ ) observed in the D'' layer. There is a number of studies on crystallographic preferred orientation (CPO) patterns of  $\text{CaIrO}_3$ -structured materials. However, the results are still under controversy, especially (010) in  $\text{CaIrO}_3$  vs (100)-(110) in  $\text{MgSiO}_3$  &  $\text{MgGeO}_3$  in the CPO patterns. Here we report a transmission electron microscopy (TEM) study on the defect microtextures of  $\text{CaIrO}_3$  ppv deformed in a laser heated diamond anvil cell (LHDAC). With a view to understanding better the deformation mechanisms at very high pressure, the results of  $\text{CaIrO}_3$  deformed under higher stress (in the order of GPa) at up to 27 GPa (higher than the previous studies in  $\text{CaIrO}_3$ ) should provide important information for discussing the difference in CPO patterns of the ppv phase.

The starting material is the orthorhombic perovskite (pv), which is pre-synthesized using a cubic-anvil type high-pressure apparatus. In *Run01 (Low-temperature deformation: LT)*, the pv phase was compressed to 13 GPa at room temperature and then converted to the ppv phase by heating it at above 1500 K for 2.5 hours. After the heating, the pressure was increased gradually to 27 GPa at room temperature. In case of *Run05 (High-temperature deformation: HT)*, after the procedure to transform the pv phase into the ppv phase, the pressure was increased gradually to 27 GPa at high temperature around 1500 K. For comparison, a transition experiment was also performed, in which the ppv phase was quenched to ambient conditions after converting from pv to ppv at 13 GPa (*Run03: Transition experiment: TR*). The microstructures of the recovered samples have been investigated using bright field (BF), dark field (DF) and weak-beam dark-field (WBDF) imaging in TEM operating at 200 kV. The

Burgers vectors ( $b$ ) of the dislocations were analyzed using the  $g \cdot b$  invisibility criterion ( $g$  is the diffraction vector) and the thickness contour fringe methods. CPOs were measured by *in situ* X-ray diffraction (*Run01*) and by analysis with electron backscatter diffraction in the SEM after the experiment (*Run03*, *Run05*).

The *in situ* XRD measurements of *Run01(LT)* imply an alignment of the (010) plane normal to the compression axis. The recovered sample shows a typical defect microtexture in TEM (Fig. 3.7-3). The centre grain has a lamella-like texture, which displays a {110} twinning relation in the selected area diffraction pattern from the lamella boundaries. In DF images with  $g = 0\bar{2}\bar{2}_{\text{matrix}}$  and  $g = 0\bar{2}\bar{2}_{\text{twin}}$ , the narrower twin lamellae (white contrast in the right image) lie between thicker matrix domains. Also, the matrix domains contain a high density of tangled dislocations. Similarly, in *Run05(HT)* the ppv phase displays polysynthetic {110} twins and a high density of [100] and [001] screw and edge dislocations on the (010) plane (Fig. 3.7-4). The crystallographic configuration of the dislocations strongly suggests that (010)[100] and (010)[001] slip systems were co-activated under the deformation at high temperature. The slip systems are consistent with a strong alignment of (010) plane, normal to the compression axis.

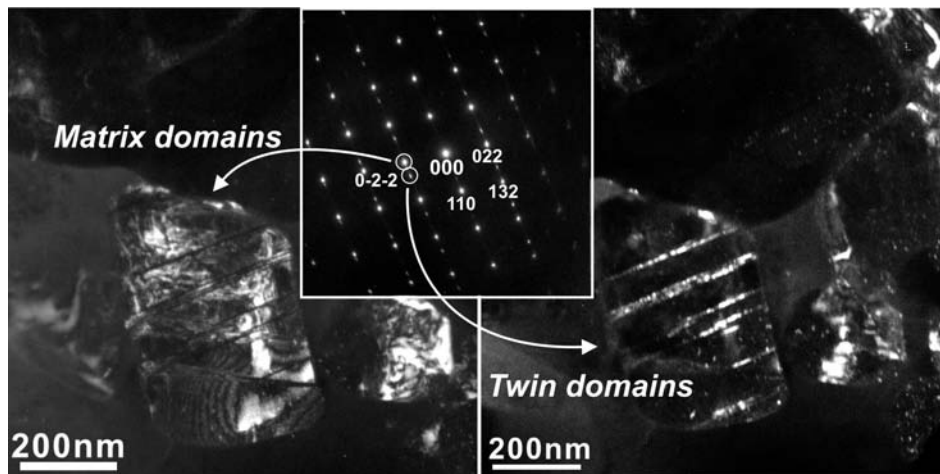


Fig. 3.7-3: DF-TEM images of the post-perovskite phase deformed at room temperature (*Run01*), with  $g = 0\bar{2}\bar{2}_{\text{matrix}}$  (Left) and  $g = 0\bar{2}\bar{2}_{\text{twin}}$  (Right). The inset (middle) is a selected area diffraction pattern from the centre grain. The grain contains thinner {110} twin lamellae.

On the other hand, the ppv phase in *Run03(TR)* does not show the twinning at the centre of the DAC sample chamber (Fig. 3.7-5), but a few twinned grains can be observed at the edge where the grains suffered a higher strain. The curved [100] dislocations and [001] edge dislocations could be nucleated due to thermal stress in the transition experiment. The character of those dislocations is consistent with the CPO patterns. In summary, the new finding of {110} twin in the ppv structure could be very important for discussing deformation textures under higher stress conditions using DAC apparatus. The effect on the plastic

behaviour of the ppv phase is currently under consideration, but it is particularly interesting in relation to the CPO pattern of  $\{110\}$  in DAC-deformed  $\text{MgSiO}_3$  and  $\text{MgGeO}_3$ .

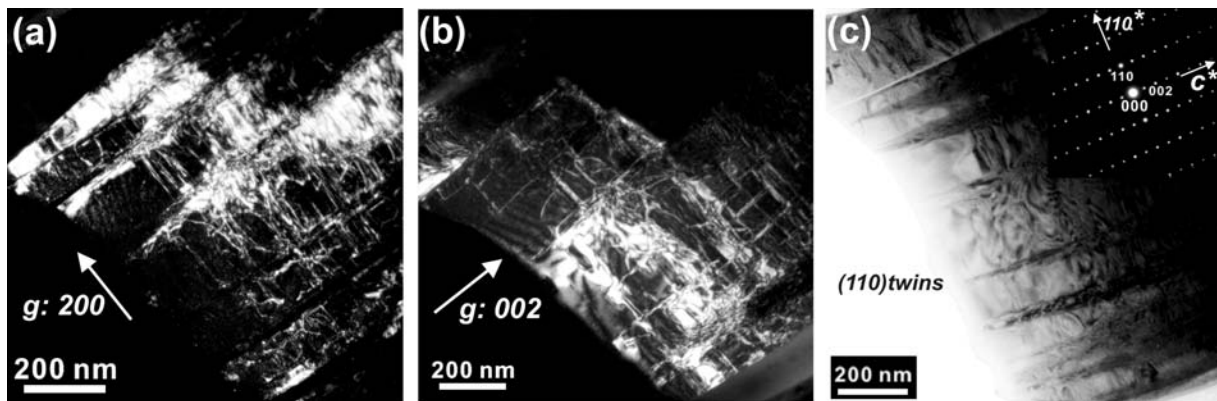


Fig. 3.7-4: Typical microtextures of the post-perovskite phase deformed at high temperature (*Run05*). WBDF-TEM images with (a)  $g = 200$  and (b) with  $g = 002$ . (c) BF-TEM image of an orientation near the  $[\bar{1}10]$  zone axis. Thinner  $(110)$  twin lamellae are visible with the dark wedge-shaped contrast.

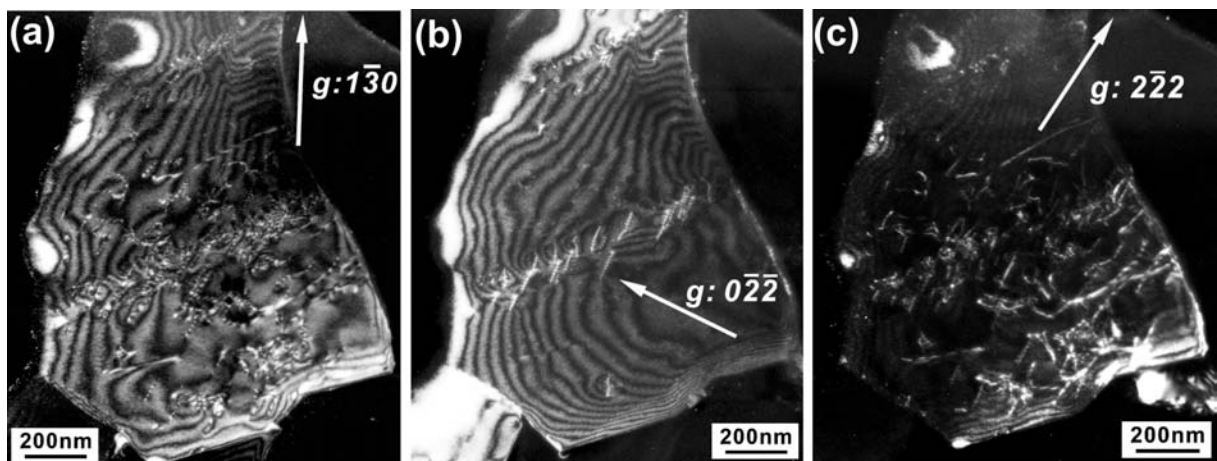


Fig. 3.7-5: WBDF-TEM images of  $[100]$  and  $[001]$  dislocations in the undeformed post-perovskite phase (*Run03*). (a)  $[100]$ -type dislocations are visible with  $g = \bar{1}30$ , (b)  $[001]$ -type dislocations are visible with  $g = 0\bar{2}\bar{2}$ , (c) Both types of dislocations are visible with  $g = 2\bar{2}\bar{2}$ .

*c. Dislocation microtextures in a Fe,Al-bearing akimotoite (N. Miyajima, J. Pickles, C.A. McCammon and D.J. Frost)*

Akimotoite is ilmenite-structured  $\text{MgSiO}_3$ , which is thought to possess strong elastic anisotropy based on the hexagonal closed packed structure ( $R\bar{3}$  space group) with a much longer  $c$ -axis than  $a$ -axis. As a solid solution between  $\text{MgSiO}_3$  and  $\text{FeAlO}_3$  components,

akimotoite is likely to be one of the main constituent minerals in subducting slabs. If the akimotoite crystals were preferentially oriented by plastic deformation, the subducted slab would be extremely anisotropic. Recently, a temperature transition in crystallographic preferred orientations (CPO) in deformed  $\text{MgSiO}_3$  akimotoite at high pressures was reported using multianvil press and electron backscatter diffraction (EBSD) techniques. The result suggested that a basal slip system of  $(0001) \langle 11\bar{2}0 \rangle$  was dominant during plastic deformation at 21-23 GPa and 1200-1300 °C. However, there have been few reports of dislocation microstructures of akimotoite. In order to confirm the mechanisms of plastic deformation, TEM investigations of dislocation properties (*e.g.*, the Burgers vector) are indispensable. Here we present a possible Burgers vector for dislocations in Fe, Al-bearing akimotoite by using transmission electron microscopic techniques.

The sample of akimotoite was synthesized from a glass with Fe, Al bearing pyroxene-stoichiometry at 24 GPa and 1260 °C. The recovered sample was first cut and polished to make a petrological thin section for optical microscopy. The TEM thin foil was then milled using a conventional Ar-milling method with a liquid nitrogen cooling stage. The TEM foil was analyzed as bright field (BF), dark field (DF) and weak beam-dark field (WBDF) images, combined with energy dispersive X-ray spectroscopy (EDXS) and electron energy-loss spectroscopy (EELS). Determination of Burgers vectors (*b*) of a perfect dislocation in the hexagonal lattice setting was performed using the well known *g.b* invisibility criterion (*g* is the diffraction vector) and thickness contour fringe methods.

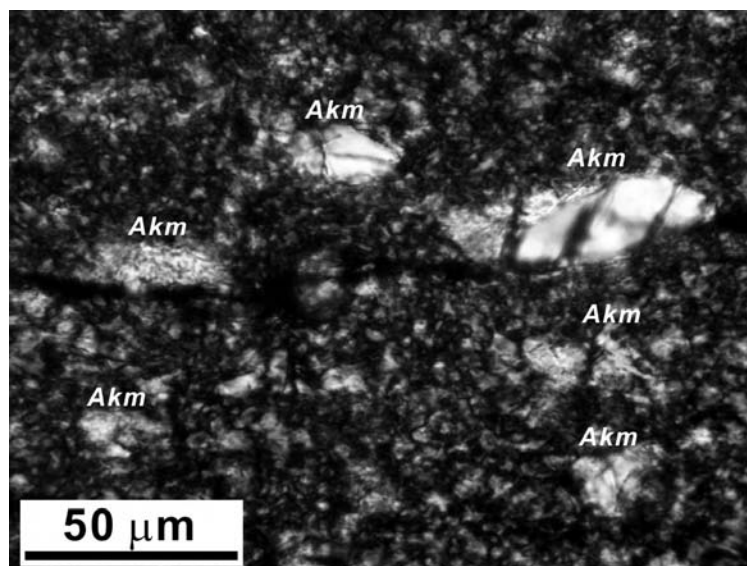


Fig. 3.7-6: Cross-polarized light optical micrograph of the recovered sample of idiomorphic akimotoite (*Akm*) and the matrix of fine grains of akimotoite and silicate perovskite.

The Fe, Al bearing akimotoite displays a bimodal grain-size distribution in a transmitted-light optical micrograph (Fig. 3.7-6). The size of the larger grains is about 50 μm in length and 15

$\mu\text{m}$  in width, while the small grains are less than  $1\ \mu\text{m}$ . The small grains frequently coexist with Fe, Al bearing silicate perovskite. The larger grains contain a high density of dislocations that are often on the basal plane of the hexagonal structure. On the other hand, fine grains of coexisting perovskite display almost no dislocations. In WBDF images of a larger grain of akimotoite (Fig. 3.7-7), straight dislocations elongated along the  $[\bar{2}110]$  axis are clearly visible with a diffraction vector of  $\mathbf{g} = \bar{2}11\bar{6}$ , while almost all dislocations with  $\mathbf{g} = 0003$  are invisible. From this invisibility criterion, the Burgers vector of the dislocations is probably  $\mathbf{b} = 1/3 [11\bar{2}0]$ , corresponding to the most common perfect dislocation for hexagonal closed packed materials. The dislocations could be nucleated due to local thermoelastic stress at high pressure and high temperature. The crystallographic configurations of an array of dislocations and the Burgers vector strongly imply a basal slip system of  $(0001) \langle 11\bar{2}0 \rangle$ , which is consistent with previous results of the end-member  $\text{MgSiO}_3$  akimotoite.

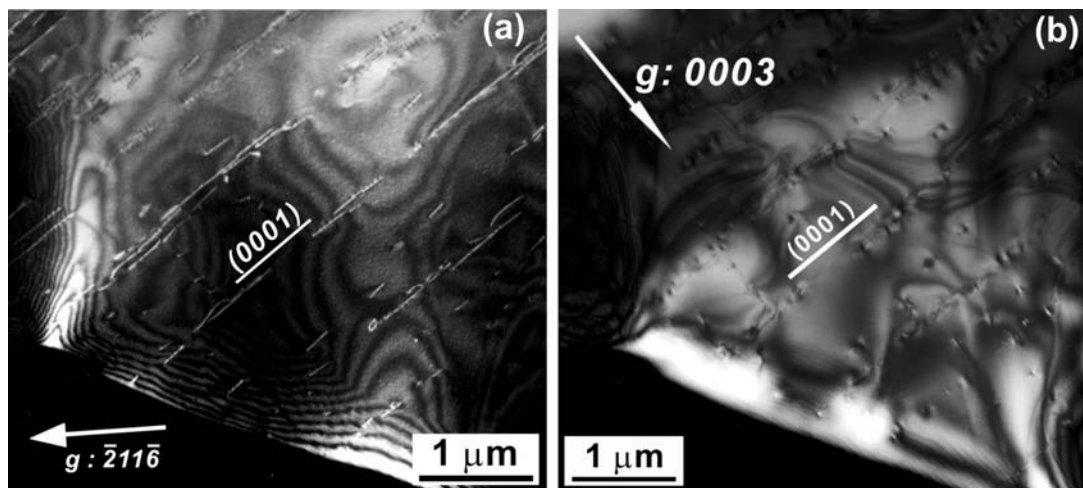


Fig. 3.7-7: Weak-beam dark-field TEM images of an idiomorphic akimotoite. The dislocations along the  $(0001)$  projection are visible with (a)  $\mathbf{g} = \bar{2}11\bar{6}$  and invisible with (b)  $\mathbf{g} = 0003$ , which are consistent with a Burgers vector of  $\mathbf{b} = 1/3 [11\bar{2}0]$ .

**d. Texture development in deformed ordered omphacite: A scanning electron microscopy study (D. Novella, N. Walte, F. Langenhorst and F. Heidelbach)**

The present study deals with the rheological properties of omphacite, which is the major phase in the high-pressure metamorphic rock eclogite. Omphacite is a Na-Al rich clinopyroxene that is stable under high-pressure metamorphic conditions and can be described by the formula  $(\text{Ca},\text{Na})(\text{Mg},\text{Fe}^{2+},\text{Al})\text{Si}_2\text{O}_6$ . This pyroxene occurs in a disordered high-temperature state and in an ordered low-temperature state below approximately  $750\ ^\circ\text{C}$  with the space groups  $C2/c$  and  $P2/n$ , respectively.

The study of omphacite can provide crucial information on the rheology of eclogite. This is due to the fact that most of the strain is accommodated by this mineral resulting in strong

lattice and shape preferred orientations in natural eclogite. Although several experimental studies have investigated the deformation behaviour of omphacite, it is still not completely clear how deformation mechanisms and LPOs in omphacite can be correlated. Additionally, even though eclogites in natural settings were often deformed at moderate temperature, no experimental study was performed so far that investigated deformation and texture formation of ordered omphacite.

For this study natural ordered omphacite samples were deformed to high bulk strain under moderate temperature conditions (approximately 650-750 °C) to remain in the low-temperature omphacite field during deformation. As a starting material we used omphacite grains from an eclogite of the locality Weissenstein, Münchberger Gneiss Massif (Bavaria, Germany); this omphacite is known to be ordered (*i.e.*, the space group is  $P2/n$ ). Five deformation experiments were performed using a D-DIA apparatus at a temperature of 650-750 °C and a confining pressure of 2 GPa (to simulate a depth of approximately 60 km). One deformation experiment was performed in simple shear configuration. In four other experiments omphacite was simply uni-axially compressed. 4 wt.% of water was added to one experiment in order to investigate its effect on the deformation behaviour. Each experiment was performed for approximately 24 hours, until a bulk shortening of about 30 % was achieved.

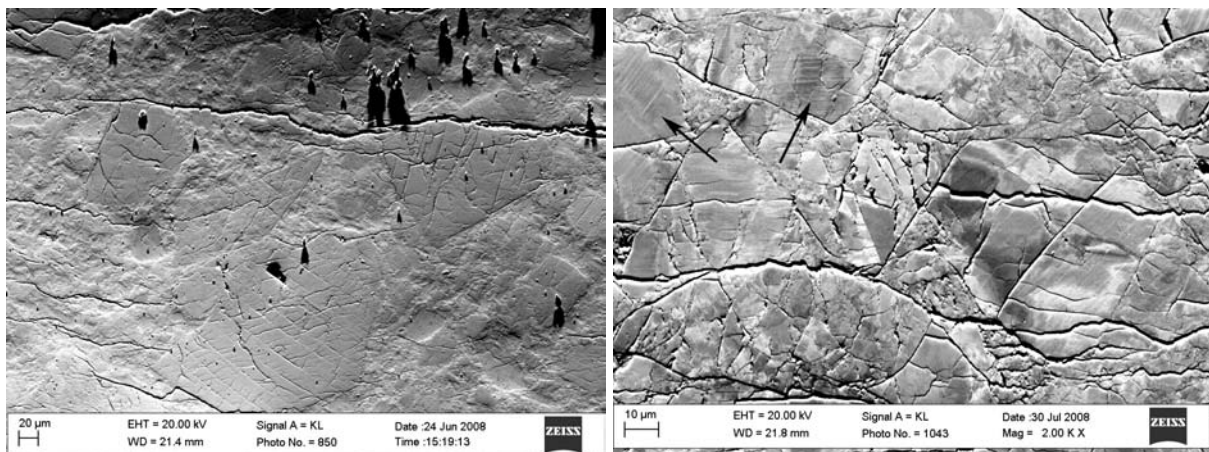


Fig. 3.7-8: SEM-OC images of samples deformed in axial compression (axis vertical); left: dry conditions; large angular omphacite grains with little internal deformation structures; right: wet conditions; large crystals show polysynthetic deformation twinning (arrows), undulose extinction and subgrain formation.

The experimentally deformed samples were analyzed by SEM orientation contrast (OC) and electron back-scattered diffraction (EBSD) technique, in order to investigate the microstructures and to measure the LPOs. OC images show how deformation differs between the dry and wet samples. In the dry experiments, the presence of big angular grains embedded in a fine-grained matrix suggests a possible localization of deformation in the matrix adjacent to the large grains (Fig. 3.7-8, left). In contrast, in the water-bearing experiment we can

observe pervasive deformation microstructures over the entire sample, even within the large grains. In the water bearing sample the omphacite grains are characterized by deformation twinning, crystal lattice bending and, apparently, by areas with sub-grain formation (Fig. 3.7-8, right).

EBSD analysis of the dry experiments result in pole figures that are characterized by irregular maxima (Fig. 3.7-9, left). The lack of a discernable texture can possibly be explained by deformation localization in the fine-grained matrix and passive rotation of the larger omphacite grains, which would prevent the formation of a strong LPO, and which is compatible with the OC images. The pole figures of the water-bearing experiment (Fig. 3-7.9, right) show a clear LPO development. It is possible to recognize a girdle around the  $\langle 001 \rangle$  direction perpendicular to the axes of compression, and an alignment of poles of the  $\{010\}$ ,  $\{110\}$  and  $\{100\}$  planes (weaker in the last case), parallel to the compression axis. Projections corresponding to the  $\langle 110 \rangle$  direction are not well defined. The added water appears to cause a switch in deformation mechanism to pervasive intracrystalline deformation in the sample, although details are currently under study.

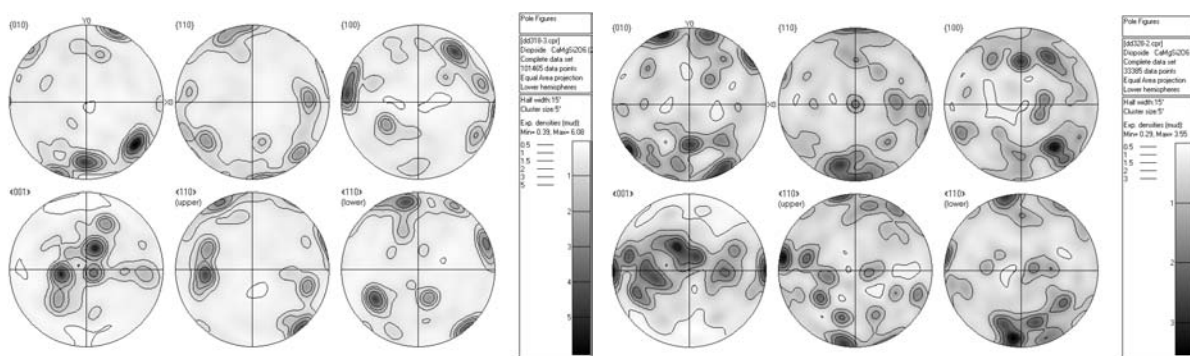


Fig. 3.7-9: Pole figures from EBSD analysis of samples from Figure 3.7-8 (equal area, lower hemisphere projections); left: dry conditions; the texture is dominated by single maxima of large grains; right: wet conditions, a deformation texture is visible of the  $\{010\}$ ,  $\{110\}$  and  $\{100\}$  planes and the  $\langle 001 \rangle$  direction..

In conclusion, the presence of water causes a variation in the textural development: the experiment under dry conditions displays no LPO and those performed under wet conditions display an S-type LPO. This could mean that the presence of water leads to a different behaviour of omphacite under axial compression under p, T, strain rate and grain size conditions of this work.

**e.** *Pressure-induced slip-system transition in polycrystalline olivine (S. Shekhar, N. Walte, D.J. Frost, F. Heidelbach, F. Langenhorst and D.C. Rubie)*

$(\text{Mg,Fe})_2\text{SiO}_4$  olivine is the dominant mineral in the upper mantle to a depth of  $\sim 400$  km. A deformation induced lattice preferred orientation (LPO) of olivine is frequently cited as being

a major cause of seismic anisotropy in these regions. The relative contribution of a particular slip system in the deformation process is dictated by the relative ease of slip under given physical and chemical conditions. Deformation experiments performed at moderate pressure and high-temperature conditions have revealed that olivine deforms by dislocation creep with [100] (Type-A) as the dominant slip direction above ~ 150 km in the upper-mantle. In A-type LPO, the polarization direction of the fast s-wave is parallel to the shear direction, which has been used for many years to interpret the direction of upper mantle flow *e.g.*, at subduction zones. There are also studies that suggest the dominant slip system changes to [001]{hk0} (Type-C) at greater depths. However, some authors have suggested that type-A, type-C and some other LPO types can also be produced at low pressure (~ 2 GPa) by varying either the water content of olivine or the differential stress. On the basis of these results, the pressure induced A-slip to C-slip system change was questioned. Since the interpretations of seismic anisotropy in the mantle depend strongly on the LPO types and on the role of the different parameters in olivine deformation, we performed several simple shear experiments at low water contents to re-examine the role of pressure. Simple-shear experiments imitate more closely the deformation conditions in the Earth than experiments performed with an axial compression configuration and allow for easier identification of the possible Burgers vectors. We have used the deformation-DIA (d-DIA) to perform deformation experiments, which offers the advantage of controlling the differential stress and strain rate.

Sample preparation was done by hot-pressing powdered dry San-Carlos olivine with a grain size 10-20  $\mu\text{m}$  in a piston-cylinder press at 1 GPa and 1200 °C for several hours. Hot-pressing ensured a consistency in the fabric and water content of the starting material. Cores were taken from the hot-pressed samples of the correct diameter and slices at 45° to the horizontal axis were obtained that were approximately 0.2 mm thick. These sections were placed between fully dense  $\text{Al}_2\text{O}_3$  pistons which were placed inside a heater in the cubic pyrophyllite assembly. Crushable and fully dense  $\text{Al}_2\text{O}_3$  cylinders were placed either side of the deformation pistons with hard and soft  $\text{Al}_2\text{O}_3$  distributed evenly but in the correct proportions to minimize deformation during cold compression.

A series of experiments were performed with hot-pressed olivine samples with a view to understand the extent of deformation being experienced by the sample during the individual stages of cold pseudo-hydrostatic compression, heating and deformation. So far, samples recovered at different stages suggest that negligible deformation occurs during the stage of hydrostatic compression and heating. Recovered samples were cut perpendicular to the shear plane and parallel to the shear direction before polishing. Imaging of the microstructures was done by SEM orientation contrast and the LPOs were measured by electron backscatter detection (EBSD). Deformation experiments done at ~ 3 GPa and at 1200 °C and a strain rate close to  $10^{-4} \text{ sec}^{-1}$  showed clear evidence of type-A slip as was expected under these conditions (Fig. 3.7-10).

Using fired pyrophyllite as the pressure cell, we were able to achieve a confining pressure above 7 GPa in the d-DIA. Preliminary experiments performed under these pressures at 1200 °C with a bulk shear strain = ~ 1 and strain rate of the order of  $10^{-4}$  shows evidence of type-C slip (Fig. 3.7-11). Due to the similar strain rate and sample preparation, we assume that the stress level and water content in the experiments performed at these different pressures were comparable. Hence, our preliminary results suggest that this transition from A-slip to C-slip was brought about by a change in pressure, which is in agreement with previous transmission electron microscopy studies of olivine slip systems and establishes surrounding pressure as another factor controlling the slip system in olivine besides water content and stress.

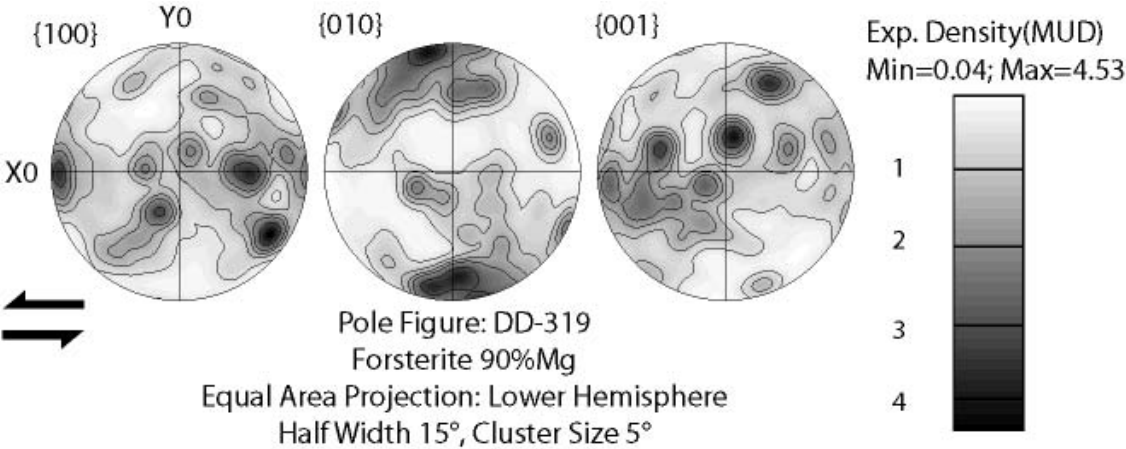


Fig. 3.7-10: Pole figure for recovered sample deformed at ~ 3 GPa and 1200 °C. Sense of shear is sinistral. Alignment of a-axes in the shear direction and b-planes in the shear plane indicates A-slip.

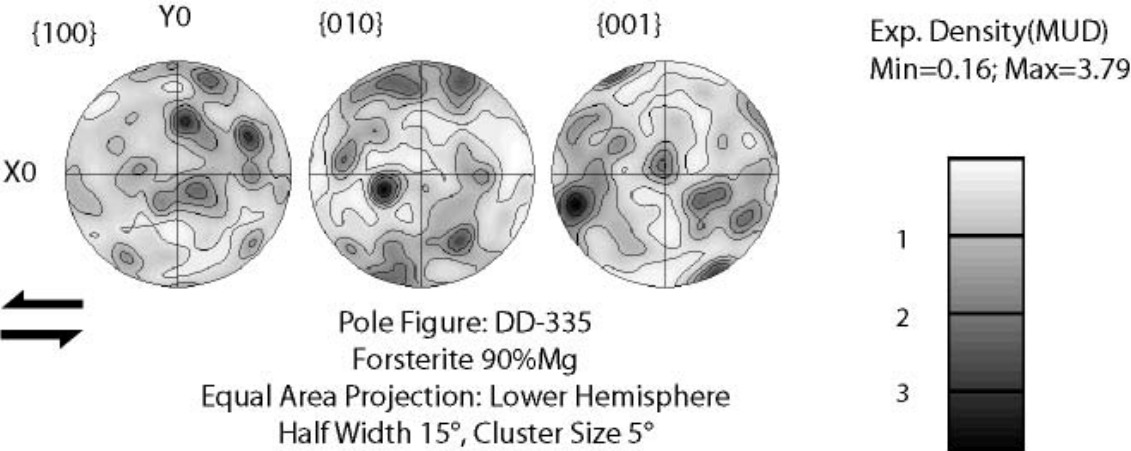


Fig. 3.7-11: Pole figure for recovered sample deformed at pressure above 7 GPa and 1200 °C. Sense of shear is sinistral. Evidence of C-slip can be observed.

**f.** *Pervasive to discrete microstructures in magmatic dense suspensions at HP-HT: Insight from SPO and CPO analysis (D. Picard, L. Arbaret, M. Pichavant and R. Champallier/Orléans; P. Launeau/Nantes and F. Heidelbach)*

Spatial and temporal relationships between structures such as mineral fabrics and shear localised zones are often used to reconstruct the flow history of crystallizing magmas. In particular, during the transition from a liquid-like to a solid-like behaviour expected within the  $40\% < \Phi < 80\%$  crystal fraction range, the change from pervasive to discrete structures and the potential influence of this change on the bulk rheological behaviour of the magma remain poorly explored. In order to constrain the evolution of the structures in this fraction range, we performed HP-HT torsion experiments at 300 MPa and 800 °C using a Paterson apparatus on synthetic plagioclase bearing suspensions. 2 series of experiments containing 52 % and 58 % of plagioclases have been realised. The shape preferred orientation (SPO) of the plagioclases was determined on [XZ] thin section using the intercept method. These 2D SPO results are compared with the crystallographic preferred orientation (CPO) acquired by using the electron back-scattered diffraction (EBSD) technique.

The sample containing 52 % of crystals was submitted to a dextral shear with a maximum finite strain of  $\gamma=1.4$ . A shape fabric oriented at 43° anticlockwise with respect to the shear plane is evidenced over the section analysed (Fig. 3.7-12, domain a). This pervasive fabric is crosscut by a dextral shear zone oriented at ~ 20° clockwise. The dextral sense of shear is marked by the progressive change of plagioclase orientation that forms the gradient zones bordering the shear zone. In this 40  $\mu\text{m}$  thick shear zone, crystals are homogeneously oriented closely parallel to the shear direction (Fig. 3.7-12, domain b). Size and aspect ratio distributions of the plagioclase crystals are similar in both orientation domains.

The CPO of the plagioclases in the pervasive fabric (Fig. 3.7-12, right) shows a maximum concentration of {010} poles at ~ 45° anticlockwise with respect to the shear plane and girdles of {001} and {100} at ~ 50°/60° clockwise with respect to the shear plane. In the shear zone (Fig. 3.7-12b), plagioclases {010} poles are oriented perpendicular to the shear plane and {001} and {100} poles shows a girdle parallel to the shear plane, defining a plano-linear crystallographic fabric.

The sample containing 58 % of crystals were submitted to a dextral shear with a maximum finite strain of  $\gamma=1.4$ . The bulk shape fabric is weak with a maxima oriented perpendicular to the shear plane (Fig. 3.7-13, domain a). This pervasive fabric corresponds to the preserved initial fabric developed during the synthesis of the sample before the deformation experiments. This shape fabric is crosscut by dextral shear zones oriented at ~ 10° clockwise with respect to the shear direction. In the shear zones, crystals are homogeneously oriented closely parallel to the shear direction (Fig. 3.7-13, domain b). All crystals are characterised by a strong reduction in size and aspect ratios compared to those preserved in the first domain. The transition between the two orientation domains is rapid without any development of gradient zones.

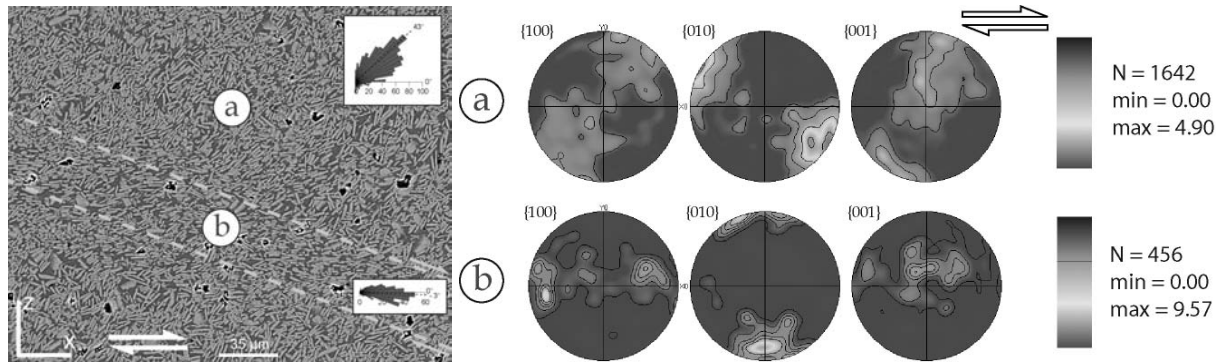


Fig. 3.7-12, left: SEM image of a deformed sample containing 52 % of crystal fraction. Plagioclases are in bright grey, glass in dark grey and bubbles in dark. The shear zone is delimited by the yellow dashed lines. Inset diagrams: SPO obtained using the intercept method in both domains; right: Pole figures of plagioclase main crystallographic axes in the pervasive fabric (a) and in the shear zone (b).

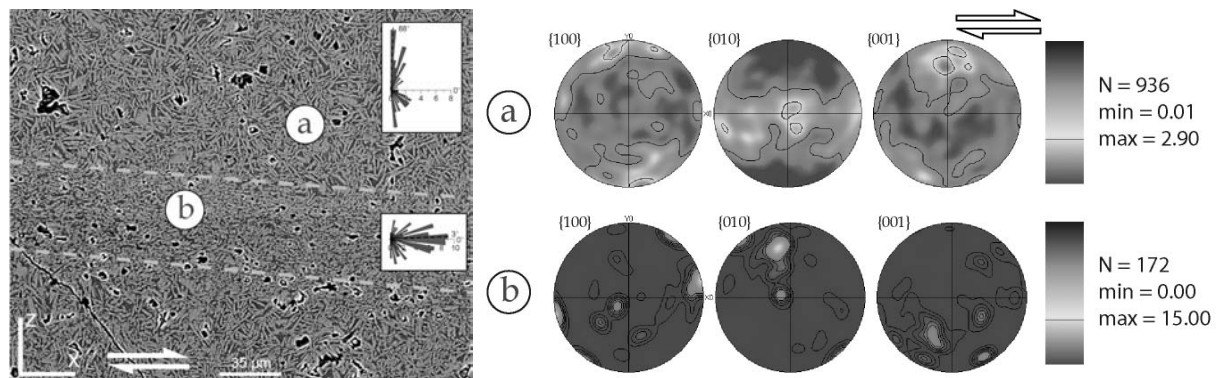


Fig. 3.7-13, left: SEM image of a 58 % deformed sample. Plagioclases are in bright grey, glass in dark grey and bubbles in dark. The shear zone is delimited by the dashed lines. Inset diagrams: SPO obtained using the intercept method; right: Pole figures of plagioclase main crystallographic axes in the undeformed fabric (a) and in the shear zone (b).

The CPO of the plagioclases in the bulk fabric (Fig. 3.7-13, domain a) shows a girdle of  $\{010\}$  poles in the shear plane and  $\{001\}$  and  $\{100\}$  oriented perpendicular to the shear plane. In the shear zone (Fig. 3.7-13, domain b), plagioclases  $\{010\}$  poles are oriented perpendicular to the shear plane and  $\{001\}$  and  $\{100\}$  poles shows a girdle in the shear plane.

The SPO and CPO of the plagioclase phase acquired in the two concentrated suspensions of plagioclase during torsion experiments point to an obvious change in structures. At 52 %, the deformation is accommodated by the development of pervasive compressive fabrics locally crosscut by rare normal synthetic, therefore extensive, shear zones. By opposite, at 58 %, the shear deformation is fully concentrated in localised planar domains, parallel to the shear plane. Because of the strain localisation, the observed strong grain size and aspect ratio reductions

may originate in the high strains and strain rates reached in these domains. The shear strain quantification in the different recognised fabric domains and the link between these fabrics and the rheological behaviour of both suspensions are in progress.

### 3.8 Metamorphism

During geological processes rocks experience changing temperature (T) and pressure (P) conditions. The rock masses and their constituents, the minerals, undergo a process of solid-state transformation that is called metamorphism. Investigation of the mineral assemblage of a metamorphic rock often allows deciphering the temperature and pressure history of the rocks, and hence provides information about geological processes that are not directly observable in nature. The key to gain quantitative information are geothermometers and barometers, minerals or mineral-assemblages whose chemical composition can be linked to precise points on a P-T path. One of the most robust thermometers is the composition of intergrown orthoclase and plagioclase feldspar that form by an exsolution of a former high-temperature feldspar. A combined experimental and computational study is presented that provides a better and more consistent calibration of this widely-used thermometer. Another recently adopted system for thermobarometry in high-grade rocks is the stability and trace element content of different TiO<sub>2</sub> modifications. An investigation of TiO<sub>2</sub> rutile inclusions in garnet from the German Erzgebirge is presented that aims to better understand that system.

Earthquakes can locally melt rocks by frictional heating along fault surfaces and form glass-rich pseudotachylites. The quickly cooling melts crystallize in a metamorphic assembly that reflects the P-T conditions of the host rock. The third contribution takes a detailed look at omphacite crystallized in an eclogite facies pseudotachylite. Surprisingly, TEM investigation of this pyroxene revealed a dislocation microstructure that is commonly associated with long-term deformation. If stresses during omphacite crystallization prove to be sufficient to cause these microstructures, a reassessment of previous TEM investigations on omphacite may become necessary.

The following contributions centre on intense short-term heating and compaction of rocks as the result of meteorite impacts. A detailed history of fractional crystallization of wadsleyite and ringwoodite is presented from shock-melt veins in a natural chondrite meteorite. In some cases unknown high-pressure mineral phases can be found in shocked meteorites. A new ultra-hard carbon modification is described here that may be interesting for applications in the material sciences. Release of greenhouse gases from carbonate rocks was suggested to contribute to climate changes after large impacts. In the final contribution a natural dolomite sample undergoes experimental shock metamorphism to investigate a resulting CO<sub>2</sub> loss. However, under the experimental condition the dolomite proved to be robust and did not release CO<sub>2</sub>.

#### **a.** *Ternary feldspar equilibria and thermodynamic modeling at the granulite-eclogite facies transition (D. Dolejš)*

The transition from eclogite to granulite facies during exhumation of high-pressure mafic rocks is characterized by the appearance of feldspar. In natural multicomponent systems the

formation of feldspar occurs between grossular + kyanite + quartz = anorthite and clinopyroxene + quartz = albite equilibria but the exact location is a function of activity-composition relationships in the K-Na-Ca (ternary) feldspars. In high-grade metamorphic rocks, re-integrated composition of feldspars, which have undergone subsequent exsolution, is a common but frequently the only tool for estimating peak metamorphic temperatures, because conventional exchange thermometers re-equilibrate by diffusion at lower temperatures. From these view points, the knowledge of thermodynamic mixing relationships in ternary feldspars at high temperatures and pressures is desirable.

Previous experimental studies defined solvus equilibria for ternary feldspars up to 900 °C and 0.2 GPa and up to 600 °C and 1.5 GPa, and were used in calibrating several thermodynamic models. Figure 3.8-1 illustrates that the current thermodynamic models are approximately consistent at 900 °C but grossly discrepant at 1100 °C and 2 GPa. The differences in solvi calculated using different models are as high as 10-15 mol.% at 900 °C and reach 50 mol.% at 1100 °C. Importantly, re-integrated ternary feldspar compositions reported in the literature span a wide composition space inside or outside of the solvus, hence use of different mixing models may lead to estimates of temperature which are erroneous by more than 200 °C.

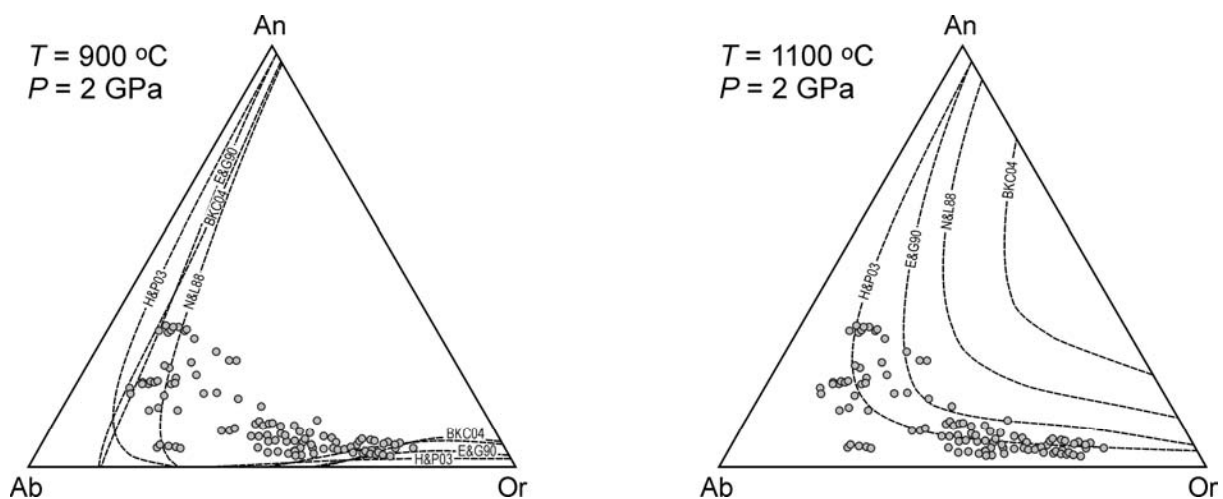


Fig. 3.8-1: Compilation of models at 2 GPa. Abbreviations for thermodynamic models: BKC04 – Benisek *et al.* (2004), E&G90 – Elkins and Grove (1990), H&P03 – Holland and Powell (2003), and N&L88 – Nekvasil & Lindsley (1988). Gray symbols represent re-integrated compositions of ternary feldspars from natural granulites.

New experiments were performed at 900-1100 °C and 2 GPa in order to define ternary feldspar solvus and to derive a new thermodynamic model. Experiments used two starting compositions: (1) synthetic glass  $Or_{35}Ab_{46}An_{20}$ , seeded with 3 wt.% K-feldspar and 3 wt.% plagioclase, and (2) natural felsic granulite powder (Miškovice, Czech Republic). All runs were performed with 0.9-2.4 wt.%  $H_2O$  leading to the presence of partial melt, which facilitated attainment of equilibrium, in addition to two coexisting feldspars. Additional dry,  $H_2O$ -poor or seedless experiments approached an incomplete equilibrium. All experiments

were carried out in a piston-cylinder apparatus, which was previously calibrated by the albite-quartz-jadeite equilibrium, and analyzed by electron microprobe. Run products using synthetic glasses with seeds and H<sub>2</sub>O produced a three-phase assemblage of K-feldspar, plagioclase and partial melt (Fig. 3.8-2a). The experiments with natural granulite preserve large amounts of relict grains and slowly approach equilibrium composition of feldspars, hence provide half-brackets (Fig. 3.8-2b).

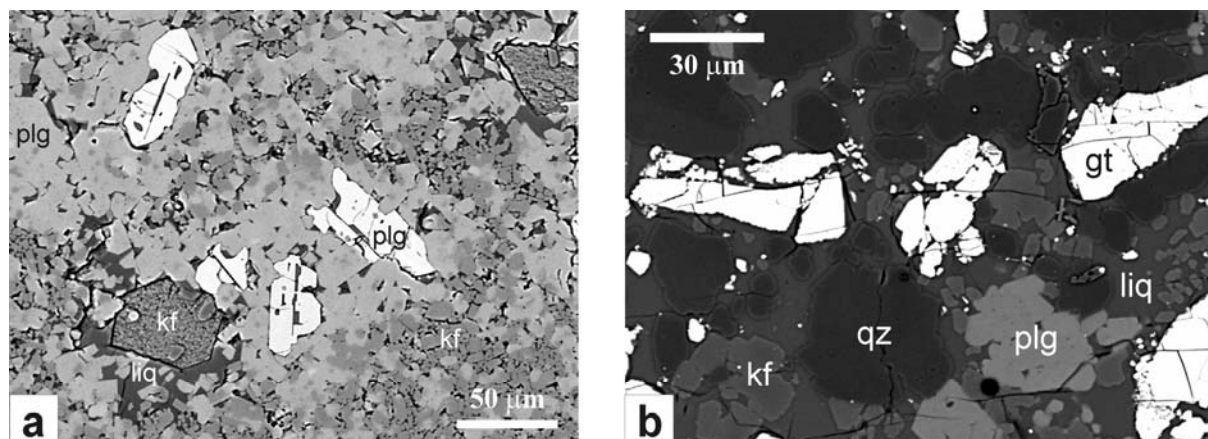


Fig. 3.8-2: Backscattered electron photomicrographs of experimental run products: (a) synthetic glass Or<sub>35</sub>Ab<sub>46</sub>An<sub>20</sub> with K-feldspar (kf) and plagioclase (plg) seeds and 0.90 wt.% H<sub>2</sub>O produces a three-phase assemblage of K-feldspar, plagioclase and hydrous feldspathic liquid (liq) at 1000 °C and 2 GPa; (b) natural granulite with 1.55 wt.% H<sub>2</sub>O produces hydrous granitic melt (liq) in equilibrium with recrystallized quartz (qz), K-feldspar and plagioclase and residual garnet (gt) at 900 °C and 2 GPa.

Experimental results are summarized in Fig. 3.8-3. None of the existing thermodynamic models describes experimental data satisfactorily and deviations between experimental and computed solvus topologies reach 25 mol.%. The distribution of experimental isotherms at 900, 1000 and 1100 °C is, however, better reproduced by the asymmetric van Laar model than by the asymmetric Margules formalism with ternary terms. The thermodynamic model of Holland and Powell (2003, *Contrib. Mineral. Petrol.* 145, 492-501) was, therefore, recalibrated using the new experimental data. The location of the experimental data within the ternary space strongly depends on the interaction term between KAlSi<sub>3</sub>O<sub>8</sub> and CaAl<sub>2</sub>Si<sub>2</sub>O<sub>8</sub> and its temperature dependence, whereas other binaries have much smaller influence. The interaction parameter was adjusted as follows:

$$W_{or-an} \text{ (J)} = 75450 - 32.75 T \text{ (K)},$$

based on current experimental results, high-temperature calorimetry of solid solutions and liquidus equilibria in the KAlSi<sub>3</sub>O<sub>8</sub>-CaAl<sub>2</sub>Si<sub>2</sub>O<sub>8</sub> binary. As shown in Fig. 3.8-3, the new calibration provides very good fit to the new experimental data.

The existence of positive excess entropy of mixing is also typical for the  $\text{KAlSi}_3\text{O}_8$ - $\text{NaAlSi}_3\text{O}_8$  binary. It probably accounts for progressive disordering on tetrahedral sites at high temperatures, which is not included in configurational entropy for simple molecular mixing with short-range order. Current experimental results provide new, experimentally based framework for geothermometry of high-temperature granulites and allow for more critical interpretation of preservation of compositional information in natural ternary feldspars and its microstructural and rheological consequences.

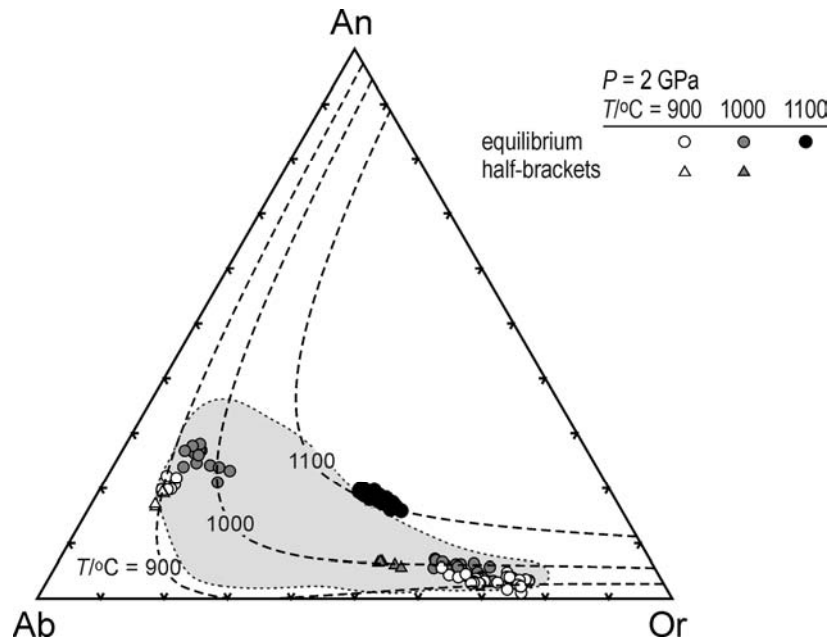


Fig. 3.8-3: Composition of coexisting feldspars in experimental run products at 2 GPa. Gray field outlines compositions of re-integrated feldspars from natural granulites. Dashed curves are solvus isotherms calculated with the new thermodynamic calibration.

**b. Microstructural and chemical characteristics of rutile in UHP metamorphic rocks (A. Escudero, N. Miyajima and F. Langenhorst)**

A high-pressure polymorph of  $\text{TiO}_2$ , without name up to now and with the  $\alpha$  -  $\text{PbO}_2$  structure, has been reported to be a potential geobarometer and an indicator of ultra-high pressure metamorphism. In the case of diamondiferous gneisses of the Saxonian Erzgebirge, Germany, the presence of  $\alpha$  -  $\text{PbO}_2$  structured  $\text{TiO}_2$  has been taken as evidence of a pressure of approximately 5 GPa and former depths of at least 130 km. However, the use of  $\text{TiO}_2$  as a geobarometer requires the clarification of some aspects, such as the P-T stability fields of its polymorphs and the influence of trace elements (*i.e.*, H, Si, Fe, Nb, Zr or Hf) on the phase boundaries.

This study on natural rutile grains from diamondiferous gneisses of the Erzgebirge focuses on:

1. Determining the trace element content in  $\text{TiO}_2$  grains to better constrain the pressure – temperature conditions using a new geothermobarometer based on the Zr content in rutile.
2. Characterizing the defect microstructure to gain insights into the deformation conditions and possible phase transformations under deep subduction zone conditions.

Rutile grains have been studied by optical microscopy, Raman spectroscopy, scanning electron microscopy with energy-dispersive X-ray microanalysis, electron microprobe analysis (EMPA) and transmission electron microscopy. Rutile grains have been observed as inclusions in garnet, with coexisting diamonds, and as isolated grains in the rock matrix. The presence of diamonds indicates former pressures of at least 3.5 - 4 GPa, depending on the temperature. The SEM images of a rutile grain in garnet presented in Fig. 3.8-4 show lamellae in well-defined and parallel planes. The EDX spectrum of the rutile grain reveals the presence of at least three trace elements: Fe, Al and Nb. The bright lamellae are richer in Fe, suggesting that they are either ilmenite or ulvöspinel.

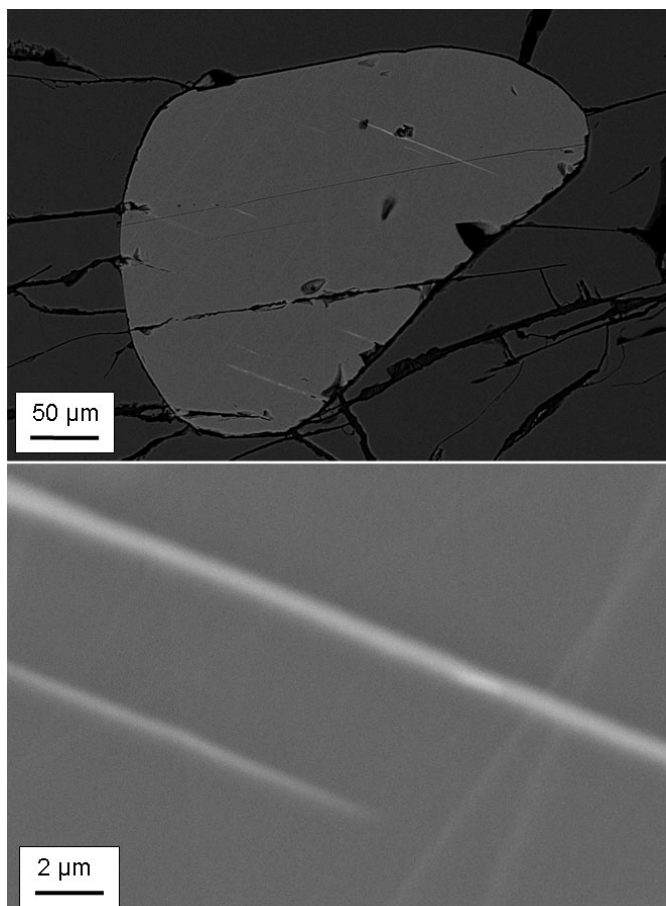


Fig. 3.8-4: SEM images of a rutile inclusion in garnet

The EMPA analysis shows that among the common trace elements in rutile, Fe and Nb are the most abundant, followed by Zr and Al, while Cr, Ca and Ta are present in very low quantities.

Moreover, it is known that the solubility of Zr in rutile has a primary temperature dependence and a secondary pressure dependence. The measured average concentrations of Zr in rutile were determined to be around 1400-1450 ppm. By using the zirconium in rutile thermometer of Tomkins (*J. Met. Geol.*, **2007**) and considering the presence of coexisting diamonds a metamorphic peak of at least 920°C and 3.95 GPa was estimated.

Ilmenite lamellae in an isolated rutile grain in the matrix have been observed by TEM and EDX. The HRTEM image presented in Fig. 3.8-5 shows that the interface between rutile and ilmenite is parallel to the  $(010)_{\text{Rt}}$  and  $(11\bar{2}0)_{\text{ilm}}$  planes. The crystallographic relationship between both phases has been determined from the electron diffraction pattern to be:  $[001]_{\text{Rt}} \parallel [1\bar{1}00]_{\text{ilm}}$  and  $[100]_{\text{Rt}} \parallel [0001]_{\text{ilm}}$ . Dislocations arranged in arrays have also been observed, indicating deformation followed by recovery at high temperature. We could not confirm the existence of  $\alpha - \text{PbO}_2$  structured  $\text{TiO}_2$  in the investigated sample.

In summary, based on the presence of coexisting diamond and rutile inclusions in garnet, the Zr solubility in rutile and the absence of the  $\alpha - \text{PbO}_2$  structured  $\text{TiO}_2$  phase, it can only be assured a minimum metamorphic peak for the diamondiferous gneisses of the Saxonian Erzgebirge of 920°C and 3.95 GPa, that corresponds to a depth of about 110 km.

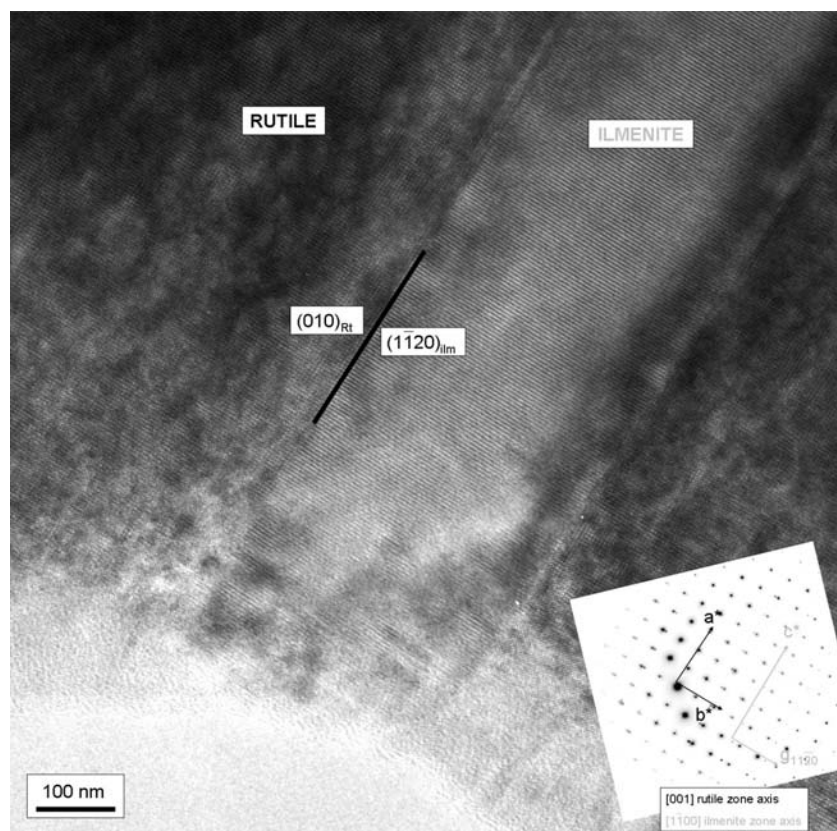


Fig. 3.8-5: HRTEM image and SAED pattern of an exsolved ilmenite lamella in a rutile grain.

*c. Textural and microstructural analysis of rapidly grown omphacite from eclogite facies pseudotachylytes (K. Pollok, F. Heidelbach and F. Langenhorst, in collaboration with T. John/Oslo)*

Eclogite facies pseudotachylytes are commonly interpreted as the petrological witness of paleo-earthquakes in the deeper crust. Faulting by frictional melting results in the formation of shear zones, which have been frequently observed to act as pathways of fluids into metastably preserved dry rocks like gabbros or granulites. This facilitates the conversion to eclogite. The present study addresses the microtextural and microstructural record of spherulitic omphacite from a pseudotachylyte of central Zambian eclogite.

Individual crystals of omphacite show a grain size of 2-3  $\mu\text{m}$ , which are typically arranged in form of spherulitic aggregates of  $\sim 150 \mu\text{m}$  in diameter (Fig. 3.8-6). A quantitative analysis of crystal orientations using EBSD yielded a common crystallographic axis for omphacites within a spherulite. Furthermore, statistics on the distribution of orientations resulted in (1) a random orientation distribution for non-neighbouring (uncorrelated) grains and (2) three distinct maxima of misorientations for neighbouring (correlated) grains (Fig. 3.8-6). The maximum at low misorientation ( $< 5^\circ$ ) is indicative for low-angle boundaries (e.g., subgrain boundaries), whereas the maxima between  $15^\circ$  and  $40^\circ$  as well as between  $140^\circ$  and  $165^\circ$  display high-angle grain boundaries formed during rapid growth of the spherulite.

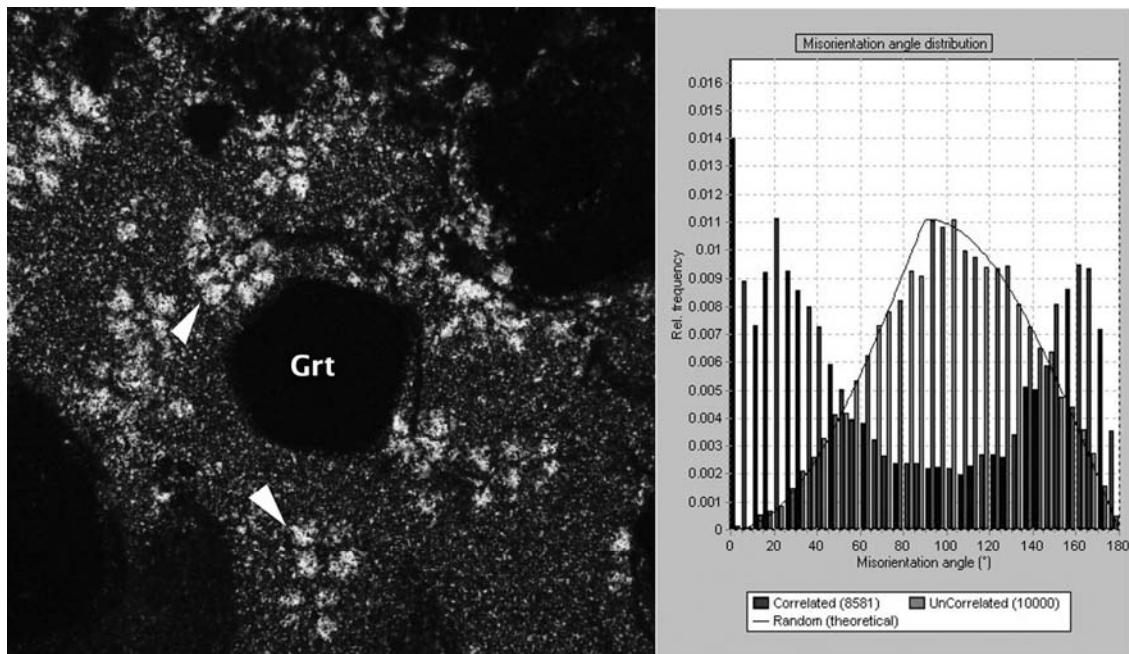


Fig. 3.8-6: Transmitted-light photomicrograph under crossed polars of garnet (grt) and fine grained omphacite. Spherulites (arrows) consist of radially oriented omphacites and show a characteristic extinction cross (left). Misorientation angle distribution of omphacite crystals in spherulites determined by EBSD. Neighbouring crystals show distinctive misorientations which are non-random (right).

Microstructural observations of omphacite grains within a spherulite have been made using transmission electron microscopy (TEM). A high dislocation density of  $10^{14} \text{ m}^{-2}$  with a heterogeneous distribution as free dislocations (dominantly  $\mathbf{b} = [001]$ ), dislocation networks and subgrain boundaries have been found (Fig. 3.8-7). High angle grain boundaries with  $120^\circ$  triple junction as well as wavy grain boundaries have been observed. Recrystallization led to the growth of small, dislocation-free grains as a result of partial healing. Other deformation microstructure include chain multiplicity faults (CMFs) with a displacement vector  $\mathbf{R} = 1/2[011]$  (Fig. 3.8-7) and deformation twin lamellae on (100). The CMFs represent an intercalation of double chains parallel  $b$  into single chain pyroxene which terminate at partial dislocations or grain boundaries. In addition to deformation microstructures, anti phase domains (APDs) are present in all grains studied. These domains arise from a phase transition  $C2/c \rightarrow P2/n$  due to diffusion controlled ordering of octahedral cations; they are characterized by a displacement vector of  $1/2[110]$ . The APDs are considerably larger ( $\sim 150 \text{ nm}$ ) in the middle of an omphacite grain and become gradually smaller towards the grain boundaries (down to less than  $20 \text{ nm}$ ).

The spherulitic microtexture is generally accepted to be formed by fast crystallization from a melt or glass after frictional melting without subsequent plastic deformation. In contrast, all microstructures (except the APDs) clearly indicate plastic deformation with partial (static?) recovery. These contradicting results might be explained by high differential stresses during mineral growth. However, this would in turn question the significance of dislocation densities and grain size as stress markers for minerals grown from frictional melts. In addition, omphacite microstructures may not only be dependent on cooling history and plastic deformation, but could also be influenced by the mineral growth rate in the presence of fluids under ultra-high pressure conditions.

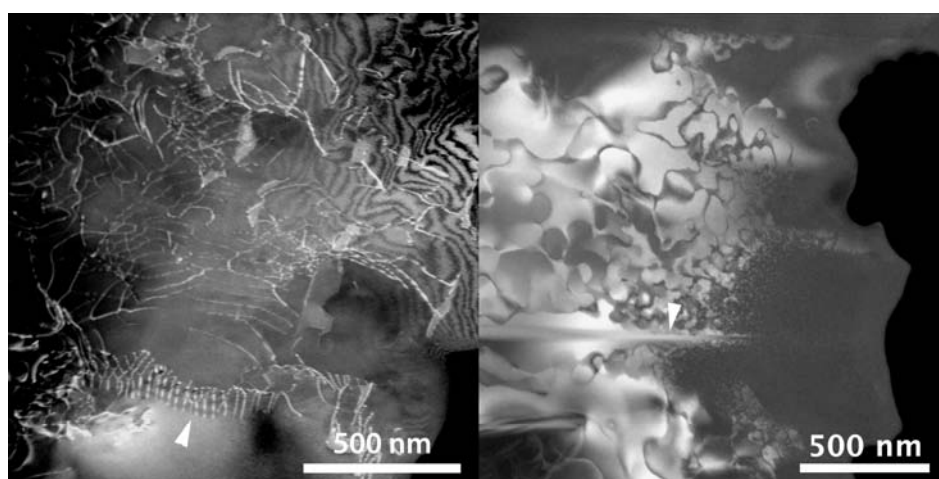


Fig. 3.8-7: Weak beam dark field TEM micrograph of dislocation networks and subgrain boundaries (arrow) in spherulitic omphacite. The microstructure suggest a high degree of plastic deformation with partial recovery (left). Dark field TEM micrograph showing chain multiplicity faults (arrow) and antiphase domains imaged using a  $h + k \neq 2n$  reflection. The antiphase domains have been formed at temperatures lower than  $650^\circ \text{C}$  by diffusion controlled ordering of cations (right).

**d. Fractional crystallization of olivine melt inclusions in a shock-induced chondritic melt vein (M. Miyahara/Sendai, A. El Goresy; E. Ohtani, S. Ozawa, T. Nagase and M. Nishijima/Sendai)**

The high-pressure polymorphs of olivine, wadsleyite and ringwoodite are the major phases in the Earth's lower mantle and transition zone. Wadsleyite and ringwoodite were also identified in shock-melt veins in ordinary chondrites. Their fabric and compositions may mimic the conditions in the Earth's interior. Formation mechanisms of shock-induced wadsleyite and ringwoodite in meteorites were investigated to constrain the magnitude of the equilibrium pressure and the time scale of the dynamic events. Previous studies discussed possibilities of the formation mechanisms, however some suggestions required durations up to 50 seconds that are unrealistically long. Recently, unique wadsleyite-ringwoodite (wadsleyite-ringwoodite) assemblages were reported in a chondrule entrained in a shock-melt vein of Peace River L6 chondrite. Surprisingly, the wadsleyite-ringwoodite crystallites interface denoted a compositional gap of < 32 mol.% fayalite without evidence for Mg-Fe interdiffusion between the crystallites. The assemblage was convincingly interpreted to have formed by fractional crystallization from olivine melts (Fa<sub>24-26</sub>) generated by the shock event.

For this study shock-melt veins in the L6 chondrites Allan Hills 78003 and Yamato 74445 were investigated. A polycrystalline ringwoodite-bearing fragment with a Mg-rich wadsleyite rim was identified in the shock-melt veins of Allan Hills 78003. Laser micro-Raman spectroscopy indicated that both wadsleyite and ringwoodite also coexisted in a similar polycrystalline ringwoodite-bearing fragment with a similar setting enclosed in the shock-melt vein of Yamato 74445. Two different settings of wadsleyite-ringwoodite assemblages were encountered; one appears to be similar to those recently reported in Peace River L6 chondrite by Miyahara *et al.* (PNAS, 2008), the other was observed for the first time during the present investigations.

The major mineral constituents of Allan Hills 78003 and Yamato 74445 in the less shocked chondritic matrix between the shock melt veins are unzoned olivine (Fa<sub>24-26</sub>), low-Ca pyroxene (Fs<sub>21-22</sub>), plagioclase feldspar (Ab<sub>83-87</sub>), troilite and metallic Fe-Ni. Shock-melt veins in both chondrites contain wadsleyite, ringwoodite, majorite, jadeite (+ amorphous SiO<sub>2</sub>) and majorite-pyrop<sub>ss</sub> in diverse settings. Lingunite and tuite (the latter a high-pressure polymorph of whitlockite) were also identified in the shock-melt veins of Yamato 74445. Many troilite and metallic Fe-Ni blebs with eutectic-like intergrowth are also present.

Ubiquitous wadsleyite-ringwoodite assemblages replaced original olivine in the shock-melt veins of both chondrites. These assemblages can be classified into two types: Type-1 wadsleyite-ringwoodite in a deformed porphyritic chondrule in a shock-melt vein and Type-2 isolated and heterogeneous wadsleyite-ringwoodite assemblage in an olivine fragment. The original olivine, now replaced by the wadsleyite-ringwoodite pair type-1 shows a complex disaggregated texture. Electron microprobe (EMPA) analyses indicate that the wadsleyite-dominated portion is slightly enriched in Mg (Fa<sub>22-26</sub>), whereas the ringwoodite-dominated portion is rich in Fe (Fa<sub>27-29</sub>). This compositional gap casts doubt of formation by a solid-state

phase transition. The original olivine monocrystal fragment of type-2 was replaced by the wadsleyite-ringwoodite pair. The wadsleyite-ringwoodite assemblage-bearing fragment is now oblong in shape as a result of flattening and plastic deformation. Fragments depicting Type-2 assemblage have a disaggregated wadsleyite-ringwoodite interior and are surrounded by continuous polycrystalline wadsleyite rims of  $< 4 \mu\text{m}$  in thickness. EMPA analyses revealed that compositions of the wadsleyite-dominated and the ringwoodite-dominated parts are  $\text{Fa}_{11-22}$  and  $\text{Fa}_{27-35}$ , respectively. The adjacent Ca-poor pyroxene  $[(\text{Mg}_{3.06}\text{Fe}_{0.82}\text{Al}_{0.01}>\text{Ca}_{0.06})\text{Si}_{4.00}\text{O}_{12}]$  grains show no sign of melting but some converted by solid-state to majorite  $[(\text{Mg}_{3.08}\text{Fe}_{0.86}\text{Al}_{0.02}\text{Ca}_{0.06})\text{Si}_{3.98}\text{O}_{12}]$  of the same composition.

Type-2 wadsleyite-ringwoodite assemblage was subsequently investigated by using a surgical FIB-TEM technique (Fig. 3.8-8a-c). We extracted two FIB slices (SP1FIB1 and SP1FIB2) from the assemblage. Both FIB slices also encompass the wadsleyite-rims. These rims consist of unfragmented polycrystalline idiomorphic wadsleyite crystallites with a sharp boundary to the following layer of wadsleyite + majorite-pyropes<sub>ss</sub> (Fig. 3.8-8a).

These crystallites depict preferred orientations. Poorly-crystallized material with chondritic- or  $(\text{Mg,Fe})_2\text{SiO}_4$ -like compositions, respectively wet these crystallites thus evidencing their crystallization from melt (Fig. 3.8-8b and 3.8-9). Some wadsleyite and ringwoodite in the interior of the enclave show granoblastic-like texture of anhedral crystallites. The compositions of the coexisting individual wadsleyite and ringwoodite grains are  $\text{Fa}_{7-10}$  and  $\text{Fa}_{28-33}$ , respectively with a compositional gap of  $< 26 \text{ mol.}\%$  fayalite. In a few places poorly crystallized material occurs as veneers wetting some of the anhedral wadsleyite and ringwoodite crystallites. The matrix of the shock-melt veins consists mainly of round majorite-pyropes<sub>ss</sub> crystallites (Fig. 3.8-8c). Troilite, iron-nickel oxides and poorly crystallized material surrounds some of the the majorite-pyropes<sub>ss</sub> crystals. The poorly crystallized material in the matrix of the shock-melt vein consists of fine-grained multiphase grains and glass that is enriched in Fe compared with those in the wadsleyite-rim (Fig. 3.8-8c).

Some wadsleyite crystals in the olivine melt enclave are surrounded by or engulfed by anhedral ringwoodite, indicating that ringwoodite crystallized subsequent to wadsleyite. Only the isolated Wadsleyite-Ringwoodite assemblages replacing the original olivine monocrystal are covered by polycrystalline wadsleyite layers (Fig. 3.8-8a-b). These layers consist of idiomorphic virgin wadsleyite crystals depicting preferred orientations. The texture of the wadsleyite-ringwoodite assemblage in the cores of the enclaves is suggestive of fragmentation and subsequent reassembly. Their fragmentation and reassembly must have taken place prior to crystallization of the idiomorphic polycrystalline wadsleyite layers (wadsleyite veneer); otherwise none of the latter would have survived without fragmentation. Xenomorphic majorite-pyropes<sub>ss</sub> crystallites interlocked with anhedral wadsleyite crystallites in the layer between the wadsleyite veneer and the chondritic melt show scalloped outlines (Fig. 3.8-9). The scalloped feature may have resulted from incipient melting either due to migration of the fragment in a hotter region of the vein or due commencing decompression. They cannot have emerged from olivine melts alone but from a mixture of olivine melt and chondritic liquid as evidenced from the composition of majorite-pyropes<sub>ss</sub>  $[(\text{Mg}_{3.18}\text{Fe}_{0.48}\text{Al}_{0.48}\text{Ca}_{0.14})\text{Si}_{3.74}\text{O}_{12}]$ .

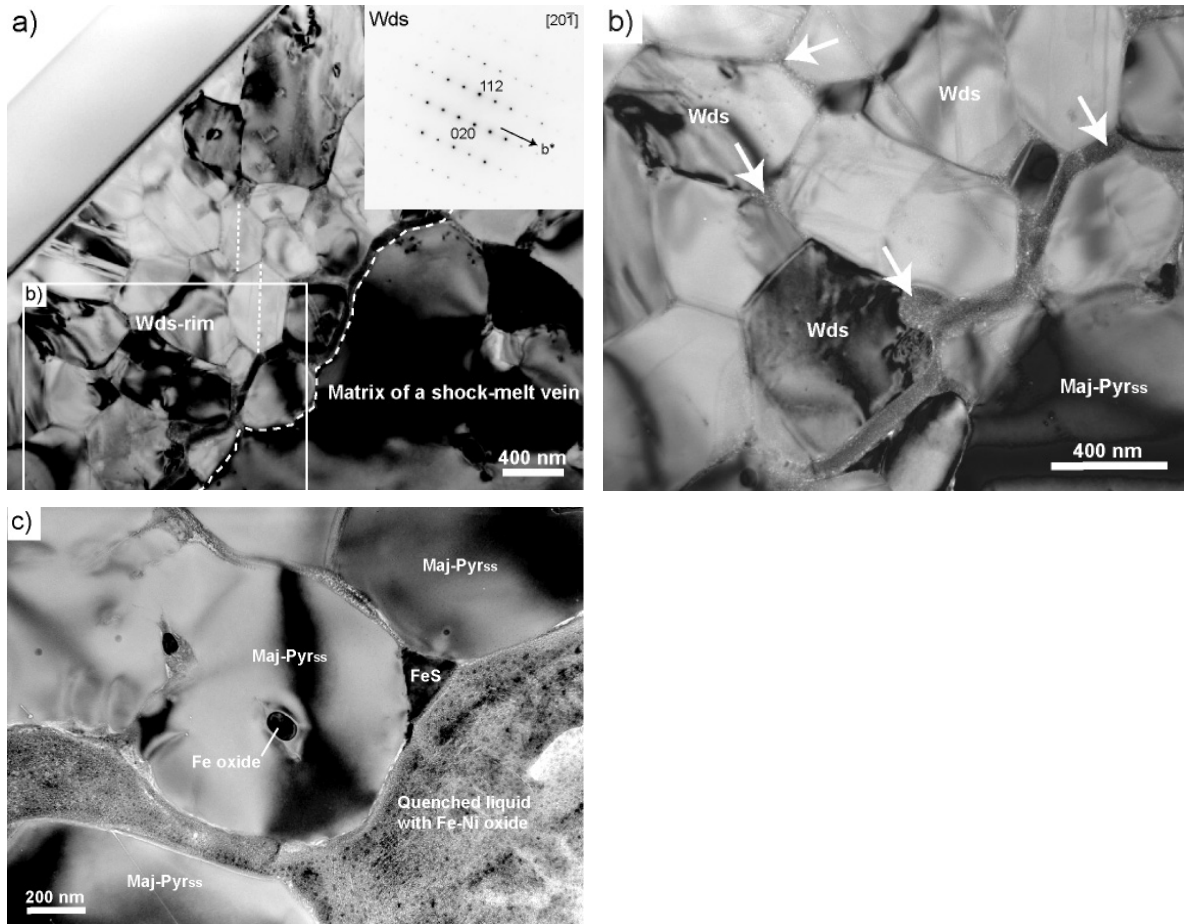


Fig. 3.8-8: TEM images of SP1FIB2 slice in Allan Hills 78003. a) Boundary between wadsleyite-rim and matrix of the shock-melt vein. Dashed white line depicts the sharp boundary between the wadsleyite rim and the matrix of the shock-melt vein consisting of majorite-pyroxene<sub>ss</sub>. Broken white lines within individual idiomorphic wadsleyite crystallites indicate their common preferred orientation. Inset box at the upper left depicts the electron diffraction pattern of wadsleyite at the zonal axis [20-1]. b) Magnified image of a box in lower left side of a) depicting poorly-crystallized materials (thick white arrows) wetting the idiomorphic wadsleyite crystallites. c) Resorbed majorite-pyroxene<sub>ss</sub> crystallite with an inclusion of iron oxide. Majorite-pyroxene<sub>ss</sub> is surrounded by quenched chondritic liquid.

The following scenario that may reflect the series of melting and crystallization events as deduced from the textural and compositional analyses of the assemblages is suggested. Large olivine and Ca-poor pyroxene fragments were cold entrained in the shock-induced chondritic melt. At these conditions, only olivine (Fa<sub>24-26</sub>) melted whereas some Ca-poor pyroxene transformed to majorite of the same chemical composition. This means that the melting temperature at the given pressure slightly exceeded the liquid line. This is followed by fractional crystallization of Mg-rich wadsleyite followed by Fe-rich ringwoodite; the latter from the residual olivine melt progressively depleted in Mg leading to a concentric growth. Ca-poor orthopyroxene transformed to either Ca-poor clinopyroxene or majorite by solid-state

inversion. Subsequently, the wadsleyite-ringwoodite intergrowth was disaggregated, fragmented and the crystallites were dispersed in the melt mesh with olivine composition and crystallites were subsequently reassembled, a consequence of the increasing shear in the vein. This is followed by crystallization of wadsleyite crystals in a veneer only around the original olivine. The wadsleyite veneer was then covered by the wadsleyite-majorite-pyrop<sub>ss</sub> pair with scalloped outlines crystallizing from a liquid mixture of olivine + chondritic melt and were subsequently subjected to partial melting.

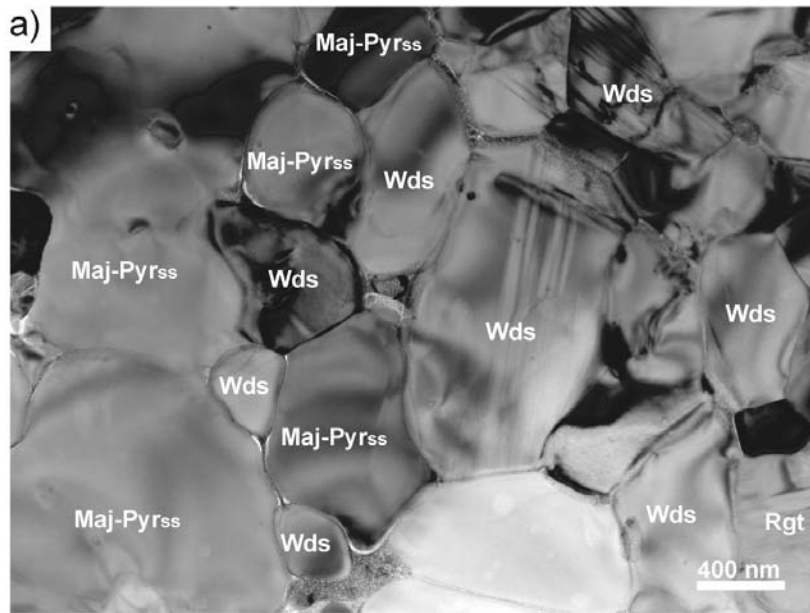


Fig. 3.8-9: A TEM image of SP1FIB1 slice in Allan Hills 78003. a) Scalloped wadsleyite and majorite-pyrop<sub>ss</sub> crystals between the wadsleyite-rim (right) and the matrix of the shock-melt vein part (left). The scalloped texture evidences partial melting after crystallization. Both wadsleyite and majorite-pyrop<sub>ss</sub> are wetted by quenched liquid best seen at the lower edge of the figure.

The formation of wadsleyite and ringwoodite from olivine melts is not restricted to the Peace River L6 chondrite, and appears to be an abundant essential mechanism probably overlooked or misinterpreted in the last 40 years since the first discovery of ringwoodite in the Tenham meteorite.

**e. Carbon polymorphism in shocked meteorites (T. Ferroir/Lyon, L.S. Dubrovinsky, A. El Goresy, A. Simionovici/Grenoble, T. Nakamura/Fukuoka and P. Gillet/Lyon)**

Since the discovery of fullerenes and carbon nanotubes, four forms of pure carbon are now recognized including diamond and graphite. These findings enhanced the interest in exploring possible further occurrences of polymorphs and polytypes of carbon. Many applications are foreseen for these new materials such as the ultrahard carbon polymorphs, possibly harder

than diamond. A new and theoretically unpredicted ultrahard carbon polymorph formed under a very intense and brief shock was found in gneisses from the Popigai impact crater and theoretically investigated afterwards. This led us to scrutinize the nature of shocked carbon materials in the ureilite class of meteorites, which contains about 3 wt.% of pure carbon.

The ureilite class of meteorites is named after the type example Novo-Urei, Russia, which fell in 1886 and is one of the unusual achondritic meteorites. Ureilites contain abundant olivine and pyroxenes with graphite-bearing veins (including tiny diamonds), Fe metal, troilite, Fe<sub>3</sub>C and other accessory phases. We studied the Haverö ureilite, which has a high abundance of carbon-bearing areas, shows a high degree of shock and complex textures of carbon species. A slice of this meteorite was cut and then polished as a thin section using diamond paste and was investigated in reflected light microscopy. We identified two carbonaceous areas forming a positive relief of more than 10 µm above the surface of the silicate matrix (Fig. 3.8-10).

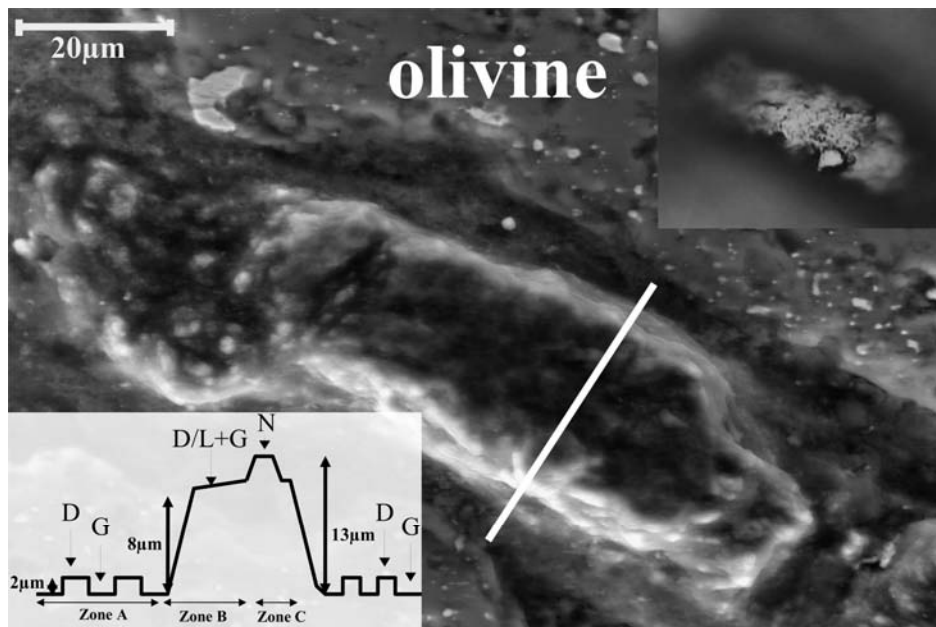


Fig. 3.8-10: One of the carbonaceous area in the Haverö ureilite. The optical microscopy image (top right) and SEM image (center) of a typical carbonaceous area in Haverö (area containing the 21R polytype). The SEM image shows the different heights in the carbonaceous area. The lower left inset shows a scheme of the spatial concentric arrangement of the different carbonaceous areas through a section represented by the solid white line on the SEM picture.

This height suggests that the carbonaceous phases were not easily polishable by a diamond paste and would therefore imply a higher polishing hardness. These high-relief zones are surrounded by flat polished culets and powdery darker areas. We investigated these areas by high-resolution Field Emission SEM (FESEM), energy-dispersive X-ray (EDX) analysis, Raman spectroscopy and we subsequently extracted them for *in situ* synchrotron microbeam X-ray fluorescence (XRF), imaging and X-ray diffraction (XRD).

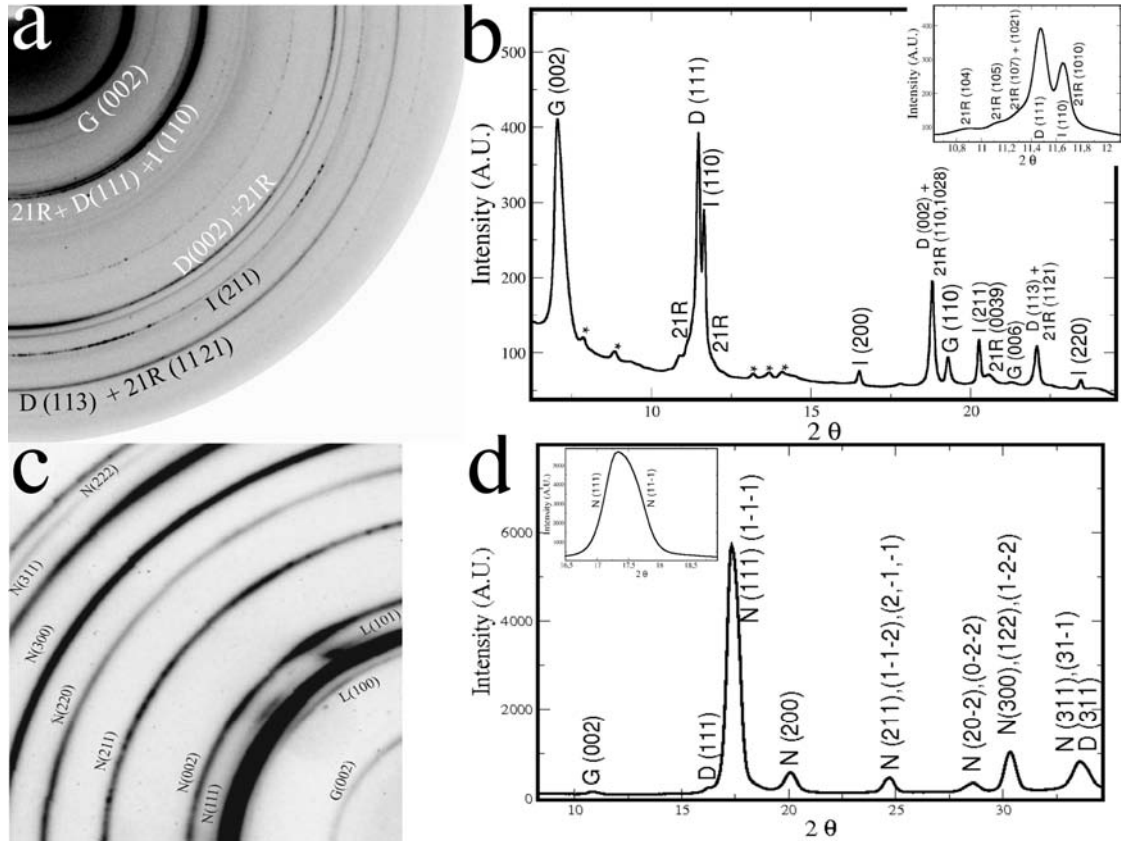


Fig. 3.8-11: (left) and integrated (right) diffraction patterns recorded from the highest relief zones of the two studied carbonaceous area. (a) The image of area 1 (Fig. 3.8-10) obtained at a wavelength of  $0.412 \text{ \AA}$  (ID09, ESRF) shows a simultaneous directional increase of the intensities of the graphite (002) and diamond (111) lines suggesting a topotaxial preferred orientation relationship between the two phases. (b) The integrated pattern was successfully indexed as a mixture of graphite (G), diamond (D), 21R polytype of diamond (21R) and bcc-structured iron-nickel alloy (I), and further refined using the LeBail algorithm as implemented in the GSAS package. \* stands for peaks originating from the lower silicate matrix. Blow-up inset figure at the top right shows the area around the diamond (111) peak where most of the 21R diffracting planes can be seen and identified unambiguously. (c) The image of area 2 obtained at a wavelength of  $0.6199 \text{ \AA}$  (ID22, ESRF) depicts diffraction lines attributed to the new super hard carbon polymorph (marked by “N” and indexed in pseudo-cubic settings), graphite (G), and reflection rings from lonsdaleite (L). The integrated diffraction pattern is interpreted as a mixture of diamond (3C polytype)(D), small amounts of compressed graphite and a new carbon phase (N) with rhombohedral symmetry and lattice parameters  $a = 3.5610(9) \text{ \AA}$ ,  $\alpha = 90.2(2)^\circ$ .

Diffraction data recorded on the first carbonaceous area is consistent with the Raman data confirming the presence of graphite, diamond and a new phase (Fig. 3.8-11a b). The analysis of the 2D diffraction images shows that diamond and graphite have strong preferred orientations and that the graphite [001] reflection is parallel to the [111] reflection of diamond. The X-ray pattern can be successfully indexed with pure iron, mainly emerging from a lower

level in the thin section, diamond 3C, secondary uncompressed graphite and a new diamond polytype, the 21R (14-17). Best fit for the 21R polytype was achieved for a R-3m space group and cell parameters of  $a=2.553(1)$  Å and  $c=44.490(6)$  Å for a volume of  $251.19(4)$  Å<sup>3</sup> close to the theoretical predictions (18-20). This polytype is reported here for the first time.

In the second area investigated, most of the X-ray reflection can be indexed as belonging to graphite, diamond and/or lonsdaleite. However, in the highest part of the carbonaceous inclusion the diffraction lines indicate the presence of: compressed graphite (with lattice parameters  $a=2.454(1)$  Å and  $c=6,372(1)$  Å versus the lattice parameters of secondary graphite  $a=2.462(1)$  Å and  $c=6.704(1)$  Å, lonsdaleite and/or diamond (3C polytype), and an entirely new carbon phase. The latter revealed a distinct diffraction pattern also different from the 21R polytype, thus indicating a new carbon polymorph.

In addition to the diffraction lines of graphite and diamond (or lonsdaleite), the pattern reveals additional lines. While the lines at 2.055 Å, 1.257 Å, 1.450 Å, and 1.185 Å are close to the lines of lonsdaleite and/or diamond, the other lines cannot be assigned to diamond or its polytype. The presence of the common texturing features on all intense diffraction lines (Fig. 3.8-11c) indicates that all of them belong to the same phase. The X-ray pattern was successfully indexed in terms of the Pm3m space group. Indeed, all lines indexed in the framework of a cubic primitive lattice with parameter  $3.559(4)$  Å for a cell volume  $V = 45.08$  Å<sup>3</sup>. Some reflections are asymmetric (particularly, the (111) reflection), while others (for example, (200)) are not. This means the actual symmetry of the new phase is lower than cubic and the best fit was obtained for a rhombohedral lattice ( $R3m$  space group) with the cell parameters  $a=3.5610(9)$  Å,  $\alpha=90.2(2)^\circ$ . Although the quality of the available diffraction data is not sufficient for a full-profile structural refinement, processing of the diffraction pattern with fixed structural positions and optimization occupancy factors indicates that the C3 and C4 positions are only partially filled which causes the density of the new phase to be intermediate between the densities of graphite and diamond. Close-up view shows the asymmetry of the N (111) peak strongly suggesting its splitting into N(111) and N(11-1) thus advocating for the rhombohedral symmetry. The presence of weak satellite reflections at 2.182 Å and 1.928 Å (if not emerging from lonsdaleite) may also indicate a significant degree of disorder of the crystal structure.

The observations of diamond 21R polytype and the new rhombohedral carbon polymorph show that the carbon system is far more complex than previously thought. The main information arising from these discoveries is that naturally shocked carbon opens a new vision of the carbon system. We emphasize that it is impossible to experimentally reproduce natural shock conditions since durations of only nano- to microseconds can be experimentally achieved, while in natural events, due to the significantly larger sizes of the impactors, durations of shock events could span several seconds. Therefore, theoretical calculations have to test if shock simulations could predict these new phases. The new carbon phases found in the Haverö ureilite are thought to be metastable at ambient conditions and indeed formed at

high pressure in a purely dynamic event. They could represent quenched intermediate states in the transformation of graphite to diamond. We assert that the study of naturally shocked samples can greatly improve our knowledge of the carbon system since, it gives access to unreachable areas of the phase space.

**f.** *Transmission electron microscopic study of experimentally shocked dolomite (R. Skála/Prague, N. Miyajima, F. Langenhorst and F. Hörz/Houston)*

The response of carbonate-dominated sediments to transient shock wave compression and subsequent unloading is essential for understanding atmospheric CO<sub>2</sub> pollution and environmental consequences of large-scale impacts on the Earth. There is however little experimental data on the deformation behaviour of dolomite under shock compression and the threshold shock pressures and temperatures for partial to complete decomposition.

Therefore, we have carried out systematic shock-recovery experiments at Johnson Space Center, Houston, using a 20-mm-caliber powder propellant gun. The starting material was a dense (0.04 % porosity) dolomite rock composed of equi-granular grains, typically 25 μm across. Pressures attained by multiple shock reverberation technique covered the range from 20 to 68 GPa. To characterize the shock defects over the entire range of conditions we prepared five shock-loaded samples (20, 26, 30, 41 and 68 GPa) and the undeformed starting material for TEM observation.

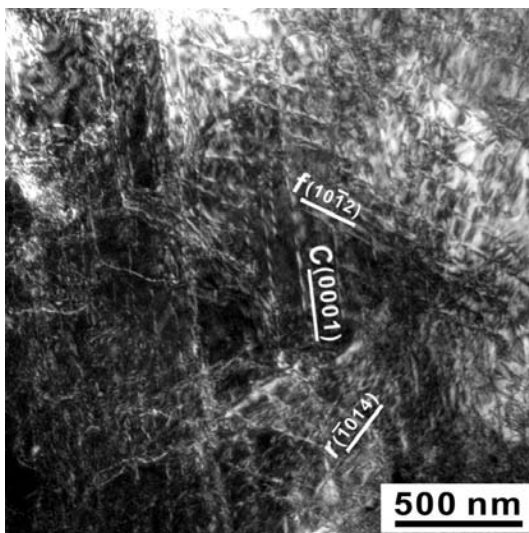


Fig. 3.8-12: Weak-beam dark-field TEM image of dislocations in *f*-, *c*- and *r*-slip systems.

Deformation features recorded in shock-loaded dolomite samples include perfect and partial dislocations, stacking faults, and microtwins. Dislocations are omnipresent in all samples; they are already present in the unshocked starting material but their density significantly increases with shock pressure. Highest dislocation densities on the order of  $10^{14} \text{ m}^{-2}$  are observed in samples shocked to medium to high shock pressures (30-68 GPa). At lower

pressures ( $< 30$  GPa), *c*-type dislocations dominate; at higher pressures ( $> 30$  GPa), *f*- and *r*-type dislocations become more important though *c*-type dislocations are still present (Fig. 3.8-12). Distinct narrow twin lamellae on *f*-planes occur exclusively in the sample shocked to 41 GPa. Partial dislocations were observed in the twin walls, indicating their mechanical nature. Stacking faults occur in all samples, however, they are more frequent in materials shocked to higher pressures. The sample shocked to 68 GPa shows weak diffuse streaks or superstructure reflections in selected area electron diffraction patterns, which might be the result of cation disordering at high post-shock temperatures (Fig. 3.8-13).

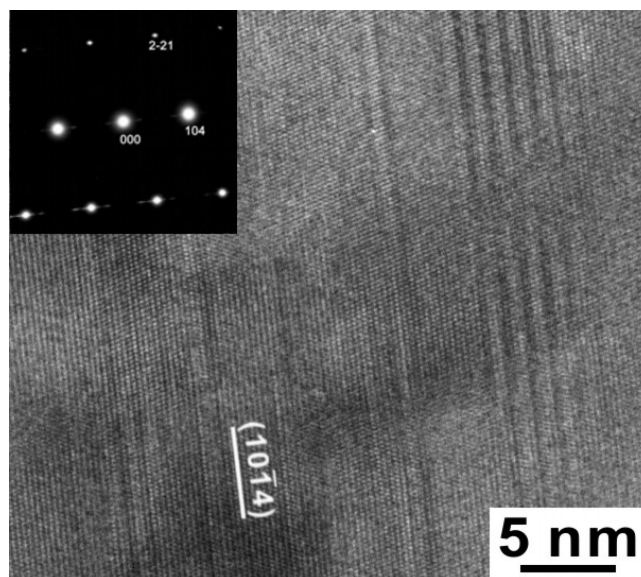


Fig. 3.8-13: High resolution TEM image of the sample shocked to 68 GPa, indicating some stacking faults along the (10 $\bar{1}$ 4) plane. The inset is the selected are electron diffraction pattern with weak diffuse streaks.

Altogether the defect microstructures document strong deformation of dolomite under shock compression but features indicating significant outgassing or melting were even not observed in dolomite shock-loaded to the highest pressure of 68 GPa. These results indicate that decomposition may only be possible if the porosity and thus the shock temperature of starting materials were high or if shock pressures were on the order of 100 GPa.

### 3.9 Materials Science

Modern mineral physics and experimental geochemistry, as branches of the Earth's sciences, widely share methodological approaches with the materials sciences. In experimental geosciences considerable progress has been achieved in the design of high-pressure and high-temperature apparatus, which allows now to tune volume, structure, electronic, magnetic, and other properties of solids of fundamental physical importance. As a result, new material scientific research centres for extreme conditions were founded in France, England, USA, Japan, while world-wide existing geoscientific high-pressure groups moved towards topics in material sciences, solid-state physics and chemistry. Although Bayerisches Geoinstitut does not have its own dedicated material science program, interests of staff scientists, cooperation with industrial partners, and collaboration within international and German research projects resulted this year in a number of contributions in the field of materials physics and chemistry. The material scientific projects at BGI are summarized in this chapter and comprise topics spanning from superhardness, semi- and superconductivity to electronic and mechanical properties.

Examples of potentially superhard, superconducting and semiconducting materials are boron-based phases. Pure boron itself is one of the most enigmatic elements. Several dozens of possible crystalline boron phases were proposed in the literature, but most of them have been proved to be impure materials such as borides. A combined experimental and theoretical study presented here resulted in the synthesis and characterization of new orthorhombic high-pressure boron phases, which are quenchable to ambient conditions and may represent promising materials that may combine superhardness and semiconducting behaviour.

The discovery of superconductivity in polycrystalline boron-doped diamond synthesized at high pressure and high temperature has stimulated recent studies on this new material, its possible applications and the origin of the superconducting state. It was suggested that boron-doping of diamond eventually leads to superconductivity. However, new detailed investigations of the microstructure reveal a complex composition of samples and suggest that superconductivity may not be related to boron-doped diamond but to an amorphous boron-rich layer at grain boundaries.

Although diamond is established so far as the hardest known material, there are continuous attempts to produce substances with comparable hardness and higher thermal stability. One of such compounds could be cubic  $BC_2N$ , synthesized as bulk sample at the Bayerisches Geoinstitut. Presently a technologically important task is the optimization of the synthesis conditions in terms of precursor, pressure, temperature, and duration of heating.

Improved optoelectronic, thermal, semiconducting or mechanical properties are the driving force for intensive recent high-pressure investigations of different nitrides and oxinitrides. Optimization of the synthesis conditions and investigation of physical properties of spinel-structured gallium oxonitride, new methods for sintering of  $Si_3N_4$ -based nano-powders, and the synthesis of unique Fe-Mg-N compounds in the multianvil apparatus are recent

approaches in developing new nitride-based compounds with potential material-scientific applications.

One important technological task relevant for a wide range of devices from mobile phones to cars is to find an effective and cheap way of accumulating electrical energy. Lithium cobaltates have been considered as useful materials to store electrical energy in high-power ion batteries. The capacity of a battery directly depends on electric and electronic properties of the material, which in turn reflects the crystal structure. High-pressure synthesis provide an opportunity to increase the variety of structure types of cobaltates, potentially useful for further electronic applications.

A major issue of modern high-pressure studies is the pressure calibration above 10 GPa. Many uncertainties and discrepancies in high-pressure experiments are due to the absence of a reliable primary pressure scale. Lithium fluoride is a material with a number of advantages for the use as internal pressure standard in diamond anvil cell experiments. First combined single crystal X-ray diffraction and Brillouin spectroscopy studies of the elastic properties of LiF under elevated pressure demonstrate that this material is potentially useful for the pressure calibration up to the Megabar range.

Organic compounds are among the most important functional materials, but their properties and behaviour at elevated pressures and temperatures only recently started to attract the attention of the high-pressure community. Studies of high-pressure crystallization of semi-crystalline polypropylene demonstrate how important the influence of even very moderate pressures and temperatures (few kilobars and 250 °C) could be for soft organic material.

**a.** *Synthesis of a high-pressure orthorhombic boron phase (E.Yu. Zarechnaya, L.S. Dubrovinsky, N. Miyajima, A. El Goresy, in collaboration with N.A. Dubrovinskaia/Heidelberg; Y. Filinchuk, D. Chernyshov and V. Dmitriev/Grenoble)*

The crystal structures of boron are based on B<sub>12</sub> icosahedra as the common building blocks. However, this basic B<sub>12</sub> unit is not stable itself with respect to the requirement of full occupancy of bonding orbitals. The formation of polymorphs with complex structures provides compensation for the deficient electrons by sharing of a small number of electrons by many atoms. Although numerous structures have been suggested, only three crystalline modifications ( $\alpha$ -,  $\beta$ -rhombohedral, and tetrahedral T-192) of elemental boron and an amorphous one are currently established. The existence of “tetragonal boron” as a true modification of pure elemental boron or as boron-rich nitride or carbide has been a subject of controversy. Resistivity measurements demonstrate metallization of boron and the occurrence of a superconducting state at about 160 GPa. However, a structural model of metallic boron is unknown. Thus, a systematic study of synthesis conditions and structure of metallic boron is of high interest.

Experiments in large-volume presses at pressures above 10 GPa and temperatures above 1500 K starting from various boron precursors with a purity higher than 99.7 % result in synthesis of an optically homogeneous reddish material. The SEM and TEM-EDS&EELS data have shown that the samples synthesized from crystalline  $\beta$ -boron powders are not contaminated regardless of the type of the capsule material (MgO, BN, or Au) used. DAC experiments revealed that  $\beta$ -boron transforms to the HPHT modification under laser heating at pressures of 5.8-8 GPa, which, in turn, can reverse to the initial  $\beta$ -boron structure upon heating if the pressure is released.

The X-ray powder diffraction pattern (Fig. 3.9-1) and the Raman spectra of the new HPHT boron are clearly different from those of any established boron phases. The structure of quenched samples was solved based on an orthorhombic unit cell ( $a=5.0563 \text{ \AA}$ ,  $b=5.6126(5) \text{ \AA}$ ,  $c=6.9710(7) \text{ \AA}$ ,  $V=197.83(3) \text{ \AA}^3$ ). It consists of 28 atoms per unit cell combining two types of icosahedra with four additional inter-icosahedra atoms forming pairs (Fig. 3.9-2). Nearly rectangular channels running along the  $a$  axis are filled with  $B_2$  dumbbells, aligned almost parallel to the  $a$  axis. In the  $Pnmm$  space group, the center of the  $B_2$  dumbbell is at  $\frac{1}{2} 0 0$ , and of  $B_{12}$  - at  $\frac{1}{2} 0 \frac{1}{2}$ . The distances B-B within the  $B_{12}$  icosahedron (1.75-1.95  $\text{\AA}$ ) are slightly longer than those within the dumbbell (1.73  $\text{\AA}$ ). The shortest distances in the structure are those between atoms linking (1) the two icosahedra - 1.64  $\text{\AA}$ , (2) the icosahedron and the dumbbell - 1.63  $\text{\AA}$ , and (3) the two boron atoms within a dumbbell - 1.73  $\text{\AA}$ .

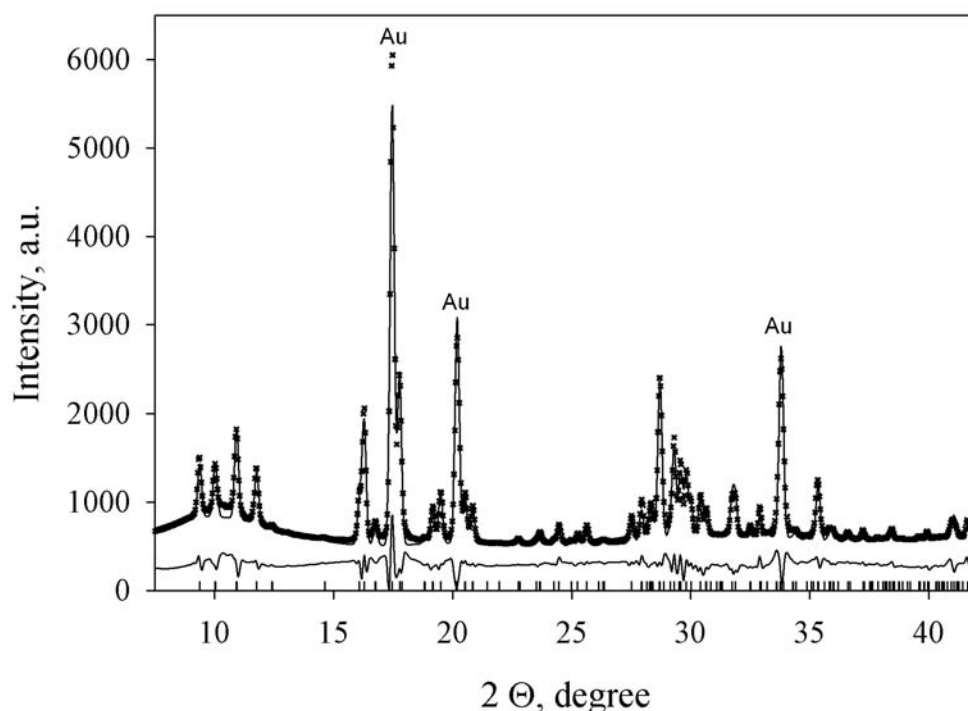


Fig. 3.9-1: The diffraction pattern of the boron phase synthesized at 14 GPa and 1800 K refined using GSAS package ( $\lambda=0.7147 \text{ \AA}$ ,  $wRp=6.5 \%$ ,  $Rp=5.5 \%$ ; space group  $Pnmm$ ). Top row of tick marks gold (residuals of capsule material), bottom row of tick marks the HPHT boron phase. The broad feature at  $\sim 10^\circ$  is due to a glass capillary.

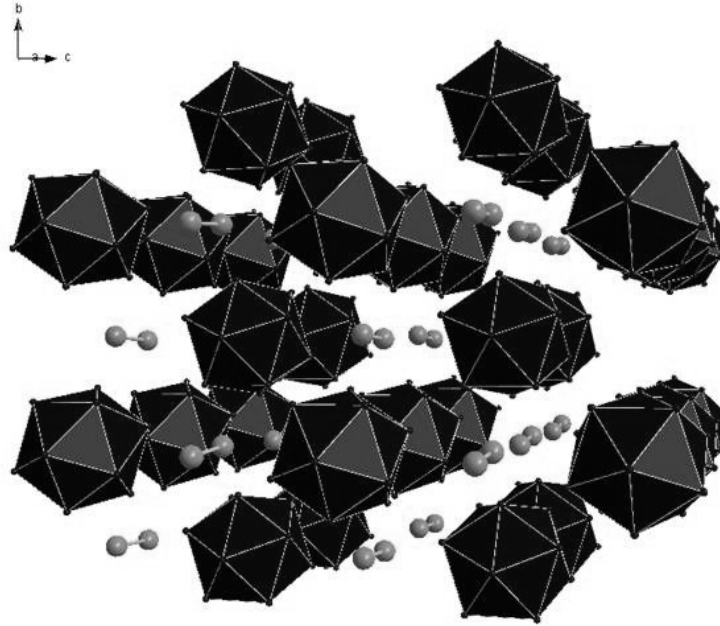


Fig. 3.9-2: The structure of the HPHT boron phase shown in the *bc* projection.

**b.** *Ab initio* study of the orthorhombic HPHT boron (E.Yu. Zarechnaya, L.S. Dubrovinsky, in collaboration with A. Mikhailushkin, S.I. Simak and I. Abrikosov/Linköping; N.A. Dubrovinskaia/Heidelberg)

The synthesis of high-pressure phases is one way to manipulate the properties in a given chemical system. Particular interest is attributed to elements with competing crystal structures such as boron. Theoretically it was predicted that the structural change of boron from the  $\alpha$ -B to the  $\alpha$ -Ga structure occurs at  $\sim 74$  GPa and is accompanied by a nonmetal-metal transition was predicted. Since we have found experimentally the existence of high-pressure and high-temperature (HPHT) orthorhombic boron, further theoretical study of the relative stability of elemental boron polymorphs is necessary.

The crystal stability and the ground state properties of the orthorhombic boron phase were studied theoretically by density-functional calculations. Best agreement with experimental structural parameters was obtained for the Perdew-Burke-Ernzerhof (PBE) parameterization. Integration over the Brillouin zone was performed via the linear tetrahedron method with Blöchl correction. For optimization of the structure with respect to internal relaxations and total energy minimization k-points of  $6 \times 6 \times 6$  were used. A convergence with tolerance of  $10^{-3}$  eV/Å was achieved.

In the framework of first principles modeling, the orthorhombic HPHT boron was found to be stable in the pressure range of 20 to 85 GPa (Fig. 3.9-3), while experimentally the transition occurs at about 5-8 GPa. Such considerable discrepancies between theory and experiment in the determination of incipient pressure of the phase transition can be attributed to the higher

temperature in experiments (calculations have been conducted for 0 K). On further compression the HPHT phase should transform into the  $\alpha$ -Ga-type structure above 90 GPa.

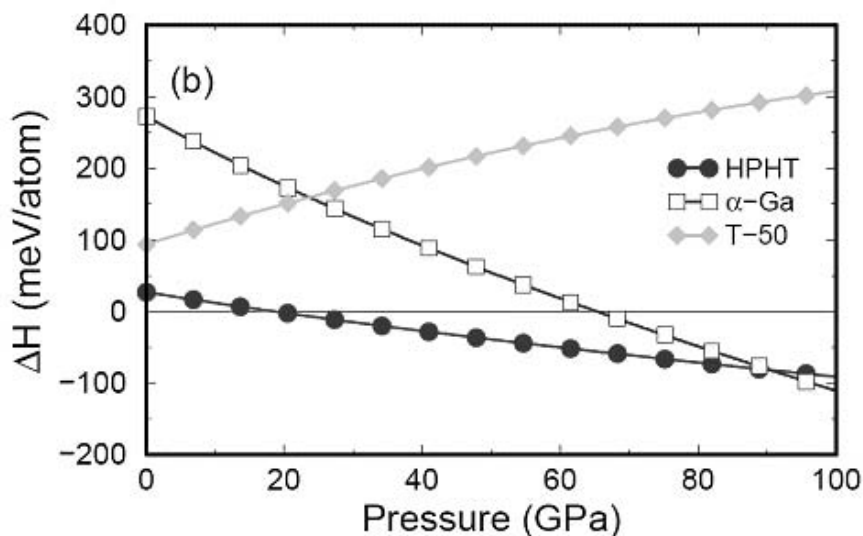


Fig. 3.9-3: Calculated enthalpy of the orthorhombic HPHT, T-50, and  $\alpha$ -Ga structured boron phases as a function of pressure with respect to the enthalpy of  $\alpha$ -B ( $T=0$  K).

The calculated value of the band gap (1.7 eV) is in a good agreement with experimental data (2.1 eV) determining the semiconducting nature of the HPHT boron. The value of the energy gap slightly decreases by  $\sim 5.88\%$  with a pressure increase up to 23 GPa (Fig. 3.9-4). Calculations suggest that the HPHT orthorhombic boron is less compressible ( $K_0=237$  GPa,  $K'=3.6$ ) than any known other boron phases.

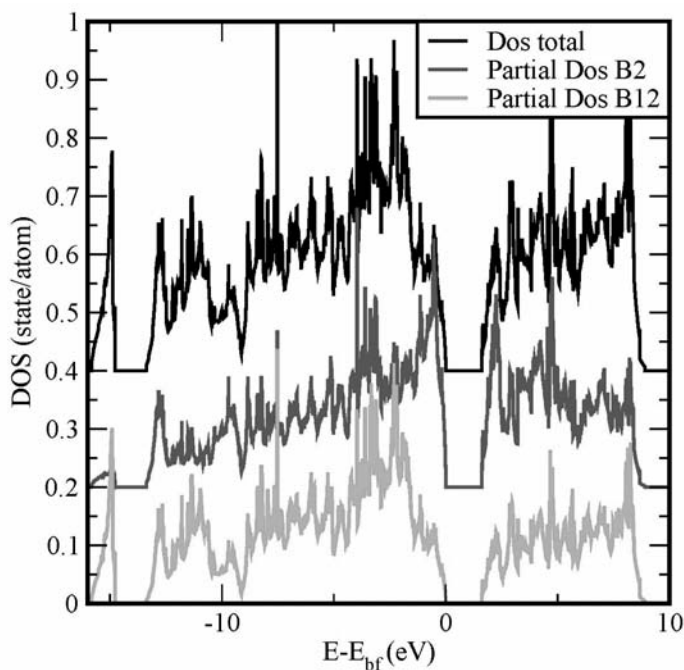


Fig. 3.9-4: Calculated DOS of the orthorhombic HPHT boron phase for several pressures. Energies  $E$  are given with respect to the chemical potential  $\mu_0$ .

*c. An insight into what superconducts in polycrystalline boron-doped diamonds based on microstructural investigations (N.A. Dubrovinskaia/Heidelberg, R. Wirth/Potsdam, J. Wosnitza and T. Papageorgiou/Dresden, H.F. Braun/Bayreuth, N. Miyajima and L.S. Dubrovinsky)*

The discovery of superconductivity in polycrystalline boron-doped diamond (BDD) synthesized under high pressure and high temperature has raised a number of questions on the origin of the superconducting state. It was suggested that the considerable boron doping of diamond eventually leads to the superconductivity. To justify this hypothesis detailed information on the microstructure of the composite materials and on the exact boron content in the diamond grains is needed. For that we utilized high-resolution transmission electron microscopy (HRTEM) as well as electron energy loss spectroscopy (EELS). For the studied superconducting BDD samples synthesized at high pressures and high temperatures the diamond grain sizes are about 1-2  $\mu\text{m}$  with a boron content between 0.2(2) and 0.5(1) at.%. The grains are separated by 10-20 nm thick layers and triangular-shaped pockets of predominantly (at least 95 at.%) amorphous boron. These results render superconductivity caused by the boron doping in diamond highly unlikely.

We investigated polycrystalline BDD samples which were synthesised at 20(1) GPa and 2300(50) K as well as at 9.0(5) GPa and 2500(50) K in a 5000-tonne press. As starting materials a mixture of graphite (referred further to as  $^{12}\text{C}$ ) or isotropically pure amorphous carbon  $^{13}\text{C}$  and  $\text{B}_4\text{C}$  in a ratio C:B = 13:1 ( $\sim 7$  at.% B) was used. Synchrotron and in-house X-ray diffraction investigations revealed for all samples studied that their main crystalline component (more than 99 %) is diamond with a small amount of boron carbide  $\text{B}_{50}\text{C}_2$ . In some samples residuals of the starting material  $\text{B}_4\text{C}$  were found.

Electron transparent foils of BDD samples were prepared by means of focused ion beam (FIB) techniques. All investigated grains are separated by layers of amorphous material along straight boundaries with thicknesses of 10 to 20 nm. The material constituting the layers along the grain boundaries also fills triangular-shaped pockets at the grain junctions (Fig. 3.9-5). The complete absence of any TEM diffraction contrast (uniform light grey contrast during sample tilting) indicates the amorphous state of the filler material. In order to probe the chemical nature of the inter- and intra-granular material in our samples, we measured the electron energy-loss spectra (EELS) of boron  $K$  and carbon  $K$  ionization edges for numerous pockets and grains. They revealed that the pocket material contains  $\sim 95$  % boron with a small amount of carbon ( $\sim 5$ -6 %, varying for the different pockets) (Fig. 3.9-6).

Based on these results, we can suggest a few hypotheses that explain the nature of superconductivity in investigated samples: (1) undistorted diamond becomes superconducting at B concentrations much lower than reported, but this strongly contradicts the results on single crystal BDD samples, which are not superconducting. This also does not agree with the experimental heat capacity data showing that only a small fraction of the sample becomes superconducting, while diamond forms its major part. (2) The graphite-like regions with comparatively moderate B-concentrations inside the grains become superconducting.

However, these innermost parts of diamond grains are not interconnected; this hypothesis can hence not explain the superconductivity observed in resistivity measurements. (3) The intergranular boron-rich material is superconducting. In our opinion, the third hypothesis is most probable, because carbon-doped amorphous boron phase, which is filling all the intergranular space in the polycrystalline samples, forms a continuous network throughout the entire sample and its amount is consistent with the estimations of a superconducting part of the sample based on the experimental heat capacity data. In order to prove superconductivity in diamonds being caused by a certain amount of boron doping one would need to measure well-characterised single crystalline BDD. Otherwise, the presence of other complex phases in the available composite materials hampers any definite conclusion.

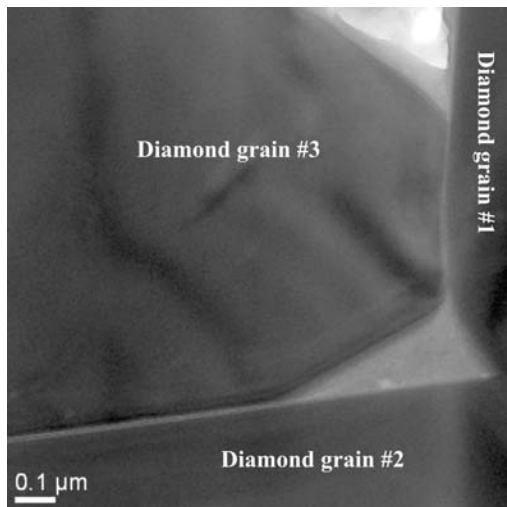


Fig. 3.9-5: Bright-field TEM image of a boron-doped diamond sample. The amorphous material constituting the layers along the grain boundaries also fills triangular-shaped pockets at the grain junctions.

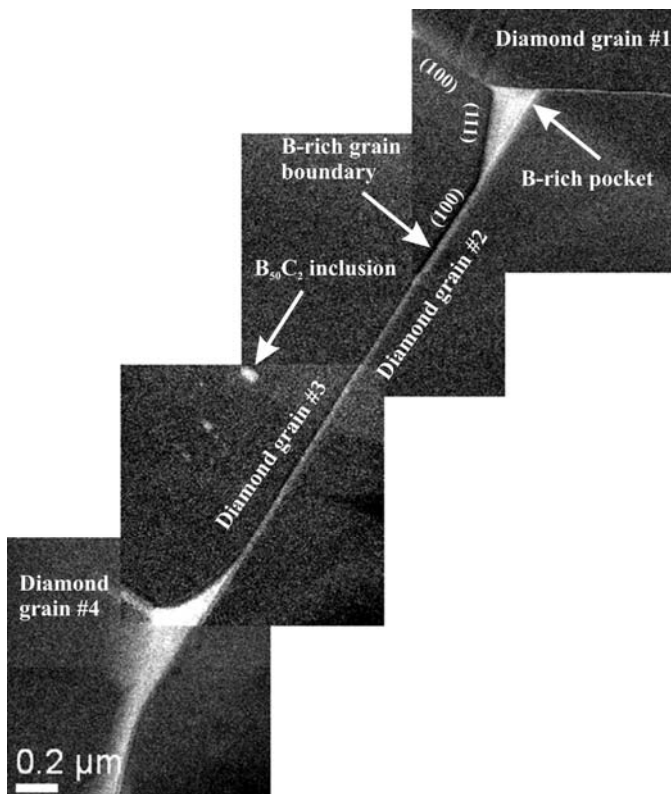


Fig. 3.9-6: Elemental B map obtained using EELS and consisting of 4 images of an intergranular area. It shows 4 diamond grains, 5 grain boundaries and two pockets. The vast majority of boron is concentrated in the grain boundaries and pockets. Boron is quite homogeneously dispersed in a very small amount within the diamond grains.

**d.** *A study on the HPHT synthesis of a c-BC<sub>2</sub>N superhard material (W.R. Matizamhuka and I. Sigalas/Johannesburg, L.S. Dubrovinsky, N.A. Dubrovinskaia/Heidelberg, N. Miyajima and O. Narygina, in collaboration with R. Riedel/Darmstadt and G. Mera/Grenoble)*

Over the years there have been tremendous efforts in the search for potential superhard materials. This has been stimulated by the need to design materials which not only approach diamond in hardness but are more useful and complimentary to the traditional superhard materials. This may include materials that are expected to be chemically and thermally more stable than diamond and harder than c-BN.

However to design new superhard materials it must be understood what makes diamond special. It is a well known fact that the diamond structure consists of short tetrahedrally bonded sp<sup>3</sup> hybridised carbon atoms forming a rigid 3-D covalent network of high symmetry with extreme resistance to shear. The short bond length implies a high atomic and mass density. Thus highly directional and strong bonding is crucial in achieving high hardness. This justifies the focus on the lighter elements boron, carbon, nitrogen and oxygen capable of forming short covalent type bonds.

Attempts to combine the properties of the two traditional superhard materials (c-BN and diamond) in order to fill the ‘hardness gap’ have resulted in increased research in the B/C/N alloy system. However the results obtained so far are controversial.

We attempted to synthesise a cubic BC<sub>2</sub>N (Z608) material under HPHT conditions in a large volume 5000 tonne multianvil press starting with a turbostratic polymer derived BC<sub>2</sub>N compound (t-BC<sub>2</sub>N hereafter). The t-BC<sub>2</sub>N was inserted into an h-BN capsule enclosed in an MgO (+ ca.5 wt.% Cr<sub>2</sub>O<sub>3</sub>) octahedron with a LaCrO<sub>3</sub> furnace for heating. The set up was placed in an 18/11 WC cube assembly and subsequently compressed to the desired pressure and heated to 2000 °C at a rate of ca. 100 °C/min and an isothermal holding time of 60s. The sample was quenched by switching off the furnace. The same experiment was reproduced in a 1200 tonne Sumitomo multianvil press with a 10/5 WC cube assembly (Table 3.9-1).

<b>Sample</b>	<b>P/GPa</b>	<b>T/°C</b>	<b>holding time/s</b>	<b>Cooling mode</b>	<b>Product</b>
Z608	20	2000	60	Quench	c-BC <sub>2</sub> N+NanoD
S4294	20	1500	120	Quench	t-BC <sub>2</sub> N
S4295	20	1920	300	Quench	t-BC <sub>2</sub> N+c-BC <sub>2</sub> N
S4306	20	2000	30	Quench	c-BC <sub>2</sub> N
S4316	20	2000	180	Quench	c-BC <sub>2</sub> N
S4311	20	-	7200	-	t-BC <sub>2</sub> N

NanoD: nano-diamond-like material.

Table 3.9-1: Summary of results on the HPHT synthesis in the multianvil presses.

Synchrotron radiation with a short monochromatic wavelength ( $\lambda = 0.7693 \text{ \AA}$ ) at the ESRF was used for X-ray analysis (Fig. 3.9-7). The XRD profile confirms the existence of a monophasic zincblende type structure. The refined lattice parameter ( $a = 0.3550(2) \text{ nm}$ ) is smaller than expected for ideal mixing of c-BN and diamond ( $a = 0.3590 \text{ nm}$ ). Furthermore, we observed the existence of a (200) peak in all transformed samples signifying an  $F-43m$  space group.

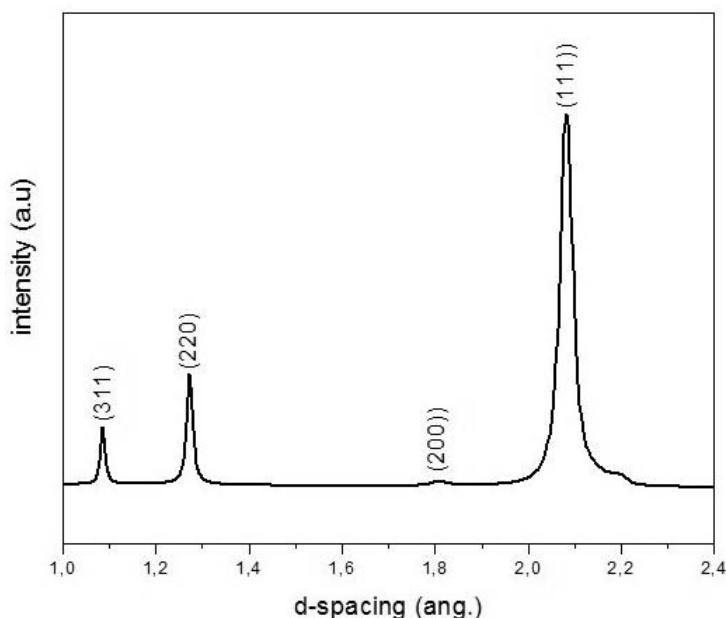


Fig. 3.9-7: Synchrotron XRD pattern of c-BC<sub>2</sub>N sample taken at ESRF. The synthesis conditions for the sample were 20 GPa and 2000 °C (60s) in a 5000t multianvil press.

A further TEM/EELS (Fig. 3.9-8) study reveals existence of an  $sp^3$  hybridised phase with nanosized crystallites (ca. 50-100nm). EELS measurements on nanocrystallites reveal the ternary composition of the phase with the B-K, N-K and C-K edges appearing concurrently in the EELS spectra. However diamond was also observed besides the BC<sub>2</sub>N signifying decomposition to some extent under the present conditions.

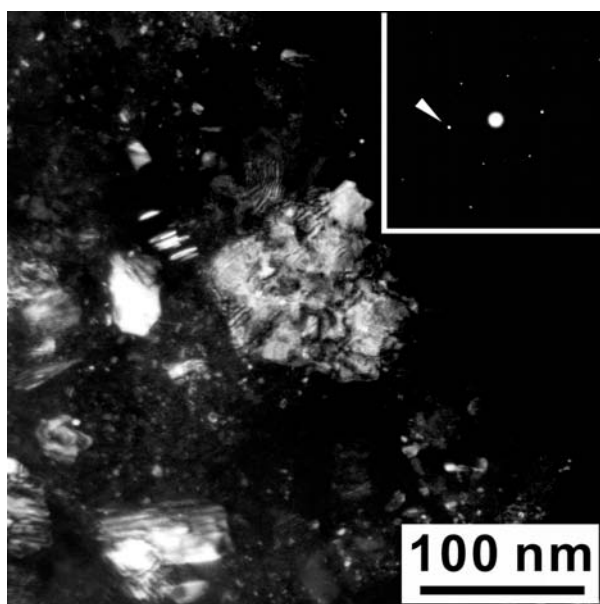


Fig. 3.9-8: Dark field image and selected area electron diffraction of the sintered B-C-N material, indicating existence of single-grained material.

e. *Diamond anvil cell syntheses and compressibility studies of the spinel-structured gallium oxonitride (C. Zvoriste/Darmstadt, I. Kinski/Dresden, S. Hering/München, H. Huppertz/Innsbruck, R. Riedel/Darmstadt, L.S. Dubrovinsky)*

Improved optoelectronic, thermal, semiconducting or mechanical properties are the driving force for an intense investigation of different oxides and nitrides during recent years. Nitride chemistry comprises a wide field. Since the increasing interest in semiconducting materials with wide band gaps for industrial applications, the research on nitrides and the anion-substituted oxonitrides focused on this class of materials that provides both good optoelectronic and mechanical properties. Intensive investigations of the pressure-temperature stability field in the system GaN-Ga<sub>2</sub>O<sub>3</sub> have been performed by our research group. To synthesize gallium oxonitride with a spinel-type phase ( $\gamma$ -Ga<sub>x</sub>O<sub>y</sub>N<sub>z</sub>) we used a precursor-derived ceramic which allowed us to obtain the spinel compound at moderate pressures. Suitable precursors were prepared by reacting bis(trisdimethylamino)gallane [Ga(NMe<sub>2</sub>)<sub>3</sub>]<sub>2</sub> with t-butanol followed by a thermal treatment at 350 °C in an ammonia atmosphere. This procedure resulted in the formation of amorphous GaON. For one of the high-pressure runs, an amorphous GaON ceramic with an N/O ratio of 1.02 has been loaded into a diamond anvil cell. *In situ* XRD and *in situ* Raman spectroscopy were used for identifying and characterizing the synthesized phases. After compression of the sample at 1 GPa and heating up to 1300 °C, a spinel-structured gallium oxonitride with a lattice parameter of 8.2042(1) Å was the only crystalline phase observed apart from LiF, which was used as the pressure medium. In order to determine the bulk modulus for the  $\gamma$ -Ga<sub>x</sub>O<sub>y</sub>N<sub>z</sub> phase, compression-decompression runs were carried out. The crystalline GaON ceramic was loaded next to a thin pallet of LiF into a DAC and compressed up to around 9 GPa. All the diffraction lines in addition to the LiF ones could be interpreted on the basis of the spinel-type structure. Up to 9 GPa no changes in the X-ray diffraction patterns were observed. Fitting the data (Fig. 3.9-9) using the second order Birch-Murnaghan equation of state ( $K' = 4$ ) gave values for the bulk modulus of  $K = 216(7)$  GPa and for the volume at zero pressure of  $V_0 = 552.9(5)$  Å<sup>3</sup>.

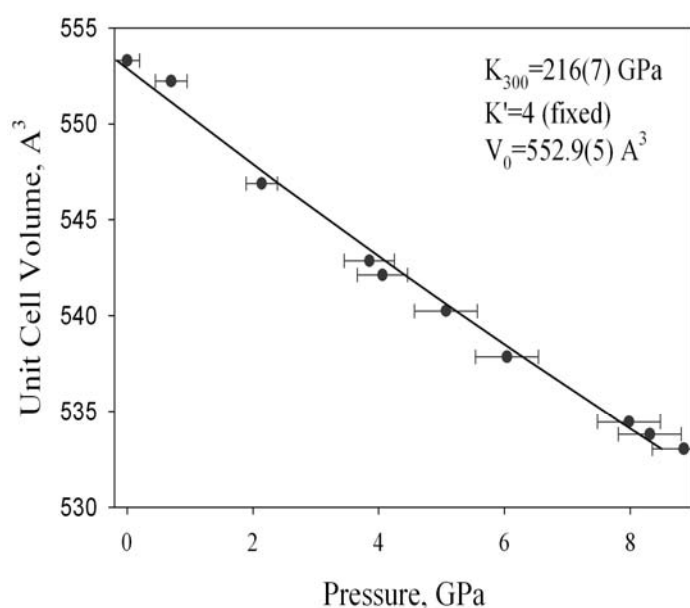


Fig. 3.9-9: Unit cell volume of the  $\gamma$ -Ga<sub>x</sub>O<sub>y</sub>N<sub>z</sub> as function of pressure. The experimental data are shown by solid circles. The solid line represents the least-squares fit of the second-order Birch-Murnaghan EOS to the experimental data.

A Raman spectrum of the sample synthesized at 3.75 GPa and around 1300 °C in a laser-heated DAC proved also the formation of the spinel-type gallium oxonitride. Although the Raman signal is weak and the spectrum is noisy, the five active modes of spinel  $\text{Ga}_x\text{O}_y\text{N}_z$  could be identified. Since the precursor-derived ceramic provided the possibility to synthesize the  $\gamma\text{-Ga}_x\text{O}_y\text{N}_z$  phase at low pressures, a new set of experiments has been started using a piston cylinder apparatus. This will allow us to obtain a higher amount of the sample in order to extend our investigations and characterization of the spinel-type gallium oxonitride.

**f. High pressure hot pressing as a method for obtaining nanostructured  $\text{Si}_3\text{N}_4$  containing materials** (I. Zalite/Riga, D.J. Frost, N. Zilinska/Riga)

Successful fabrication of nano-structural materials from ceramic nanopowders with the traditional compacting methods (sintering, hot pressing etc.) is complicated due to the high chemical activity and agglomeration tendency of nanopowders, ending in rapid grain growth during compaction. These problems could be partially solved by high pressure hot pressing. High pressures could partially destroy agglomerates and sintering at high pressures may require lower temperature and shorter time of thermal treatment.

Plasma-produced nanopowders of different  $\text{Si}_3\text{N}_4$  containing compounds:  $\text{Si}_3\text{N}_4\text{-SiC-C}_{\text{free}}$  (sample 1),  $\text{Si}_3\text{N}_4\text{-SiC}$  (samples 2 and 3) and  $\text{Si}_3\text{N}_4\text{-TiN}$  (sample 4) were used for subsequent investigations.

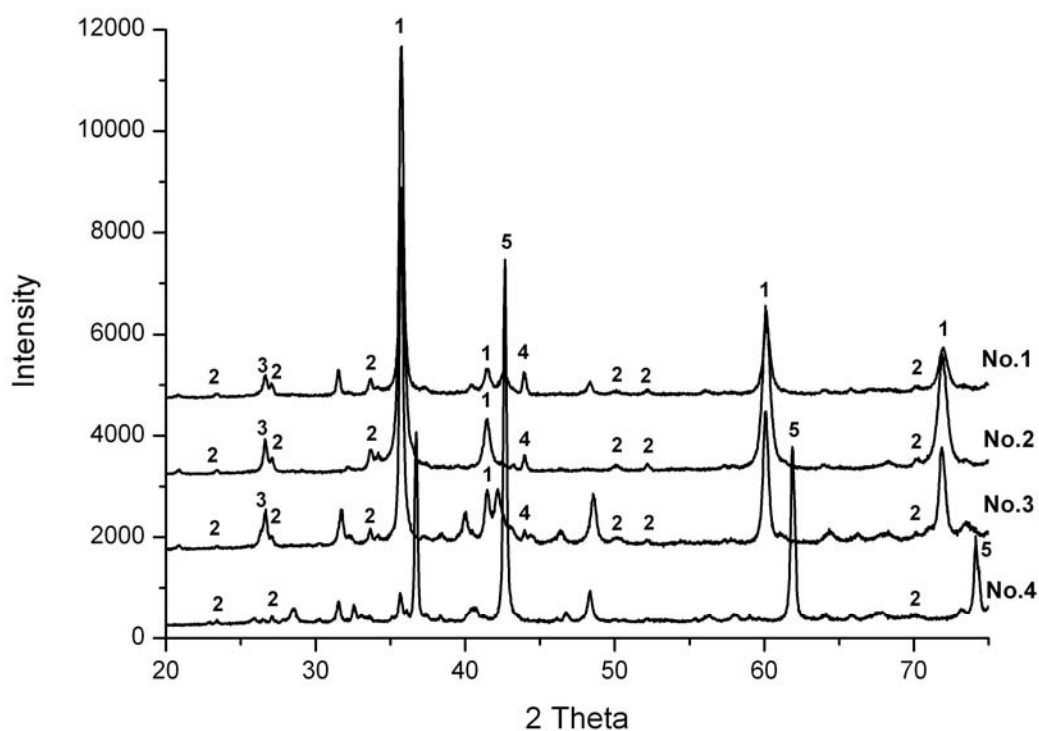


Fig. 3.9-10: The phase analysis of samples No.1, 2, 3 and 4. Labels: 1 -  $\beta\text{-SiC}$ , 2 -  $\beta\text{-Si}_3\text{N}_4$ , 3 - C(graphite), 4 - C(diamond), 5 - TiN.

Compact materials were prepared by high pressure hot pressing to 8 GPa and sintering at temperatures of 1400-1800 °C. The temperature was increased at an approximate rate of 100 °C/min and samples were annealed at the highest temperature for 3 to 10 minutes.

Practically in all cases a dense material with the grain size smaller than 200 nm was obtained. The phase analysis shows that at compaction conditions of our experiments the same phases formed that have also been obtained by other methods:  $\beta$ -SiC and some small amount of  $\beta$ -Si<sub>3</sub>N<sub>4</sub> in samples No.1, 2 and 3 and TiN and  $\beta$ -Si<sub>3</sub>N<sub>4</sub> in sample No.4. Notably, in carbide-containing samples, especially those with free carbon, we also found a small amount of graphite and diamond (Fig. 3.9-10).

The microhardness of sample No.3 is rather high ( $H_{\mu} = 35 \pm 5$  GPa at the load of 200 g). This high microhardness probably could be explained by a densified structure of nanograins. Note however, that free carbon containing SiC nanopowders, as described in the literature, treated thermally at high pressures (~ 5 GPa) also exhibit high hardness (up to 39 GPa) due to carbon excess in the silicon carbide.

**g.** *High pressure and temperature synthesis of metal nitrides (A.J. McGaff and G. Serghiou/Edinburgh, in collaboration with D.J. Frost)*

In an effort to prepare novel alloys and ceramics containing transition metals and alkali and alkaline earths, we have investigated the effect of high pressure and temperature on magnesium iron mixtures in the presence of sodium azide (NaN<sub>3</sub>) in a multianvil press. Several interstitial iron nitride phases are known and a magnesium nitride phase has also been reported. On the other hand neither magnesium nor iron metal form compounds with sodium at ambient pressure. We present here scanning electron microscopy of chemical and morphological aspects of the reaction products.

Mg is light and strong and is thus a desirable alloying component and Fe itself is central to most everyday metal-based constructions. The prospect thus of incorporating the two in the same structure is appealing technologically. The ambient pressure experiments reveal no reaction between magnesium and iron, consistent with their ambient pressure phase diagram and no reaction takes place between iron and Mg<sub>3</sub>N<sub>2</sub>, formed upon heating in nitrogen. The reaction product recovered from 15 GPa however reveals two principal chemistries, namely a Fe-Mg-N and a Fe-Mg-Na-N phase (Fig. 3.9-11).

Alloys can be broadly categorized into solid solutions and intermetallic compounds. Mg, however, does not form either a solid solution or an intermetallic alloy with iron at ambient conditions. With regards to solid solution formation, principal reasons for the absence of reactions are that the Mg-Fe atomic radii ratios are well outside the 15 % tolerance ratio. In

addition their crystal structures are different. With regard to intermetallic alloy formation, empirical criteria based on differences in electronegativity and charge density of elements have been developed, which for Mg and Fe predict a positive value for the heat of formation and thus no reaction. Our new results on the combined effect of high pressure and nitridation of Mg, Fe, and Na opens a new dimension in novel dense nitride formation and its applications. For the particular case of multianvil syntheses, and accompanying diamond cell studies, the interplay between sodium containing and sodium free nitrides is being explored to target an expanded region of one or the other nitride phase.

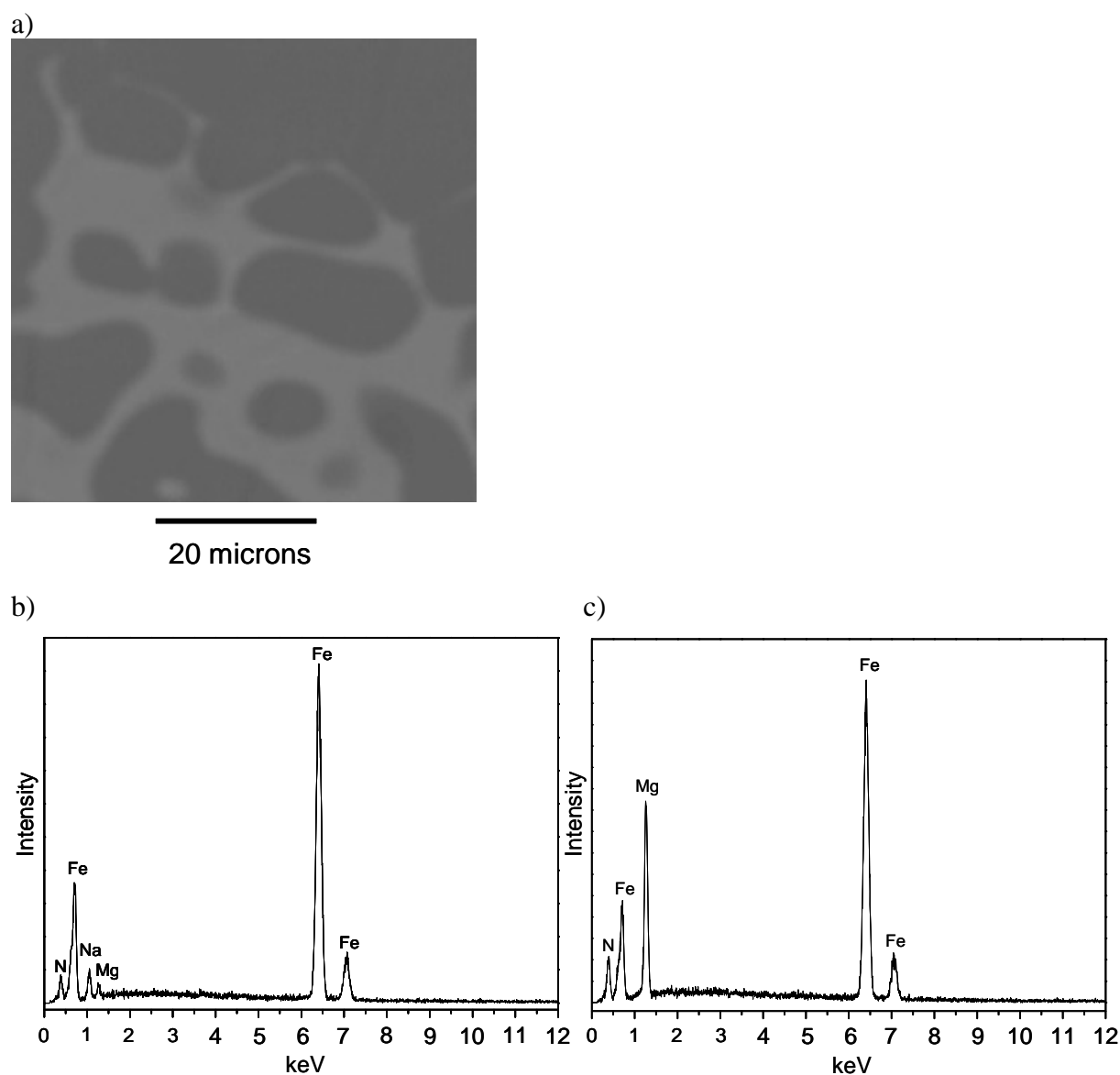


Fig. 3.9-11: (a) Backscattered scanning electron microscopy (BSE) images of a Mg-Fe-N phase (dark contrast regions) and a Mg-Na-Fe-N phase (light contrast regions) recovered after heating intimately mixed Fe and Mg with sodium azide at 15 GPa and 1800 K followed by temperature quenching. Energy dispersive X-ray analysis (EDX) spectra from the (b) dark contrast and the (c) light contrast regions.

**h.** *Structural stability of the  $\sigma$  phase FeCr under pressures up to 77 GPa (V.F. Degtyareva/Chernogolovka, L.S. Dubrovinsky, A. Kurnosov and I.Yu. Kantor; V. Prakapenka/Chicago)*

Iron-based alloys are important for the technology of steel production and for geosciences with respect to the Earth's core. The Fe – Cr alloy system, with both constituent elements crystallizing in a body-centered cubic structure, contains an intermediate phase of anequiatomic composition with complex crystal structure. The structure of this phase, called  $\sigma$  phase, is tetragonal with 30 atoms in the unit cell, space group  $P4_2/mnm$ , lattice parameters  $a = 8.7995 \text{ \AA}$ ,  $c = 4.5442 \text{ \AA}$ ,  $c/a = 0.516$ . The  $\sigma$  phase occurs in a number of binary and ternary systems involving transition-group elements. This structure has been found in two pure elements: one of the allotropic forms of uranium ( $\beta$ -U) and a metastable crystalline modification of tantalum ( $\beta$ -Ta). The interest in the  $\sigma$  phase goes far beyond its technological properties and is related to the fundamental problem of structure stability in crystal chemistry and physics of metals and alloys.

The equiatomic FeCr alloy is isoelectronic to manganese that crystallizes at ambient conditions in a complex cubic structure ( $\alpha$ -Mn). It was shown that the  $\alpha$ -Mn structure is stable at high pressures up to 165 GPa where a new diffraction peak appeared indicating a phase transition. One of the main factors for the stability of such complex low-symmetry structures is the valence electron energy contribution to the total crystal energy that increases under compression. Therefore structural high-pressure studies provide new data for an understanding of the formation and stability of the complex low-symmetry phases.

High-pressure studies of the  $\sigma$  phase were performed with a diamond anvil cell using a Re gasket and a ruby chip for pressure measurements. X-ray powder diffraction measurements were made with an in-house high-brilliance system (BGI) and synchrotron radiation at IDD-13 of the Advanced Photon Source (Argonne National Lab). The diffraction data were analyzed with the Rietveld method using GSAS. The volume compressibility data were fitted with the third-order Birch - Murnaghan equation of state.

Collected X-ray diffraction patterns showed that the  $\sigma$  phase FeCr remained stable up to 77GPa, the highest pressure reached in this study. The diffraction pattern of the FeCr alloy at 77 GPa is shown in Fig. 3.9-12. The Rietveld refinement on the basis of the tetragonal  $\sigma$ -type structure, space group  $P4_2/mnm$ , resulted in lattice parameters  $a = 8.2441(3) \text{ \AA}$ ,  $c = 4.2552(2) \text{ \AA}$ , assuming the same atomic positions as at ambient pressure. These values correspond to a cell volume compression of  $V/V_0=0.817$ .

Analysis of the pressure dependence of cell volume results in the equation of states given in Fig. 3.9-13 with the values of bulk modulus  $K_0=217(5) \text{ GPa}$  and its pressure derivative  $K_0'=5.8(2)$ . It is interesting to compare the compressibility of the  $\sigma$  phase FeCr to that of the constituent elements. The bulk modulus  $K_0$  for bcc structured Cr and Fe is 161 and 173 GPa for antiferromagnetic Cr and ferromagnetic Fe, respectively and is lower than that of the  $\sigma$  phase. For the paramagnetic  $\epsilon$ -Fe, the value of  $K_0$  was found to be 163(8) GPa, which is still

lower than that of the  $\sigma$  phase FeCr. Thus, the FeCr in its  $\sigma$  structure appears to be less compressible than the phases of the constituent elements. In contrast, the pure element Mn, isoelectronic to the FeCr alloy, has much lower value of the bulk modulus,  $K_0 = 158$  GPa.

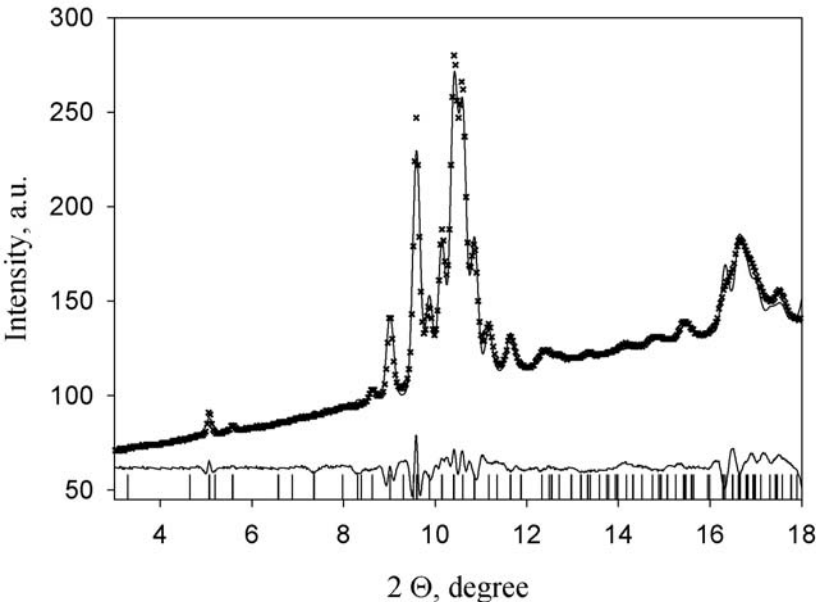


Fig. 3.9-12: Diffraction pattern of the FeCr alloy at 77 GPa ( $\lambda=0.3344$  Å). The tetragonal  $\sigma$ -type structure has lattice parameters  $a = 8.2441(3)$  Å,  $c = 4.2552(2)$  Å. Calculated peak positions are indicated by tick marks below the spectrum; the curve below the tick marks is the difference between observed and calculated spectrum.

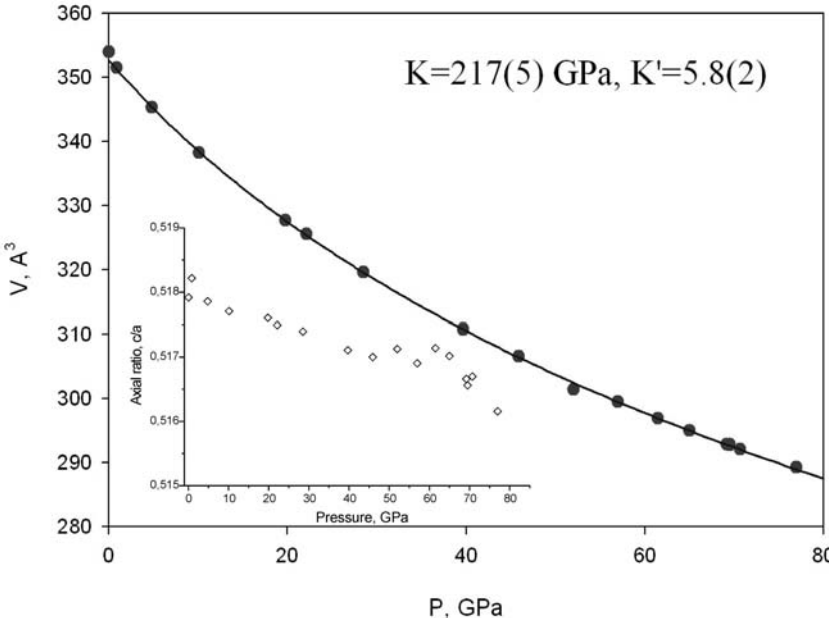


Fig. 3.9-13: Variation of the cell volume for the  $\sigma$  phase in FeCr with pressure. Circles show experimental data (the experimental error is smaller than the symbol size); solid curve is the EoS fit with  $K_0 = 217(5)$  GPa and  $K'_0 = 5.8(2)$ . The pressure dependence of the axial ratio  $c/a$  for the tetragonal cell is shown in the inset.

It should be noted that the tetragonal structure of the  $\sigma$  phase FeCr is compressed slightly anisotropically as can be concluded from the  $c/a$  behaviour under pressure (see insert in Fig. 3.9-13). The compressibility along the  $c$  axis is noticeably higher than along the  $a$  axis, at a pressure of 77 GPa  $c/a$  decreases at ambient pressure from 0.5185(1) to 0.5161(1).

In conclusion, the structural stability of the complex, low-symmetry phase of FeCr was observed in the pressure range up to 77 GPa. This observation provides evidence for the importance of the electronic energy contribution to the total energy and the increase of this factor on compression. The stability of the  $\sigma$  phase can be related to the Hume-Rothery effect based on the configuration of the large Brillouin-Jones zone.

*i. First-principles phase diagram calculations for the HfC-TiC, ZrC-TiC and HfC-ZrC solid solutions (O. Adjaoud and G. Steinle-Neumann, in collaboration with B.P. Burton/Gaithersburg and A. van de Walle/Pasadena)*

Transition metal carbides have extremely high melting points and are therefore referred to collectively as the “refractory carbides.” In addition to their stability at high temperatures, these compounds exhibit interesting physical properties such as high hardness, high electrical conductivity and superconductivity. These properties make them suitable as bulk or thin film materials in many technological applications. They are used as first-wall coatings for fusion reactors, protective coatings for cutting tools, and low-friction coatings for bearings. Their hardness is retained to very high temperatures, and they have low chemical reactivity.

Experimental investigations of the phase diagrams of pseudobinary systems formed by non-stoichiometric compounds are extremely difficult. It is almost impossible to find by experimental means the position of the liquidus line in a system formed by compounds with melting points of 3000 K and higher or to find in such a system a latent solid-phase decomposition region. At the same time, calculations make it possible to establish the shape of the phase diagram to a sufficient degree of accuracy if the dependence on temperature and composition of the parameters describing the interaction in the system is known. Several semi-empirical methods exist to construct phase diagrams based on approximate free energy functions fitted to existing thermodynamic data such as the model of subregular solutions, which takes into account the dependence on temperature and composition of the interchange energies in the different phases. Hence these methods are all useful to obtain phase diagrams and thermodynamic functions strictly from knowledge of the constituent atoms. Such a first principles approach to calculating the phase diagrams of compounds has long been a goal for computational material physics and faces enormous challenges. In order to calculate phase equilibria the Gibbs free energy must be known for the competing structures over a wide range of concentrations. The energies of formation for a large number of phases over a range of stoichiometries need to be determined.

In the present study, we have used first-principle phase diagram calculations in order to study the HfC-TiC, ZrC-TiC and HfC-ZrC solid solutions. A first principles calculation seeks to determine the properties of a material without relying on any experimental input, starting solely from the knowledge of the atomic number of the constituents. Here we have used the Alloy Theoretic Automated Toolkit (ATAT), which takes in account configurational and vibrational contributions to free energy. Our calculations predict miscibility gaps in the quasibinary systems HfC-TiC, TiC-ZrC, and HfC-ZrC (Fig. 3.9-14) with consolute temperatures (the maximum temperature of the miscibility gap)  $T_C$  of 2120K, 2695K, and 238K, respectively. Miscibility gaps are approximately symmetric in the phase diagram for HfC-TiC and asymmetric in the phase diagrams for HfC-ZrC and TiC-ZrC. The reductions in  $T_C$  induced by the inclusion of vibrational contribution to the free energy result in considerably improved agreement with available experimental data.

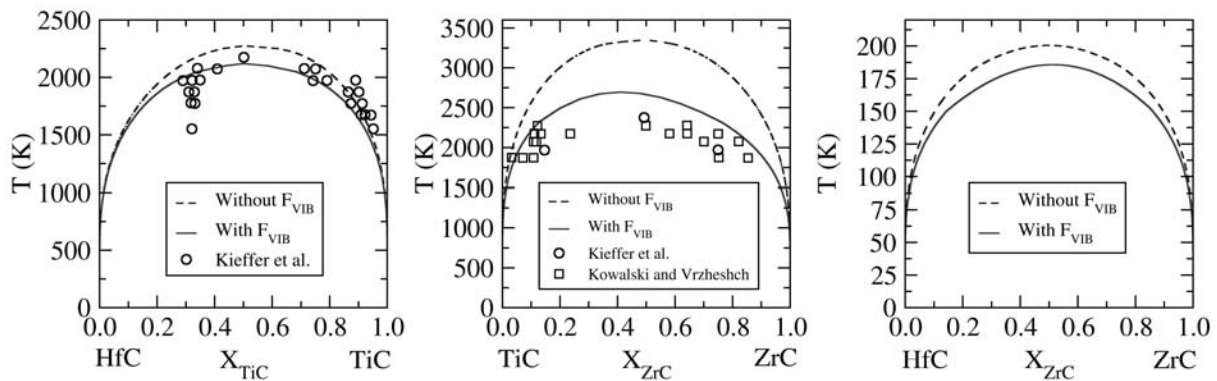


Fig. 3.9-14: Calculated phase diagrams for the systems: (a) HfC-TiC, (b) TiC-ZrC, and (c) HfC-ZrC. Dashed curves are for calculations that did not include  $F_{vib}$ , and solid curves are for calculations that did. Symbols show different experimental data.

**j.** *Pressure-induced modifications of crystal and magnetic structure of  $La_{0.33}Ca_{0.67}MnO_3$  (D.P. Kozlenko/Dubna, L.S. Dubrovinsky, B.N. Savenko/Dubna and V.I. Voronin/Ekaterinburg)*

Perovskite manganites  $R_{1-x}A_xMnO_3$  ( $R$  – rare earth,  $A$  – alkali earth elements) exhibit a rich variety of fascinating physical phenomena extensively studied during last years – colossal magnetoresistance, charge and orbital ordering, and mesoscopic phase separation. In compounds  $R_{1-x}Ca_xMnO_3$  ( $R = La, Pr, Nd$ ) with a small average ( $R,A$ ) site ionic radius  $\langle r_A \rangle$  charge localization effects become pronounced and for  $x$  values corresponding to ideal ratios of  $Mn^{3+}$  and  $Mn^{4+}$  ions - 1:1, 2:3, etc. a number of more complicated charge ordered (CO) AFM ground states occur – CE-type AFM ( $x = 0.5$ ) and “wigner-crystal” (WC,  $x = 0.67$ ) AFM ones. Recently we found that the CE-type AFM state remains stable in  $La_{0.5}Ca_{0.5}MnO_3$  with increasing  $T_{CO}$  and  $T_N$  values at high pressure, resulting in a monoclinic distortion of the crystal structure. Unlike half-doped systems, the high-pressure effects on manganites with more complex AFM states realized for  $x \sim 2/3$  remain unexplored. In the present X-ray and

neutron diffraction study of the crystal and magnetic structures of  $\text{La}_{0.33}\text{Ca}_{0.67}\text{MnO}_3$  compound with the largest  $T_{\text{CO}} = 260$  K for  $\text{La}_{1-x}\text{Ca}_x\text{MnO}_3$  family we demonstrate that the WC AFM state is remarkably unstable at high external pressure and completely destroyed in favor of C-type AFM state, which is a ground state for manganites with larger radii  $\langle r_A \rangle$ .

At high pressures up to 50 GPa,  $\text{La}_{0.33}\text{Ca}_{0.67}\text{MnO}_3$  exhibits strongly anisotropic compression of pseudo-tetragonal character with the most compressible  $b$ -axis of the orthorhombic structure of  $Pnma$  symmetry (Fig. 3.9-15).

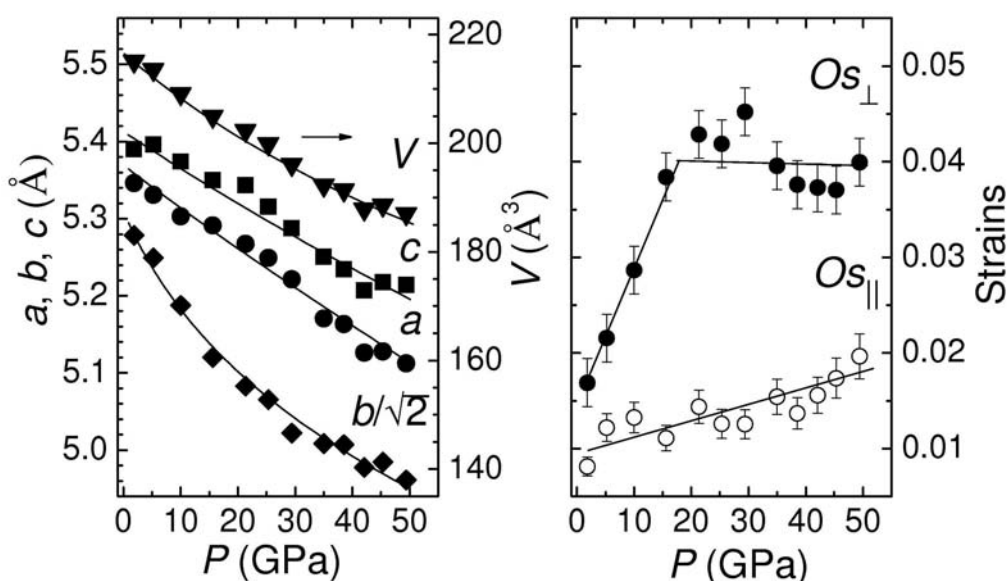


Fig. 3.9-15: Lattice parameters, unit cell volume and orthorhombic strains of  $\text{La}_{0.33}\text{Ca}_{0.67}\text{MnO}_3$  as function of pressure at ambient temperature.

The compression anisotropy can be characterized by “orthorhombic” strains  $Os_{\parallel} = 2(c-a)/(c+a)$  in the  $(ac)$  plane and  $Os_{\perp} = 2(a+c-b\sqrt{2})/(a+c+b\sqrt{2})$  along the  $b$  axis. The  $Os_{\parallel}$  increases nearly linearly under pressure, while  $Os_{\perp}$  grows more rapidly and exhibits a slope change at  $P \sim 20$  GPa.

In neutron diffraction patterns at ambient pressure a coexistence of the WC and C-type AFM phases with similar volume fractions was observed. At  $P \geq 2$  GPa on cooling the intensity of the strongest magnetic lines  $(2/3 \ 1 \ 1/2)$  and  $(1/3 \ 1 \ 1/2)$  from the WC AFM state ( $T_{\text{N}} = 140$  K) were fully suppressed, while the intensity of the  $(1/2 \ 1 \ 1/2)$  magnetic line from the C-type AFM state increases noticeably (Fig. 3.9-16). This corresponds to the total suppression of the WC AFM state in favor of the C-type AFM one. The value of the ordered magnetic moment at  $T = 10$  K is about the same,  $\mu_{\text{C}} \approx 2.2(1) \mu_{\text{B}}$ , over a 2-5 GPa pressure range. The  $T_{\text{N-C}}$  value increases significantly from 155 to 235 K in 0-2 GPa pressure range. No further changes in

diffraction patterns were found at high pressures up to 5 GPa, indicating the stability of the C-type AFM state.

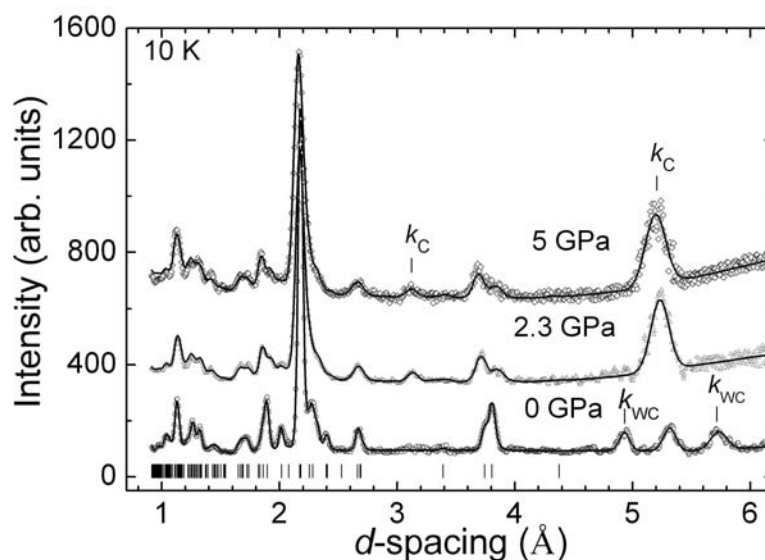


Fig. 3.9-16: Neutron diffraction patterns of  $\text{La}_{0.33}\text{Ca}_{0.67}\text{MnO}_3$  at different pressures and  $T = 10 \text{ K}$ , processed by the Rietveld method.

**k.** *Raman spectroscopic study of  $\text{PbCO}_3$  at high pressure and temperature (R. Minch/Kiel, L.S. Dubrovinsky and A. Kurnosov)*

A high P-T Raman spectroscopic investigation of cerussite has been carried out up to 17.2(2) GPa. The high-pressure Raman spectra in the  $100\text{-}1200 \text{ cm}^{-1}$  frequency range were collected using a LABRAM system spectrometer (BGI, Bayreuth) with a 514.5 nm  $\text{Ar}^+$  ion laser as the excitation light source. The spectra were obtained using the standard diamond anvil cell (DAC) technique, a 25x microscope objective and three accumulations with 60 s integration time. Neon was used as pressure transmitting medium.

Two pressure induced phase transitions were observed at about 8.0(2) and 7.0(2) GPa, respectively. The post-aragonite transition at 8.0(2) GPa is accompanied by the mode softening of the  $\nu_2$ -out-of-plane band of  $\text{CO}_3^{2-}$  group and disappearance of the  $\text{B}_{1g}$  ( $\nu_4$ -in-plane band of  $\text{CO}_3^{2-}$  group) mode. The increased mode shifts of the carbonate vibrations after the phase transition suggest that the new structure is more compressible. The formation of the second high-pressure polymorph begins at about 10 GPa. It is accompanied by the occurrence of 3 new peaks at different pressures and splitting of the  $\nu_1$ -symmetric C-O stretching of  $\text{CO}_3^{2-}$  group. The transitions are reversible when pressure was released. A semi-quantitative phase diagram for  $\text{PbCO}_3$  as a function of pressure and temperature is proposed (Fig. 3.9-17).

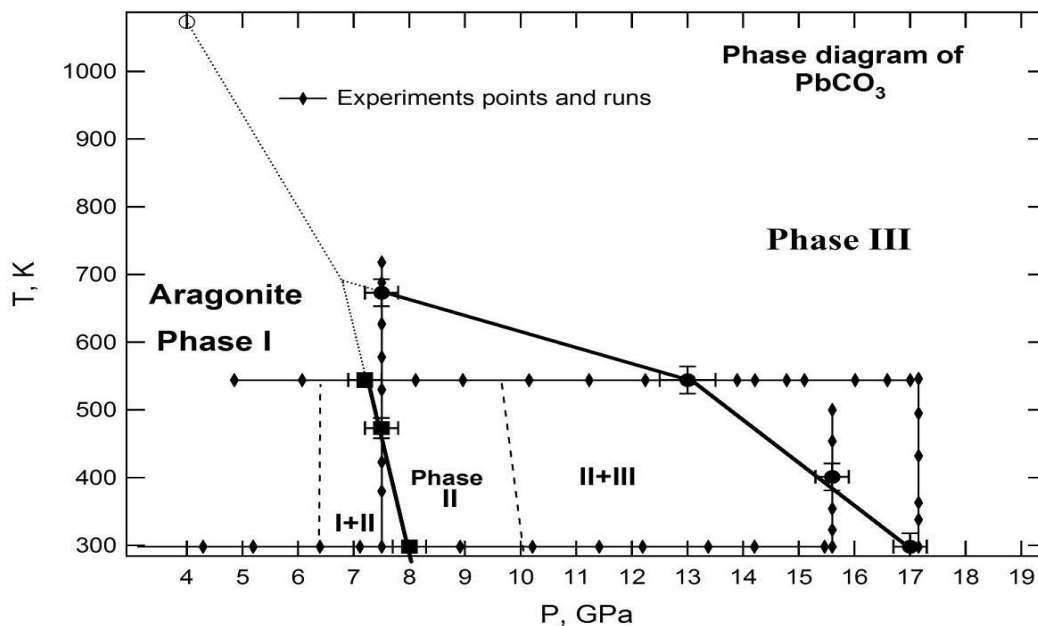


Fig. 3.9-17: A model of the tentative phase diagram of the lead carbonate. I - orthorhombic phase at ambient conditions; II - new high-pressure phase; III - high-pressure phase ( $P2_122$  or  $P-3c$ ). Open circle denotes literature data. Closed connected rhombuses denote conditions at which experiments were run. The heavy solid lines are the supposed phase boundaries. The dashed lines indicate continuation of phase boundaries outside the field of our data and the I-III phase boundary.

**I. High-pressure effect on the formation of layered lithium cobaltates with Li occupying the Co-site (R. Stoyanova, E. Shinova and M. Yoncheva/Sofia; C.A. McCammon and T. Boffa Ballaran)**

Lithium cobaltates,  $\text{LiCoO}_2$ , have been considered as materials of great scientific importance due to their high-power lithium ion batteries application. The structure of  $\text{LiCoO}_2$  consists of  $\text{CoO}_2$ -layers composed by edge-sharing  $\text{CoO}_6$ -octahedra. The same triangular  $\text{CoO}_2$ -layers form also building blocks in sodium cobaltates  $\text{Na}_x\text{CoO}_2$ . However, only  $\text{Na}_x\text{CoO}_2$  displays thermoelectric properties. In order to understand the unusual physical properties of alkaline cobaltates, there is a need for detailed structural investigations in the Li-Co-O systems.

The project is focused on the high-pressure preparation of novel compositions in the Li-Co-O systems having Li-to-Co ratios higher than 1,  $\text{Li}_{1+x}\text{Co}_{1-x}\text{O}_2$ . By variation of the Li content, it is possible to change the number of conduction electrons in the triangular Co-layers, which will induce new electrical and magnetic properties.

The target compositions were prepared by solid state reaction between  $\text{Li}_2\text{O}_2$  and  $\text{Co}_3\text{O}_4$  spinels under high pressure (up to 3 GPa) using the piston cylinder type apparatus. The use of  $\text{Li}_2\text{O}_2$  ensures an  $\text{O}_2$  rich environment during formation of  $\text{Li}_{1+x}\text{Co}_{1-x}\text{O}_2$ . If the Li-to-Co ratio

in the precursor mixture is lower than 1.2,  $\text{LiCoO}_2$  with layered crystal structure is obtained (Fig. 3.9-18). The incorporation of extra Li into  $\text{LiCoO}_2$  leads to the increase in the mean  $\text{Co(Li)-O}$  bond length. By increasing the Li-to-Co ratio in the precursor mixture, a new structural modification is obtained. The crystal structure can be described as spinel modification, where Li and Co occupy 16d and 16c spinel positions (Fig. 3.9-18). The refinement of the structure is slightly improved if a small amount of Li occupies the Co-site. However, the exact amount of Li incorporated into the Co position is difficult to quantify from X-ray data due to low scattering factor of Li. Note, that when oxide is prepared at atmospheric pressure the incorporation of Li in  $\text{LiCoO}_2$  by formation of  $\text{Li}_{1+x}\text{Co}_{1-x}\text{O}_2$  spinels is limited.

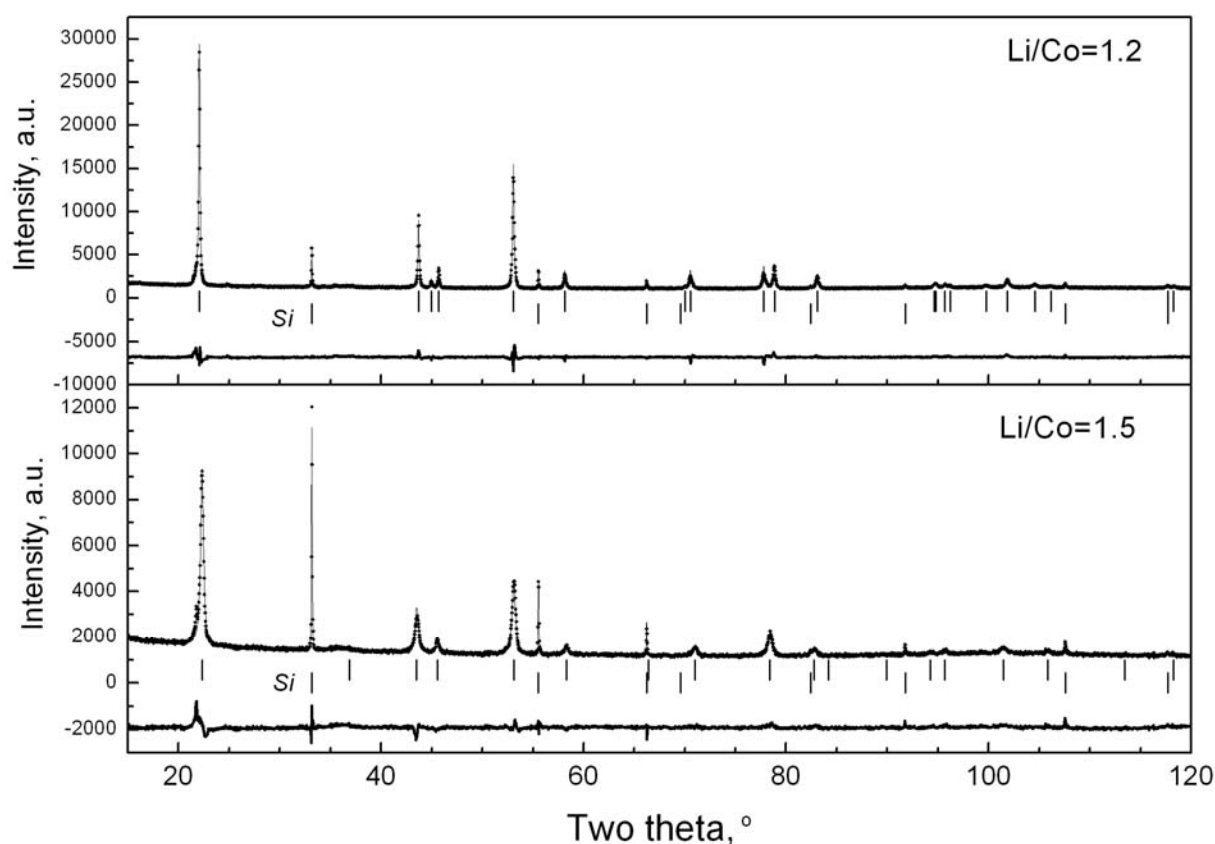


Fig. 3.9-18: X-ray diffraction patterns of layered and spinel  $\text{Li}_{1+x}\text{Co}_{1-x}\text{O}_2$  modifications obtained at 700 °C under 3 GPa from the precursors with Li/Co=1.2 and 1.5, respectively.

**m.** *Elastic behaviour of lithium fluoride under high pressure (A. Kantor, L.S. Dubrovinsky, in collaboration with I.Yu. Kantor, V. Prakapenka, S. Sinogeikin/Chicago)*

Lithium fluoride is used as an internal pressure standard for high-pressure experiments in the diamond anvil cell (DAC). Advantages of lithium fluoride are its high chemical stability and transparency in a wide optical spectral range. It can also be used as a thermal insulator in

laser-heating DAC experiments. LiF shows no structural transitions at least up to 100 GPa (it remains in a cubic B1 structure) and, therefore, LiF single crystals can be used for the construction primary pressure scale that goes to much higher pressures than in case of the widely used NaCl that has a phase transition at 30 GPa. In addition, LiF absorbs significantly less water from air than hygroscopic NaCl. A single crystal LiF was studied at pressures up to 20 GPa with on-line Brillouin spectroscopy combined with high resolution micro X-ray diffraction technique (for details see *Rev. Sci. Inst.* 77, 103905, 2006) at GSCEARS (Sector 13, Advanced Photon Source, Argonne, USA). The 20 microns thick LiF sample was loaded in a DAC along with Ne pressure transmitting medium. Brillouin spectra were collected at room temperature and elevated pressures using a 80° platelet scattering geometry. Fig. 3.9-19 shows an example of a Brillouin spectrum, collected at 6.3 GPa. Diffraction data were collected at each pressure point to determine unit cell volume and density of the sample. The elastic constants of LiF are found to be as follows:  $C_{11}=113.05$  GPa,  $C_{12}=47.86$  GPa and  $C_{44}=62.82$  GPa with a measured density of  $2.61 \text{ g/cm}^3$ . Pressure derivatives of the elastic constants are 11.3, 3.5 and 0.03, respectively.

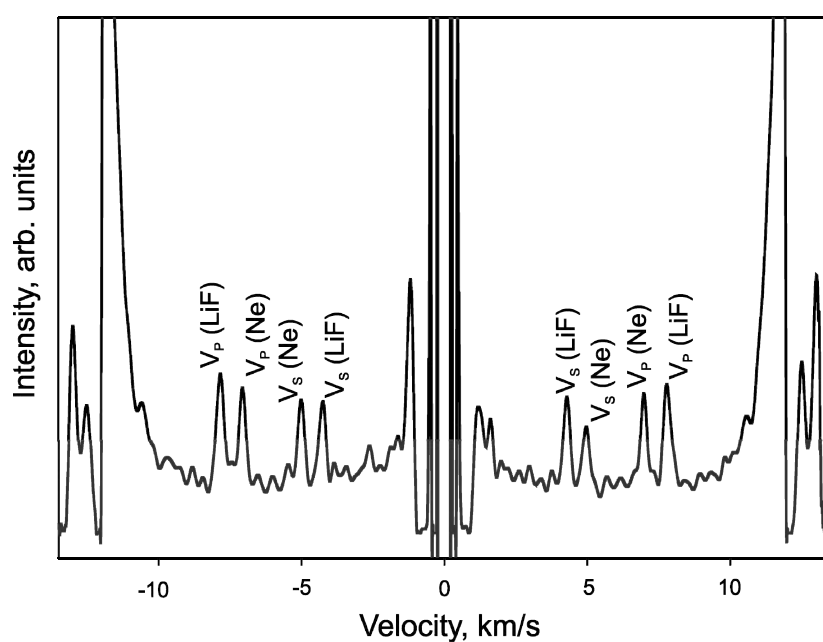


Fig. 3.9-19: Brillouin spectrum of a single crystal LiF standard collected at 6.3 GPa.

**n.** *High-pressure crystallization of semi-crystalline polypropylene* (S. Mazzullo and A. Fait/Ferrara, T. Boffa Ballaran, C.A. McCammon)

The effect of pressure on phase change transition of semi-crystalline polymers during cooling from the molten state was examined both experimentally and on the basis of a mathematical model. The reference experimental data are the so-called Pressure-Volume-Temperature (PVT) state diagrams, typically obtained at near equilibrium cooling rate of  $1 \text{ }^\circ\text{C/min}$  from the molten state and at pressures up to 1.5 kbar. Our modeling effort was aimed, mainly, at

identifying a state equation, resembling a *van der Waals* equation, capable to describe the experimental state diagrams. In this model the pressure appears, explicitly, in the equation describing the specific volume of the polymer, while it also affects, implicitly, other thermodynamic parameters of the polymer, that is, the equilibrium melting temperature  $T_m$ , the glass transition temperature  $T_g$  and the kinetic constant of crystallization  $k(T)$ . The theoretical model suggests that similarly to real fluids described by the *van der Waals* equation, semi-crystalline polymers could display a critical tern ( $P^*, V^*, T^*$ ) at which the phase change could take place without volume variation, provided:  $dT_g/dP > dT_m/dP$ . This condition means that the rate of variation of  $T_g$  is higher than the rate of variation of  $T_m$  with respect to pressure. The experimental confirmation of this theoretical prediction could open unexpected practical applications in the technology of polymer processing.

In order to validate the model predictions, 13 crystallization experiments in piston-cylinder apparatus on polypropylene were performed at pressures of 1.0, 4.1, 7.0, 9.9, 15.5 and 40.0 kbar. The experimental procedure was as follows: an isobaric experiment was started at an initial temperature of 250 °C and then automatically cooled down at 1 °C/min to 100 °C. The material studied was broad molecular weight homo-polymer (Melt Index = 2.8) synthesized by succinate-based Ziegler-Natta catalyst. In order to minimize the dead space in the Pt sample holder, polymer pellets were previously prepared by extrusion, with an outside diameter that matched with the internal diameter of the Pt capsule. All samples, after the BGI isobaric experiments, were analyzed off-site, at the Lyondell Basell R&D Centre of Ferrara, in terms of wide angle X-ray diffraction (WAXRD), differential scanning calorimetry (DSC) and optical microscopy under polarized light. The results of the analyses can be summarized by the help of a (T,P) state diagram (Fig. 3.9-20) in which, besides the experimental points, we plotted also the inclined straight lines of the provisional pressure variation of the equilibrium melting temperature, crystallization-solidification temperatures and glass transition temperature, with a slope coherent with the off-site analyses. The position of the first sample point, at 1.0 kbar, is slightly above the equilibrium melting temperature at that pressure and, coherently, it gives rise to the formation of  $\beta$ -form spherulite (average size 200 microns), because compressive strain was applied to the melt for a longer time with respect to the rest of experiments. The position of the second sample point, at 4.1 kbar, is between the equilibrium melting temperature and the crystallization temperature at that pressure. Under these conditions we observe the formation of  $\alpha$ -form type I spherulites (average size 300 microns) and a relatively high enthalpy of first run DSC melting. The position of the third sample point, at 9.9 kbar, is midway between the solidification temperature and the glass transition temperature at that pressure and, coherently, it gives rise to the formation of crystallographic  $\gamma$ -form, because of the presence of compressive strain in the solid. For the first time we also obtained an extremely high enthalpy of first run DSC melting associated to an unusually high DSC peak melting temperature. The morphology shows either type I spherulites (average size: 40 microns), or cooperative crystallization of elongated monorifringent spherulites (average size: 50 microns). The position of the fourth sample point, at 15.5 kbar, is across the glass transition temperature at that pressure. Coherently, it still allows residual solid/solid crystallization, while it essentially behaves like a rigid body, maintaining

the  $\alpha$ -form structure of the stress free sample. The position of the fifth sample point, at 40.0 kbar, is well below the glass transition temperature at that pressure and, coherently, it behaves like a rigid body, essentially, maintaining the  $\alpha$ -form structure of the stress free sample, in terms of enthalpy of melting and DSC peak melting temperature. Contrary to expectations, the off-site analyses are better represented in the light of the scenario in which the pressure derivatives of  $T_g$  and  $T_m$  are equal:  $dT_g/dP = dT_m/dP = 23 \text{ }^\circ\text{C/kbar}$ .

Once this preliminary result is confirmed by a specific campaign of further experiments aimed at this purpose, we could definitely conclude that pressure affects crystallization of polypropylene only by shifting the crystallization window to higher temperatures.

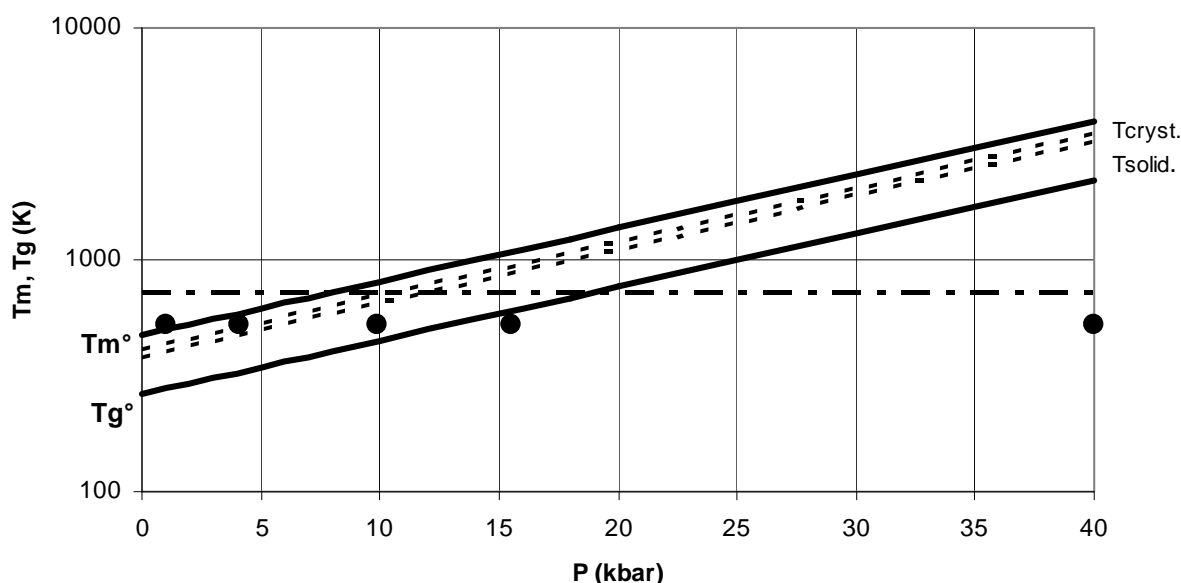


Fig. 3.9-20: State diagram of polypropylene. Provisional identification of the pressure variation of equilibrium melting temperature  $T_m$  and glass transition temperature  $T_g$  equal the one to the other:  $dT_m/dP = dT_g/dP = 23 \text{ }^\circ\text{C/kbar}$ , based on experiments (circles) and  $T_m^\circ$ ,  $T_g^\circ$  at room pressure. The horizontal dotted line indicates the pyrolysis temperature of polypropylene.

**o. Catalytic oxidative dehydrogenation of ethylbenzene on nanocrystalline iron oxides and carbon nanotubes (K. Pollok, in collaboration with B. Nigrovski, P. Scholz, M. Müller and B. Ondruschka/Jena)**

Styrene is an important chemical, used for the production of styrene polymers and copolymers, like polystyrene, styrene–butadiene rubber and acrylonitrile–butadiene–styrene. The catalytic dehydrogenation of ethylbenzene to produce styrene accounts for > 90 % of the world capacity, with 25 million tons of monomer produced annually. In industrial production the catalysis is realized at high temperature (600-700  $^\circ\text{C}$ ) using a hematite catalyst and other promoting compounds. Alternative developments look for catalysts with high selectivity and long term stability combined with low manufacturing and energy costs.

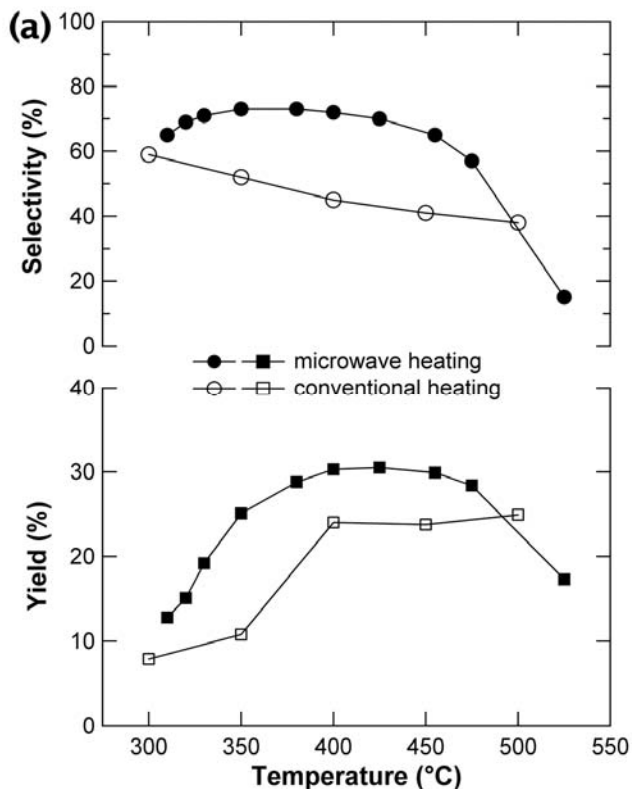
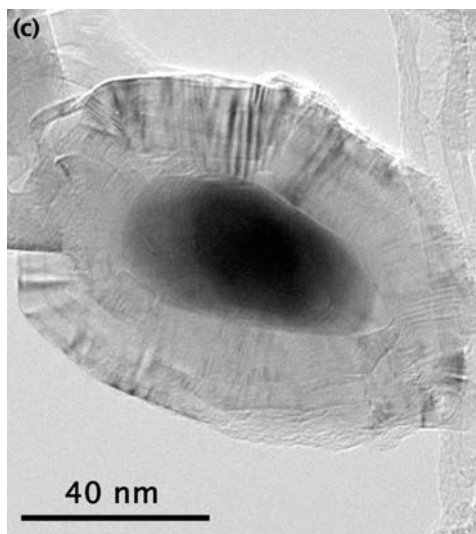
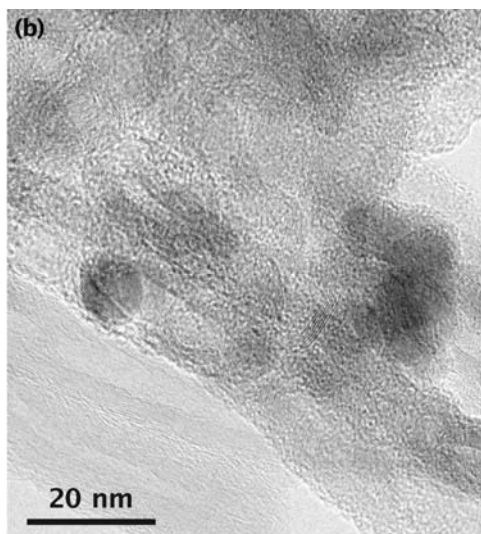


Fig. 3.9-21: (a) Effect of reaction temperature in oxidative dehydrogenation of ethylbenzene over a MWCNT catalyst loaded with 3 wt.% iron oxide on styrene selectivity and yield. (b) HRTEM image of the catalyst after conventionally heated reaction with disordered carbon at the nanotube walls and unreacted hematite nanocrystals. (c) HRTEM image of iron metal encapsulated by newly formed polyhedral graphite shells.



The catalytic performance of multi-walled carbon nanotubes (MWCNTs) modified by nanocrystalline iron oxides has been investigated for oxidative dehydrogenation of ethylbenzene in an integral fixed-bed reactor conventionally-heated and under microwave-assisted conditions (Fig. 3.9-21). The morphology and microstructural characteristics of the obtained composites before and after the catalytic reaction were characterized by transmission electron microscopy and X-ray diffraction. A content of 3 wt.% hematite with a particle size of 10 nm supported on MWCNTs was found optimal in respect of the ethylbenzene conversion and styrene selectivity. All prepared composites were found more selective in a

microwave field in the temperature range 380-450 °C. For the conventionally heated process a deposition of highly disordered carbon at the outer surface of the nanotubes has been found (Fig. 3.9-21b) which is well known to exhibit a lower catalytic selectivity. In contrast, microwave heating leads to the conversion of hematite into Fe nanocrystals encapsulated by highly-ordered, polyhedral graphite shells that provide active sides for the gas phase and increase the selective properties of the catalyst (see Fig. 3.9-21c).

### 3.10 Methodological Developments

The development of novel experimental and analytical techniques represents one of the backbones of modern geoscience. Although such developments typically are time- and cost-intensive, they are well worth pursuing because they allow fundamental breakthroughs which are necessary to compete at high scientific level. The emphasis this year was on diamond anvil cell techniques, fluid inclusion synthesis and numerical modeling.

A new, portable laser heating system for diamond anvil cells allows this equipment be moved easily from one analytical facility to the other. This is of particular importance for *in situ* studies by synchrotron radiation, as only very few beamlines worldwide are equipped with (stationary) laser heating systems. Another major improvement is represented by the development of a new resistive heated diamond anvil cell with full 90° solid angle opening from both sides, allowing simultaneous sample characterization by both optical spectroscopy and X-ray scattering techniques. In the field of fluid geochemistry a new method was developed to synthesize large fluid inclusions at conditions at which one normally would obtain only very small inclusions, with the additional advantage that the fluid can be trapped after a specific time of pre-equilibration. Furthermore, a new numerical code for modeling geodynamic processes in 2D is presented which allows complex scenarios be modeled at comparatively low computational cost on simple desktop computers.

**a.** *Portable laser heating system for diamond anvil cells (L.S. Dubrovinsky, K. Glazyrin, O. Narygina and C.A. McCammon; N.A. Dubrovinskaia/Heidelberg and J. Bock/Gaggenau)*

The diamond anvil cell (DAC) technique initiated in the late 1950s provides many opportunities for high-pressure researchers dealing with Mössbauer, infrared and Raman spectroscopy, resistivity measurements, X-ray diffraction and inelastic scattering. During the last few decades, the DAC technique has become the most successful method of pressure generation capable for working in the multimegabar pressure range. However, there are still a number of problems related to high-temperature experiments in DACs. There are two major methods of heating in DACs – laser and electrical. Electrical heating is very efficient at temperatures below ~1000 K at pressures over 250 GPa, but experiments become very demanding if higher temperatures are required. Laser heating techniques cover a wide P-T field:  $P > 200$  GPa,  $T = 1300$ -5000 K. The sample preparation for laser-heating experiments is relatively easy and there is practically no risk to the diamonds due to heating. There are numerous DAC laser heating facilities in geo-, material-, physics- and chemistry-oriented laboratories (including BGI), and there are a number of examples of successful coupling of an *in situ* laser-heating system with synchrotron radiation facilities, including specialized beamlines at European Synchrotron Radiation Facilities (ESRF), Advanced Photon Source (APS), and at Spring-8. However, so far all existing DAC laser-heating systems are stationary, they are linked either to certain equipment (an optical or Raman spectrometer, for example) or a beam-line. Studies of various physical properties and chemical reactions at high pressures and temperatures in diamond anvil cells require mobility of the laser-heating system, for example,

the ability to move laser heating equipment (preferably together with the same DAC, at the same pressure) between different analytical facilities, including transfer from in-house to a synchrotron. We have developed a portable laser heating system for DACs.

The system consists of two major components – the source of the laser light (in our case it is a 100 W Modulated High Power Fiber Laser SPI100, SPI Lasers UK Ltd., with a weight of 40 kg) and the universal laser-heating head (UniHead) (Fig. 3.10-1). The UniHead is based on the finite cutting laser head produced by Precitec KG (Germany) (weight of about 4.5 kg).



Fig. 3.10-1: The Universal laser-heating head (UniHead) mounted at ID18 beam line at ESRF (see inset) for nuclear inelastic scattering experiments in diamond anvil cells (1 – the connector for SPI100 fiber laser, 2 – the illumination unit, 3 – the lenses unit for focusing of the incoming laser light, 4 – the digital video camera, 5 – the module for spectroscopic measurements, 6 – the diamond anvil cell mounted inside the holder).

The functions of the UniHead are to focus incoming laser light on the sample within the DAC, to provide illumination by white light for sample observation, and to give access for various optical spectroscopic measurements (multiwavelength spectroradiometry, ruby fluorescence measurements, Raman spectroscopy, etc.). For focusing of the 1064 nm laser radiation, the UniHead employs a bending mirror and a set of lenses with the 50 mm working

distance. The position of the mirror and the lenses can be adjusted in order to achieve an optimum (circular) beam shape and its centering with respect to the optical axis of the instrument. Illumination of the sample is achieved due to a built-in halogen 50 W lamp. For observation of the sample in the DAC and for the process of laser-heating we use a high-resolution GiqE uEye™ (SUXGA, 2048x1536) digital camera. The module for spectroscopic measurements includes an objective for coupling with an optical fibre mounted on a small 3D stage, a lens with a 100 mm focal distance on an adjustable mount, and a bifurcated optical fibre. One end of the fibre is connected to a small solid-state 100 mW 532 nm laser (used for exciting ruby fluorescence), and another one is attached to the Ocean Optics QE65000 spectrometer. (That could be used either for ruby fluorescence measurements, for measurements of thermal radiation emitted by a laser-heated sample, or for Raman spectroscopy in a laser-heated cell.)

The portable laser heating system has been successfully used at BGI in-house for routine DAC experiments as well as DACs coupled with Mössbauer spectrometer. Moreover, the portable laser-heating system was transferred to ESRF (Grenoble, France) for experiments at the beam-line ID18. The nuclear inelastic scattering (NIS) of the iron-nickel alloy  $\text{Fe}_{0.9}\text{Ni}_{0.1}$ , ferropicalase ( $\text{Mg}_{0.875}\text{Mg}_{0.125}\text{O}$ ), and silicate perovskite ( $\text{Mg}_{0.88}\text{Fe}_{0.12}\text{SiO}_3$ ) was studied at pressures over 100 GPa and temperatures up to 1500 K. Figure 3.10-2 shows an example of the NIS spectra of ( $\text{Mg}_{0.88}\text{Fe}_{0.12}\text{SiO}_3$ ) perovskite at 75(2) GPa and 1100(50) K (temperature determined from intensities of Stoke and anti-Stoke parts of the spectra).

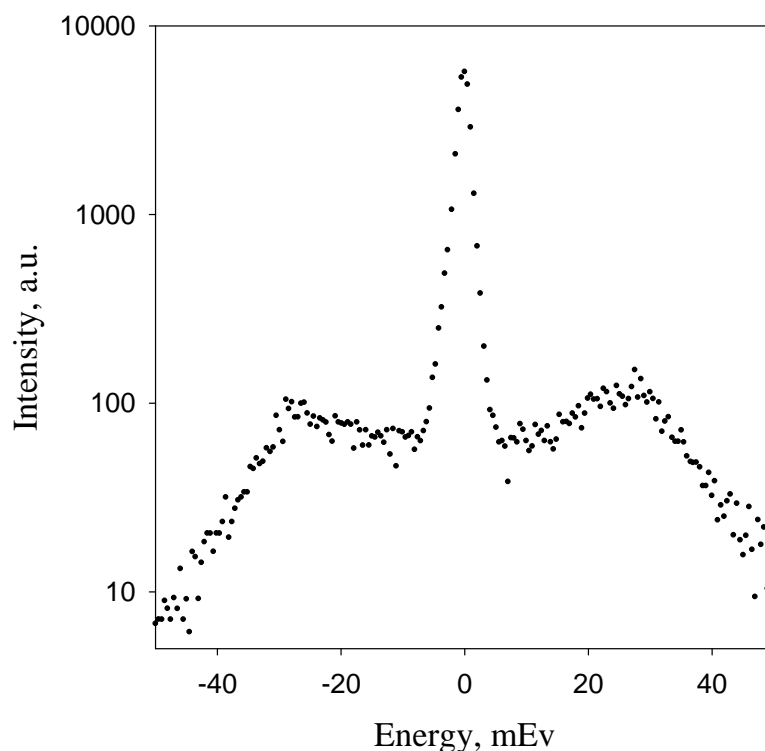


Fig. 3.10-2: Nuclear inelastic scattering spectrum of silicate perovskite ( $\text{Mg}_{0.88}\text{Fe}_{0.12}\text{SiO}_3$ ) at 75(2) GPa and 1100(50) K collected at the ID18 beam line at ESRF (Grenoble, France) in a laser-heated diamond anvil cell.

**b. Universal diamond anvil cell for combined optical and X-ray studies (I.Yu. Kantor, in collaboration with V. Prakapenka and P. Dera/Chicago; L.S. Dubrovinsky)**

We made a new design of a diamond anvil cell (DAC). The main purpose of the new resistive heater ready symmetrical DAC is its universal application for *in situ* studies of materials in the Mbar pressure range with a combination of different techniques: optical spectroscopy (Brillouin scattering, optical absorption etc), conventional Mössbauer and high-resolution X-ray scattering (powder, single crystal and non-crystalline materials). One of the main requirements for optical spectroscopy experiments as well as for X-ray scattering techniques is to provide the widest optical angular access to the sample as possible. The new DAC (called BX-90 – Brillouin and X-ray 90-degrees opening cell) has full 90° solid angle opening from both sides.

BX-90 (Fig. 3.10-3a) cell has a symmetric piston (3)-cylinder (4) construction that provides the highest stability at high loadings needed for Mbar pressure range experiments. Together with the Belleville disc spring washers (5) on four compression screws (6) it guarantees very smooth and parallel movement of diamond anvils (1) and significantly reduces the risk of diamond breakage at very high pressures. The location of the internal screws provides large enough space around the sample to mount a resistive electrical heater measuring up to 20 mm in diameter and up to 4 mm thickness, which is impossible for convenient symmetric piston-cylinder DACs. Four side-cuts on the cylinder part give access for the heater and thermocouple wiring, and also prevent the cell from stacking during external heating experiments due to different thermal expansion of the piston and cylinder parts of the DAC as result of temperature gradient.

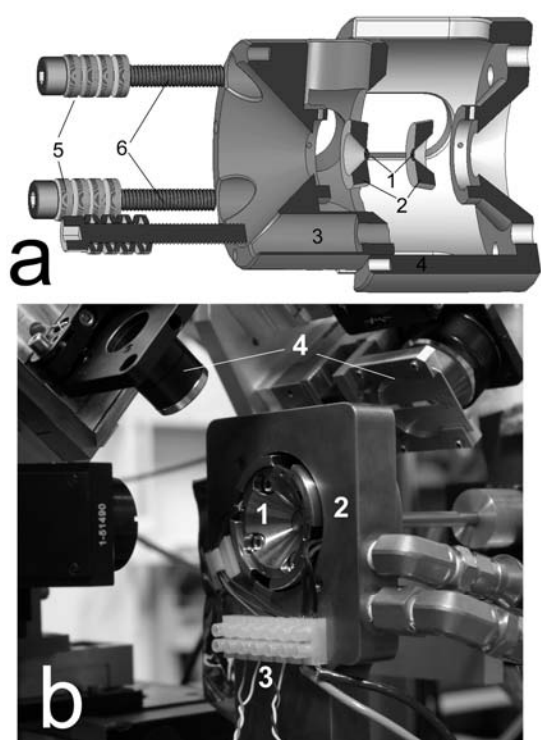


Fig. 3.10-3: Schematic illustration of the BX-90 diamond anvil cell. a) 3D-model section cut of the BOX-90 cell. 1 – diamonds, 2 – supporting plates, 3 – piston part, 4 – cylinder part, 5 – spring Belleville washers, 6 – compression screws. b) Simultaneous X-ray diffraction and Brillouin scattering experiment at high pressure and temperature at GSECARS BMD-13 sector at the Advanced Photon Source. 1 – BOX-90 cell, 2 – water-cooled DAC holder, 3 – heater and thermocouples wires, 4 – Brillouin optics at 80° geometry.

Two first models of the new cell have been manufactured at the Bayerisches Geoinstitut (University of Bayreuth), Germany. During the pilot experiments, pressures over 100 GPa have been reached. Test experiments at GSECARS (APS sector 13 BMD station) also showed high stability during external heating with simultaneous Brillouin scattering and X-ray diffraction measurements (Fig. 3.10-3b).

*c. A method to synthesize large fluid inclusions in quartz at controlled times and under unfavorable growth conditions (Y. Li and A. Audéat)*

Synthesis of fluid inclusions in quartz or other transparent minerals is a popular method to study phase relations, P-V-T-X properties and mineral solubilities in high-P/T fluids. Limitations may be set by the inclusion size (required detection limits may not be reached if the inclusions are too small), and by the fact that fluid can be trapped before it has reached equilibrium with respect to all components of the system. The latter problem has been addressed by the *in situ* fracturing method developed by Mike Sterner in 1992, in which the cracks required for fluid entrapment are generated during the experiment after a certain time of pre-equilibration. However, a disadvantage of this technique is that the resulting fluid inclusions typically are rather small (< 20  $\mu\text{m}$ ), especially if the experiments are conducted at conditions of low quartz solubility. To overcome this drawback we developed a method in which large, primary fluid inclusions are grown at conditions of high quartz solubility, and then are re-opened by *in situ* fracturing during a second experiment at less favorable growth conditions. Here we report the results of a feasibility study in which primary inclusions were produced at 700 °C / 200 MPa, and were re-opened during a second experiment at 500 °C / 70 MPa in the presence of a compositionally different fluid. Both experiments were performed in a cold-seal pressure vessel equipped with a rapid-quench setup. The first experiment was conducted in the presence of an aqueous fluid containing 9.54 wt.% NaCl and ~ 1000 ppm each of Rb, Sr, Cs and Mn, using an etched quartz piece as substrate for fluid entrapment. Because quartz solubility at 700 °C/200 MPa is high, numerous large (> 40  $\mu\text{m}$ ) fluid inclusions formed during this run. The retrieved quartz piece was then sealed with a solution containing 9.6 wt.% KCl and ~ 1000 ppm Ba into a new capsule which was run at 500 °C/70 MPa. After 24 hours of pre-equilibration the capsule was quickly moved from the hot end of the pressure vessel to the cold end, which caused numerous cracks to develop within the quartz piece. The capsule was then moved back to the hot end of the pressure vessel and left there for three days such that the crack generated by *in situ* fracturing could heal. A typical example of a refilled inclusion is shown in Fig. 3.10-4.

In order to quantify the efficiency of fluid replacement in re-opened fluid inclusions we analyzed eight primary and eleven refilled inclusions by Laser-Ablation ICP-MS. The results (Fig. 3.10-5) suggest that in all eleven refilled inclusions the efficiency of fluid replacement was better than 97.5 %, and in eight of them even better than 99 %. Thus, the refilled inclusions contain fluid that is representative of the fluid in the second experiment at the time of *in situ* fracturing. The fluid replacement efficiencies calculated based on Na are systematically higher than those calculated based on Cs, Rb and Sr, which we regard as

evidence that Na was gained from nearby unopened inclusions by diffusion after the refilled inclusions had sealed.

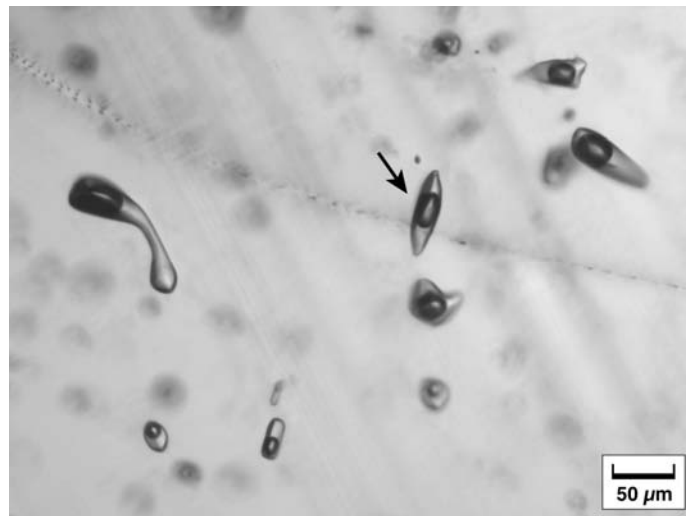


Fig. 3.10-4: Photomicrograph of the quartz sample after the second experiment, showing several primary inclusions and one inclusion that was re-opened by *in situ* fracturing during the second experiment. Note the much smaller size of the fluid inclusions that formed along the crack by simple crack healing (transmitted light).

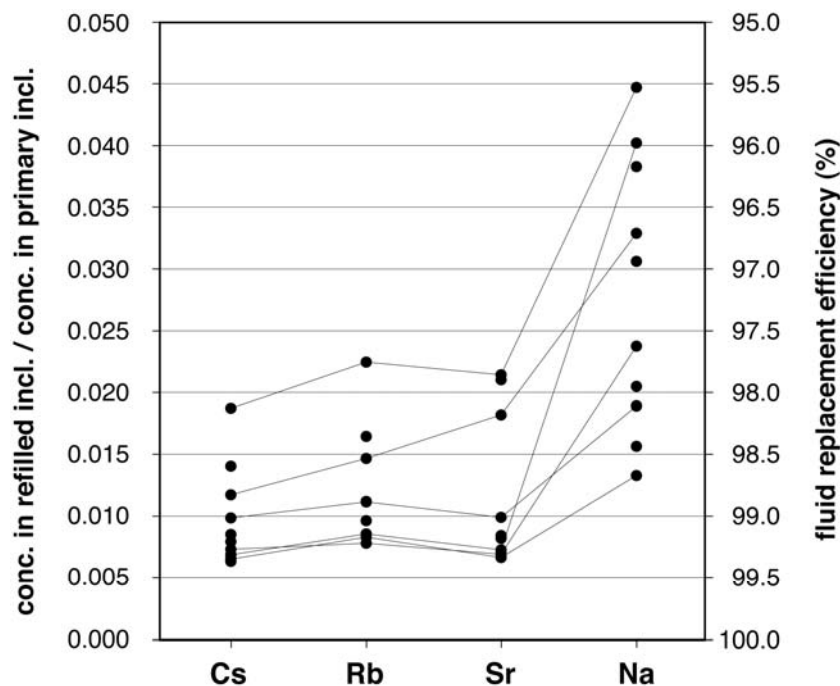


Fig. 3.10-5: Concentration of Cs, Rb, Sr and Na in refilled inclusions normalized to the average concentration of these elements in primary inclusions. The vertical scale on the right indicates corresponding fluid replacement efficiencies in weight percent. Notice that replacement efficiencies calculated based on Cs, Rb and Sr agree well with each other, whereas those calculated based on Na are higher and less systematic.

We conclude that the new method is suitable to trap representative aliquots of fluid in form of large inclusions at conditions under which one normally would obtain only small inclusions, plus it has the advantage that it allows fluid to be trapped after a specific time of pre-equilibration.

**d. *STREAMV*: A fast, robust and modular numerical code for modeling various 2D geodynamic scenarios (H. Samuel)**

Although physico-chemical processes of interest in geosciences occur in 3-dimensional space, many geodynamic situations can be well approximated in 2D space.

While 3D modeling can be achieved in some cases, the obvious advantage (and need) for reducing the number of degree of freedom is the resulting simplicity and the possibility to explore systematically the parameter space at an affordable computational cost.

To this end, I developed *STREAMV*, an Eulerian, particle-in-cell, Finite Difference /Finite Volume numerical code that solves for the conservation of mass, momentum, energy and composition for an incompressible, multi-component viscous fluid:

$$\nabla \cdot \mathbf{U} = 0 \quad (3)$$

$$\frac{1}{Pr} \frac{D\mathbf{U}}{Dt} = -\nabla p + \nabla \cdot (\eta \boldsymbol{\varepsilon}) + (Ra^{local} \mathbf{T} - Rb^{local}) \mathbf{e}_g \quad (4)$$

$$\frac{DT}{Dt} = \nabla \cdot (k \nabla T) + H \quad (5)$$

$$\frac{DC^i}{Dt} = \nabla \cdot (\kappa_c^i \nabla C^i) \quad (6)$$

where the dimensionless quantities  $\mathbf{U}$ ,  $t$ ,  $T$ ,  $p$ ,  $\boldsymbol{\varepsilon}$ ,  $k$ ,  $\kappa_c^i$ ,  $C^i$ ,  $H$ ,  $\mathbf{e}_g$  are respectively, the velocity vector, time, potential temperature, dynamic pressure, deviatoric strain rate tensor, thermal conductivity, composition for material “ $i$ ”, chemical diffusivity of material “ $i$ ”, internal heating, a unit vector aligned in the direction of the gravity field.  $Pr$  is the Prandtl number;  $Ra^{local}$  and  $Rb^{local}$  are thermal and compositional Rayleigh numbers depending on the local composition.

To solve the momentum equation (4) *STREAMV* uses a formal stream function formulation on a staggered grid, which satisfies exactly mass conservation (3) (Fig 3.10-6c). Although the code is Eulerian, it uses Lagrangian tracers for solving the advective part of the conservation of energy and the conservation of composition with a 4<sup>th</sup> order Runge-Kutta integration scheme. This formalism easily allows one to solve accurately Equation (6) for  $\kappa_c^i = 0$  with negligible numerical diffusion. In addition, the Lagrangian tracers can be used to calculate in

real time, stirring properties or anisotropy induced by the flow. Tracers also carry out information on material properties such as viscosity, density, thermal expansion and thermal conductivity. This Eulerian-Lagrangian formalism allows handling very large and sharp contrasts in material properties. For instance, viscosity contrasts of more than five orders of magnitude across a single cell are easily handled by *STREAMV*.

At present state, the code has been successfully benchmarked against analytic solutions or published benchmarks for thermal and thermo-chemical flows with infinite  $Pr$  and constant or variable viscosity.

Figure 3.10-6 illustrates the various possible geodynamic scenarios that can be studied with *STREAMV* such as high Rayleigh Number finite or infinite Prandtl number thermal convection, subduction dynamics, axisymmetric thermal and thermo-chemical plumes, core formation via negative diapirism, long term thermo-chemical mantle evolution, convection with heterogeneous surface stress and temperature boundary conditions.

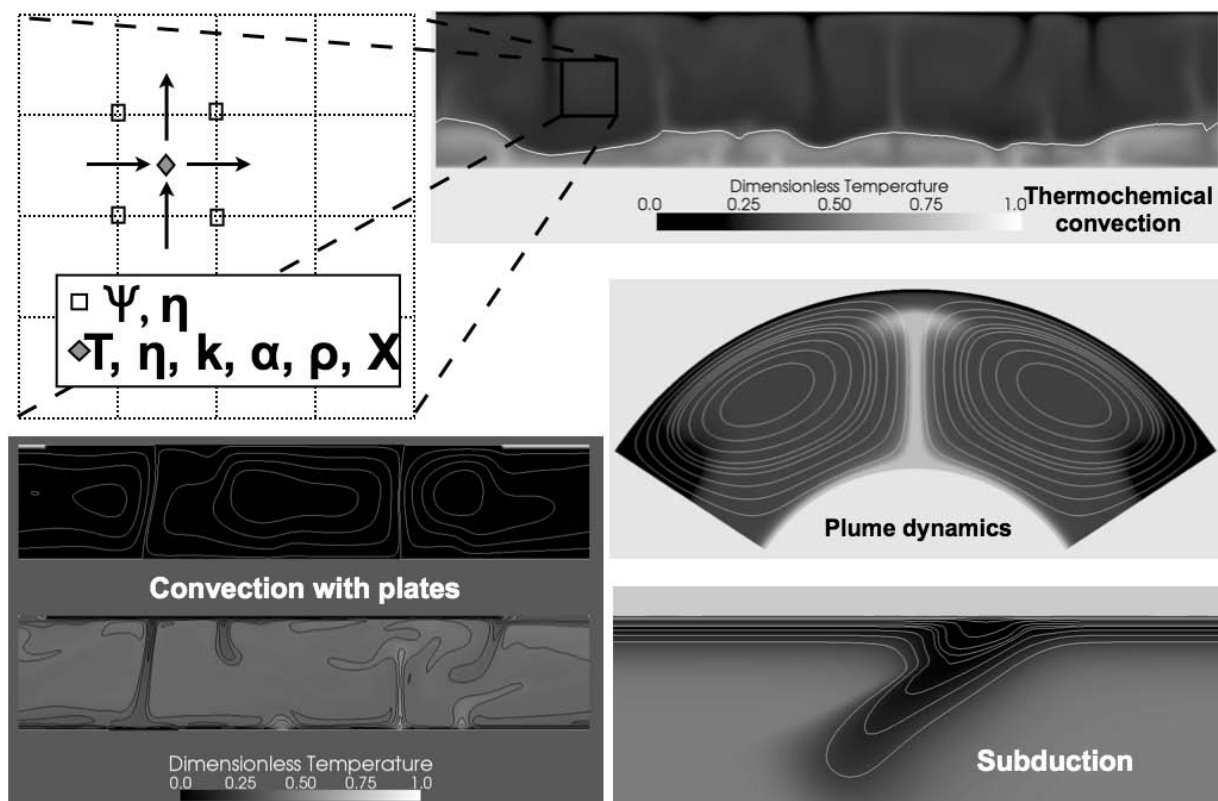


Fig. 3.10-6: Schematic representation of the numerical grid used and examples of geodynamic scenarios modeled with *STREAMV*. The Stream function is defined at nodal points while other scalar values are defined at cell center. Viscosity is defined at both nodal and center cell locations. Velocity components (arrows) calculated from stream function values are then located at center of cell surface, therefore leading to a natural volume-control configuration.

*STREAMV* is written in *FORTRAN 95*, in a modular fashion using operator stencils, making the implementation of various 2D geometries (*e.g.*, cylindrical, axisymmetric) relatively straightforward.

The code uses efficient direct or iterative multigrid methods to solve the governing equations. Although further improvement can be made in these directions, *STREAMV* can solve a million degree of freedom /points in a few minutes on a single processor with enough memory. This means that for most of the geodynamic scenarios mentioned above, the computational time should generally not exceed a few hours on a simple desktop computer.



#### **4. International Graduate School – Elitenetzwerk Bayern/Elite Network of Bavaria "Structure, Reactivity and Properties of Oxide Materials" (OXIDES)**

The interdisciplinary Graduate School is funded by the State of Bavaria and it encompasses three cooperating institutes: Bayerisches Geoinstitut (BGI), Institute of Inorganic Chemistry I (LAC), both in Bayreuth, and the Fraunhofer Institute for Silicate Research (ISC) in Würzburg. These institutes provide their experimental and analytical facilities, complementary expertise in basic and applied material research, and commitment to capitalize on synergies as well as international contacts to other leading research institutes all over the world.

The Graduate School is chaired by Prof. David Rubie, Ph.D. (BGI) and it includes ten other faculty members and one coordinator. Two additional Ph.D. positions became available in this school in 2008 based on the recommendations of an external evaluation committee in 2007. Enrollment in 2008 was eleven doctoral students on a full-time basis at all three institutes (BGI, LAC, ISC) and, in addition, thirteen doctoral students have associate status in the school which provides them with full access to all educational activities. Research projects include element partitioning between silicate materials and core-forming alloys at high pressures, thermodynamics of mantle phases, hydroxyl defects in minerals, synthesis and investigation of new layer silicates as well as experimental and computer simulations of solid and liquid matter.

During 2008, five students have graduated:

<i>Anastasia Kantor</i> (M.A. 2003, Moscow) on 05.02.2008	Elasticity measurements at extreme conditions: application to FeO and FeNi-alloy <u>Supervisors:</u> PD Dr. L. Dubrovinsky, Prof. S. Jacobsen/Chicago
<i>Ashima Saikia</i> (M.Sc. 2002, Delhi) on 06.02.2008	Experimental constraints on silicate perovskite forming reactions and elastic properties: geophysical implications for chemical heterogeneity in the deep mantle <u>Supervisors:</u> Dr. D. Frost, Prof. D. Rubie
<i>Ute Mann</i> (Dipl.-Geol. 2003, Tübingen) on 13.02.2008	Physical and chemical constraints on core-mantle differentiation in terrestrial planets <u>Supervisor:</u> Dr. D. Frost, Prof. D. Rubie
<i>Eva Holbig</i> (Dipl.-Ing. 2005, Berlin) on 29.04.2008	The effect of Zr-doping and crystallite size on the mechanical properties of TiO <sub>2</sub> rutile and anatase <u>Supervisors:</u> PD Dr. L. Dubrovinsky, Dr. G. Steinle-Neumann
<i>Polina Gavrilenko</i> (M.Sc. 2004, Moscow) on 16.10.2008	Water solubility in diopside <u>Supervisor:</u> Prof. H. Keppler, Dr. T. Boffa Ballaran

Three students (*Alexander Baumgartner, Ram Sai Yelamanchili, Alexander Konschak*) have submitted their theses towards the end of 2008.

In 2008 three new students were accepted to the doctoral program:

- |  |   |
|--|---|
| <i>Dunja Hirsemann</i><br>(Dipl.-Chem. 2008, Bayreuth)<br>since 01.04.2008 | Development of innovative Janus-particles based on the layered silicate kaolinite<br><u>Supervisors:</u> Prof. J. Senker, Prof. J. Breu                                 |
| <i>Sushant Shekhar</i><br>(M.Sc. 2008, Kharagpur)<br>since 01.06.2008      | Rheological properties of olivine-pyroxene-garnet assemblage at P-T conditions applicable to subduction zones<br><u>Supervisors:</u> Dr. D. Frost, Prof. F. Langenhorst |
| <i>Konstantin Glazyrin</i><br>(M.Sc. 2004, Moscow)<br>since 20.07.2008     | Iron oxide systems under high pressure<br><u>Supervisors:</u> PD Dr. L. Dubrovinsky, Dr. C. McCammon  |

Five new associate students were accepted to the doctoral program in 2008:

- |   |   |
|---|---|
| <i>Geertje Ganskow</i><br>(Dipl.-Geol. 2006, Jena)<br>since 01.01.2008        | Hydrous minerals in the Martian mantle<br><u>Supervisors:</u> Prof. F. Langenhorst, Prof. D. Rubie  |
| <i>Julien Chantel</i><br>(M.Sc. 2008, Clermont-Ferrand)<br>since 07.05.2007   | Measurement of elastic properties of silicates at realistic mantle pressures and temperatures<br><u>Supervisors:</u> Dr. Dan Frost, Prof. F. Langenhorst                  |
| <i>Dennis Harries</i><br>(Dipl.-Geowiss. 2008, Göttingen)<br>since 01.09.2008 | TEM microstructural characterization of mono-sulphides and their behaviour during aqueous alteration processes<br><u>Supervisors:</u> Dr. K. Pollok, Prof. F. Langenhorst |
| <i>Linda Lerchbaumer</i><br>(Dipl.-Geol. 2008, Vienna)<br>since 01.09.2008    | Experimental studies on the fractionation of metals between vapor and brine<br><u>Supervisors:</u> Dr. A. Audétat, Prof. H. Keppler                                       |
| <i>Willem van Mierlo</i><br>(M.Sc. 2007, Utrecht)<br>since 04.01.2008         | Exsolution of accessory minerals from garnets in UHP rocks<br><u>Supervisors:</u><br>Prof. F. Langenhorst, Dr. G. Steinle-Neumann   |

*Juliane Hopf*  
(Dipl.-Biol. 2005, Bayreuth)  
since 25.02.2008

Interactions between minerals and microbes  
Supervisors:  
Prof. F. Langenhorst, Prof. E. Kothe/Jena

Descriptions of some student research projects are listed in Chapter 3 of this yearbook. Students gave presentations at several major international meetings in 2008: EMPG XII: 12th International Conference on Experimental Mineralogy, Petrology and Geochemistry, (Innsbruck, Austria), European Geosciences Union General Assembly 2008 (Vienna, Austria), 86th Annual Meeting of the German Mineralogical Society (Berlin, Germany), 9th International Kimberlite Conference (Frankfurt/M., Germany), American Geophysical Union Fall Meeting (San Francisco, USA), International Alloy Conference – V (Ruegen, Germany), Goldschmidt 2008 – 'from Sea to Sky', (Vancouver, Canada), 33rd International Geological Congress (Oslo, Norway), Acoustics '08, (Paris, France), EuroMinSci Conferences (Giens and Obernai, France). The list of presentations and publications may be found in Chapter 5.

As part of program requirements, all students undergo an intensive training program, in addition to their research project, that encompasses lectures, short courses, research colloquium, doctoral seminar, seminars by invited leading experts and weekend seminars on soft skills such as scientific writing, ethics and team work. Invited speakers from overseas and Europe gave 13 lectures during the last year and presented novel experimental techniques and current research results.

The following weekend seminars were held in 2008:

- |                   |  |
|-------------------|--|
| 26.-27.01.2008    | 3 <sup>rd</sup> Joint Student Meeting on Geo- & Material Sciences<br>Regensburg-Kunreuth<br>Graduate schools <i>Oxides</i> (Univ. Bayreuth, ISC Würzburg) and<br>Master Course <i>Advanced Materials and Processes (MAP)</i> (Univ.<br>Erlangen) |
| 31.07.-01.08.2008 | Two-day industrial excursion to chemical production plants in<br>southern Bavaria ( <i>SGL Group/The Carbon Company</i> , Meitingen<br>and <i>AlzChem-Gruppe/Trostberg</i> , Hart a.d. Alz)  |

Three students (*O. Adjaoud, L.M. Arefin and P. Gavrilenko*) and the speaker of the graduate school, *Prof. D. Rubie*, participated in the Graduation Ceremony of the Elite Network of Bavaria with the State Minister Dr. W. Heubisch in Nuernberg on November 4, 2008.



Industrial excursion: Demonstration of carbon products in the exhibition center of SGL Group/Meitingen



ENB Graduation Ceremony 2008: State Minister Dr. W. Heubisch with P. Gavrilenko, L. Arefin and O. Adjaoud (from right)

Students of the graduate school participated in several short courses during 2008:

- "Data analysis in Earth sciences with MATLAB" (23.-26.09.2008), held by PD Dr. M. Trauth/Potsdam in Bayreuth
- a soft skill course with the topic "Effective presentation and communication fluency" (02.-05.10.2008) organized by the ENB administration at Beilngries
- a LINUX Cluster workshop in Garching at the Computer Center Garching (LRZ), 08.-09.12.2008
- a workshop on *ab initio* calculations in geosciences in Cracow, Poland (22.-25.10.2008), organized by the EU c2c programme

In fulfillment of the program requirements, one graduate student carried out a research stay at an institute abroad:

*Micaela Longo*      11.09.-13.12.2008      University of British Columbia, Earth and Oceanic Sciences Department – Vancouver, Canada;  
*Cathodoluminescence studies of alluvial diamonds from Archean conglomerates of Eastern Canada*

Students and members of the graduate program received six international awards for their research excellence; these awards are listed in Section 7.2.

Detailed information on the Graduate School "Structure, Reactivity and Properties of Oxide Materials" can be found at <http://www.uni-bayreuth.de/elitenetzwerk/oxides>.

## 5. Publications, Conference Presentations, Seminars

### 5.1 Publications (published)

Supplement to **2007** (papers published at the end of 2007):

CARACAS, R.; COHEN, R.E. (2007): Post-perovskite phase in selected sesquioxides from density-functional calculations. *Physical Review B* 76, 184101

LIU, J.; DUBROVINSKY, L.S.; BOFFA BALLARAN, T.; CRICHTON, W. (2007): Equation of state and thermal expansivity of LiF and NaF. *High Pressure Research* 27 (4), 483-489

## 2008

### a) Refereed international journals

ADJAOUD, O.; STEINLE-NEUMANN, G.; JAHN, S. (2008): Mg<sub>2</sub>SiO<sub>4</sub> liquid under high pressure from molecular dynamics. *Chemical Geology* 256, 185-192

ANTONANGELI, D.; BENEDETTI, L.R.; FARBER, D.L.; STEINLE-NEUMANN, G.; AUZENDE, A.-L.; BADRO, J.; HANFLAND, M.; KRISCH, M. (2008): Anomalous pressure evolution of the axial ratio *c/a* in hcp cobalt: Interplay between structure, magnetism, and lattice dynamics. *Applied Physics Letters* 92, 111911

AUDÉTAT, A.; PETTKE, T.; HEINRICH, C.A. (2008): The composition of magmatic-hydrothermal fluids in barren and mineralized intrusions. *Economic Geology* 103, 877-908

BAIER, J.; AUDÉTAT, A.; KEPLER, H. (2008): The origin of the negative niobium tantalum anomaly in subduction zone magmas. *Earth and Planetary Science Letters* 267, 290-300

BALI, E.; ZANETTI, A.; SZABÓ, Cs.; PEATE, D.W.; WAIGHT, T.E. (2008): A micro-scale investigation of melt production and extraction in the upper mantle based on silicate melt pockets in ultramafic xenoliths from the Bakony-Balaton Highland Volcanic Field (Western Hungary). *Contributions to Mineralogy and Petrology* 155, 165-179

BALI, E.; ZAJACZ, Z.; KOVÁCS, I.; SZABÓ, Cs.; HALTER, W.; VASELLI, O.; TÖRÖK, K.; BODNAR, R.J. (2008): A quartz-bearing orthopyroxene-rich websterite xenolith from the Pannonian Basin, Western Hungary: Evidence for release of quartz-saturated melts from a subducted slab. *Journal of Petrology* 49, 421-439

BALI, E.; BOLFAN-CASANOVA, N.; KOGA, K. (2008): Pressure and temperature dependence of H solubility in forsterite in the MgO-SiO<sub>2</sub>-H<sub>2</sub>O system and a model of the activity of water at high depths. *Earth and Planetary Science Letters* 268, 354-363

BESTMANN, M.; HABLER, G.; HEIDELBACH, F.; THÖNI, M. (2008): Dynamic recrystallization of garnet and related diffusion processes. *Journal of Structural Geology* 30, 777-790

- BURTON, B.P.; ROBINSON P.; MCENROE, S.A.; FABIAN K.; BOFFA BALLARAN, T. (2008): A low-temperature phase diagram for ilmenite-rich compositions in the system  $\text{Fe}_2\text{O}_3 - \text{FeTiO}_3$ . *American Mineralogist* 93, 1260-1272
- CORGNE, A.; KESHAV, S.; WOOD, B.J.; MCDONOUGH, W.F.; FEI, Y. (2008): Metal-silicate partitioning and constraints on the composition of the Earth's core and oxygen fugacity during Earth's accretion. *Geochimica et Cosmochimica Acta* 72, 574-589
- CREIGHTON, S.; STACHEL, T.; MATVEEV, S.; HÖFER, H.; MCCAMMON, C.; LUTH, R.W. (2008): Oxidation of the Kaapvaal lithospheric mantle driven by metasomatism. *Contributions to Mineralogy and Petrology*. doi: 10.1007/s00410-008-0348-3
- DOLEJŠ, D.; WAGNER, T. (2008): Thermodynamic modeling of non-ideal mineral-fluid equilibria in the system Si-Al-Fe-Mg-Ca-Na-K-H-O-Cl at elevated temperatures and pressures: Implications for hydrothermal mass transfer in granitic rocks. *Geochimica et Cosmochimica Acta* 72, 526-553
- DUBROVINSKAIA, N.; DUBROVINSKY, L.; PAPAGEORGIOU, T.; BOSSAK, A.; KRISCH, M.; BRAUN, H.; WOSNITZA, J. (2008): Large carbon-isotope shift of T-C in boron-doped diamond. *Applied Physics Letters* 92, 132506
- DUBROVINSKAIA, N.; WIRTH, R.; WOSNITZA, J.; PAPAGEORGIOU, T.; BRAUN, H.F.; MIYAJIMA, N.; DUBROVINSKY, L. (2008): An insight into what superconducts in polycrystalline boron-doped diamonds based on investigations of microstructure. *Proceedings of the National Academy of Sciences* 105, 11619-11622
- EL GORESY, A.; DERA, P.; SHARP, T.G.; PREWITT, C.T.; CHEN, M.; DUBROVINSKY, L.; WOPENKA, B.; BOCTOR, N.Z.; HEMLEY, R.J. (2008): Seifertite, a dense orthorhombic polymorph of silica from the Martian meteorites Shergotty and Zagami. *European Journal of Mineralogy* 20, 523-528
- FERROIR, T.; BECK, P.; VAN DE MOORTELE, B.; BOHN, M.; REYNARD, B.; SIMIONOVICI, A.; EL GORESY, A.; GILLET, P. (2008): Akimotoite in the Tenham meteorite: Crystal chemistry and high-pressure formation mechanisms. *Earth and Planetary Science Letters* 275, 26-31
- FROST, D.J.; MCCAMMON, C.A. (2008): The redox state of Earth's mantle. *Annual Review of Earth and Planetary Sciences* 36, 389-420
- FROST, D.J. (2008): The upper mantle and transition zone. *Elements* 4 (3), 171-176
- FROST, D.J.; MANN, U.; ASAHARA, Y.; RUBIE D.C. (2008): The redox state of the mantle during and just after core formation. *Philosophical transactions of the Royal Society A-366*, 4315-4337
- GATTA, G.D.; ROTIROTI, N.; BOFFA BALLARAN, T.; PAVESE, A. (2008): Leucite at high-pressure: elastic behaviour, phase stability and petrological implications. *American Mineralogist* 93, 1588-1596
- GUILLAUME, C.; MORNIROLI, J.P.; FROST, D.J.; SERGHIOU, G. (2008): Synthesis of metal nitrides using high pressures and temperatures. *Journal of Physics: Conference Series* 121, 092005-092009
- HEINEMANN, R.; KROLL, H.; LANGENHORST, F. (2008): Relationship between Guinier-Preston zones and the kinetics of the intracrystalline  $\text{Fe}^{2+}$ ,Mg exchange reaction in Johnstown meteoritic orthopyroxene. *European Journal of Mineralogy* 20, 551-561

- HEZEL, D.; DUBROVINSKY, L.; NASDALA, L.; CAUZID, J.; SIMIONOVICI, A.; GELLISSEN, M.; SCHONBECK, T. (2008): *In situ* micro-Raman and X-ray diffraction study of diamonds and petrology of the new ureilite UAE 001 from the United Arab Emirates. *Meteoritics and Planetary Science* 43, 1127-1136
- HOLBIG, E.; DUBROVINSKY, L.; MIYAJIMA, N.; SWAMY, V.; WIRTH, R.; PRAKAPENKA, V.; KUZNETSOV, A. (2008): Stiffening of nanoscale anatase  $\text{Ti}_{0.9}\text{Zr}_{0.1}\text{O}_2$  upon multiple compression cycles. *Journal of Physics and Chemistry of Solids* 69, 2230-2233
- HOLBIG, E.S.; GROVE, T.L. (2008): Mantle melting beneath the Tibetan Plateau: Experimental constraints on ultrapotassic magmatism. *Journal of Geophysical Research* 113, B04210
- HOLL, C.M.; SMYTH, J.R.; JACOBSEN, S.D.; FROST, D.J. (2008): Effects of hydration on the structure and compressibility of wadsleyite,  $\beta\text{-(Mg}_2\text{SiO}_4)$ . *American Mineralogist* 93, 598-607
- IACONO MARZIANO, G.; GAILLARD, F.; PICHAVANT, M. (2008): Limestone assimilation by basaltic magmas: an experimental re-assessment and application to Italian volcanoes. *Contributions to Mineralogy and Petrology* 155, 719-738
- IDRISSI, H.; CORDIER, P.; JACOB, D.; WALTE, N. (2008): Dislocations and plasticity of experimentally deformed coesite. *European Journal of Mineralogy* 20, 665-671
- JACOBSEN, S.D.; JIANG, F.; MAO, Z.; DUFFY, T.S.; SMYTH, J.R.; HOLL, C.M.; FROST, D.J. (2008): Effects of hydration on the elastic properties of olivine. *Geophysical Research Letters* 35, L14303, 10.1029/2008GL034398
- KANTOR, A.; KANTOR, I.Yu.; KURNOSOV, A.; DUBROVINSKY, L.S.; KRISCH, M.; BOSSAK, A.; JACOBSEN, S. (2008): Anelasticity of  $\text{Fe}_x\text{O}$  at high pressure. *Applied Physics Letters* 93, 034106
- KANTOR, I.Yu.; KURNOSOV, A.V.; MCCAMMON, C.A.; DUBROVINSKY, L.S. (2008): Monoclinic FeO at high pressures. *Zeitschrift für Kristallographie* 223, 461-464
- KEGLER, Ph.; HOLZHEID, A.; FROST, D.J.; RUBIE, D.C.; DOHMEN, R.; PALME, H. (2008): New Ni and Co metal-silicate partitioning data and their relevance for an early terrestrial magma ocean. *Earth and Planetary Science Letters* 268, 28-40
- KEPPLER, H.; DUBROVINSKY, L.S.; NARYGINA, O.; KANTOR, I.Yu. (2008): Optical absorption and radiative thermal conductivity of silicate perovskite to 125 GPa. *Science* 322, 1529-1532
- KLOTZ, S.; STEINLE-NEUMANN, G.; STRÄSSLE, Th.; PHILIPPE, J.; HANSEN, Th.; WENZEL, M.J. (2008): Magnetism and the Verwey transition in  $\text{Fe}_3\text{O}_4$  under pressure. *Physical Review B* 77, 012411
- KOMABAYASHI, T.; HIROSE, K.; SUGIMURA, E.; SATA, N.; OHISHI, Y.; DUBROVINSKY, L.S. (2008): Simultaneous volume measurements of post-perovskite and perovskite in  $\text{MgSiO}_3$  and their thermal equations of state. *Earth and Planetary Science Letters* 265, 515-524
- KONZETT, J.; FROST, D.J.; PROYER, A.; ULMER, P. (2008): The Ca-Eskola component in eclogitic clinopyroxene as a function of pressure, temperature and bulk composition: an experimental study to 15 GPa with possible implications for the formation of oriented  $\text{SiO}_2$ -inclusions in omphacite. *Contributions to Mineralogy and Petrology* 155, 215-228

- KOZLENKO, D.P.; DUBROVINSKY, L.S.; SAVENKO, B.N.; VORONIN, V.I.; KISELEV, E.A.; PROSKURNINA, N.V. (2008): Pressure-induced suppression of Wigner-crystal antiferromagnetic state in  $\text{La}_{0.33}\text{Ca}_{0.67}\text{MnO}_3$ . *Physical Review B* 77, 104444
- KURNOSOV, A.; KANTOR, I.; BOFFA BALLARAN, T.; LINDHARDT, S.; DUBROVINSKY, L.; KUZNETSOV, A.; ZEHNDER, B.H. (2008): A novel gas-loading system for mechanically closing of various types of diamond anvil cells. *Review of Scientific Instruments* 79, 45110
- LEE, K.K.M.; STEINLE-NEUMANN, G. (2008): *Ab initio* study of the effects of pressure and chemistry on the electron-capture radioactive decay constants of  $^7\text{Be}$ ,  $^{22}\text{Na}$  and  $^{40}\text{K}$ . *Earth and Planetary Science Letters* 267, 628-636
- LEROUX, H.; RIETMEIJER, F.J.M.; VELBEL, M.A.; BREARLEY, A.J.; JACOB, D.; LANGENHORST, F.; BRIDGES, J.C.; ZEGA, T.J.; STROUD, R.M.; CORDIER, P.; HARVEY, R.P.; LEE, M.; GOUNELLE, M.; ZOLENSKY, M.E. (2008): A TEM study of thermally modified comet 81P/Wild 2 dust particles by interactions with the aerogel matrix during the Stardust capture process. *Meteoritics & Planetary Science* 43 (1-2), 97-120
- LIN, J.-F.; WATSON, H.; VANKÓ, G.; ALP, E.E.; PRAKAPENKA, V.B.; DERA, P.; STRUZHKIN, V.V.; KUBO, A.; ZHAO, J.; MCCAMMON, C.; EVANS, W.J. (2008): Predominant intermediate-spin ferrous iron in lowermost mantle post-perovskite and perovskite. *Nature Geoscience* 1, 688-691
- MANN, U.; FROST, D.J.; RUBIE, D.C. (2008): The wetting ability of Si-bearing liquid Fe-alloys in a solid silicate matrix-percolation during core formation under reducing conditions? *Physics of the Earth and Planetary Interiors* 167, 1-7
- MAO, Z.; JACOBSEN, S.D.; JIANG, F.M.; SMYTH, J.R.; HOLL, C.M.; FROST, D.J.; DUFFY, T.S. (2008): Single-crystal elasticity of wadsleyites,  $\beta\text{-Mg}_2\text{SiO}_4$ , containing 0.37-1.66 wt.%  $\text{H}_2\text{O}$ . *Earth and Planetary Science Letters* 268, 540-549
- MCCAMMON, C.; KANTOR, I.; NARYGINA, O.; ROUQUETTE, J.; PONKRATZ, U.; SERGUEEV, I.; MEZOUAR, M.; PRAKAPENKA, V.; DUBROVINSKY, L. (2008): Stable intermediate-spin ferrous iron in lower mantle perovskite. *Nature Geoscience* 1, 684-687
- MÉDARD, E.; MCCAMMON, C.A.; BARR, J.A.; GROVE, T.L. (2008): Oxygen fugacity, temperature reproducibility, and  $\text{H}_2\text{O}$  content for nominally dry piston-cylinder experiments using graphite capsules. *American Mineralogist* 93, 1838-1844
- MIYAHARA, M.; EL GORESY, A.; OHTANI, E.; NAGASE, T.; NISHIJIMA, M.; VASHAEI, Z.; FERROIR, T.; GILLET, P.; DUBROVINSKY, L.; SIMIONOVICI, A. (2008): Evidence for fractional crystallization of wadsleyite and ringwoodite from olivine melts in chondrules entrained in shock-melt veins. *Proceedings of the National Academy of Sciences* 105, No. 25, 8542-8547
- MÜLLER, W.F.; WALTE, N.; MIYAJIMA, N. (2008): Experimental deformation of ordered natural omphacite: a study by transmission electron microscopy. *European Journal of Mineralogy* 20, 835-844
- NAKASHIMA, D.; OTT, U.; HOPPE, P.; EL GORESY, A. (2008): Search for extinct  $^{36}\text{Cl}$ : Vigarano CAIs, the Pink Angel from Allende, and a Ningqiang chondrule. *Geochimica et Cosmochimica Acta* 72, 6141-6153

- NESTOLA, F.; BOFFA BALLARAN, T.; BALIC ZUNIC, T.; SECCO, L.; DAL NEGRO, A. (2008): The high-pressure behavior of an Al and Fe-rich natural orthopyroxene. *American Mineralogist* 93, 644-652
- NESTOLA, F.; BOFFA BALLARAN, T.; LIEBSKE, C.; THOMPSON, R.M; DOWNS, R.T. (2008): The effect of the hedenbergitic substitution on the compressibility of jadeite. *American Mineralogist* 93, 1005-1013
- NESTOLA, F.; BOFFA BALLARAN, T.; OHASHI, H. (2008): The high-pressure  $C2/c$ - $P2_1/c$  phase transition along the  $\text{LiAlSi}_2\text{O}_6$ - $\text{LiGaSi}_2\text{O}_6$  solid solution. *Physics and Chemistry of Minerals* 35, 477-484
- NEUFELD, K.; RING, U.; HEIDELBACH, F.; DIETRICH, S.; NEUSER, R.D. (2008): Omphacite textures in eclogites of the Tauern Window: Implications for the exhumation of the Eclogite Zone, Eastern Alps. *Journal of Structural Geology* 30, 976-992
- NIGROVSKI, B.; ZAVYLOVA, U.; SCHOLZ, P.; MÜLLER, M.; POLLOK, K.; ONDURSCHKA, B. (2008): Microwave-assisted catalytic oxidative dehydrogenation of ethylbenzene on iron oxide loaded carbon nanotubes. *Carbon* 46, 1678-1686
- OHGUSHI, K.; MATSUSHITA, Y.; MIYAJIMA, N.; KATSUYA, Y.; TANAKA, M.; IZUMI, F.; GOTOU, H.; UEDA, Y.; YAGI, T. (2008):  $\text{CaPtO}_3$  as a novel post-perovskite oxide. *Physics and Chemistry of Minerals* 35, 189-195
- PAVARINI, E.; TARANTINO, S.C.; BOFFA BALLARAN, T.; ZEMA, M.; GHIGNA, P.; CARRETTA, P. (2008): Effect of high pressure on competing exchange couplings in  $\text{Li}_2\text{VOSiO}_4$ . *Physical Review B* 77, 014425
- POLLOK, K.; LLOYD, G.E.; AUSTRHEIM, H.; PUTNIIS, A. (2008): Complex replacement patterns in garnets from Bergen Arcs eclogites: A combined EBSD and analytical TEM study. *Geochemistry* 68, 177-191
- PRESNALL, D.C.; GUDFINNSSON, G.H. (2008): Origin of the oceanic lithosphere. *Journal of Petrology* 49, 615-632
- RAFAJA, D.; KLEMM, V.; MOTYLENKO, M.; SCHWARZ, M.R.; BARSUKOVA, T.; KROKE, E.; FROST, D.; DUBROVINSKY, L.; DUBROVINSKAIA, N. (2008): Synthesis, microstructure and hardness of bulk ultrahard BN nanocomposites. *Journal of Materials Research* 23, 981-993
- ROUQUETTE, J.; DOLEJŠ, D.; KANTOR, I.Yu.; MCCAMMON, C.A.; FROST, D.J.; PRAKAPENKA, V.B.; DUBROVINSKY L.S. (2008): Iron-carbon interactions at high temperatures and pressures. *Applied Physics Letters* 92, 121912
- ROUQUETTE, J.; KANTOR, I.; MCCAMMON, C.A.; DMITRIEV, V.; DUBROVINSKY, L.S. (2008): High-pressure studies of olivine  $(\text{Mg}_{0.9}\text{Fe}_{0.1})_2\text{SiO}_4$  using Raman spectroscopy, X-ray diffraction and Mössbauer spectroscopy. *Inorganic Chemistry* 47, 2668-2673
- SAIKIA, A.; FROST, D.J.; RUBIE, D.C. (2008): Splitting of the 520-kilometer seismic discontinuity and chemical heterogeneity in the mantle. *Science* 319, 1515-1518
- SAMUEL, H.; TACKLEY, P.J. (2008): Dynamics of core formation and equilibration by negative diapirism. *Geochemistry, Geophysics, Geosystems (G-cubed)* 9, Q06011, doi: 10.1029/2007GC001896

- SCHRINNER, M.; PROCH, S.; MEI, Y.; KEMPE, R.; MIYAJIMA, N.; BALLAUFF, M. (2008): Stable bimetallic gold-platinum nanoparticles immobilized on spherical polyelectrolyte brushes: synthesis, characterization and application for the oxidation of alcohols. *Advanced Materials* 20, 1928-1933, doi: 10.1002/adma.200702421
- SHUSHKANOVA, A.V.; DUBROVINSKY, L.; DUBROVINSKAIA, N.; LITVIN, Yu.A.; URUSOV, V.S. (2008): Synthesis and *in situ* Raman spectroscopy of nanodiamonds. *Doklady Physics* 53, 1-4
- STEINLE-NEUMANN, G. (2008): Magneto-elastic effects in compressed cobalt from first principles. *Physical Review B* 77, 104109
- ŠTEMPROK, M.; DOLEJŠ, D.; MÜLLER, A.; SELTMANN, R. (2008): Textural evidence of magma decompression, devolatilization and disequilibrium quenching: an example from the Western Krusne hory/Erzgebirge granite pluton. *Contributions to Mineralogy and Petrology* 155, 93-109
- ŠTEMPROK, M.; SEIFERT, T.; HOLUB, F.V.; CHLUPÁČOVÁ, M.; DOLEJŠ, D.; NOVÁK, J.K.; PIVEC, E.; LANG, M. (2008): Petrology and geochemistry of Variscan dykes from the Jáchymov (Joachimsthal) ore district, Czech Republic. *Journal of Geosciences* 53, 65-104
- SWAMY, V.; HOLBIG, E.; DUBROVINSKY, L.; PRAKAPENKA, V.; MUDDLE, B.C. (2008): Mechanical properties of bulk and nanoscale TiO<sub>2</sub> phases. *Journal of Physics and Chemistry of Solids* 69, 2332-2335
- TARANTINO, S.C.; ZEMA, M.; BOFFA BALLARAN, T.; GHIGNA, P. (2008): Room-temperature equation of state of Li<sub>2</sub>VOSiO<sub>4</sub> up to 8.5 GPa. *Physics and Chemistry of Minerals* 35, 71-76
- TERASAKI, H.; FROST, D.J.; RUBIE, D.C.; LANGENHORST, F. (2008): Percolative core formation in planetesimals. *Earth and Planetary Science Letters* 273, 132-137
- TRIBAUDINO, M.; NESTOLA, F.; BOFFA BALLARAN, T.; LIEBSKE, C.; BRUNO, M. (2008): Thermal expansion along the NaAlSi<sub>2</sub>O<sub>6</sub> – NaFe<sup>3+</sup>Si<sub>2</sub>O<sub>6</sub> and NaAlSi<sub>2</sub>O<sub>6</sub> – CaFe<sup>2+</sup>Si<sub>2</sub>O<sub>6</sub> solid solutions. *Physics and Chemistry of Minerals* 35, 241-248
- VAN ORMAN, J.A.; KESHAV, S.; FEI, Y. (2008): High pressure, high temperature partitioning of Re, Os, and Pt between solid/molten metal alloy in the system Fe-S. *Earth and Planetary Science Letters* 274, 250-257
- VANPETEGHEM, C.B.; ANGEL, R.A.; ZHAO, J.; ROSS, N.L.; REDHAMMER, G.J.; SEIFERT, F. (2008): The effect of oxygen vacancies and aluminium substitution on the high-pressure properties of brownmillerite-structured Ca<sub>2</sub>Fe<sub>2-x</sub>Al<sub>x</sub>O<sub>5</sub>. *Physics and Chemistry of Minerals* 35, 493-594
- WALTER, M.J.; BULANOVA, G.; ARMSTRONG, L.S.; KESHAV, S.; BLUNDY, J.D.; GUDFINNSSON, G.H.; LORD, O.; LENNIE, A.; CLARK, S.M.; SMITH, C.; GOBBO, L.; (2008): Primary carbonatite melt from deeply subducted oceanic crust. *Nature* 454, 622-625
- WEIGEL, C.; CORMIER, L.; CALAS, G.; GALOISY, L.; BOWRON, D.T. (2008): Nature and distribution of iron sites in a sodium silicate glass investigated by neutron diffraction and EPSR simulation. *Journal of Non-Crystalline Solids* 354, 5378-5385

- WOOD, I.G.; VOCADLO, L.; DOBSON, D.P.; PRICE, G.D.; FORTES, A.D.; COOPER, F.J.; NEALE, J.W.; MARSHALL, W.G.; TUCKER, M.G.; FRANCIS, D.J.; STONE, H.J.; MCCAMMON, C.A. (2008): Thermoelastic properties of magnesiowüstite, (Mg<sub>1-x</sub>Fe<sub>x</sub>)O: Determination of the Anderson-Grüneisen parameter by time-of-flight powder neutron diffraction at simultaneous high pressures and temperatures. *Journal of Applied Crystallography* 41, 886-896
- YUAN, J.; SCHMALZ, H.; XU, Y.; MIYAJIMA, N.; DRECHSLER, M.; MÖLLER, M.W.; SCHACHER, F.; MÜLLER, A.H.E. (2008): Room-temperature growth of uniform tellurium nanorods and the assembly of tellurium or Fe<sub>3</sub>O<sub>4</sub> nanoparticles on the nanorods. *Advanced Materials* 20, 947-952, doi: 10.1002/adma.200701756
- ZARECHNAYA, E.Y.; ISAEV, E.I.; SIMAK, S.I.; VEKILOV, Y.H.; DUBROVINSKY, L.; DOUBROVINSKAIA, N.; ABRIKOSOV, I. (2008): Ground-state properties of boron-doped diamond. *Journal of Experimental and Theoretical Physics* 106, 781-787
- ZAVYALOVA, U.; NIGROVSKI, B.; POLLOK, K.; LANGENHORST, F.; MÜLLER, B.; SCHOLZ, P.; ONDRUSCHKA, B. (2008): Gel-combustion synthesis of nanocrystalline spinel catalysts for VOCs elimination. *Applied Catalysis B: Environmental* 83 (3-4), 221-228
- ZOLENSKY, M.; NAKAMURA-MESSENGER, K.; RIETMEIJER, F.; LEROUX, H.; MIKOUCHI, T.; OHSUMI, K.; SIMON, S.; GROSSMAN, L.; STEPHAN, T.; WEISBERG, M.; VELBEL, M.; ZEGA, T.; STROUD, R.; TOMEOKA, K.; OHNISHI, I.; TOMIOKA, N.; NAKAMURA, T.; MATRAJT, G.; JOSWIAK, D.; BROWNLEE, D.; LANGENHORST, F.; KROT, A.; KEARSLEY, A.; ISHII, H.; GRAHAM, G.; DA, Z.R.; CH, M.; BRADLEY, J.; HAGIYA, K.; GOUNELLE, M.; KELLER, L.; BRIDGES, J. (2008): Comparing Wild 2 particles to chondrites and IDPs. *Meteoritics & Planetary Science* 43 (1-2), 261-272

*b) Popular scientific magazines*

- KEPPLER, H.; AUDÉTAT, A. (2008): Die Physik von Vulkaneruptionen. *Physik in unserer Zeit* 39, 132-138
- KEPPLER, H. (2008): Migration geologischer Fluide. *Nova Acta Leopoldina* 97, 87- 101
- LANGENHORST, F. (2008): Vom Staubkorn zum Planeten. *Spektrum – Uni Bayreuth* 2/08, 9-11
- MCCAMMON, C.A. (2008): Chasing light beams. *Nature Geoscience* 1, 718
- MCCAMMON, C.A.; KANTOR, I.Yu.; NARYGINA, O.; ROUQUETTE, J.; PONKRATZ, U.; SERGUEEV, I.; MEZOUAR, M.; PRAKAPENKA, V.; DUBROVINSKY, L. (2008): Earth's interior contains unusual electron structure. *ESRF News* 48, 16
- MCCAMMON, C.A.; KANTOR, I.Yu.; NARYGINA, O.; ROUQUETTE, J.; PONKRATZ, U.; SERGUEEV, I.; MEZOUAR, M.; PRAKAPENKA, V.; DUBROVINSKY, L. (2008): Intermediate-spin iron in lower mantle silicate perovskite. *ESRF Highlights* 2007, 21-23

POLLOK, K.; LANGENHORST, F.; HOPF, J.; KOTHE, E.; GEISLER, T.; PUTNIS, C.V.;  
PUTNIS, A. (2008): Microstructural controls on monosulfide weathering and heavy metal  
release (MIMOS). GEOTECHNOLOGIEN Science Report 12, 79-88  
STEINLE-NEUMANN, G. (2008): Eisen im Mittelpunkt. Physik Journal 7 (11), 27-32

### *5.2 Publications (submitted, in press)*

ANGEL, R.J.; GATTA, G.D.; BOFFA BALLARAN, T.; CARPENTER, M.A.: The  
mechanism of coupling in the modulated structure of nepheline. Can. Min. JV Smith  
Memorial Volume (in press)

AREFIN, M.L.; RAETHER, F.; DOLEJŠ, D; KLIMERA, A.: Experimental study of phase  
formation during liquid phase sintering of ZnO ceramics. Journal of Materials Science  
(submitted)

AUDÉTAT, A.; BALI, E.: A new technique to seal volatile-rich samples into platinum  
capsules. American Mineralogist (submitted)

BECERRO, A.I.; ESCUDERO, A.; MANTOVANI, M.: Application of  $^{29}\text{Si}$  and  $^{27}\text{Al}$  MAS  
NMR spectroscopy to the study of the reaction mechanism of kaolinite to illite/muscovite.  
Geochimica et Cosmochimica Acta (submitted)

BOFFA BALLARAN, T.; NESTOLA, F.; TRIBAUDINO, M.; OHASHI, H.: Bulk modulus  
variation along the diopside – kosmochlor solid solution. European Journal of Mineralogy  
(submitted)

COMODI, P.; NAZZARENI, S.; DUBROVINSKY, L.S.; MERLINI, M.: The high pressure-  
high temperature behaviour of bassanite. European Journal of Mineralogy (submitted)

DÉGI, J.; ABART, R.; TÖRÖK, K.; WIRTH, R.; BALI, E.; RHEDE, D.: Symplectite  
formation during decompression induced garnet breakdown in lower crustal mafic  
granulite xenoliths: mechanisms and rates. Contributions to Mineralogy and Petrology  
(submitted)

DEGTYAREVA, V.F.; DUBROVINSKY, L.; KURNOSOV, A.: Structural stability of the  
sigma phase FeCr under pressure to 77 GPa. Paper to Journal of Physics: Condensed  
Matter (submitted)

ELLIOTT, P.; KOLITSCH, U.; GIESTER, G.; LIBOWITZKY, E.; MCCAMMON, C.;  
PRING, A.; BIRCH, W.D.: Description and crystal structure of plimerite, the Zn-analogue  
of rockbridgeite and frondelite, from Broken Hill, New South Wales, Australia. American  
Mineralogist (submitted)

FERROIR, T.; DUBROVINSKY, L.S.; EL GORESY, A.; SIMIONOVICI, A.;  
NAKAMURA, T.; GILLET, Ph.: Carbon polymorphisms in shocked meteorites. PNAS  
(submitted)

FROST, D.J.; MCCAMMON, C.A.: The effect of ferric iron on the olivine to wadsleyite  
transformation: implications for remote sensing of mantle redox state at the 410 km  
seismic discontinuity. American Mineralogist (submitted)

- GHOSH, S.; KESHAV, S.; GUDFINNSSON, G.H.: Detailed structure of the carbonated peridotite solidus ledge in the system CaO-MgO-Al<sub>2</sub>O<sub>3</sub>-SiO<sub>2</sub>-CO<sub>2</sub>: consequences for primary calcic carbonatites and high carbon dioxide (CO<sub>2</sub>) solubilities in mantle-derived magmas. *Geochimica et Cosmochimica Acta* (submitted)
- GUILLAUME, C.; SERGHIOU, G.; THOMSON, A.; MORNIROLI, J.P.; FROST, D.J.; ODLING, N.; MEZOUAR, M.: Novel Ge<sub>0.9</sub>Sn<sub>0.1</sub> solid solution formation at 10 GPa after heating. *Science* (submitted)
- HEIDELBACH, F.; TERRY, M.P.; BYSTRICKY, M.; HOLZAPFEL, C.; MCCAMMON, C.A.: A simultaneous deformation and diffusion experiment: Quantifying the role of deformation in enhancing metamorphic reactions. *Earth and Planetary Science Letters* (in press)
- HOLZAPFEL, C.; CHAKRABORTY, S.; RUBIE, D.C.; FROST, D.J.: Fe-Mg interdiffusion in wadsleyite: the role of pressure, temperature and composition and the magnitude of jump in diffusion rates at the 410 km discontinuity. *Physics of the Earth and Planetary Interiors* (in press)
- HOPF, J.; LANGENHORST, F.; POLLOK, K.; MERTEN, D.; KOTHE, E.: Influence of microorganisms on biotite dissolution: an experimental approach. *Chemie der Erde – Geochemistry* (submitted)
- HUSHAR, A.; MANGHNANI, M.H.; SMYTH, J.R.; NESTOLA, F.; FROST, D.J.: Crystal chemistry of hydrous forsterite and its vibrational properties up to 41 GPa. *American Mineralogist* (in press)
- KANTOR, I.Yu.; DUBROVINSKY, L.S.; MCCAMMON, C.A.; STEINLE-NEUMANN, G.; KANTOR, A.; SKORODUMOVA, N.; PASCARELLI, S.; AQUILANTI, G.: Short-range order in (Mg,Fe)O: Evidence for Fe clusterization under high pressure. *Physical Review B* (submitted)
- KESHAV, S.; GUDFINNSSON, G.H.; PRESNALL, D.C.: Widespread carbonatitic melts at depths of 400-600 km in the Earth. *Nature* (submitted)
- KESHAV, S.; GUDFINNSSON, G.H.: Survival of carbonate to great depths in the Earth: results from the solidus determination of carbonated eclogite in the system CaO-MgO-Al<sub>2</sub>O<sub>3</sub>-SiO<sub>2</sub>-CO<sub>2</sub>. *Journal of Geophysical Research* (submitted)
- LEE, K.K.M.; STEINLE-NEUMANN, G.; AKBER-KNUTSON, S.: *Ab initio* predictions of potassium partitioning between Fe and Al-bearing MgSiO<sub>3</sub> perovskite and post-perovskite. *Physics of the Earth and Planetary Interiors* (in press), doi: 10.1016/j.pepi.2008.09.003
- LI, Y.; AUDÉTAT, A.: A method to synthesize large fluid inclusions in quartz at controlled times and under unfavorable growth conditions. *American Mineralogist* (in press)
- MANTOVANI, M.; ESCUDERO, A.; ALBA, M.D.; BECERRO, A.I.: Stability of phyllosilicates in Ca(OH)<sub>2</sub> solution. Influence of layer nature, octahedral occupation, presence of tetrahedral Al and degree of crystallinity. *Applied Geochemistry* (submitted)
- MARIANI, E.; MECKLENBURGH, J.; WHEELER, J.; PRIOR, D.J.; HEIDELBACH, F.: Microstructure evolution and recrystallization during creep of MgO single crystals. *Acta Materialia* (in press)

- MARTIN, A.; MCCAMMON, C.: Oxygen fugacity of the Antarctic shallow upper mantle: Results from Mössbauer spectroscopy. *Contributions to Mineralogy and Petrology* (submitted)
- MCCAMMON, C.A.; LONGO, M.; NESTOLA, F.; BOFFA BALLARAN, T.; ROSS, N.; O'NEILL, H.: Constraints on the formation of Yakutian eclogites derived from the crystal chemistry of iron in clinopyroxene and garnet. *Lithos* (submitted)
- MCCAMMON, C.A.; MCENROE, S.A.; ROBINSON, P.; BURTON, B.P.: Single-grain investigation of lamellar magnetism in ilmeno-hematite using Mössbauer spectroscopy. *Earth and Planetary Science Letters* (submitted)
- MCGAFF, A.J.; SERGHIOU, G.; FROST, D.J.: Metal nitride and alloy synthesis using high pressures and temperatures. *High Pressure Research* (in press)
- MIYAHARA, M.; KIMURA, M.; EL GORESY, A.; OHTANI, E.; OZAWA, O.; NAGASE, T.; NISHIJIMA, M.: Fractional crystallization of olivine melt inclusions in shock-induced chondritic melt vein. *Nature* (submitted)
- MIYAJIMA, N.; YAGI, T.; ICHIHARA, M.: Dislocation microstructures of MgSiO<sub>3</sub> perovskite at a high pressure and temperature condition. *Physics of Earth and Planetary Interior* (in press)
- MIYAJIMA, N.; WALTE, N.: Burgers vector determination on deformed perovskite and post-perovskite in CaIrO<sub>3</sub> using thickness-fringes in weak beam dark field images. *Ultramicroscopy* (in press)
- MOSENFELDER, J.L.; ASIMOW, P.D.; FROST, D.J.; RUBIE, D.C.; AHRENS, T.J.: The MgSiO<sub>3</sub> system at high pressure: Thermodynamic properties of perovskite, post-perovskite, and melt from global inversion of shock and static compression data. *Journal of Geophysical Research* (in press)
- NARYGINA, O.V.; KANTOR, I.Yu.; WU, X.; PASCARELLI, S.; AQUILANTI, G.; MCCAMMON, C.; DUBROVINSKY, L.S.: XANES study of spin crossover in Fe-bearing silicate perovskite. *Phase Transitions* (submitted)
- SCHIAVI, F.; KOBAYASHI, K.; MORIGUTI, T.; NAKAMURA, E.; POMPILIO, M.; TIEPOLO, M.; VANNUCCI, R.: Degassing, crystallization and eruption dynamics at Stromboli: trace elements and lithium isotopes evidence from 2003 ashes. *Earth and Planetary Science Letters* (submitted)
- SCHUBERTH, B.; BUNGE, H.-P.; STEINLE-NEUMANN, G.; MODER, C.; OESER, J.: Thermal vs. elastic heterogeneity in high-resolution mantle circulation models with pyrolite composition: high plume excess temperatures in the lowermost mantle. *Geochemistry, Geophysics, Geosystems* (in press)
- SHIRYAEV, A.A.; ZUBAVICHUS, Y.V.; MCCAMMON, C.; VELIGZHANIN, A.A.: Iron in fibrous diamonds from different localities: X-ray absorption and Mössbauer data. *Lithos* (submitted)
- SKÁLA, R.; LANGENHORST, F.; DEUTSCH, A.: Geochemical characteristics of basement target rocks and suevitic glasses from the Eyreville B drill core, Chesapeake Bay impact structure. *Special volume, Geological Society of America* (submitted)

- SKÁLA, R.; STRNAD, L.; MCCAMMON, C.; CADA, M.: Moldavites from the Cheb Basin, Czech Republic. *Geochimica et Cosmochimica Acta* (submitted)
- STEBBINS, J.F.; PANERO, W.R.; SMYTH, J.R.; FROST, D.J.: Forsterite, wadsleyite, and ringwoodite:  $^{29}\text{Si}$  NMR constraints on structural disorder and effects of paramagnetic impurity ions. *American Mineralogist* (submitted)
- SZABÓ, Cs.; HIDAS, K.; BALI, E.; ZAJACZ, Z.; KOVÁCS, I.; YANG, K.; GUZMICS, T.; TÖRÖK, K.: Mafic melt peridotite wall rock interaction as shown by silicate melt inclusions in upper mantle xenoliths from the central Pannonian Basin. *Island Arc* (in press)
- TERRY, M.P.; HEIDELBACH, F.; COUVY, H.; BROMILEY, G.D.; CARSWELL, D.A.: Deformation and metamorphism of the Kvalvika peridotite, Norway: Conditions and timing for olivine c-slip and exhumation at ultrahigh pressure. *Journal of Metamorphic Petrology* (submitted)
- TIRONE, M.; KESHAV, S.; MORGAN, J.P.: Petrological geodynamic modeling of a plume under a moving plate: a realistic scenario. *Journal of Geophysical Research* (submitted)
- TSUNO, K.; OHTANI, E.: Eutectic temperatures and melting relations in the Fe-O-S system at high pressures and temperatures. *Physics and Chemistry of Minerals* (in press), doi: 10.1007/s00269-008-0254-2
- UVAROVA, Y.; SOKOLOVA, E.; HAWTHORNE, F.C.; MCCAMMON, C.; KAZANSKY, V.I.; LOBANOV, K.V.: Amphiboles from the Kola Superdeep Borehole:  $\text{Fe}^{3+}$  contents from crystal-chemical analysis and Mössbauer spectroscopy. *Mineralogical Magazine* (submitted)
- WALTE, N.; HEIDELBACH, F.; MIYAJIMA, N.; FROST, D.J.; RUBIE, D.C.; DOBSON, D.: Transformation textures in post-perovskite: Understanding mantle flow in the D" layer of the Earth. *Geophysical Research Letters* (in press)
- WENDLER, F.; BECKER, J.K.; NESTLER, B.; BONNS, P.D.; WALTE, N.P.: Phase-field simulations of partial melts in geological materials. *Computers and Geoscience* (submitted)
- WILLIAMS, H.M.; NIELSEN, S.G.; RENAC, C.; GRIFFIN, W.L.; O'REILLY, S.Y.; MCCAMMON, C.A.; PEARSON, N.; VILJOEN, F.; ALT, J.C.; HALLIDAY, A.N.: Fractionation of oxygen and iron isotopes in the mantle: implications for crustal recycling and the source regions of oceanic basalts. *Earth and Planetary Science Letters* (submitted)
- WU, X.; STEINLE-NEUMANN, G.; NARYGINA, O.; KANTOR, I.Yu.; MCCAMMON, C.A.; PASCARELLI, S.; AQUILANTI, G.; PRAKAPENKA, V.; DUBROVINSKY, L.S.: Iron oxidation state of  $\text{FeTiO}_3$  under high pressure. *Physical Review B* (submitted)
- WU, X.; KANZAKI, M.; QIN, S.; STEINLE-NEUMANN, G.; DUBROVINSKY, L.S.: Structural study of  $\text{FeP}_2$  at high pressure. *High Pressure Research* (in press)
- XIONG, X.; KEPPLER, H.; AUDÉTAT, A.; GUDFINNSSON, G.H.; SUN, W.; SONG, M.; XIAO, W.; LI, Y.: Experimental constraints on rutile saturation during partial melting of hydrous basalt at the amphibolite to eclogite transition, with applications to TTG genesis. *American Mineralogist* (submitted)
- YELAMANCHILI, R.S.; LU, Y.; LUNKENBEIN, T.; MIYAJIMA, N.; YAN, Li-T.; BALLAUFF, M.; BREU, J.: Shaping colloidal rutile into thermally stable and porous mesoscopic titania-balls. *Small* (in press)

ZARECHNAYA, E.Yu.; DUBROVINSKY, L.S.; DUBROVINSKAIA, N.; FILINCHUK, Y.; CHERNYSHOV, D.; DMITRIEV, V.; MIYAJIMA, N.: Synthesis of an orthorhombic high-pressure boron phase. *Science and Technology of Advanced Materials* (submitted)

ZARECHNAYA, E.Yu.; DUBROVINSKY, L.S.; DUBROVINSKAIA, N.A.; FILINCHUK, Y.; CHERNICHOV, D.; DMITRIEV, V.; MIYAJIMA, N.; EL GORESY, A.; BRAUN, H.F.; VAN SMAALEN, S.; KANTOR, I.Yu.; KANTOR, A.; PRAKAPENKA, V.; HANFLAND, M.; MIKHAILUSHKIN, A.; SIMAK, S.I.; ABRIKOSOV, I.A.: Optically transparent high-pressure phase of boron. *Science* (submitted)

ZÖLLER, L.; BLANCHARD, H.; MCCAMMON, C.A.: The partial heat-longest plateau technique for TL dating of Middle and Upper Quaternary volcanic eruptions. *Chemical Geology* (submitted)

### 5.3 Presentations at scientific institutions and at congresses

ADJAOUD, O.; STEINLE-NEUMANN, G.; BURTON, B.P.: 19.-21.09.2008, EU c2c Meeting, Adeje, Tenerife, Spain: "Computing phase diagrams from *ab initio*-Group IV carbides as an example"

ADJAOUD, O.; STEINLE-NEUMANN, G.; BURTON, B.P.: 22.-25.10.2008, Workshop on *ab initio* calculations in geosciences, Cracow, Poland: "First principles phase diagram calculations in group IV carbides"

ASAHARA, Y.; RUBIE, D.C.; MIYAJIMA, N.; DUBROVINSKY, L.S.; FROST, D.J.; HOLZAPFEL, C.; OHTANI, E.; MIYAHARA, M.; SAKAI, T.: 23.-31.08.2008, XXI Congress and General Assembly of the International Union of Crystallography, IUCr 2008, Osaka, Japan: "Oxygen partitioning between magnesiowüstite and Fe-liquid: Implication to the Earth's core"

AUDÉTAT, A.: 13.-18.04.2008, European Geosciences Union General Assembly 2008, Vienna, Austria (*keynote lecture*): "Fluid-melt partitioning in experiments and nature", *Geophysical Research Abstracts* 10, EGU2008-A-09133, 2008

AUDÉTAT, A.: 26.05.2008, Ringvorlesung SS 2008, 'Structure-property relations in materials: From crystal structures to textures to macroscopic properties', Bayreuth, Germany: "Fluid-melt partitioning in experiments and nature"

AUDÉTAT, A.: 29.06.-04.07.2008, Gordon Research Conference on Geochemistry of Mineral Deposits, Lucca, Italy (*invited*): "Identifying fertile vs. barren magmatic complexes: new evidence from fluid, melt and solid inclusions"

AUDÉTAT, A.: 06.-14.08.2008, 33<sup>rd</sup> International Geological Congress, Oslo, Norway (*keynote lecture*): "Formation of porphyry-Cu and porphyry-Mo deposits: insights gained through the study of fluid, melt and solid inclusions"

AUDÉTAT, A.: 26.09.2008, Perkin Elmer Anorganica Meeting, Nürnberg, Germany: "Vorteile und Limitationen der Laser-Ablation ICP-MS Analytik in den Geowissenschaften"

- AUDÉTAT, A.; BALI, E.; LI, Y.; LERCHBAUMER, L.: 30.10.2008, ETH Zürich, Switzerland: "Synthetic fluid inclusions: experimental techniques, advantages and limitations"
- BALI, E.; TÖRÖK, K.; SZABÓ, Cs.: 06.-14.08.2008, 33<sup>rd</sup> International Geological Congress, Oslo, Norway: "Origin and evolution of garnet pyroxenite xenoliths from the Bakony Balaton Highland Volcanic Field, western Hungary"
- BALI, E.; AUDÉTAT A.; KEPLER, H.: 08.-10.09.2008, EMPG XII, Innsbruck, Austria<sup>\*1</sup>: "U-mobility at high pressure and temperature - a synthetic fluid inclusion study"
- BERNINI, D.; AUDÉTAT, A.; DOLEJŠ, D.; KEPLER, H.: 08.-10.09.2008, EMPG XII, Innsbruck, Austria<sup>\*1</sup>: "Zircon solubility in aqueous fluids at high pressure and temperature conditions"
- BOFFA BALLARAN, T.; SAIKIA, A.; FROST, D.J.: 08.-10.09.2008, EMPG XII, Innsbruck, Austria (*key note*)<sup>\*1</sup>: "The effect of Fe and Al substitution on the high-pressure behaviour of MgSiO<sub>3</sub> perovskite: a single-crystal X-ray diffraction study"
- BOFFA BALLARAN, T.; FROST, D.J.; POZZOBON, R.: 15.-19.12.2008, AGU Fall Meeting, San Francisco, USA<sup>\*4</sup>: "Structure and density of perovskite from subducted oceanic crust in the lower mantle", EOS Trans. AGU, 89(53), Fall Meet. Suppl., Abstract MR53A-1712, 2008
- CARACAS, R.; DUBROVINSKY, L.S.; MCCAMMON, C.A.; KANTOR, I.Yu.; NARYGINA, O.: 13.-18.07.2008, Goldschmidt 2008 – 'from Sea to Sky', Vancouver, Canada: "A computational and experimental study of (Fe<sup>2+</sup>,Mg)SiO<sub>3</sub> perovskite at lower mantle conditions", Geochimica et Cosmochimica Acta, 72 (12), Suppl. 1, A136
- COMODI, P.: 07.-12.09.2008, 1<sup>st</sup> SIMP-AIC Joint Meeting, Sestri Levante, Italy (*keynote lecture*): "HP-HT phase stability of Ca-sulphates"
- COMODI, P.; NAZZARENI, S.; DUBROVINSKY, L.S.; MERLINI, M.: 07.-12.09.2008, 1<sup>st</sup> SIMP-AIC Joint Meeting, Sestri Levante, Italy: "High pressure and high temperature behaviour of bassanite"
- COMODI, P.: 28.09.-01.10.2008, EU RITA User workshop, Verbania, Italy<sup>\*3</sup>: "HP-HT phase stability of Ca-sulphates"
- COMODI, P.: 06.-09.10.2008, Workshop CECAM on Mineral spectroscopy by theory and experiment, Lausanne, Switzerland (*invited*): "HP-HT phase stability of Ca-sulphates"
- DE KOKER, N.; MOOKHERJEE, M.; STEINLE-NEUMANN, G.: 15.-19.12.2008, AGU Fall Meeting, San Francisco, USA<sup>\*4</sup>: "High pressure behavior of phase X", EOS Trans. AGU, 89(53), Fall Meet. Suppl., Abstract MR53A-1719, 2008
- DEGTYAREVA, V.F.; DUBROVINSKY, L.S.; KURNOSOV, A.: 23.-31.08.2008, XXI Congress and General Assembly of the International Union of Crystallography, IUCr 2008, Osaka, Japan: "Structural stability of the FeCr sigma phase under pressure to 77 GPa"
- DEGTYAREVA, V.F.; DUBROVINSKY, L.S.; KURNOSOV, A.: 11.-14.09.2008, International Alloy Conference – V (IACV), Rügen, Germany: "Structural stability of the sigma phase FeCr under pressure to 77 GPa"
- DEUTSCH, A.; LANGENHORST, F.; LUETKE, S.; BERNDT, J.: 13.-18.07.2008, Goldschmidt 2008 – 'from Sea to Sky', Vancouver, Canada: "A combined LA-ICP-MS and DEGAS study on Bediasites and Ivory Coast tektites", Geochimica et Cosmochimica Acta, 72 (12), Suppl. 1, A214

- DOLEJŠ, D.: 19.03.2008, Charles University, Institute of Petrology and Structural Geology, Prague, Czech Republic: "Magmatic degassing & reactive fluid flow in the vicinity of granitic plutons"
- DOLEJŠ, D.: 13.-18.04.2008, European Geosciences Union General Assembly 2008, Vienna, Austria: "Redox state of the subducting slab: Thermodynamic constraints from multicomponent phase equilibria", Geophysical Research Abstracts 10, EGU2008-A-05291, 2008
- DOLEJŠ, D.: 28.-30.04.2008, Charles University, Institute of Petrology and Structural Geology, Prague, Czech Republic: "Physical-chemical principles of metamorphic, magmatic and hydrothermal processes"
- DOLEJŠ, D.: 29.06.-04.07.2008, Gordon Research Conference on Geochemistry of Mineral Deposits, Lucca, Italy: "Thermochemistry of crystallization and vapor-brine exsolution in granitic and rhyolitic systems"
- DOLEJŠ, D.: 19.-21.09.2008, EU c2c Meeting, Adeje, Tenerife, Spain: "When do granitic and rhyolitic magmas exsolve two fluids simultaneously?"
- DOLEJŠ, D.: 19.-21.09.2008, EU c2c Meeting, Adeje, Tenerife, Spain: "Redox state in subduction zones: a thermodynamic perspective"
- DUBROVINSKAIA, N.A.; WIRTH, R.; WOSNITZA, J.; PAPAGEORGIOU, T.; BRAUN, H.F.; MIYAJIMA, N.; DUBROVINSKY, L.S.: 23.-31.08.2008, XXI Congress and General Assembly of the International Union of Crystallography, IUCr 2008, Osaka, Japan: "Microstructure and superconductivity in polycrystalline boron-doped diamonds"
- DUBROVINSKY, L.S.: 23.-31.08.2008, XXI Congress and General Assembly of the International Union of Crystallography, IUCr 2008, Osaka, Japan: "High pressure synthesis of nanocrystalline superhard materials"
- EL GORESY, A.; MIYAHARA, M.; OHTANI, E.; KIMURA, M.; NAGASE, T.; NISHIJIMA, M.; VASHAEI, Z.: 27.07.-01.08.2008, 71<sup>st</sup> Annual Meeting of the Meteoritical Society, Matsue, Japan: "Evidence for fractional crystallization of wadsleyite and ringwoodite from individual olivine melt pockets in chondrules entrained in shock melt veins"
- EL GORESY, A.: 29.09.2008, Kyushu University, Fukuoka, Japan: "Polychromatic pigment decorations in temples and tombs in pharaonic Egypt: Artistic selection patterns of natural minerals and manufacture technology of synthetic pigments in three millennia"
- EL GORESY, A.; CHENNAOUI-AUDJEHANE, H.; CAILLET, C.; JAMBON, A.: 30.09.2008, Kyushu University, Fukuoka, Japan: "Origin of metallic copper in FeNi metal and coexisting sulfides in chondritic meteorites"
- EL GORESY, A.; ZINNER, E.; PELLAS, P.: 01.10.2008, Kyushu University, Fukuoka, Japan: "Diverse graphite morphologies with contrasting C- and N-isotopic compositions in the Acapulco meteorite: Clues to the evolution of acapulcoite meteorites in the Early Solar System"
- EL GORESY, A.; DUBROVINSKY, L.S.; GILLET, Ph.; SIMIOMOVICI, A.: 02.10.2008, Kyushu University, Fukuoka, Japan: "New very super-hard carbon polymorphs in ureilitic meteorites"

- EL GORESY, A.; MIYAHARA, M.; OHTANI, E.; NAGASE, T.; NISHIJIMA, M.; VASHAEI, Z.: 03.10.2008, Kyushu University, Fukuoka, Japan: "Evidence for fractional crystallization of Mg-rich wadsleyite and Fe-rich ringwoodite in olivine porphyritic chondrules entrained in shock-melt veins in the Peace River L-6 chondrite: Constraints to the duration of shock-events on chondritic asteroids and possible time of the destruction of the parent body"
- EL GORESY, A.; CHENNAOUI-AUDJEHANE, H.; CAILLET, C.; JAMBON, A.: 06.10.2008, Tohoku University, Sendai, Japan: "Origin of metallic copper in FeNi metal and coexisting sulfides in chondritic meteorites: Not produced by shock"
- EL GORESY, A.: 10.10.2008, Tohoku University, Sendai, Japan: "Polychromatic pigment decorations in temples and tombs in pharaonic Egypt: Artistic selection patterns of natural minerals and manufacture technology of synthetic pigments in three millennia"
- EL GORESY, A.; ZINNER, E.; PELLAS, P.: 14.10.2008, Tohoku University, Sendai, Japan: "A menagerie of graphite morphologies with diverse carbon and nitrogen isotopic compositions of graphite in the Acapulco meteorite: Clues to the evolution of acapulcoite meteorites in the Early Solar System"
- EL GORESY, A.; MIYAHARA, M.; OHTANI, E.; NAGASE, T.; NISHIJIMA, M.; VASHAEI, Z.: 27.10.2008, The 1<sup>st</sup> Workshop on 'Planetary Collisions and Evolution of the Solar System', Tohoku University, Sendai, Japan (*invited*): "Evidence for fractional crystallization of Mg-rich wadsleyite and Fe-rich ringwoodite in olivine porphyritic chondrules entrained in shock-melt veins in the Peace River L-6 chondrite: Constraints to the duration of shock-events on chondritic asteroids and possible time of the destruction of the parent body"
- EL GORESY, A.; MIYAHARA, M.; OHTANI, E.; NAGASE, T.; NISHIJIMA, M.; VASHAEI, Z.: 04.11.2008, Gakushuin University, Tokyo, Japan: "Evidence for fractional crystallization of Mg-rich wadsleyite and Fe-rich ringwoodite in olivine porphyritic chondrules entrained in shock-melt veins in the Peace River L-6 chondrite: Constraints to the duration of shock-events on chondritic asteroids and possible time of the destruction of the parent body"
- ESCUADERO, A.: 08.-12.09.2008, Universidad de Sevilla, Instituto de Ciencia de Materiales de Sevilla, CSIC Postgraduate Course, Sevilla, Spain (*invited*): "Structure determination of real solids. Nuclear magnetic Resonance Technique"
- ESCUADERO, A.; MIJAYIMA, N.; LANGENHORST, F.: 14.-17.09.2008, 86. Jahrestagung der DMG, Berlin, Germany<sup>\*2</sup>: "Microstructural characteristics of rutile in diamondiferous gneisses of the Saxonian Erzgebirge, Germany", Abstract Volume, 306
- ESCUADERO, A.: 19.-21.09.2008, EU c2c Meeting, Adeje, Tenerife, Spain: "Microstructural and chemical characteristics of rutile in diamondiferous gneisses of the Saxonian Erzgebirge, Germany"
- FROST, D.J.; STAGNO, V.: 06.-14.08.2008, 33<sup>rd</sup> International Geological Congress, Oslo, Norway: "Carbonate stability as a function of oxygen fugacity in the deep Earth"
- FROST, D.J.; ASAHARA, Y.; RUBIE, D.C.: 08.-10.09.2008, EMPG XII, Innsbruck, Austria<sup>\*1</sup>: "Experimental observations and thermodynamic modelling of liquid immiscibility in the Fe-O system at high pressure and temperature", Abstract Volume, 25

- FROST, D.J.; ASAHARA, Y.; RUBIE, D.C.: 14.-17.09.2008, 86. Jahrestagung der DMG, Berlin, Germany<sup>\*2</sup>: "Liquid immiscibility in the Fe-O system: implications for the light element in the Earth's core", Abstract Volume, 310
- FROST, D.J.: 11.11.2008, GeoForschungsZentrum, Potsdam, Germany: "Core formation and Early differentiation of the Earth – perspectives from high pressure and temperature experiments"
- FROST, D.J.: 18.11.2008, University College London, U.K.: "In the beginning: The origin of the Earth according to experimental petrology"
- FROST, D.C.; ASAHARA, Y.; TSUNO, K.; RUBIE, D.C.; PICKLES, J.: 15.-19.12.2008, AGU Fall Meeting, San Francisco, USA<sup>\*4</sup>: "An experiment-based model describing the partitioning of oxygen between Earth's mantle and core", EOS Trans. AGU, 89(53), Fall Meet. Suppl., Abstract MR32A-01, 2008
- GANSKOW, G.; LANGENHORST, F.; FROST, D.J.: 28.-29.02.2008, 5<sup>th</sup> Colloquium, DFG Priority Programme SPP 1115 'Mars and the terrestrial planets', Münster, Germany: "Stability of hydrous ringwoodite in the  $MgFeSiO_4 - H_2O$  system"
- GANSKOW, G.; LANGENHORST, F.; FROST, D.J.: 13.-18.04.2008, European Geosciences Union General Assembly 2008, Vienna, Austria: "Stability of hydrous ringwoodite in the  $(Mg_1Fe_1)SiO_4 - H_2O$  system"
- GANSKOW, G.; LANGENHORST, F.; FROST, D.J.: 08.-10.09.2008, EMPG XII, Innsbruck, Austria<sup>\*1</sup>: "Hydrous phases in the  $(Mg_1Fe_1)SiO_4 - H_2O$  system up to 25 GPa"
- GAVRILENKO, P.; KEPPLER, H.: 31.03.-02.04.2008, 2<sup>nd</sup> EuroMinSci Conference, Giens, France: "Water solubility in diopside"
- GAVRILENKO, P.; KEPPLER, H.: 28.09.-01.10.2008, EU RITA User workshop, Verbania, Italy<sup>\*3</sup>: "Water solubility in diopside"
- GAVRILENKO, P.; KEPPLER, H.: 24.-26.11.2008, Final EuroMinSci Conference, Obernai, France: "Water solubility in diopside"
- GHOSH, S.; KESHAV, S.; GUDFINNSSON, G.H.; PRESNALL, D.C.: 15.-19.12.2008, AGU Fall Meeting, San Francisco, USA<sup>\*4</sup>: "Detailed structure of the carbonated peridotite solidus ledge in the system  $CaO-MgO-Al_2O_3-SiO_2-CO_2$ ", EOS Trans. AGU, 89(53), Fall Meet. Suppl., Abstract MR43A-1798, 2008
- GREENBERG, E.; ROZENBERG, G.Kh.; XU, W.M.; PASTERNAK, M.P.; KURNOSOV, A.; DUBROVINSKY, L.S.; HANFLAND, M.: 28.09.-01.10.2008, EU RITA User workshop, Verbania, Italy<sup>\*3</sup>: "The dilemma of post-spinel structure of  $MFe_2O_4$  (M=Mg, Co, Zn) ferrite spinels: Mössbauer, Raman and XRD studies"
- GUDFINNSSON, G.H.; KESHAV, S.; PRESNALL, D.C.: 15.-19.12.2008, AGU Fall Meeting, San Francisco, USA<sup>\*4</sup>: "Water-rich carbonatites at low pressures and kimberlites at high pressures", EOS Trans. AGU, 89(53), Fall Meet. Suppl., Abstract MR43A-1799, 2008
- GUZMICS, T.; KODOLANYI, J.; ZAJACZ, Z.; SZABO, C.; BALI E.; MÁRTA, B.; AUDÉTAT, A.: 06.-14.08.2008, 33<sup>rd</sup> International Geological Congress, Oslo, Norway: "Liquid immiscibility between a P-bearing and a silicate-bearing carbonatite melts reflected by primary carbonatite melt inclusions in mantle xenoliths"

- GUZMICS T.; BALI E.; AUDÉTAT A.; BERKESI, M.; SZABÓ, C.: 28.09.-01.10.2008, EU RITA User workshop, Verbania, Italy<sup>\*3</sup>: "Liquid immiscibility between a phosphorous carbonatite melt and a carbonate-bearing alkali aluminosiliceous melt, coexisting with apatite, K-feldspar and diopside at 1200 °C and 2.2 GPa: implications for carbonatite metasomatism in the mantle"
- HEIDELBACH, F.: 21.01.2008, University of Lausanne, Institute for Geology, Lausanne, Switzerland: "Fabric analysis with backscattered electrons in the SEM: Examples from natural and experimental metamorphic rocks"
- HEIDELBACH, F.: 25.04.2008, South Dakota School of Mines and Technology, Rapid City, USA: "Fabric analysis of rocks with backscattered electrons in the SEM"
- HEIDELBACH, F.; WALTE, N.: 19.-21.09.2008, EU c2c Meeting, Adeje, Tenerife, Spain: "Plastic deformation of aragonite"
- HEWENER, B.; NARYGINA, O.; SCHÜNEMANN, V.; MCCAMMON, C.A.; DUBROVINSKY, L.S.; CHUMAKOV, S.; WOLNY, J.; MUFFLER, K.: 16.-18.06.2008, 2. Berichtskolloquium DFG Priority Program 1236, Freiberg, Germany: "Iron dynamics in iron-nickel alloy and Earth mantle minerals probed by Mössbauer spectroscopy using synchrotron radiation"
- HOPF, J.; HAFERBURG, G.; POLLOK, K.; KOTHE, E.; LANGENHORST, F.: 14.-17.09.2008, 86. Jahrestagung der DMG, Berlin, Germany<sup>\*2</sup>: "Bioprecipitation of phosphates and sulfates in experiments with *Streptomyces acidiscabies*", Abstract Volume, 603
- HOPF, J.; HAFERBURG, G.; POLLOK, K.; KOTHE, E.; LANGENHORST, F.: 22.-23.10.2008, 7<sup>th</sup> Symposium on Remediation 'Metal-stress: biotic and abiotic factors', University of Jena, Germany: "New phosphates and sulfates produced by a *Streptomyces acidiscabies* strain"
- IRIFUNE, T.; SHINMEI, T.; TANGE, Y.; SANEHIRA, T.; FUNAKOSHI, K.; MCCAMMON, C.A.; MIYAJIMA, N.; FROST, D.J.; RUBIE, D.C.: 06.-14.08.2008, 33<sup>rd</sup> International Geological Congress, Oslo, Norway: "Development of multianvil high-pressure technology with sintered diamond anvils and phase transitions in pyrolite under the lower mantle P-T conditions"
- IRIFUNE, T.; SHINMEI, T.; TANGE, Y.; SANEHIRA, T.; FUNAKOSHI, K.; MCCAMMON, C.; MIYAJIMA, N.; FROST, D.; RUBIE, D.: 15.-19.12.2008, AGU Fall Meeting, San Francisco, USA<sup>\*4</sup>: "Iron partitioning in pyrolite and its relevance to the spin transition in magnesiowustite under the lower mantle P-T conditions", EOS Trans. AGU, 89(53), Fall Meet. Suppl., Abstract MR23A-03, 2008
- KANTOR, A.; JACOBSEN, S.; KANTOR, I.Yu.; DUBROVINSKY, L.S.; REICHMANN, H.-J.: 29.06.-04.07.2008, Acoustics'08, Paris, France (*invited*): "GHz ultrasonic interferometry at high pressure and temperature: geophysical implications"
- KANTOR, A.: 03.07.2008, Institut de Minéralogie et de Physique des Milieux Condensés, Paris, France: "Single crystal elasticity measurements at extreme conditions"
- KEGLER, P.; HOLZHEID, A.; FROST, D.J.; RUBIE, D.C.; PALME, H.: 28.-29.02.2008, 5<sup>th</sup> Colloquium, DFG Priority Programme SPP 1115 'Mars and the terrestrial planets', Münster, Germany: "Partitioning behaviour of moderately siderophile elements: implications to terrestrial core formation scenarios", Abstract Volume, 4

- KEGLER, P.; HOLZHEID, A.; MCCAMMON, C.A.; RUBIE, D.C.; PALME, H.: 08.-10.09.2008, EMPG XII, Innsbruck, Austria<sup>\*1</sup>: "First results on pressure and temperature dependences of metal-silicate partitioning of copper"
- KEPPLER, H.: 04.07.2008, Bavarian Academy of Sciences, Munich, Germany: "Von der Kruste bis zum Erdkern: Geowissenschaftliche Hochdruckforschung"
- KEPPLER, H.; DUBROVINSKY, L.S.; NARYGINA, O.; KANTOR, I.Yu.: 14.-17.09.2008, 86. Jahrestagung der DMG, Berlin, Germany<sup>\*2</sup>: "Optical absorption spectra of silicate perovskite to 1.25 Mbar", Abstract Volume, 70
- KESHAV, S.: 14.01.2008, Winter School in Experimental Petrology, University of Delhi, Delhi, India: "Strict topological analysis of partial fusion in the Earth's mantle"
- KESHAV, S.: 16.01.2008, Winter School in Experimental Petrology, University of Delhi, Delhi, India: "Coupling experimentally derived melting models with numerical simulations: a few applications to magma generation beneath mid-ocean ridges"
- KESHAV, S.: 25.02.2008, National High Magnetic Field Lab, Tallahassee, USA: "Carbonatite melt generation at great depths in the Earth"
- KESHAV, S.: 26.02.2008, National High Magnetic Field Lab, Tallahassee, USA: "Alkaline volcanism in ocean-islands: are we being fooled by temperature versus source compositions?"
- KESHAV, S.: 19.-21.09.2008, EU c2c Meeting, Adeje, Tenerife, Spain: "Watery carbonatites at low pressures and kimberlites at high pressures"
- KESHAV, S.: 05.11.2008, University of Trieste, Department of Earth Sciences, Trieste, Italy: "Melting beneath Hawaii: some stringent phase equilibrium controls"
- KESHAV, S.; TIRONE, M.; GUDFINNSSON, G.H.; PRESNALL, D.C.: 15.-19.12.2008, AGU Fall Meeting, San Francisco, USA<sup>\*4</sup>: "Melting in the system CaO-MgO-Al<sub>2</sub>O<sub>3</sub>-SiO<sub>2</sub>-FeO-Cr<sub>2</sub>O<sub>3</sub> spanning the plagioclase-spinel lherzolite transition at 7 to 10 kbar: experiments versus thermodynamics", EOS Trans. AGU, 89(53), Fall Meet. Suppl., Abstract V43B-2150, 2008
- KOPYLOVA, M.; NAVON, O.; DUBROVINSKY, L.S.; KHACHATRYAN, G.: 13.-18.07.2008, Goldschmidt 2008 – 'from Sea to Sky', Vancouver, Canada: "Mineralogy of natural diamond-forming fluids", *Geochimica et Cosmochimica Acta*, 72 (12), Suppl. 1, A490
- LANGENHORST, F.: 27.-28.03.2008, International Graduate School, ENB, Nördlingen, Germany: "Shock metamorphism of minerals"
- LANGENHORST, F.: 21.05.2008, Inaugural Lecture, University of Bayreuth, Germany: "Stardust – Kometenstaub unter dem Mikroskop"
- LANGENHORST, F.; ESCUDERO, A.: 01.-05.09.2008, 14<sup>th</sup> European Microscopy Congress, Aachen, Germany: "New insights into ultra-high pressure metamorphism from TEM studies"
- LANGENHORST, F.; LEROUX, H.; JACOB, D.; ZOLENSKY, M.: 14.-17.09.2008, 86. Jahrestagung der DMG, Berlin, Germany<sup>\*2</sup>: "TEM observations of sulfide and enstatite dust particles sampled by the Stardust mission", Abstract Volume, 524

- LEE, K.K.M.; STEINLE-NEUMANN, G.: 15.-19.12.2008, AGU Fall Meeting, San Francisco, USA<sup>\*4</sup>: "Ab initio predictions of potassium partitioning between lower mantle phases", EOS Trans. AGU, 89(53), Fall Meet. Suppl., Abstract DI41A-1749, 2008
- LIN, J.; WATSON, H.C.; VANKO, G.; ALP, E.; PRAKAPENKA, V.; DERA, P.; STRUZHUKIN, V.V.; KUBO, A.; ZHAO, J.; MCCAMMON, C.; EVANS, W.J.: 15.-19.12.2008, AGU Fall Meeting, San Francisco, USA<sup>\*4</sup>: "Predominant intermediate-spin ferrous iron in lowermost mantle post-perovskite and perovskite", EOS Trans. AGU, 89(53), Fall Meet. Suppl., Abstract MR31A-1821, 2008
- LONGO, M.; MCCAMMON, C.A.: 10.-15.08.2008, 9<sup>th</sup> International Kimberlite Conference, Frankfurt/M., Germany: "Iron oxidation state in (Mg,Fe)O: Calibration of the flank method (EPMA) as a new technique for diamond inclusion studies", 9<sup>th</sup> International Kimberlite Conference Extended Abstract No. 9IKC-A-00248, 2008
- LONGO, M.; MCCAMMON, C.A.; BULANOVA, G.; KAMINSKY, F.: 15.-19.12.2008, AGU Fall Meeting, San Francisco, USA<sup>\*4</sup>: "Iron oxidation state in (Mg,Fe)O: Calibration of the flank method on synthetic samples and application to natural inclusions in lower mantle diamonds", EOS Trans. AGU, 89(53), Fall Meet. Suppl., Abstract MR53A-1728, 2008
- MARTIN, A.; COOPER, A.; PALIN, M.; MCCAMMON, C.A.: 06.-14.08.2008, 33<sup>rd</sup> International Geological Congress, Oslo, Norway: "Plagioclase-Spinel – 5 phase lherzolite from a cratonic rift setting: fugacity and trace element geochemistry of an understudied mantle field"
- MARTIN, A.; COOPER, A.; PALIN, M.; MCCAMMON, C.A.: 22.-26.09.2008, AGU Chapman Conference on Shallow Mantle Composition and Dynamics Fifth Orogenic Lherzolite Conference, Mount Shasta, USA: "Plagioclase-spinel and spinel lherzolite xenoliths from a continental rift environment, Antarctica: Preliminary petrography, chemistry and implications"
- MAZZULLO, S.; FAIT, A.; MCCAMMON, C.A.; BOFFA BALLARAN, T.: 28.09.-01.10.2008, EU RITA User workshop, Verbania, Italy<sup>\*3</sup>: "High pressure crystallization of semicrystalline polypropylene"
- MCCAMMON, C.A.; DUBROVINSKY, L.; NARYGINA, O.; KANTOR, I.; ROUQUETTE, J.; SCHÜNEMANN, V.; HEWENER, B.; WOLNY, J.; MUFFLER, K.; PONKRATZ, U.; SERGUEEV, I.; CHUMAKOV, A.: 31.05.-01.06.2008, High-Resolution Inelastic X-ray Scattering on Earth Materials using Synchrotron Radiation Workshop, Argonne, USA: "Nuclear resonant studies of deep mantle and core phases using an externally heated diamond anvil cell"
- MCCAMMON, C.A.; DUBROVINSKY, L.; KANTOR, I.; NARYGINA, O.; WU, X.; CHUMAKOV, A.; SERGUEEV, I.: 16.-18.06.2008, 2. Berichtskolloquium DFG Priority Program 1236, Freiberg, Germany: "New results from *in situ* high P,T studies of lower mantle minerals"
- MCCAMMON, C.A.; LONGO, M.; NESTOLA, F.; BOFFA-BALLARAN, T.; ROSS, N.; O'NEILL, H.S.C.: 10.-15.08.2008, 9<sup>th</sup> International Kimberlite Conference, Frankfurt/M., Germany: "Constraints on the formation of Yakutian eclogites derived from the crystal chemistry of iron in clinopyroxene and garnet", 9<sup>th</sup> International Kimberlite Conference Extended Abstract No. 9IKC-A-00359, 2008

- MCCAMMON, C.A.; DUBROVINSKY, L.; NARYGINA, O.; KANTOR, I.; ROUQUETTE, J.; SCHÜNEMANN, V.; HEWENER, B.; WOLNY, J.; MUFFLER, K.; PONKRATZ, U.; SERGUEEV, I.; CHUMAKOV, A.: 08.-10.09.2008, EMPG XII, Innsbruck, Austria<sup>\*1</sup>: "Nuclear resonant studies of deep Earth phases at high P, T"
- MCCAMMON, C.A.: 06.-09.10.2008, Workshop CECAM on Mineral spectroscopy by theory and experiment, Lausanne, Switzerland: "Results from nuclear resonance spectroscopic methods: Where theory and experiment meet (or not)"
- MCCAMMON, C.A.; DUBROVINSKY, L.; KANTOR, I.; NARYGINA, O.; WU, X.; ROUQUETTE, J.; PONKRATZ, U.; SERGUEEV, I.; CHUMAKOV, A.: 09.-10.10.2008, 50 Years After – the Mössbauer Effect Today and in Future, Garching, Germany: "Nuclear resonant studies of deep mantle phases at high pressure and high temperature using an externally heated diamond anvil cell"
- MCCAMMON, C.A.; DUBROVINSKY, L.; NARYGINA, O.; KANTOR, I.; WU, X.; SERGUEEV, I.; CHUMAKOV, A.: 21.-24.10.2008, Transport Properties of the Lower Mantle Workshop, Yunishigawa, Japan: "Intermediate- and low-spin iron in (Mg,Fe)(Si,Al)O<sub>3</sub> perovskite and consequences for the properties and dynamics of the deep mantle"
- MCCAMMON, C.A.; DUBROVINSKY, L.; KANTOR, I.; NARYGINA, O.; WU, X.; CHUMAKOV, A.; SERGUEEV, I.: 15.-19.12.2008, AGU Fall Meeting, San Francisco, USA<sup>\*4</sup>: "Elastic wave velocities of lower mantle perovskite with intermediate-spin iron and consequences for mantle properties and dynamics", EOS Trans. AGU, 89(53), Fall Meet. Suppl., Abstract MR23A-07, 2008
- MIKHAYLUSHKIN, A.S.; SIMAK, S.I.; DUBROVINSKY, L.S.; DUBROVINSKAIA, N.A.; JOHANSSON, B.; ABRIKOSOV, I.A.: 13.-18.04.2008, European Geosciences Union General Assembly 2008, Vienna, Austria: "Pure iron compressed and heated to extreme conditions", Geophysical Research Abstracts 10, EGU2008-A-02286, 2008
- MIYAHARA, M.; OHTANI, E.; EL GORESY, A.; KIMURA, M.; OZAWA, S.; NAGASE, T.; NISHIJIMA, M.: 15.-19.12.2008, AGU Fall Meeting, San Francisco, USA<sup>\*4</sup>: "The scrutinization of shock textures by a FIB-TEM technique", EOS Trans. AGU, 89(53), Fall Meet. Suppl., Abstract V33B-2217, 2008
- MIYAJIMA, N.: 28.05.2008, Ringvorlesung SS 2008, 'Structure-property relations in materials: From crystal structures to textures to macroscopic properties', Bayreuth, Germany: "Dislocation microtextures of perovskite and post-perovskite: TEM studies from CaIrO<sub>3</sub> analogues to MgSiO<sub>3</sub>"
- MIYAJIMA, N.; WALTE, N.: 01.-05.09.2008, 14<sup>th</sup> European Microscopy Congress, Aachen, Germany: "Burgers vector determinations in deformed perovskite and post-perovskite of CaIrO<sub>3</sub>, using thickness-fringes in weak beam dark field images"
- MIYAJIMA, N.: 28.09.-01.10.2008, EU RITA User workshop, Verbania, Italy<sup>\*3</sup>: "Burgers vector determination in deformed perovskite and post-perovskite of CaIrO<sub>3</sub> using thickness-fringes in weak beam dark field images"
- MOOKHERJEE, M.; FROST, D.J.: 15.-19.12.2008, AGU Fall Meeting, San Francisco, USA<sup>\*4</sup>: "Chemistry of low degree hydrous partial melt at high pressures", EOS Trans. AGU, 89(53), Fall Meet. Suppl., Abstract MR43A-1797, 2008

- NARYGINA, O.; DUBROVINSKY, L.S.; KANTOR, I.Yu.; PRAKAPENKA, V.: 31.03.-02.04.2008, 2<sup>nd</sup> EuroMinSci Conference, Giens, France: "Carbon influence on phase relations in iron-nickel"
- NARYGINA, O.; KANTOR, I.Yu.; MCCAMMON, C.A.; PASCARELLI, S.; MEZOUAR, M.; SERGUEEV, I.; PONKRATZ, U.; PRAKAPENKA, V.; DUBROVINSKY, L.S.: 13.-18.04.2008, European Geosciences Union General Assembly 2008, Vienna, Austria: "Iron spin state in perovskite structure: Moessbauer spectroscopy, X-ray diffraction spectroscopy and XANES", Geophysical Research Abstracts 10, EGU2008-A-11671, 2008
- NARYGINA, O.; DUBROVINSKY, L.S.; MCCAMMON, C.A.; FROST D.J.; MIYAJIMA, N.; PRAKAPENKA V.: 11.-14.09.2008, International Alloy Conference – V (IACV), Ruegen, Germany: "Fe-Ni-C system at high pressure"
- NARYGINA, O.; DUBROVINSKY, L.S.; MCCAMMON, C.A.; FROST, D.J.; MIYAJIMA, N.; PRAKAPENKA V.: 15.-19.12.2008, AGU Fall Meeting, San Francisco, USA<sup>\*4</sup>: "Fe-Ni-C system at high pressure", EOS Trans. AGU, 89(53), Fall Meet. Suppl., Abstract DI43A-1763, 2008
- OTSUKA, K.; MCCAMMON, C.A.; KARATO, S.: 21.-24.10.2008, Transport Properties of the Lower Mantle Workshop, Yunishigawa, Japan: "Site occupation and solubility of ferric iron in (Mg,Fe)O at high pressures studied by Mössbauer spectroscopy"
- OTSUKA, K.; MCCAMMON, C.A.; KARATO, S.: 15.-19.12.2008, AGU Fall Meeting, San Francisco, USA<sup>\*4</sup>: "Tetrahedral occupancy of ferric iron in (Mg,Fe)O at high pressures", EOS Trans. AGU, 89(53), Fall Meet. Suppl., Abstract MR53A-1720, 2008
- POLLOK, K.: 14.-17.09.2008, 86. Jahrestagung der DMG, Berlin, Germany<sup>\*2</sup>: "Microstructural controls on pyrrhotite weathering and secondary mineral formation: A TEM study", Abstract Volume, 399
- POLLOK, K.: 22.-23.09.2008, 7. Jenaer Sanierungskolloquium, Jena, Germany: "Pyrrhotite weathering and secondary mineral formation: A first survey on microstructural controls"
- POLLOK, K.; LANGENHORST, F.; HOPF, J.; KOTHE, E.; GEISLER, T.; PUTNIS, C.V.; PUTNIS, A.: 13.-14.10.2008, Kick-off-Meeting 'Mineral Surfaces – From Atomic Processes to Industrial Applications', München, Germany: "Microstructural controls on monosulfide weathering and heavy metal release (MIMOS)"
- PICKLES, J.; MCCAMMON, C.A.; KURNOSOV, A.; FROST, D.J.: 15.-19.12.2008, AGU Fall Meeting, San Francisco, USA<sup>\*4</sup>: "Displacement of lower mantle material into the upper mantle and its potential effect on mantle and surface redox reactions", EOS Trans. AGU, 89(53), Fall Meet. Suppl., Abstract DI53A-1693, 2008
- PRESNALL, D.C.; GUDFINNSSON, G.H.: 13.-18.04.2008, European Geosciences Union General Assembly 2008, Vienna, Austria: "Plumeless oceanic volcanism challenges whole-mantle convection", Geophysical Research Abstracts 10, EGU2008-A-05872, 2008
- ROZENBERG, G.Kh.; PASTERNAK, M.P.; XU, W.M.; KURNOSOV, A.; DUBROVINSKY, L.S.; PASCARELLI, S.; MUNOZ, M.; HANFLAND, M.: 07.-12.09.2008, 46<sup>th</sup> European High Pressure Research Group (EHPRG) Conference, Valencia, Spain (*invited*): "Electronic/magnetic phenomena and related structural transitions in iron(II,III) compounds under high pressure", Abstracts, p. 60, 2008

- ROZENBERG, G.Kh.; PASTERNAK, M.P.; XU, W.M.; KURNOSOV, A.; DUBROVINSKY, L.S.; PASCARELLI, S.; MUNOZ, M.; HANFLAND, M.: 11.-14.09.2008, International Alloy Conference – V (IACV), Ruedgen, Germany: "Metallization of TM compounds under pressure and accompanying magnetic/electronic phenomena", Abstracts, p. 37, 2008
- RUBIE, D.C.; TERASAKI, H.; ASAHARA, Y.; TSUNO, K.; MANN, U.; DUBROVINSKY, L.; MIYAJIMA, N.; LANGENHORST, F.; FROST, D.J.; KEGLER, P.; HOLZHEID, A.; PALME, H.; MIYAHARA, M.; SAKAI, T.; OHTANI, E.: 28.-29.02.2008, 5<sup>th</sup> Colloquium, DFG Priority Programme SPP 1115 'Mars and the terrestrial planets', Münster, Germany: "New constraints on core formation and planetary accretion", Abstract Volume, 1
- RUBIE, D.C.: 17.03.2008, University of Hawaii, Honolulu, USA: "Core formation and accretion history of the Earth"
- RUBIE, D.C.; MANN, U.; FROST, D.J.; TSUNO, K.; KEGLER, P.; HOLZHEID, A.; PALME, H.: 21.-23.03.2008, The 3<sup>rd</sup> COE-21 International Symposium 'Origin, Evolution and Dynamics of the Earth', Misasa, Japan: "Core formation and accretion of the Earth", Abstract Volume, 23
- RUBIE, D.C.; FROST, D.J.; MANN, U.; TSUNO, K.; ASAHARA, Y.; KEGLER, P.; HOLZHEID, A.; PALME, H.: 29.06.-04.07.2008, Ascona conference, 'Origin and Evolution of Planets 2008', Ascona, Switzerland: "Core formation and Heterogeneous Accretion of the Earth", Abstract Volume, 24
- RUBIE, D.C.; FROST, D.J.; MANN, U.; TSUNO, K.; ASAHARA, Y.; KEGLER, P.; HOLZHEID, A.; PALME, H.: 14.-17.09.2008, 86. Jahrestagung der DMG, Berlin, Germany<sup>\*2</sup>: "The light element content of the Earth's core: constraints from models of core formation", Abstract Volume, 276
- RUBIE, D.C.; FROST, D.J.; ASAHARA, Y.; TSUNO, K.; MANN, U.: 21.-24.10.2008, Transport Properties of the Lower Mantle Workshop, Yunishigawa, Japan: "The light elements in the Earth's core and implications for reactions at the core-mantle boundary"
- RUBIE, D.C.; MANN, U.; FROST, D.J.; TSUNO, K.; ASAHARA, Y.: 15.-19.12.2008, AGU Fall Meeting, San Francisco, USA<sup>\*4</sup> (*invited*): "Estimates of the light element content of the Earth's core from models of core formation", EOS Trans. AGU, 89(53), Fall Meet. Suppl., Abstract MR31B-01, 2008
- SAMUEL, H.; TACKLEY, P.J.: 13.-18.04.2008, European Geosciences Union General Assembly 2008, Vienna, Austria: "Heat partitioning during core formation in terrestrial planets", Geophysical Research Abstracts 10, EGU2008-A-03356, 2008
- SAMUEL, H.; TACKLEY, P.J.: 29.06.-04.07.2008, Ascona conference, 'Origin and Evolution of Planets 2008', Ascona, Switzerland: "Heat partitioning in terrestrial planets during core formation"
- SAMUEL, H.; TACKLEY, P.J.: 15.07.2008, Geophysics seminar, Ludwig-Maximilians-Universität München, Germany (*invited*): "The early thermo-chemical evolution of terrestrial planets"
- SAMUEL, H.; TACKLEY, P.J.: 30.09.-02.10.2008, Geodynamik Workshop 2008, Neustadt an der Weinstraße, Germany: "Scaling laws for heat partitioning in terrestrial planets during core formation"

- SCHIAVI, F.; WALTE, N.; KEPPLER, H.: 06.-14.08.2008, 33<sup>rd</sup> International Geological Congress, Oslo, Norway: "Optical *in situ* observation of crystallization processes in basaltic melt with the moissanite anvil cell"
- SCHIAVI, F.; WALTE, N.; KEPPLER, H.: 08.-10.09.2008, EMPG XII, Innsbruck, Austria<sup>\*1</sup>: "First *in situ* observation of the crystallization of a basaltic magma"
- SCHIAVI, F.; WALTE, N.; KEPPLER, H.: 14.-17.09.2008, 86. Jahrestagung der DMG, Berlin, Germany<sup>\*2</sup>: "First *in situ* observation of the crystallization of basalts", Abstract Volume, 160
- SCHUBERTH, B.; BUNGE, H.-P.; STEINLE-NEUMANN, G.; MODER, C.; OESER, J.: 15.-19.12.2008, AGU Fall Meeting, San Francisco, USA<sup>\*4</sup> (*invited*): "Thermal vs. elastic heterogeneity in high-resolution mantle circulation models with pyrolite composition: high plume excess temperatures in the lowermost mantle", EOS Trans. AGU, 89(53), Fall Meet. Suppl., Abstract DI34A-08, 2008
- SERGHIOU, G.: 27.-30.01.2008, International Workshop on High Pressure Science and Technology, Max-Planck-Gesellschaft, Schloss Ringberg, Rottach-Egern, Germany: "Synthesis and stability of silicates, nitrides and alloys using extreme conditions"
- SERGHIOU, G.; GUILLAUME, C.; MORNIROLI, J.P.; FROST, D.J.: 07.-12.09.2008, 46<sup>th</sup> European High Pressure Research Group (EHPRG) Conference, Valencia, Spain: "Metal-nitride and alloy synthesis using high pressures and temperatures"
- SHCHEKA, S.; KEPPLER, H.; WIEDENBECK, M.; FROST, D.J.: 06.-09.09.2008, 8<sup>th</sup> Workshop 'Deep-seated magmatism, its sources and plumes', Vladivostok, Russia: "Carbon speciation in the Earth's mantle "
- SHIRYAEV, A.A.; ZUBAVICHUS, Y.V.; MCCAMMON, C.A.; VELIGZHANIN, A.A.: 10.-15.08.2008, 9<sup>th</sup> International Kimberlite Conference, Frankfurt/M., Germany: "Iron in fibrous diamonds from different localities: X-ray Absorption and Mössbauer data", 9<sup>th</sup> International Kimberlite Conference Extended Abstract No. 9IKC-A-00074, 2008
- STAGNO, V.; DOLEJŠ, D.: 13.-18.04.2008, European Geosciences Union General Assembly 2008, Vienna, Austria: "Experimental study and thermodynamic model for chlorine solubility in polymerized aluminosilicate melts", Geophysical Research Abstracts 10, EGU2008-A-03224, 2008
- STAGNO, V.; FROST, D.J.: 10.-15.08.2008, 9<sup>th</sup> International Kimberlite Conference, Frankfurt/M., Germany: "When elemental carbon turns into carbonate; redox conditions of a carbonate-rich melt source", 9<sup>th</sup> International Kimberlite Conference Extended Abstract No. 9IKC-A-00246, 2008
- STEINLE-NEUMANN, G.; LEE, K.K.M.; AKBER-KNUTSON, S.: 27.-30.01.2008, International Workshop on High Pressure Science and Technology, Max-Planck-Gesellschaft, Schloss Ringberg, Rottach-Egern, Germany: "K-partitioning in the deep Earth from *ab initio* computations"
- STEINLE-NEUMANN, G.: 04.03.2008, Polish Academy of Sciences, Institute of Nuclear Physics, Krakow, Poland: "Structure of the Earth's deep mantle: insight from computational mineral physics"

- STEINLE-NEUMANN, G.: 31.03.2008, German Science Foundation Roundtable 'Supercomputing and E-Infrastructure in the Earth Sciences', Tutzing, Germany: "Computational methods in mineral physics"
- STEINLE-NEUMANN, G.: 05.08.2008, Norwegian Geological Survey, Trondheim, Norway: "Structure of the Earth's deep mantle: insight from computational mineral physics"
- STEINLE-NEUMANN, G.; LEE, K.K.M.: 06.-14.08.2008, 33<sup>rd</sup> International Geological Congress, Oslo, Norway: "Potassium partitioning in the Earth's deep Interior from *ab initio* computations"
- STEINLE-NEUMANN, G.: 22.-25.10.2008, Workshop on *ab initio* calculations in geosciences, Cracow, Poland: "Magneto-elastic coupling in compressed cobalt"
- STEINLE-NEUMANN, G.: 30.10.2008, SFB 574 'Volatiles and Fluids in Subduction Zones' Retreat, Flensburg, Germany: "The fate of subducted material: the c2c network"
- STEINLE-NEUMANN, G.; MOOKHERJEE, M.: 15.-19.12.2008, AGU Fall Meeting, San Francisco, USA<sup>\*4</sup>: "Elasticity of hollandite", EOS Trans. AGU, 89(53), Fall Meet. Suppl., Abstract DI41A-1750, 2008
- ŠTEMPROK, M.; SEIFERT, T.; HOLUB, F.V.; DOLEJŠ, D.; CHLUPÁČOVÁ, M.: 12.-13.06.2008, 59. Berg- und Hüttenmännischer Tag, Freiberg, Germany: "Dikes and mineralization of the Jáchymov ore district (Western Krušné hory, Czech Republic)"
- TANG, Z.; STEINLE-NEUMANN, G.: 19.-21.09.2008, EU c2c Meeting, Adeje, Tenerife, Spain: "Magnetic and electronic structure of Fe<sub>2</sub>SiO<sub>4</sub> fayalite from first principles"
- TANG, Z.; STEINLE-NEUMANN, G.: 22.-25.10.2008, Workshop on *ab initio* calculations in geosciences, Cracow, Poland: "Magnetic and electronic structure of Fe<sub>2</sub>SiO<sub>4</sub> fayalite from first principles"
- TRØNNES, R.G.; BOFFA BALLARAN, T.; FROST, D.J.; BALIC-ZUNIC, T.; OLSEN, L.A.; STØLEN, S.: 28.09.-01.10.2008, EU RITA User workshop, Verbania, Italy<sup>\*3</sup>: "Phase relations and mineral physics of the lowermost mantle - the analogue compositional approach"
- TSUNO, K.; FROST, D.J.; RUBIE, D.C.: 06.-14.08.2008, 33<sup>rd</sup> International Geological Congress, Oslo, Norway: "The effect of Ni and S on partitioning of O between magnesiowüstite and metallic Fe-liquid at high pressures", PIP04703L (Oral)
- VAN MIERLO, W.; LANGENHORST, F.; FROST, D.; MIYAJIMA, N.: 19.-21.09.2008, EU c2c Meeting, Adeje, Tenerife, Spain: "Diffusion in the enstatite/majorite – pyrope system"
- VAN MIERLO, W.: 28.09.-01.10.2008, EU RITA User workshop, Verbania, Italy<sup>\*3</sup>: "Diffusion experiments in the enstatite/majorite - pyrope system"
- VAN MIERLO, W.; LANGENHORST, F.; FROST, D.; MIYAJIMA, N.: 22.-25.10.2008, Workshop on *ab initio* calculations in geosciences, Cracow, Poland: "Diffusion in the enstatite/majorite – pyrope system"
- VAN ORMAN, J.A.; KESHAV, S.; FEI, Y.: 25.-28.06.2008, COMPRES Seventh Annual Meeting, Colorado Springs, USA: "High pressure solid-metal/liquid-metal partitioning of Os, Re, and Pt in the Fe-FeS system transactions"
- WAGNER, T.; DOLEJŠ, D.; KULIK, D.: 29.06.-04.07.2008, Gordon Research Conference on Geochemistry of Mineral Deposits, Lucca, Italy: "Novel geochemical models for fluid-rock equilibria: a key element in computer simulations of hydrothermal systems"

- WALTE, N.; HEIDELBACH, F.; RUBIE, D.C.; FROST, D.J.: 31.03.-02.04.2008, 2<sup>nd</sup> EuroMinSci Conference, Giens, France: "Transition textures in CaIrO<sub>3</sub>: Reconciling experiments with seismic evidence in the core-mantle region"
- WALTE, N.; MIYAJIMA, N.; HEIDELBACH, F.; RUBIE, D.; FROST, D.J.: 21.-24.10.2008, Transport Properties of the Lower Mantle Workshop, Yunishigawa, Japan: "The non-hydrostatic CaIrO<sub>3</sub> pv-ppv phase transition: Implications for lattice preferred orientations and seismic anisotropy in the D" layer"
- WEIGEL, C.; KEPPLER, H.; MCCAMMON, C.A.; DUBROVINSKY, L.S.: 28.09.-01.10.2008, EU RITA User workshop, Verbania, Italy<sup>\*3</sup>: "Fe-bearing silicate glasses : Mössbauer studies at high pressure and at high temperature"
- WEIGEL, C.; CORMIER, L.; CALAS, G.; BOWRON, D.T.; MCCAMMON, C.A.; ROSSANO, S.: 03.-05.09.2008, Workshop 'New opportunities and challenges for liquid and amorphous materials science', ESRF, Grenoble, France: "Intermediate range order in (Fe,Al) framework glasses determined by neutron diffraction coupled with numerical modelisation"
- ZALITE, I.; FROST, D.J.; ZILINSKA, N.: 22.-25.04.2008, 1<sup>st</sup> International Scientific Conference 'Nanostructured Materials – 2008: Belarus – Russia – Ukraine', Minsk, Belarus: "High-pressure hot pressing of some nanosized refractory compounds", Abstract Volume, 67-68
- ZALITE, I.; ZILINSKA, N.; FROST, D.J.: 28.09.-01.10.2008, EU RITA User workshop, Verbania, Italy<sup>\*3</sup>: "High pressure hot pressing as a method for obtaining of nanostructured Si<sub>3</sub>N<sub>4</sub> containing material"
- ZARECHNAYA, E.: 11.-14.09.2008, International Alloy Conference – V (IACV), Ruegen, Germany: "A new high pressure high temperature phase of boron"

<sup>\*1</sup> **EMPG XII: 12<sup>th</sup> International Conference on Experimental Mineralogy, Petrology and Geochemistry, 08.-10.09.2008, Innsbruck, Austria**

<sup>\*2</sup> **DMG: 86. Jahrestagung der Deutschen Mineralogischen Gesellschaft (86<sup>th</sup> Annual Meeting of the German Mineralogical Society), 14.-17.09.2008, Berlin, Germany**

<sup>\*3</sup> **EU: FP6 "Research Infrastructure – Transnational Access" Programme (RITA) User workshop 'The Structure and Properties of Materials at High Pressure', 28.09.-01.10.2008, Verbania-Pallanza, Italy**

<sup>\*4</sup> **AGU: American Geophysical Union Fall Meeting, 15.-19.12.2008, San Francisco, USA – EOS Transactions, American Geophysical Union, 89(53), AGU Fall Meeting 2008 Supplement**

#### 5.4 Lectures and seminars at Bayerisches Geoinstitut

- BALI, E., Bayerisches Geoinstitut, Bayreuth, Germany: "Application of synthetic fluid inclusion technique for the study of mantle fluids", 23.10.2008
- BAUMGARTNER, L., Université de Lausanne, Faculty of Geosciences and Environment, Lausanne, France: "There is more to metamorphic petrology than phase diagrams: rates!", 13.02.2008
- BORISOV, A., Russian Academy of Sciences, Moscow, Russia: "The effects of silica on metal solubilities in silicate melt: an experimental study and petrological applications", 07.02.2008
- CHEMIA, Z., Uppsala University, Department of Earth Sciences, Uppsala, Sweden: "Modeling internal deformation of salt structures targeted for radioactive waste disposal", 25.09.2008
- COTTENIER, S., Katholieke Universiteit Leuven, Nuclear and Radiation Physics, Leuven, Belgium: "Hyperfine interactions at lanthanide and actinide impurities in bcc Fe", 12.06.2008
- DAVAILLE, A., Institut de Physique du Globe de Paris, Laboratoire de Dynamique des Systèmes Géologiques, Paris, France: "Penetrative convection in an heterogeneous mantle: hot spots, cratons and the episodic evolution of the Earth", 29.05.2008
- DAVAILLE, A., Institut de Physique du Globe de Paris, Laboratoire de Dynamique des Systèmes Géologiques, Paris, France: "How to model multi-scale convection in the mantle: A *fishtank approach*", 30.05.2008
- EL GORESY, A., Bayerisches Geoinstitut, Bayreuth, Germany: "Polychromatic pigment decorations in pharaohic temples and tombs in Egypt in time and space", 26.02.2008
- ETZEL, K., Universität Kiel, Germany: "Biological dissolution of synthetic pyrite surfaces", 25.09.2008
- EVONUK, M., ETH Zürich, Switzerland: "Thermal convection and vorticity generation in a fully convective density stratified giant planet", 18.01.2008
- FISCHER, K., Brown University, Geological Sciences, Providence, USA: "The continental lithosphere-asthenosphere boundary", 07.05.2008
- FISCHER, K., Brown University, Geological Sciences, Providence, USA: "Subduction zone structure, dynamics and melting processes: Lessons from Central America", 08.05.2008
- FUMAGALLI, P., Università degli Studi di Milano, Dipartimento di Scienze della Terra, Milano, Italy: "Subsolidus phase relations in ultramafic compositions up to 6.0 GPa and their geodynamic implications", 13.11.2008
- GANSKOW, G., Bayerisches Geoinstitut, Bayreuth, Germany: "Stability of hydrous mantle phases in the MgFeSiO<sub>4</sub> - H<sub>2</sub>O system", 06.11.2008
- GUDFINNSSON, G.H., Bayerisches Geoinstitut, Bayreuth, Germany: "Melting of hydrous, carbonate-bearing mantle peridotite at 3-7 GPa", 06.03.2008
- HOPF, J., Friedrich-Schiller-Universität Jena, Germany: "Influence of microorganisms on biotite dissolution: an experimental approach", 06.11.2008
- IRIFUNE, T., Ehime University, Geodynamics Research Center, Matsuyama, Japan: "High P, T generation with sintered diamond anvils and some applications", 30.07.2008

- JACKSON, J., California Institute of Technology, Division of Geological & Planetary Sciences, Pasadena, USA: "The behaviour of iron-bearing mineral assemblages in Earth's lower mantle", 27.10.2008
- JONNALAGADDA, M., University of Pune, Department of Geology, Pune, India: "Petrographic and geochemical characterization of the Dyke rocks in Kutch, NW India", 28.02.2008
- KESHAV, S., Bayerisches Geoinstitut, Bayreuth, Germany: "Deep mantle carbonatites: they can run, but they cannot hide", 24.01.2008
- KING, S., Virginia Tech, Geosciences, Blacksburg, USA "Mercury and Mars: A geodynamical tale of two planets", 15.05.2008
- LIN, J.-F., The University of Texas at Austin, Department of Geological Sciences, Austin, USA: "Spin transitions of iron in Earth's lower mantle", 11.09.2008
- LIN, J.-F., The University of Texas at Austin, Department of Geological Sciences, Austin, USA: "Hot dense iron, water, and silica", 12.09.2008
- MAINPRICE, D., Université Montpellier 2, France: "Seismic anisotropy of subduction zone minerals – contribution of hydrous phases", 20.11.2008
- MANTHILAKE, G., Okayama University, Institute for the Study of Earth's Interior, Tottori, Japan: "Laboratory measurements of electrical conductivity and their application to structure and composition of the mantle", 18.09.2008
- MARTIN, A., Bayerisches Geoinstitut, Bayreuth, Germany: "The first direct measurement of mantle  $\text{Fe}^{3+}/\Sigma\text{Fe}$  from Antarctica: A glimpse of fugacity and geology from 4- and 5- phase lherzolites", 28.02.2008
- MATAS, J., École normale supérieure de Lyon, France: "Lower mantle structure: Can anelasticity change the story?", 15.05.2008
- MATAS, J., École normale supérieure de Lyon, France: "Anelasticity and seismic attenuation in the lower mantle", 16.05.2008
- MAYNARD, H., University of Edinburgh, School of Physics, Edinburgh, U.K.: "High-pressure crystallography of methane", 07.05.2008
- MCDONOUGH, W., University of Maryland, Department of Geology, Geochemistry Laboratory, College Park, USA: "Antineutrino detection, geoneutrinos and heat production in the Earth", 18.08.2008
- MCDONOUGH, W., University of Maryland, Department of Geology, Geochemistry Laboratory, College Park, USA: "K-U-Th abundances of the mantle: Consequences for  $^{40}\text{Ar}$  and U/Pb", 20.08.2008
- NI, H., University of Michigan, Department of Geological Sciences, Ann Arbor, USA: "Driving volcanic eruptions:  $\text{H}_2\text{O}$  diffusion in calc-alkaline melts", 26.05.2008
- OHTANI, E., Tohoku University, Institute of Mineralogy, Petrology and Economic Geology, Sendai, Japan: "Experimental study on the role of hydrogen in the mantle transition zone and lower mantle", 12.08.2008
- PASCARELLI, S., ESRF Grenoble, France: "An introduction to X-ray absorption spectroscopy", 03.04.2008

- PASCARELLI, S., ESRF Grenoble, France: "Examples of XAS studies of matter at high pressure", 04.04.2008
- PENTCHEVA, R., Ludwig-Maximilians-Universität, Department für Geo- und Umweltwissenschaften, München, Germany: "Charge disproportionation and origin of magnetism at iron oxide interfaces: insights from correlated band theory", 17.01.2008
- PETTKE, T.; OBERLI, F.; AUDÉTAT, A.; WIECHERT, U.; HARRIS, C.R.; HEINRICH, C.A.: 13.-18.07.2008, Goldschmidt 2008 – 'from Sea to Sky', Vancouver, Canada: "Precise and accurate lead isotopic analysis of fast transient signals by laser-ablation MC-ICP-MS", *Geochimica et Cosmochimica Acta*, 72 (12), Suppl. 1, A741
- PICKLES, J., Bayerisches Geoinstitut, Bayreuth, Germany: "Oxidation and melting at the top of the lower mantle", 28.02.2008
- PRESNALL, D., University of Texas at Dallas, Richardson, USA: "Fracture-induced oceanic volcanism without mantle plumes", 30.10.2008
- RAY, S., Indian Institute of Technology, Department of Earth Sciences, Bombay, India: "Reaction induced rheological inversion: a case study from a suit of mafic dyke and felsic rock from Chotonagpur Granitic Gneissic Complex (CGGC), India", 12.12.2008
- RODRÍGUEZ, J.L.P., Universidad de Sevilla, Instituto de Ciencia de Materiales de Sevilla, Spain: "Damage to and preservation of cultural heritage", 08.01.2008
- RODRÍGUEZ, J.L.P., Universidad de Sevilla, Instituto de Ciencia de Materiales de Sevilla, Spain: "Ultrasonic treatment of clay minerals", 09.01.2008
- RUDNICK, R., University of Maryland, Department of Geology, Geochemistry Laboratory, College Park, USA: "Recycling of the deep lithosphere beneath the North China Craton", 19.08.2008
- SAIKIA, A., Bayerisches Geoinstitut, Bayreuth, Germany: "A compressibility study on single crystals of Al,Fe bearing Mg perovskite", 10.01.2008
- STEIN, H., Colorado State University, Department of Geosciences, Fort Collins, USA: "Re-Os dating and tracer studies - from ore deposits to shales", 26.06.2008
- TACKLEY, P., ETH Zürich, Institut für Geophysik, Zürich, Switzerland: "Modelling the thermochemical structure and evolution of Earth's mantle using self-consistent mineralogy and petrology", 14.02.2008
- TSUCHIYA, T., Ehime University, Geodynamics Research Center, Matsuyama, Japan, "*Ab initio* study on the iron-bearing lower mantle phases", 28.10.2008
- VIEIRA CONCEIÇÃO, R. Universidade Federal do Rio Grande do Sul, Porto Alegre, Brasil: "Melting and metasomatism in the mantle wedge beneath the extra back arc Patagonia, inferred from mantle xenoliths and basalts", 22.04.2008
- WU, X., Okayama University, Japan: "The high-pressure behaviour of FeTiO<sub>3</sub>", 16.10.2008
- YANG, X., University of Science and Technology of China, School of Earth and Space Sciences, Hefei, China: "Water content and H-O-Li isotopes of lower crustal granulite minerals in eastern China", 25.06.2008
- YAO, L., Universität Karlsruhe, Laboratorium für Elektronenmikroskopie, Karlsruhe, Germany: "High pressure synthesis, physical properties and TEM study of the layered perovskite-like compounds", 07.10.2008

### 5.5 Conference organization

- 06.03.-07.03.2008, Annual meeting of the section Chemistry, Physics and Crystallography of Minerals, German Mineralogical Society (DMG), Erlangen, Germany (PÖLLMANN, H.; LANGENHORST, F.)
- 13.-18.04.2008, European Geosciences Union General Assembly 2008, Vienna, Austria: Convener for the IS4 session: "The Early Earth: inside out and alive" (SAMUEL, H.)
- 29.06.-04.07.2008, International Conference on Origin and Evolution of Planets 2008, Ascona, Switzerland: Main Co-organizers (RUBIE, D.C.; SAMUEL, H.)
- 06.-14.08.2008, 33<sup>rd</sup> International Geological Congress, Oslo, Norway: Symposium EID-02: "Properties and dynamics of mantle and core" (OHTANI, E.; STEINLE-NEUMANN, G.; STEINBERGER, B.; CONNOLLY, J.)
- 14.09.-17.09.2008, 86<sup>th</sup> Annual Meeting of the German Mineralogical Society (DMG), Berlin, Germany: Symposia S10 & S13, "New Insights from New Analytical Method" (LANGENHORST, F.; WEYER, S.)
- 30.09.-02.10.2008, Geodynamik Workshop 2008, Neustadt an der Weinstraße, Germany: Convener for the session "Core related dynamics" (SAMUEL, H.)
- 21.-24.10.08, International Workshop on "Transport Properties in the Lower Mantle", Yunishigawa, Tochigi, Japan: Co-organizer (RUBIE, D.C.)
- 22.-25.10.2008, Workshop on *ab initio* calculations in geosciences, Cracow, Poland: (JOCHYM, P.; STEINLE-NEUMANN, G.)



## 6. Visiting scientists

### *6.1 Visiting scientists funded by the Bayerisches Geoinstitut*

- BAUMGARTNER, L., Université de Lausanne, Faculty of Geosciences and Environment, Lausanne, France: 12.-14.02.2008
- DOBSON, D., University College London, Department of Earth Sciences, London, U.K.: 09.-11.12.2008
- ETZEL, K., Universität Kiel, Institut für Geowissenschaften, Mineralogie – Kristallographie, Kiel, Germany: 24.-26.09.2008
- GEISLER-WIERWILLE, T., Westfälische Wilhelms-Universität Münster, Institut für Mineralogie, Münster, Germany: 28.-30.07.2008
- GHOSH, S., Indian Institute of Technology, Kharagpur, India: 26.05.-11.07.2008
- HOLZHEID, A., Universität Kiel, Institut für Geowissenschaften, Kiel, Germany: 09.-11.12.2008
- ITO, E., Okayama University, Institute for Study of the Earth's Interior, Misasa, Japan: 04.-06.11.2008
- JACKSON, J., California Institute of Technology, Division of Geological & Planetary Sciences, Pasadena, USA: 25.-28.10.2008
- KATSURA, T., Okayama University, Institute for Study of the Earth's Interior, Okayama, Japan: 07.-12.12.2008
- KING, S., Virginia Polytechnic Institute and State University, Geosciences, Blacksburg, USA: 12.-18.05.2008
- KUZMINA, E., Institute of Precambrian Geology and Geochronology (IPGG), St. Petersburg, Russia: 05.-10.04.2008
- LEE, K.K.M., New Mexico State University, Physics Department, Las Cruces, USA: 08.05.-18.06.2008
- LEHRMANN, B., Wolfsburg, Germany: 13.-14.03.2008
- LERCHBAUMER, L., Universität Wien, Erdwissenschaftliches Zentrum, Wien, Austria: 15.-16.05.2008
- MANTHILAKE, G., Okayama University, Institute for the Study of Earth's Interior, Tottori, Japan: 16.-21.09.2008
- MAYNARD, H., University of Edinburgh, School of Physics, Edinburgh, U.K.: 06.-10.05.2008
- MELOSH, J., University of Arizona, Lunar and Planetary Lab, Tucson, USA: 06.-11.07.2008
- NESTOLA, F., Università degli Studi di Padova, Dipartimento di Mineralogia e Petrologia, Padova, Italy: 18.08.-06.09.2008
- NI, H., University of Michigan, Department of Geological Sciences, Ann Arbor, USA: 23.-29.05.2008
- NOVELLA, D., Università degli Studi di Padova, Dipartimento di Mineralogia e Petrologia, Padova, Italy: 26.-27.02.2008

OHTANI, E., Tohoku University, Institute of Mineralogy, Petrology and Economic Geology, Sendai, Japan: 10.-14.08.2008

PAMATO, M., Università degli Studi di Padova, Dipartimento di Geoscienze, Padova, Italy: 02.-09.09.2008

PANDOLFO, F., Università degli Studi di Padova, Dipartimento di Geoscienze, Padova, Italy: 01.07.-31.08.2008

PENTCHEVA, R., LMU München, Department für Geo- und Umweltwissenschaften, München, Germany: 17.-18.01.2008

PICKLES, J., University of Bristol, Department of Earth Sciences, Bristol, U.K.: 06.-13.07.2008

POZZOBON, R., Università degli Studi di Padova, Dipartimento di Geoscienze, Padova, Italy: 03.06.-25.07.2008, 04.-09.08.2008

PRESNALL, D., University of Texas at Dallas, Department of Geosciences, Richardson, USA: 11.03.-12.04.2008, 01.-31.10.2008

PREWITT, C., University of Arizona, Department of Geosciences, Tucson, USA: 20.-23.04.2008

QUETSCHER, A., Braunschweig, Germany: 11.-12.03.2008

RADCHENKO, T., N.A.S.U., Institute for Metal Physics, Department of Solid State Theory, Kiev, Ukraine: 13.04.-25.05.2008

REICHMANN, H.-J., GeoForschungsZentrum, Potsdam, Germany: 01.-02.12.2008

RUSKOV, T., Bulgarian Academy of Sciences, Institute for Nuclear Research and Nuclear Energy, Sofia, Bulgaria: 05.-09.05.2008

SEIFERT, D., Fachhochschule Jena, Germany: 23.-25.07.2008

SEIFERT, F., Berlin, Germany: 25.-26.02.2008

SHARMA, R., Chaudhary Devi Lal University, Sirsa Haryana, India: 16.-19.11.2008

SMYTH, J.R., University of Colorado at Boulder, Geological Sciences, Boulder, USA: 24.01.-11.02.2008

STEIN, H., Colorado State University, Department of Geosciences, Fort Collins, USA: 26.-27.06.2008

TACKLEY, P., ETH Zürich, Institut für Geophysik, Zürich, Switzerland: 14.-15.02.2008

VAN WESTRENEN, W., VU University Amsterdam, Faculty of Earth and Life Sciences, Amsterdam, The Netherlands: 10.-11.12.2008

VIEIRA CONCEIÇÃO, R. Universidade Federal do Rio Grande do Sul, Porto Alegre, Brasil: 19.-27.04.2008

WALTER, M., University of Bristol, Department of Earth Sciences, Bristol, U.K.: 10.-11.12.2008

WOODLAND, A., Johann Wolfgang Goethe-Universität Frankfurt/M., Institut für Geowissenschaften, Frankfurt/M., Germany: 06.-17.01.2008

YANG, X., University of Science and Technology of China, School of Earth and Space Sciences, Hefei, China: 23.-28.06.2008

YAO, L., Universität Karlsruhe, Laboratorium für Elektronenmikroskopie, Karlsruhe, Germany: 07.-08.10.2008

## 6.2 Visiting scientists supported by other externally funded BGI projects

- ARÉVALO, Á., Universidad Complutense de Madrid, Departamento de Química Inorgánica I, Madrid, Spain: *"High pressure synthesis of perovskite and related materials"*, 20.-28.04.2008, 06.-14.07.2008 (RITA<sup>\*A</sup>)
- BEJINA, F., Université Paul Sabatier, CNRS – Observatoire Midi-Pyrénées, Toulouse, France: *"Self-diffusion of hydrogen in wadsleyite and ringwoodite: Toward an estimation of water concentration in the transition zone"*, 04.-14.11.2008 (RITA<sup>\*A</sup>)
- BERRY, A., Imperial College London, Department of Earth Sciences and Engineering, London, U.K.: *"High-resolution <sup>17</sup>O NMR of hydrous wadsleyite and hydrous ringwoodite"*, 01.-12.06.2008 (RITA<sup>\*A</sup>)
- BOLFAN-CASANOVA, N., Université Clermont-Ferrand, Laboratoire Magmas et Volcans, Clermont-Ferrand, France: *"Study of the aluminum substitution in magnesium silicate perovskite by X-ray single crystal diffraction and Raman spectroscopy in-situ at high pressure"*, 04.-14.11.2008 (RITA<sup>\*A</sup>)
- CARACAS, R., École normale supérieure de Lyon, France: 20.-28.02.2008 (c2c<sup>\*C</sup>)
- CHANTEL, J., Université Clermont-Ferrand, Laboratoire Magmas et Volcans, Clermont-Ferrand, France: 05.-08.05.2008 (ENB<sup>\*D</sup>)
- CHEMIA, Z., Uppsala University, Department of Earth Sciences, Solid Earth Geology, Uppsala, Sweden: 22.-26.09.2008 (c2c<sup>\*C</sup>)
- COMBES, R., Université de Marne-la-Vallée, Laboratoire des Géomatériaux, Marne-la-Vallée, France: *"Evolution of chondrite materials at high pressure and temperature under different redox conditions: Implications for planetary mantle mineralogy"*, 14.-25.07.2008 (RITA<sup>\*A</sup>)
- COMODI, P., Università degli Studi di Perugia, Dipartimento di Scienze della Terra, Perugia, Italy: *"HP-HT behaviour of gypsum and its dehydration products: A spectroscopic study"*, 06.-12.07.2008 (RITA<sup>\*A</sup>)
- CORDIER, P., Université des Sciences et Technologies de Lille, Laboratoire de Structure et Propriétés de l'Etat Solide, Villeneuve d'Ascq, France: *"Deformation mechanisms in MgSiO<sub>3</sub> majorite garnet"*, 14.-26.07.2008 (RITA<sup>\*A</sup>)
- COTTENIER, S., Katholieke Universiteit Leuven, Nuclear and Radiation Physics, Leuven, Belgium: 12.-13.06.2008 (c2c<sup>\*C</sup>)
- DAVAILLE, A., Institut de Physique du Globe de Paris, Laboratoire de Dynamique des Systèmes Géologiques, Paris, France: 27.-31.05.2008 (ENB<sup>\*D</sup>)
- DEMOUCHY, S., Université Montpellier II, Laboratoire Géosciences Montpellier, UMR CNRS 5243 - CC060, Montpellier, France: *"Inheritance of crystal preferred orientation during phase transformation: olivine > wadsleyite"*, 19.10.-08.11.2008, 16.-25.11.2008 (RITA<sup>\*A</sup>)
- DOBSON, D., University College London, Department of Earth Sciences, London, U.K.: *"The effect of the spin collapse transition in Fe on elastic properties of silicate perovskite"*, 23.06.-04.07.2008 (RITA<sup>\*A</sup>)

- DOS SANTOS-GARCIA, A., Universidad Complutense de Madrid, Departamento de Quimica Inorganica I, Madrid, Spain: *"High pressure synthesis of perovskite based materials"*, 20.-28.04.2008 (RITA<sup>\*A</sup>)
- DOLEJŠ, D., Charles University, Institute of Petrology and Structural Geology, Prague, Czech Republic: 03.-04.11.2008, 08.-09.12.2008 (c2c<sup>\*C</sup>)
- FAIT, A., Basell Poliolefins, 'Giulio Natta' Research Centre, Ferrara, Italy: *"High pressure crystallization of semicrystalline polypropylene"*, 02.-05.12.2008 (RITA<sup>\*A</sup>)
- FABIAN, K., Geological Survey of Norway, Trondheim, Norway: *"Magnetic exchange bias in synthetic samples from the ilmenite-hematite solid solution series: Magnetic properties, nanoscale exsolution and chemical ordering"*, 08.-13.09.2008 (RITA<sup>\*A</sup>)
- FERNÁNDEZ SANJULIÁN, J., Universidad Complutense de Madrid, Departamento de Quimica Inorganica I, Madrid, Spain: *"High pressure synthesis of perovskite and related materials"*, 06.-14.07.2008 (RITA<sup>\*A</sup>)
- FERNANDEZ SANJULIAN, J., Universidad Complutense de Madrid, Departamento de Quimica Inorganica I, Madrid, Spain: *"High pressure synthesis of perovskite based materials"*, 23.-29.11.2008 (RITA<sup>\*A</sup>)
- FISCHER, K., Brown University, Geological Sciences, Providence, USA: 06.-09.05.2008 (ENB<sup>\*D</sup>)
- FUMAGALLI, P., Università degli Studi di Milano, Dipartimento di Scienze della Terra, Milano, Italy: 12.-14.11.2008 (ENB<sup>\*D</sup>)
- GATTA, G.D., Università degli Studi di Milano, Dipartimento di Scienze della Terra, Milano, Italy: *"High-pressure behaviour of pollucite, a rare Cs-bearing open framework silicate"*, 27.07.-09.08.2008 (RITA<sup>\*A</sup>)
- GLAZYRIN, K., Moscow State Institute of Steel and Alloys, Moscow, Russia: 02.-08.02.2008 (ENB<sup>\*D</sup>)
- GREENBERG, E., Tel Aviv University, School of Physics & Astronomy, Tel Aviv, Israel: *"High pressure properties of  $MFe_2O_4$  and  $FeM_2O_4$  ( $M=Cr, Co, Al, Mg, Zn$ ) ferrite spinels"*, 01.-15.06.2008 (RITA<sup>\*A</sup>)
- GUZMICS, T., Eötvös University, Department of Petrology and Geochemistry, Lithosphere Research Group, Budapest, Hungary: *"Carbonatite melt research with additional components of apatite and K feldspar at high P and T"*, 21.04.-04.05.2008 (RITA<sup>\*A</sup>)
- HARRIES, D., Universität Göttingen, Germany: 21.-23.04.2008 (ENB<sup>\*D</sup>)
- HIEMSTRA, T., Wageningen University, Soil Quality Department, Wageningen, The Netherlands: *"Reactive surface area of iron oxides in natural sample"*, 07.-11.11.2008 (RITA<sup>\*A</sup>)
- HIRAI, S., The University of Edinburgh, Centre for Science at Extreme Conditions, Edinburgh, U.K.: *"High-pressure behaviour of  $CaMnO_3$  and the perovskite phase transition"*, 09.-13.06.2008 (RITA<sup>\*A</sup>)
- HOBBS, L., University of Bristol, Department of Earth Sciences, Bristol, U.K.: *"Exploring volcanism: Distribution of sulphur between silicate melt and aqueous fluids, and adsorption of HCl onto volcanic ash"*, 15.11.-31.12.2008 (AtG<sup>\*B</sup>)

- INGRIN, J., Université Paul Sabatier, CNRS – Observatoire Midi-Pyrénées, Toulouse, France: *"Self-diffusion of hydrogen in wadslyite and ringwoodite: Toward an estimation of water concentration in the transition zone"*, 04.-14.11.2008 (RITA<sup>\*A</sup>)
- IVANOVA, S., Bulgarian Academy of Sciences, Sofia, Bulgaria: *"High pressure effect on the formation of layered lithium cobaltates with Li occupying the Co-site"*, 29.06.-07.07.2008 (RITA<sup>\*A</sup>)
- JONNALAGADDA, M., University of Pune, Department of Geology, Pune, India: 26.02.-04.03.2008 (ENB<sup>\*D</sup>)
- KARIPIDIS, T., Lomonosov Moscow State University, Moscow, Russia: 04.-08.02.2008 (ENB<sup>\*D</sup>)
- KREBS, C., Wageningen University, Soil Quality Department, Wageningen, The Netherlands: *"Reactive surface area of iron oxides in natural sample"*, 07.-14.11.2008 (RITA<sup>\*A</sup>)
- KURAKEVYCH, O., Université Paris Nord, LPMTM-CNRS, Institut Galilée, Villetaneuse, France: *"B-P system at high pressure and temperature – DAC and MA studies"*, 20.04.-08.05.2008, 19.-26.10.2008 (RITA<sup>\*A</sup>)
- LEE, K.K.M., New Mexico State University, Physics Department, Las Cruces, USA: 12.-22.10.2008 (c2c<sup>\*C</sup>)
- LIN, J.-F., The University of Texas at Austin, Department of Geological Sciences, Austin, USA: 07.-13.09.2008 (ENB<sup>\*D</sup>)
- MAINPRICE, D., Université Montpellier II, Laboratoire Géosciences Montpellier, UMR CNRS 5243 - CC060, Montpellier, France: *"Inheritance of crystal preferred orientation during phase transformation: olivine > wadsleyite"*, 16.-25.11.2008 (RITA<sup>\*A</sup>)
- MALAVERGNE, V., Université de Marne-la-Vallée, Laboratoire des Géomatériaux, Marne-la-Vallée, France: *"Evolution of chondrite materials at high pressure and temperature under different redox conditions: Implications for planetary mantle mineralogy"*, 14.-25.07.2008 (RITA<sup>\*A</sup>)
- MARTIN, A., University of Otago, Department of Geology, Dunedin, New Zealand: *"Mantle redox conditions beneath Antarctica"*, 01.01.-29.02.2008 (AtG<sup>\*B</sup>)
- MARTIN, A., University of Otago, Department of Geology, Dunedin, New Zealand: 25.-29.08.2008 (AtG<sup>\*B</sup>)
- MATAS, J., École normale supérieure de Lyon, France: 15.-16.05.2008 (ENB<sup>\*D</sup>)
- MAZZULLO, S., Basell Poliolefins, 'Giulio Natta' Research Centre, Ferrara, Italy: *"High pressure crystallization of semicrystalline polypropylene"*, 02.-05.12.2008 (RITA<sup>\*A</sup>)
- MCDONOUGH, W., University of Maryland, Department of Geology, Geochemistry Laboratory, College Park, USA: 17.-21.08.2008 (ENB<sup>\*D</sup>)
- MCENROE, S., Geological Survey of Norway, Trondheim, Norway: *"Magnetic exchange bias in synthetic samples from the ilmenite-hematite solid solution series: Magnetic properties, nanoscale exsolution and chemical ordering"*, 07.-13.09.2008 (RITA<sup>\*A</sup>)
- MCGAFF, A., The University of Edinburgh, School of Engineering & Electronics, Edinburgh, U.K.: *"Synthesis of new nitrides and their alloy precursors at high pressures and temperatures"*, 20.-27.01.2008 (RITA<sup>\*A</sup>)

- MCGAFF, A., The University of Edinburgh, School of Engineering & Electronics, Edinburgh, U.K.: *"Metal nitride and alloy synthesis using high pressures and temperatures"*, 24.-30.08.2008 (RITA<sup>\*A</sup>)
- MINCH, R., Universität Kiel, Institut für Geowissenschaften, Kiel, Germany: 14.07.-01.08.2008 (DFG<sup>\*E</sup>)
- NAZZARENI, S., Università degli Studi di Perugia, Dipartimento di Scienze della Terra, Perugia, Italy: *"HP-HT behaviour of gypsum and its dehydration products: A spectroscopic study"*, 29.06-01.07.2008 (RITA<sup>\*A</sup>)
- OKAMOTO, H., University of Oslo, Department of Chemistry, Oslo, Norway: *"High pressure synthesis of novel cobalt oxide, RECoO<sub>3</sub> with RE = Yb and Lu"*, 18.-29.05.2008 (RITA<sup>\*A</sup>)
- PAL, A., Indian Institute of Technology Roorkee, Department of Earth Sciences, Roorkee, India: 19.-25.01.2008 (ENB<sup>\*D</sup>)
- PASCARELLI, S., European Synchrotron Radiation Facility, Grenoble, France: 02.-04.04.2008 (ENB<sup>\*D</sup>)
- PICARD, D., Institut des Sciences de la Terre d'Orléans (ISTO), Orléans, France: *"Shear zones in magmatic dense suspensions at HP-HT: Insight from CPO and SPO analysis"*, 28.04.-06.05.2008 (RITA<sup>\*A</sup>)
- PICKLES, J., University of Bristol, Department of Earth Sciences, Bristol, U.K.: *"Lower mantle to upper mantle: The back reaction and redox relations during mantle upwelling and avalanche"*, 01.01.-29.02.2008 (AtG<sup>\*B</sup>)
- PICKLES, J., University of Bristol, Department of Earth Sciences, Bristol, U.K.: *"Trace element thermobarometry of coexisting garnet and CPX"*, 26.10.-02.11.2008 (RITA<sup>\*A</sup>)
- POKROVSKI, G., Université Paul Sabatier, LMTG, Toulouse, France: *"In situ Raman spectroscopy study of sulphur speciation in high-temperature high-pressure aqueous fluids using the hydrothermal diamond-anvil cell"*, 02.-15.11.2008 (RITA<sup>\*A</sup>)
- RAY, S., Indian Institute of Technology, Department of Earth Sciences, Bombay, India: 10.-17.12.2008 (ENB<sup>\*D</sup>)
- ROZENBERG, G., Tel Aviv University, School of Physics & Astronomy, Tel Aviv, Israel: *"High pressure properties of MFe<sub>2</sub>O<sub>4</sub> and FeM<sub>2</sub>O<sub>4</sub> (M=Cr, Co, Al, Mg, Zn) ferrite spinels"*, 01.-15.06.2008 (RITA<sup>\*A</sup>)
- RUDNICK, R., University of Maryland, Department of Geology, Geochemistry Laboratory, College Park, USA: 17.-21.08.2008 (ENB<sup>\*D</sup>)
- SERGHIOU, G., University of Edinburgh, The School of Engineering and Electronics, Edinburgh, U.K.: *"Synthesis of new nitrides and their alloy precursors at high pressures and temperatures"*, 23.-27.01.2008 (RITA<sup>\*A</sup>)
- SHINOVA, E., Bulgarian Academy of Sciences, Institute of General and Inorganic Chemistry, Sofia, Bulgaria: *"Structural characterization of lithium-nickel-cobalt-manganese oxides obtained under high pressure"*, 08.-24.01.2008 (RITA<sup>\*A</sup>)
- SKÁLA, R., Academy of Sciences of the Czech Republic, Institute of Geology, Prague, Czech Republic: *"Experimental shock deformation in dolomite: A transmission electron microscopic study"*, 08.-25.06.2008 (RITA<sup>\*A</sup>)

- SMYTH, J.R., University of Colorado at Boulder, Geological Sciences, Boulder, USA: 12.-14.02.2008, 30.07.-10.08.2008 (RITA<sup>\*A</sup>)
- SOKOLOV, P., Université Paris Nord, LPMTM-CNRS, Institut Galilée, Villetaneuse, France: *"Synthesis and investigation of cubic FeO-ZnO solid solutions at high pressures"*, 19.-26.10.2008 (RITA<sup>\*A</sup>)
- SOLOZHENKO, V., Université Paris Nord, LPMTM-CNRS, Institut Galilée, Villetaneuse, France: *"B-P system at high pressure and temperature – DAC and MA studies"*, 20.04.-08.05.2008, 19.-26.10.2008 (RITA<sup>\*A</sup>)
- SOLOZHENKO, V., Université Paris Nord, LPMTM-CNRS, Institut Galilée, Villetaneuse, France: *"Synthesis and investigation of cubic FeO-ZnO solid solutions at high pressures"*, 19.-26.10.2008 (RITA<sup>\*A</sup>)
- SYASSEN, K., Max Planck Institute for Solid State Research, High Pressure Group, Stuttgart, Germany: 05.08.2008 (RITA<sup>\*A</sup>)
- TALYZIN, A., Umeå University, Experimental Physics, Umeå, Sweden: *"New carbon nanomaterials by high temperature high pressure exfoliation"*, 07.-18.01.2008 (RITA<sup>\*A</sup>)
- TRAUTH, M., Universität Potsdam, Institut für Geowissenschaften, Potsdam-Golm, Germany: 22.-26.09.2008 (ENB<sup>\*D</sup>)
- TSUCHIYA, T., Ehime University, Geodynamics Research Center, Matsuyama, Japan: 25.-29.10.2008 (c2c<sup>\*C</sup>)
- WENG, L., Wageningen University, Soil Quality Department, Wageningen, The Netherlands: *"Reactive surface area of iron oxides in natural sample"*, 02.-08.11.2008 (RITA<sup>\*A</sup>)
- WILLIAMS, H., Oxford University, Department of Earth Sciences, Oxford, U.K.: *"The effects of core formation on the Pb- and Tl- isotopic composition of the silicate Earth"*, 07.-17.12.2008 (RITA<sup>\*A</sup>)
- WOOD, B., Oxford University, Department of Earth Sciences, Oxford, U.K.: *"The effects of core formation on the Pb- and Tl- isotopic composition of the silicate Earth"*, 24.03.-02.04.2008, 07.-17.12.2008 (RITA<sup>\*A</sup>)
- YONCHEVA, M., Bulgarian Academy of Sciences, Sofia, Bulgaria: *"High pressure effect on the formation of layered lithium cobaltates with Li occupying the Co-site"*, 29.06.-07.07.2008 (RITA<sup>\*A</sup>)

\*A) RITA: EU "Research Infrastructures: Transnational Access" Programme

\*B) AtG: EU Marie Curie Actions "Atomic to Global" Training Programme

\*C) c2c: EU Marie Curie Research Training Network - the fate of subducted material

\*D) ENB: International Graduate School under the Elitenetzwerk Bayern

\*E) DFG: Deutsche Forschungsgemeinschaft

### 6.3 Visitors (externally funded)

ANGEL, R., Virginia Polytechnic Institute and State University, Geosciences, Blacksburg, USA: 21.-28.06.2008

BLAESS, U., Friedrich-Schiller-Universität Jena, Institut für Geowissenschaften, Mineralogie und Geochemie, Jena, Germany: 04.02.2008, 26.-29.08.2008

BRAUN, C., LMU München, Department Chemie und Biochemie, München, Germany: 28.-30.07.2008

CAILLET, C., Muséum National d'Histoire Naturelle, Paris, France: 15.-19.09.2008

CAPALBO, C., Università degli Studi di Perugia, Dipartimento di Scienze della Terra, Perugia, Italy: 26.05.-25.08.2008 (Erasmus Student Placement)

CHAREEV, D., Institute of Experimental Mineralogy, Chernogolovka, Moscow region, Russia: 15.06.-01.08.2008

CHRISTOFIDES, G., Aristotle University of Thessaloniki, School of Geology, Department of Mineralogy, Petrology and Economic Geology, Thessaloniki, Greece: 19.-26.06.2008

DEUTSCH, A., Universität Münster, Institut für Planetologie, Münster, Germany: 08.-11.06.2008

GANNOUN, M., Laboratoire Magmas et Volcans, UMR CNRS 6524, Observatoire de Physique du Globe, Clermont-Ferrand, France: 14.-19.12.2008

HEWENER, B., Technische Universität Kaiserslautern, AG Biophysik und Medizinische Physik, Kaiserslautern, Germany: 10.07.-01.08.2008

IRIFUNE, T., Ehime University, Geodynamics Research Center, Matsuyama, Japan: 07.-09.04.2008, 26.07.-06.08.2008

KAKEGAWA, T., Tohoku University, Graduate School of Science, Sendai, Japan: 16.-18.06.2008

KEGLER, P., Christian-Albrechts-Universität zu Kiel, Institut für Geowissenschaften, Abteilung Mineralogie – Petrologie, Kiel, Germany: 11.-13.11.2008

KLEIN, R., Gesellschaft für Schwerionenforschung mbH, Darmstadt, Germany: 04.-08.02.2008

KONZETT, J., Universität Innsbruck, Institut für Mineralogie und Petrographie, Innsbruck, Austria: 18.02.-02.03.2008

LITVIN, Y.A., Russian Academy of Sciences, Institute of Experimental Mineralogy, Chernogolovka, Russia: 29.03.-13.04.2008

MALASPINA, N., Università degli Studi di Milano, Dipartimento di Scienze della Terra, Milano, Italy: 12.-14.11.2008

MANAKOV, A., Novosibirsk Institut of Inorganic Chemistry, Siberian Division of Russian Academy of Sciences, Novosibirsk, Russia: 05.-07.05.2008

MANTOVANI, M., Universidad de Sevilla, Instituto de Ciencia de Materiales (ICMSE), Sevilla, Spain: 23.02.-01.03.2008, 06.10.-07.11.2008

MARQUARDT, H., GeoForschungsZentrum, Potsdam, Germany: 06.08.2008

MATIZAMHUKA, W.R., University of the Witwatersrand, School of Chemical & Metallurgical Engineering, Johannesburg, South Africa: 01.03.-30.04.2008, 06.09.-06.11.2008

MINCH, R., Universität Kiel, Institut für Geowissenschaften, Kiel, Germany: 05.-16.05.2008

NESTOLA, F., Università degli Studi di Padova, Dipartimento di Mineralogia e Petrologia, Padova, Italy: 27.02.2008

OGIENKO, A., Novosibirsk Institut of Inorganic Chemistry, Siberian Division of Russian Academy of Sciences, Novosibirsk, Russia: 05.-07.05.2008

OSADCHII, E., Institute of Experimental Mineralogy, Chernogolovka, Moscow region, Russia: 27.07.-01.08.2008

OTSUKA, K., Yale University, Department of Geology and Geophysics, New Haven, USA: 05.-30.07.2008

PASQUAL, D., Università degli Studi di Padova, Dipartimento di Mineralogia e Petrologia, Padova, Italy: 15.-19.07.2008

POLLOK, K., Friedrich-Schiller-Universität Jena, Institut für Geowissenschaften, Mineralogie und Geochemie, Jena, Germany: 27.-28.02.2008

REICHMANN, H.-J., GeoForschungsZentrum, Potsdam, Germany: 06.08.2008

REINHARD, B., Universität Heidelberg, Mineralogisches Institut, Heidelberg, Germany: 18.-19.12.2008

SCHÄRER, U., Université de Nice Sophia Antipolis, Nice, France: 24.-25.04.2008

SCHMÄDICKE, E., Friedrich-Alexander-Universität Erlangen-Nürnberg, Lehrstuhl für Mineralogie, Germany: 28.03.2008

SCHOLLENBRUCH, K., Johann Wolfgang Goethe-Universität Frankfurt/M., Institut für Geowissenschaften, Frankfurt/M., Germany: 15.-25.01.2008, 10.-14.03.2008, 07.-11.04.2008, 14.-18.07.2008, 17.-21.11.2008

SINDERN, S., RWTH Aachen, Germany: 24.07.2008

SITTE, J., Friedrich-Schiller-Universität Jena, Institut für Ökologie, Forschungsgruppe Limnologie, Jena, Germany: 24.-28.11.2008

SMYTH, J.R., University of Colorado at Boulder, Geological Sciences, Boulder, USA: 26.05.-13.06.2008

SWAMY, V., Monash University, Department of Materials Engineering, Victoria, Australia: 11.-21.02.2008

SZABÓ, C., Eötvös University, Budapest, Hungary: 01.-04.05.2008

WOODLAND, A., Johann Wolfgang Goethe-Universität Frankfurt/M., Institut für Geowissenschaften, Frankfurt/M., Germany: 08.-12.10.2008

ZACHARIAS, J., Charles University Prague, Czech Republic: 22.-23.01.2008

ZVORISTE, C., Technische Universität Darmstadt, Fachbereich Materialwissenschaft, Darmstadt, Germany: 25.-29.02.2008, 14.04.-09.05.2008, 04.-15.08.2008



## 7. Additional scientific activities

### 7.1 Ph.D. theses

GAVRILENKO, P.: Water solubility in diopside

HOLBIG, E.: TiO<sub>2</sub>-ZrO<sub>2</sub> solid solution at high pressure and temperature

KANTOR, A.: Elasticity measurements at extreme conditions: application to FeO and FeNi-alloy

MANN, U.: Physical and chemical constraints on core-mantle differentiation in terrestrial planets

SAIKIA, A.: Experimental constraints on silicate perovskite forming reactions and elastic properties: geophysical implications for chemical heterogeneity in the deep mantle

### 7.2 Honours and awards

Wieland DIETRICH received the student poster award (see section 3.1 c.) at the 13<sup>th</sup> non-linear dynamics meeting in October 2008

Innokenty KANTOR received the 2008 Mineral and Rock Physics Outstanding Student Award of the American Geophysical Union (AGU)

Hans KEPPLER was elected a member of the German National Academy of Sciences (Leopoldina) and of the Bavarian Academy of Sciences

Olga NARYGINA received the award of "Best student presentation" at the 2<sup>nd</sup> conference of the European Mineral Sciences Initiative (EuroMinSci), April 2008, Giens/Toulon, France

David RUBIE received the Schlumberger Award of the Mineralogical Society of Great Britain and Ireland

David RUBIE received the Abraham-Gottlob-Werner Medaille of the German Mineralogical Society (Deutsche Mineralogische Gesellschaft)

Federica SCHIAVI was awarded the "Student Prize" of the Italian Mineralogical and Petrological Society (SIMP) for her outstanding thesis

### 7.3 Editorship of scientific journals

DOLEJŠ, D. Editorial Advisory Board of "Journal of Geosciences"

DUBROVINSKY, L.S. Member of the Editorial Board of the "High Pressure Research - International Journal"

HEIDELBACH, F. Associate Editor "American Mineralogist"

KEPPLER, H. Editorial Advisory Board "Elements"

Editorial Board "Contributions to Mineralogy and Petrology"

LANGENHORST, F.	Associate editor "Geochemistry/Chemie der Erde"
MCCAMMON, C.A.	Editor "Physics and Chemistry of Minerals"
RUBIE, D.C.	Editor-in-Chief "Physics of the Earth and Planetary Interiors"

*7.4 Membership of scientific advisory bodies*

DUBROVINSKY, L.S.	Elected Chair of the Special Interest Group "Crystallography at extreme conditions" of the European Crystallography Union Member of the Review Panel of the Canadian Light Source Member of the Review Panel of the European Science Foundation
KEPPLER, H.	Member, Committee of Visitors, Deep Earth Section, National Science Foundation (USA) Chairman, Research Council of the German Mineralogical Society (Forschungskollegium Mineralogie der DMG) Member, Abraham Gottlob Werner Medal Committee, German Mineralogical Society (DMG) Member, Commission for Research of Bayreuth University (Präsidialkommission für Forschung und wissenschaftlichen Nachwuchs) Member, German National Academy of Sciences (Leopoldina) Member, Bavarian Academy of Sciences
LANGENHORST, F.	National Representative of the German Mineralogical Society (DMG) within the European Mineralogical Union (EMU) Member, Abraham Gottlob Werner Medal Committee, German Mineralogical Society (DMG) Chairman, Section Chemistry, Physics and Crystallography of Minerals, German Mineralogical Society (DMG) Vice-President, German Mineralogical Society (DMG) Member, "DFG-Senatskommission für geowissenschaftliche Gemeinschaftsforschung (Geokommission)"
MCCAMMON, C.A.	IMA Medal Committee of the International Mineralogical Association, Member MSA Lecture Program Committee of the Mineralogical Society of America, Member Fellows Committee of the Volcanology, Geochemistry & Petrology Section of the American Geophysical Union, Chairman Executive Committee of the Volcanology, Geochemistry & Petrology Section of the American Geophysical Union, Member

RUBIE, D.C.

Executive Committee of the Mineral and Rock Physics Focus  
Group of the American Geophysical Union, Member  
Advisory Board of "Mössbauer Information Exchange"  
International Advisory Board of the Mössbauer Effect Data  
Center

Member of AGU Mineral and Rock Physics Executive  
Committee

Member of Dana Medal Committee, Mineralogical Society of  
America

Member of Forschungskollegium Physik des Erdkörpers  
(FKPE)



## 8. Scientific and Technical Personnel

Name		Position	Duration in 2008	Funding source
ADJAOUD, Omar	M.Sc. (Physics)	Wiss. Mitarbeiter		BGI/IGS
AREFIN, Mohammad Lutful	M.Sc. (Nanomaterials)	Wiss. Mitarbeiter	to 31.12.	BGI/IGS <sup>1</sup>
AUDÉTAT, Andreas	Dr.	Akad. Rat z.A.		BGI
BALI, Enikő	Dr.	Wiss. Angestellte		BGI/VP
BAUMGARTNER, Alexander	Dipl.-Chem.	Wiss. Mitarbeiter	to 30.09.	BGI/IGS <sup>2</sup>
BEHRINGER, Nicole	Reg. Inspektorin	Verwalt. Beamtin		BGI
BERNINI, Diego	Dipl.-Geol.	Gastwissenschaftler		EU
BÖHM, Ulrich		Mechaniker		BGI
BOFFA BALLARAN, Tiziana	Dr.	Akad. Rätin		BGI
BORISOV, Alexander	Dr.	Wiss. Angestellter	01.02.-30.04.	BGI/VP
BUCHERT, Petra		Fremdsprachen- sekretärin		BGI
CARACAS, Razvan	Dr.	Forschungsstipendiat	01.07.-30.11.	AvH
CHANTEL, Julien	M.Sc.	Gastwissenschaftler	from 01.10.	EU
DE KOKER, Nico	Dr.	Gastwissenschaftler	from 01.09.	EU
DITTMANN, Uwe		Präparator		BGI
DOLEJŠ, David	Dr.	Wiss. Angestellter	to 31.10.	BGI/IGS
DUBROVINSKY, Leonid	PD Dr.	Akad. Oberrat		BGI
EL GORESY, Ahmed	Prof. Dr.			BGI/VP <sup>3</sup>
ESCUDERO, Alberto	Dr.	Wiss. Angestellter	01.02.-31.07. 01.08.-30.09. 01.10.-30.11. from 01.12.	EU/Jena DFG BMBF DFG
ETZEL, Katja	Dr.	Wiss. Angestellte	from 01.12.	BMBF
FISCHER, Heinz		Mechaniker		BGI
FROST, Daniel	Dr.	Akad. Direktor		BGI
GANSKOW, Geertje	Dipl.-Geol.	Wiss. Mitarbeiterin	01.01.-19.07.	BGI/IGS
		Wiss. Angestellte	from 20.07.	DFG
GAVRILENKO, Polina	M.Sc. (Geol.)/ Dr.	Wiss. Mitarbeiterin	01.01.-31.05 from 01.06.	BGI/IGS DFG
GLAZYRIN, Konstantin	Ing. Phys.	Wiss. Mitarbeiter	from 22.07.	BGI/IGS
GOLLNER, Gertrud		Chem.-Techn. Assistentin		BGI
GUDFINNSSON, Gudmundur	Dr.	Wiss. Angestellter	to 31.08.	EU
HARRIES, Dennis	Dipl. Geosciences	Wiss. Mitarbeiter	01.09.-31.12. 01.10.-31.12.	DFG <sup>4</sup> BMBF
HEIDELBACH, Florian	Dr.	Wiss. Mitarbeiter	01.01.-10.12. 11.12.-31.12.	EU BGI/IGS
HERRMANN, Elisabeth	MTA	Chem.-Techn. Assistentin		BGI

HIRSEMANN, Dunja	Dipl.-Chem.	Wiss. Mitarbeiterin	from 01.04.	BGI/IGS <sup>2</sup>
HOLBIG, Eva	Dipl.-Min.	Wiss. Mitarbeiterin	to 28.02.	Industry
HOPF, Juliane	Dipl.-Biol.	Wiss. Angestellte	from 01.02.	DFG/Jena
HUANG, Xianliang	M.E. (Material Science)	Wiss. Mitarbeiter		BGI/IGS <sup>1</sup>
KANTOR, Anastasia	Cand. of Science/Dr.	Wiss. Angestellte		DFG
KANTOR, Innokenty	Dr.	Wiss. Angestellter	to 14.03.	Industry
KEPPLER, Hans	Prof. Dr.	Leiter		BGI
KESHAV, Shantanu	Dr.	Wiss. Angestellter		BGI/VP
KEYSSNER, Stefan	Dr.	Akad. Oberrat		BGI
KISON-HERZING, Lydia		Sekretärin		BGI
KLASINSKI, Kurt	Dipl.-Ing. (FH)	Techn. Angestellter		BGI
KRAUßE, Detlef	Dipl.-Inform. (FH)	Techn. Angestellter		BGI
KRIEGL, Holger		Haustechniker		BGI
KUMBAR, Suresh	M.Sc. (Inorg. Chem.)	Wiss. Mitarbeiter		BGI/IGS <sup>2</sup>
KUNZ, Daniel	Dipl.-Chem.	Wiss. Mitarbeiter	from 01.10.	BGI/IGS <sup>2</sup>
KURNOSOV, Alexander	Dr.	Wiss. Angestellter	to 31.08.	BGI/VP
LANGENHORST, Falko	Prof. Dr.			BGI
LERCHBAUMER, Linda	Mag. rer. nat.	Wiss. Angestellte	from 01.09.	DFG
LI, Yuan	B.Sc.	Stipendiat		EU
LIEBL, Mario	Dipl.-Chem.	Wiss. Mitarbeiter	15.01.-14.07. from 01.09.	BGI/IGS <sup>2</sup> BGI/IGS <sup>2</sup>
LINHARDT, Sven		Elektrotechniker		BGI
LONGO, Micaela	Dipl.-Min.	Gastwissenschaftlerin		EU
MANN, Ute	Dipl.-Geol./ Dr.	Wiss. Mitarbeiterin	01.01.-14.01. 15.01.-14.04.	BGI/IGS EU
MANNING, Craig	Prof.	Forschungspreisträger	03.07.-31.08.	AvH
MCCAMMON, Catherine	Dr.	Akad. Oberrätin		BGI
MIYAJIMA, Nobuyoshi	Dr.	Akad. Rat z.A.		BGI
MOOKHERJEE, Mainak	Dr.	Wiss. Angestellter	from 14.04.	BGI/VP
NARYGINA, Olga	M.Sc. (Physics)	Wiss. Angestellte	01.01.-14.07. from 15.07.	DFG BGI/IGS
NOVELLA, Davide	B.Sc.	stud. Hilfskraft	from 15.04.	BGI
PAMATO, Martha	B.Sc.	stud. Hilfskraft	from 15.10.	DFG
POLLOK, Kilian	Dr.	Akad. Rat a.Z.	from 01.04.	BGI
POTZEL, Anke		Chem.-Techn. Assistentin		BGI
RAMMING, Gerd		Elektroniker		BGI
RAUSCH, Oliver		Mechaniker		BGI
ROSCHEER Elisabeth		Wissensch. Techn. Assistentin		BGI
RUBIE, David C.	Prof. Dr.	Stellvertr. Leiter		BGI
SAIKIA, Ashima	M.Sc. (Geol.)/ Dr.	Wiss. Mitarbeiterin	to 31.03.	BGI/IGS

SAMUEL, Henri	Prof. Dr.	Juniorprofessor		Stiftung <sup>5</sup>
SCHIAVI, Federica	Dr.	Wiss. Mitarbeiterin	01.01.-14.01. 15.01.-14.07. 15.07.-31.10. from 01.11.	BGI/VP DFG BGI DFG
SCHULZE, Hubert		Präparator		BGI
SHCHEKA, Svyatoslav	Dr.	Wiss. Angestellter		DFG
SHEKHAR, Sushant	M.Sc.	Wiss. Mitarbeiter	from 17.06.	BGI/IGS
STAGNO, Vincenzo	Dipl.-Geol.	Gastwissenschaftler		EU
STEINLE-NEUMANN, Gerd	Dr.	Akad. Rat		BGI
TANG, Zhengning	M.E. (Material Science)	Gastwissenschaftler		EU
TSUNO, Kyusei	Dr.	Wiss. Mitarbeiter		DFG/ BGI/VP
ÜBELHACK, Stefan		Mechaniker		BGI
VAN MIERLO, Willem	M.Sc.	Gastwissenschaftler	from 04.01.	EU
WALTE, Nicolas	Dr.	Wiss. Angestellter		DFG
WEIGEL, Coralie	Dr.	Wiss. Angestellte		BGI/VP
WESTON, Lesley	Dr.	Wiss. Angestellte	to 31.05.	BGI/VP
WU, Xiang	Dr.	Forschungsstipendiat		AvH
YELAMANCHILI, Ram Sai	Dipl.-Chem.	Wiss. Mitarbeiter	to 31.08.	BGI/IGS <sup>2</sup>
ZARECHNAYA, Evgeniya	M.Sc.	Wiss. Mitarbeiterin		BGI/IGS

#### Abbreviations/explanations:

AvH	Alexander von Humboldt Foundation
BGI	Staff Position of Bayerisches Geoinstitut
BGI/VP	Visiting Scientists' Program of Bayerisches Geoinstitut
BMBF	Federal Ministry of Education and Research
DFG	German Science Foundation
EU	European Union
IGS	International Graduate School under the Elitenetzwerk Bayern "Structure, Reactivity and Properties of Oxide Materials"

---

<sup>1</sup> Fraunhofer ISC Würzburg

<sup>2</sup> Chair of Inorganic Chemistry I, Prof. Breu

<sup>3</sup> partially funded by the Visiting Scientists' Program of Bayerisches Geoinstitut

<sup>4</sup> Leibniz award Prof. Langenhorst

<sup>5</sup> Juniorprofessorship for Geodynamic Modeling funded by  
Stifterverband für die Deutsche Wissenschaft

## Index

Abrikosov, I. ....	174
Adjaoud, O. ....	186
Akber-Knutson, S. ....	43
Antonangeli, D. ....	93
Aquilanti, G. ....	47, 80
Arbaret, L. ....	151
Asahara, Y. ....	35, 38
Audétat, A. ....	63, 118, 134, 201
Auzende, A.-L. ....	93
Badro, J. ....	93
Bali, E. ....	118, 134
Benedetti, L.R. ....	93
Berkesi, M. ....	134
Bernini, D. ....	120
Bock, J. ....	197
Boffa Ballaran, T. ....	68, 69, 73, 101, 102, 103, 108, 190, 192
Borisov, A. ....	130
Braun, H.F. ....	176
Bruno, E. ....	68
Bulanova, G. ....	48
Bunge, H.-P. ....	31
Bureau, H. ....	41
Burton, B.P. ....	108, 186
Busse, F. ....	25
Capalbo, C. ....	101
Champallier, R. ....	151
Charee, D. ....	88
Chernyshov, D. ....	172
Chumakov, A. ....	29
Combes, R. ....	41
Comodi, P. ....	71, 101
Degtyareva, V.F. ....	184
Dera, P. ....	200
Dietrich, W. ....	25
Dmitriev, V. ....	172
Dobson, D. ....	140
Dolejš, D. ....	43, 120, 127, 154
Dubrovinskaia, N.A. ....	88, 172, 174, 176, 178, 197
Dubrovinsky, L.S. ....	27, 29, 47, 71, 77, 80, 83, 86, 88, 91, 165, 172, 174, 176, 178, 180, 184, 187, 189, 191, 197, 200

El Goresy, A. ....	162, 165, 172
Escudero, A. ....	157
Fabian, K. ....	108
Fait, A. ....	192
Farber, D.L. ....	93
Ferroir, T. ....	165
Filinchuk, Y. ....	172
Frost, D.J. ....	35, 36, 38, 40, 41, 45, 51, 54, 60, 73, 74, 95, 102, 112, 144, 148, 181, 182
Gallien, J.P. ....	41
Ganskow, G. ....	95
Gatta, G.D. ....	103
Gavrilenko, P. ....	123
Ghosh, S. ....	56
Gillet, P. ....	165
Glazyrin, K. ....	86, 197
Greenberg, E. ....	77
Gudfinnsson, G.H. ....	56, 58
Guzmics, T. ....	134
Hanfland, M. ....	93
Harries, D. ....	65
Heidelberg, F. ....	142, 146, 148, 151, 160
Hering, S. ....	180
Hörz, F. ....	169
Holbig, E. ....	91
Holzheid, A. ....	35
Hopf, J. ....	124
Hunt, S. ....	140
Huppertz, H. ....	180
Jacob, D. ....	96
John, T. ....	160
Kaminsky, F. ....	48
Kantor, A. ....	191
Kantor, I.Yu. ....	27, 80, 83, 184, 191, 200
Kegler, P. ....	35
Keppler, H. ....	27, 118, 120, 121, 123, 125, 127, 131, 135
Keshav, S. ....	56, 58
Kinski, I. ....	180
Koch-Müller, M. ....	68
Konschak, A. ....	125
Konzett, J. ....	60
Kopylova, M. ....	114
Kothe, E. ....	124

Kozlenko, D.P. ....	187
Krisch, M. ....	93
Kurnosov, A. ....	71, 77, 88, 184, 189
Langenhorst, F. ....	65, 95, 96, 105, 112, 124, 146, 148, 157, 160, 169
Launeau, P. ....	151
Lee, K.K.M. ....	43
Leroux, H. ....	96
Li, Y. ....	201
Litvin, Y. ....	88
Longo, M. ....	48, 114
Malavergne, V. ....	41
Mann, U. ....	35
Matizamhuka, W.R. ....	178
Mazzullo, S. ....	192
McCammon, C.A. ....	29, 48, 54, 83, 86, 130, 131, 144, 190, 192, 197
McEnroe, S.A. ....	105, 108
McGaff, A.J. ....	182
Mera, G. ....	178
Merten, D. ....	124
Mikhailushkin, A. ....	174
Minch, R. ....	189
Miyahara, M. ....	162
Miyajima, N. ....	105, 108, 112, 142, 144, 157, 169, 172, 176, 178
Mookherjee, M. ....	98
Müller, M. ....	194
Nagase, T. ....	162
Nakamura, T. ....	165
Narygina, O. ....	27, 29, 47, 80, 83, 86, 88, 178, 197
Nazzareni, S. ....	71, 101
Nestola, F. ....	68, 73
Nigrovski, B. ....	194
Nishijima, M. ....	162
Niwa, K. ....	142
Novella, D. ....	146
Ohgushi, K. ....	142
Ohtani, E. ....	162
Ondruschka, B. ....	194
Osadshii, E. ....	88
Ozawa, S. ....	162
Palme, H. ....	35
Pandolfo, F. ....	68
Papageorgiou, T. ....	176

Pascarelli, S. ....	47, 80
Picard, D. ....	151
Pichavant, M. ....	151
Pickles, J. ....	45, 144
Pollok, K. ....	65, 124, 160, 194
Pozzobon, R. ....	40, 73, 102
Prakapenka, V. ....	83, 184, 191, 200
Presnall, D. ....	58
Riedel, R. ....	178, 180
Robinson, P. ....	105, 108
Rozenberg, G.Kh. ....	77
Rubie, D.C. ....	35, 36, 38, 148
Samuel, H. ....	22, 24, 25, 203
Savenko, B.N. ....	187
Schiavi, F. ....	135
Schollenbruch, K. ....	74
Scholz, P. ....	194
Schuberth, B.S.A. ....	31
Serghiou, G. ....	182
Sergueev, I. ....	29
Shcheka, S. ....	121
Shekhar, S. ....	148
Shinova, E. ....	190
Sigalas, I. ....	178
Simak, S.I. ....	174
Simionovici, A. ....	165
Sinogeikin, S. ....	191
Skála, R. ....	169
Spiess, R. ....	73
Stagno, V. ....	51, 54, 127
Steinle-Neumann, G. ....	31, 43, 83, 86, 90, 91, 93, 98, 186
Stoyanova, R. ....	190
Swamy, V. ....	83
Szabó, C. ....	134
Tackley, P. ....	22, 24
Tang, Z. ....	90
Tarantino, S.C. ....	69
Terry, M.P. ....	105
Tirone, M. ....	58
Tsuno, K. ....	35, 36, 45
van de Walle, A. ....	186
van Mierlo, W. ....	112

Voronin, V.I. ....	187
Walte, N. ....	135, 140, 146, 148
Wang, Y. ....	74
Weigel, C. ....	131
Wirth, R. ....	176
Woodland, A. ....	74
Wosnitza, J. ....	176
Wu, X. ....	29, 47, 80, 83, 91
Yagi, T. ....	142
Yoncheva, M. ....	190
Zalite, I. ....	181
Zanetti, A. ....	101
Zarechnaya, E. ....	172, 174
Zema, M. ....	69
Zilinska, N. ....	181
Zimmermann, W. ....	25
Zolensky, M.E. ....	96
Zvoriste, C. ....	180